

---

# **Formation of Colloidal Semiconductor Nanocrystals – The Aspect of Nucleation –**

**Stefan Kudera**

---



München, 2007



---

# **Formation of Colloidal Semiconductor Nanocrystals – The Aspect of Nucleation –**

**Stefan Kudera**

---

Dissertation  
an der Fakultät für Physik  
der Ludwig-Maximilians-Universität  
München

vorgelegt von  
Stefan Kudera  
aus Dortmund

München, den 17. August 2007

Erstgutachter: Prof. Dr. Wolfgang J. Parak

Zweitgutachter: Prof. Dr. Joachim Rädler

Tag der mündlichen Prüfung: 25. Oktober 2007

# Abstract

The present work describes different techniques to control some major parameters of colloidal nanocrystals. The individual techniques rely on the manipulation of the nucleation event. The sensitive control of the nanocrystals' size and shape is discussed. Furthermore the formation of hybrid nanocrystals composed of different materials is presented. The synthesis technique for the production of the different samples involves organic solvents and surfactants and reactions at elevated temperatures.

The presence of magic size clusters offers a possibility to control the size of the nanocrystals even at very small dimensions. The clusters produced comprise ca. 100 atoms. In the case of CdSe, nanocrystals of this size emit a blue fluorescence and therefore extend the routinely accessible spectrum for this material over the whole visible range. Samples fluorescing in the spectral range from green to red are produced with standard recipes. In this work a reaction scheme for magic size clusters is presented and a theoretical model to explain the particular behaviour of their growth dynamics is discussed. The samples are investigated by optical spectroscopy, transmission electron microscopy, X-ray diffraction and elemental analysis.

Shape controlled nanocrystals might be of interest for a variety of applications. The size dependent properties of nanocrystals are dominated by their smallest dimension. Therefore anisotropically shaped nanocrystals exhibit similar optical and electronic properties as spherical nanocrystals with a compatible diameter. This makes nanorods and nanowires an appealing object for electronics. Another possible application for these materials is to incorporate them into synthetic materials to influence their mechanical stability. Here, a method to form branched nanocrystals is discussed. It turned out that the presence of small impurities in the reaction vessel triggers the formation of branching points. Furthermore this synthesis technique offers some insights into the architecture of the branching point. The branching point is analysed by high resolution transmission electron microscopy and proves for the occurrence of a multiple twinned structure are strengthened by simulation of the observed patterns.

Incorporation of a second material into a nanocrystal adds different functionality to the entire object. Ideally both materials contribute with their own functionality and they are not affected by the presence of the other material. Two different techniques to generate nanocrystals of this type are presented. The first relies on a seeded growth approach in which the nucleation of the second material is allowed only on defined sites of the seeds. Anisotropic nanorods show a reactivity that varies for the individual facets. Using such nanorods as seeds dumbbell structures are formed. The second technique uses the tips of pre-formed nano-dumbbells as sacrificial domains. The material on the tips is replaced by gold.

In any of the processes a different aspect of the nucleation event or the earliest stage of the growth is of relevance. In the growth of the magic size clusters the nucleation event itself is slowed down to a pace at which the experimenter can follow any step. The occurrence of branching can be traced down to the emergence of defects in the crystalline structure in the earliest stage of the growth. Hybrid materials are formed by a seeded-growth mechanism. Pre-formed nanocrystals provide the nucleation sites for the second material.



# Zusammenfassung

In der vorliegenden Arbeit werden verschiedene Techniken vorgestellt, mit denen wichtige Eigenschaften von kolloidalen Nanokristallen variiert werden können. Sie beeinflussen den Keimbildungsprozeß auf verschiedene Arten. Neben der Kontrolle von Größe und Form der Nanokristalle können auch Hybride aus verschiedenen Materialien hergestellt werden. Die hier dargestellten Techniken beschränken sich auf Synthesen, die in organischen Lösungsmitteln mit entsprechend angepaßten Netzmitteln durchgeführt werden.

Besonders kleine, aber sehr stabile Nanokristalle lassen sich dank der Existenz von Clustern mit hoher Symmetrie, den sogenannten Magic Size Clustern, herstellen. Diese Cluster enthalten etwa 100 Atome. Cluster dieser Größe aus CdSe zeigen eine blaue Fluoreszenzlinie, so daß mit ihrer Hilfe das mögliche Emissionsspektrum von CdSe Nanokristallen über den gesamten sichtbaren Spektralbereich ausgedehnt wird. In dieser Arbeit wird ein Protokol zur Synthese dieser Klasse von Nanokristallen vorgestellt und für die spezielle Dynamik des Wachstumsprozesses wird ein Modell aufgestellt. Die optischen Spektren, transmissions-elektronenmikroskopische Aufnahmen, Röntgenbeugungsexperimente und eine Elementaranalyse der Cluster werden diskutiert.

Etwas komplexere Nanokristalle können erzeugt werden, wenn auch die Form der Kristalle eingestellt werden kann. Nachdem die optischen und elektronischen Eigenschaften von Nanokristallen vor allem von der kleinsten charakteristischen Länge dieser Strukturen bestimmt werden, fluoreszieren Nanostäbchen in etwa bei derselben Wellenlänge wie kugelförmige Nanokristalle mit dem gleichen Durchmesser. Somit sind Nanostäbchen und Nanodrähte von großem Interesse für Anwendungen als elektroische Bauteile. Außerdem wird erwartet, daß der Einfluß von anisotropen Nanokristallen in Kunststoffen Einfluß auf deren Stabilität nehmen kann. In dieser Arbeit wird eine Methode zur Erzeugung von Nanokristallen mit einer verzweigten Geometrie dargestellt. Es wird gezeigt, daß kleine Verunreinigungen in der Synthese sind für diese Verzweigungen verantwortlich sind. Durch die Möglichkeit, die Zahl der Verzweigungen zu kontrollieren, besteht auch die Möglichkeit, die kristallographische Struktur des Verzweigungspunkts zu untersuchen. Dies geschieht vor allem mit Hilfe von hochauflösenden Transmissions-Elektronenmikroskopaufnahmen. Zwillingsebenen können in einfachen Strukturen direkt beobachtet werden, in komplexeren Kristallen kann deren Existenz mit Hilfe von Simulationen der Aufnahmen nachgewiesen werden.

Wird ein weiteres Material in einen Nanokristall eingebunden, dann addieren sich idealerweise die Eigenschaften der einzelnen Materialien ohne Abstriche. So können Hybrid-Materialien hergestellt werden, deren Eigenschaften exakt auf mögliche Anwendungen zugeschnitten werden. Hier werden zwei Techniken zur Herstellung solcher Materialien vorgestellt. Die erste Technik nutzt fertige Nanokristalle als Keime für das Wachstum des zweiten Materials. Speziell bei anisotrop geformten Keimen ist es möglich, die unterschiedliche Reaktivität der Seiten- und Grundflächen auszunutzen, um hantelförmige Nanokristalle zu synthetisieren. Die zweite Technik geht von solchen Hanteln aus, und ersetzt die Köpfe der Hantel durch Gold.

In jedem dieser drei Prozesse wird ein anderer Aspekt der Keimbildung und der frühen Wachstumsphase der Nanokristalle beleuchtet. Bei der Synthese der Magic-Size Cluster wird die Keimbildung selbst so weit verlangsamt, daß einzelne Schritte in diesem Prozess sichtbar werden. Verzweigte Nanokristalle entstehen durch das Auftreten von Fehlstellen vor allem während der ersten Wachstumsphase. Hybride aus mehreren Materialien werden durch heterogene Keimbildung erzeugt. Vorhandene Nanokristalle werden als Kondensationskerne benutzt.



# Contents

<b>Abstract</b>	<b>v</b>
<b>Zusammenfassung</b>	<b>viii</b>
<b>Contents</b>	<b>ix</b>
<b>List of Figures</b>	<b>xi</b>
<b>Acronyms</b>	<b>xiii</b>
<b>1 Introduction</b>	<b>1</b>
1.1 General Interest in Nanocrystals and Applications . . . . .	1
1.2 Synthesis Technique . . . . .	2
1.3 Nucleation . . . . .	4
1.4 Growth . . . . .	6
1.5 Contribution of this Work . . . . .	11
<b>2 Size Control - Magic Size Clusters</b>	<b>13</b>
2.1 Synthesis of Magic Size Clusters . . . . .	14
2.2 Growth-Mechanism of the Magic Size Clusters . . . . .	18
2.3 Structural Analysis . . . . .	21
<b>3 Shape Control</b>	<b>27</b>
3.1 Origin of Branching – Polymorphism vs. Octa-Twin . . . . .	30
3.2 Synthesis of Tetrapods . . . . .	33
3.3 Structure of the Tetrapod-Core . . . . .	34
3.4 Discussion of the Growth-Mode . . . . .	36
<b>4 Composition Control - Hybrid Materials</b>	<b>39</b>
4.1 Growth Strategies . . . . .	40
4.2 Synthesis of PbSe-Tipped Nano-Dumbbells . . . . .	41
4.3 Synthesis of Au-Tipped Nano-Dumbbells . . . . .	43
<b>Conclusion</b>	<b>47</b>
<b>Bibliography</b>	<b>49</b>
<b>Acknowledgements</b>	<b>63</b>

<b>Publications</b>	<b>65</b>
<b>A Magic Size Clusters</b>	<b>69</b>
A.1 Sequential Growth of Magic-Size CdSe Nanocrystals . . . . .	69
A.2 Blue light emitting diodes based on fluorescent CdSe/ZnS nanocrystals . . . . .	88
<b>B Tetrapods</b>	<b>93</b>
B.1 Multiple Wurtzite Twinning in CdTe Nanocrystals Induced by Methylphosphonic Acid . . . . .	93
B.2 Shape and Phase Control of Colloidal ZnSe Nanocrystals . . . . .	109
B.3 Optical properties of tetrapod-shaped CdTe nanocrystals . . . . .	127
B.4 Electron-Hole Dynamics in CdTe Tetrapods . . . . .	131
B.5 Confinement Effects on Optical Phonons in Polar Tetrapod Nanocrystals Detected by Resonant Inelastic Light Scattering . . . . .	137
B.6 Shape Dependence of the Scattering Processes of Optical Phonons in Colloidal Nanocrystals Detected by Raman Spectroscopy . . . . .	146
B.7 Confinement effects on optical phonons in spherical, rod- and tetrapod-shaped nanocrystals detected by Raman spectroscopy . . . . .	151
B.8 Confined Optical Phonon Modes in Aligned Nanorod Arrays Detected by Resonant Inelastic Light Scattering . . . . .	156
<b>C Hybrid Colloidal Nanocrystals</b>	<b>165</b>
C.1 Selective Growth of PbSe on One or Both Tips of Colloidal Semiconductor Nanorods . . . . .	165
C.2 Selective reactions on the tips of colloidal semiconductor nanorods . . . . .	178
C.3 Synthesis and Micrometer-Scale Assembly of Colloidal CdSe/CdS Nanorods Prepared by a Seeded Growth Approach . . . . .	184
<b>D Reviews and Conference Proceedings</b>	<b>209</b>
D.1 On the Development of Colloidal Nanoparticles towards Multifunctional Structures and their Possible Use for Biological Applications . . . . .	209
D.2 Synthesis and perspectives of complex crystalline nano-structures . . . . .	226
D.3 Synthesis routes for the growth of complex nanostructures . . . . .	235
<b>E Water-Solubility, Applications and Further Characterisation</b>	<b>243</b>
E.1 Hydrophobic nanocrystals coated with an amphiphilic polymer shell: a general route to water soluble nanocrystals . . . . .	243
E.2 Cytotoxicity of Colloidal CdSe and CdSe/ZnS Nanoparticles . . . . .	268
E.3 Quantum Dots on Gold: Electrodes For Photoswitchable Cytochrome c Electrochemistry . . . . .	300
E.4 Catalytic and seeded shape-selective synthesis of II–VI semiconductor nanowires . . . . .	304
E.5 Temperature and Size Dependence of Nonradiative Relaxation and Exciton-Phonon Coupling in Colloidal CdTe Quantum Dots . . . . .	309

# List of Figures

1.1	Transmission electron microscopy (TEM) images and optical spectra of CdTe-dots . . . . .	2
1.2	General setup for the synthesis . . . . .	3
1.3	Sketch of the potential landscape for the nucleation . . . . .	5
1.4	Sketch of the growth rate of the nanocrystals in units of the critical size ( $r^*$ ) . . . . .	8
1.5	Effect of size-focussing in the synthesis of CdSe nanocrystals . . . . .	9
1.6	Effect of the size-selective precipitation . . . . .	10
2.1	A series of different clusters . . . . .	14
2.2	Characteristic absorption spectra of the CdSe-magic size clusters (MSCs) . . . . .	15
2.3	Size-selective precipitation of two sample of magic size clusters . . . . .	16
2.4	Fluorescence spectra of the growing magic size clusters . . . . .	17
2.5	Sketch of the potential landscape in the growth of CdSe magic-size-clusters	20
2.6	Low resolution TEM-images of MSC of family 6 . . . . .	22
2.7	Mass spectra of large magic size clusters . . . . .	23
2.8	Possible models for the first five magic size clusters . . . . .	25
3.1	Examples of faceting of nanocrystals . . . . .	27
3.2	TEM-images of nanocrystals with different aspect ratios . . . . .	28
3.3	TEM-image of tetrapods of CdTe . . . . .	29
3.4	Model of a (1122) twin boundary in the wurtzite (WZ) structure . . . . .	32
3.5	Comparison between the polymorphism and the octa-twin model . . . . .	32
3.6	Effect of methyl phosphonic acid (MPA) on the growth of CdTe-tetrapods	33
3.7	High-Resolution TEM images of a branching region . . . . .	35
3.8	High-Resolution TEM images of a tetrapod's core . . . . .	36
3.9	Sketch of the architecture of the tetrapod . . . . .	37
4.1	Sketch of dumbbell-structures . . . . .	40
4.2	Nano-dumbbells of PbSe-CdSe-PbSe . . . . .	42
4.3	Formation of matchsticks of PbSe-CdS . . . . .	43
4.4	Gold tips grown on nanorods with different methods . . . . .	44
4.5	Highly branched CdTe-nanocrystals with gold dots on their tips . . . . .	46



# Acronyms

$\sigma$  surface energy of a crystalline facet

**CdE** CdS, CdSe or CdTe

**CdO** cadmium oxide

**DDAB** didodecyldimethyl ammonium bromide

**DDPA** dodecyl phosphonic acid

$d_m$  density of the monomers in the crystal

**fcc** face-centred cubic structure

**HPA** hexyl phosphonic acid

$k_B$  Boltzmann's constant

**kDa** kilo-Dalton

**MALDI-TOF** Matrix-assisted laser desorption ionization time of flight

**MPA** methyl phosphonic acid

**MSC** magic size cluster

$n$  Number of monomers in a nanocrystal

**OA** oleic acid

**ODPA** octadecyl phosphonic acid

$r^*$  critical size of the growth-process

$r_c$  critical size of the nucleation event

**SSP** size-selective precipitation

**TBP** tri-n-butylphosphine

**TEM** transmission electron microscope

**TDPA** tetradecyl phosphonic acid

**TOP** tri-n-octylphosphine

**TOPO** tri-n-octylphosphine oxide

**WZ** wurtzite structure

**XRD** X-ray diffraction

**ZB** zinc-blende structure

# 1 Introduction

## 1.1 General Interest in Nanocrystals and Applications

Nanotechnology is considered a key-technology for the upcoming century. As it unites many different fields, it is quite an appealing and challenging branch of science. Chemistry with preparation methods, physics with investigation methods and biology with a wide range of functional molecules contribute all together to the development of the field. Influences are taken even from astronomy. [1] And in the same way each of the disciplines can take some profit from the others. For instance chemically prepared colloidal nanocrystals can be used as probes in living cells [2–4]. An example for the interaction between physics and chemistry are single molecule based transistors. [5, 6] Since ca. 20 years an important branch of the nanotechnology research is occupied with the synthesis and characterisation of colloidal nanocrystals.

Colloidal nanocrystals are small, soluble crystals, which comprise a few hundred to several thousands of atoms. [7] They are obtained by interrupting the crystal growth at a very early stage and can be synthesised for a wide variety of materials. [8, 9] The property that makes these objects attractive for a great variety of fields is in fact their flexibility. Already in the early eighties it was pointed out that semiconductor crystals of a size below the Bohr-radius of the bulk materials exciton exhibit a strong dependence of their properties on the size. [10] For instance the Bohr radius of bulk CdS is of the order of 60nm. So, particles of a size below ca. 50nm experience already the confinement of the exciton. In a simple way the dependence of the energy of an exciton in these structures can be explained by the behaviour of a particle in a box. [7, 11–13] The energy levels are discrete and their spacing depends inversely on the particles size. Therefore semiconductor nanocrystals can be considered as an intermediate species between the molecular regime with its well-defined energy levels and the bulk material with continuous bands. [14, 15] As an example in Figure 1.1 the absorption and fluorescence spectra of different samples of CdTe-nanocrystals are shown. They show a strong dependence on the size and furthermore discrete levels can be discerned. Also the properties of metallic nanocrystals show a dependence on the size, as for instance the susceptibility and the specific heat of Pd. [16] It is also interesting to note the strong size-dependence of the melting temperature of nanocrystals. [7, 17] Ideally, the chemical behaviour of the nanocrystals remains unaffected by the variation of their size. Nanocrystals of CdSe with a diameter of ca. 5 nm emit red light, whereas nanocrystals of the same material, only with a smaller diameter of ca. 2 nm emit green light. The chemical properties, i.e. the chemical interaction with the surrounding, of the two types of nanocrystals are unaffected as they depend only on the surface-properties. Due to their versatility, nano-

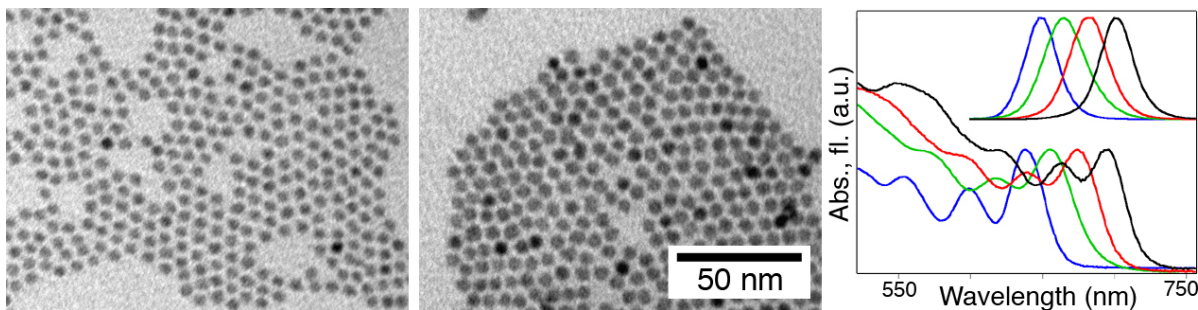


**Figure 1.1: Transmission electron microscopy (TEM) images and optical spectra of CdTe-dots.** The dots on the TEM images have a diameter of ca. 4 nm (left panel) and 5.5 nm (middle panel). Absorption (bottom) and fluorescence (top) spectra for a series of spherical CdTe-nanocrystals are shown in the right panel. The smallest nanocrystals (4 nm) show the first exciton peak in the absorption-spectrum at 640 nm and the fluorescence peak at 650 nm. The largest nanocrystals of this series (6nm) show the exciton peak at 700 nm and the fluorescence peak at 705 nm. In the absorption spectrum of the smallest nanocrystals (blue line) the higher energy levels of the exciton can be identified clearly.

crystals offer a wide spectrum of possible applications, spanning from the construction of photovoltaic devices [18, 19], to medical applications [4]. Also, nanocrystals are employed to produce antireflective glasses [20], and transistors with single nanocrystals as active elements have been realised. [21–23]

In addition to the size-dependency, also the shape of the nanocrystals might be taken into account when designing nanomaterials for special applications. In the easiest case, the anisotropy of the crystals might be tuned, changing the shape of the crystals from a sphere to a rice-structure and even to a rod- or wire-shape. [24–26] Finally an even higher level of complexity can be reached by uniting different materials in only one nanocrystal. These hybrid materials promise to offer an even higher flexibility for applications. [27–29]

## 1.2 Synthesis Technique

The nanocrystals presented in this work are synthesised exclusively in an organic solvent. For certain purposes the synthesis may also be performed in aqueous solution [30, 31] or in reverted micelles. [32] Using organic solvent has the advantage that one can tune the reaction temperature over a wide range, and also in this environment the specific reactants are exhaustively explored. As we will explain later, temperature and composition of the solvent are taking strong influence the growth-kinetics and on the shape of the crystals. [33, 34] Also, through the reaction environment the crystal-phase of the material can be influenced. For instance, CdTe nanocrystals generally grow in wurtzite structure. [35] But by a careful control of the reaction conditions, the crystalline phase can be selected between either zinc-blende or wurtzite. [36]

In general the solvent serves two purposes. Evidently its main purpose is to solubilise

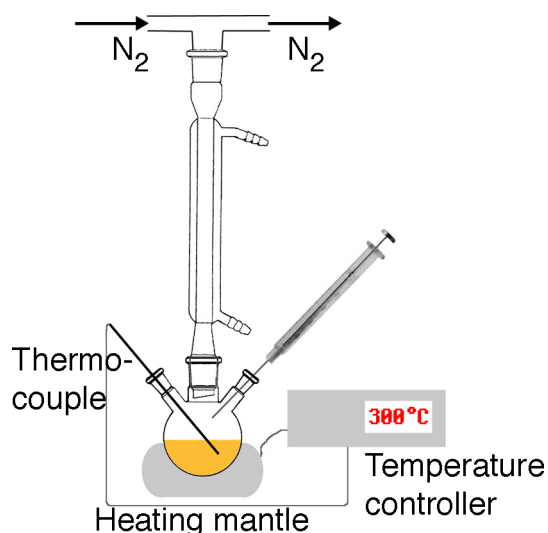


**Figure 1.2: General setup for the synthesis.** The reaction line is connected to a Schlenk-line and can be evaporated to remove residual air and volatile impurities. The reaction is carried out under inert conditions either in an argon or a nitrogen atmosphere.

the crystals and the reactants involved in the growth. The second task is to control the speed of the reaction. To do so, the solvent-molecules need to bind and unbind dynamically on the surface of the growing crystals. Once a molecule detached from the surface of the crystal, new atomic species (monomers) can be incorporated into the crystal, thus it can grow. When referring to these characteristics of the solvent molecules, they are termed “surfactant”. In a synthesis the solvent can be a mixture of the different species, including pure solvent and pure surfactants.

Especially the role as surfactant is of great interest. In general the surfactant molecules exhibit two domains, one non-polar, generally a long alkyl-chain, and a polar head-group. As it will be described in chapter 3 their functionality depends on both domains. The shape of the non-polar group as well as the binding strength of the polar group influence on the growth dynamics. Briefly, the non-polar tail biases the diffusion-properties (a consequence of this effect is demonstrated in article B.1), whereas the polar head-group mainly affects the binding-efficiency.

The most frequently used surfactants comprise tri-n-octylphosphine oxide (TOPO), tri-n-octylphosphine (TOP) as used in the work of Murray et al. [35]. But also different amines and carboxylic acids are frequently used as surfactants. [37, 38] Most of these compounds are solid at room-temperature, and melt only at ca. 50°C.

The reaction is performed in a 3-necked-flask connected to a Schlenk-line with one of the necks, as displayed in Figure 1.2. The remaining two necks are sealed with rubber septa and serve for the measurement of the temperature inside the flask and for the injection of reactants. The reaction is carried out under an inert atmosphere, as some of the reactants are pyrophoric and also the nanocrystals are sensitive to air. After loading the flask with the reactants, the organic reactants are molten and the flask is evacuated and kept under vacuum at ca. 130–180°C for 10–20 minutes to remove volatile impurities. This step is crucial for most synthesis. Before starting the actual reaction the flask is flushed with an inert gas (generally nitrogen or argon).

The monomers can be introduced in many different ways. At least one species should be in liquid form. Through this the experimenter can start the formation of nanocrystals

by the quick injection of this compound and thus determine a sharp nucleation event. The chalcogens are introduced into the reaction as a complex with either TOP or tri-n-butylphosphine (TBP). The complex is formed by mixing the chalcogen in form of a power and the liquid TOP or TBP. Generally, for the formation of the complex it is sufficient to simply vortex this solution for some minutes. Only for the preparation of a Te-solution this solution has to be heated to above 200°C for at least one hour. Residual undissolved tellurium-powder is removed by centrifugation. In the early synthesis of CdE (E= S, Se or Te) nanocrystals dimethyl Cadmium was used as precursor. [35] This liquid compound along with Se:TOP is injected into the reaction-solution to initiate the growth of CdSe-nanocrystals, but unfortunately it is unstable, highly toxic and pyrophoric. In the following this compound was replaced by CdO. At a temperature of ca. 300°C the Cd-ion binds to the surfactants, which are either phosphonic acid like tetradecyl phosphonic acid (TDPA), octadecyl phosphonic acid (ODPA) or dodecyl phosphonic acid (DDPA) [37, 39, 40] or oleic acid (OA) [37, 41]. This reaction is accompanied by formation of steam and a colour-change of the solution, which turns from dark red to translucent. In this reaction scheme only the chalcogen-complex is injected and the nucleation sets in shortly after this injection.

## 1.3 Nucleation

The first step in the growth of any sort of crystal is evidently the nucleation. Through a density-fluctuation of the medium several atoms assemble to a small crystal that is thermodynamically stable, and thus does not decay to free atoms or ions. In that sense the nucleation can be understood as the overcoming of a barrier. This section will explain briefly the origin of this barrier. In the following we will distinguish between the crystalline phase, in which the atoms are bound to a crystal, and the solution phase, in which the atoms are dispersed freely in the solution. The nucleation in a solution at constant temperature and constant pressure is driven by the difference in the free energy between the two phases. At the simplest the driving forces in the nucleation event can be reduced to two, the gain in the chemical potential and the increase of the surface energy. The gain in chemical potential can be understood as the energy freed by the formation of the bonds in the growing crystal. The surface term takes into account the correction for the incomplete saturation of the surface bonds. Upon formation of a nucleus consisting of  $n$  atoms the total free energy of the system changes by the value

$$\Delta G = n(\mu_c - \mu_s) + 4\pi r^2\sigma \quad (1.1)$$

( $\mu_c$  and  $\mu_s$  are the chemical potentials of the crystalline phase and the solution-phase, respectively,  $r$  is the radius of the nucleus and  $\sigma$  the surface tension.) In this equation the surface-term constitutes the main difference between nanomaterials and bulk crystals. Bulk materials are dominated by the volume-effects and thus the surface energy can be neglected, whereas in nanocrystals the majority of atoms might be situated on the surface.

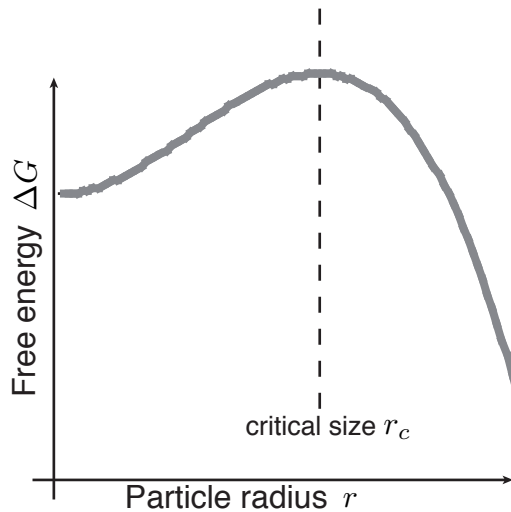


**Figure 1.3: Sketch of the potential landscape for the nucleation.** as described in equation (1.2). Only at small values of the radius  $r$  the  $r^2$ -term of the surface energy outcompetes the  $r^3$ -contribution of the chemical potential, so that a barrier is imposed at the critical size  $r_c$ .

In equation (1.1) the surface energy  $\sigma$  is assumed to be constant for any size and morphology of the crystal, which is a very rough approximation. The surface tension definitively depends on the class of the limiting facets. The individual facets have different densities of atoms and also different arrangements of the dangling bonds. Therefore it is comprehensible that the surface energy should be different for the individual facets of the nucleus. And certainly it also depends on the size of the particle. When considering the surface tension as the interaction of the surface atoms with the bulk of the crystals, it is evident that it is actually reduced for smaller crystallites as there are no long-range-interactions. It has been calculated that under the assumption of a Lennard-Jones interaction between the atoms the surface energy of a general cluster of 13 atoms (as sketched in Figure 2.1) is reduced by 15% with respect to the surface energy of a plane surface. [42] The uniformity of the surface energy in equation (1.1) refers to a liquid bubble model for the nucleation. In a more refined model also geometric peculiarities of the nucleating crystal have to be considered. An example of this effect is discussed qualitatively in chapter 2 and in article A.1.

Assuming a spherical shape for the nanocrystals and neglecting any variation of the surface energy  $\sigma$ , the number of atoms  $n$  in the first term of equation (1.1) can be expressed by the radius  $r$  of the crystal, taking into account the density  $d_m$  of monomers in the nanocrystals. Then the equation reads:

$$\Delta G = \frac{4\pi d_m}{3} r^3 (\mu_c - \mu_s) + 4\pi r^2 \sigma \quad (1.2)$$

In the case that the chemical potential in the solution is inferior to that of an atom of the crystal, the minimum of the free energy is given when all atoms are unbound, and so no

stable crystals are formed. Here we are interested in the opposite case with the chemical potential of atoms in solution being greater than that of bound atoms. In that case the first term becomes negative, and thus the free energy reaches a maximum for a certain radius  $r_c$ , termed *critical size*, at which a nucleation barrier is imposed, see Figure 1.3. For small nuclei the surface energy dominates the free energy, whereas only for crystals much larger than  $r_c$  the growth is dominated by the gain in chemical potential and in principle the crystals grows to an infinite size. The amplitude of the nucleation barrier controls the rate at which crystals nucleate. [43]

## 1.4 Growth

The actual process of the deposition of monomers onto the growing nanocrystal can be split into two steps. First the monomers have to be transported onto the surface of the crystal and in a second process they have to react with the crystal. Generally the first process is accomplished through diffusion and thus at a rate dominated by the diffusion-constant  $D$ , whereas the speed of the second process is given by the rate of reaction between free monomers and the crystal-surface.

In the following the dynamics of the growth-process will be outlined briefly. The discussion will start from a mechanistic view of the growth in which the growth rate  $\dot{r}$  of a crystal of radius  $r$  depends only on the rate at which monomers are incorporated into the crystal. This later rate is simply the time-derivative of the number of monomers  $n$  in the crystal and it describes the number of monomers that go through the two processes mentioned above (diffusion and reaction) during a unit of time. We can write the growth rate  $\dot{r}$  as:

$$\frac{dr}{dt} = \frac{\dot{n}}{4\pi r^2 d_m} \quad (1.3)$$

In this equation  $d_m$  denotes the density of monomers in the crystal, thus the inverse of the volume occupied by one monomer. This equation is the time-derivative of  $n$  solved for  $\dot{r}$ . In the following the behaviour of the deposition rate of monomers  $\dot{n}$  will be discussed for two extreme cases.

In an experiment, generally a huge amount of free monomers is injected to initiate the growth process. Under these conditions the effect of the diffusion process can be virtually neglected due to the high concentration of monomers. Monomers are available whenever there is a free site for their incorporation into a growing crystal. In this case the incorporation rate  $\dot{n}$  depends only on the rate of the reaction monomer – crystal. This rate is proportional to the surface area of the crystal. Therefore the growth rate  $\dot{r}$  in equation (1.3) is independent of the radius of the crystal. This growth regime is called *reaction-controlled growth* and it is important only at very high concentrations of monomers. In this regime the width of the size-distribution  $\Delta r$  does not vary with time. Only the relative width  $\Delta r/\bar{r}$  decreases with time. ( $\bar{r}$  denotes the mean radius of the crystals) [44]

After a while the reservoir of monomers is partially depleted and the growth rate is

dictated by the rate at which monomers reach the surface of the crystal.<sup>1</sup> The flux  $J$  of monomers towards a growing crystal is driven by a gradient of the concentration  $C$  of the monomers. The surface of a nanocrystal represents a sink for free monomers and thus a minimum for the monomer-concentration. In the model the monomer concentration is assumed constant on any sphere of radius  $x$  (greater than  $r$ ) around the crystal. On the surface of the crystal the flux  $J$  is equal to the incorporation rate  $\dot{n}$  of monomers:

$$J(x = r) = \dot{n} \quad (1.4)$$

For any radius greater than  $r$  the flux through a spherical surface is determined by Fick's law of diffusion:

$$J(x > r) = 4\pi x^2 D \frac{dC}{dx} \quad (1.5)$$

Here  $D$  is the diffusion constant. In a steady state, this flux  $J$  is independent of the distance  $x$ :

$$\begin{aligned} \frac{dJ}{dx}(x > r) &= 4\pi D \left( 2x \frac{dC}{dx} + x^2 \frac{d^2C}{dx^2} \right) = 0 \\ \Rightarrow \frac{d^2C}{dx^2} &= -\frac{2}{x} \frac{dC}{dx} \end{aligned} \quad (1.6)$$

Once the profile of the concentration is calculated from this differential equation, it can be inserted into equation 1.5 to quantify the flux  $J$ . To solve (1.6) boundary conditions are imposed. The monomer-concentration  $C_i$  on the surface of a crystal as well as the monomer-concentration  $C_b$  in the bulk of the solution, i.e. far from any crystal, are considered.<sup>2</sup> Then equation (1.5) for the flux towards a crystal of radius  $r$  reads:

$$J = 4\pi D r (C_b - C_i) \quad (1.7)$$

With this result the growth rate of a crystal in (1.3) can be written as:

$$\frac{dr}{dt} = \frac{D}{r d_m} (C_b - C_i) \quad (1.8)$$

To this point an infinite stability of the nanocrystals is assumed. This assumption cannot be maintained. The Gibbs-Thompson effect actually introduces a competing effect to the growth. [43] Crystals – or particles and droplets in general – have a higher vapour pressure the smaller they are, and thus monomers evaporate more easily from smaller crystals than from larger ones. This can be understood on a molecular level when considering the higher curvature of smaller crystals. Due to this the surface-atoms are more exposed to the surrounding and at the same time experience a weaker binding-strength to the smaller crystal core. Experimentally this effect is seen in the lower melting temperature of smaller nanocrystals. [7, 17]

<sup>1</sup>The following can be understood as the limit of a infinite diffusion layer in the argumentation presented in reference [44].

<sup>2</sup>From equation (1.6) the general form the concentration-profile around a crystal is derived as:

$$C(x) = C_b - \frac{r(C_b - C_i)}{x}$$

and thus the derivative of  $C$  reads:  $\frac{dC}{dx} = \frac{r(C_b - C_i)}{x^2}$

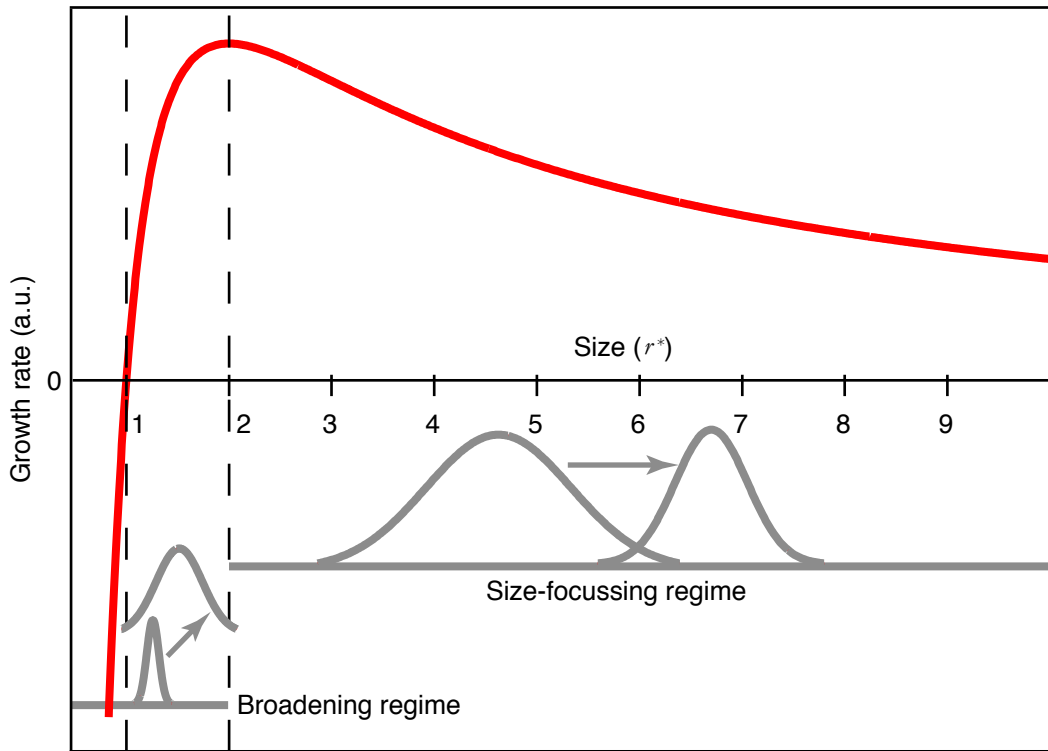


**Figure 1.4: Sketch of the growth rate of the nanocrystals in units of the critical size ( $r^*$ ).**  
 As examples two size-distributions are displayed and how they develop with time. Note that in the example for the broadening regime, the smallest particles are larger than  $r^*$ . Therefore the mean-size of the particles still increases. The situation would be different if the size-distribution would comprise nanocrystals smaller than  $r^*$ .

With the help of the Gibbs-Thompson-equation the vapour pressures of a crystal of radius  $r$  can be calculated. Through the general gas-equation these vapour pressures can be expressed as the concentrations of monomers in the vicinity of the surface:

$$C_i = C_\infty \exp^{\frac{2\sigma}{rd_m k_B T}} \approx C_\infty \left( 1 + \frac{2\sigma}{rd_m k_B T} \right) \quad (1.9)$$

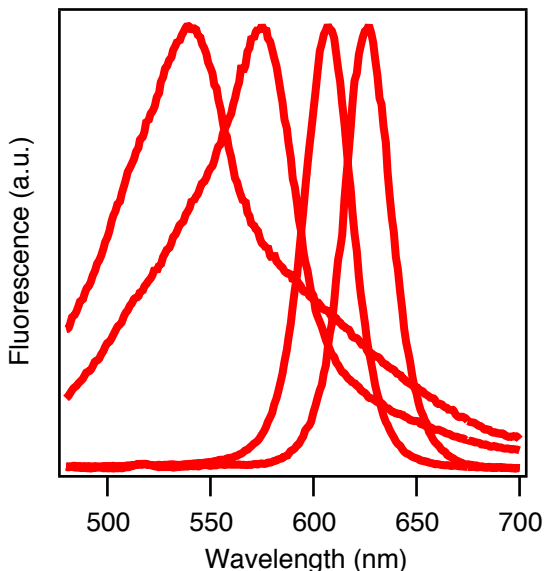
In this equation  $C_\infty$  is the vapour pressure of a flat surface,  $\sigma$  is the surface energy. Formally the same reasoning is applied to the concentration  $C_b$ . The radius of a crystal in equilibrium with the concentration of monomers in the bulk is introduced as the critical size ( $r^*$ ) of the growth process [44]:

$$C_b = C_\infty \exp^{\frac{2\sigma}{r^* d_m k_B T}} \approx C_\infty \left( 1 + \frac{2\sigma}{r^* d_m k_B T} \right) \quad (1.10)$$

With these two quantities the growth rate from equation (1.8) can be calculated as:

$$\frac{dr}{dt} = \frac{2\sigma D C_\infty}{d_m^2 k_B T} \frac{1}{r} \left( \frac{1}{r^*} - \frac{1}{r} \right) \quad (1.11)$$

**Figure 1.5: Effect of size-focussing in the synthesis of CdSe nanocrystals.** The synthesis was performed at very high temperature (370°C). Aliquots were taken every 20 seconds during the run of the synthesis and fluorescence spectra were recorded. The first aliquot (leftmost spectrum) shows a broad fluorescence spectrum and thus a wide size-distribution, whereas the fluorescence line of the latest aliquot (rightmost spectrum) is very narrow with a FWHM of 28nm.



The critical size is characterised by a zero growth rate, as a crystal of this size is in equilibrium with the solution. For crystals smaller than  $r^*$  the growth rate is negative, the dissociation of monomers is more important than the supply of fresh monomers, and therefore these crystals melt. Here it becomes evident that the quantity  $r^*$  is actually equal to the critical size  $r_c$  that characterises the position of the energy barrier in the nucleation event.

The general dependence of the growth rate on the radius of the crystal is illustrated in Figure 1.4. It is interesting to notice the presence of a maximum at a radius of  $2r^*$ . If all crystals present in the solution have a radius larger than this value, the smallest crystals grow the fastest, and therefore the size-distribution becomes narrower over time. The value of  $r^*$  depends mainly on the overall concentration of free monomers, but also on the reaction temperature and the surface energy. Especially the latter effect will be discussed in chapter 3. During the run of the reaction the concentration of monomers decreases and the critical size shifts to higher values. If  $r^*$  is sufficiently small, as discussed above, the system is said to be in the *narrowing- or size-focussing regime*. As soon as  $2r^*$  has reached a value situated in the lower end of the size-distribution of crystals, the system enters in the *broadening regime*. Ultimately, when  $r^*$  is larger than the radius of the smallest crystals present, the system enters into the *Ostwald-ripening-regime*, which is characterised by an large broadening of the size-distribution and – more important – by a decrease of the total concentration of the crystals. The smallest crystals melt to free monomers that are incorporated into the larger crystals.

In an experiment the effect of the size-focusing is limited by the broadness of the initial size-distribution, in other words, the nucleation event has a strong influence on the size-distribution of the final sample. [45] Ideally the nucleation-event should be finished well before the system enters into the diffusion-controlled growth regime. The sharpness of this event is therefore of great importance.

In the case of fluorescent nanocrystals, the width of the fluorescence line is a good

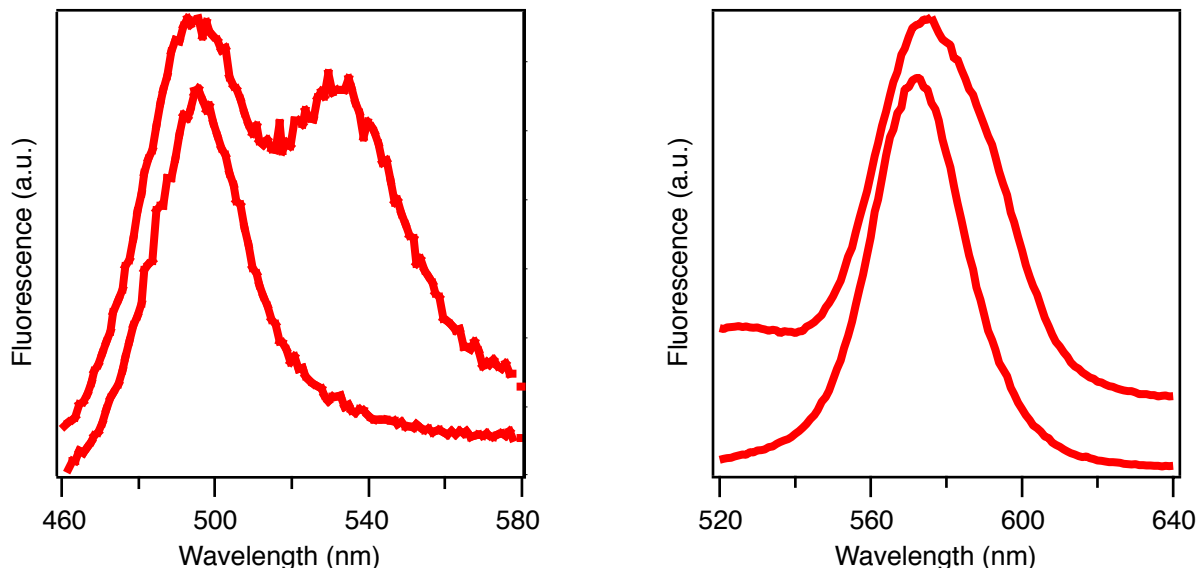


**Figure 1.6: Effect of the size-selective precipitation.** By careful addition of methanol to samples of CdSe nanocrystals with a bimodal (left) or simply broadened (right) size-distribution the largest particles, i.e. those with an emission at higher wavelength, can be precipitated by centrifugation while the smaller particles remain in solution. The upper spectra show the fluorescence of the initial samples, whereas the lower spectra show the fluorescence of the supernatants. In the right example a further contamination of small, i.e. blue-fluorescent, nanocrystals has been removed by a second precipitation.

indicator for the quality of the size-distribution. Samples of CdSe or CdTe nanocrystals generally have a linewidth of ca. 30nm or less. In Figure 1.5 an example for the focussing of the size-distribution is displayed. In this example the synthesis was carried out under conditions that favour the size-focussing. The nanocrystals were synthesised at a very high temperature, which reduces the nucleation-event to a very short time-span. Also, the concentration of monomers was sufficiently high to prevent the system to enter into the broadening-regime.

In some synthesis schemes it is inevitable to consume the reservoir of monomers and thus obtain a broadening of the fluorescence lines. In these cases the system can be maintained in focussing-regime by repeated injections of fresh monomers. [35, 46] Experimentally it is not always possible to obtain a perfect size-distribution. In some cases the distribution is broadened or shows several distinct peaks. A possible – but laborious – way to improve the size-distribution is to perform a size-selective precipitation after the synthesis is completed. In order to do so, a non-solvent is added slowly and carefully. The larger particles become unstable in the solution at lower concentrations of the non-solvent than the smaller particles, and thus they precipitate first. [47] This process has been successfully applied for instance in the synthesis of CdTe [48] and CdSe [35]. In Figure 1.6 an example of a size-selective precipitation is shown.

## 1.5 Contribution of this Work

This work is divided into three parts. Each of them is describing a different aspect of the nucleation event. And in each of the steps a different level of complexity is introduced into the geometry of nanocrystals. Size, shape and composition of the nanocrystals are controlled.

Chapter 2 presents a process in which the nucleation event is slowed down significantly. By this the mechanics of the growth at this stage can be studied nicely. In the particular synthesis scheme presented a series of energetic barriers is found that leads to the formation of several particularly stable nanocrystals, the so-called MSCs. The growth mechanism is discussed and a model is proposed.

In chapter 3 first a modification to the classical growth-model is shown. The focus of this chapter is on a different aspect of the early stage of the growth of nanocrystals. A too large oversaturation of free and reactive monomers can lead to the introduction of defects in the crystalline structure. In this chapter a process is demonstrated that exploits these defects to form nanocrystals of a complex geometry.

In chapter 4 a strategy to control the composition of the nanomaterial is presented. In the case that preformed nanocrystals are present in the growth solution the event of free nucleation can be suppressed and instead the preformed nanocrystals serve as nucleation sites. In certain processes this might enhance the monodispersity of the sample as the system immediately enters into the size-focussing regime. The process presented in chapter 4 exploits this scheme to control the site on which a second material is deposited on the shape-controlled nanocrystals.



## 2 Size Control - Magic Size Clusters

For many applications it is of interest to have materials at hand that exhibit a high fluorescence yield and at the same time can be packed very densely. Through this many light emitting units can be packed into a small volume and the overall fluorescence yield of the material is enhanced as an eventually low fluorescence quantum yield might be overcome by a larger number of light emitting sites. Also, in applications as markers the size of the fluorophore is a limiting factor. Most techniques to produce water-soluble nanocrystals involve the generation of a shell of organic molecules around the nanocrystals. [4,49] This additional shell contributes to the total size of the nanocrystals. The sole core has a molecular weight ranging between 30kDa for green emitting CdSe nanocrystals with a diameter of ca. 2nm and a several hundred kDa for red emitting CdSe nanocrystals. The contribution of the surfactants is certainly of the range of several 10kDa. In comparison to this fluorescing molecules are quite small, Rhodamine 6G has a molecular weight of 480Da, and the green fluorescent protein GFP has a molecular weight of ca. 27kDa.

With published synthesis schemes for CdSe particles [35, 40] generally nanocrystals with a diameter of 2-8nm are produced. To synthesise routinely nanocrystals with a smaller diameter, a different concept has to be employed. Already in the reported synthesis-schemes of the CdSe-nanocrystals the existence of highly stable and very small CdSe-clusters was observed. [50] In the size-regime below 2nm the stability of these clusters can be explained with the concept of magic sizes. Several clusters exhibit a higher stability as compared to others. Generally their high stability coincides with a high symmetry in their structure. The magic size clusters (MSCs) could be considered as those clusters that possess complete shells of atoms. [51] A classical example is the series of truncated octahedra (“cubo octahedra”). The first member of this series is a single atom along with its 12 nearest neighbours in the *fcc*-structure. The larger clusters can be constructed from the previous ones by covering each of the exposed facets with one layer of atoms. Thus the smallest cluster contains 13 atoms, the second 55 atoms and the third 147 atoms, as sketched in figure 2.1. [52] These clusters differ only little from a sphere and therefore minimise the contribution of the surface atoms to the entire structure. On the larger clusters the surface structure is obvious. Two types of facets are exposed: The (111)-facets with a triangular shape and the (100)-facets with quadratic shape. Clusters comprising 13 atoms have been shown for instance for Au and Rh. [53, 54] The cluster Au<sub>55</sub> has been identified by Mößbauer-spectroscopy [55] and it has been proven to be exceptionally stable against oxidation [56]. The same cluster has been prepared for several other metals. [57] Larger clusters with a forth shell have been synthesised of palladium [58] or platinum [59]. Clusters with different geometry can be constructed with a similar approach. [51]

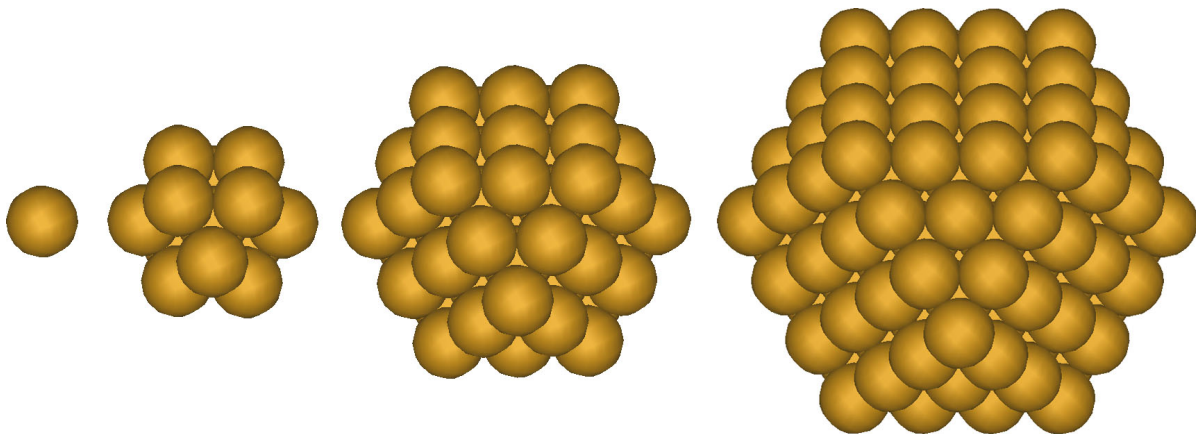


**Figure 2.1: A series of different clusters.** Cubo-octahedra of 1, 13, 55 and 147 atoms in fcc-structure. Each of the presented clusters represents the core of the subsequent cluster. Note that the percentage of surface atoms is far above 50% for all structures.

In this chapter and in article A.1 a synthesis scheme for the production of MSC of CdSe is presented and discussed. Due to their small size the CdSe-MSCs emit blue light. Therefore these clusters extend the spectrum of the accessible fluorescence colours of CdSe-nanocrystals. A method to exploit this for the production of blue emitting diodes is presented in article A.2.

## 2.1 Synthesis of Magic Size Clusters

In literature one can find protocols for the synthesis of several magic-size-clusters. [60–63] In these reaction schemes for each different cluster size a different technique is employed. For this reason also the structure and nature of the surfactants is different for each of the different clusters. In article A.1 we present a reaction scheme through which a series of magic-size-clusters can be synthesised sequentially one after another with only one synthesis-scheme. The size of the cluster is determined only by the reaction time.

The synthesis as described in article A.1 is derived from the standard synthesis [35, 39, 40] of the green to red nanocrystals, i.e. of nanocrystals with a size of 2-6nm. The most important difference between this synthesis and the synthesis of the magic size cluster is the reaction temperature. In general the synthesis of semiconductor nanocrystals in organic solvents is performed at temperatures between 200 and 300°C.

Apart from the difference in temperature, the cited protocols also use either highly flammable or expensive precursors to introduce Cd-ions into the synthesis. In the early recipes [35] dimethyl-cadmium was used, which is a very unstable compound. In later protocols this was replaced by a complex formed by Cd and a long-chain phosphonic acid, usually tetradecyl phosphonic acid (TDPA) or dodecyl phosphonic acid (DDPA). [39, 40] The disadvantage of the phosphonic acids is that the reaction-solutions tend to form a gel after the synthesis. In some reaction schemes this event is quite uncontrolled. A

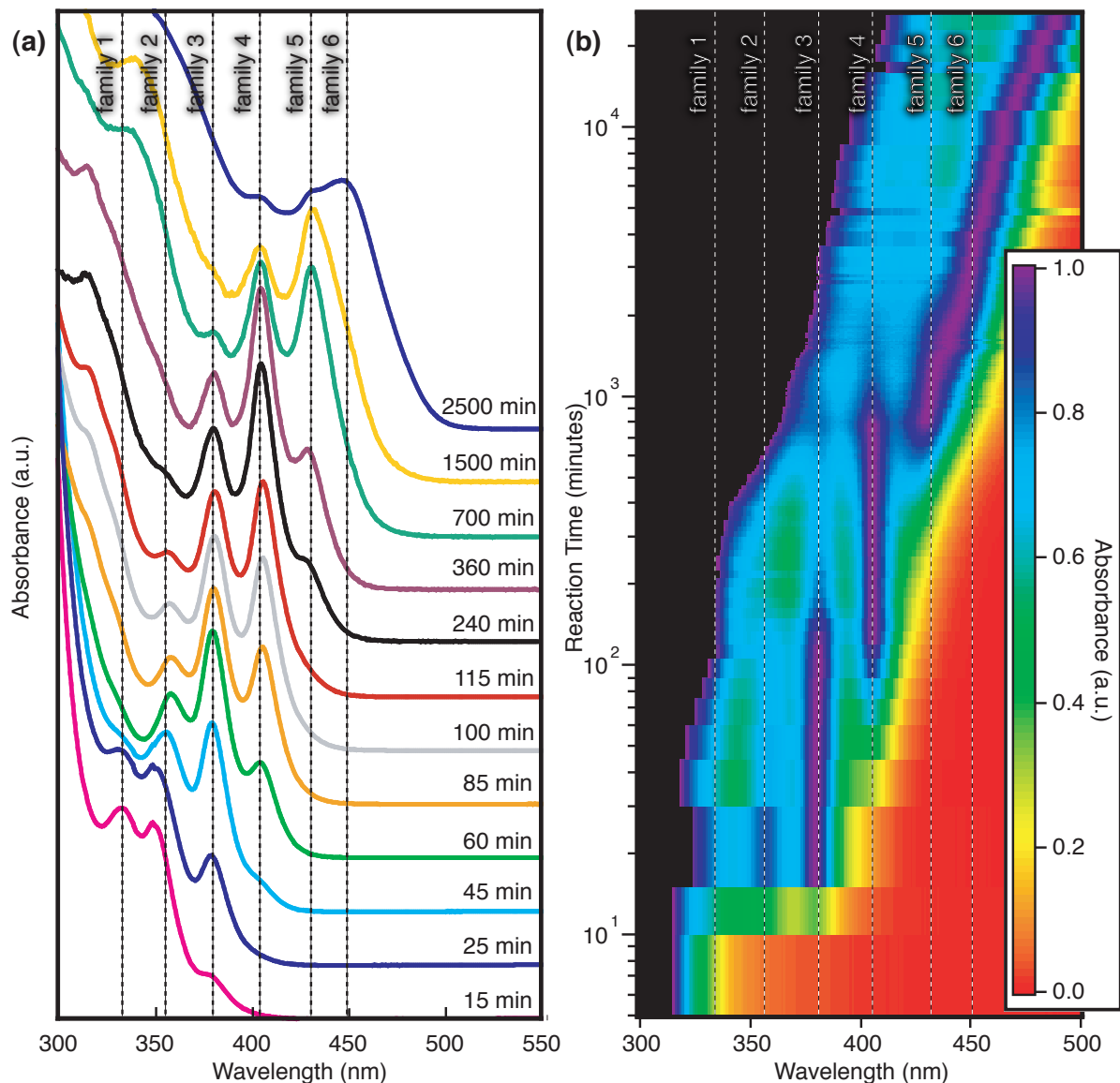


**Figure 2.2: Characteristic absorption spectra of the CdSe-magic size clusters (MSCs).** Absorption spectra of aliquots taken during the synthesis of magic-size-clusters in two different representations. In both cases the spectra are normalised to the amplitude of the dominant peak. At the early stage of the reaction, only distinct peaks are visible at 330 nm (*family 1*), 360 nm, 384 nm, 406 nm, 431 nm and 447 nm (*family 6*). In the upper right part of (b) the transition from the discrete growth-dynamics to a continuous-growth-mode can be observed.

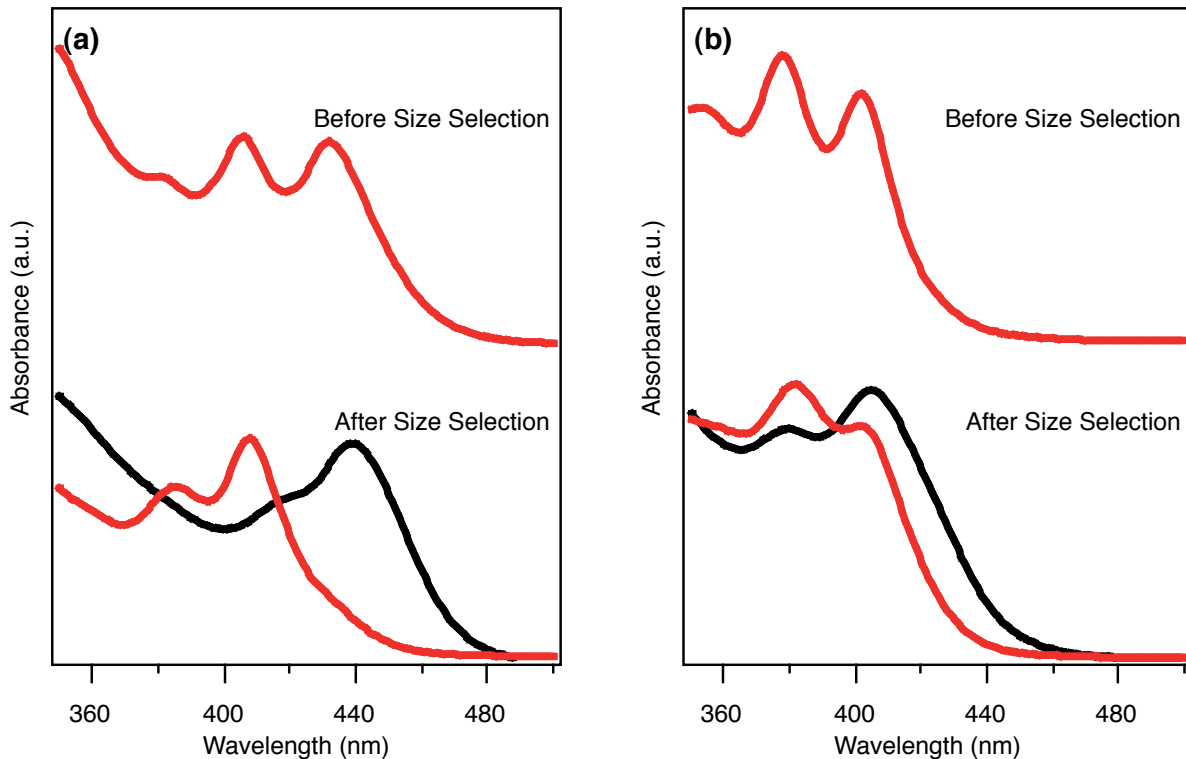


**Figure 2.3: Size-selective precipitation of two sample of magic size clusters.** Methanol was added carefully to the cooled-down reaction solution (upper spectra) and the mixture was centrifuged. In the spectrum of the first precipitates (black lines) the amplitude of the first peak is increased with respect to the other peaks. In the spectrum of a later supernatants (red lines, lower spectra) the situation is inverted and the second peak is more pronounced than the first.

possible way to suppress the formation of the gel is to add a carboxylic acid in a large excess to the reaction solution after it is cooled to ca. 100°C. At this temperature in the pure reaction solution the growth is virtually stopped. But upon addition of the carboxylic acid in some cases a second fluorescence line appears as shown in Figure 1.6. In the same way as the position of the absorption peak is related to the size of the crystals, also the position of the fluorescence peak is an indication for the size.

It has been proven experimentally [37] and theoretically [64] that a carboxylic acid is a weak ligand that enables the rapid growth of CdSe nanocrystals. In the present case we can therefore assume that new crystals with carboxylic acid as a ligand nucleate and grow even at that low temperature and thus give rise to the second fluorescence peak.

A synthesis of CdSe nanocrystals in carboxylic acid (nonanoic acid) and amine (dodecyl amine) (see article A.1) at relatively low temperatures (ca. 80°C) shows a quite remarkable result. In the absorption spectra, instead of a continuously shifting peak one can find a series of peaks that appear one after another and only vary in their relative amplitude. The position of the individual peaks remains almost constant over time. As

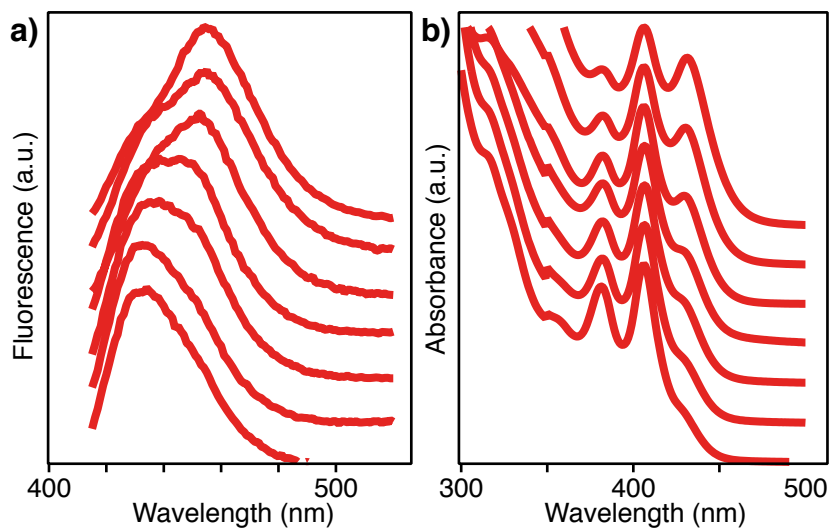


**Figure 2.4: Fluorescence spectra of the growing magic size clusters.** Fluorescence spectra (a) were recorded at different instances of the growth process and for comparison the relative absorption spectra are shown in (b). For clarity the spectra recorded at later stages of the growth are shifted upwards. Even though not as clearly as in the case of absorption, the fluorescence spectra are composed of discrete peaks. The first (lowest) fluorescence spectrum shows a strong peak centred at ca. 430 nm with a small shoulder at higher wavelengths. The latest spectrum has a strong peak at ca. 450 nm and a shoulder at lower wavelengths. Intermediate spectra show a broadened peak. By comparison with the amplitude of the first two absorption peaks, one can infer that the quantum yield of the larger clusters, i.e. those fluorescing at 450 nm, is superior to that of the smaller clusters.

the position of a peak is related to the size of the absorbing nanocrystal, this result points towards the sequential appearance of different sizes. The co-existence of clusters with different sizes in the solution can be proven by a size-selective precipitation. It is possible to separate the fraction of the solution that is producing the peak situated at red edge of the spectrum. This fraction is found to be the clusters that precipitate the first, thus the largest particles. By a careful treatment of the remaining supernatant it is even possible to eliminate the peak related to these large clusters almost completely, as shown in Figure 2.3(a). In the following the clusters are divided into six families, each of them characterised by a different peak in the absorption spectrum (see Figure 2.2).

In the spectra of the size-selected sample and generally in spectra recorded after a purification of the MSCs a red-shift of the peaks can be noticed. This shift is most likely due to the partial stripping-off of some surfactants from the clusters. The shift is of the order of ca. 10 nm. Upon addition of free surfactants to the solution the peaks can be shifted back. The recovery is not complete and also it bears the disadvantage that fresh organic material is introduced into the solution as impurity.

Another indication for the discontinuous size-distribution can be found in the fluorescence spectra. As shown in the Figure 2.4 the fluorescence spectra at late stages

of the reaction, i.e. when the families 4–6 are present, are composed of a series distinct peaks, similar to the behaviour of the absorption spectra. The observation of the discontinuity in the fluorescence spectra is limited by the low fluorescence efficiency of the bare clusters. Especially the smallest clusters (families 1–3) show almost no sharp band-edge-fluorescence. For applications (as shown in article A.2) the fluorescence-yield is enhanced by covering the clusters with a shell of ZnS. Generally this process strongly influences the position of the absorption features.<sup>1</sup>

Once a cluster has reached the size relative to family 6, the growth mode changes. The further growth proceeds in a classical continuous mode as normally observed in the nanocrystal-growth [46]. This behaviour is clearly evident in the colour plot in Figure 2.2(b). At the first stage of the synthesis, the behaviour of the spectra is discontinuous. The vertical features represent the appearance and disappearance of the peak along with their stability in position. At later stages, i.e. after more than 1000 minutes of reaction and once family 6 is populated the principal absorption feature shifts continuously to larger wavelengths with the proceeding of the reaction, as can be discerned from the diagonal feature in the plot.

## 2.2 Growth-Mechanism of the Magic Size Clusters

It is of great interest to understand the mechanism of formation of the magic size clusters. In the preceding section it was shown that the individual peaks actually point towards the non-continuous size-distribution. In this section the mechanism of growth will be discussed under the assumption of this non-continuous size-distribution. Certainly it is different from the standard models for the growth of nanocrystals. One can imagine two several reasonable, but yet competing models to rationalise the behaviour of the spectra.

**Coalescence model** Two or more clusters coalesce to form a bigger cluster.

**Continuous growth** Growth proceeds through continuous addition of monomers, but there is an energy barrier between the individual particle-size which has to be overcome through thermodynamic fluctuations.

These two models state that there has been a nucleation event as described in section 1.3. In both cases the appearance of the smallest cluster size is a spontaneous event. According to the coalescence model, first some very small building blocks nucleate, and then these entities fuse together to form a nanocrystal of a second family. Then either two particles of the second family fuse to form a particle of a third family or a cluster of the first family is deposited onto one of the second family. This model is widely applied for observed growth processes, the so-called oriented attachment. [65–68] In 1998 a model

<sup>1</sup>An alternative to a shell of ZnS is the growth of a shell of CdS. For this the MSC are dissolved in TOP. A flask containing CdO, TOPO and ODPA is prepared, and after removal of the volatile impurities in the reactants heated to 370°C. Then the solution of the MSC along with Se:TOP is injected rapidly and the heating source is removed immediately. Even though with this process the exact fluorescence colour of the resulting sample is relatively unpredictable, it yields brightly fluorescent particles with a narrow fluorescence line centred in a range between 470 nm and 500 nm.

for CdSe-MSCs was proposed that described the clusters as composed of pyramids fused at their edges (*Koch-pyramids*) so that in the centre a void is generated. [69] In this case four subunits need to coalesce in order to give rise to the subsequent cluster-size.

The second model is a variation of a continuous-growth-model. The growing crystal is exposed to a flux of monomers. And in the same way as in a normal growth-model, the monomers dynamically bind and unbind onto the crystal. Only here the ratio between binding- and unbinding-rate depends on the size of the crystal. The magic sizes represent sizes of extraordinary stability. If the crystal is slightly larger than a magic-size-cluster, the release of the outer atoms is more probable than the deposition of other monomers. Accordingly, crystals slightly smaller than a magic-size-cluster have a high affinity for monomers to reach the closed-shell-structure. In the normal growth-model in contrast, generally the binding-rate dominates for all crystal-sizes above the critical size, so that the crystals grow continuously.

To decide between the two models a control-experiment was carried out. Magic size clusters were synthesised and then purified. The purification was performed in a way to ensure the complete precipitation of all clusters present in the solution. For this aim an unusually large amount of methanol was added and the solution was centrifuged for a long time. Then a reaction flask containing only surfactants and no monomers was prepared and the purified MSCs were injected into the solution. Absorption spectra were recorded, but the spectra remained unchanged for several hours. This actually cannot be explained by the coalescence-model. In this case the growth would have continued. This behaviour can only be explained by the continuous deposition of monomers onto the particles.

A way to rationalise the stability of the MSCs is to introduce a slight modification to the energy landscape as presented in section 1.3. The MSCs represent minima in the potential landscape as sketched in figure 2.5. The sketch is a simplified model for the one-dimensional case. In principle the modified growth-model can be understood as a subsequent nucleation. The growth proceeds only through a series of jumps over potential barriers. In the potential a preferential direction is inscribed. A given MSC can evolve only into a larger MSC. The melting, i.e. the evolution to a smaller MSC, of the MSCs is virtually suppressed. Clusters that grow leave their own family  $i$  and after they have overcome the potential barrier, they become part of the subsequent family  $i+1$ . In the same way the depopulation of the preceding family  $i-1$  feeds the population of family  $i$ . Therefore the evolution of the concentration  $c_i$  of MSCs of family  $i$  can be described by only two rate-constants. The concentration of MSCs of family  $i$  grows at the rate  $\alpha_{i-1}c_{i-1}$  and decreases at the rate  $\alpha_i c_i$ :

$$\frac{dc_i}{dt} = \alpha_{i-1}c_{i-1} - \alpha_i c_i \quad (2.1)$$

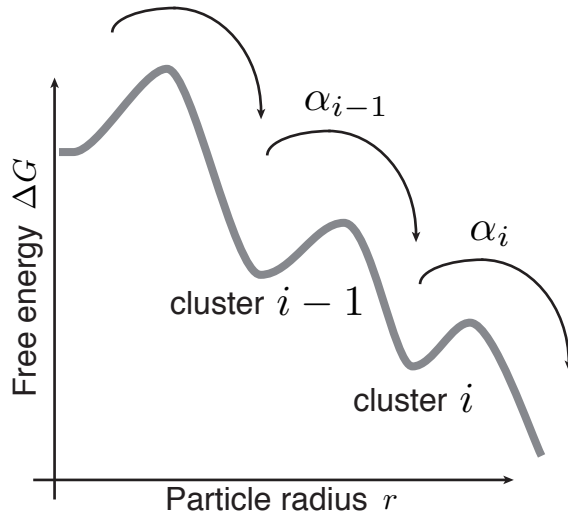


**Figure 2.5: Sketch of the potential landscape in the growth of CdSe magic-size-clusters.**  
For simplicity it is sketched only in one dimension. The model is to be understood as a modification to the classical nucleation-potential as shown in Figure 1.3.

The differential equations for the individual families can be summarised in a vectorial form:

$$\frac{d}{dt} \begin{pmatrix} c_0 \\ c_1 \\ c_2 \\ \vdots \\ c_n \end{pmatrix} = \begin{pmatrix} -\alpha_0 & 0 & 0 & \dots & 0 \\ \alpha_0 & -\alpha_1 & 0 & \dots & 0 \\ 0 & \alpha_1 & -\alpha_2 & & 0 \\ \vdots & & & \ddots & 0 \\ 0 & 0 & 0 & & -\alpha_n \end{pmatrix} \begin{pmatrix} c_0 \\ c_1 \\ c_2 \\ \vdots \\ c_n \end{pmatrix} \quad (2.2)$$

In the coefficient matrix it is interesting to notice the singular role of the families 0 and  $n$ . Family  $n$  is exceptional only for a trivial reason. It represents the last family described by the matrix. Clusters that leave this family enter into a different growth regime. From the data represented in Figure 2.2(b) it can be deduced that this growth regime is a continuous growth. More interesting is family 0. It is not fed by any other family, thus the clusters of this family must exist from the beginning of the reaction. At that moment only free monomers are found in the solution. Therefore the clusters of family 0 can at maximum be single atoms, which actually cannot be discerned from the other atoms. It is difficult to find a physical relevance for the number  $c_0$ . But actually the rate of depopulation of family 0 can be interpreted nicely. It is also the rate at which clusters of family 1 appear. In other words the rate  $\alpha_0 c_0$  can be interpreted as the nucleation rate of the system. This becomes evident when calculating the total concentration of MSCs:

$$c_{\text{total}} = \sum_{i=0}^n c_i \quad (2.3)$$

As long as the largest family  $n$  is not populated, this number is constant over time. A reasonable boundary condition to solve equation (2.2) is to set all concentrations to zero at  $t = 0$ , except for  $c_0$ , which will take a finite value. If we would exclude family 0 from the sum, the total concentration of clusters would be zero at the beginning of the reaction and then increase until it reaches a saturation value. It will remain stable until the first clusters appear in family  $n$ .

In article A.1 it is shown that with the solutions of equation (2.2) it is possible to reproduce the general behaviour of the absorption spectra shown in Figure 2.2. Actually through this explanation the coalescence model is not entirely excluded. One can still imagine the existence of small entities such as molecules consisting of few atoms (rings of the form  $(\text{CdSe})_3$ ) that are deposited as building block onto the clusters.

## 2.3 Structural Analysis

So far the analysis of the MSCs was restricted to optical measurements. In this section some methods for a more detailed analysis will be presented and also some plausible atomistic models for the structure of the MSCs will be shown. The experimental methods used to determine the size of the MSCs comprise X-ray diffraction (XRD), elemental analysis, TEM and mass spectroscopy.

XRD-spectra were recorded on dried samples of MSCs of different sizes. Unfortunately these spectra cannot be interpreted unambiguously to reveal the precise structure of the clusters. The signal, as displayed in the supporting information of article A.1, shows relatively broad peaks. This broadness is partially due to the small size of the clusters and most probably also to effects of surface-reconstruction. [62, 70, 71] Nevertheless, the spectra can be fitted better assuming a cubic zinc-blende (ZB)-structure than a hexagonal WZ-structure. This observation of the ZB-structure is in agreement with the general observation of a higher stability of ZB-structure with respect to the WZ-structure. [72] Especially at the low temperature of the growth it is more probable to find the clusters in this ZB-structure.

A second insight into the structure of the MSCs was gained by an elemental analysis. In principle with this technique the total number of atoms of one species in the sample can be determined. For the measurements, fresh samples of different MSCs were produced and a size-selective precipitation was performed to isolate only the largest clusters present in the solution. As the concentration of the MSCs is unknown, only the ratio Cd:Se in the individual samples could be determined. In all samples a higher concentration of Cd than of Se was found. This imbalance is also found in larger CdSe-nanocrystals with a different technique [73] and can be explained by an overrepresentation of Cd on the surface of the clusters due to the higher affinity of the surfactants to the Cd atoms than to the Se atoms.

TEM-measurements of the MSCs were limited by the difficulty to descry between the actual particles and the modulations of the image due to the support. Only the largest clusters (family 6) could be identified clearly (see Figure 2.6). From the TEM-images a diameter of these clusters could be determined as 2.1nm. Due to the limitations in the

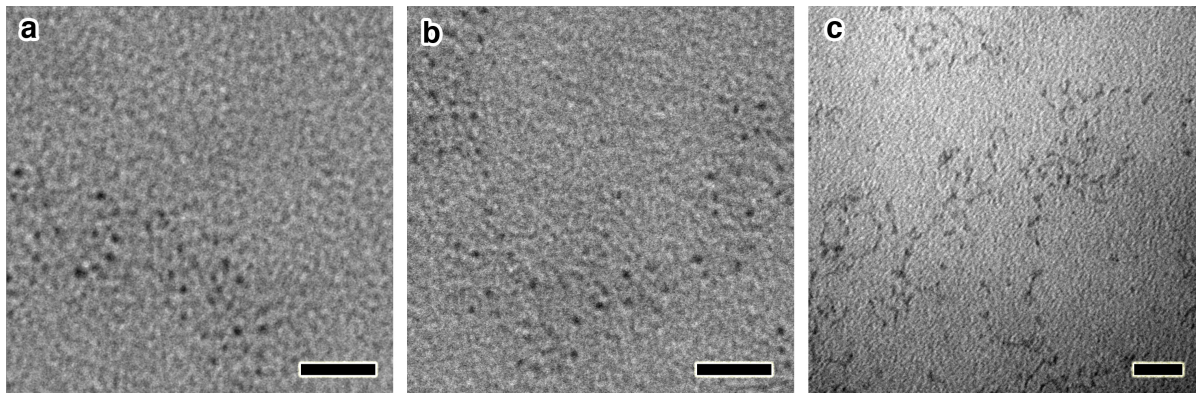


**Figure 2.6: Low resolution TEM-images of MSC of family 6.** Individual MSCs can be identified in (a) and (b). Their diameter is measured as ca. 2.1nm. (c) On the TEM-grid frequently rod-like structures are observed, which probably represent a matrix of residual organic molecules with MSCs incorporated. Generally these aggregates hinder the observation of individual particles especially when they are of small sizes. Also in (a) and (b) this matrix can be seen as a slight shadow. The scale-bars represent 20 nm.

imaging system of the TEM this value is to be considered as an upper limit.

In previous publications mass-spectroscopy was employed to characterize MSCs of CdSe. [62, 74] Unfortunately this technique does not seem to be appropriate for the MSCs presented in this work. Matrix-assisted laser desorption ionization time of flight (MALDI-TOF) experiments were performed on size-selected and purified samples. As shown in the supplementary information of article A.1 the mass-spectra show peaks relative to clusters of the type  $(\text{CdSe})_{13}$ ,  $(\text{CdSe})_{33}$  and  $(\text{CdSe})_{34}$  like those found also by Kasuya and co-workers. [62, 74] But actually these clusters were found for any CdSe sample exceeding a certain size (i.e. with an absorption peak at a wavelength of 432nm and greater, families 5 and 6). But the fact that we find the same clusters for any CdSe sample larger than MSCs of family 4 and even in classical nanocrystals with a diameter of ca. 3nm must be interpreted as a general limitation of the technique for the inquiry of our samples. It seems that the clusters actually become reshaped under the strong laser excitation, most probably by stripping off of the outermost atoms and the surfactants. The peak relative to the cluster  $(\text{CdSe})_{13}$  appears for clusters of the families 5 and 6 but only very weakly – if at all – for clusters of family 4, whereas the peaks of  $(\text{CdSe})_{33}$  and  $(\text{CdSe})_{34}$  do not appear at all for this sample. From this we can deduce that MSCs of family 4 are smaller than  $(\text{CdSe})_{33}$ .

From the absorption spectra one can infer the size of the nanocrystals. In literature one can find a reference curve that attributes a size to the position of the first exciton peak in the absorption spectrum. [75] When assuming a perfect zinc-blende structure the size gives an indication of the number of atoms in the individual MSCs. These results are reported in Table 2.1. The size of the clusters of family 6 determined by this technique correlates nicely with the TEM measurements.

Given the results summarized in the upper part of Table 2.1 one can try to develop

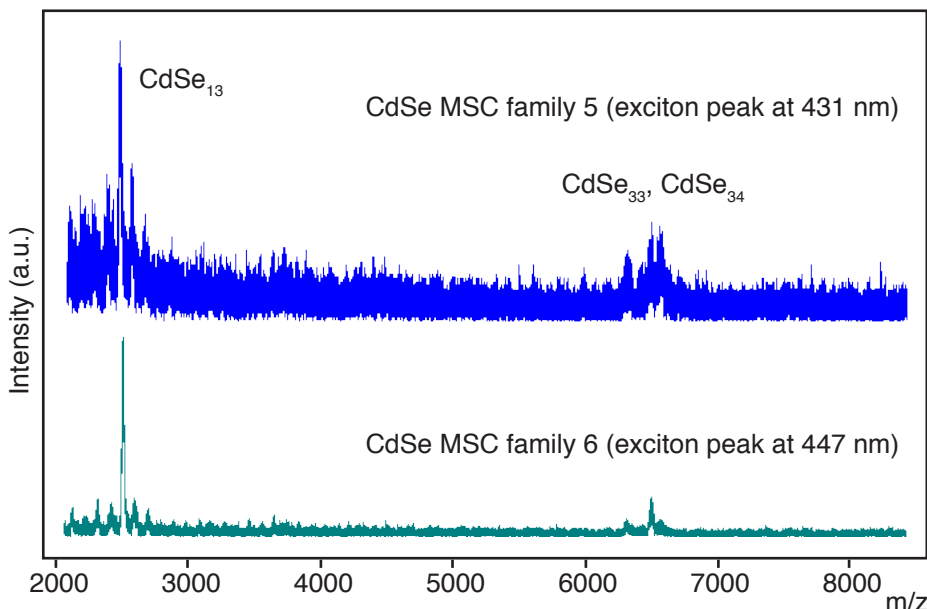


**Figure 2.7: Mass spectra of large magic size clusters.** Matrix-assisted laser desorption ionization time of flight spectra (MALDI-TOF) were recorded on samples of families 5 and 6. The peak at ca. 2500 mass units can be attributed to clusters of the form  $\text{CdSe}_{13}$ , the peaks around 6500 mass units are relative to clusters  $\text{CdSe}_{33}$  and  $\text{CdSe}_{34}$ . Mass spectra of larger nanocrystals show a similar pattern (see article A.1).

models for the structure of the MSCs. The measurement of the ratio Cd:Se has turned out to be the most valuable information for this purpose. As mentioned above the imbalance between Cd and Se can be explained by the number of the relative atoms on the surface. A way to rationalize this imbalance in models is to restrict the number of allowed dangling bonds for the surface atoms. If Cd-atoms are allowed to have 2 or less dangling bonds, Se-atoms only 1 dangling bond, clusters can be generated that show a higher number of Cd atoms than of Se atoms. This model reflects the behaviour of the surfactants. We can speculate that the carboxylic acids offers two binding sites for the Cd-atoms, whereas the Se forms only a single bond with TOP. The cluster models were generated by a *perl* script, which randomly generated clusters of a given size and geometry (spheres, tetrahedra, cubes) in perfect ZB structure. Subsequently Cd surface atoms with 3 dangling bonds and Se surface atoms with 2 or 3 dangling bonds were removed so that the surface atoms of the remaining cluster showed the imposed number of dangling bonds. With this approach ca. 400 different clusters containing less than 200 atoms and having the restricted amounts of dangling bonds were found. Out of these models six clusters fulfilled the stronger restriction that Cd-atoms have either two or no dangling bonds, but not just one single dangling bond. This series actually has sizes similar to those determined by the optical absorption measurements. Furthermore the clusters are based on a tetrahedral architecture. Similar clusters could be identified in previous works by crystallization of the clusters and X-ray diffraction. [60, 61, 76, 77]

**Table 2.1: Overview of the characteristics of the different magic size clusters (MSCs).**

The positions of the absorption- and fluorescence-peaks are measured on non purified samples. From the position of the absorption peak the diameter of the particles is estimated through a calibration curve from literature. [75] Assuming a perfect ZB-structure the number of atoms per cluster can be estimated from the diameter. The ratio Cd:Se is measured by elemental analysis on purified samples. In the lower part the characteristics of the proposed models are summarised (see Figure 2.8).

Family	1	2	3	4	5	6
<b>Measurements</b>						
Absorption peak (nm)	327	360	384	406	432	447
Fluorescence peak (nm)	–	–	–	430	450	475
Diameter (nm)	0.9	1.2	1.4	1.6	1.8	1.9
Number of atoms	13	31	53	78	113	135
Measured ration Cd:Se	–	–	–	1.10–1.22	1.28–1.29	1.24–1.26
<b>Proposed models (see Figure 2.8)</b>						
Number of atoms	10	29	59	75	102	142
Ratio Cd:Se	1.50	1.23	1.11	1.34	1.04	1.29

In those reported cases, however, the Se- or S-atoms were overrepresented on the surface of the clusters, which is due to the employment of strong ligands for Se or S. Therefore the tetrahedra in those reports can be understood as the inverted structure of those proposed here. In this series (See Figure 2.8) the smallest cluster has the structure of adamantane. The two subsequent clusters are obtained basically by the addition of a triangular layer on the base of the precedent cluster. This geometrical feature would nicely explain the existence of the barriers in the growth-process. To grow from one tetrahedral size to the next, a new layer has to be added. The addition of the less atoms than necessary for the entire layer produces an unstable cluster. Only when a sufficient number of atoms is assembled in the layer, it is likely that the missing atoms are added to form the complete layer before the unstable atoms are removed. This can be understood as a nucleation barrier for the growth of the individual layers.

In the model-structure for larger cluster intermediate clusters between two full tetrahedra have to be introduced. These clusters (clusters 4 and 6) show small cage-like structures on their four flat surfaces. A possible explanation for these structures is that the entire cluster restructures when this size is reached. In this case not only the barrier for the nucleation of a new shell but also a barrier for the conformational change would have to be overcome to reach this size. Another explanation would be that this structure is intermediate in the sense that not the entire triangular layer has to be deposited onto one facet. Once a certain size is overcome, domains smaller than a full facet could be stable. In the case of cluster 4 in Figure 2.8 this is an adamantane cage in the centre of the triangular facets. One can also imagine that this cage is formed only on one of the

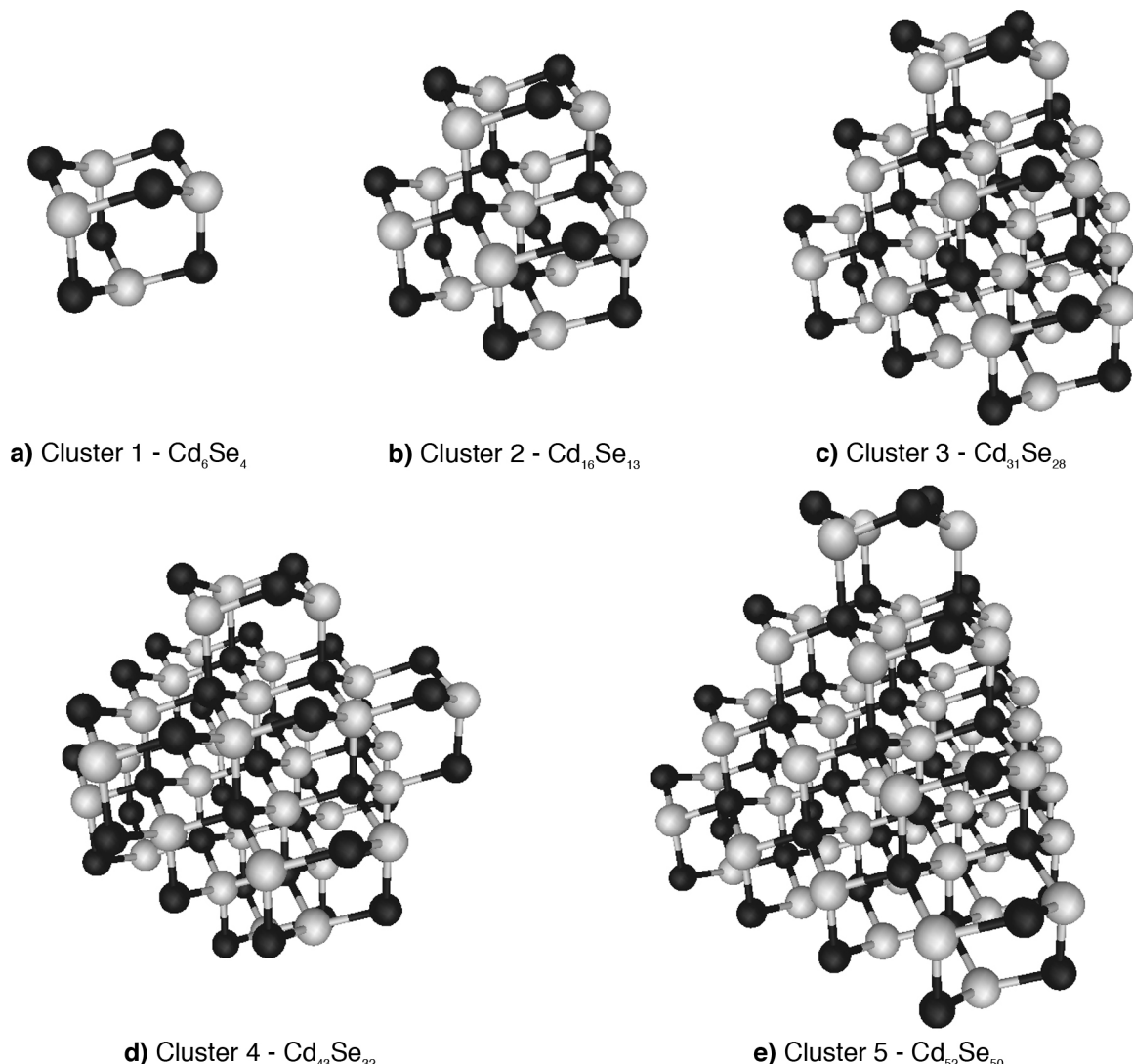


**Figure 2.8: Possible models for the first five magic size clusters.** A series of clusters in ZB-structure that show similar architecture so that the addition of few atoms onto one cluster can lead to the subsequent structure. The series meets the observed ratio Cd:Se, the estimated sizes of the clusters.

four facets. The subsequent cluster size is then reached by completion of the layer.



### 3 Shape Control

The nanocrystals discussed so far were of almost spherical shape. But already in very small nanocrystals such as the magic size clusters presented in the previous chapter different crystalline facets can be identified. But due to the small size of these facets the deposition of only few atoms onto one of them changes its nature completely. In Figure 3(a) an example of an almost spherical nanocrystals is shown. In this nanocrystal the hexagonal facets can be identified clearly. On larger nanocrystals the faceted shape becomes more obvious, as for instance on PbSe-nanocrystals (see Figure 3(b)). [67] Indeed the growth of perfectly spherical crystals is more an exception than the rule. For instance macroscopic quartz is frequently found in an elongated shape with six large facets that intersect under an angle of  $120^\circ$ . The tip of the crystal shows a series of facets, all inclined with respect to the long axis of the crystal. Generally the shape of a crystal depends on the relative speeds at which the individual facets grow. Here, the speed of growth of a facet is measured as the speed at which the distance of its centre to the centre of the entire crystal increases. The faster a crystal grows on one facet the more likely to disappear is this facet. [78] To rationalise the differences in the growth speeds let us reconsider the discussion of section 1.4 on the growth process. There the exact nature of the surface or the existence of facets of the growing crystal was not taken into account. The introduction of the critical size ( $r^*$ ) in the growth process was actually based on the values of the vapour pressure of a flat surface ( $C_\infty$ ) and the surface energy ( $\sigma$ ), but in equation (1.10) implicitly these values were assumed constant for all facets. In fact these two quantities depend strongly on the exact nature of the facet in consideration. Especially the surface energy of the different facets can

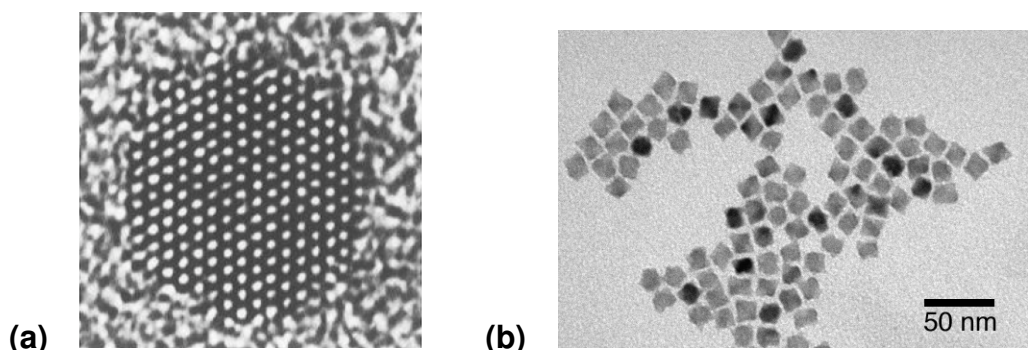


**Figure 3.1: Examples of faceting of nanocrystals.** TEM-images of a hexagonally shaped CdSe-dot in WZ-structure (a, picture taken from reference [7]) and of a sample of octagonally shaped PbSe-nanocrystals. (b)

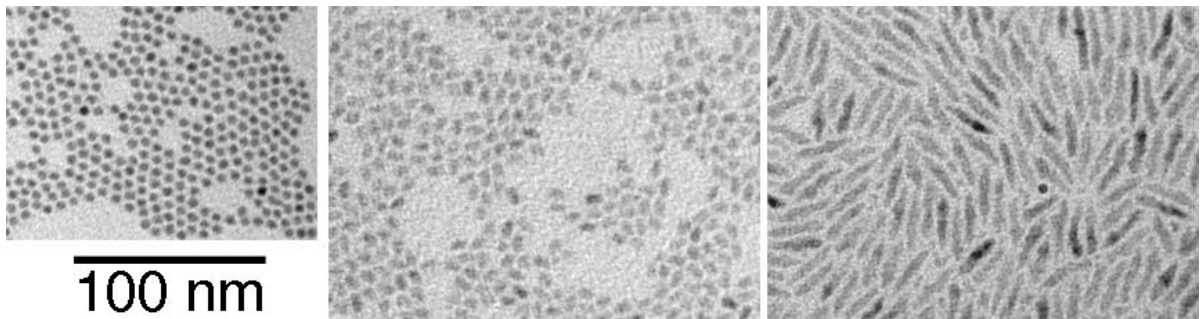


**Figure 3.2: TEM-images of nanocrystals with different aspect ratios.** Spherical CdTe-nanocrystals (left), rice- and rod-shaped CdSe-nanocrystals

be influenced strongly by the choice of the surfactants. [64, 79–81] If the surfactants bind stronger to one facet than to its neighbouring facets, new monomers are more likely to be incorporated into these neighbouring facets. In other words, those facets onto which the surfactants bind stronger have a lower surface energy, as the area of this facet is extended easier than that of a facet with weak ligands. In literature this relation between growth-speed on the different facets and their individual surface energy is known as the Curie-Gibbs-Wulff-theorem. [44]

This effect is seen on many different nanomaterials, where nanocrystals of different shapes can be synthesised, as for instance cubes can be formed from Cu<sub>2</sub>O, gold, silver or PbSe [82–84], stars from PbSe and PbS [85, 86], disks of cobalt, silver and iron oxide [87–90], rods or wires of gold [91, 92].

In the wurtzite (WZ)-structure the choice of the growth axis is relatively straightforward. Through its high symmetry the unique *c*-axis is distinguished from the other axes. In CdE nanocrystals it serves as the directional axis for the asymmetric growth. [93] In the case of Co-nanocrystals in the  $\epsilon$ -phase growth along this axis is suppressed. [87] But the asymmetric growth is not restricted to materials that expose a hexagonal structure. [94] CaF<sub>2</sub>-nanorods grow in the cubic fluorite structure along the (111)-axis [95]. PbSe grows in the highly symmetric cubic rock salt structure, but by the help of bulky surfactants a unique growth-direction can be assigned and nanowires are formed. [84] For the materials of interest in this chapter (CdS, CdSe and CdTe) generally the crystalline structure is the WZ-structure. For instance, nanorods of CdSe (as shown in Figure 3.2) preferentially grow in WZ-structure, as can be inferred from XRD-measurements and high-resolution-TEM. [96] A nice demonstration of the existence of the well-developed facets in the rods can be seen in honeycomb-structures, in which the nanorods align vertically and in TEM-images the rods can be seen along the long axis, or parallel to the lateral facets. In this case the hexagonal boundaries of each rod can be observed clearly. [96] It is interesting to notice that for thin nanorods the WZ structure is favoured even in conditions where the bulk material favours the cubic ZB-structure due to the reduced number of dangling bonds on the surface. [97, 98]

A higher level of complexity is observed in branched nanocrystals (see Figure 3.3. An

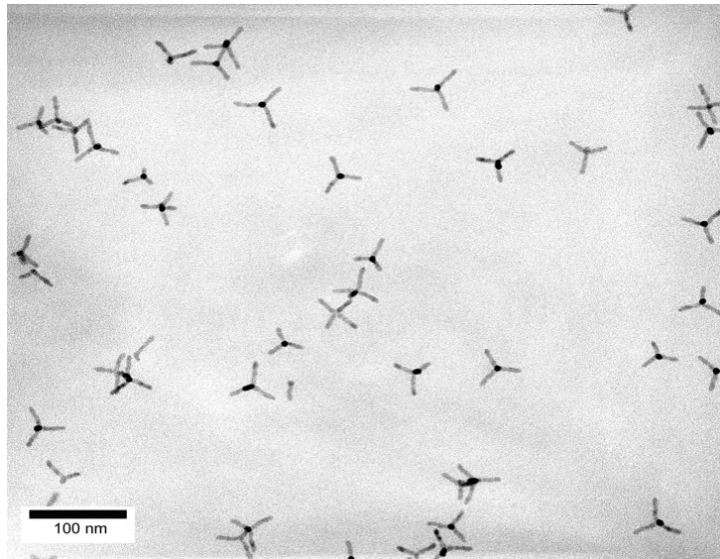


**Figure 3.3: TEM-image of tetrapods of CdTe.** The particles consist of four rods that are fused together in one point and that span the tetrahedral angle between two legs. In the projection of the TEM, three legs can easily be identified, the forth legs points directly upwards. Due to the longer distance that the electron beam has to travel through the material this leg appears as a dark spot.

intriguing example of such structures is the tetrapod. It is composed of four rods that are fused together in a central core. This shape is observed in several materials, such as ZnO [99], ZnSe ([100] and article B.2), ZnS [101], CdSe ([102, 103] and article B.7), CdTe ([104] and article B.1), Pt [105] and Fe<sub>2</sub>O<sub>3</sub> [106]. Generally, the growth mode of the tetrapods is driven by the same mechanism as the growth of the rods. During growth monomers are deposited onto the high-energy facets of the arms, that is on their tips, whereas deposition of monomers onto the lateral facets of the arms is hindered. The main difference in the growth process resides in the nucleation event and the very early stage of the growth, when the core of the tetrapod is formed, as will be discussed in the following sections and article B.1.

Shape controlled nanocrystals are interesting for many aspects. The nanorods show linearly polarised emission [107] and are proven of advantage in solar cells [19, 108]. The appealing feature of the nanorods is their behaviour as quasi one-dimensional objects. Their quantum-properties can be tuned merely over the diameter, the total length of the nanorods affects its electronic properties only for nanorods with a low aspect ratio. [109] That makes them an appealing system for electronic devices. For instance nanowires<sup>1</sup> of different materials can be embedded into electric circuits to act as transistors or other active elements [110, 111], electroluminescence is observed from CdSe-nanorods [112] and CdSe- and CdSe/ZnS-nanorods have been proven to be of advantage as lasing medium [113, 114]. Their symmetry facilitates the alignment of nanorods. In some cases it is sufficient to slowly evaporate the solvent to obtain large areas of aligned rods. [115–118] Better results are achieved when the nanorods are oriented by an electric field. (See references [119–122] and articles B.8 and C.3)

Tetrapods offer the possibility to expand this spectrum of applications. When three of the arms are contacted electrically, one of the arms can be used as a gate to control the

<sup>1</sup>The terms nanowires and nanorods are used interchangeably here. There is no strict differentiation between the two terms. A tendency is to call long nanorods, i.e. with a length superior to ca. 500 nm, nanowires.

current through the entire structure. [23] Also, these nanocrystals can be of advantage in solar-cells. They exhibit a large surface on which charges can be separated, and still provide through their complex and extended geometry a pathway to transport charges to an electrode. [123] Furthermore tetrapods exhibit an interesting structure of their excited states. Electrons and holes can be localised in the core-region of in the arms and the overlap between the two wave-functions differs considerably from one excited state to another. [124]

### Contribution of this work

In articles B.1 and B.2 synthetic methods to obtain branched nanocrystals of CdTe and ZnSe are described. In article B.1 a model for the origin of the branching is proposed. The architecture of the tetrapods according to this model and the experimental evidence for it are also presented in the present chapter.

In article B.3 the presence of two radiating levels in the tetrapod is demonstrated. This effect is explained by the high overlap of the wave-functions of the second excited level, compared to the overlap between these wave-functions with first level.

Article B.4 deals with the polarisation-effect on the absorbance of a tetrapod. By means of time-resolved spectroscopy the decay of the excited states can be observed. Interestingly, at short time delays (several picoseconds) after the excitation, the exited state is still localised in one arm of the tetrapod. Only after a few tens of picoseconds the energy is spread over the entire structure and therefore the probed levels are anisotropic.

A series of Raman-experiments is described in the articles B.5–B.8. In article B.5 resonance of confined phonon modes with different exciton levels in CdTe tetrapods is detected, article B.6 describes the influence of the shape, especially the anisotropy, on the measured Raman-spectra.

In article B.7 the sensitivity of surface-optical phonons on the dimensions of rod- and tetrapod-like CdSe nanocrystals is shown.

In article B.8 we describe a method to align CdSe-nanorods by means of a strong field. The success of this alignment is demonstrated directly by SEM- and also by Raman-measurements. In aligned nanorods those surface-optical phonons with a potential extended significantly to the surrounding of the rods are suppressed by the influence of the neighbouring nanorods on the dielectric medium. Furthermore the dependence of Raman-lines on the polarisation of the exciting laser provides an additional evidence of the success of the alignment. Low-frequency-modes appear only when the incident laser-light is polarised perpendicularly to the axis of the nanorods.

## 3.1 Origin of Branching – Polymorphism vs. Octa-Twin

To understand the dynamics of the growth of tetrapods, first the intrinsic structure of these peculiar nanocrystals should be discussed. One can actually find two competing models to rationalise the four-arm shape. One model – the *octatwin model* – has been discussed and supported since the early nineties for tetrapods of ZnO and ZnS. [100] This model is based on the controlled formation of twin-planes. The second model –

the *polymorphism model* – relies on the polymorphism of the materials and has been assumed to describe the formation of CdTe-tetrapods. [104] In this model the core of the tetrapod is grown in Zinc Blende structure, whereas the arms grow in Wurtzite structure.

### 3.1.1 Polymorphism Model

Being a tetrahedrally coordinated binary compound, CdTe can grow either in the hexagonal Wurtzite or the cubic Zinc Blende structure. The different structures have different energies of formation. Thus, at lower reaction-temperatures growth in the zinc-blende-phase is favoured, whereas at higher temperatures the crystals preferentially grow in the wurtzite structure. [72, 125] The injection of precursors induces a drop in temperature and thus enables the formation of zinc-blende-nuclei. Due to the small difference in energy the later growth – after the temperature has recovered – takes place in the wurtzite-phase, giving rise to the development of the arms. Apart from the temperature-effect, the change in the crystalline phase is also supported by the affinity of the ligand – namely the phosphonic acids – to the lateral facets of the rods in WZ-structure, i.e. to the arms of the tetrapod. [126] At the very early stage the surfactants are too bulky to efficiently bind to these facets and thus support their formation.

The fact that only four out of the eight  $\{111\}$ -facets of ZB-structure allow for the growth of the arms is explained by the atomic difference between the  $(111)$  and the opposed  $(\bar{1}\bar{1}\bar{1})$  facets. In the same way as in the WZ-structure on one of the facets the Cd-atoms expose three dangling bonds, whereas on the other facet they expose only one. The latter can be efficiently passivated by surfactants and thus the growth on this facet is hindered. [126] Therefore only on four of the eight facets of the  $\{111\}$ -family a wurtzite arm can grow.

This polymorphism model is accepted widely in literature for the growth of CdE-tetrapods. [102, 104, 127]

### 3.1.2 Octa-Twin Model

A different model describes the tetrapod as composed of several domains that are exclusively in wurtzite-structure. According to this twinning-model, the core is composed of eight WZ-domains. These domains have a tetrahedral shape and can be of two different types. In one type (type A) the basal facet is a  $(0001)$ -facet of the WZ-structure, in the other type (type B) it is a  $(000\bar{1})$ -facet. The other three facets of the tetrahedra are either of the family  $\{11\bar{2}\bar{2}\}$  (type A) or of the family  $\{11\bar{2}2\}$  (type B). Two tetrahedra of different type are interconnected through a twin-plane as shown in Figure 3.4. This twin-structure shows an inverted symmetry. As domains of type A are connected preferentially to domains of type B and vice versa, the octahedron formed by eight of these domains exposes an alternating pattern of  $(0001)$ - and  $(000\bar{1})$ -facets. These facets exhibit hexagonally organised atoms, identically to the  $\pm(111)$ -facets of the ZB-structure. Therefore this octahedron is chemically identical to an octahedron formed of ZB-structure. In both cases the Cd-atoms on the individual facets exhibit one dangling

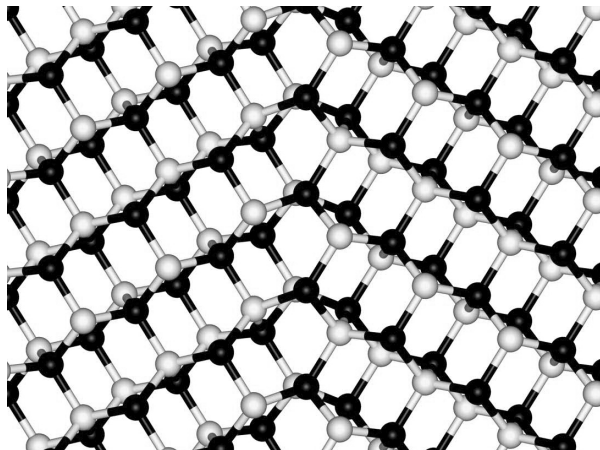


**Figure 3.4: Model of a  $(11\bar{2}2)$  twin boundary in the WZ structure.** The symmetry operation necessary for the formation of this structure involves mirroring on the  $(11\bar{2}2)$  plane, exchange of the atom-type and a shift along the  $c$ -axis. Due to the exchange of the type of atoms the twin boundary shows an inverted symmetry. If the  $c$ -axis in the left domain points upwards, it points downwards in the right domain. Consequently the two fused domains are of different type (see text).

bond on four facets of the octahedron and on the remaining four facets three dangling bonds.

The *octa-twin*-model (“octahedral multiple twin model”) was first proposed to describe the architecture of ZnO and ZnS tetrapods. [99,128] The structure of the core, as constructed according to this model, does not necessarily fill the volume of the octahedron. In fact it is very likely that the individual domains are formed such that, when assembling eight of them, they do not perfectly fill the volume. The stress induced by this mismatch is released in the formation of cracks along the twin-planes leading to a deviation from the ideal tetrahedral angle. The successful measurement of this deviation on ZnO-tetrapods supports the octa-twin model. [129]

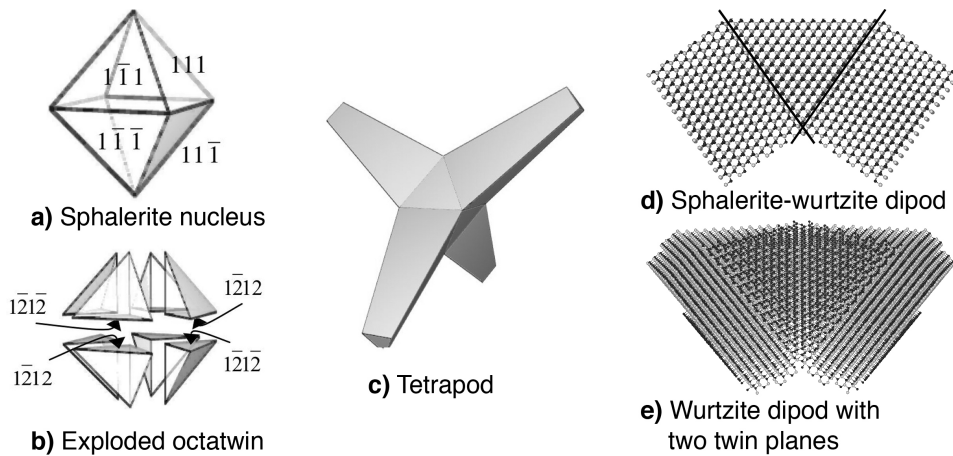


**Figure 3.5: Comparison between the polymorphism and the octa-twin model.** An octahedral core can be formed either in ZB-structure (a) or out of eight tetrahedral WZ-domains (b). In both cases only four of the eight facets allow the growth of a rod, so that a tetrapod (c) can be formed. A detail of the different architectures are sketch in (d) and (e) on the example of a dipod, i.e. a junction of two rods.

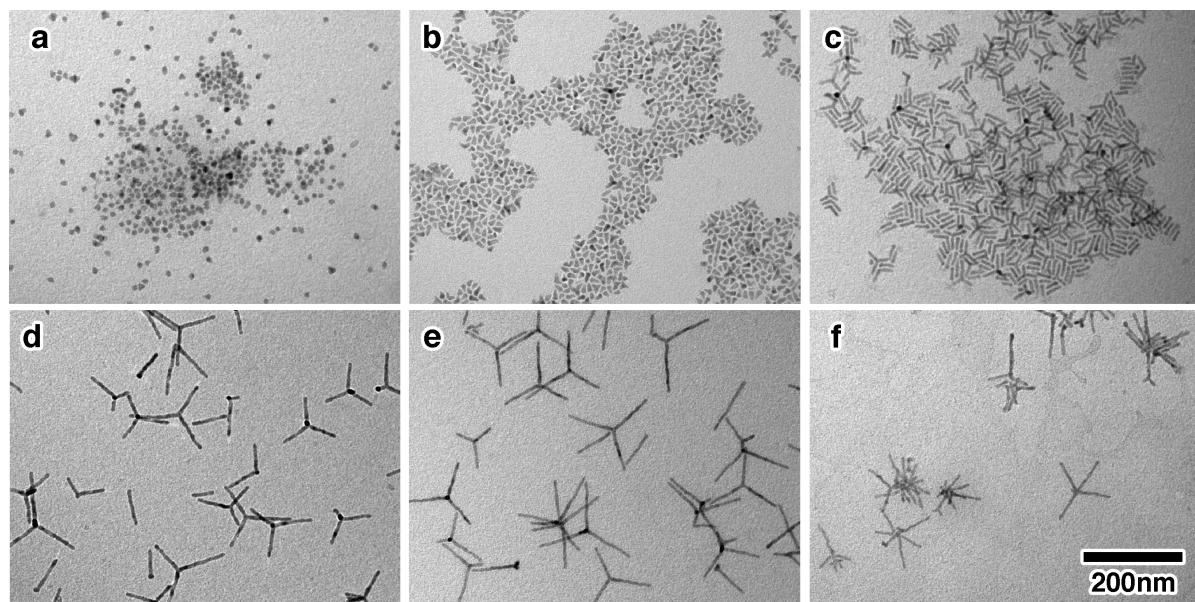


**Figure 3.6: Effect of methyl phosphonic acid (MPA) on the growth of CdTe-tetrapods.**  
For the synthesis of the different samples the molar ratio [MPA]:[ODPA] was adjusted to: (a) 0%, (b) 2.6%, (c) 5.3%, (d) 8.1%, (e) 9.3% and (f) 17.6%.

## 3.2 Synthesis of Tetrapods

Experimentally tetrapods of CdTe are synthesised in a mixture of phosphonic acid, TOPO and TOP. [104] Through the ratios of the surfactants (mainly the phosphonic acid) and the precursors of Cd and Te, the length and the width of the arms of the tetrapods can be regulated. A high concentration of precursors or monomers enables the growth of long arms [104], quite in the same way as it is observed also in the formation of CdSe-nanorods [34]. In the early recipes for the synthesis of CdTe-tetrapods only one type of phosphonic acid was used, octadecyl phosphonic acid (ODPA). In 2004 the supplier for this reactant changed its production-process and delivered the reactant in a higher purity. It turned out that actually the impurities were responsible for the success of the tetrapod-synthesis and this finding led to a deeper understanding of the mechanism of growth and motivated a deeper investigation on the crystalline structure of the CdTe-tetrapods, as discussed in article B.1

The impurities present in the old batches of ODPA comprised phosphonic acids with short alkyl chains and esters of the different phosphonic acids. By the addition of a short-chain phosphonic acid, in particular methyl phosphonic acid (MPA), to the reaction solution, the number of arms in the tetrapod can be controlled. If no MPA is present in the solution, the CdTe-nanocrystals grow in almost spherical shape (see Figure 3.6). When increasing gradually the molar ratio of MPA/ODPA the nanocrystals first grow into elongated structures (ratio of ca. 5%) and at even higher ratios branched structures dominate the sample. At a ratio of ca. 9% the sample is rich in tetrapods.

Given the difference in molecular weight the mass of the MPA used in a synthesis of tetrapods is about 3% of the mass of the ODPA. In that sense the MPA can be regarded as an impurity in the synthesis. When employing even higher concentrations, nanocrystals with an even higher number of arms can be synthesised. The synthesis scheme is presented in more details in article B.1. A similar behaviour is reported for the use of a slightly longer phosphonic acid, propyl phosphonic acid, as impurity. [130]

The knowledge on influence of this impurity on the branching can be also employed in the synthesis of CdSe-tetrapods. The first successful synthesis of CdSe-nanorods was performed in technical grade TOPO. [96] Again, in this case the technical grade compounds supplied the impurities necessary for the growth of the nanorods. This impurity was, as explained in the introduction to this chapter, a phosphonic acid. Later, a better control over the anisotropy of the nanorods was achieved by the use of two types of phosphonic acids, namely hexyl phosphonic acid (HPA) and tetradecyl phosphonic acid (TDPA). In this synthesis TDPA can be exchanged by ODPA. Addition of a high quantity of MPA actually leads to the formation of tetrapods also in CdSe. Nanocrystals of this type have been investigated by Raman-spectroscopy, as described in article B.7.

### 3.3 Structure of the Tetrapod-Core

An evidence for the nature of tetrapods core is given already by the ability to tune the number of arms per nanocrystal with only one parameter, i.e. with the amount of the short-chain phosphonic acid MPA. Given the high symmetry of a ZB-core as proposed in the polymorphism model, this effect is hard to explain. If one of the four equal arms is affected by the presence of the MPA, the same should count for the remaining three arms. Thus, the polymorphism model could only account for arms of different length, but not for the complete absence of several arms, i.e. the selective formation of rods, dipods etc. In the octa-twin-model in turn, one can actually ascribe the probability of twin-formation to the presence of the MPA. In this model a minimum of two twin planes, i.e. of three twin-domains, has to be formed to give rise to the simplest branched structure, the dipod.

But this discussion is just an indication for deciding for one or the other model. For a deeper insight a crystallographic determination of the cores' structure is necessary. The samples were examined by XRD and high-resolution TEM. XRD-measurements on branched CdTe-nanocrystals show only peaks relative to the wurtzite-structure. But the absence of signals from the ZB-core cannot be considered as an ultimate proof for the non-existence of this phase in the tetrapods. As most of the material is found in the arms the reflexes of the core-region might be too weak to be discerned from the strong WZ-signal of the arms. In one-dimensional CdTe-nanostructure such as matchsticks and dipods the presence of type-(11 $\bar{2}$ 2) twin boundaries in CdTe-nanocrystals can be shown directly by means of high-resolution-TEM (see Figure 3.8b). Unfortunately in tetrapods such direct observation of the core region is not feasible. The view onto the core is hindered by the presence of the upstanding arm. Only by tilting of the sample in the electron-beam this problem could be partially overcome. But still no direct

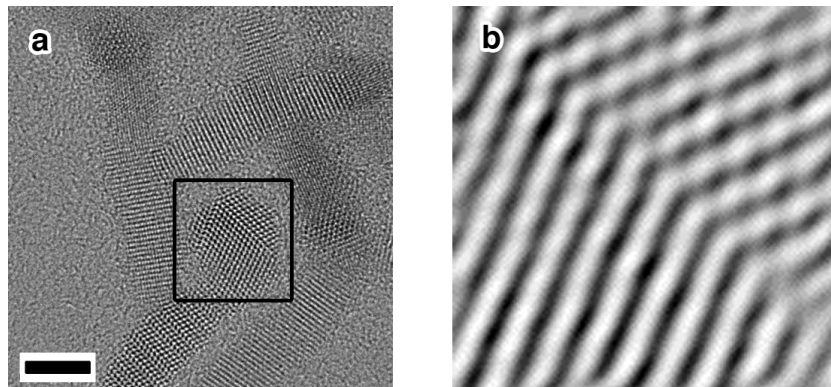


**Figure 3.7: High-Resolution TEM images of a branching region.** (a) Some matchstick structures like in Figure 3.6c. The scalebar represents 5 nm. (b) Magnified view of a  $3.5 \text{ nm} \times 3.5 \text{ nm}$  area from the head-region of the nanocrystals marked in (a). The pattern shows the same symmetry as the model represented in Figure 3.4 and thus can be identified as a twin-plane with inverted symmetry.

and unambiguous identification of the twin-boundaries is possible. One reason is the difficulty to align the zone-axis of the observed tetrapod with the twin-planes. Another reason is the general complexity of the structure. In most cases other domains of the tetrapod hide the interesting regions. Therefore the TEM-images have to be analysed more carefully. In the present case the TEM-image of a tilted tetrapods core could be simulated by a dipod-structure consisting of three wurtzite domains, thus by the most elemental branched structure accessible in the framework of the octa-twin model. The result of the simulation is shown in Figure 3.8g. The main characteristics of the TEM data are reproduced nicely by the simulation.

In conclusion the data presented here and in article B.1 is supporting strongly the octa-twin-model. But the proof is mainly based on high resolution TEM images, i.e. on the measurement on individual nanocrystals. Therefore the possibility to find also individual tetrapods formed according to the polymorphism model cannot be excluded. In different works the authors come to the conclusion that the polymorphism model is the dominating architectural principle for CdE tetrapods. [104, 127] And in fact the crystalline phase could be varied from ZB to WZ by only minor modifications in the synthesis scheme. [36] Therefore none of the two models can be considered as the unique model. Instead the samples might consist of a mixture of nanocrystals based on both architectures. To ultimately decide for one model a deeper analysis would be necessary, for instance by a statistical analysis of the angles between the arms of a large number of tetrapods as it was demonstrated in the case of ZnO-tetrapods. [129]

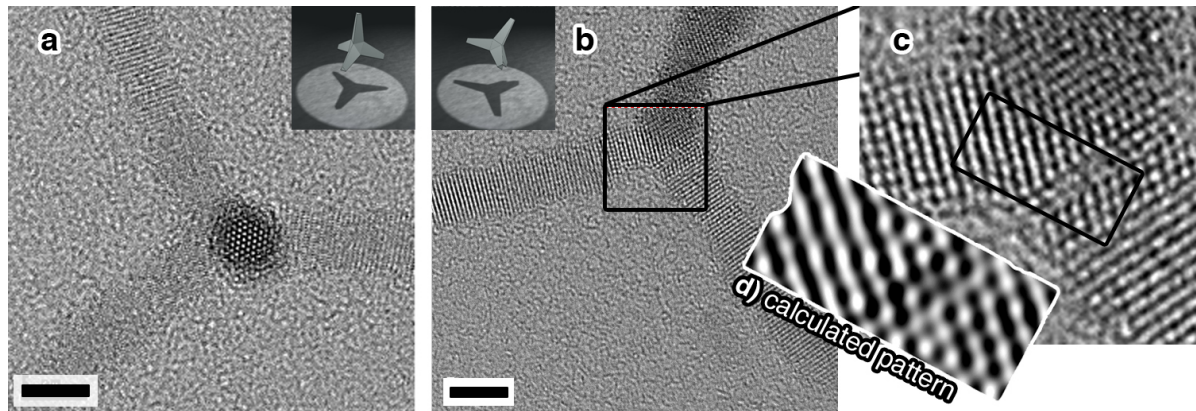


**Figure 3.8: High-Resolution TEM images of a tetrapod's core.** (a) A tetrapod in high resolution. On the upstanding arm the hexagonal structure can be recognised clearly. (b) The same tetrapod as in (a), only tilted with respect to the electron beam. (The insets in (a) and (b) illustrate schematically the orientation of the sample.) (c) Enlarged view on the tilted core, as marked in (b). The central region of this image could be simulated using a dipod-model such as shown in Figure 3.5(e). The result of the simulation is displayed in (d). The scale-bars represent 5 nm.

### 3.4 Discussion of the Growth-Mode

In the previous sections it was shown that the peculiar shape of the tetrapod is the result of the formation of twin-planes and that the growth of tetrapods can be triggered by the presence of a specific molecule. In this section we will discuss a possible model for the growth of the tetrapods.

Evidently the shape of the tetrapod is determined already at the beginning of the growth-process, i.e. during the nucleation of the particles or shortly after this event. First the tetrapod-cores have to form, and only after this stage the arms can grow to their final length. And apparently the short-chain phosphonic acid MPA plays an important role in this process. Its influence on the nucleation process is also supported by the observation of an acceleration of the nucleation-event at higher concentrations of MPA. The event of nucleation can be identified from the colour change of the reaction from clear to black or dark-brown. When no MPA is present the nucleation occurs only after ca. 60 seconds and later, whereas at high concentrations nucleation is observed within the first 30 seconds after the injection of the Te-TOP.

MPA is introduced into the synthesis as a precursor for the Cd-ions. The reactants present in the flask before the injection of tellurium comprise TOPO, ODPA, MPA and CdO. At high temperatures the CdO decomposes, but only in the presence of the phosphonic acids in sufficient amount, if the molar ratio phosphonic acid:Cd is higher than 2. The decomposition can be inferred from a colour change and the release of water, i.e. the formation of steam. After all CdO is decomposed, tellurium is injected in the form of Te-TOP. Therefore at the early stage of the reaction the monomers are

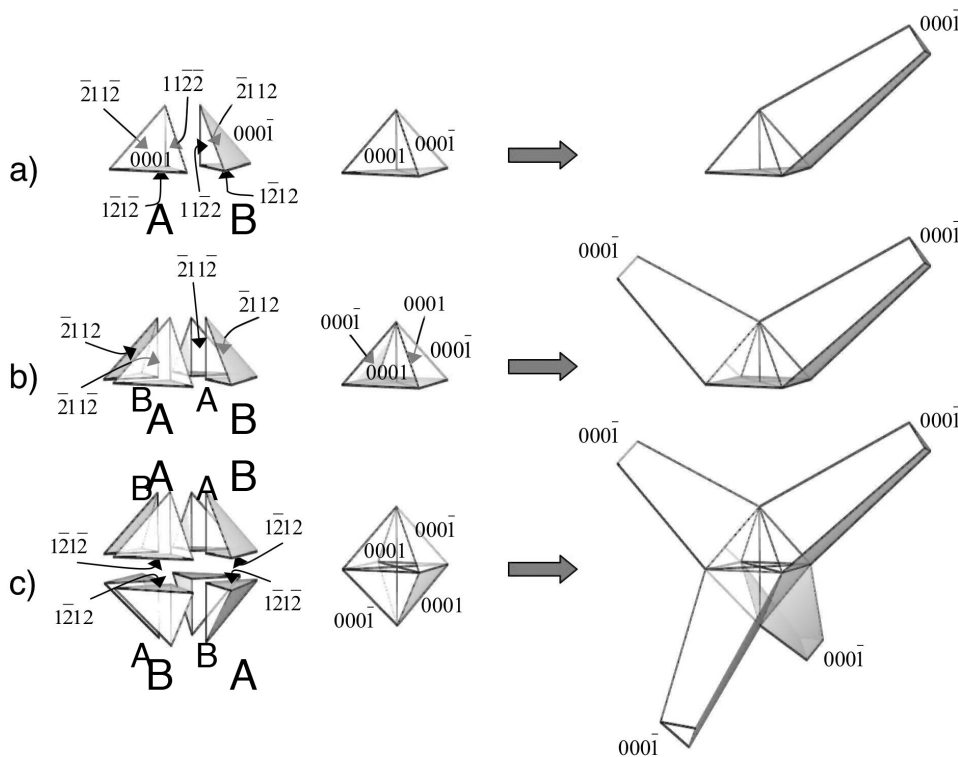


**Figure 3.9: Sketch of the architecture of the tetrapod.** The multiple-twin model describes the core of the tetrapod as composed of several wurtzite domains, but only every second of these domains is able to grow into a nanorod. There are two types of domains (*type A* and *type B*) and only domains of different type can be interconnected through a twin plane. Only domains of type B can evolve into a rod. The shape of the evolved nanocrystal, as sketched in the rightmost column at the base depends on the number of twins in its core. To form a dipod at least two twin planes have to be present as shown in the second line. The role of the MPA in the experiments is to trigger the formation of twin planes. The number of branches in the nanocrystal increases with the concentration of MPA. (see Figure 3.6)

present as complexes of the form Cd-ODPA, Cd-MPA and Te-TOP.

The principal difference between MPA and ODPA is the length of the alkyl chain. The ODPA is relatively bulky and heavy compared to the small MPA. The molecular weight of the complex Cd-ODPA is more than the double of that of Cd-MPA, and the volume (as estimated from the number of atoms other than H) is scaled by a factor of more than 4. From this we can assume that the diffusion coefficient of Cd-MPA is inferior to that of Cd-ODPA. Thus, especially at the beginning of the growth-process, we can expect that the Cd-monomers deposited onto the nanocrystal are mainly those bound to the shorter phosphonic acid. Due to the higher diffusion-coefficient their rate of deposition is much higher than that of the Cd-monomers stemming from the complexes Cd-ODPA. Overall the deposition-rate of Cd is the higher the more MPA is present. Here we assume that the reaction rate of Cd is much lower than that of

Te, therefore whenever a Cd-atom is deposited onto the crystals, also an atom of Te will be deposited. Under normal growth-conditions, the formation of twin-planes is actually not favoured energetically (see article B.1). But under the influence of the high deposition rate apparently it is favourable to form twin boundaries instead of growing on the lateral facets of the hexagonal structure. In fact, it is known that the formation of defects – and as such we have to consider the twin-boundary here – occurs when the growing crystal is not in thermodynamic equilibrium with its surrounding. [131] By the introduction of the twin planes the growth becomes more or less anisotropic. Instead of only one fast-growing facet in the case of non-twinned nanocrystals the number of fast-growing facets increases with the number of twin planes and thus material can be deposited more rapidly. A similar behaviour has also been reported on the growth of CdE-nanocrystals. [34, 50, 132] In these reports the shape-evolution was reduced to the effect of the monomer-concentration. By increasing the total concentration of available monomers the growth could be tuned from dots over rods to tetrapods.

Here, we should note that the presence of a small amount of MPA apparently offers a possibility to influence selectively on the early stage of the growth process. As soon as the MPA is consumed, i.e. when the complexes Cd-MPA are broken, the growth proceeds as the normal rod growth and only the arms of the tetrapods grow in their length.

## 4 Composition Control - Hybrid Materials

The relative ease to tune the properties of the nanocrystals is considered their main feature. But actually the range of accessible properties for one type of material is still relatively limited. Semiconductor nanocrystals function nicely as fluorescence markers, but it is still difficult to direct them specifically towards areas of interest. It would be therefore of advantage to design nanostructures that consist of different domains, each of these domains contributing with its particular properties to the entire object. There are several strategies to reach this target. A simple approach is to assemble different nanocrystals through pairs of complementary biomolecules such as single strands of DNA into larger structures. [133] By a more careful choice of the DNA-sequences, even dimers or chains of nanocrystals can be formed. [134,135] The big disadvantage of these nanostructures is their instability. The linker is stable under precisely defined conditions, otherwise it just releases the individual nanocrystals. A more promising approach is to fuse two materials together into a covalently bound object. This idea arose already shortly after a stable synthesis scheme for semiconductor nanocrystals was established. The fluorescence yield of these samples is relatively low, but it can be enhanced by covering the nanocrystals with a shell of a different material with a higher bandgap. By this the confinement can be improved and more importantly the surface of the luminescent core-material is more defined. Fluorescence quantum yield is reduced mainly due to nonradiative recombination of the exciton on sites of distorted lattice structure. Their number is reduced by the epitaxial deposition of a second material with a higher bandgap onto the surface of the nanocrystals, as demonstrated for *core-shell-nanocrystals* of CdSe/ZnS [136, 137] and CdSe/CdS [138]. In this case the band-edges of the core material are situated inside the bandgap of the shell, so that a stronger confinement of the exciton is achieved. But the shell-material also contributes as a passivation layer to the overall property of the nanocrystal (see article E.2). If the bands of the two materials are aligned in a staggered way, such that only one band-edge is placed in the bandgap of the other material, the fluorescence line is drastically red-shifted as recombination can occur in the interfacial region from the lower conduction-band to the higher valence-band. [139, 140] These core-shell-nanocrystals are the demonstration of the manipulation of only one property of the material, in the case mentioned above the fluorescence quantum yield is increased or shifted. But also hybrid nanostructures with a more sophisticated geometry have been prepared that meet the claim of uniting the functionality of two domains in one particle. Heterodimers of a fluorescent and a

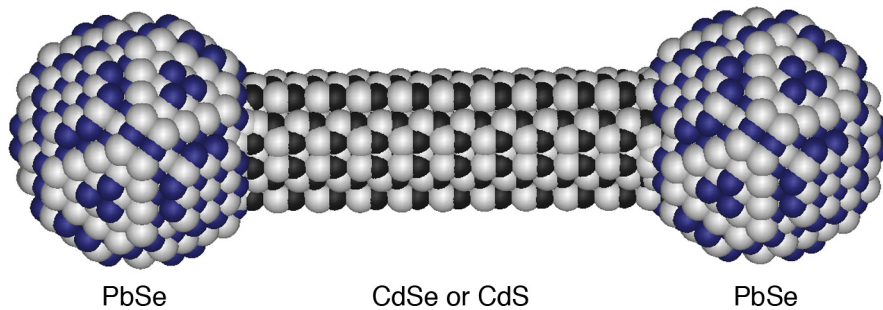


**Figure 4.1: Sketch of dumbbell-structures.** as discussed in this chapter. The central nanorod is of either CdS or CdSe, the tips are of either PbSe (in rock-salt structure as sketched), CdTe or Au.

magnetic fraction have been prepared. [141]<sup>1</sup> Other dimer structures involve domains of gold, which are of advantage for the attachment of functional molecules, such as Au-CoPt<sub>3</sub> [142] or Au-Fe<sub>3</sub>O<sub>4</sub> [143, 144]. Also heterodimers of materials with different wettability can be prepared. In this case the interfacial tension between a hexane- and water-phase can be influenced. [145]

Especially for the construction of hybrid nanocrystals based on spherical units there are different strategies. [29] In this chapter we will discuss two different approaches to synthesise hybrid nanocrystals based on a rod-structure. Nanorods are decorated with tips of a different material to form *nanodumbbells*. Examples of these structures are also discussed in more detail in the articles C.1 and C.2. Another way to circumvent the problems of an extended nucleation event is shown in article C.3. Here the synthesis of nanorods with a narrow size distribution is demonstrated. Spherical nanocrystals are used as seeds for the rods. By this the nucleation event for the nanorods is suppressed and the growth time is similar for all nanorods leading to very homogeneous samples.

## 4.1 Strategies for the Growth of Hybrid Materials

The techniques presented here rely on the heterogeneous nucleation of some material on nanocrystals present in the growth-solution. The first technique (see article C.1) is a pure demonstration of this principle. The second technique (see article C.2) is partially an extension of it and also an application.

It is known that in the presence of inhomogeneities or impurities the formation of nuclei is favoured. This can be observed as a hindrance in the synthesis of gold-nanocrystals according to the protocol of Brust et al. [146], in which slight impurities result in a broad size-distribution, as the nucleation event is no longer restricted to a short moment of high oversaturation in the liquid. The height of the nucleation-barrier is reduced

<sup>1</sup>It is actually under discussion in our group if the synthesis described in this reference [141] can be reproduced. It seems that the measurement of fluorescence from these nanostructures is impossible or simply stems from isolated CdS domains.

by the presence of nucleation-sites. [43] In the case of bubble-formation in a liquid this can be understood in a quite intuitive way. Small gas-filled cavities on the surface of the vessel are considered as the impurities. These cavities are initially filled with gas by simply flowing the liquid over the surface. If the radius of the meniscus of the gas bubbles is superior to the critical radius of the nucleation event (see Figure 1.3) the nucleation barrier is basically by-passed and the visible formation of free bubbles is controlled only by the growth of the bubbles in and on the cavity to a size sufficient for their detachment. After detachment some gas remains in the cavity as a seed for the subsequent bubble. [147] Generally, when depositing one material on top of another, the effect of the seed is to manipulate the curvature of the nucleus' surface. In dependence of the wettability of the nucleating material on the seed, the surface exhibits a more or less flat surface and in the nucleation event less material has to be assembled to obtain this curvature. [43]

In the experiments demonstrated in article C.1, the nucleation sites are the tips of nanorods. It has been discussed in the previous chapter that the binding strength of the surfactants depends sensitively on the type of the facet. Phosphonic acids bind strongly to the lateral facets of the rod, but only weakly to their basal facets. In the synthesis of the rods this enables the growth of these structures. In the experiments shown here, PbSe is grown on nanorods of CdS or CdSe. Due to the effect of the surfactants the lateral surfaces of the rods are completely passivated for the nucleation of PbSe as they offer no binding sites. As a result of this selective nucleation, *dumbbell*-structures of the form PbSe-CdSe-PbSe can be produced.

In article C.2 the starting point are dumbbell-structures as prepared in article C.1. In a subsequent step the material on the tips can be exchanged by gold-tips. This offers the possibility to access gold-tipped nanostructures based on materials on which the direct deposition of gold is impossible or relatively hard to achieve, as for instance on CdS-nanorods.

## 4.2 Synthesis of PbSe-Tipped Nano-Dumbbells

The synthesis of PbSe-tipped CdSe and especially CdS nanorods offers some insights into the growth mechanics of the nanorods. In both cases first the nanorods were prepared and purified. Then the synthesis of PbSe was carried out in the presence of the nanorods. As a solvent for the synthesis of PbSe diphenyl ether was used. It turned out that in this solvent the nanorods show a high stability. In higher co-ordinating solvents such as TOPO these nanostructures actually undergo a change of the shape at high temperatures. The solution in diphenyl ether instead could be heated to above 200°C without any visible effect on the shape of the nanocrystals. In the case of the synthesis of CdSe-based dumbbells, the Pb- and Se-precursors had to be injected slowly at a moderate temperature (130°C) to obtain samples with few loose PbSe-dots and a high yield of dumbbell-structures. An example of the structures synthesised with this method is shown in Figure 4.2.

In a different synthesis CdS-nanorods were used as nucleation sites for the PbSe. In

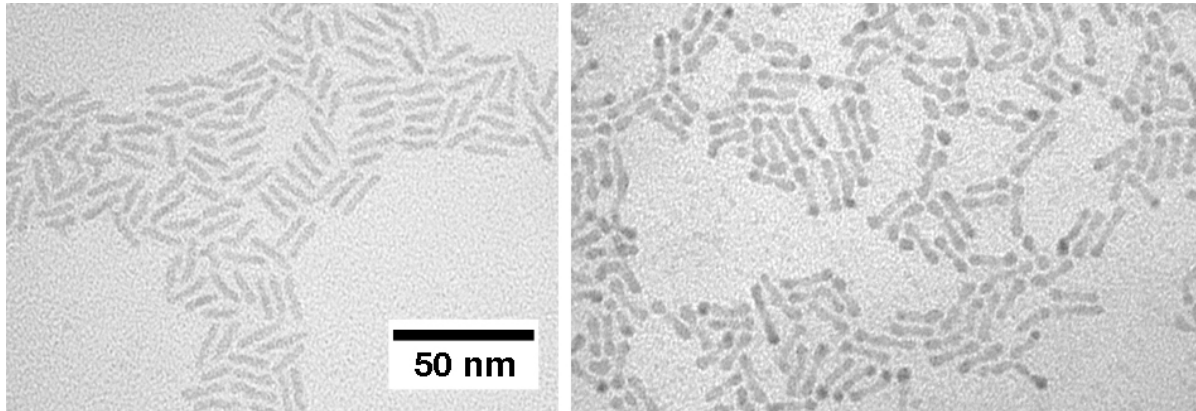


**Figure 4.2: Nano-dumbbells of PbSe-CdSe-PbSe.** The left panel shows pure CdSe-rods. These rods were used as backbone for the synthesis of PbSe-CdSe-PbSe dumbbells. The PbSe-fraction of the nanostructures can be identified from the slight broadening and darkening of the tip.

in this case the slow injection of PbSe yielded almost only separated PbSe-dots and CdS-nanorods. The nucleation of the PbSe-dots sets in after a considerable amount of PbSe-precursors was injected. In order to grow the PbSe onto the tips of the CdS-nanorods, the entire stock of the PbSe-precursors had to be injected rapidly into a hot (ca. 180°C) solution of CdS-nanorods. This process is always accompanied by the formation of free dots of PbSe, which are partially removed during the washing process. By variation of the amount of precursors a different coverage could be obtained, i.e. in one case the majority of nanocrystals showed a dumbbell-shape (PbSe-CdS-PbSe), in the other case the majority was in matchstick-shape (PbSe-CdS, see Figure 4.3). When a higher amount of precursors was used, the formation of dumbbells was preferred.

Apart from TEM-measurements also by means of optical absorption spectroscopy a sample of CdS-based matchsticks can be discerned from a sample of dumbbells. The low-bandgap material PbSe shows an absorption-feature in the infrared spectral region, in the range 1300–1800 nm, whereas the absorption feature of CdS- and CdSe-nanorods is situated between 400nm and 600nm. In the case of the PbSe-CdSe-PbSe-dumbbells the absorption peak relative to CdSe disappears entirely (see article C.1). We can speculate that the band-structure of the whole dumbbell is dominated also in the higher levels by the PbSe-sections. Furthermore it is interesting to notice that the nanocrystals can be excited in both the CdSe- and the PbSe-section, but electrons and holes will localise in the tips. [148] In the case of CdS-based matchsticks and dumbbells the influence of the CdS on the absorption is partially preserved, i.e. the absorption peak of the CdS-domain is still visible after the addition of the PbSe-dots. The difference between the two materials is certainly due to the different efficiency to form dumbbell structures. In the CdS-based samples always a considerable amount of matchstick is present, and the matchsticks are likely to show absorption features similar to the bare CdS nanorods.

A clear difference between the deposition of PbSe onto CdS and CdSe can be noticed.

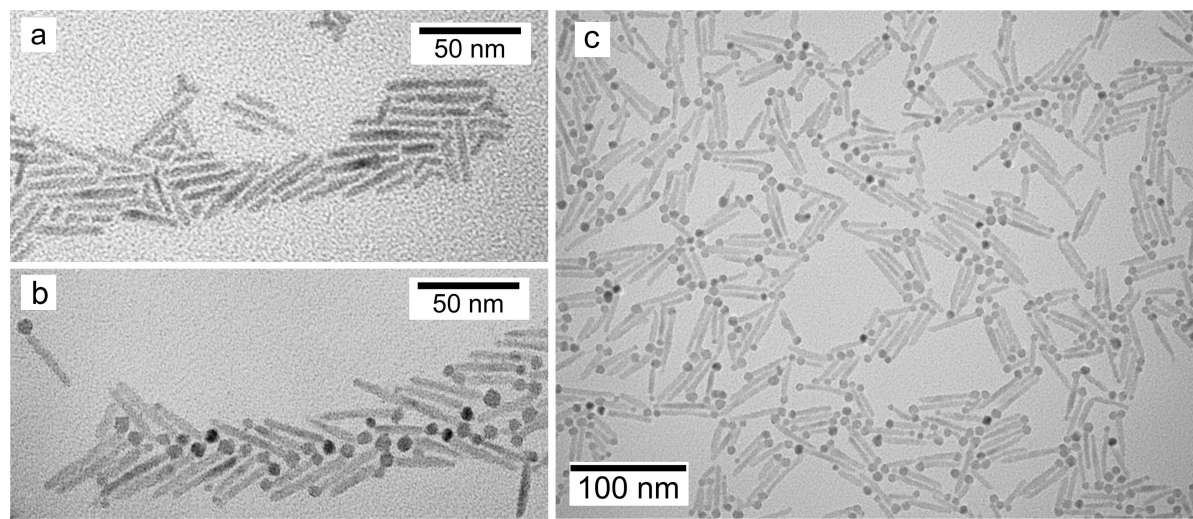


**Figure 4.3: Formation of matchsticks of PbSe-CdS.** (a) CdS-nanorods before the reaction with PbSe. (b) Area showing a high percentage of matchstick-structures. (c) Wide-field TEM-image of the sample shown in (b).

Apart from the different reaction-conditions also the morphology of the obtained samples is quite different. The tips of the CdSe-nanorods are completely covered with PbSe, whereas the PbSe-dots share only little surface with the CdS-nanorods. In the latter case the PbSe-dots are almost spherical and are interconnected with the CdS-nanorods seemingly only in one point. This drop-formation is the general behaviour of liquids that do not wet their surface. From this we can infer that the PbSe shows only a reduced wettability on the CdS-nanorods. This reduced wettability can also explain the difficulty to nucleate the domains of PbSe onto the CdS. As discussed in the previous section the nucleation barrier, in this case is reduced only by a small amount due to the low wettability. Therefore nucleation of PbSe on the tips of CdS does not take place during the slow addition of the precursors. It only occurs when the supersaturation of PbSe is sufficient to allow also the nucleation of free PbSe-nanocrystals. During the slow addition of monomers the supersaturation approaches slowly the value necessary for an efficient nucleation of PbSe-dots.

## 4.3 Synthesis of Au-Tipped Nano-Dumbbells

Gold nanocrystals are frequently used as model-systems for envisaged applications. [133, 134, 149, 150] The synthesis of these nanocrystals is developed for both organic [146, 151] and aqueous solutions [152, 153], they are relatively inert and furthermore this material is of great interest due to its surface-chemistry. Through a thiol-group, organic molecules and biomolecules can be easily reacted with gold-surfaces [151] whereas the bond between thiols and CdE-sections is stable only under well-defined conditions, such as a high pH-value [154, 155]. Also the electronic contact between CdE-nanocrystals and metallic

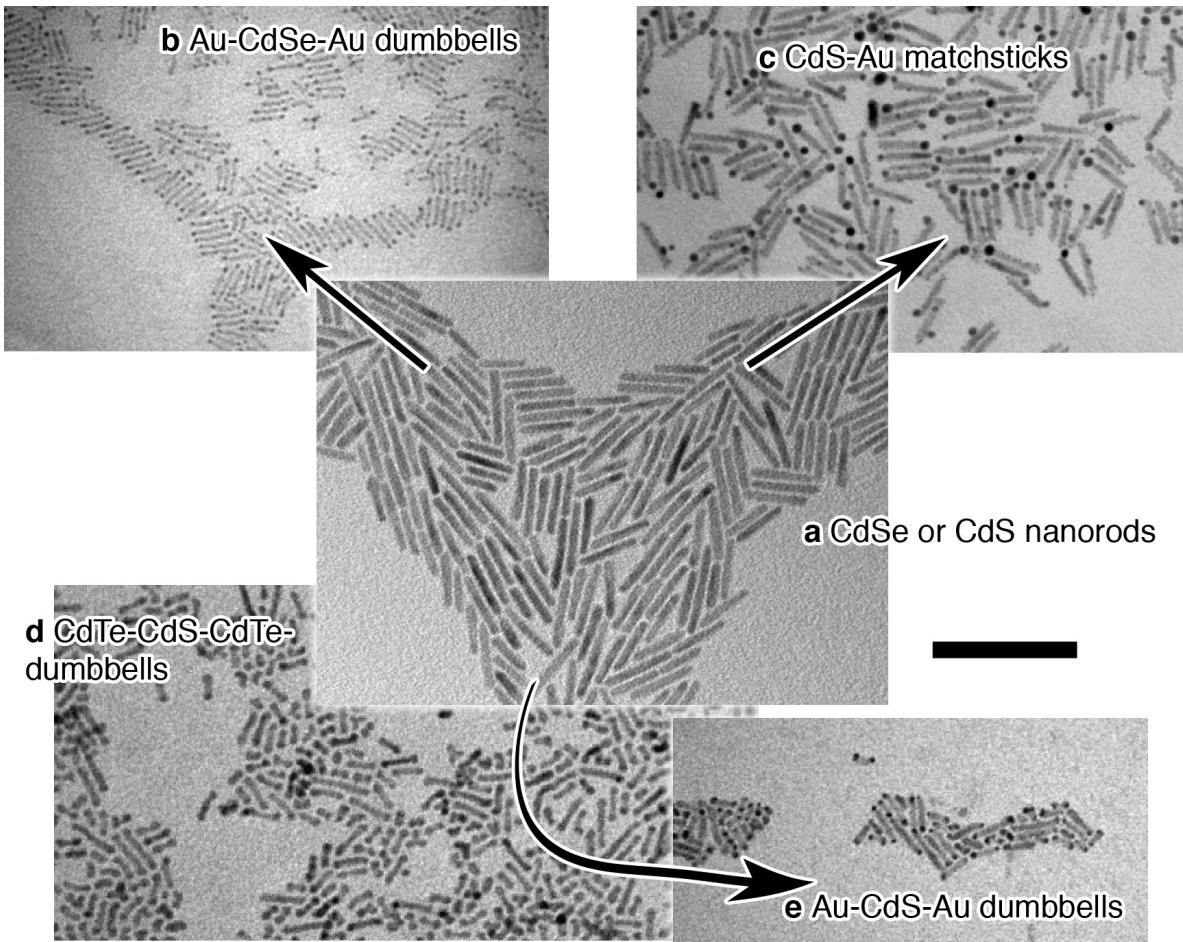


**Figure 4.4: Gold tips grown on nanorods with different methods.** Au-tips can be grown either directly (b,c) onto semiconductor nanorods (a shows CdS-nanorods) or through a sacrificial domain such as CdTe- or PbSe-tips (d,e). The scale bar is 100 nm.

electrodes is relatively weak but it might be improved by the epitaxial deposition of metals onto the nanocrystals.

The deposition of gold-tips on nanorods is relatively simple when CdSe-nanorods are employed. In this case the addition of a small amount of gold-ions leads to the formation of the tips. [156] An example is shown in Figure 4.4(b). By a careful adjustment of the experimental conditions one can produce either dumbbell- or matchstick-structures. [157] Only here the mechanism for the formation of the dumbbells is different from the mechanism for the formation of matchsticks of CdS-PbSe. First dumbbells of the form Au-CdSe-Au are produced which transform into Au-CdSe-matchsticks upon the continued addition of gold-precursors. In reference [157] the reason for this transformation is ascribed to a ripening-process in which one tip grows at the expenses of the other tip.

In the same way as in the case of PbSe-CdE-PbSe-nanodumbbells, the efficiency of

formation of these tips depends strongly on the material employed as template. The reaction between gold and CdS-nanorods is relatively slow, opening up the possibility to discern between the reactivity of the two different basal facets of the nanorods. [158] An example of CdS-Au-matchsticks is shown in Figure 4.4(c). In the case of CdTe, the growth of the Au-tips is possible only under highly controlled conditions. A too high amount of gold ions added to the CdTe-nanocrystals leads to agglomeration and dissolution of the CdTe-nanocrystals. This might be avoided by carrying out the reaction on a surface, see Figure 4.5. This synthesis-scheme is limited in as far as the nanocrystals are fixed on the surface. Another difficulty of the reaction of gold with CdE, but especially with CdTe-nanocrystals, is the fact that the nanocrystals might be strongly oxidised and thus lose length.

In article C.2 a different approach for the deposition of gold-tips on CdE-nanorods is described. It exploits the fact that CdTe and PbSe is easily oxidised by the gold-ions. In principle the CdTe or PbSe acts as a sacrificial material and is replaced by a gold-domain. The reaction-scheme is as follows. First rods of CdS or CdSe are synthesised. In case CdTe-tips should be grown onto the rods, the growth of the rods is quenched by the injection of a high quantity of Te:TOP. This complex has a reactivity that is higher than that of the corresponding complexes of selenium or sulphur and thus the material deposited after the injection is CdTe. This process is similar to that described in reference [159], only the surfactant ODPA is now used in a higher purity. In the same way as described in chapter 3 the CdTe therefore grows in a spherical shape instead of the branched morphology described in the reference. PbSe-tips are grown in the two-step synthesis as described in article C.1.

After the semiconductor tips are deposited, the sample is washed carefully and then reacted with gold. The stock solution for gold is prepared according to the protocol of reference [156]. This solution is relatively unstable and can be conserved only for a few hours before gold dots nucleate freely. Stable stock-solutions can be produced by splitting it into two parts. The gold-ions are dissolved separately from the surfactant dodecylamine. In one vial 6 g toluene, 80 mg chloroauric acid ( $\text{HAu(III)Cl}_4$ ) and 200 mg didodecyldimethyl ammonium bromide (DDAB) are mixed and sonicated to obtain a clear red solution. In a separate vial 350 mg dodecylamine are dissolved in 6 g toluene. In order to obtain a reactive solution the two solutions are combined in equal parts. After a while the colour of the mixture turns to pale yellow. This solution is added dropwise to a diluted solution of semiconductor dumbbells. A darkening of the nanocrystal solution indicates the formation of the gold-tips. On the TEM-images the success of the process can be inferred from the darkening of the tip-region (see Figure 4.4e).

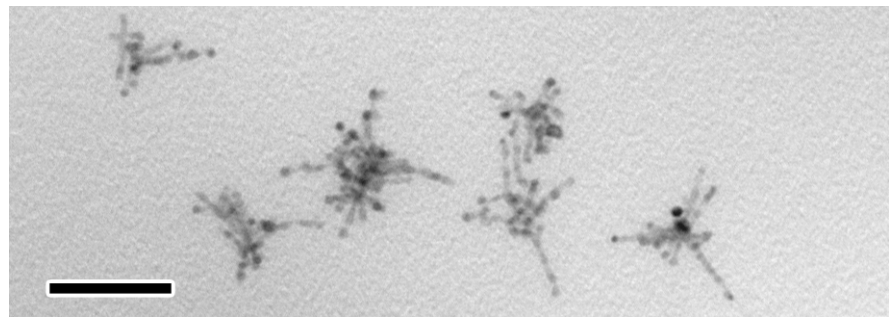


**Figure 4.5: Highly branched CdTe-nanocrystals with gold dots on their tips.** The reaction was carried out by first depositing the CdTe-nanocrystals on a surface, in this case on a TEM-grid. In a second step a solution of gold-ions was prepared and the TEM-grid was dipped into it for ca. 30 seconds. The scale-bar represents 100 nm.

# Conclusions

In this work the control over three different parameters of colloidal nanocrystals is demonstrated and discussed. These parameters comprise the size, the shape and the composition of the nanocrystals.

With standard protocols the size of colloidal semiconductor nanocrystals can be controlled relatively precisely for sizes above 2 nm. In this work a method for the synthesis of even smaller nanocrystals has been discussed for the case of CdSe. By this the accessible spectral range for the fluorescence of this material spans the entire visible spectrum from ca. 450 nm to ca. 700 nm. Contrary to the classical growth-mode that ultimately leads to the Ostwald-ripening, the growth of the smallest nanocrystals proceeds step-wise. Only several crystal-sizes are stable, the so-called *magic size clusters*. In this work their growth mechanism has been described experimentally and theoretically. Plausible models for the atomic structure of the individual clusters have been proposed. Future studies should primally investigate on the exact structure of the clusters for instance by means of X-ray-diffraction. Ligands seem to have a strong influence on the optical properties of the magic size clusters. The investigation on this effect and its correlation with eventual structural changes might be of great interest also for the understanding of the growth process. One could imagine that structural fluctuations induced by the binding and unbinding of ligands play an important role in this process.

Nanocrystals with an anisotropic shape can be synthesised. By controlling carefully the composition of the reaction solution the nanocrystals can be grown into a *branched structure*, of which the *tetrapod* with four arms joined in a central point is the most symmetric. One of the contributions of this work is the experimental identification of a dominant chemical additive that triggers the branching in CdTe nanocrystals, a phosphonic acid with a short alkyl chain, and the crystallographic discussion of the architecture of the branching point. In the future, research on these structures should be focused on applications. CdTe as a material is of interest for solar cells as it shows a broad absorbance over the entire visible spectral range. But to achieve higher efficiencies the individual nanocrystal need to be interconnected to ensure the transport of generated carriers onto the electrodes. Also, the exact nature of the branching point needs to be understood in more detail. For this aim extensive TEM-studies are necessary. Besides, it is also challenging to find optical or electronic properties that help to distinguish between the two models for the branching point.

A higher level of complexity can be attained by introducing domains of a different material into the nanocrystals. Two techniques to realise this formation of *hybrid structures* have been presented. The hybrid nanocrystals are based on rod-shaped backbones of CdSe or CdS. The tips of these rods are decorated with different materials, comprising metals (Au) and semiconductors (PbSe and CdTe). These materials are promising

candidates for many applications. For instance the semiconductor dumbbells PbSe-CdSe-PbSe with the wide bandgap material CdSe in between two domains of the low bandgap material PbSe could be exploited as nano-transistors. Efficient transport along the rod is possible only in the excited state. The synthesis scheme might be extended also to different materials. For instance one could imagine to use seeds of a more symmetric structure, as for example the *fcc*– or the rock-salt structure. In the case of *fcc* seeds one would expect that arms in the wurtzite structure would grow in four or even eight directions, similar to the polymorphism model presented for the growth of tetrapods. Rock-salt seeds should lead to the formation of six branches.

# Bibliography

- [1] H. W. Kroto, J. R. Heath, S. C. O'Brien, R. F. Curl, and R. E. Smalley. C60: Buckminsterfullerene. *Nature*, 318(6042):162–163, 1985.
- [2] Xavier Michalet, Fabien Pinaud, Thilo D. Lacoste, Maxime Dahan, Marcel P. Bruchez, A. Paul Alivisatos, and Shimon Weiss. Properties of fluorescent semiconductor nanocrystals and their application to biological labeling. *Single Molecules*, 2(4):261–276, 2001.
- [3] X. Michalet, F. F. Pinaud, L. A. Bentolila, J. M. Tsay, S. Doose, J. J. Li, G. Sundaresan, A. M. Wu, S. S. Gambhir, and S. Weiss. Quantum dots for live cells, in vivo imaging, and diagnostics. *Science*, 307(5709):538–544, 2005.
- [4] W. J. Parak, T. Pellegrino, and C. Plank. Labelling of cells with quantum dots. *Nanotechnology*, 16(2):R9–R25, 2005.
- [5] A. Nitzan and M. A. Ratner. Electron transport in molecular wire junctions. *Science*, 300(5624):1384–1389, 2003.
- [6] W. Haiss, C. S. Wang, I. Grace, A. S. Batsanov, D. J. Schiffrin, S. J. Higgins, M. R. Bryce, C. J. Lambert, and R. J. Nichols. Precision control of single-molecule electrical junctions. *Nature Materials*, 5(12):995–1002, 2006.
- [7] A. P. Alivisatos. Perspectives on the physical chemistry of semiconductor nanocrystals. *J. Phys. Chem.*, 100(31):13226–13239, 1996.
- [8] O. Masala and R. Seshadri. Synthesis routes for large volumes of nanoparticles. *Annual Review of Materials Research*, 34:41–81, 2004.
- [9] Brian L. Cushing, Vladimir L. Kolesnichenko, and Charles J. O'Connor. Recent advances in the liquid-phase synthesis of inorganic nanoparticles. *Chem. Rev.*, 104:3893–3946, 2004.
- [10] L. E. Brus. Electron–electron and electron–hole interactions in small semiconductor crystallites: The size dependence of the lowest excited electronic state. *J. Chem. Phys.*, 80(9):4403–4409, 1984.
- [11] S.V. Gaponenko. *Optical Properties of Semiconductor Nanocrystals*. Cambridge Studies in Modern Optics. Cambridge University Press, Cambridge, 1998.
- [12] Al. L. Efros and M. Rosen. The electronic structure of semiconductor nanocrystals. *Annu. Rev. Mater. Sci.*, 30:475–521, 2000.

- [13] G. Pellegrini, G. Mattei, and P. Mazzoldi. Finite depth square well model: Applicability and limitations. *Journal of Applied Physics*, 97(7):–, 2005.
- [14] A. P. Alivisatos. Nanocrystals: Building blocks for modern materials design. *Endeavour*, 21(2):56–60, 1997.
- [15] Wolfgang Johann Parak, Liberato Manna, Friedrich Christian Simmel, Daniele Gerion, and Paul Alivisatos. Quantum dots. In Günter Schmid, editor, *Nanoparticles: From Theory to Application*, pages 4–49. Wiley-VCH, Weinheim, 2004.
- [16] Y. Volokitin, J. Sinzig, L. J. deJongh, G. Schmid, M. N. Vargaftik, and I. I. Moiseev. Quantum-size effects in the thermodynamic properties of metallic nanoparticles. *Nature*, 384(6610):621–623, 1996.
- [17] Ph. Buffat and J-P. Borel. Size effect on the melting temperature of gold particles. *Physical Review A*, 13(6):2287–2298, 1976.
- [18] Michael Grätzel. Photoelectrochemical cells. *Nature*, 414(6861):338, 2001.
- [19] Wendy U. Huynh, Janke J. Dittmer, and A. Paul Alivisatos. Hybrid nanorod-polymer solar cells. *Science*, 295(5564):2425–2427, 2002.
- [20] D. Lee, M. F. Rubner, and R. E. Cohen. All-nanoparticle thin-film coatings. *Nano Letters*, 6(10):2305–2312, 2006.
- [21] David L. Klein, Paul L. McEuen, Janet E. Bowen Katari, Richard Roth, and A. Paul Alivisatos. An approach to electrical studies of single nanocrystals. *Applied Physics Letters*, 68(18):2574–2576, 1996.
- [22] David L. Klein, Richard Roth, Andrew K. L. Lim, A. Paul Alivisatos, and Paul L. McEuen. A single-electron transistor made from a cadmium selenide nanocrystal. *Nature*, 389(6652):699, 1997.
- [23] Y. Cui, U. Banin, M. T. Bjork, and A. P. Alivisatos. Electrical transport through a single nanoscale semiconductor branch point. *Nano Lett.*, 5(7):1519–1523, 2005.
- [24] Charles M. Lieber. One-dimensional nanostructures: Chemistry, physics & applications. *Solid State Communications*, 107(11):607–616, 1998.
- [25] Y. N. Xia, P. D. Yang, Y. G. Sun, Y. Y. Wu, B. Mayers, B. Gates, Y. D. Yin, F. Kim, and Y. Q. Yan. One-dimensional nanostructures: Synthesis, characterization, and applications. *Advanced Materials*, 15(5):353–389, 2003.
- [26] Sandeep Kumar and Thomas Nann. Shape control of ii-vi semiconductor nanomaterials. *Small*, 2(3):316–329, 2006.
- [27] Yadong Yin and A. Paul Alivisatos. Colloidal nanocrystal synthesis and the organic-inorganic interface. *Nature*, 437(7059):664, 2005.

[28] M. Green. The organometallic synthesis of bifunctional core/shell nanoparticles. *Small*, 1(7):684–686, 2005.

[29] Pantaleo Davide Cozzoli, Teresa Pellegrino, and Liberato Manna. Synthesis, properties and perspectives of hybrid nanocrystal structures. *Chemical Society Reviews*, 35(11):1195–1208, 2006.

[30] T. Vossmeyer, L. Katsikas, M. Giersig, I. G. Popovic, K. Diesner, A. Chemseddine, A. Eychmüller, and H. Weller. CdS nanoclusters: Synthesis, characterization, size dependent oscillator strength, temperature shift of the excitonic transition energy, and reversible absorbance shift. *J. Phys. Chem.*, 98(31):7665–7673, 1994.

[31] A. L. Rogach, A. Kornowski, M. Y. Gao, A. Eychmüller, and H. Weller. Synthesis and characterization of a size series of extremely small thiol-stabilized CdSe nanocrystals. *Journal of Physical Chemistry B*, 103(16):3065–3069, 1999.

[32] Janos H. Fendler. Atomic and molecular clusters in membrane mimetic chemistry. *Chem. Rev.*, 87(5):877–899, 1987.

[33] Liberato Manna, Erik C. Scher, and A. Paul Alivisatos. Synthesis of soluble and processable rod-, arrow-, teardrop-, and tetrapod-shaped CdSe nanocrystals. *Journal of the American Chemical Society*, 122(51):12700–12706, 2000.

[34] Z. A. Peng and X. G. Peng. Mechanisms of the shape evolution of CdSe nanocrystals. *Journal of the American Chemical Society*, 123:1389–1395, 2001.

[35] C. B. Murray, D. J. Norris, and M. G. Bawendi. Synthesis and characterization of nearly monodisperse CdE (E = S, Se, Te) semiconductor nanocrystallites. *Journal of the American Chemical Society*, 115:8706–8715, 1993.

[36] W. William Yu, Y. Andrew Wang, and Xiaogang Peng. Formation and stability of size-, shape-, and structure-controlled CdTe nanocrystals: Ligand effects on monomers and nanocrystals. *Chem. Mater.*, 15:4300–4308, 2003.

[37] L. Qu, Z. Peng, and X. Peng. Alternative routes toward high quality CdSe nanocrystals. *Nano Letters*, 1(6):333–337, 2001.

[38] Bifeng Pan, Rong He, Feng Gao, Daxiang Cui, and Yafei Zhang. Study on growth kinetics of CdSe nanocrystals in oleic acid/dodecylamine. *Journal of Crystal Growth*, 286(2):318, 2006.

[39] Z. Adam Peng and Xiaogang Peng. Formation of high-quality CdTe, CdSe, and CdS nanocrystals using CdO as precursor. *Journal of the American Chemical Society*, 123(1):183–184, 2001.

[40] Peter Reiss, Joël Bleuse, and Adam Pron. Highly luminescent CdSe/ZnSe core/shell nanocrystals of low size dispersion. *Nanoletters*, 2(7):781–784, 2002.

- [41] W. William Yu and Xiaogang Peng. Formation of high-quality CdS and other ii-vi semiconductor nanocrystals in noncoordinating solvents: Tunable reactivity of monomers. *Angewandte Chemie International Edition*, 41(13):2368–2371, 2002.
- [42] G. C. Benson and R. Shuttleworth. The surface energy of small nuclei. *The Journal of Chemical Physics*, 19(1):130–131, 1951.
- [43] Ivan V. Markov. *Crystal growth for beginners*. World Scientific, 2 edition, 2003.
- [44] Tadao Sugimoto. Preparation of monodispersed colloidal particles. *Advances in Colloid and Interface Science*, 28:65, 1987.
- [45] Victor K. LaMer and Robert H. Dinegar. Theory, production and mechanism of formation of monodispersed hydrosols. *Journal of the American Chemical Society*, 72(11):4847, 1950.
- [46] Xiaogang Peng, J. Wickham, and A. P. Alivisatos. Kinetics of II-VI and III-V colloidal semiconductor nanocrystal growth: “focusing” of size distributions. *Journal of the American Chemical Society*, 120(21):5343–5344, 1998.
- [47] P. S. Shah, J. D. Holmes, K. P. Johnston, and B. A. Korgel. Size-selective dispersion of dodecanethiol-coated nanocrystals in liquid and supercritical ethane by density tuning. *Journal of Physical Chemistry B*, 106(10):2545–2551, 2002.
- [48] D. V. Talapin, S. Haubold, A. L. Rogach, A. Kornowski, M. Haase, and H. Weller. A novel organometallic synthesis of highly luminescent CdTe nanocrystals. *J. Phys. Chem. B*, 105(12):2260–2263, 2001.
- [49] J.M. Klostranec and W.C.W. Chan. Quantum dots in biological and biomedical research: Recent progress and present challenges. *Advanced Materials*, 18(15):1953–1964, 2006.
- [50] Z. Adam Peng and Xiaogang Peng. Nearly monodisperse and shape-controlled CdSe nanocrystals via alternative routes: Nucleation and growth. *Journal of the American Chemical Society*, 124(13):3343–3353, 2002.
- [51] T.P. Martin. Shells of atoms. *Physics Reports*, 273:199–241, 1996.
- [52] Günter Schmid. Von Metallclustern und Clustermetallen. *Nachr. Chem. Tech. Lab.*, 35(3):249–254, 1987.
- [53] V. G. Albano, A. Ceriotti, P. Chini, G. Ciani, S. Martinengo, and W. M. Anker. Hexagonal close packing of metal atoms in new polynuclear anions  $[\text{rh}_{13}(\text{co})_{24}\text{h}_5\text{n}]^n$  (n=2 or 3) - x-ray structure of  $[(\text{ph}_3\text{p})_2\text{n}]_2[\text{rh}_{13}(\text{co})_{24}\text{h}_3]$ . *Journal of the Chemical Society-Chemical Communications*, (20):859–860, 1975.

[54] C. E. Briant, B. R. C. Theobald, J. W. White, L. K. Bell, D. M. P. Mingos, and A.J. Welch. Synthesis and X-ray structural characterization of the centered icosahedral gold cluster compound  $[\text{Au}_{13}(\text{PMe}_2\text{Ph})_{10}\text{Cl}_2](\text{PF}_6)_3$  - the realization of a theoretical prediction. *Journal of the Chemical Society-Chemical Communications*, (5):201–202, 1981.

[55] Günter Schmid, Reinhard Pfeil, Roland Boese, Friedhelm Bandermann, Sonja Meyer, Gijs H. M. Calis, and Jan W. A. van der Velden.  $\text{Au}_{55}[\text{P}(\text{C}_6\text{H}_5)_3]_{12}\text{Cl}_6$  - ein Goldcluster ungewöhnlicher Grösse. *Chemische Berichte*, 114(11):3634–3642, 1981.

[56] H. G. Boyen, G. Kästle, F. Weigl, B. Koslowski, C. Dietrich, P. Ziemann, J. P. Spatz, S. Riethmuller, C. Hartmann, M. Möller, G. Schmid, M. G. Garnier, and P. Oelhafen. Oxidation-resistant gold-55 clusters. *Science*, 297(5586):1533–1536, 2002.

[57] G. Schmid and W. Huster. Large transition-metal clusters, IV –  $\text{Ru}_{55}^-$ ,  $\text{Rh}_{55}^-$  and  $\text{Pt}_{55}^-$ -clusters. *Zeitschrift Für Naturforschung Section B*, 41(8):1028–1032, 1986.

[58] M. N. Vargaftik, V. P. Zagorodnikov, I. P. Stolyarov, I. I. Moiseev, V. A. Likhlobov, D. I. Kochubey, A. L. Chuvilin, V. I. Zaikovsky, K. I. Zamaraev, and G. I. Timofeeva. A novel giant palladium cluster. *Journal of the Chemical Society-Chemical Communications*, (14):937–939, 1985.

[59] G. Schmid, B. Morun, and J. O. Malm.  $\text{Pt}_{309}\text{Phen}_{36}^*\text{O}_{30\pm 10}$ , a 4-shell platinum cluster. *Angewandte Chemie-International Edition in English*, 28(6):778–780, 1989.

[60] Silke Behrens, Marco Bettenhausen, Andreas Eichhöfer, and Dieter Fenske. Synthesis and crystal structure of  $[\text{Cd}_{10}\text{Se}_4(\text{SePh})_{12}(\text{PPh}_3)_4]$  and  $[\text{Cd}_{16}(\text{SePh})_{32}(\text{PPh}_3)_2]$ . *Angewandte Chemie International Edition*, 36(24):2797–2799, 1997.

[61] V. N. Soloviev, A. Eichhofer, D. Fenske, and U. Banin. Size-dependent optical spectroscopy of a homologous series of CdSe cluster molecules. *J. Am. Chem. Soc.*, 123(10):2354–2364, 2001.

[62] A. Kasuya, R. Sivamohan, Y. A. Barnakov, I. M. Dmitruk, T. Nirasawa, V. R. Romanuk, V. Kumar, S. V. Mamykin, K. Tohji, B. Jeyadevan, K. Shinoda, T. Kudo, O. Terasaki, Z. Liu, R. V. Belosludov, V. Sundararajan, and Y. Kawazoe. Ultra-stable nanoparticles of CdSe revealed from mass spectrometry. *Nature Materials*, 3(2):99–102, 2004.

[63] N. Zheng, X. Bu, H. Lu, Q. Zhang, and P. Feng. Crystalline superlattices from single-sized quantum dots. *J. Am. Chem. Soc.*, 127(34):11963–11965, 2005.

[64] Aaron Puzder, Andrew J. Williamson, Natalia Zaitseva, Giulia Galli, Liberato Manna, and A. Paul Alivisatos. The effect of organic ligand binding on the growth

of CdSe nanoparticles probed by ab initio calculations. *Nanoletters*, 4(12):2361–2365, 2004.

[65] R. Lee Penn and Jillian F. Banfield. Oriented attachment and growth, twinning, polytypism, and formation of metastable phases: Insights from nanocrystalline  $\text{TiO}_2$ . *American Mineralogist*, 83(Sep-Oct):1077–1082, 1998.

[66] Zhiyong Tang, Nicholas A. Kotov, and Michael Giersig. Spontaneous organization of single CdTe nanoparticles into luminescent nanowires. *Science*, 297(5579):237–240, 2002.

[67] Kyung-Sang Cho, Dmitri V. Talapin, Wolfgang Gaschler, and Christopher B. Murray. Designing PbSe nanowires and nanorings through oriented attachment of nanoparticles. *Journal of the American Chemical Society*, 127:7140–7147, 2005.

[68] R. L. Penn. Kinetics of oriented aggregation. *Journal of Physical Chemistry B*, 108(34):12707–12712, 2004.

[69] V. Platschek, T. Schmidt, M. Lerch, G. Müller, L. Spanhel, A. Emmerling, J. Fricke, A.H. Foitzik, and E. Langer. Quantized aggregation phenomena in ii-vi-semiconductor colloids. *Berichte der Bunsen-Gesellschaft-Phys. Chem.*, 102(1):85–95, 1998.

[70] A. Puzder, A. J. Williamson, F. Gygi, and G. Galli. Self-healing of CdSe nanocrystals: First-principles calculations. *Physical Review Letters*, 92(21):217401, 2004.

[71] J. Frenzel, J. O. Joswig, P. Sarkar, G. Seifert, and M. Springborg. The effects of organisation, embedding and surfactants on the properties of cadmium chalcogenide (CdS, CdSe and CdS/CdSe) semiconductor nanoparticles. *European Journal of Inorganic Chemistry*, 2005(18):3585–3596, 2005.

[72] Chin-Yu Yeh, Z. W. Lu, S. Froyen, and Alex Zunger. Zinc-blende-wurtzite polytypism in semiconductors. *Physical Review B-Condensed Matter*, 46:10086–10097, 1992.

[73] Jason Taylor, Tadd Kippeny, and Sandra J. Rosenthal. Surface stoichiometry of CdSe nanocrystals determined by rutherford backscattering spectroscopy. *Journal of Cluster Science*, 12(4):571–582, 2001.

[74] A. Kasuya, Y. Noda, I. Dmitruk, V. Romanyuk, Y. Barnakov, K. Tohji, V. Kumar, R. Belosludov, Y. Kawazoe, and N. Ohuchi. Stoichiometric and ultra-stable nanoparticles of II-VI compound semiconductors. *European Physical Journal D*, 34(1-3):39–41, 2005.

[75] W. William Yu, Lianhua Qu, Wenzhuo Guo, and Xiaogang Peng. Experimental determination of the extinction coefficient of CdTe, CdSe, and CdS nanocrystals. *Chem. Mater.*, 15(14):2854–2860, 2003.

[76] Silke Behrens, Marco Bettenhausen, Anne C. Devenson, Andreas Eichhöfer, Dieter Fenske, Almut Lohde, and Ulrike Woggon. Synthesis and structure of nanoclusters  $[\text{Hg}_{32}\text{Se}_{14}(\text{SePh})_{36}]$ ,  $[\text{Cd}_{32}\text{Se}_{14}(\text{SePh})_{36}(\text{PPh}_3)_{12}]$ ,  $[\text{P}(\text{Et})_2(\text{Ph})\text{C}_4\text{H}_8\text{OSiMe}_3]_5[\text{Cd}_{18}\text{I}_{17}(\text{PSiMe}_3)_{12}]$  and  $[\text{N}(\text{Et})_3\text{C}_4\text{H}_8\text{OSiMe}_3]_5[\text{Cd}_{18}\text{I}_{17}(\text{PSiMe}_3)_{12}]$ . *Angewandte Chemie International Edition*, 35(19):2215–2218, 1996.

[77] V. N. Soloviev, A. Eichhofer, D. Fenske, and U. Banin. Molecular limit of a bulk semiconductor: Size dependence of the band gap in CdSe cluster molecules. *J. Am. Chem. Soc.*, 122(11):2673–2674, 2000.

[78] Will Kleber, Hans-Joachim Bautsch, and Joachim Bohm. *Einführung in die Kristallographie*. Verlag Technik, Berlin, 18. edition, 1998.

[79] L. Manna, L. W. Wang, R. Cingolani, and A. P. Alivisatos. First-principles modeling of unpassivated and surfactant-passivated bulk facets of wurtzite CdSe: A model system for studying the anisotropic growth of CdSe nanocrystals. *Journal of Physical Chemistry B*, 109(13):6183–6192, 2005.

[80] J. Y. Rempel, B. L. Trout, M. G. Bawendi, and K. F. Jensen. Properties of the CdSe(0001), (0001), and (1120) single crystal surfaces: Relaxation, reconstruction, and adatom and admolecule adsorption. *Journal of Physical Chemistry B*, 109(41):19320–19328, 2005.

[81] J. Y. Rempel, B. L. Trout, M. G. Bawendi, and K. F. Jensen. Density functional theory study of ligand binding on CdSe (0001), (0001), and (1120) single crystal relaxed and reconstructed surfaces: Implications for nanocrystalline growth. *Journal of Physical Chemistry B*, 110(36):18007–18016, 2006.

[82] L. F. Gou and C. J. Murphy. Solution-phase synthesis of  $\text{Cu}_2\text{O}$  nanocubes. *Nano Letters*, 3(2):231–234, 2003.

[83] Y. G. Sun and Y. N. Xia. Shape-controlled synthesis of gold and silver nanoparticles. *Science*, 298(5601):2176–2179, 2002.

[84] E. Lifshitz, M. Bashouti, V. Kloper, A. Kigel, M. S. Eisen, and S. Berger. Synthesis and characterization of PbSe quantum wires, multipods, quantum rods, and cubes. *Nano Letters*, 3(6):857–862, 2003.

[85] Sang-Min Lee, Young-wook Jun, Sung-Nam Cho, and Jinwoo Cheon. Single-crystalline star-shaped nanocrystals and their evolution: Programming the geometry of nano-building blocks. *Journal of the American Chemical Society*, 124:11244–11245, 2002.

[86] N. Zhao and L. M. Qi. Low-temperature synthesis of star-shaped pbs nanocrystals in aqueous solutions of mixed cationic/anionic surfactants. *Advanced Materials*, 18(3):359–+, 2006.

[87] V. F. Puntes, D. Zanchet, C. K. Erdonmez, and A. P. Alivisatos. Synthesis of hcp-Co nanodisks. *Journal of the American Chemical Society*, 124(43):12874–12880, 2002.

[88] S. H. Chen, Z. Y. Fan, and D. L. Carroll. Silver nanodisks: Synthesis, characterization, and self-assembly. *Journal of Physical Chemistry B*, 106(42):10777–10781, 2002.

[89] M. Maillard, S. Giorgio, and M. P. Pileni. Silver nanodisks. *Advanced Materials*, 14(15):1084–1086, 2002.

[90] M. F. Casula, Y. W. Jun, D. J. Zaziski, E. M. Chan, A. Corrias, and A. P. Alivisatos. The concept of delayed nucleation in nanocrystal growth demonstrated for the case of iron oxide nanodisks. *Journal of the American Chemical Society*, 128(5):1675–1682, 2006.

[91] N. R. Jana, L. Gearheart, and C. J. Murphy. Seed-mediated growth approach for shape-controlled synthesis of spheroidal and rod-like gold nanoparticles using a surfactant template. *Advanced Materials*, 13(18):1389–1393, 2001.

[92] X. C. Jiang and M. P. Pileni. Gold nanorods: Influence of various parameters as seeds, solvent, surfactant on shape control. *Colloids and Surfaces a-Physicochemical and Engineering Aspects*, 295(1-3):228–232, 2007.

[93] G. M. Dalpian, M. L. Tiago, M. L. del Puerto, and J. R. Chelikowsky. Symmetry considerations in CdSe nanocrystals. *Nano Letters*, 6(3):501–504, 2006.

[94] Philip B. Allen. Nanocrystalline nanowires: 1. Structure. *Nano Letters*, 7(1):6–10, 2007.

[95] Y. B. Mao, F. Zhang, and S. S. Wong. Ambient template-directed synthesis of single-crystalline alkaline-earth metal fluoride nanowires. *Advanced Materials*, 18(14):1895–1899, 2006.

[96] Xiaogang Peng, Liberato Manna, Weidong Yang, Juanita Wickham, Erik Scher, Andreas Kadavanich, and A P Alivisatos. Shape control of CdSe nanocrystals. *Nature*, 404(6773):59–61, 2000.

[97] Peter Lawaetz. Stability of the wurtzite structure. *Physical Review B-Condensed Matter*, 5(10):4039–4045, 1972.

[98] T. Akiyama, K. Nakamura, and T. Ito. Structural stability and electronic structures of inp nanowires: Role of surface dangling bonds on nanowire facets. *Physical Review B*, 73(23):235308, 2006.

[99] Koji Nishio, Toshiyuki Isshiki, Motoi Kitano, and Makoto Shiojiri. Structure and growth mechanism of tetrapod-like zno particles. *Philosophical Magazine A*, 76(4):889–904, 1997.

[100] Junqing Hu, Yoshio Bando, and Dmitri Golberg. Sn-catalyzed thermal evaporation synthesis of tetrapod-branched ZnSe nanorod architectures. *small*, 1(1):95–99, 2005.

[101] Ying-Chun Zhu, Yoshio Bando, Dong-Feng Xue, and Dmitri Golberg. Nanocable-aligned ZnS tetrapod nanocrystals. *Journal of the American Chemical Society*, 125(52):16196–16197, 2003.

[102] Q. Pang, L. J. Zhao, Y. Cai, D. P. Nguyen, N. Regnault, N. Wang, S. H. Yang, W. K. Ge, R. Ferreira, G. Bastard, and J. N. Wang. CdSe nano-tetrapods: Controllable synthesis, structure analysis, and electronic and optical properties. *Chemistry of Materials*, 17(21):5263–5267, 2005.

[103] Subashini Asokan, Karl M. Krueger, Vicki L. Colvin, and Michael S. Wong. Shape-controlled synthesis of CdSe tetrapods using cationic surfactant ligands. *small*, 3(7):1164–1169, 2007.

[104] Liberato Manna, Delia J. Milliron, Andreas Meisel, Erik C. Scher, and A. Paul Alivisatos. Controlled growth of tetrapod-branched inorganic nanocrystals. *Nature Materials*, 2:382–385, 2003.

[105] Xiaowei Teng and Hong Yang. Synthesis of platinum multipods: An induced anisotropic growth. *Nano Lett.*, 5(5):885–891, 2005.

[106] P. D. Cozzoli, E. Snoeck, M. A. Garcia, C. Giannini, A. Guagliardi, A. Cervellino, F. Gozzo, A. Hernando, K. Achterhold, N. Ciobanu, F. G. Parak, R. Cingolani, and L. Manna. Colloidal synthesis and characterization of tetrapod-shaped magnetic nanocrystals. *Nano Letters*, 6(9):1966–1972, 2006.

[107] Jiangtao Hu, Liang-shi Li, Weidong Yang, Liberato Manna, Lin-wang Wang, and A. Paul Alivisatos. Linearly polarized emission from colloidal semiconductor quantum rods. *Science*, 292(15 June):2060–2063, 2001.

[108] Ilan Gur, Neil A. Fromer, Michael L. Geier, and A. Paul Alivisatos. Air-stable all-inorganic nanocrystal solar cells processed from solution. *Science*, 310(5747):462–465, 2005.

[109] Oded Millo, David Katz, Dov Steiner, Eli Rothenberg, Taleb Mokari, Miri Kazes, and Uri Banin. Charging and quantum size effects in tunnelling and optical spectroscopy of CdSe nanorods. *Nanotechnology*, 15(1):R1, 2004.

[110] Y. Huang, X. F. Duan, Y. Cui, L. J. Lauhon, K. H. Kim, and C. M. Lieber. Logic gates and computation from assembled nanowire building blocks. *Science*, 294(5545):1313–1317, 2001.

[111] X. F. Duan, Y. Huang, Y. Cui, J. F. Wang, and C. M. Lieber. Indium phosphide nanowires as building blocks for nanoscale electronic and optoelectronic devices. *Nature*, 409(6816):66–69, 2001.

- [112] M. S. Gudiksen, K. N. Maher, L. Ouyang, and H. Park. Electroluminescence from a single-nanocrystal transistor. *Nano Letters*, 5(11):2257–2261, 2005.
- [113] M. Kazes, D. Y. Lewis, Y. Ebenstein, T. Mokari, and U. Banin. Lasing from semiconductor quantum rods in a cylindrical microcavity. *Advanced Materials*, 14(4):317–321, 2002.
- [114] H. Htoon, J. A. Hollingworth, A. V. Malko, R. Dickerson, and V. I. Klimov. Light amplification in semiconductor nanocrystals: Quantum rods versus quantum dots. *Applied Physics Letters*, 82(26):4776–4778, 2003.
- [115] L. S. Li, J. Walda, L. Manna, and A. P. Alivisatos. Semiconductor nanorod liquid crystals. *Nanoletters*, 2(6):557–560, 2002.
- [116] F. Dumestre, B. Chaudret, C. Amiens, M. Respaud, P. Fejes, P. Renaud, and P. Zurcher. Unprecedented crystalline super-lattices of monodisperse cobalt nanorods. *Angewandte Chemie-International Edition*, 42(42):5213–5216, 2003.
- [117] D. V. Talapin, E. V. Shevchenko, C. B. Murray, A. Kornowski, S. Forster, and H. Weller. CdSe and CdSe/CdS nanorod solids. *Journal of the American Chemical Society*, 126(40):12984–12988, 2004.
- [118] Liang-Shi Li and A. Paul Alivisatos. Semiconductor nanorod liquid crystals and their assembly on a substrate. *Advanced Materials*, 15(5):408–411, 2003.
- [119] Oliver Harnack, Claudia Pacholski, Horst Weller, Akio Yasuda, and Jurina M. Wessels. Rectifying behavior of electrically aligned zno nanorods. *Nanoletters*, 3(8):1097–1101, 2003.
- [120] K. M. Ryan, A. Mastroianni, K. A. Stancil, H. T. Liu, and A. P. Alivisatos. Electric-field-assisted assembly of perpendicularly oriented nanorod superlattices. *Nano Letters*, 6(7):1479–1482, 2006.
- [121] S. Gupta, Q. L. Zhang, T. Emrick, and T. P. Russell. Self-corralling nanorods under an applied electric field. *Nano Letters*, 6(9):2066–2069, 2006.
- [122] Z. H. Hu, M. D. Fischbein, C. Querner, and M. Drndic. Electric-field-driven accumulation and alignment of CdSe and CdTe nanorods in nanoscale devices. *Nano Letters*, 6(11):2585–2591, 2006.
- [123] I. Gur, N. A. Fromer, C. P. Chen, A. G. Kanaras, and A. P. Alivisatos. Hybrid solar cells with prescribed nanoscale morphologies based on hyperbranched semiconductor nanocrystals. *Nano Lett.*, 7(2):409–414, 2007.
- [124] J. B. Li and L. W. Wang. Shape effects on electronic states of nanocrystals. *Nano Letters*, 3(10):1357–1363, 2003.

- [125] S. Wei and S. Zhang. Structure stability and carrier localization in CdX (X=S, Se, Te) semiconductors. *Physical Review B*, 62(11):6944, 2000.
- [126] L. Manna, E. C. Scher, and A. P. Alivisatos. Shape control of colloidal semiconductor nanocrystals. *Journal of Cluster Science*, 13(4):521–532, 2002.
- [127] J. Y. Zhang and W. W. Yu. Formation of CdTe nanostructures with dot, rod, and tetrapod shapes. *Applied Physics Letters*, 89(12):123108, 2006.
- [128] S. Takeuchi, H. Iwanaga, and M. Fujii. Octahedral multiple-twin model of tetrapod zno crystals. *Philosophical Magazine A*, 69(6):1125–1129, 1995.
- [129] Hiroshi Iwanaga, Mitsuhiro Fujii, and Shin Takeuchi. Inter-leg angles in tetrapod zno particles. *Journal of Crystal Growth*, 183(1-2):190–195, 1998.
- [130] A. G. Kanaras, C. Sonnichsen, H. Liu, and A. P. Alivisatos. Controlled synthesis of hyperbranched inorganic nanocrystals with rich three-dimensional structures. *Nano Lett.*, 5(11):2164–2167, 2005.
- [131] N.W. Ashcroft and N.D. Mermin. *Festkörperphysik*. Oldenbourg, München, 2001.
- [132] X. Peng. Mechanisms for the shape-control and shape-evolution of colloidal semiconductor nanocrystals. *Advanced Materials*, 15(5):459–463, 2003.
- [133] C. A. Mirkin, R. L. Letsinger, R. C. Mucic, and J. J. Storhoff. A dna-based method for rationally assembling nanoparticles into macroscopic materials. *Nature*, 382:607–609, 1996.
- [134] A. P. Alivisatos, K. P. Johnsson, X. G. Peng, T. E. Wilson, C. J. Loweth, M. P. Bruchez, and P. G. Schultz. Organization of 'nanocrystal molecules' using dna. *Nature*, 382(6592):609–611, 1996.
- [135] Wolfgang J Parak, Daniele Gerion, Teresa Pellegrino, Daniela Zanchet, Christine Micheel, Shara C Williams, Rosanne Boudreau, Mark A Le Gros, Carolyn A Larabell, and A Paul Alivisatos. Biological applications of colloidal nanocrystals. *Nanotechnology*, 14:R15–R27, 2003.
- [136] Margaret A. Hines and Philippe Guyot-Sionnest. Synthesis and characterization of strongly luminescing ZnS-capped CdSe nanocrystals. *Journal of Physical Chemistry*, 100(2):468–471, 1996.
- [137] B. O. Dabbousi, J. Rodriguez-Viejo, F. V. Mikulec, J. R. Heine, H. Mattoussi, R. Ober, K. F. Jensen, and M. G. Bawendi. (CdSe)ZnS core-shell quantum dots: Synthesis and characterization of a size series of highly luminescent nanocrystallites. *Journal of Physical Chemistry B*, 101(46):9463–9475, 1997.

[138] X. G. Peng, M. C. Schlamp, A. V. Kadavanich, and A. P. Alivisatos. Epitaxial growth of highly luminescent CdSe/CdS core/shell nanocrystals with photostability and electronic accessibility. *Journal of the American Chemical Society*, 119(30):7019–7029, 1997.

[139] S. Kim, B. Fisher, H. J. Eisler, and M. Bawendi. Type-II quantum dots: CdTe/CdSe(core/shell) and CdSe/ZnTe(core/shell) heterostructures. *J. Am. Chem. Soc.*, 125(38):11466–11467, 2003.

[140] K. Yu, B. Zaman, S. Romanova, D. S. Wang, and J. A. Ripmeester. Sequential synthesis of type ii colloidal CdTe/CdSe core-shell nanocrystals. *Small*, 1(3):332–338, 2005.

[141] Hongwei Gu, Rongkun Zheng, XiXiang Zhang, and Bing Xu. Facile one-pot synthesis of bifunctional heterodimers of nanoparticles: A conjugate of quantum dot and magnetic nanoparticles. *Journal of the American Chemical Society*, 126(18):5664–5665, 2004.

[142] T. Pellegrino, A. Fiore, E. Carlino, C. Giannini, P. D. Cozzoli, G. Ciccarella, M. Respaud, L. Palmirotta, R. Cingolani, and L. Manna. Heterodimers based on CoPt<sub>3</sub>-Au nanocrystals with tunable domain size. *J. Am. Chem. Soc.*, 128(20):6690–6698, 2006.

[143] H. Yu, M. Chen, P. M. Rice, S. X. Wang, R. L. White, and S. Sun. Dumbbell-like bifunctional Au-Fe<sub>3</sub>O<sub>4</sub> nanoparticles. *Nano Lett.*, 5(2):379–382, 2005.

[144] H. Gu, Z. Yang, J. Gao, C. K. Chang, and B. Xu. Heterodimers of nanoparticles: Formation at a liquid-liquid interface and particle-specific surface modification by functional molecules. *J. Am. Chem. Soc.*, 127(1):34–35, 2005.

[145] N. Glaser, D. J. Adams, A. Böker, and G. Krausch. Janus particles at liquid-liquid interfaces. *Langmuir*, 22(12):5227–5229, 2006.

[146] M. Brust, M. Walker, D. Bethell, D.J. Schiffrin, and R. Whyman. Synthesis of thiol-derivatised gold nanoparticles in a two-phase liquid-liquid system. *J. Chem. Soc., Chem. Commun.*, 1994:801–802, 1994.

[147] S. F. Jones, G. M. Evans, and K. P. Galvin. Bubble nucleation from gas cavities - a review. *Advances in Colloid and Interface Science*, 80(1):27–50, 1999.

[148] A. Franceschetti, L. W. Wang, G. Bester, and A. Zunger. Confinement-induced versus correlation-induced electron localization and wave function entanglement in semiconductor nano dumbbells. *Nano Lett.*, 6(5):1069–1074, 2006.

[149] Christof M. Niemeyer. Nanoparticles, proteins, and nucleic acids: Biotechnology meets materials science. *Angewandte Chemie International Edition*, 40:4128–4158, 2001.

- [150] Andrea Schroedter and Horst Weller. Ligand design and bioconjugation of colloidal gold nanoparticles. *Angewandte Chemie International Edition*, 41(17):3218–3221, 2002.
- [151] M. Brust, J. Fink, D. Bethell, D. J. Schiffrin, and C. Kiely. Synthesis and reactions of functionalized gold nanoparticles. *Journal of the Chemical Society-Chemical Communications*, (16):1655–1656, 1995.
- [152] J. Turkevich, P. C. Stevenson, and J. Hillier. A study of the nucleation and growth processes in the synthesis of colloidal gold. *Discussions of the Faraday Society*, (11):55–75, 1951.
- [153] G. Schmid and A. Lehnert. The complexation of gold colloids. *Angewandte Chemie-International Edition in English*, 28(6):780–781, 1989.
- [154] J. Aldana, Y. A. Wang, and X. Peng. Photochemical instability of CdSe nanocrystals coated by hydrophilic thiols. *Journal of the American Chemical Society*, 123(36):8844–8850, 2001.
- [155] D. Gerion, F. Pinaud, S. C. Williams, W. J. Parak, D. Zanchet, S. Weiss, and A. P. Alivisatos. Synthesis and properties of biocompatible water-soluble silica-coated CdSe/ZnS semiconductor quantum dots. *Journal of Physical Chemistry B*, 105(37):8861–8871, 2001.
- [156] Taleb Mokari, Eli Rothenberg, Inna Popov, Ronny Costi, and Uri Banin. Selective growth of metal tips onto semiconductor quantum rods and tetrapods. *Science*, 304:1787–1790, 2004.
- [157] Taleb Mokari, Claudia G. Sztrum, Asaf Salant, Eran Rabani, and Uri Banin. Formation of asymmetric one-sided metal-tipped semiconductor nanocrystal dots and rods. *Nature Materials*, 4(11):855–863, 2005.
- [158] A. E. Saunders, I. Popov, and U. Banin. Synthesis of hybrid CdS-Au colloidal nanostructures. *Journal of Physical Chemistry B*, 110(50):25421–25429, 2006.
- [159] Delia J Milliron, Steven M Hughes, Yi Cui, Liberato Manna, Jingbo Li, Lin-Wang Wang, and A Paul Alivisatos. Colloidal nanocrystal heterostructures with linear and branched topology. *Nature*, 430(6996):190–195, 2004.



# Acknowledgements

Even though this work is declared to be written by only one person, many dear people have their share in its completion. Here I would like to express my gratitude to them.

- I am especially grateful to my long-time supervisor Wolfgang J. Parak. Already in the early days of my studies he offered me the possibility to obtain some insights into lab-work and the secrets of cookie-eating. Later he gave me the opportunity to work as a PhD-student in his project. During this time I have hopefully learned from his persistence. I am also thankful for his support during my stage in Lecce.
- To Liberato Manna for being my supervisor and advisor both in Munich and in Lecce. Also for being a seemingly inexhaustible source of ideas. Discussions with him were always fruitful and motivating.
- In Lecce I found a very dear and motivated colleague, Luigi Carbone, with whom I shared not only long sessions in front of the hood and in the TEM-chamber (even though also to me some of his activities in this room are a mystery). He was always willing to show me the nicest parts of his country. I am glad that I can consider him as a friend.
- To Roman Krahne for all his help, his company and regular 12:45-meetings at the Scaccia. Many thanks also to his wife Kirsten Wulf for the phantastic polpette and to their children Kolya and Luca for the countless nice and adventurous days.
- To Joachim P. Spatz for his support during the last stage of the thesis and for offering me a possibility to prosecute my work in Stuttgart.
- To Hermann E. Gaub for hosting the group of Wolfgang Parak in his institute and for being responsible or the unique atmosphere in the Gambicrew.
- To Teresa Pellegrino for being a dear friend and a fantastic co-worker.
- To Christian Kirchner for the all the wasted hours and to the “Koreaner” for inventing the Schweinebauch.
- Hermann Gumpp for all the discussions on any subject, the cocktails and the willingness to share my praises.
- To Manuel Piacenza for all the espressi and for always finding good reasons to have them. I enjoyed the visits in the palazzina A.

- To Concetta Nobile for her patience with my Italian, her regular lessons and her nice way to become upset.
- To Angelika Kardinal for her nice personality. The early parts of this work would not have been possible without her help and without her patience with our “dirty” work.
- Verena Thalhammer: Vielen Dank für Deine strengen Ermahnungen.
- To my numerous office mates, especially to those from Sommerfeldkeller who gave me always a nice welcome when I was in Munich. I hope we will manage to have an “Amerikaner” one day soon, Elias, Julia, Julchen and Robert. Also to the container-crew for all the entertainment: Albert, Allesandra, Angela, Benedetta, Eva, Gianvito, Philo, Riccardo and Marianna.
- To all the other colleagues from the NNL and the Gambi-Crew: Almu, Beno, Betty, Davide, Hendrik, Larissa, Gianvito, Monica, Ralph, Sonia, Stefania, Tim.
- To Mirja for proof-reading and her assistance, patience and for sometimes taking an air-plane to Puglia.

# Publications

---

## On Magic Size Clusters

---

**A.1** 69  
“Sequential Growth of Magic-Size CdSe Nanocrystals”  
S. Kudera, M. Zanella, C. Giannini, A. Rizzo, Y. Li, G. Gigli, R. Cingolani, G. Ciccarella, W.J. Parak, L. Manna  
*Adv. Mat.* **19**(4), pp. 548–552, 2007

**A.2** 88  
“Blue light emitting diodes based on fluorescent CdSe/ZnS nanocrystals”  
A. Rizzo, Y. Li, S. Kudera, F. Della Sala, M. Zanella, W.J. Parak, R. Cingolani, L. Manna, G. Gigli  
*Appl. Phys. Lett.* **90**(5), pp. 051106, 2007

---

## On Shape-Control and Shape-controlled Nanocrystals

---

**B.1** 93  
“Multiple Wurtzite Twinning in CdTe Nanocrystals Induced by Methylphosphonic Acid”  
L. Carbone, S. Kudera, E. Carlino, W.J. Parak, C. Giannini, R. Cingolani, L. Manna  
*J. Am. Chem. Soc.* **128**(3), pp. 748–755, 2006

**B.2** 109  
“Shape and Phase Control of Colloidal ZnSe Nanocrystals”  
P.D. Cozzoli, L. Manna, M.L. Curri, S. Kudera, C. Giannini, M. Striccoli, A. Agostiano  
*Chem. Mater.* **17**(6), pp. 1296–1306, 2005

**B.3** 127  
“Optical properties of tetrapod-shaped CdTe nanocrystals”  
D. Tarì, M. De Giorgi, F. Della Sala, L. Carbone, R. Krahne, L. Manna, R. Cingolani, S. Kudera, W.J. Parak  
*Appl. Phys. Lett.* **87**(22), pp. 224101, 2005

**B.4** 131  
“Electron-Hole Dynamics in CdTe Tetrapods”  
S. Malkmus, S. Kudera, L. Manna, W. J. Parak, M. Braun  
*J. Phys. Chem. B* **110**(35), pp. 17334–17338, 2006

**B.5** 137  
“Confinement Effects on Optical Phonons in Polar Tetrapod Nanocrystals Detected by Resonant Inelastic Light Scattering”  
R. Krahne, G. Chilla, G., C. Schüller, L. Carbone, S. Kudera, G. Mannarini, L. Manna, D. Heitmann, R. Cingolani  
*Nano Letters* **6**(3), pp. 478–482, 2006

**B.6** 146  
“Shape Dependence of the Scattering Processes of Optical Phonons in Colloidal Nanocrystals Detected by Raman Spectroscopy”  
R. Krahne, G. Chilla, C. Schüller, S. Kudera, D. Tarì, M. De Giorgi, D. Heitmann, R. Cingolani, L. Manna  
*J. Nanolectron. Optoelectron.* **1**(1), pp. 104–107, 2006

**B.7** 151  
“Confinement effects on optical phonons in spherical, rod- and tetrapod-shaped nanocrystals detected by Raman spectroscopy”  
C. Nobile, S. Kudera, A. Fiore, L. Carbone, G. Chilla, T. Kipp, D. Heitmann, R. Cingolani, L. Manna, R. Krahne  
*Phys. stat. sol. (a)* **204**(2), pp. 483–486, 2007

**B.8** 156  
“Confined Optical Phonon Modes in Aligned Nanorod Arrays Detected by Resonant Inelastic Light Scattering”  
C. Nobile, V.A. Fonoberov, S. Kudera, A. Della Torre, A. Ruffino, G. Chilla, T. Kipp, D. Heitmann, L. Manna, R. Cingolani, A.A. Balandin, R. Krahne  
*Nano Letters* **7**(2), pp. 476–479, 2007

---

## On Hybrid Nano-Materials

---

**C.1** 165  
“Selective Growth of PbSe on One or Both Tips of Colloidal Semiconductor Nanorods”  
S. Kudera, L. Carbone, M.F. Casula, R. Cingolani, A. Falqui, E. Snoeck, W.J. Parak, L. Manna  
*Nano Letters* **5**(3), pp. 445–449, 2005

**C.2** 178

“Selective reactions on the tips of colloidal semiconductor nanorods”  
L. Carbone, S. Kudera, C. Giannini, G. Ciccarella, R. Cingolani, P.D. Cozzoli, L. Manna  
*J. Mater. Chem.* **16**(40), pp. 3952–3956, 2006

**C.3** 184

“Synthesis and Micrometer-Scale Assembly of Colloidal CdSe/CdS Nanorods Prepared by a Seeded Growth Approach”  
L. Carbone, C. Nobile, M. De Giorgi, F. Della Sala, G. Morello, P. Pompa, M. Hytch, E. Snoeck, A. Fiore, I.R. Franchini, M. Nadasan, A.F. Silvestre, L. Chiodo, S. Kudera, R. Cingolani, R. Krahne, L. Manna  
*Nano Letters* **7**(10), pp. 2942–2950, 2007

---

**Reviews and Conference Proceedings**

---

**D.1** 209

“On the Development of Colloidal Nanoparticles towards Multifunctional Structures and their Possible Use for Biological Applications”  
T. Pellegrino, S. Kudera, T. Liedl, A. Muñoz Javier, L. Manna, W.J. Parak  
*small* **1**(1), pp. 48–63, 2005

**D.2** 226

“Synthesis and perspectives of complex crystalline nano-structures”  
S. Kudera, L. Carbone, M. Zanella, R. Cingolani, W.J. Parak, L. Manna  
*Phys. stat. sol. (a)* **203**(6), pp. 1329–1336, 2006

**D.3** 235

“Synthesis routes for the growth of complex nanostructures”  
S. Kudera, L. Carbone, E. Carlino, R. Cingolani, P.D. Cozzoli, L. Manna  
*Physica E* **37**(1–2), pp. 128–133, 2007

---

**Water-Solubility, Applications and Further Characterisation**

---

**E.1** 243

“Hydrophobic nanocrystals coated with an amphiphilic polymer shell: a general route to water soluble nanocrystals”  
T. Pellegrino, L. Manna, S. Kudera, T. Liedl, D. Koktysh, A.L. Rogach, S. Keller, J. Rädler, G. Natile, W.J. Parak  
*Nano Letters* **4**(4), pp. 703–707, 2004

**E.2** 268  
“Cytotoxicity of Colloidal CdSe and CdSe/ZnS Nanoparticles”  
C. Kirchner, T. Liedl, S. Kudera, T. Pellegrino, A. Muñoz Javier, H.E. Gaub, S. Stölzle, N. Fertig, W.J. Parak  
*Nano Letters* **5**(2), pp. 331–338, 2005

**E.3** 300  
“Quantum Dots on Gold: Electrodes For Photoswitchable Cytochrome c Electrochemistry”  
C. Stoll, S. Kudera, W.J. Parak, F. Lisdat  
*small* **2**(6), pp. 741–743, 2006

**E.4** 304  
“Catalytic and seeded shape-selective synthesis of II–VI semiconductor nanowires”  
A. Fasoli, A. Colli, S. Kudera, L. Manna, S. Hofmann, C. Ducati, J. Robertson, A.C. Ferrari  
*Physica E* **37**(1–2), pp. 138–141, 2007

**E.5** 309  
“Temperature and Size Dependence of Nonradiative Relaxation and Exciton-Phonon Coupling in Colloidal CdTe Quantum Dots”  
G. Morello, M. De Giorgi, S. Kudera, L. Manna, R. Cingolani, M. Annici  
*J. Phys. Chem. C* **11**(16), pp. 5846–5849, 2007

# A Magic Size Clusters

## A.1 Sequential Growth of Magic-Size CdSe Nanocrystals

S. KUDERA, M. ZANELLA, C. GIANNINI, A. RIZZO, Y. LI, G. GIGLI, R. CINGOLANI, G. CICCARELLA, W.J. PARAK, L. MANNA  
*Adv. Mat.* **19**(4), pp. 548–552, 2007

DOI: 10.1002/adma.200601015

## Sequential Growth of Magic-Size CdSe Nanocrystals\*\*

By Stefan Kudera, Marco Zanella, Cinzia Giannini, Aurora Rizzo, Yanqin Li, Giuseppe Gigli, Roberto Cingolani, Giuseppe Ciccarella, Werner Spahl, Wolfgang J. Parak, and Liberato Manna\*

Colloidal semiconductor nanocrystals have been exploited in several applications in which they serve as fluorophores, because of the tunability of the wavelength of the emitted light.<sup>[1-3]</sup> The possibility of exactly controlling the size of nanocrystals is of great importance in the development of these materials, as this will lead to nano-objects with well-defined and reproducible properties. Whereas this goal seems to be hard to achieve with large nanocrystals, it might be viable for clusters consisting of a few tens or hundreds of atoms, as in this size regime a handful of structures can have an exceptionally high stability and therefore would form preferentially over any other combination of atoms. This concept is already well-known for several metal clusters, as for some of them several "magic" structures exist that are formed by closed shells of atoms.<sup>[4-7]</sup> Cluster molecules that can be considered as the smallest building units of semiconductors have been investigated in the past.

As an example several tetrahedral cluster molecules based on the general formula  $[E_wM_x(SR)_y]^{z-}$  (where E = S or Se; M = Zn or Cd; and R = alkyl or aryl) or similar were reported some years ago.<sup>[8,9]</sup> The series was formed only by clusters

containing a well-defined number of atoms, and therefore, characterized by particularly stable structures; thus, these structures can also be termed "magic-size clusters" (MSCs). Different families of almost monodisperse CdS clusters of sizes down to 1.3 nm were reported by Vossmeyer et al.,<sup>[10]</sup> whereas CdSe MSCs were observed later in the solution growth of colloidal nanocrystals<sup>[11]</sup> and the various cluster sizes found were explained as arising from the aggregation of smaller clusters. Soloviev et al. synthesized and crystallized a homologous series of CdSe cluster molecules<sup>[12,13]</sup> (very similar in structure to those reported earlier<sup>[8,9]</sup>) that were capped by selenophenol ligands. Also in many high-temperature organometallic syntheses of colloidal CdSe nanocrystals, either the transient formation of ultrasmall, highly stable CdSe clusters was noticed,<sup>[14,15]</sup> or these clusters could be isolated using size-selective precipitation.<sup>[16,17]</sup> Recently, one type of CdSe MSC has been synthesized in a water-in-oil reverse-micelle system.<sup>[18]</sup>

Here, we report a method for controlling the sequential growth in solution of CdSe MSCs of progressively larger sizes. Each of these types of clusters is characterized by a sharp optical-absorption feature at a well-defined energy. During the synthesis, the relative populations of the different families of MSCs varied, as smaller MSCs evolved into larger MSCs. We can model the time evolution of the concentration of the various magic sizes using a modification of a continuous-growth model, by taking into account the much higher stability of the various MSCs over nanocrystals of any intermediate size.

For the synthesis of the CdSe MSCs reported here a mixture of dodecylamine and nonanoic acid was used to decompose cadmium oxide at 200 °C under an inert atmosphere. The resulting solution was stabilized at 80 °C and a stock solution of selenium in trioctylphosphine was injected into the flask. The temperature was kept at 80 °C throughout the synthesis. The low temperature ensured both slow nucleation and growth, as it produced large activation barriers for the two processes. The optical spectra of several aliquots taken during the synthesis are shown in Figure 1a. Some minutes after the injection, two well-defined absorption peaks appeared at 330 and 350–360 nm, as well as a shoulder around 384 nm. Over time, the peak at 330 nm disappeared, the peak at 360 nm kept losing intensity, the shoulder at 384 nm became a well-distinct peak, and a new peak showed up at 406 nm. Later, another shoulder appeared at longer wavelengths, which developed into a new absorption peak centered at 431 nm, followed by yet another peak at 447 nm. The position of all these peaks remained constant over time, whereas their rela-

[\*] Dr. L. Manna, S. Kudera, A. Rizzo, Dr. Y. Li, Prof. G. Gigli, Prof. R. Cingolani, Dr. G. Ciccarella  
National Nanotechnology Laboratory of CNR-INFM  
Distretto Tecnologico – ISUFI  
Via Arnesano, 73100 Lecce (Italy)  
E-mail: liberato.manna@unile.it  
S. Kudera, M. Zanella, Prof. W. J. Parak  
Center for Nanoscience  
Ludwig Maximilians Universität  
Amalienstraße 54, 80799 München (Germany)  
Dr. C. Giannini  
CNR-Istituto di Cristallografia (IC)  
Via Amendola 122/O, 70126 Bari (Italy)  
Dr. W. Spahl  
Department of Chemistry and Biochemistry  
Ludwig Maximilians Universität  
Butenandtstr. 5-13 F, 81377 München (Germany)

[\*\*] S. Kudera and M. Zanella contributed equally to this work. This work was supported by the European projects SA-NANO (contract number STRP 013698) and OLLA (contract number IST 004607), by the Italian MIUR 297 project (contract number 13587) by the Italian project FIRB NG-lab (contract number RBLA03ER38) and by the German research foundation (DFG, Emmy Noether program). We acknowledge Dr. Davide Cozzoli, Dr. Elvio Carlino, and Hermann Gumpf for many inspiring discussions. Supporting information is available online from Wiley InterScience or from the author.

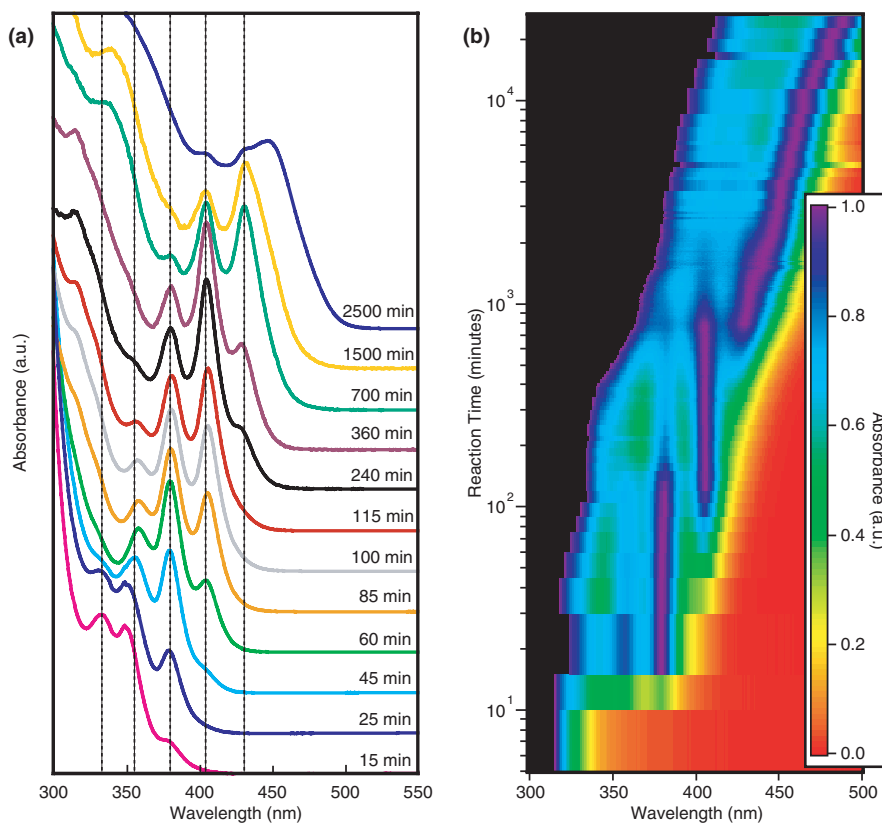


**Figure 1.** a) Absorption spectra of the growth solution recorded at different times and containing different populations of MSCs. b) This graph is built by stacking several horizontal stripes on top of each other, each of which corresponds to a color-coded plot of an optical-absorption spectrum, which were collected at progressively longer reaction times.

tive intensities varied so that the peak at the longest wavelength exhibited increasing intensity with respect to those at shorter wavelength, which eventually disappeared.

This behavior points to a size evolution through different families of increasingly larger clusters with high stabilities. If in fact these peaks corresponded to various excitonic transitions of a single family of cluster sizes in solution, and these clusters were steadily growing in size, then the spectral positions of the peaks would be shifting gradually towards longer wavelengths, and in addition their relative separation and their width would change (as their electronic structure is strongly sensitive to size<sup>[19]</sup>). Instead, the time evolution of the optical spectra did not point to a continuous growth but rather to the formation of new families of MSCs having larger sizes. Also the optical emission spectra of diluted samples of the growth solution showed the contribution of different families of MSCs (see Supporting Information). Over time, the average cluster size within each family remained constant, whereas the relative population of the various families changed in favor of the one with the largest size.

The graph in Figure 1b is built by stacking several horizontal stripes on top of each other, each of which corresponds to

a color-coded plot of an optical absorption spectrum that had been collected at progressively longer reaction times. Each spectrum, that is, each horizontal stripe, is normalized to the intensity of its dominant peak. Spectra were recorded roughly every 15 min. On the overall plot, therefore, the wavelength is reported on the horizontal axis, whereas the reaction time is reported on the vertical axis. At shorter reaction times ( $t < 10^2$  min) only a limited number of spectra could be collected and therefore the corresponding plots were replicated along the time scale until a new plot was available. As a consequence of this approach in constructing the overall plot, artificially sharp transitions are seen in it at these short times. The overall plot shows clearly the persistence over time of the peaks at 350–360 nm, 384 nm, 406 nm, and 431 nm, which therefore appear as vertical stripes. Once the various families of MSCs have evolved such that the peaks at 431–447 nm are the most intense ones, the overall spectral trends reflect rather the “continuous” size evolution of traditional nanocrystal growth kinetics.

The width of the various absorption peaks (see Fig. 1a) suggests that the size distribution within each family was quite narrow. As an example, the width-at-half-maximum of the

peak centered at 406 nm was approximately 20 nm (150 meV), which is rather close to the one reported by Kasyua et al.<sup>[18]</sup> for ultrasmall, extremely monodisperse CdSe nanoparticles prepared in reverse micelles and absorbing strongly at 415 nm (also approximately 20 nm or only slightly narrower). The overall growth kinetics did not change much neither for syntheses carried out at lower temperatures (peak widths could not be narrowed further) nor at moderately higher temperatures (peak widths were slightly broader), as in both cases the changes over time in the relative populations of the various families of MSCs followed the same trend as above.

The mechanism by which the growth of these clusters proceeded in solution is definitely fascinating. At the very simplest level, the size evolution of a nanocrystal can be thought of as being the result of a competition between the attachment and detachment of single atoms to its surface. Based on this picture, we have developed a growth model that reproduces the time evolution of the relevant absorption features of the various families of MSCs. The experimental parameters for the various families of MSCs were extracted by performing a Gaussian deconvolution of the absorption spectra. For this fit we assumed that the contribution of a single family of MSCs consisted of a narrow Gaussian function that represents the lowest exciton peak and of a much broader Gaussian that models the absorbance at shorter wavelengths (see the Supporting Information for details). The key assumption of our model states that once a cluster has grown to a magic size, such a size is so stable that no atoms can detach from it. Therefore it can only grow further, but it cannot shrink. Any cluster with a size intermediate between two magic sizes can either grow to reach the larger of the two magic sizes, or shrink to the smaller one. Figure 2 reports with different marker types the intensities of the exciton peaks from the various families of MSCs over reaction time as derived from the fit to the experimental spectra, whereas solid lines represent the trends in the intensities of such peaks as derived from the pro-

posed growth model. This fitting procedure reflects qualitatively the actual trends in the growth of the various families of MSCs.

A control experiment that supports our model was carried out. A synthesis of MSCs was performed and thereby the nanocrystals were extracted from the solution using precipitation and purified by repeated washing. This sample, which contained different families of MSCs, was redissolved in the same mixture of surfactants used for the synthesis of MSCs and the mixture was heated at 80 °C for several hours. Therefore, all conditions were similar to those used for the synthesis of MSCs, with the only difference being that no free monomers were present in this experiment. Optical-absorption spectra on aliquots taken from this mixture at different times during the heating did not show any remarkable variation in the intensity of the various peaks, nor any shift in their positions, indicating no further evolution in the distribution of the families of MSCs. The results of this control experiment have two important implications. One is that the various MSCs were stable and that they did not undergo any shrinking or ripening process, as opposed to the classical case of a sample containing a wide distribution of colloidal crystal sizes, for which Oswald-ripening processes dominate if there is a shortage of monomers.<sup>[20]</sup> The other is that no aggregation occurred among smaller clusters to form larger clusters. Both implications support our growth model.

The novelty of the synthetic approach developed here is that it yields only MSCs. These are not a side product of a synthesis that yields much larger nanocrystals, nor are much larger nanocrystals formed as a side product in our syntheses. Furthermore, as the growth is slow, the synthesis is reproducible and indeed it can be stopped whenever a given distribution of various families of MSCs is reached. Then, from this final solution, the largest family of MSCs present can be isolated using a size-selective precipitation. A typical set of optical absorption spectra before and after size-selective precipitation is reported in Figure 3a. The isolation of MSCs of smaller sizes from this solution is in principle possible but laborious, as they are contaminated by a small percentage of the largest MSCs.

Transmission electron microscopy (TEM) analysis on aliquots extracted from the growth solution and on size-selected samples revealed that these MSCs have roughly spherical shapes and that they are not aggregated. However, a more detailed analysis based on electron microscopy and aimed at determining average sizes and size distributions was strongly limited by the extremely small sizes of such clusters. Wide-angle X-ray diffraction analysis on size-selected samples indicated cluster sizes ranging from 1.5 to 2.0 nm for the families of largest MSCs (those absorbing strongly at 406, 431, and 447 nm, respectively) and elemental analysis of these size-selected and purified clusters showed that they are all Cd-rich, with Cd/Se ratios ranging from 1.1 to 1.3. No further structural information could be inferred from mass spectrometry, as the ionization of these samples in a matrix-assisted laser desorption ionization time-of-flight mass spectrometry (MALDI-

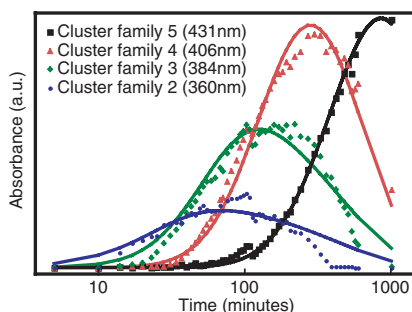


**Figure 2.** Development over time of the intensities of the individual absorption peaks from the various MSCs. These were extracted from the normalized optical absorption spectra, as shown in Figure 1. The families of smallest MSCs as identified from the optical spectra (those showing a peak at 330 nm) were not considered in the fit, as their absorption spectra became too weak a few minutes after their formation. Solid lines represent the fits to these trends using the proposed growth model.

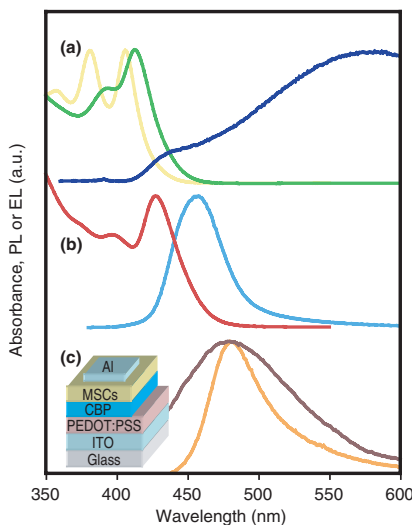


**Figure 3.** a) Optical absorption spectra of a sample (yellow) before size-selective precipitation, and optical absorption (green) and fluorescence spectra (blue) after size-selective precipitation. b) Optical absorption (red) and fluorescence spectra (cyan) of the CdSe/ZnS core-shell nanocrystals prepared from the size-selected sample of MSCs shown in (a). c) Photoluminescence from a film of core-shell nanocrystals (light brown) and EL (brown) from a light-emitting diode based on these nanocrystals. The inset displays the schematic layout of the EL device.

TOF-MS) setup yielded very similar fragmentation patterns, even for nanocrystals as large as 3 nm in diameter, but did not yield any clear fingerprints of the original clusters.

The synthesis of different families of MSCs is of technological interest as it yields nanocrystals that always have the same sizes and, therefore, reproducible optical properties, such as, for instance, the range of emitted light. The CdSe clusters reported in this work displayed considerable emission from trap states (see Fig. 3a) and band-edge emission was only clearly visible at very high dilutions. So, after size-selective precipitation, the absorption features were slightly broadened and red-shifted. Both effects could be the result of stripping off of some molecules from the surface of the MSCs during cleaning. This might have resulted in a partial reconstruction of the nanocrystal surface, with a concomitant variation of the overall electronic properties of the clusters.<sup>[21,22]</sup> By adding fresh surfactants, we could partially cancel this effect. Light emission from these clusters occurred almost exclusively from trap states. However, when a ZnS shell was grown on the size-selected nanocrystals, such as, for instance, on those originally absorbing at 406 nm, the resulting core/shell nanocrystals emitted only from band-edge states (Fig. 3b). The photoluminescence (PL) quantum yield from these samples varied from synthesis to synthesis (in the range between 35 and 60 %), but remained constant for each sample, even for a few months after the synthesis.

A potential application of the blue-light-emitting nanocrystals synthesized in this work is, for instance, a light-emitting

diode. There have been several studies of nanocrystal-based light-emitting diodes in the last years,<sup>[23–28]</sup> but only a few devices have been reported so far in which the blue emission originated from nanocrystals.<sup>[26]</sup> We built a blue-light-emitting diode in which the active layer was a blend of the blue-light-emitting CdSe/ZnS nanocrystals, prepared as described above, and 4,4',*N,N'*-diphenylcarbazole (CBP). The device, whose geometry and characteristics are displayed in Figure 3c, showed an electroluminescence (EL) peak at 485 nm, which is attributed to the emission of the CdSe/ZnS nanocrystals, in agreement with the PL spectra from a solid film of the same nanocrystals (Fig. 3c). The red-shift in the emission for the clusters in the film relative to that for the clusters in solution is attributed to the energy transfer within the sample.<sup>[29]</sup> The increase in peak width of the EL is likely to be an effect of both environmental broadening and local heating of the sample under current flow.<sup>[25]</sup>

In conclusion, we have reported a method to control the sequential growth of CdSe magic-size clusters of progressively larger sizes. We modeled the time evolution of the concentration of the various magic sizes using a slight modification of a continuous-growth model. After the synthesis, we could isolate MSCs of a given size and grow a ZnS shell on them. Finally, we demonstrated the fabrication of a hybrid organic/inorganic light-emitting diode based on these nanocrystals with blue-light emission. The concept of sequential growth of different families of MSCs reported here is of general interest and can be potentially extended to other materials, provided that suitable conditions are found to slow down the nucleation and the growth rate of the nanocrystals. In addition, we believe that this approach can be followed to synthesize more elaborate nanostructures, such as, for instance, doped nanocrystals.<sup>[30–36]</sup> A route to prepare doped nanocrystals could for instance be through the controlled formation of extremely small clusters, such as those reported in this work, but having a certain number of doping atoms already embedded in them. It might be likely, for instance, that such small cluster molecules could gain an additional stability (and therefore could be formed preferentially) if one or more “impurity atoms” were present in their structure. This possibility is currently under investigation in our groups.

## Experimental

**Synthesis of Magic-Size CdSe Nanocrystals:** 1 g of cadmium oxide (99.99 %), 4 g of dodecylamine (98 %), and 4 g of nonanoic acid (97 %) were mixed in a three-necked flask. The flask was pumped to vacuum at 100 °C for 15 min and then heated to above 200 °C under nitrogen to decompose the CdO. The temperature was then lowered to 80 °C and 20 g of a solution of Se in triethylphosphine (10 % in weight of Se) was injected. After the injection the temperature dropped and it was allowed to recover to 80 °C (but not higher). During the growth, 0.1 mL of the growth solution was extracted at time intervals ranging from 3 min (at the early stages of growth) to several hours (after several hundred minutes of growth) and diluted into a known amount of toluene. Therefore, all spectra could be scaled according to the dilution factor.

**Size-Selective Precipitation:** After the synthesis, the growth solution was transferred to a glove-box. Ethyl acetate was added to this solution, followed by methanol until a persistent cloudiness was observed. An amount of methanol ranging from 50 to 150 mL was required, depending on the distribution of MSCs present in the solution. Ethyl acetate was needed to prevent phase segregation, as methanol and tri-octylphosphine have a low miscibility. This solution was centrifuged and the precipitate was washed again by adding few milliliters of ethyl acetate and methanol. The final precipitate was redissolved in toluene. By using this procedure, the largest MSCs are almost quantitatively separated from the smaller MSCs present.

**ZnS Shell Growth:** This was carried out following standard published procedures [37], except for the shell-growth temperature, which was set at 80 °C for the first injection and then steadily raised to 120 °C during the following injections. The starting MSCs could not resist the heating in trioctylphosphine/trioctylphosphine oxide above 80 °C for too long.

**Fabrication and Characterization of the Electroluminescent Devices:** Devices consisting of ITO/PEDOT-PSS/CBP:CdSe/ZnS/Al were fabricated as follows. A hole-transporting layer (100 nm) of poly(3,4-ethylenedioxythiophene):poly(styrenesulfonate) (PEDOT:PSS), used to lower the hole-injection barrier at the indium tin oxide (ITO) surface, was spin-deposited onto a cleaned ITO-coated glass substrate (120 nm, 15 Ω square<sup>-1</sup>). The layer was then heated at 110 °C for 10 min to remove residual solvent. Then, a layer of a blend of CdSe/ZnS nanocrystals and CBP (100 nm) was spin-coated from a chloroform solution on the surface of the PEDOT:PSS layer. Finally, a 150 nm thick Al layer was deposited by thermal-evaporation at a pressure of 4 × 10<sup>-6</sup> mbar (1 bar = 10<sup>5</sup> Pa). PL spectra were recorded on thin films and CHCl<sub>3</sub> solutions, by using a Cary Eclipse fluorescence spectrophotometer with an intense Xenon flash lamp. Absorption measurements were carried out using a Cary 5000 UV-vis spectrophotometer. The EL spectra were measured by a Spectroradiometer OL 770. All the measurements were carried out at room temperature under air.

Received: May 9, 2006

Revised: September 18, 2006

Published online: January 24, 2007

- [1] X. Michalet, F. F. Pinaud, L. A. Bentolila, J. M. Tsay, S. Doose, J. J. Li, G. Sundaresan, A. M. Wu, S. S. Gambhir, S. Weiss, *Science* **2005**, *307*, 538.
- [2] I. L. Medintz, H. T. Uyeda, E. R. Goldman, H. Mattoussi, *Nature Mater.* **2005**, *4*, 435.
- [3] W. J. Parak, T. Pellegrino, C. Plank, *Nanotechnology* **2005**, *16*, R9.
- [4] J. Pedersen, S. Bjornholm, J. Borggreen, K. Hansen, T. P. Martin, H. D. Rasmussen, *Nature* **1991**, *353*, 733.
- [5] T. P. Martin, T. Bergmann, H. Gohlich, T. Lange, *J. Phys. Chem.* **1991**, *95*, 6421.
- [6] T. P. Martin, *Phys. Rep.* **1996**, *273*, 199.
- [7] W. Ekardt, *Z. Phys. B: Condens. Matter* **1997**, *103*, 305.
- [8] G. S. H. Lee, D. C. Craig, J. Ma, M. L. Scudder, T. D. Bailey, I. G. Dance, *J. Am. Chem. Soc.* **1988**, *110*, 4863.
- [9] N. Herron, J. C. Calabrese, W. E. Farneth, Y. Wang, *Science* **1993**, *259*, 1426.
- [10] T. Vossmeye, L. Katsikas, M. Giersig, I. G. Popovic, K. Diesner, A. Chemseddine, A. Eychmüller, H. Weller, *J. Phys. Chem.* **1994**, *98*, 7665.
- [11] V. Platschek, T. Schmidt, M. Lerch, G. Müller, L. Spanhel, A. Emmerling, J. Fricke, A. H. Foitzik, E. Langer, *Ber. Bunsenges. Phys. Chem.* **1998**, *102*, 85.
- [12] V. N. Soloviev, A. Eichhöfer, D. Fenske, U. Banin, *J. Am. Chem. Soc.* **2000**, *122*, 2673.
- [13] V. N. Soloviev, A. Eichhöfer, D. Fenske, U. Banin, *J. Am. Chem. Soc.* **2001**, *123*, 2354.
- [14] H. Z. Wang, A. Tashiro, H. Nakamura, M. Uehara, M. Miyazaki, T. Watari, H. Maeda, *J. Mater. Res.* **2004**, *19*, 3157.
- [15] Z. A. Peng, X. G. Peng, *J. Am. Chem. Soc.* **2002**, *124*, 3343.
- [16] C. B. Murray, D. J. Norris, M. G. Bawendi, *J. Am. Chem. Soc.* **1993**, *115*, 8706.
- [17] A. L. Rogach, A. Kornowski, M. Y. Gao, A. Eychmüller, H. Weller, *J. Phys. Chem. B* **1999**, *103*, 3065.
- [18] A. Kasuya, R. Sivamohan, Y. A. Barnakov, I. M. Dmitruk, T. Nirasawa, V. R. Romanyuk, V. Kumar, S. V. Mamykin, K. Tohji, B. Jeyadevan, K. Shinoda, T. Kudo, O. Terasaki, Z. Liu, R. V. Belosludov, V. Sundararajan, Y. Kawazoe, *Nat. Mater.* **2004**, *3*, 99.
- [19] A. L. Efros, M. Rosen, *Annu. Rev. Mater. Sci.* **2000**, *30*, 475.
- [20] T. Sugimoto, *Adv. Colloid Interface Sci.* **1987**, *28*, 65.
- [21] A. Puzder, A. J. Williamson, F. Gygi, G. Galli, *Phys. Rev. Lett.* **2004**, *92*, 217401.
- [22] J. Frenzel, J. O. Joswig, P. Sarkar, G. Seifert, M. Springborg, *Eur. J. Inorg. Chem.* **2005**, 3585.
- [23] S. Coe, W. K. Woo, M. Bawendi, V. Bulovic, *Nature* **2002**, *420*, 800.
- [24] N. Tessler, V. Medvedev, M. Kazes, S. H. Kan, U. Banin, *Science* **2002**, *295*, 1506.
- [25] J. L. Zhao, J. Y. Zhang, C. Y. Jiang, J. Bohnenberger, T. Basche, A. Mews, *J. Appl. Phys.* **2004**, *96*, 3206.
- [26] J. S. Steckel, J. P. Zimmer, S. Coe-Sullivan, N. E. Stott, V. Bulovic, M. G. Bawendi, *Angew. Chem. Int. Ed.* **2004**, *43*, 2154.
- [27] Y. Q. Li, A. Rizzo, M. Mazzeo, L. Carbone, L. Manna, R. Cingolani, G. Gigli, *J. Appl. Phys.* **2005**, *97*, 113501.
- [28] S. Coe-Sullivan, J. S. Steckel, W. K. Woo, M. G. Bawendi, V. Bulovic, *Adv. Funct. Mater.* **2005**, *15*, 1117.
- [29] C. R. Kagan, C. B. Murray, M. G. Bawendi, *Phys. Rev. B: Condens. Matter* **1996**, *54*, 8633.
- [30] F. V. Mikulec, M. Kuno, M. Bennati, A. D. Hall, R. G. Griffin, M. G. Bawendi, *J. Am. Chem. Soc.* **2000**, *122*, 2532.
- [31] D. J. Norris, N. Yao, F. T. Charnock, T. A. Kennedy, *Nano Lett.* **2001**, *1*, 3.
- [32] K. M. Hanif, R. W. Meulenberg, G. F. Strouse, *J. Am. Chem. Soc.* **2002**, *124*, 11495.
- [33] D. Yu, C. J. Wang, P. Guyot-Sionnest, *Science* **2003**, *300*, 1277.
- [34] D. A. Schwartz, N. S. Norberg, Q. P. Nguyen, J. M. Parker, D. R. Gamelin, *J. Am. Chem. Soc.* **2003**, *125*, 13205.
- [35] S. C. Erwin, L. J. Zu, M. I. Hafnel, A. L. Efros, T. A. Kennedy, D. J. Norris, *Nature* **2005**, *436*, 91.
- [36] N. Pradhan, D. Goorskey, J. Thessing, X. G. Peng, *J. Am. Chem. Soc.* **2005**, *127*, 17586.
- [37] B. O. Dabbousi, J. Rodriguez Viejo, F. V. Mikulec, J. R. Heine, H. Mattoussi, R. Ober, K. F. Jensen, M. G. Bawendi, *J. Phys. Chem. B* **1997**, *101*, 9463.

# ADVANCED MATERIALS

**Supporting Information**

for

*Advanced Materials*, adma.200601015

© Wiley-VCH 2007  
69451 Weinheim, Germany

## Sequential growth of magic size CdSe nanocrystals

*Stefan Kudera<sup>1,2†</sup>, Marco Zanella<sup>2†</sup>, Dr. Cinzia Giannini<sup>3</sup>, Aurora Rizzo<sup>1</sup>, Dr. Yanqin Li<sup>1</sup>, Prof. Giuseppe Gigli<sup>1</sup>, Prof. Roberto Cingolani<sup>1</sup>, Dr. Giuseppe Ciccarella<sup>1</sup>, Dr. Werner Spahl<sup>4</sup>, Prof. Wolfgang J. Parak<sup>2</sup>, and Dr. Liberato Manna<sup>1\*</sup>*

<sup>1</sup> *National Nanotechnology Laboratory of CNR-INFM, 73100 Lecce, Italy*

<sup>2</sup> *Center for Nanoscience, Ludwig Maximilians Universität, 80799 München, Germany*

<sup>3</sup> *CNR-Istituto di Cristallografia (IC), via Amendola 122/O, 70126 Bari, Italy*

<sup>4</sup> *Department of Chemistry and Biochemistry, Ludwig Maximilians Universität, München, Germany*

<sup>†</sup> *These authors have contributed equally to this work*

[\*] Dr. Liberato Manna

National Nanotechnology Laboratory of CNR-INFM

Distretto Tecnologico – ISUFI, Via Arnesano

email: liberato.manna@unile.it

## Supporting information

### 1. Estimation of the concentration of the various nanocrystal families in solution

*Modeling the time evolution of the absorption spectra.* In order to extract the concentration of the various clusters present, we attributed to each magic cluster size an absorption spectrum similar to that of a highly monodisperse nanocrystal sample of relatively small size.<sup>[1, 2]</sup> This is roughly characterized by a strong exciton peak and by a broad, rising absorption towards shorter wavelengths. We modeled the exciton peak with a sharp Gaussian function and the broad contribution with a broad Gaussian function whose peak is at a variable position below 300 nm, in order to place it relatively far from the exciton peak. The width of this broad Gaussian is varied in order to make it vanish for wavelengths longer than those corresponding to the exciton peak position. The curves shown in Figure S1 are examples of how the modeled absorption spectra look like for two different families of MSCs.

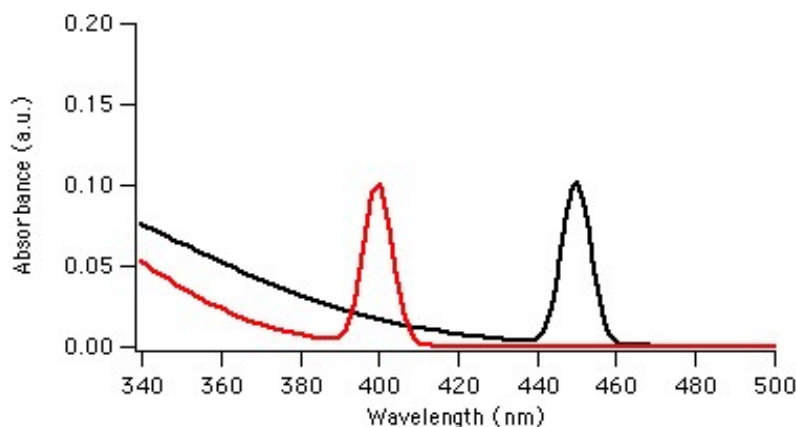


**Figure S1.** Modeled absorption spectra of two different families of MSCs.

The optical absorption spectrum of an aliquot extracted during the synthesis contained the contribution of several families of MSCs. Therefore, this spectrum had to be fitted with several Gaussian functions. The most important constraint of the fitting procedure was that the position of the individual peaks was kept almost constant for all spectra. The peak positions could vary only in the range of a few nanometers. Also, the peak widths could vary only by a relatively small amount. The short wavelength part of the spectrum was fitted by a single, broad Gaussian function, centered far apart from the area of interest. Through this approach, we could extract the absorption spectra of the single families of clusters. An example of this fit is shown in Figure S2.

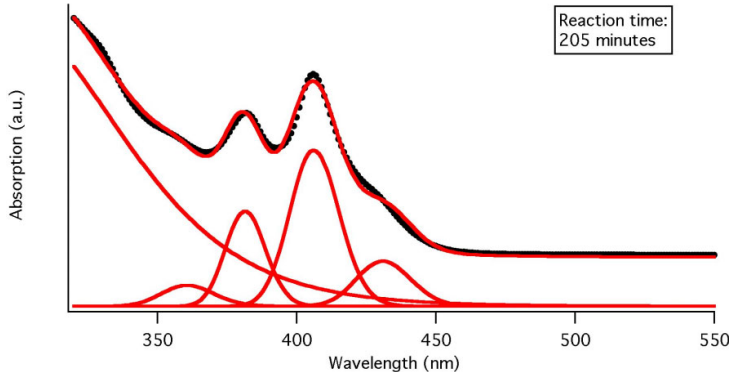


**Figure S2:** Example of a fit of the optical absorption spectrum (top, the black line is the experimental spectrum, the red line is the result of the fit) with a collection of Gaussian functions (bottom).

## 2. Simulation of the nanocrystal growth

*General description of the model.* The basic concept of the model is that the size evolution of a cluster in solution is a process governed by the addition (as well as by the removal) of atoms to (from) its surface. The model describes certain cluster sizes as much more stable than others, so these clusters are actually the “magic size clusters” (MSCs) that we observe in our experiments. The key assumption of the model is that once a cluster has reached such a magic size, it cannot shrink to sizes smaller than this one. Any cluster whose size is intermediate between two magic sizes is unstable and its lifetime in solution will be relatively short. Therefore, either such cluster will grow, by adding a sufficient number of monomers to reach its nearest larger magic size, or it will shrink ultimately to its nearest smaller magic size. As a consequence of this assumption, the dynamics of the growth of a cluster can be considered as unidirectional: Throughout a series of events, a cluster will evolve from one magic size to a larger magic size, and so on.

Let us consider a series of families of MSCs of increasing sizes, with the index  $i$  indicating the  $i^{\text{th}}$  family of this series (a larger  $i$  refers to a family of larger MSCs). Let us define with  $\alpha_i$  the rate at which a MSC belonging to the  $i^{\text{th}}$  family evolves to a MSC of the  $(i+1)^{\text{th}}$  family. This rate can be understood as the depopulation rate of the  $i^{\text{th}}$  family, and at same as the population rate of the  $(i+1)^{\text{th}}$  family.

Let us indicate with  $c_i$  the concentration of the MSCs belonging to the  $i^{\text{th}}$  family. In general, the time evolution of  $c_i$  is described by the following differential equation:

$$\frac{dc_i}{dt} = \alpha_{i-1}c_{i-1} - \alpha_i c_i$$

The first term indicates the rate at which clusters of the  $(i-1)^{\text{th}}$  family evolve to the clusters of the  $i^{\text{th}}$  family, while the second term describes the depopulation rate of the  $i^{\text{th}}$  family. This set of differential equations can be solved analytically. The solutions consist of a sum of differently weighted exponential decays, with decay rates equal to the rate constants  $\alpha_i$ .

*Fitting the model to the experimental results.* In applying the fitting procedure to extract the concentrations of the various magic clusters, we considered only the first five families of magic clusters that we observed experimentally. The family of the smallest MSCs (denoted with the index 1) was assumed to be the one absorbing strongly at 330 nm. Therefore, the families of the larger MSCs considered here were the ones absorbing at 360 (family 2), 384 (family 3), 406 (family 4) and 431 nm (family 5), respectively. This assignment was based on the fact that no transient peak below 330 nm was observed in our experiments.

*Solution of the differential equations.* In order to solve the set of differential equations we had to introduce one initial species, denoted with the index 0, whose population is not fed by any smaller clusters. This species was assumed to be the only family present in the solution at time  $t=0$ . Therefore this species can be regarded as the subset of monomers that evolves into MSCs. More importantly, the rate of depopulation of this species, which is equal to the rate of population of the family of the smallest MSCs (family 1), can be interpreted as the nucleation rate in the system.

*Estimation of the extinction coefficients.* In order to fit the optical absorption data reported in Figure 2 of the manuscript, we had to take into account the fact that the individual families of MSCs have different extinction coefficients. Unfortunately, reliable experimental data exists only for larger clusters. For instance, the calibration curve reported by Yu and co-workers<sup>[3]</sup> is reliable only for nanocrystals with diameters down to 2 nm. However, as we were interested only in the relative concentrations of the various MSCs in solution, we decided to set the extinction coefficient of the largest MSCs equal to an arbitrary value, and assumed that the extinction coefficients of all MSCs depend linearly on the spectral position of their exciton peak. We were able to fit accurately the time dependence of the optical spectra (Figure 2 of manuscript) even if we varied the slope of this linear dependence over a wide range. The only constraint was that the extinction coefficient  $\epsilon$  of the smaller clusters had to be larger than the extinction coefficient of the larger clusters. For the maximum slope that we considered, the extinction coefficient of the smallest MSCs (those absorbing at 360 nm) was 6.6 times larger than that of the MSCs absorbing at 431 nm. For the minimum slope, this was only 1.5 times larger. Such trends in the extinction coefficients are in qualitative agreement with those reported by Soloviev and co-workers.<sup>[4]</sup>

### 3. Fluorescence spectra of MSCs

*Multimodal distributions in fluorescence.* In addition to optical absorption spectra, the presence of different families of MSCs in the growth solution can be inferred from the fluorescence spectra of diluted aliquots. Figure S3 reports a set of fluorescent spectra (a) and of absorption spectra (b) for aliquots extracted at different times during the growth and diluted in toluene. In order to be able to record fluorescent spectra that showed significant emission from band-edge states, the samples had to be significantly diluted, such that for instance the optical density at the exciton peak centred at 406 nm (in absorption) was well below 0.1. In these experiments, the excitation wavelength was peaked at 400 nm.

In principle, a diluted solution containing a sample of fluorescent nanocrystals with a multimodal distribution of sizes would show distinct fluorescence peaks, each corresponding to the band-edge emission from a subset of nanocrystals sizes, if excited with a radiation having an energy higher than all the band gaps present. Indeed, the fluorescence spectra of figure S3 clearly show the contribution from two distinct peaks, whose weight varies over the synthesis in favour of the peak centered at longer

wavelengths, as this is clearly due to a increasing enrichment in the population of the family of largest MSCs during the synthesis run.

Each of the fluorescence spectra reported in Figure S3(a) was fitted with two Gaussians functions, one centered at 528-532 nm (this corresponds to the emission from the family of MSCs absorbing at 406 nm), and the other one centered at 550-552 nm (this corresponds to the emission from the family of MSCs absorbing at 431 nm). The peak heights of the two Gaussian functions for the various spectra are reported in Figure S3(c). As the fluorescence quantum efficiency for the different families of MSCs is not known, we cannot estimate the relative population of the two families of MSCs from this interpolation, so that the trends reported in the left plot of figure S3 are simply indicative of depletion, over time, of the smaller family of MSCs in favour of the larger family. Nevertheless, one should notice that the larger family of MSCs shows a significant contribution in the fluorescence spectrum even when in absorption its contribution is still low (therefore when the population of this family is still relatively small). Consequently, we can easily infer that in this sample the larger MSCs have a much higher fluorescence quantum yield than the smaller MSCs.

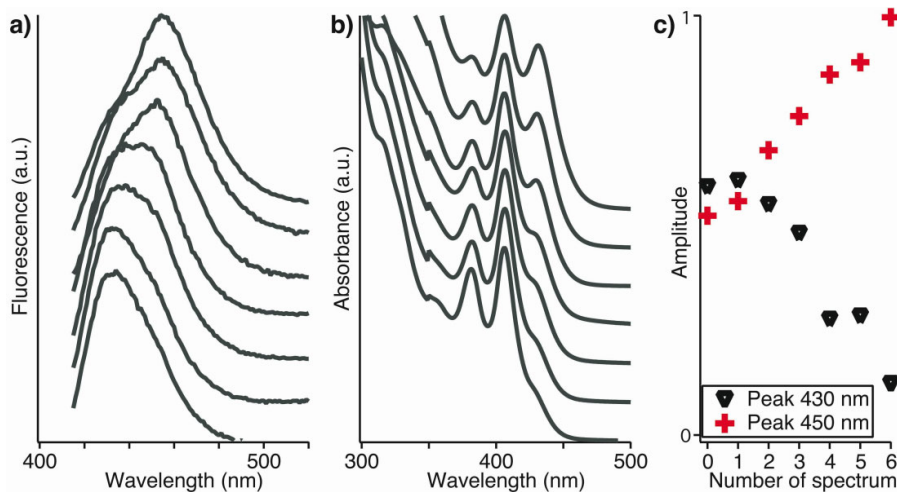


**Figure S3:** Fluorescence spectra (a) and the corresponding absorption spectra (b) of aliquots extracted from the growth solution at different stages of the synthesis. Spectra recorded at later stages of the reaction are shifted vertically. The fluorescence spectra are normalized to the maximum intensity, the absorptions are normalized to the amplitude of the peak at 406nm. (c) Trends in the relative amplitudes of the two Gaussians functions used to fit the fluorescence spectra shown in (a).

*Band-edge and trap emission.* One remarkable aspect of the fluorescence spectrum from a solution of MSCs is that at concentrations of MSCs higher than the ones discussed in the previous section, for instance when the optical density of the solution is around 0.2 at 406 nm, this is dominated by a broad band that spans the whole visible range (see for instance the spectrum 1 of Figure S4 or the one shown in Figure 5 of the paper). This band can be attributed to emission from trap states. However, when this solution is diluted further (roughly by a factor of 10-20) the band-edge fluorescence increases in intensity over the broad band, as can be seen in the spectra 2 and 3 of Figure S4.

To our opinion, it is unlikely that the almost complete suppression of band edge emission from moderately concentrated samples is due to some self-absorption effect, since at optical densities around 0.2 self-absorption should be still negligible. On the other hand, we know that the solution of MSCs is

contaminated by several un-reacted chemical species and surfactants, which might be adsorbed to the surface of MSCs and which might somehow suppress their band-edge emission. This effect should be less relevant at higher dilutions. This interpretation is however only speculative and more detailed studies are under way in our groups.

At wavelengths below 400 nm the dominant contribution to the fluorescence spectra is the emission from toluene, which takes place between 330 nm and 390 nm. In the range around 600 nm and above in addition to the original signal we find as a main feature the replica of the scattered incident excitation light (peaked at 600 nm), and the replicas of any signal between 300nm and 400nm. This becomes more obvious in spectra 3 and 4.

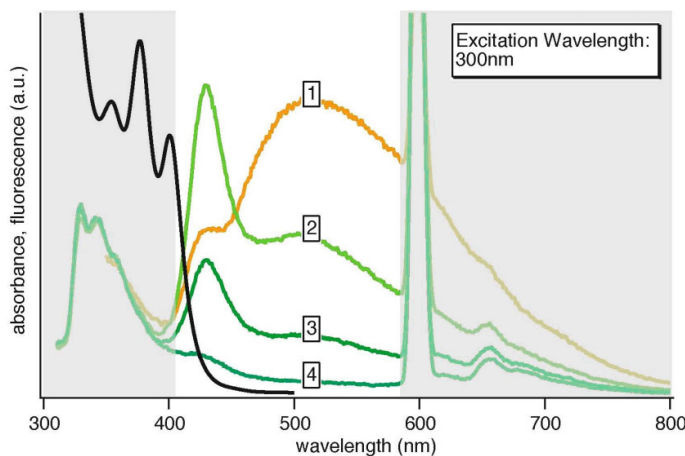


**Figure S4:** Series of fluorescence spectra (coloured) from the same sample of MSCs in toluene (absorption spectrum in black) but at different concentrations. The concentration of MSCs is reduced gradually from spectrum 1 to spectrum 4 by addition of toluene. The concentration used for spectrum 1 is slightly lower than that used for the spectrum shown in Figure 5a of the paper.

#### 4. Size Selective Precipitation

When the synthesis of MSCs is stopped, the growth solution contains a given distribution of various families of MSCs. In principle, in order to isolate the various families of magic size clusters, a so-called “size selective precipitation” can be carried out, a method that is widely used to isolate monodisperse nanocrystals from a batch containing a broad distribution of sizes. The idea behind this type of separation is that nanocrystals are coated with hydrophobic stabilizing molecules, which cause them to be soluble in non-polar solvents. In a non-polar solvent (such as toluene), surfactant-coated nanocrystals are stabilized by means of hydrophobic interactions between the tails of the surfactant molecules coating the nanocrystals’ surface and the solvent molecules (surfactant-solvent interactions). In addition, the inorganic cores of the nanoparticles cannot touch each other as they are ultimately stabilized by the hydrophobic layers of adjacent nanocrystals. If a polar solvent (such as methanol) is gradually added to this solution, the surfactant-solvent interactions are progressively disrupted. As soon as a certain threshold of solvent polarity has been crossed, the nanocrystals start aggregating. This happens because the hydrophobic interactions among the surfactant tails of different nanocrystals (surfactant-surfactant interactions) become much more favourable than the surfactant-solvent interactions. As a consequence of this aggregation, the nanocrystals start precipitating from the

solution. Since larger nanoparticles have a larger radius of curvature than smaller crystals, inter-particle aggregation between larger particles will be significant already in a moderately polar solution. Upon addition of a polar solvent, the larger nanoparticles precipitate first, whereas the smaller particles are still soluble. When large particles are precipitated, the solution is centrifuged so that the larger nanoparticles settle down as a compact precipitate, whereas the smaller ones remain in the solution. The precipitate is then separated from the solution that now contains only the smaller particles (the supernatant). Finally, the precipitate is re-dissolved in a fresh organic solvent, yielding a solution that contains only the largest nanoparticles from the original sample. This process can be applied again to the supernatant obtained from the centrifugation, and so on, so that fractions with different nanoparticles sizes can be obtained from a starting batch of nanocrystals.

In the present case of a solution containing different families of MSCs, the first step of the size-selective precipitation procedure aims at isolating the largest family of MSCs present. Typical optical absorption spectra of an aliquot of the growth solution prior to size selective precipitation, and of the corresponding size-selected largest MSCs, for syntheses stopped at different stages of the growth, are reported in Figure S5.

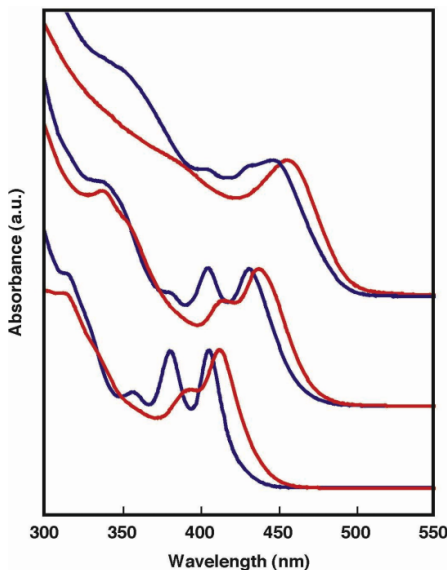


**Figure S5.** Optical absorption spectra of an aliquot from the growth solution prior to size selective precipitation, and of the corresponding size-selected largest MSCs, for three syntheses stopped at different stages of the growth. The spectrum of each solution before size selective precipitation (diluted in toluene) is reported in blue, while the spectrum of the size-selected largest MSCs, re-dissolved in toluene, is shown in red. The possible reason for the red shift in the absorption spectra of the size-selected samples is discussed in the main paper.

One general limitation of the size selective precipitation is that such a separation procedure is not quantitative and therefore a sample of size-selected nanocrystals is always contaminated by a small fraction of nanocrystals having significantly different sizes. This limitation is particularly critical for the separation of different families of MSCs and this can be seen clearly in Figure S6. The figure reports, for two different syntheses (a, b), the optical absorption spectra of an aliquot from the growth solution prior to size selective precipitation (top), and of the corresponding supernatant solution as well as the solution containing the size-selected, largest MSCs (bottom).

In both cases, one can notice that the solution containing the size-selected largest MSCs is contaminated by a tiny fraction of smaller MSCs. However, more critical is the contamination of the supernatant by the family of largest MSCs (so the precipitation of that family was not quantitative). Consequently, a new size selective precipitation carried out on this supernatant solution yields a precipitate that is certainly richer in the MSCs with intermediate size, but that contains inevitably fractions of both larger and smaller MSCs.

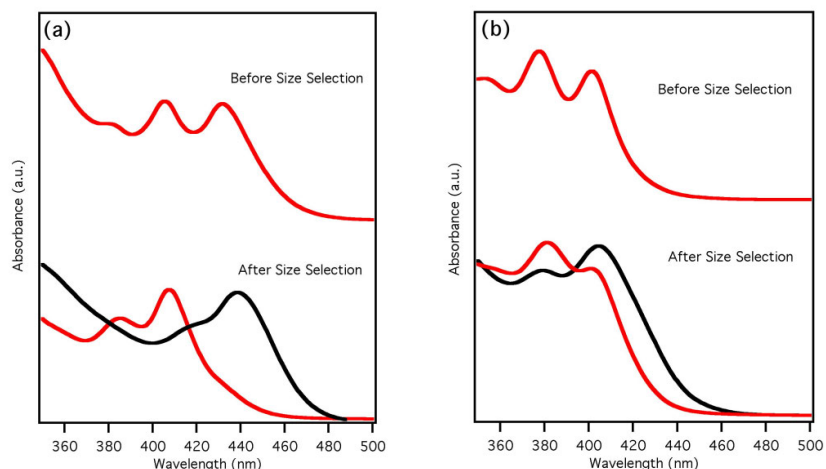


**Figure S6:** Exemplary optical absorption spectra of precipitate and supernatant solutions after size-selective precipitation. The upper spectra are recorded from the growth solution before size-selective precipitation. The lower spectra are those of the precipitate, i.e. the largest MSCs, (black) and of the supernatant (which contains mainly the families of smaller MSCs, red).

The results of these experiments therefore show that the isolation of a sample that contains virtually only one family of MSCs may be quite laborious. In addition, the size selective precipitation of magic size nanocrystals requires large amounts of methanol, and therefore becomes increasingly unpractical for isolating smaller MSCs from a starting batch. Moreover, MSCs of extremely small sizes, such as those absorbing below 400 nm, cannot be precipitated even by large additions of methanol (several hundreds of ml). As a consequence of these intrinsic difficulties, we found out that it is more favorable to simply carry out a synthesis and stop it when the required family of MSCs is the one present with the largest size. This family will be easy to isolate and will contain as contaminants only smaller MSCs.

## 5. Elemental analysis and Mass spectrometry

An inductively coupled plasma atomic emission spectrometer (Varian Vista AX) was used to investigate the elemental composition of the nanocrystals. Samples were dissolved in  $\text{HCl}/\text{HNO}_3$  3:1 (v/v) by using a CEM “MARS 5” microwave digester. For a control experiment, elemental analysis on large CdSe nanocrystals (6 nm diameter) yielded a Cd:Se ratio equal to 1.06, in close agreement with the values reported earlier on large CdSe nanocrystals with the aid of other techniques.<sup>[5]</sup> Elemental analysis of size-selected and purified clusters (for instance those absorbing strongly at 406, 431 and 447 nm, respectively) showed that they are all Cd-rich, with Cd:Se ratios ranging from 1.1 to 1.3 (see

also table 1 at the end of the supporting information). These findings are in accordance with previous work, as for instance Rosenthal and co-workers found that CdSe nanocrystals are in general Cd-rich.<sup>[6]</sup> Mass Spectra were recorded on a MALDI/TOF mass spectrometer (Bruker Daltonics autoflex II) without use of a matrix substance. A sample solution was deposited on an anchor chip target plate, dried at ambient temperature and then ionised. Mass spectra of MSCs absorbing at 431 nm and 447 nm, as well as of larger nanocrystals (of roughly 3 nm in diameter) showed that the ionization of all these samples yields naked  $(\text{CdSe})_{13}$ ,  $(\text{CdSe})_{33}$  and  $(\text{CdSe})_{34}$  clusters, regardless of the starting type of cluster (Figure S7). This indicates that a complete stripping off of surfactant molecules occurs from the surface of the nanocrystals, and that fragmentation of the MSCs could not be avoided, even with such a soft ionisation source as the one used in MALDI/TOF. Similar spectra had been observed previously, with the same technique, on CdSe MSCs prepared in reverse micelles.<sup>[2]</sup> Such clusters represent very stable aggregates of atoms in the gas phase, as already postulated and observed for similar systems (i.e.  $\text{ZnS}^{[7]}$ ). As these clusters have no direct relation with the CdSe MSCs synthesised in solution, we deduce that the latter might have a rather different structure. Mass spectra on smaller MSCs, those absorbing at 406 nm, did not show any of the characteristic peaks of the  $(\text{CdSe})_{13}$ ,  $(\text{CdSe})_{33}$  and  $(\text{CdSe})_{34}$  clusters. We deduce therefore that the stripping off of surfactants from these smaller MSCs and their fragmentation leads to the formation of clusters that are even smaller than the smallest “magic”  $(\text{CdSe})_{13}$  clusters observed in the gas phase.

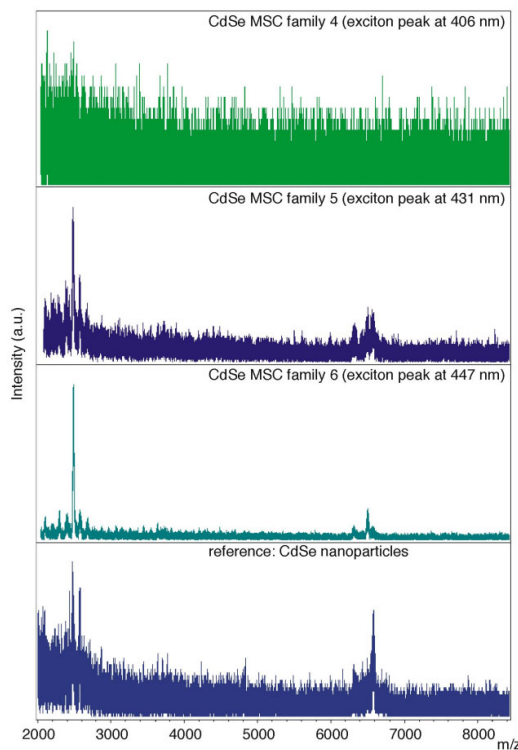


**Figure S7.** Mass spectra samples of three different MSC families and of a reference sample (bottom) which is based on CdSe nanocrystals having a diameter of about 3 nm.

## 6. X-ray diffraction spectra

X-ray diffraction spectra were collected with a D8 Bruker diffractometer equipped with a Goebel mirror and a two-bounce V-groove monochromator on the primary beam and a scintillator counter as detector. Samples were deposited on miscut silicon and measured in reflection geometry. The diffraction spectra of these size-selected clusters resemble a zinc-blende like structure. However, for clusters with diameters in the 1-2 nm range, as those reported here, the ratio of surface-to-volume atoms can exceed 50%, adding important surface stress contributions that can strongly affect the internal structure of these clusters.<sup>[1, 2, 8, 9]</sup> Therefore, the present data cannot be used to fully identify the correct structural model of these clusters. Work is in progress to carry out diffraction experiments with a synchrotron source, in order to possibly distinguish among several structural models.

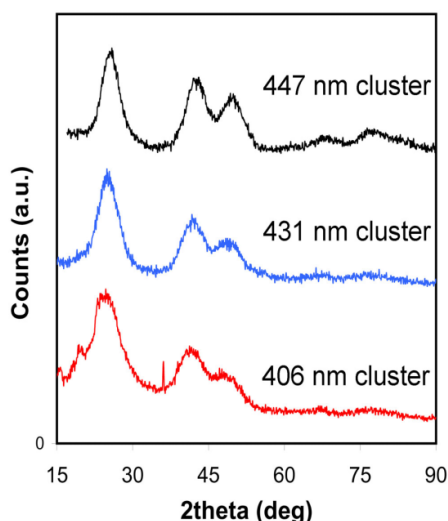


**Figure S8.** Wide angle, XRD spectra of three different size-selected families of MSCs.

## 7. Transmission electron microscopy analysis

The samples for transmission electron microscopy (TEM) were prepared by dispersing dilute solutions of nanocrystals onto carbon-coated copper grids. Low-magnification TEM images were recorded on a Jeol Jem 1011 microscope operated at 100 KV. TEM observations were particularly difficult due to extremely small size of such clusters, for which the contrast variation under the beam often did not differ sufficiently enough from the normal fluctuations of the carbon support film. In the case of samples absorbing at 406 nm, which have a size around 1.5-1.6 nm (close to the resolution limit of the microscope) we did not succeed to identify clearly the particles. Figure S9 reports TEM micrographs of two different aliquots extracted at different times during the growth, one in which the largest MSCs present are those absorbing at 431 nm (left), and the other in which largest MSCs present are those absorbing at 447 nm (right). On these images it is not possible to carry out a reliable statistical analysis that reveals the relative population of the various families of MSCs, neither we could determine their sizes with an acceptable margin of error. One reason is the limited resolution of the instrument, as the

uncertainty in the size measurement on these images is definitely higher than the separation of two adjacent sizes. Also, as said before, at such small sizes the contrast variation of the carbon support itself introduces critical artefacts in the analysis. Despite these limitations, the TEM images show that MSCs are well dispersed (no aggregation is seen) and that they have a roughly spherical morphology.

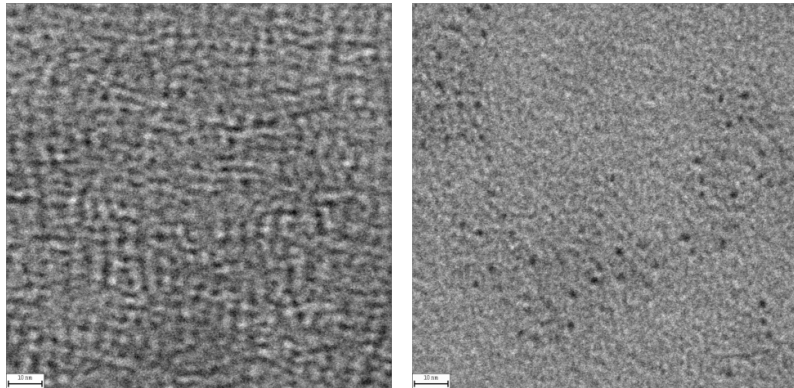


**Figure S9:** Transmission electron micrographs of a sample with the first absorption feature centred at 431 nm (left) and of a sample with the first absorption feature centred at 447 nm (right). The scale bar is 10 nm.

Peak position (nm)	Diameter (Peng) <sup>[3]</sup> (nm)	Calculated number of atoms	Cd:Se ratio from elemental analysis
330	0,898	14	-
360	1,185	31	-
384	1,410	53	-
406	1,606	78	1.10 - 1.22
431	1,817	113	1.28 - 1.29
447	1,929	136	1.24 - 1.26

**Table 1.** Comparison of experimental data with data from the literature. Starting from the measured peak position in the optical absorption spectra of aliquots extracted from the growth solution (Column 1), and by assuming clusters with spherical shape, we estimated a cluster diameter using the calibration curve reported by of Yu co-workers<sup>[3]</sup> (Column 2) and the number of atoms in each cluster (Column 3). Column 5 reports, for each size-selected family of clusters, the Cd:Se ratio as derived from the elemental analysis.

**References**

- [1] C. B. Murray, D. J. Norris, M. G. Bawendi, *J. Am. Chem. Soc.* **1993**, *115*, 8706.
- [2] A. Kasuya, R. Sivamohan, Y. A. Barnakov, I. M. Dmitruk, T. Nirasawa, V. R. Romanyuk, V. Kumar, S. V. Mamykin, K. Tohji, B. Jeyadevan, K. Shinoda, T. Kudo, O. Terasaki, Z. Liu, R. V. Belosludov, V. Sundararajan, Y. Kawazoe, *Nat. Mater.* **2004**, *3*, 99.
- [3] W. W. Yu, L. H. Qu, W. Z. Guo, X. G. Peng, *Chem. Mat.* **2003**, *15*, 2854.
- [4] V. N. Soloviev, A. Eichhofer, D. Fenske, U. Banin, *J. Am. Chem. Soc.* **2000**, *122*, 2673.
- [5] J. E. B. Katari, V. L. Colvin, A. P. Alivisatos, *J. Phys. Chem.* **1994**, *98*, 4109.
- [6] J. Taylor, T. Kippeny, S. J. Rosenthal, *J. Cluster Sc.* **2001**, *12*, 571.
- [7] T. P. Martin, *Phys. Rep.-Rev. Sec. Phys. Lett.* **1996**, *273*, 199.
- [8] A. Puzder, A. J. Williamson, F. Gygi, G. Galli, *Phys. Rev. Lett.* **2004**, *92*, art. n. 217401.
- [9] J. Frenzel, J. O. Joswig, P. Sarkar, G. Seifert, M. Springborg, *Eur. J. Inorg. Chem.* **2005**, 3585.

## A.2 Blue light emitting diodes based on fluorescent CdSe/ZnS nanocrystals

A. RIZZO, Y. LI, S. KUDERA, F. DELLA SALA, M. ZANELLA, W.J. PARAK, R. CINGOLANI, L. MANNA, G. GIGLI  
*Appl. Phys. Lett.* **90**(5), pp. 051106, 2007

The authors report on the blue electroluminescence from CdSe/ZnS core/shell nanocrystals prepared from ultrasmall, magic size CdSe clusters that have a diameter of less than 2 nm. The light emitting device consists of an active layer of nanocrystals blended with 4,4',*N,N'*- diphenylcarbazole and an evaporated electron transporting/hole blocking layer made of 2,9-dimethyl-4,7-diphenyl-1,10-phenanthroline. A blue, stable electroluminescence at 485 nm from the hybrid device was observed, in good agreement with the photoluminescence spectra of a solid film of the same nanocrystals used for the device.

### Blue light emitting diodes based on fluorescent CdSe/ZnS nanocrystals

Aurora Rizzo,<sup>a,b)</sup> Yanqin Li, Stefan Kudera, and Fabio Della Sala

*National Nanotechnology Laboratory (NNL), CNR-INFM, Università degli Studi Lecce, Via per Arnesano Km 5, 73100 Lecce, Italy*

Marco Zanella and Wolfgang J. Parak

*Center for Nanoscience, Ludwig Maximilians Universität, Amalienstraße 54 80799 München, Germany*

Roberto Cingolani, Liberato Manna, and Giuseppe Gigli<sup>c)</sup>

*National Nanotechnology Laboratory (NNL), CNR-INFM, Università degli Studi Lecce, Via per Arnesano Km 5, 73100 Lecce, Italy*

(Received 20 September 2006; accepted 28 November 2006; published online 30 January 2007)

The authors report on the blue electroluminescence from CdSe/ZnS core/shell nanocrystals prepared from ultrasmall, magic size CdSe clusters that have a diameter of less than 2 nm. The light emitting device consists of an active layer of nanocrystals blended with 4,4',*N,N'*-diphenylcarbazole and an evaporated electron transporting/hole blocking layer made of 2,9-dimethyl-4,7-diphenyl-1,10-phenanthroline. A blue, stable electroluminescence at 485 nm from the hybrid device was observed, in good agreement with the photoluminescence spectra of a solid film of the same nanocrystals used for the device. © 2007 American Institute of Physics.

[DOI: 10.1063/1.2426899]

Over the last few years, colloidal semiconductor nanocrystals, also termed as colloidal quantum dots (QDs), have attracted much interest because of their high potential for optoelectronic applications such as organic light emitting diodes (OLEDs)<sup>1–3</sup> and solar cells.<sup>4</sup> The appealing features of these materials, when properly synthesized, are their high fluorescence efficiency,<sup>5</sup> their narrow band emission,<sup>5</sup> their chemical stability,<sup>6</sup> and their tunable light emission. Among the various types of fluorescent colloidal nanocrystals, core/shell CdSe/ZnS nanocrystals are of peculiar interest for practical applications due to the possibility to finely tune their emission wavelength in the visible spectrum by varying their size.<sup>5,7</sup>

Different approaches have been reported so far for the fabrication of light emitting diodes (LEDs) based on colloidal QDs. Hybrid organic/inorganic LEDs, for instance, were fabricated using host/guest systems consisting of a polymer doped with CdSe or CdSe/ZnS nanocrystals.<sup>1</sup> Bilayer structures were also reported which were based on a hole transporting layer made of conductive polymers and an electron transporting layer of QDs.<sup>2</sup> Coe-Sullivan *et al.* have fabricated high luminance devices with electrochemical emission in the green-red region by exploiting the phase segregation between organic molecules, such as 4,4',*N,N'*-diphenylcarbazole (CBP) and *N,N'*-diphenyl-*N,N'*-bis(3-methylphenyl)-(1,1'-biphenyl)-4,4'-diamine, and aliphatically capped QDs.<sup>3,7</sup> In this approach the problem of poor charge conductivity of QDs, due to the insulating layer of surfactants that coat their surface, was in fact overcome elegantly by the formation of a single monolayer of QDs sandwiched between a hole and an electron transporting organic layer. This geometry separated the charge recombination process (which occurred in the QD layer) from the charge conduction process (which occurred in the two organic layers).

Despite the reported advances in the field, to date LEDs based on core/shell CdSe/ZnS nanocrystals that emit pure blue light have remained difficult to fabricate. This is due to the lack of appropriate synthetic routes to synthesize CdSe nanocrystals with diameters that are sufficiently small (of the order of 1.5 nm) to shift their light emission to the blue-UV region of the visible spectrum, which in addition have a narrow size distribution, good quantum efficiency, chemical stability, and which can be routinely prepared in high yields. These limitations prevent the exploitation of the nanocrystal-based technology in full-color flat display applications, for which chromophores emitting in all the three primary colors are required in order to obtain white light.

In a recent work we have reported a synthetic approach to blue emitting CdSe/ZnS QDs which was based on the sequential growth of CdSe magic size clusters (MSCs) with progressively larger sizes.<sup>8</sup> The method allowed us to grow extremely small colloidal CdSe nanocrystals in a mixture of three surfactants (trioctyl phosphine, dodecylamine, and nonanoic acid) at temperatures (80 °C) that are much lower than those involved in conventional organometallic syntheses of CdSe nanocrystals. Small nanocrystals can be grown as both nucleation and growth rates are considerably reduced, due to the large activation barriers for the two processes at such low temperature.

In order to synthesize blue emitting nanocrystals, we interrupted the growth when the largest MSCs present were the one characterized by an absorption peak at 406 nm. These clusters, which had a diameter of approximately 1.5–1.6 nm, were isolated from smaller MSCs present in the growth solution by size selective precipitation with methanol,<sup>8</sup> and a ZnS shell was grown on them in order to passivate defects and to enhance their band-edge emission. In Fig. 1 we report the absorption and the photoluminescence spectra of core/shell CdSe/ZnS nanocrystals that were prepared from such size-selected MSCs. In a chloroform solution the absorption and PL showed maximum peaks at 427 and 454 nm, respectively. In the solid state, for samples prepared by drop casting the solution of nanocrystals in chloroform on a cleaned

<sup>a)</sup> Author to whom correspondence should be addressed; FAX: 0039-0832-298238.

<sup>b)</sup> Electronic mail: aurora.rizzo@unile.it

<sup>c)</sup> Electronic mail: gigli@mailing.unile.it

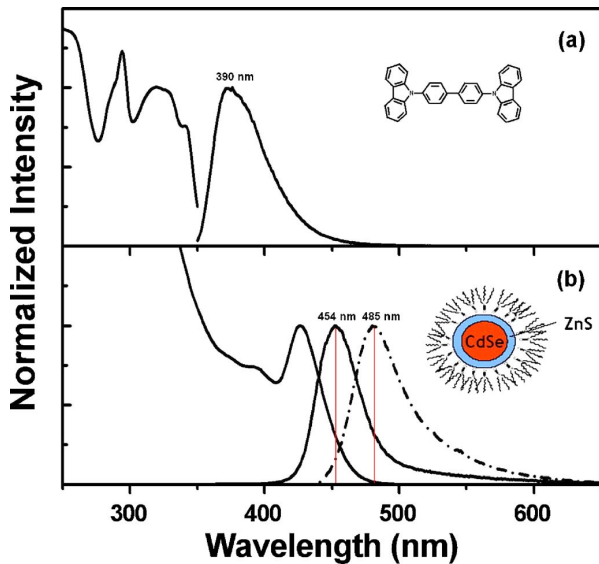


FIG. 1. (Color online) Optical properties of the materials involved in the fabrication of the LED. (a) Absorption and photoluminescence spectra of CBP in chloroform. (Inset) Molecular structure of CBP. (b) Absorption and photoluminescence spectra of core/shell CdSe/ZnS nanocrystals in chloroform (solid) and in film (dash dot). (Inset) Simplified structure of a CdSe/ZnS nanocrystal.

quartz glass, the PL spectrum showed a 30 nm redshift (Fig. 1). It is likely that this shift is due to the Förster energy transfer from smaller (donor) to larger (acceptor) dots within the film, and in nanocrystals it increases with increasing non-homogeneity of the sample.<sup>9</sup> In the present case, the process of ZnS shell growth leads inevitably to a broadening of the size distribution of the clusters, which is initially remarkably narrow. The Förster theory relates the efficiency of energy transfer due to donor-acceptor dipole-dipole interaction to the spectral overlap of donor emission and acceptor absorption.<sup>10</sup> For a random orientation of transition dipoles, the rate of this process is given by

$$k_F = \tau_D^{-1} \left( \frac{R_0}{r} \right)^6, \quad (1)$$

whereas the Förster radius is

$$R_0 \propto \left( \frac{\varphi_D}{n^4} \int_0^\infty F_D(\tilde{\nu}) \varepsilon_A(\tilde{\nu}) \frac{d\tilde{\nu}}{\tilde{\nu}^4} \right)^{1/6}. \quad (2)$$

In the former expressions,  $\tau_D$  is the lifetime of the donor in the absence of the acceptor,  $r$  is the distance between the donor and the acceptor,  $\varphi_D$  is the luminescence quantum yield of the donor,  $n$  is the refractive index of the QD solid,  $F_D(\tilde{\nu})$  is the normalized spectrum of the donor emission, and  $\varepsilon_A(\tilde{\nu})$  is the molar extinction coefficient for acceptor absorption.  $R_0$  is a measure of transfer efficiency and defines the distance at which  $k_F$  equals the rate of donor deexcitation by competing mechanisms. In our samples, we estimated a Förster radius of about 23 Å from the spectra in Fig. 1, by assuming  $n \approx 2.26$ ,<sup>11</sup> and a molar extinction coefficient at the peak of the first excited state of  $2.4 \times 10^4 \text{ M}^{-1} \text{ cm}^{-1}$ .<sup>12</sup> In a recent report by Kasuya *et al.*, the nearest-neighbor interparticle distance for close-packed films of MSCs that were very similar in size to the size-selected MSCs prepared by us was of the order of 16 Å.<sup>13</sup> Such interparticle distance certainly

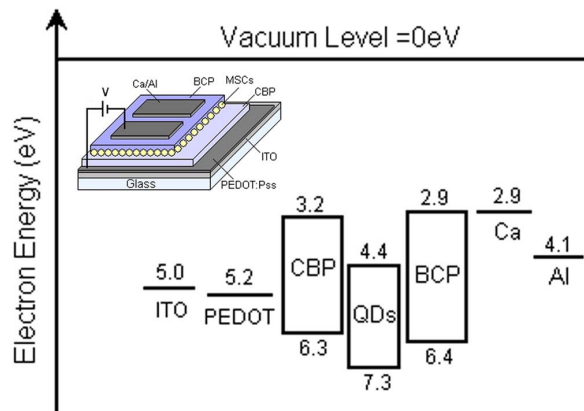


FIG. 2. (Color online) Proposed energy level diagram of the device: ITO||PEDOT:PSS||CBP:MSCs||BCP||Ca/Al. (Inset) Sketch of the device.

increases in close-packed films of core-shell nanocrystals, as in the present case, but should not be larger than 20 Å, and is therefore shorter than the Förster radius estimated above. We want to remark, however, that the estimate of such Förster radius is certainly affected by large errors, which are due mainly to the large uncertainties in the values of the refractive index and the molar extinction coefficient for nanocrystals with such small sizes. In addition, it is likely that other effects are also responsible for the observed shift. We observed in the absorption spectrum in the film a broadening as well as a very small redshift (about 1.4 nm) of the first absorption peak as compared to the spectrum recorded on the same sample in solution (data not shown). The latter effect can be justified by considering the formation of delocalized states due to the interactions among nanocrystals.<sup>14,15</sup> The small redshift can be explained by considering the changes in the surrounding environment,<sup>15–17</sup> such as the dielectric constant discontinuity at the QD boundary, which is known to increase the exciton ground state energy significantly.<sup>17</sup> However, in our case the effect might be strongly reduced by the presence of the organic surfactants.<sup>18</sup>

PL efficiency of CdSe/ZnS nanocrystals in chloroform solution varied from synthesis to synthesis, in a 30%–60% range. These blue emitting nanocrystals, dispersed in a matrix of (CBP), were used as active emissive layer in OLED devices with a multilayered structure [Fig. 2 inset]. In particular, in order to increase the hole injection from the indium tin oxide (ITO) anode into the active materials and also to improve the film forming properties, a thin layer of poly(3,4-ethylenedioxythiophene):poly(styrenesulfonate) (PEDOT:PSS) was spin deposited onto the cleaned ITO-coated glass substrate and then heated at 110 °C for 10 min. The nanocrystals and the host material (CBP) were deposited in a single spin-casting step from a chloroform solution.<sup>19</sup> To improve the electron injection in the nanocrystals layer a 35 nm electron transporting/hole blocking layer of 2,9-dimethyl-4,7-diphenyl-1,10-phenanthroline (BCP) was evaporated. Finally, a Ca/Al (50 nm/150 nm) cathode was thermal evaporated at a pressure of  $4 \times 10^{-6}$  mbar using a contact shadow mask.

The electroluminescence spectrum of the device is reported in Fig. 3. It is peaked at the same wavelength as the PL spectrum, although it has a broader line shape. Differences between photo- and electroluminescence are attributed to AIP license or copyright, see <http://apl.aip.org/apl/copyright.jsp>

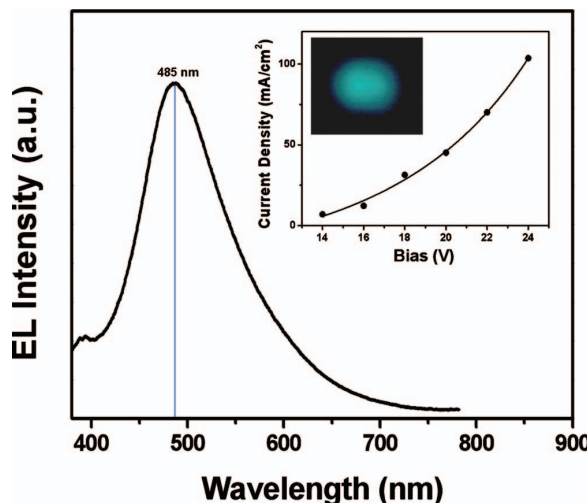


FIG. 3. (Color) Electroluminescence spectrum for the device. (Inset)  $V$ - $I$  characteristic of the device and a photo taken from the working device.

to the environmental effects, such as energy and charge transfer among nanocrystals or between nanocrystals and the organic molecules.<sup>20</sup> The small shoulder located at 390 nm from CBP is probably due to incomplete exciton energy transfer from CBP molecules to the nanocrystals. We report in Fig. 2 the energy level diagram of the device in order to clarify the processes occurring in the device. Work functions ( $\Phi$ ), band gaps ( $E_g$ ), ionization energies (IE), and electron affinities (EA) of ITO ( $\Phi=-5.0$  eV), PEDOT ( $IE=-5.2$  eV), Al ( $\Phi=-2.9$  eV), Ca ( $\Phi=-4.1$  eV), CBP ( $E_g=3.1$  eV,  $IE=-6.3$  eV), and BCP ( $E_g=3.5$  eV, EA = -2.9 eV) were taken from literature.<sup>1,21,22</sup> The IE of the nanocrystals can be obtained approximately by adding the quantization energy to the bulk CdSe IE.<sup>23</sup> For simplicity we treated the nanocrystals as a CdSe sphere of diameter of 1.6 nm and neglected the influence of the ZnS shell on the effective band gap. Atomistic calculations predict for this system a hole quantization energy of about 0.7 eV.<sup>24,25</sup> The resulting IE is thus -7.3 eV, and by subtracting the nanocrystal's optical gap (2.9 eV) estimated from the absorption measurements, we obtain a value of -4.4 eV for the EA.

Based on this diagram, the generation of excitons in the nanocrystals can occur either through direct charge injection or by the Förster energy transfer from the organic molecules. Electrons are injected from the Ca/Al contact through the BCP, due to the energy alignment of the EA of the nanocrystals and the lowest unoccupied molecular orbitals of CBP and BCP. They are eventually transported to the nanocrystals, where they are better confined due to their higher electron affinity. In charged nanocrystals the barrier for hole injection from CBP is reduced, and therefore the holes injected from the anode (ITO) through the PEDOT:PSS into the CBP layer can be trapped on the nanocrystals. By this mechanism excitons are formed on nanocrystals by direct charge injection from CBP and BCP. Excitons as well can be formed on the organic molecules placed in the interstitial spaces of the MSC layer, and then transferred to the nanocrystals by the Förster energy transfer process. According to the Förster energy transfer theory, one of the necessary conditions for an efficient process is a strong overlap of the acceptor absorp-

tion and donor photoluminescence spectra.<sup>26,27</sup> As is shown in Fig. 1 this condition is satisfied in the case of the reported device, as the PL of CBP (donor) and the absorption of nanocrystals (acceptor) are well overlapped.

In conclusion, we have fabricated a blue light emitting device based on blue emitting CdSe/ZnS nanocrystals blended in a host material (CBP). A thin layer of a hole blocking/electron transporting material (BCP) is used to control and to balance the emission process. This work demonstrates the potentiality of colloidal semiconductor nanocrystals as blue emitters for light emitting diodes. Furthermore, when mixed with nanocrystals emitting in other colors, they can be exploited for full-color displays and lighting technology.

This work was supported by the European project SA-NANO (contract number STRP 013698) and by the Italian projects MIUR 297 (contract number 13587), FIRB Synergy (RBNE03S8XZ) and FIRB NG-LAB (contract number RBLA03ER38).

- <sup>1</sup>Y. Q. Li, A. Rizzo, M. Mazzeo, L. Carbone, L. Manna, R. Cingolani, and G. Gigli, *J. Appl. Phys.* **97**, 113501 (2005).
- <sup>2</sup>H. Mattoussi, L. H. Radzilowski, B. O. Daboussi, E. L. Thomas, M. G. Bawendi, and M. F. Rubner, *J. Appl. Phys.* **83**, 7965 (1998).
- <sup>3</sup>S. Coe, W. K. Woo, M. G. Bawendi, and V. Bulovic, *Nature* (London) **420**, 800 (2002).
- <sup>4</sup>I. Gur, N. A. Fromer, M. L. Geier, and A. P. Alivisatos, *Science* **310**, 462 (2005).
- <sup>5</sup>B. O. Daboussi, J. Rodriguez-Viejo, F. V. Mikulec, J. R. Heine, H. Mattoussi, R. Ober, K. F. Jensen, and M. G. Bawendi, *J. Phys. Chem. B* **101**, 9463 (1997).
- <sup>6</sup>V. I. Klimov, *Los Alamos Sci.* **28**, 214 (2003).
- <sup>7</sup>S. Coe-Sullivan, J. S. Steckel, W. K. Woo, M. G. Bawendi, and V. Bulovic, *Adv. Funct. Mater.* **15**, 1117 (2005).
- <sup>8</sup>S. Kudera, M. Zanella, C. Giannini, A. Rizzo, Y. Q. Li, G. Gigli, R. Cingolani, G. Ciccarella, W. Spahl, W. J. Parak, and L. Manna, *Adv. Mater.* (Weinheim, Ger.) (in press).
- <sup>9</sup>C. R. Kagan, C. B. Murray, and M. G. Bawendi, *Phys. Rev. B* **54**, 8633 (1996).
- <sup>10</sup>T. Förster, *Discuss. Faraday Soc.* **27**, 7 (1959).
- <sup>11</sup>The refractive index for CdSe cores is calculated from the Moss rule  $n^4=77/E_g$  (eV);  $E_g=2.95$  eV was estimated from the first optical absorption peak.
- <sup>12</sup>W. Y. Yu, L. Qu, W. Guo, and X. Peng, *Chem. Mater.* **15**, 2854 (2003).
- <sup>13</sup>A. Kasuya, R. Sivamohan, Y. A. Barnakov, I. M. Dmitruk, T. Nirasawa, V. R. Romanyuk, V. Kumar, S. V. Mamykin, K. Tohji, B. Jeyadevan, K. Shinoda, T. Kudo, O. Terasaki, Z. Liu, R. V. Belosludov, V. Sundararajan, and Y. Kawazoe, *Nat. Mater.* **3**, 99 (2004).
- <sup>14</sup>M. V. Artemyev, A. I. Bibik, L. I. Gurinovich, S. V. Gaponenko, and U. Woggon, *Phys. Rev. B* **60**, 1504 (1999).
- <sup>15</sup>H. Döllefeld, H. Weller, and A. Eychmüller, *J. Phys. Chem. B* **106**, 5604 (2002).
- <sup>16</sup>C. A. Leatherdale and M. G. Bawendi, *Phys. Rev. B* **63**, 165315 (2001).
- <sup>17</sup>V. A. Fonoberov, E. P. Pokatilov, and A. A. Balandin, *Phys. Rev. B* **66**, 085310 (2002).
- <sup>18</sup>B. S. Kim, M. A. Islam, L. E. Brus, and I. P. Herman, *J. Appl. Phys.* **89**, 8127 (2001).
- <sup>19</sup>J. S. Steckel, J. P. Zimmer, S. Coe-Sullivan, N. E. Stott, V. Bulovic, and M. G. Bawendi, *Angew. Chem.* **43**, 2154 (2004).
- <sup>20</sup>J. L. Zhao, J. Y. Zhang, C. Y. Jiang, J. Bohnenberger, T. Basche, and A. Mews, *J. Appl. Phys.* **96**, 3206 (2004).
- <sup>21</sup>I. G. Hill and A. Kahn, *J. Appl. Phys.* **84**, 5583 (1998).
- <sup>22</sup>I. G. Hill and A. Kahn, *J. Appl. Phys.* **86**, 4515 (1999).
- <sup>23</sup>A. H. Nethercot, *Phys. Rev. Lett.* **33**, 1088 (1974).
- <sup>24</sup>L. W. Wang and A. Zuger, *Phys. Rev. B* **53**, 9579 (1996).
- <sup>25</sup>S. Sapra and D. D. Sarma, *Phys. Rev. B* **69**, 125304 (2004).
- <sup>26</sup>S. E. Shaheen, B. Kippelen, and N. Peyghambarian, *J. Appl. Phys.* **85**, 7939 (1999).
- <sup>27</sup>M. Anni, L. Manna, R. Cingolani, D. Valerini, A. Creti, and M. Lomascolo, *Appl. Phys. Lett.* **85**, 4169 (2004).



## B Tetrapods

### B.1 Multiple Wurtzite Twinning in CdTe Nanocrystals Induced by Methylphosphonic Acid

L. CARBONE, S. KUDERA, E. CARLINO, W.J. PARAK, C. GIANNINI, R. CINGOLANI, L. MANNA  
*J. Am. Chem. Soc.* **128**(3), pp. 748–755, 2006

Branching in semiconductor nanocrystals, which leads to tetrapods and to more complex architectures, is the subject of intensive investigation. Here we support the model according to which branching in CdTe nanocrystals is driven by the formation of multiple wurtzite twins. This is in contrast to previous models for this material. We found that twinning, as well as anisotropic growth, can be triggered by the presence of suitable molecules, such as for instance methylphosphonic acid. In the case of CdTe nanocrystals, we designed a robust growth scheme in which the variation of a single parameter (the concentration of methylphosphonic acid in solution) leads to the controlled formation of nanocrystals with shapes ranging from spheres to anisotropic structures with varying level of branching, as both twinning and anisotropic growth are progressively favored. We believe that these concepts can be extended to other nanocrystal systems.



Published on Web 12/24/2005

## Multiple Wurtzite Twinning in CdTe Nanocrystals Induced by Methylphosphonic Acid

Luigi Carbone,<sup>†</sup> Stefan Kudera,<sup>‡</sup> Elvio Carlino,<sup>§</sup> Wolfgang J. Parak,<sup>‡</sup> Cinzia Giannini,<sup>†</sup> Roberto Cingolani,<sup>†</sup> and Liberato Manna<sup>\*,†</sup>

*Contribution from the National Nanotechnology Laboratory of CNR-INFM, 73100 Lecce, Italy,  
Center for Nanoscience, Ludwig Maximilians Universität, München, Germany,  
TASC-INFM-CNR National Laboratory, Area Science Park - Basovizza, 34012 Trieste, Italy,  
and CNR-Istituto di Cristallografia (IC), via Amendola 122/O, 70126 Bari, Italy*

Received July 21, 2005; E-mail: liberato.manna@unile.it

**Abstract:** Branching in semiconductor nanocrystals, which leads to tetrapods and to more complex architectures, is the subject of intensive investigation. Here we support the model according to which branching in CdTe nanocrystals is driven by the formation of multiple wurtzite twins. This is in contrast to previous models for this material. We found that twinning, as well as anisotropic growth, can be triggered by the presence of suitable molecules, such as for instance methylphosphonic acid. In the case of CdTe nanocrystals, we designed a robust growth scheme in which the variation of a single parameter (the concentration of methylphosphonic acid in solution) leads to the controlled formation of nanocrystals with shapes ranging from spheres to anisotropic structures with varying level of branching, as both twinning and anisotropic growth are progressively favored. We believe that these concepts can be extended to other nanocrystal systems.

### Introduction

The synthesis of nanocrystals with complex shapes is an exciting development in nanoscience<sup>1</sup> as it paves the way to materials with tailored, geometry-dependent properties and to new concepts of self-assembly arising from the mutual interaction of such nanocrystals. The tetrapod, for instance (Figure 1), is a shape that occurs frequently in several materials ( $\text{ZnO}$ ,<sup>2–11</sup>  $\text{ZnSe}$ ,<sup>12</sup>  $\text{ZnS}$ ,<sup>13</sup>  $\text{CdS}$ ,<sup>14–16</sup>  $\text{CdSe}$ ,<sup>17</sup>  $\text{CdTe}$ ,<sup>18–20</sup>  $\text{CuCl}$ ,<sup>21</sup>

and  $\text{Pt}^{22}$ ) and is formed by four arms that branch out at tetrahedral angles from a central region. Tetrapod-shaped nanocrystals present promising potential for building blocks in solar cells,<sup>23,24</sup> as active components in nanoscale transistors,<sup>25</sup> as field emitters, and might open up new possibilities to create unique architectures that cannot be realized with spherical or rod-shaped nanocrystals.

Understanding the mechanism of branching in colloidal nanocrystals is of fundamental importance, as this is a prerequisite for unfolding the detailed structure and the intrinsic electronic properties of these nanocrystals<sup>26</sup> and for achieving a better control over the fabrication of more elaborate nanoparticle shapes. In the case of solution-grown nanocrystals of II–VI semiconductors, several reports have proposed the model of the tetrapod (Figure 1f) as formed by a sphalerite nucleus (Figure 1a), onto which wurtzite arms have developed by

<sup>†</sup> National Nanotechnology Laboratory of CNR-INFM.  
<sup>‡</sup> Center for Nanoscience, Ludwig Maximilians Universität.  
<sup>§</sup> TASC-INFM-CNR National Laboratory.  
<sup>†</sup> CNR-Istituto di Cristallografia (IC).

(1) Burda, C.; Chen, X. B.; Narayanan, R.; El-Sayed, M. A. *Chem. Rev.* **2005**, *105*, (4), 1025–1102.  
(2) Kitano, M.; Hamabe, T.; Maeda, S.; Okabe, T. *J. Cryst. Growth* **1991**, *108*, (1–2), 277–284.  
(3) Fujii, M.; Iwanaga, H.; Ichihara, M.; Takeuchi, S. *J. Cryst. Growth* **1993**, *128*, (1–4), 1095–1098.  
(4) Takeuchi, S.; Iwanaga, H.; Fujii, M. *Philos. Mag. A* **1994**, *69*, (6), 1125–1129.  
(5) Nishio, K.; Isshiki, T.; Kitano, M.; Shiojiri, M. *Philos. Mag. A* **1997**, *76*, (4), 889–904.  
(6) Iwanaga, H.; Fujii, M.; Takeuchi, S. *J. Cryst. Growth* **1998**, *183*, (1–2), 190–195.  
(7) Dai, Y.; Zhang, Y.; Wang, Z. L. *Solid State Commun.* **2003**, *126*, (11), 629–633.  
(8) Yan, H. Q.; He, R. R.; Pham, J.; Yang, P. D. *Adv. Mater.* **2003**, *15*, (5), 402–405.  
(9) Chen, Z.; Shan, Z. W.; Cao, M. S.; Lu, L.; Mao, S. X. *Nanotechnology* **2004**, *15*, (3), 365–369.  
(10) Yu, W. D.; Li, X. M.; Gao, X. D. *Cryst. Growth Des.* **2005**, *5*, (1), 151–155.  
(11) Wang, F. Z.; Ye, Z. Z.; Ma, D. W.; Zhu, L. P.; Zhuge, F. *J. Cryst. Growth* **2005**, *274*, (3–4), 447–452.  
(12) Hu, J. Q.; Bando, Y. S.; Golberg, D. *Small* **2005**, *1*, (1), 95–99.  
(13) Zhu, Y. C.; Bando, Y.; Xue, D. F.; Golberg, D. *J. Am. Chem. Soc.* **2003**, *125*, (52), 16196–16197.  
(14) Jun, Y. W.; Lee, S. M.; Kang, N. J.; Cheon, J. *J. Am. Chem. Soc.* **2001**, *123*, (21), 5150–5151.

(15) Chen, M.; Xie, Y.; Lu, J.; Xiong, Y. J.; Zhang, S. Y.; Qian, Y. T.; Liu, X. *M. J. Mater. Chem.* **2002**, *12*, (3), 748–753.  
(16) Shen, G. Z.; Lee, C. J. *Cryst. Growth Des.* **2005**, *5*, (3), 1085–1089.  
(17) Manna, L.; Scher, E. C.; Alivisatos, A. P. *J. Am. Chem. Soc.* **2000**, *122*, (51), 12700–12706.  
(18) Yu, W. W.; Wang, Y. A.; Peng, X. G. *Chem. Mater.* **2003**, *15*, (22), 4300–4308.  
(19) Bunge, S. D.; Krueger, K. M.; Boyle, T. J.; Rodriguez, M. A.; Headley, T. J.; Colvin, V. L. *J. Mater. Chem.* **2003**, *13*, (7), 1705–1709.  
(20) Manna, L.; Milliron, D. J.; Meisel, A.; Scher, E. C.; Alivisatos, A. P. *Nat. Mater.* **2003**, *2*, (6), 382–385.  
(21) Li, Q.; Shao, M. W.; Yu, G. H.; Wu, J.; Li, F. Q.; Qian, Y. T. *J. Mater. Chem.* **2003**, *13*, (2), 424–427.  
(22) Teng, X.; Yang, H. *Nano Lett.* **2005**, *5*, (5), 885–891.  
(23) Huynh, W. U.; Dittmer, J. J.; Alivisatos, A. P. *Science* **2002**, *295*, (5564), 2425–2427.  
(24) Sun, B. Q.; Marx, E.; Greenham, N. C. *Nano Lett.* **2003**, *3*, (7), 961–963.  
(25) Cui, Y.; Banin, U.; Bjork, M. T.; Alivisatos, A. P. *Nano Lett.* **2005**, *5*, (7), 1519–1523.  
(26) Li, J. B.; Wang, L. W. *Nano Lett.* **2003**, *3*, (10), 1357–1363.

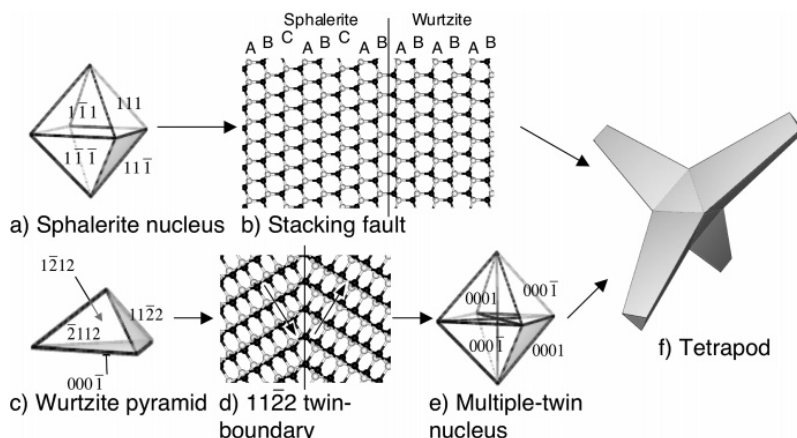


**Figure 1.** Two different models that rationalize the tetrapod shape. (a) A sphalerite nucleus with four equivalent  $\{111\}$  facets and four equivalent  $\{1\bar{1}1\}$  facets. (b) By generation of stacking faults on the four fast growing facets, the growth on these facets would continue in the hexagonal phase, leading to a tetrapod shape (f). (e) A multiple-twin nucleus formed by eight pyramid-shaped wurtzite crystals (c). (d) Structural details of the  $(11\bar{2}2)$  twin boundary present in this type of nucleus. The lattice boundary is observed from the  $(1010)$  zone axis. The arrows in (d) indicate the direction of the polarity in the two wurtzite domains.

continuation of growth from four equivalent  $\{111\}$  facets. This occurs through generation of stacking faults (Figure 1b).<sup>14,15,17,18,20</sup> This model is plausible, since the coexistence of wurtzite and sphalerite phases in II–VI semiconductors is frequent, due to the low energy of formation of stacking faults in these materials.<sup>27,28</sup> However, this model has not been fully proven thus far, due to the lack of detailed TEM investigations. Data from existing studies either do not allow for a unambiguous conclusion about the structure of the tetrapod because the central seed is too small to be clearly identified as a sphalerite domain,<sup>15</sup> or can be interpreted by different models.

Another popular model that rationalizes the tetrapod shape (for instance, in ZnO and ZnSe<sup>4–7,12,29,30</sup>) proposes that the initial nucleus is formed by eight wurtzite domains connected to each other through  $(11\bar{2}2)$  twin boundaries (Figure 1c,e). For each couple of domains sharing a twin plane there is a head-to-tail configuration of the polarity (Figure 1d). This particular type of boundary has a low energy of formation (higher, however, than that of a stacking fault) because it does not involve the creation of dangling bonds and requires little lattice distortion. Ideally, the multiple-twin nucleus is then terminated by four  $(0001)$  and by four  $(000\bar{1})$  wurtzite facets. The growth rate between these two groups of facets is remarkably different;<sup>17,31</sup> hence, four out of the eight domains making up the nucleus are “fast growing”, and the remaining four are “slow growing”. Therefore, the initial nucleus evolves to a tetrapod (Figure 1f). This more elaborate model has been supported by the statistical analysis of the inter-leg angles in ZnO tetrapods<sup>6</sup> (which agree with the angles that are generated by complete relaxation of the octahedral nucleus<sup>32</sup>) and has been confirmed in part also by transmission electron microscopy.<sup>7</sup>

The synthesis of tetrapod-shaped CdTe nanocrystals is well documented,<sup>18–20</sup> and as such this material can be considered as a model system for studying the branching in nanocrystals. In the present work, we support the model according to which the branching in colloidal CdTe nanocrystals is due to the formation of multiple wurtzite twins, which we are able to trigger. The nanocrystals were synthesized at high temperatures in a mixture of surfactants. We show that a small molecule, such as methylphosphonic acid (MPA) is a powerful additive to control both branching and anisotropic growth. When no MPA was added, roughly spherical nanocrystals were always formed. When MPA was present, the shape of the synthesized nanocrystals varied from short, pear-like shapes to structures that were progressively more branched and that grew more anisotropically, depending on the concentration of MPA. High-resolution transmission electron microscopy (HRTEM) revealed that the branching region in tetrapods is characterized by the presence of multiple wurtzite domains. In structures with a number of arms lower than four this region could be studied in more detail and showed the occurrence of twins. In particular, the  $11\bar{2}2$  twin boundary with a head-to-tail polarity configuration was identified clearly and unambiguously in nanocrystals in which a single arm departed from a multiple-twinned region. Other types of wurtzite twins could be present in CdTe nanocrystals, although among them the  $11\bar{2}2$  twin boundary has the lowest energy of formation and therefore the highest probability of occurrence. Twinned wurtzite regions were also observed by HRTEM in tetrapods. Due to the more complicated geometry of the latter experiments, the HRTEM images were compared to the relevant simulations of the twinned core of a branched nanocrystal generated by using atomistic models based on multiple wurtzite domains joined by  $11\bar{2}2$  twin boundaries. Therefore, we are confident that these data can explain the tetrapod shape in the light of the multiple-twin model, although

(27) Takeuchi, S.; Suzuki, K.; Maeda, K., *Philos. Mag. A* **1984**, *50*, (2), 171–178.

(28) Yeh, C. Y.; Lu, Z. W.; Froyen, S.; Zunger, A. *Phys. Rev. B* **1992**, *46*, (16), 10086–10097.

(29) Iwanaga, H.; Fujii, M.; Takeuchi, S. *J. Cryst. Growth* **1993**, *134*, (3–4), 275–280.

(30) Iwanaga, H.; Fujii, M.; Ichihara, M.; Takeuchi, S. *J. Cryst. Growth* **1994**, *141*, (1–2), 234–238.

(31) Kudera, S.; Carbone, L.; Casula, M. F.; Cingolani, R.; Falqui, A.; Snoeck, E.; Parak, W. J.; Manna, L. *Nano Lett.* **2005**, *5*, (3), 445–449.

(32) The formation of the octa-twin requires in fact the accumulation of a large strain if the various pyramids have to join to form a perfect octahedron. However, past a certain critical size for the nucleus, this strain must be released by the generation of cracks along the twin boundaries, and this disrupts the perfect tetrapod geometry, which has indeed never been observed in actual samples.

## ARTICLES

we cannot rule out that some branched nanocrystals form as a consequence of wurtzite–sphalerite polymorphism. We believe that these concepts can be applied also to other nanocrystalline materials that show similar shapes in solution (i.e., CdSe and CdS), and as such they can deepen our knowledge on the formation of these systems.

## Experimental Section

**Chemicals and Stock Solutions.** Cadmium oxide (CdO, 99.999%), trioctylphosphine oxide (TOPO 99%), trioctylphosphine (TOP, 97%), and tellurium (99.999%) were purchased from Strem Chemicals. Octadecylphosphonic acid (ODPA, 99%) was purchased from Polycarbon Industries. Methylphosphonic acid (MPA, 98%) was purchased from Aldrich. All solvents used were anhydrous and were manipulated in a nitrogen drybox. A stock solution of MPA in distilled water (18.2 MΩ) was prepared as 2.9% in weight. A solution of Te in TOP (10% in weight) was prepared by mixing 1 g of Te powder with 9 g of TOP under nitrogen, and then by heating the mixture to 250 °C for several hours until the tellurium was completely dissolved. When cooled to room temperature, the resulting yellow solution was centrifuged at 4000 rpm for several hours to separate it from undissolved products, which were collected as a tiny, white-grayish precipitate.

**Synthesis of CdTe Nanocrystals.** All syntheses were carried out under nitrogen atmosphere. In all experiments, the molar ratio of cadmium to phosphonic acids (ODPA + MPA) was set to 1.0:3.2, the molar ratio of cadmium to tellurium was set to 3.5:1.0, and the total amount of surfactants (TOPO + ODPA + MPA) was kept to 4.1–4.2 g. The only parameter that was changed was the MPA:ODPA molar ratio, which was varied from 0 (only ODPA present) to 0.18. As an example of a typical synthesis of CdTe nanocrystals that yielded mainly tetrapods, 52 mg of CdO were mixed in a 50 mL three-neck flask with 3.75 g of TOPO, 0.385 g of ODPA, and 0.358 g of the MPA solution. The resulting solution was pumped to vacuum for 30 min at 100 °C. To decompose the CdO, the solution was heated to 350 °C under nitrogen until it turned completely transparent and clear. The temperature was stabilized at 320 °C and 0.146 g of the Te:TOP solution, diluted with additional TOP (to a total weight of 0.450 g) was quickly injected in the flask. In all syntheses, the crystals were allowed to grow for 10 min at 320 °C, after which the reaction was stopped by removing the heating mantle. When the solution was cooled to 50 °C, 3–5 mL of chloroform was added to it and the whole content of the flask was transferred in the drybox. The nanocrystals were purified by repeated precipitation with methanol and solubilization in chloroform.

**Transmission Electron microscopy (TEM).** The samples were prepared by dispersing dilute solutions of nanocrystals onto carbon-coated copper grids. Low-magnification TEM images were recorded on a JEOL Jem 1011 microscope operated at 100 KV. Further TEM and scanning TEM (STEM) experiments were performed at room temperature on a JEOL JEM 2010F UHR TEM/STEM electron microscope, with field-emission gun, operating at 200 kV ( $\lambda = 0.0025$  nm), with a measured spherical aberration coefficient  $C_s$  of 0.47 ± 0.01 mm and producing a relevant interpretable resolution limit in HRTEM of 0.19 nm.<sup>33</sup> For Z-contrast imaging, the STEM attachment was equipped with a YAP high angle annular dark field (HAADF) detector. The theoretical resolution achievable in Z-contrast mode with the available electron optics is 0.126 nm.<sup>34</sup> Z-contrast micrographs were recorded with a collection angle  $84^\circ \leq 2\theta \leq 224$  mrad. TEM/STEM observations were performed to identify unambiguously the crystal Bravais lattice of the branching region and thus to assess whether this had wurtzite or sphalerite structure. For this purpose, several nanocrystals were imaged which were oriented along some particular zone

(33) Spence, J. C. H. *Experimental High-Resolution Electron Microscopy*, 2nd ed.; Oxford University Press: Oxford, 1988; p 87.

(34) Pennycook, S. J. *Advances in Imaging and Electron Physics*; Academic: New York, 2002; Vol. 123, p 140.

Carbone et al.

axes that allowed distinguishing between the two types of lattices from the analysis of their diffraction patterns. This differentiation is straightforward: for instance if the orientation of the particles is such that the symmetry of their diffraction pattern is characterized by six diffraction spots placed on the vertex of a regular hexagon. This pattern symmetry is peculiar of both the  $\langle 111 \rangle$  zone axis of the sphalerite structure and of the  $\langle 0001 \rangle$  zone axis of the wurtzite structure. However, in the sphalerite case the diffraction spots are due to the six  $\{202\}$  families of planes, which are spaced by 0.229 nm, whereas in the wurtzite case they are due to both the  $\{100\}$  and the  $\{\bar{1}10\}$  families of planes, which are spaced by 0.398 nm. Hence, by measuring the lattice spacings, the two structures can be distinguished from each other.

**X-ray Diffraction (XRD).** XRD measurements were performed with a D8 Discover-Bruker diffractometer equipped with a 3 kW ceramic tube with a copper anode, a Goebel type parabolic mirror and two-bounces monochromator (V Groove) as primary optics, and a NaI(Tl) scintillator detector. A coupled  $\theta - 2\theta$  movement was chosen for data collection. Concentrated nanocrystal solutions were spread on top of a silicon substrate and then the sample was allowed to dry and was measured in reflection geometry.

**Calculations.** The simulations of the HRTEM images were carried out in the framework of the Multislice approach.<sup>35</sup> This approach allows managing supercells containing thousands of atoms, which are necessary to correctly describe the central region of the tetrapods. In practice, the simulations were performed using the program MACTEMPAS ([www.totalresolution.com](http://www.totalresolution.com)).

Ab initio, DFT calculations of the twin formation energy were performed using the PEtot software, which is based on a plane wave expansion and uses the density functional theory.<sup>36</sup> The exchange-correlation functional was evaluated within the local density approximation (LDA).<sup>37,38</sup> Pseudopotentials<sup>39</sup> for Cd and Te atoms were generated according to the improved Troullier and Martins method,<sup>40</sup> with the Ceperly–Alder exchange-correlation function<sup>41</sup> and using 12 valence electrons for Cd ( $4d^{10}5s^2$ ) and 6 valence electrons for Te ( $5s^25p^4$ ) without core correction, respectively. For Cd, the 5s electrons were used for the local part of the pseudopotential. The plane wave cutoff energy for the wave function was set to 45 Ryd, while the cutoff energy for the charge density was set to 150 Ryd. The cell used to model the twin boundary contained 64 atoms (for a total of 576 valence electrons) and was adapted from the cell used by Yan and co-workers to model the same type of defect in ZnO.<sup>42</sup> Eight symmetry-reduced special k-points for the supercell calculations were used. The atomic positions were optimized to minimize the forces acting on the atoms.

## Results

The results of the syntheses performed at MPA:ODPA molar ratios ranging from 0 to 0.18 are summarized in Figure 2. The clear trend here is that the higher the MPA:ODPA ratio, the more branched and elongated the nanocrystals grow. A statistical analysis was also carried out on the TEM images of these samples to determine the average number of branches per nanocrystal (Figure 2, inset). From this analysis and from an overall glance at Figure 2, one can deduct that tetrapods (four branches per nanocrystal) are best synthesized at MPA:ODPA ratios around 0.08–0.09 (Figure 2d,e). Slightly lower ratios

(35) Goodman, P.; Moodie, A. F. *Acta Crystallogr., Sect. A* **1974**, *A30*, 280–290.

(36) Wang, L. W. *Petot: A Parallel Plane Wave Pseudopotential Program for Atomistic Total Energy Calculation Based on Density Functional Theory*, Version 2; Berkeley, 2004.

(37) Hohenberg, P.; Kohn, W. *Phys. Rev.* **1964**, *136*, 864B.

(38) Kohn, W.; Sham, L. J. *Phys. Rev.* **1965**, *140*, 1133A.

(39) Heine, V. In *Solid State Physics*; Ehrenreich, H., Seitz, F., Turnbull, D., Eds.; Academic Press: New York, 1970; Vol. 24, pp 1–36.

(40) Troullier, N.; Martins, J. L. *Phys. Rev. B* **1991**, *43*, (3), 1993–2006.

(41) Perdew, J. P.; Zunger, A. *Phys. Rev. B* **1981**, *23*, (10), 5048–5079.

(42) Yan, Y. F.; Al-Jassim, M. M.; Chisholm, M. F.; Boatner, L. A.; Pennycook, S. J.; Oxley, M. *Phys. Rev. B* **2005**, *71*, (4), art. no.-041309.

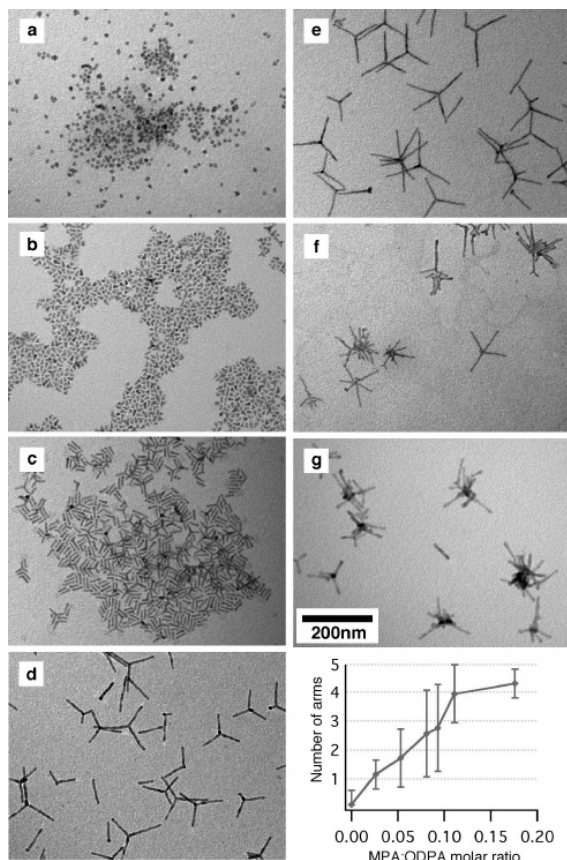


**Figure 2.** Low-magnification TEM images and results of statistical analysis of a series of samples prepared at increasing MPA:ODPA molar ratios. (a) 0, (b) 0.026, (c) 0.053, (d) 0.081, (e) 0.093, (f) 0.111, and (g) 0.176. All syntheses were run for 10 min. In the statistical analysis, the number of branches for each nanocrystal was assigned as follows: zero for spherical nanocrystals; 1, 2, 3, and 4, for rods, dipods, tripods, and tetrapods, respectively, while multibranched objects were simply assigned five arms. The large errors are due to the fact that often the determination of the number of branches in a nanocrystal is not straightforward, especially for highly branched structures. Also, highly branched structures are not weighted adequately by the analysis, leading to an artificial shift toward smaller numbers on average.

(0.05–0.08) will tend to yield more regular tetrapods but accompanied with a large number of nanocrystals having a lower number of arms (rods, dipods, tripods).

When only ODPA was used in the syntheses, almost spherical nanocrystals were obtained (Figure 2a and Figure 3a,b). X-ray diffraction (Supporting Information) indicated that this sample contained a mixture of wurtzite and sphalerite nanocrystals. The formation of branched nanocrystals was rarely observed. On the other hand, the nanocrystals showed a remarkable occurrence of stacking faults. In Figure 3c,d two representative nanocrystals from this sample are shown which present a “branching region”. In the nanocrystal of Figure 3d, the central region between the two lobes can be indexed as the (214) zone axis (or  $(10\bar{1}4)$  in the Miller–Bravais notation) of the wurtzite structure. Also, the two arms have wurtzite structure, and therefore the whole nanocrystal represents a multiple twin.

At a molar ratio of MPA to ODPA as low as 0.026 (corresponding to a weight percentage of MPA in the mixture of phosphonic acids of less than 1%) the nucleation rate

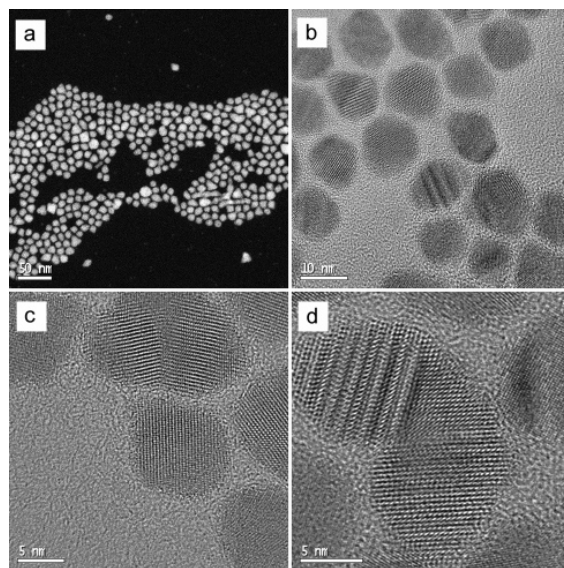


**Figure 3.** (a) Low-magnification HAADF image of nanocrystals grown in the absence of MPA, which shows that the shapes of most clusters are roughly isotropic and that there is no contrast variation inside them. (b–d) HRTEM images of some representative nanocrystals, highlighting the presence of stacking faults (b), and of occasional wurtzite twins (c, d).

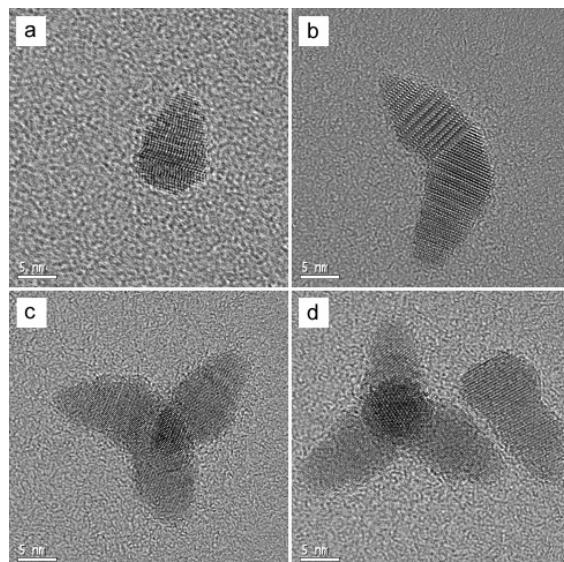


**Figure 4.** HRTEM images of some representative nanocrystals of the sample grown at MPA:ODPA molar ratio equal to 0.026 (see also Figure 2b). In the branched nanocrystals shown in (c, d) the spacings in the arms can be compatible with the sphalerite structure, except for the arm pointing upward. It is very unlikely that the structure of this fourth arm is different from that of the other arms in both nanocrystals, whereas it is more plausible that the peculiar spacing of the wurtzite structure for the arms touching the substrate are not clearly distinguishable under this orientation.

increased with respect to the previous synthesis, as a color change of the solution from pale yellow (the color of the injected Te:TOP solution) to brown (nanocrystals) occurred much earlier after the injection. The synthesis yielded mainly anisotropic nanocrystals with pearl-like shapes, along with dipods, tripods and some tetrapods (Figure 2b and Figure 4). These nanocrystals were either single wurtzite domains or were made by wurtzite

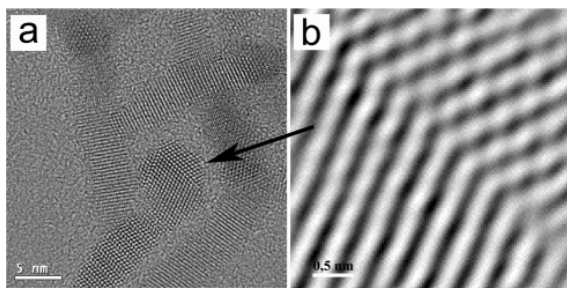


**Figure 5.** (a) Matchstick-shaped nanocrystal revealing several twins in the head of the matchstick. The region indicated by the arrow is shown in (c) at higher magnification. This area is close to the  $[1\bar{1}00]$  zone axis. The defect contrast can be identified as a (1122) twin boundary, with a head-to-tail configuration of the crystal polarity. The arrangement of the atoms close to the boundary corresponds to the one shown in the model of Figure 1d.

twins (Figure 4). In all cases the domains were elongated along the  $c$  axis. The presence of sphalerite nanocrystals was very seldom observed. This in addition indicates that the presence of MPA decreased the probability of formation of sphalerite phase considerably.

At higher MPA:OPDA ratios, the branching increased further, as well as the anisotropic growth (Figure 2c–g). Ratios in the range 0.08–0.09 yielded mainly tripods and tetrapods, whereas nanocrystals with multiple branching points dominated at ratios higher than 0.10.

X-ray diffraction spectra of the branched samples (for instance, the samples shown in Figure 2d and 2f, see Supporting Information), resembled in their shape those of wurtzite nanorods.<sup>17,43</sup> They show, in fact, a high degree of distortion of the intensity ratios due to shape anisotropy, in particular with an enhancement of the reflections associated with crystalline domains along the  $c$  axis of the wurtzite structure.

Extensive HRTEM observations were carried out on nanocrystals. To uncover the nature of the branching in tetrapods, it would be desirable to image the central region. Unfortunately, such a direct observation is often made difficult by the presence of the arms, which hinder most of this region. A more straightforward analysis can be carried out on structures missing several arms, such as tripods, dipoles (Figures 3d and 4b), or matchstick-shaped nanocrystals, often present together with branched nanocrystals (Figure 2c–e). These latter structures are characterized by the presence of easily identifiable twinned domains, of which only one has been able to grow anisotropically and has developed to an arm. Therefore, the twinned region is always localized on one side of the CdTe rod, and so it forms the head of the resulting matchstick shape. One of these matchsticks is shown in more detail in Figure 5a. In particular, the region indicated by the arrow is close to the  $[1\bar{1}00]$  zone axis. The twin of interest can be seen at higher magnification at Scherzer defocus in Figure 5b. Here, the defect contrast is the same as the one reported recently by Yan et al. for wurtzite  $\text{ZnO}$ <sup>42</sup> and can be identified as a (1122) twin boundary. The different positions of the fringes at the opposite sides of the twin boundary indicate that the two domains are not mirror images of each other, but instead the arrangement of the atoms corresponds to the one shown in the model of Figure 1d. Therefore, this is a

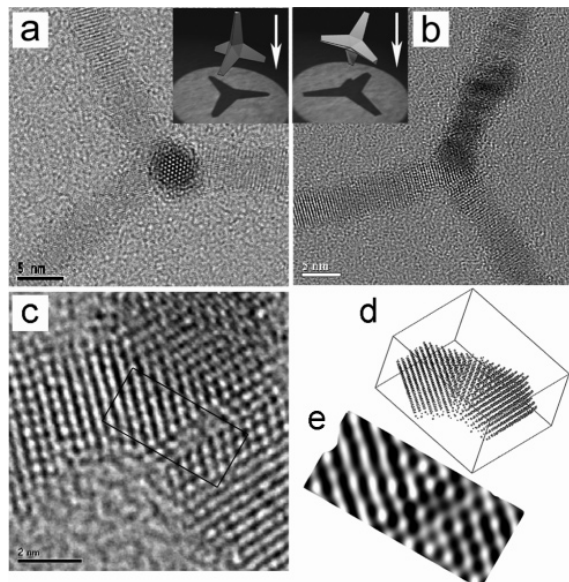


**Figure 6.** (a) HRTEM image of a CdTe tetrapod with one arm pointing upward. (Inset) Orientation of the nanocrystal with respect to the electron beam (white arrow). The analysis of the symmetry and of the lattice spacing of the arms of several tetrapods indicates a wurtzite structure (space group  $P6_3mc$ ) with lattice parameters corresponding to  $a = 0.458$  nm and  $c = 0.75$  nm, respectively. (b) Tilted tetrapod. (Inset) Orientation again of the nanocrystal with respect to the electron beam (white arrow). In particular, in this geometry two arms are superimposed. (c) Central region of the tetrapod shown in (b) is imaged here at higher magnification. The rectangular contour is the region that is the object of the image simulation. (d) Supercell containing the atomistic model used to simulate the HRTEM image of the central region of the tetrapod, viewed along its 247 zone axis and rotated around this axis (which is perpendicular to the plane of the image) so that the model has the same orientation as the real nanocrystal in the HRTEM image in (c). (e) Simulated HRTEM image of the core region of the tetrapod contoured in (c).

(1122) twin boundary with a head-to-tail configuration of the polarities of the two wurtzite domains.

Branching in CdTe nanocrystals is occurring only if more than two wurtzite domains are present in the nanocrystal, such as for instance in the dipod shown in Figure 3d. In that case, the central wurtzite domain is a “slow growing” domain (as discussed in the Introduction), and this is attached to “two fast growing” wurtzite domains. Therefore, at least two twin planes are present in a branched nanocrystal (in this case the branched nanocrystal is a dipod). Unfortunately, the visualization of these planes from a favorable zone axis is made difficult by the orientation of the nanocrystal with respect to the electron beam, and a tilting experiment rarely improves this view.

In the case of a tetrapod, a view of the central core region can be obtained by tilting the particle from its natural orientation on the substrate (which is the one with one upstanding arm as in Figure 6a), so that its TEM image is, for instance, that shown in Figure 6b (the core region is seen at higher magnification in Figure 6c). Due to the small size of the structures studied here, it is not possible to align precisely a convenient zone axis, but it is only possible, with great efforts, to tilt the region of interest close to a zone axis with an uncertainty of a few degrees. In the present case, the two arms that point downward are as sketched in the model shown in the inset of Figure 6b. In such a nanocrystal, the geometry of the HRTEM experiment is more

(43) Peng, X. G.; Manna, L.; Yang, W. D.; Wickham, J.; Scher, E.; Kadavanich, A.; Alivisatos, A. P. *Nature* **2000**, *404*, (6773), 59–61.

complicated with respect to the case shown in Figure 5, and to understand the HRTEM image contrast it is necessary to have a comparison with the relevant simulated image. Hence, a simulation of the HRTEM image of the central region between the two lower arms was carried out (Figure 6e). The atomistic model (Figure 6d) was built by joining three hexagonal domains sharing the  $(1\bar{1}2\bar{2})$  twin boundary, the same as the one present in the matchsticks of Figure 5. Two domains represent the arms, joined to a central domain. The atomistic model used for this purpose is actually a dipod, as this contains the minimum number of twins necessary to model the region of interest (in this region, the electron beam would cross only these three domains). As can be seen from Figure 6e, the calculated HRTEM image qualitatively reproduces the experimental image. Considering the supercell structure used to model this image (Figure 6d) the HRTEM image has been successfully simulated by considering such supercell as oriented along its  $[2\bar{4}7]$  zone axis. In this projection, the domain on the left (the left arm) is hiding part of the central domain. It is worth noting that this simulation shows how a tilt of the structure produces a not intuitive image of the tetrapod and in particular of the twinned region. Therefore, the way to proper understand a HRTEM image contrast of such a complex object is to compare the experimental image to the relevant simulation.

The occurrence of twins in CdTe must be promoted if their energy of formation is low, or if the growth environment contributes to lower such energy of formation. Although several types of wurtzite twin planes have been observed in other materials (such as  $\text{ZnO}^5$ ) and are likely to be present also in CdTe, we choose to focus on the  $(1\bar{1}2\bar{2})$  twin boundary. Our LDA-DFT calculations show that in bulk CdTe the energy of formation for the  $(1\bar{1}2\bar{2})$  twin boundary with a head-tail polarity configuration is of the order of  $70 \text{ mJ/m}^2$ , which is intermediate between that of  $\text{ZnO}$  ( $40 \text{ mJ/m}^2$ ) or  $\text{InN}$  ( $51 \text{ mJ/m}^2$ ) and that of other wurtzite semiconductors, such as  $\text{AlN}$  and  $\text{GaN}$  ( $109$  and  $107 \text{ mJ/m}^2$ , respectively), as reported by Yan et al.<sup>42</sup> Therefore,  $(1\bar{1}2\bar{2})$  twinning should not form in CdTe easily, unless the presence of an additional perturbation could promote somehow its formation. This seems to be the effect of adding MPA in our syntheses, together with the enhancement of anisotropic growth (these two features could be interconnected). The possible roles of MPA in this process are highlighted in the discussion section. We point out that  $(1\bar{1}2\bar{2})$  twin boundaries, with tail-to-tail or head-to-head configuration would have a much higher energy of formation, in analogy with other materials,<sup>42</sup> as they would involve the formation of unsaturated bonds and the build-up of considerable strain at the twin interface. The occurrence of these types of twins in CdTe would be justified if we could find dipods with only one twin plane (i.e. two fast growing wurtzite domains joined together). This twin plane would be localized at the center of the branching region of these dipods. However, we did not find such types of dipods in our samples.

### Discussion

The synthesis of colloidal CdTe nanocrystals in a mixture of surfactants highlights the intrinsic complexity of the crystal growth process and how this can be influenced by the presence of impurities. Several reports on the growth of CdTe tetrapods have appeared recently.<sup>18–20</sup> In one of them,<sup>20</sup> tetrapods of varying arm length and diameters were synthesized in a mixture

of TOPO, TOP, and ODPA. Later, we found out that the commercially available ODPA contained, until recently, various impurities.<sup>44</sup> When we performed the synthesis of CdTe nanocrystals in a purer ODPA (99%, prepared by Polycarbon Industries according to a new protocol), we could obtain only roughly spherical nanocrystals (Figures 2a and 3). The series of experiments reported in this work, in which MPA is present at a known concentration in the mixture of surfactants, reveals that the active component that controls branching and anisotropic growth can be a phosphonic acid with a short alkyl chain. We cannot exclude that other molecules, as for instance alkyl phosphonic acids with intermediate chain lengths, or closely related molecules, might have comparable effects. As an example, syntheses performed with propylphosphonic acid yielded similar results (data not shown).

On the basis of the experimental evidence, we are confident that twinning is responsible for the branching of CdTe nanocrystals. The nanocrystal shapes observed in our experiments indicate in fact that, the higher the concentration of MPA in the growing medium, the higher the average number of twins in the starting nuclei will be, and also the more anisotropically the nanocrystals will grow. Following these observations, we can propose a model that explains the branching behavior. According to this model, which is sketched in Figure 7, the number of arms formed in the nanocrystals depends on the number and on the type of twins present in the starting nucleus. When no MPA is present, twinning has low probability of occurrence. Also, the formed nuclei will grow more or less isotropically, yielding roughly spherical or faceted nanocrystals (as for instance in Figure 2a). At low concentrations of MPA, the nuclei either will be still single domains or will be formed mainly by two wurtzite domains sharing a twin plane (Figure 7a). Both types of nuclei will expose, in addition to other facets, one polar  $(0001)$  facet and one polar  $(000\bar{1})$  facet. Of these two polar facets, one will grow much faster than the other, resulting in a pear- or matchstick-shaped nanocrystal (Figure 7a). These shapes can be seen in most nanocrystals of Figure 2b (pears) and Figure 2c (matchsticks). At higher concentrations of MPA, the nuclei will be formed by a higher number of twins (Figure 7b,c). Therefore, these nuclei will show more than one fast growing facet and so will develop more arms, becoming for instance a dipod (Figure 7b), a tripod, or a tetrapod (Figure 7c). At even higher concentration of MPA, twinning will be favored not only at nucleation but also during growth. In these cases, each arm can branch further, as in the hyper-branched structures of Figure 2f,g.

We would like to stress that the proposed mechanism, with perfectly shaped and nicely matching domains, all developing boundaries at the same time (as shown in Figure 7), represents a highly idealized view of the structure of the initial nucleus and of the overall shape evolution. More irregular shapes, often observed in our samples, indicate that the actual branching mechanism is likely to be more complex than the one depicted here. It is quite likely that additional branching pathways exist, which are based on the formation of multiple twins other than those due to the  $(1\bar{1}2\bar{2})$  type. This is particularly true for nanocrystals in which there is a high level of branching. In addition, we cannot exclude here the formation of branched

(44) See the Supporting Information for the description of impurities present in ODPA.

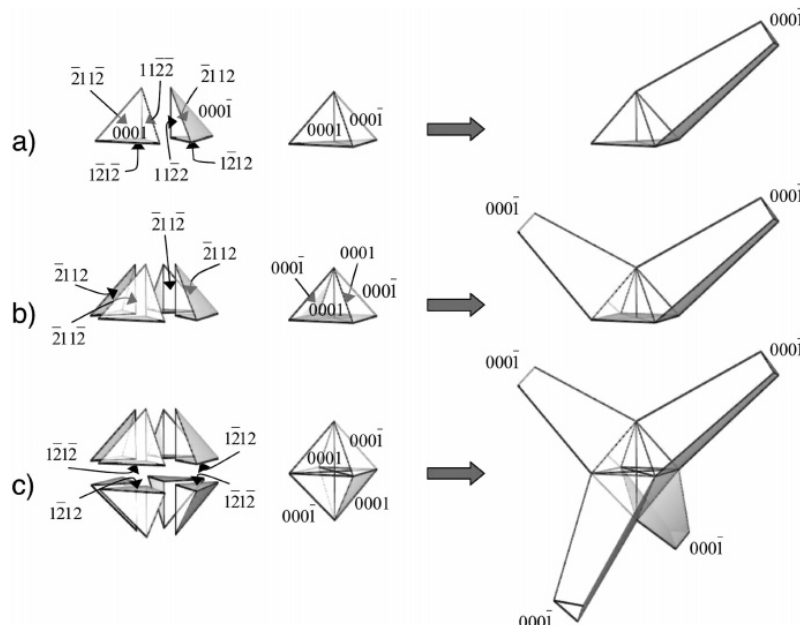


**Figure 7.** Sketch of the multiple-twin model. The left column shows an exploded view of three different types of nuclei (middle column) that could rationalize the formation of rods (a), dipods (b), and tetrapods (c). Two types of domains are considered in this model (as shown in a, left side). One domain exposes a (0001) facet (we call it type I domain), whereas the other domain exposes a (0001̄) facet (type II domain). In a multiple-twin nanocrystal the two types of domains are connected to each other by a twin boundary. Of these two types of domains, only one can grow to an elongated structure, although our present knowledge does not allow us to identify which one of the two domains this will be. To help the reader understand the model better, we assume here that the "fast growing" domain is of the type I. Therefore, the nucleus from which a rod (or a matchstick) evolves is composed of at least one domain which is of type I. This domain can be joined to one type II domain (as shown in a) or to more type II domains (up to three) by (1122) twin boundaries. These will be the slow growing domains. Then, if a second twin boundary is generated between any of these type II domains and yet a new type I domain, a second arm will form (a possible case for this situation is shown in b). In the most crowded situation, eight domains can join together to form an octahedral crystal (as shown in c). Four of these domains can be of type I, and four of type II, and in this case four arms will branch out from this core, forming a tetrapod.

structures also based on the occurrence of wurtzite–sphalerite polymorphic modifications.

A small molecule such as MPA can play different roles in the growth kinetics of CdTe nanocrystals. We can try to elucidate these possible roles based on our experimental results and on previous work on nanocrystals. First of all, the Cd precursor in solution is a complex of  $\text{Cd}^{2+}$  with phosphonate molecules.<sup>45</sup> Therefore, the higher the concentration of MPA relative to that of ODPA, the more likely it will be for  $\text{Cd}^{2+}$  to be bound to methyl phosphonates. This sort of complex will be much more mobile than the bulkier complex formed by  $\text{Cd}^{2+}$  with octadecylphosphonate molecules, and in addition the  $\text{Cd}^{2+}$  ions will be less hindered and so more reactive (in other words they will be more *available*). This accounts for the observed increase in nucleation and growth rate of the nanocrystals at increasing concentration of MPA. It can also account for the elongated growth that is observed in the nanocrystals. Looking at the series of TEM images from Figure 2, a–c, it is clear that long arms are formed at higher concentrations of MPA. Anisotropic growth, in fact, can be sustained only if there is fast supply of monomers from the bulk of the solution.<sup>46–48</sup> In addition, crystal defects are generated more easily at high growth rates,<sup>49</sup> and therefore the presence of MPA could also rationalize the much higher probability of formation of twins, which are a

particular type of planar defect. This behavior is consistent with earlier observations on a similar system (CdSe nanocrystals<sup>47</sup>), in which an increase in the concentration of precursors resulted in higher nucleation and growth rates of nanocrystals, but also promoted the formation of multibranched nanocrystals.

Another (or an additional) mechanism by which we can imagine that the presence of MPA induces twinning could be a templating effect mediated by the MPA molecules that are passivating the surface of the nanocrystals during nucleation and growth. In other words, it might be possible for these MPA molecules to promote an arrangement between the atoms on the surface of the crystal and those approaching the surface from the solution, which could favor the formation of a twin boundary. To decide by which mechanism the formation of twins occurs, extensive studies would be necessary, which go beyond the scope of this work.

## Conclusions

In this work, we have reported a simple and robust protocol for the synthesis of CdTe nanocrystals with a good control over their branching. Detailed HRTEM experiments and HRTEM image simulations have revealed that the branching region is characterized by the presence of multiple twins, among which the  $11\bar{2}2$  twin boundary with a head-to-tail polarity configuration was identified in matchstick-shaped nanocrystals. The presence of this type of twin supports the tetrapod shape on the light of

(45) In the synthesis, CdO dissolves in the mixture of surfactants via decomposition by alkylphosphonic acids. The reaction leads to the formation of a cadmium phosphonate complex and releases water as a byproduct.

(46) Peng, Z. A.; Peng, X. G. *J. Am. Chem. Soc.* **2001**, *123*, (7), 1389–1395.

(47) Peng, Z. A.; Peng, X. G. *J. Am. Chem. Soc.* **2002**, *124*, (13), 3343–3353.

(48) Peng, X. G. *Adv. Mater.* **2003**, *15*, (5), 459–463.

(49) Markov, I. V. *Crystal Growth for Beginners: Fundamentals of Nucleation, Crystal Growth, and Epitaxy*; World Scientific: Singapore, 2003.

*Multiple Wurtzite Twinning in CdTe Nanocrystals*

**ARTICLES**

the multiple-twin model discussed above and facilitates the rationalization of other shapes obtained in these types of syntheses, such as matchsticks, dipods, tripods, and multi-branched nanocrystals. The formation of these shapes would be difficult to explain by the model based on a cubic sphalerite nucleus. A sphalerite nucleus exposes four equivalent, fast growing facets, and therefore this type of object would naturally evolve into a tetrapod shape. There is apparently no reason why only some of these four equivalent, fast growing facets, would grow much faster than the others, generating structures with a number of arms lower than four.

We found that twinning, as well as anisotropic growth, can be favored by the presence of suitable molecules, such as MPA. We have also drawn some hypotheses on the possible microscopic mechanisms that trigger the formation of twins and, consequently, of branched nanocrystals. Additional studies (both theoretical and experimental) by our group on this matter are in progress and will be the subject of a future work.

**Acknowledgment.** This work was supported in part by the European project SA-NANO (Contract Number STRP 013698), by the Italian MIUR 297 project (Contract Number 13587) and

by the German research foundation (DFG, Emmy Noether program). For the calculations, this work used the resources of the U.S. National Energy Research Scientific Computing Center at NERSC (U.S. Department of Energy under Contract No. DE-AC03-76SF00098). We acknowledge Dr. Yanfa Yan (National Renewable Energy Laboratory, Golden, CO 80401, U.S.A.) for having given us the geometrical details of the ZnO supercell which we adapted for our calculations on CdTe. We would like to acknowledge Professor A.P. Alivisatos (UC Berkeley) and Dr. L.W. Wang (NERSC Berkeley) for many inspiring discussions.

**Supporting Information Available:** Description of the impurities often present in ODPAs; XRD characterization of spherical and branched nanocrystals; geometrical details of the computations (derivation of cell parameters and atomic positions for the twin formation energy; atomistic model of the multiple-twinning region used for the simulation of the HRTEM image). This material is available free of charge via the Internet at <http://pubs.acs.org>.

JA054893C

# Multiple wurtzite twinning in CdTe nanocrystals induced by methylphosphonic acid

*Luigi Carbone<sup>a</sup>, Stefan Kudera<sup>b</sup>, Elvio Carlino<sup>c</sup>, Wolfgang J. Parak<sup>b</sup>, Cinzia Giannini,<sup>d</sup> Roberto Cingolani<sup>a</sup> and Liberato Manna<sup>a\*</sup>*

<sup>a</sup> National Nanotechnology Laboratory of CNR-INFM, 73100 Lecce, Italy

<sup>b</sup> Center for Nanoscience, Ludwig Maximilians Universität, München, Germany

<sup>c</sup> TASC-INFM-CNR National Laboratory, Area Science Park - Basovizza, 34012 Trieste, Italy

<sup>d</sup> CNR-Istituto di Cristallografia (IC), via Amendola 122/O, 70126 Bari, Italy

## Supporting Information

[liberato.manna@unile.it](mailto:liberato.manna@unile.it)

**RECEIVED DATE (to be automatically inserted after your manuscript is accepted if required according to the journal that you are submitting your paper to)**

\*Corresponding author:

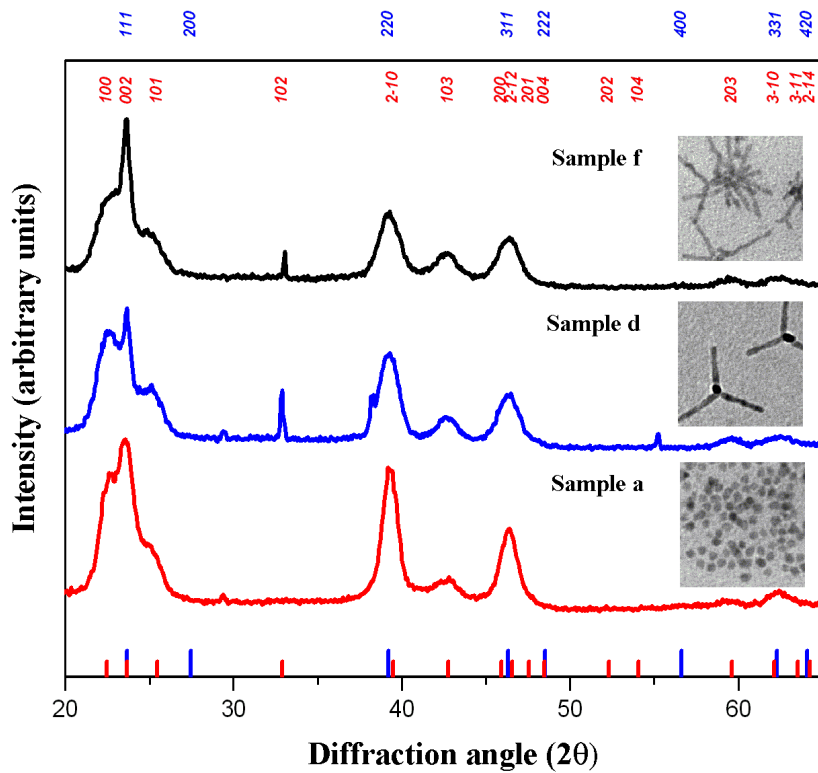
liberato.manna@unile.it; tel. +39 0832 298 207; fax +39 0832 298 238

**Impurities in old batches of Octadecylphosphonic acid**

The impurities previously present in ODPA, as declared by the vendor (Polycarbon Industries Inc.), were the following: ethyl phosphonic acid, ethyl esters of ethyl phosphonic acid (mono and di-esters), octadecyl esters of ethyl phosphonic acid (mono and di-esters), mixed esters of the above, ethyl esters of ODPA (mono and di-esters), octadecyl esters of ODPA (mono and di-esters), mixed esters of the above. It is likely that other vendors provided ODPA with similar impurities in the past.

**Diffraction Data**

**Figure S1.** We report here the XRD spectra of the samples shown in Figure 2a, 2d and 2f of the manuscript. These samples are prepared at the following MPA:OPDA ratios: (a) 0.026; (d) 0.081; (f) 0.111. At the bottom of the plot, on the x-axis, the red lines correspond to the positions of the peaks in bulk wurtzite CdTe, while the blue lines correspond to the positions of the peaks in bulk sphalerite CdTe. On the top of the plot, these diffraction peaks are indexed.



Model of a multiple wurtzite twinned nanocrystal (a dipod) viewed at different tilts

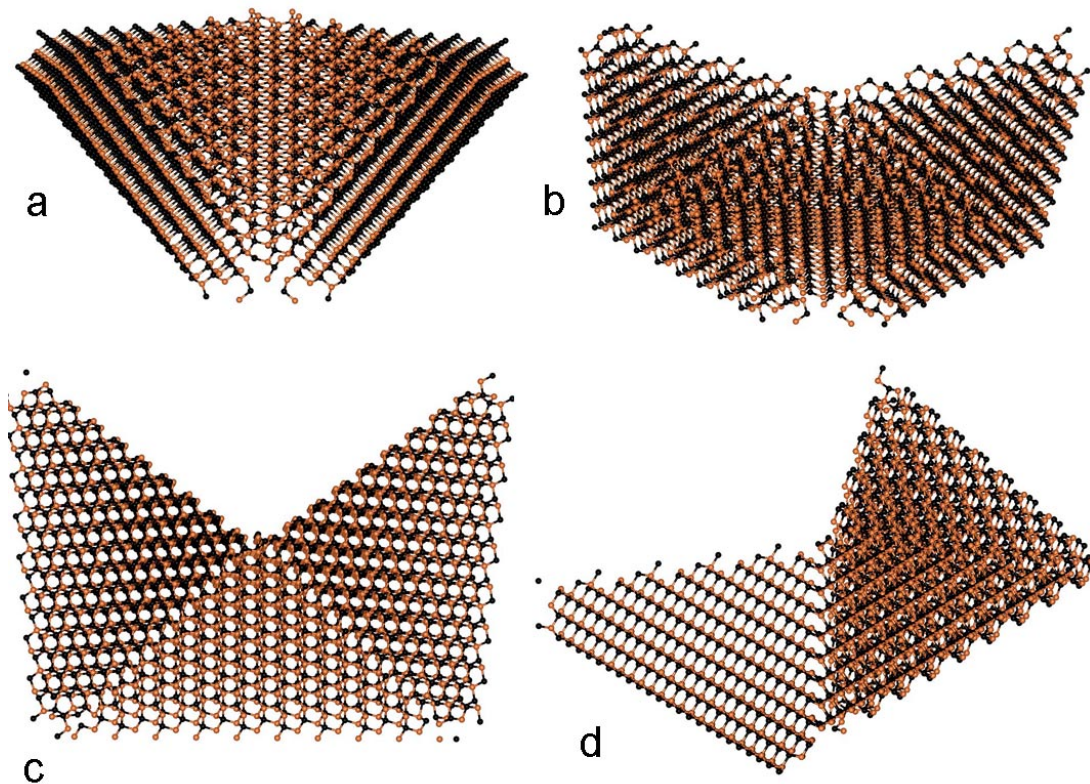


**Figure S2.** Different views of a dipod based on a multiple wurtzite twinned nanocrystal (the one used for the HRTEM image simulation, see figure 6 of the manuscript). The images have the purpose to show that the unambiguous identification of a given type of twin plane is difficult to achieve, unless the crystal has a particularly favourable orientation. This favourable orientation is for instance the one depicted in Figure S2-d. In this case, the domain on the left and the central domain are both viewed along their  $(10\bar{1}0)$  zone axes (the same as in figure 1d of the manuscript). Unfortunately, the central domain overlaps with the domain on the right and this makes the view less clear. Moreover, this orientation is rather difficult to achieve in a real TEM experiment, as the domain on the right should be pointing upwards (or downwards), while the domain on the left should lie flat. The atomic positions near the twin boundaries have not been relaxed, as opposed to

the case depicted in figures S3 and S4. As a consequence, some stretched or compressed bonds are present in the model (See also the structure file of the dipod included as supporting material).

### Geometrical details of the LDA-DFT computations

We report here the geometrical parameters of the *orthorombic* supercell used to model the  $1\bar{1}\bar{2}2$  twin boundary, along with the atomic positions in the cell. The supercell used to model the twin boundary contained 64 atoms (for a total of 576 valence electrons) and was adapted from the supercell used by Yan and coworkers to model the same type of defect in ZnO. If we indicate with  $a$  and  $b$  the lattice parameters for the hexagonal cell of bulk wurtzite CdTe, the lattice parameters for the supercell are calculated as follows:

$$\begin{aligned}l_1 &= 8a \cdot \cos(\arctan(a/c)) \\l_2 &= a/\sin(\arctan(a/c)) \\l_3 &= 2a \cdot \cos(\pi/6)\end{aligned}$$

As can be seen from Figures S3 and S4, each cell intersects two twin planes. Therefore, the twin plane formation energy is calculated as follows:

$$E_{\text{boundary}} = (E_{\text{supercell}} - E_{\text{bulk}})/2A$$

Here,  $E_{\text{bulk}}$  corresponds to the energy per unit cell of bulk wurtzite CdTe, and  $A$  is the twin plane area intersected by a single supercell, which corresponds to  $l_2 \cdot l_3$ .

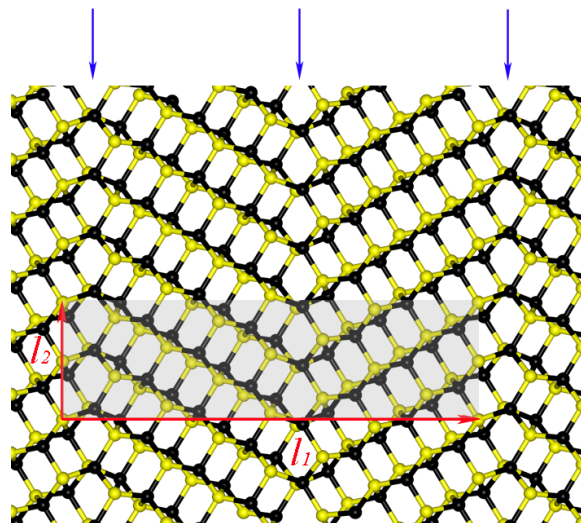


**Figure S3.** Lattice used to model the  $11\bar{2}2$  twin boundary, side view. The shaded area corresponds to a single supercell. It contains 64 atoms (32 Cd and 32 Te). The blue arrows indicate the positions of the twin planes in the lattice.

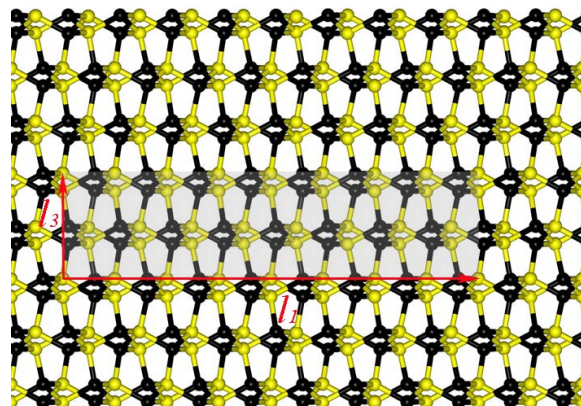


**Figure S4.** Lattice used to model the  $11\bar{2}2$  twin boundary, top view. The shaded area corresponds to a single supercell.

**Cell parameters:**  $l_1 = 31,167 \text{ \AA}$   
 $l_2 = 8,777 \text{ \AA}$   
 $l_3 = 7,897 \text{ \AA}$

**Atomic positions in the cell (along  $l_1$ ,  $l_2$ , and  $l_3$ , respectively):**

Te	0.484792276	0.633448318	0.324374777
Te	0.233392040	0.604490987	0.166535178
Te	0.733472620	0.515843578	0.166811465
Te	0.608373364	0.797662140	0.165787235
Te	0.233379049	0.104510736	0.333489332
Te	0.173644375	0.468289588	0.666978980
Te	0.858289392	0.240028713	0.169650262
Te	0.985103391	0.481757787	0.323249028
Te	0.298257572	0.746371744	0.666868506
Te	0.357990061	0.880996596	0.169781022
Te	0.484790563	0.133538251	0.175475216
Te	0.985108023	0.981646755	0.176654796
Te	0.923687838	0.089965769	0.665745972
Te	0.108712461	0.316856571	0.165816202
Te	0.423143530	0.029659331	0.664457596
Te	0.048567065	0.213537898	0.663091435
Te	0.673477765	0.648150368	0.666419799
Te	0.798451074	0.372105969	0.666741280
Te	0.858281818	0.740041814	0.330316217
Te	0.923696982	0.589943934	0.834213598
Te	0.733463989	0.015816978	0.333195193
Te	0.548306016	0.401534209	0.837154643
Te	0.423155068	0.529593575	0.835656800
Te	0.673470407	0.148162723	0.833614020
Te	0.798433581	0.872113709	0.833210129
Te	0.608375126	0.297563898	0.334124197
Te	0.298266182	0.246378969	0.833223467
Te	0.548316701	0.901520767	0.662924548
Te	0.357988170	0.380999617	0.330297088
Te	0.048557743	0.713554190	0.836929973
Te	0.173628787	0.968322287	0.833040397
Te	0.108698262	0.816892118	0.334182017
Cd	0.686618827	0.243985207	0.167595774
Cd	0.436411445	0.410196024	0.165305761
Cd	0.626940885	0.376372416	0.669010243
Cd	0.876104177	0.818334074	0.664720095
Cd	0.561195117	0.525452266	0.164364859
Cd	0.311289989	0.653441076	0.332069133
Cd	0.811383223	0.967764761	0.167411188
Cd	0.311295934	0.153412033	0.168008686
Cd	0.186642217	0.876791973	0.168241434
Cd	0.251591100	0.018322254	0.666437799
Cd	0.000573802	0.493013763	0.669020638
Cd	0.811375055	0.467741180	0.332571203
Cd	0.936381515	0.705155239	0.165893797
Cd	0.375930490	0.302332568	0.664695957
Cd	0.061515589	0.588568611	0.163542439
Cd	0.127095141	0.239595986	0.830498095
Cd	0.436356734	0.910155787	0.334713877
Cd	0.561189496	0.025562910	0.335637689
Cd	0.375940155	0.802281292	0.835506562
Cd	0.000544187	0.992992967	0.831080659
Cd	0.876120646	0.318287959	0.835262600
Cd	0.061511231	0.088560233	0.336334779
Cd	0.686605102	0.743942927	0.332367216
Cd	0.751510776	0.100169144	0.667013214
Cd	0.936379525	0.205231275	0.334049430
Cd	0.751512256	0.600128771	0.832996492
Cd	0.186638706	0.376619323	0.331688504
Cd	0.626923189	0.876364310	0.830986891
Cd	0.251598903	0.518360155	0.833592253
Cd	0.500329278	0.122571993	0.830104151
Cd	0.500325435	0.622319394	0.670091488
Cd	0.127091959	0.739548454	0.669596226

## B.2 Shape and Phase Control of Colloidal ZnSe Nanocrystals

P.D. COZZOLI, L. MANNA, M.L. CURRI, S. KUDERA, C. GIANNINI, M. STRICCOLI,  
A. AGOSTIANO

*Chem. Mater.* **17**(6), pp. 1296–1306, 2005

Shape- and phase-controlled ZnSe nanocrystals are synthesized in hot mixtures of long-chain alkylamines and alkylphosphines. The variation in the rate of precursor addition, down to low and controlled levels, allows the nucleation, as well as the growth of the nanocrystals, to switch between the wurtzite and the zinc blend structures. Such a level of control leads to a variety of shapes, from spheres to rods to three-dimensional structures formed by rod sections interconnected through branching points. The temperature- and time-dependence of the chemical potentials for the monomer species in solution are the most relevant parameters involved in the growth mechanism.

## Shape and Phase Control of Colloidal ZnSe Nanocrystals

P. Davide Cozzoli,<sup>\*,†</sup> Liberato Manna,<sup>‡</sup> M. Lucia Curri,<sup>§</sup> Stefan Kudera,<sup>||</sup> Cinzia Giannini,<sup>†</sup> Marinella Striccoli,<sup>§</sup> and Angela Agostiano<sup>†,§</sup>

Dipartimento di Chimica, Università di Bari, Via Orabona 4, 70126 Bari, Italy, National Nanotechnology Laboratory of INFM, Via Arnesano Km 5, 73100 Lecce, Italy, CNR-Istituto per i Processi Chimico-Fisici (IPCF), sez. Bari, via Orabona 4, 70126 Bari, Italy, Center for Nanoscience, Ludwig Maximilians Universität München, Munich, Germany, and CNR-Istituto di Cristallografia (IC), via Amendola 122/O, 70126 Bari, Italy

Received December 7, 2004

Shape- and phase-controlled ZnSe nanocrystals are synthesized in hot mixtures of long-chain alkylamines and alkylphosphines. The variation in the rate of precursor addition, down to low and controlled levels, allows the nucleation, as well as the growth of the nanocrystals, to switch between the wurtzite and the zinc blend structures. Such a level of control leads to a variety of shapes, from spheres to rods to three-dimensional structures formed by rod sections interconnected through branching points. The temperature- and time-dependence of the chemical potentials for the monomer species in solution are the most relevant parameters involved in the growth mechanism.

### 1. Introduction

The recognition of the strongly size- and shape-dependent physical–chemical properties of inorganic matter at the nanoscale<sup>1–4</sup> has stimulated efforts toward the fabrication of nanocrystals in a systematic and controlled manner.<sup>5–22</sup>

\* Corresponding author. E-mail: d.cozzoli@ba.ipcf.cnr.it. Phone: +39 080 544207. Fax: +39 080 5442118.

<sup>†</sup> Università di Bari.

<sup>‡</sup> National Nanotechnology Laboratory of INFM.

<sup>§</sup> CNR-Istituto per i Processi Chimico-Fisici.

<sup>||</sup> Ludwig Maximilians Universität München.

<sup>†</sup> CNR-Istituto di Cristallografia.

- (a) Alivisatos, A. P. *Science* **1996**, *271*, 933. (b) Banin, U.; Cao, Y. W.; Katz, D.; Millo, O. *Nature* **1999**, *400*, 542. (c) El-Sayed, M. A. *Acc Chem. Res.* **2001**, *34*, 257.
- (a) Hu, J.; Li, L.; Yang, W.; Manna, L.; Wang, L.; Alivisatos, A. P. *Science* **2001**, *292*, 2060. (b) Wang, J. F.; Gudiksen, M. S.; Duan, X. F.; Cui, Y.; Lieber, C. M. *Science* **2001**, *293*, 1455.
- (a) Hong, B. H.; Bae, S. C.; Lee, C.-W.; Jeong, S.; Kim, K. S. *Science* **2001**, *294*, 348. (b) *Future Trends in Microelectronics: The Nano Millennium*; Luryi, S.; Xu, J.; Zaslavsky, A., Eds.; Wiley-Interscience: New York, 2002. (c) Huynh, W. U.; Dittmer, J. J.; Alivisatos, A. P. *Science* **2002**, *295*, 2425.
- (a) Narayanan, R.; El-Sayed, M. A. *J. Am. Chem. Soc.* **2004**, *126*, 7194. (b) Narayanan, R.; El-Sayed, M. A. *J. Am. Chem. Soc.* **2003**, *125*, 8340. (c) Narayanan, R.; El-Sayed, M. A. *J. Phys. Chem. B* **2003**, *107*, 12416.
- (a) Gates, B.; Mayers, B.; Cattle, B.; Xia, Y. *Adv. Func. Mater.* **2002**, *12*, 219. (b) Gates, B.; Mayers, B.; Crossman, A.; Xia, Y. *Adv. Mater.* **2002**, *14*, 1749. (c) Mayer, B.; Xia, Y. *Adv. Mater.* **2002**, *14*, 279.
- (a) Barrelet, C. J.; Wu, Y.; Bell, D. C.; Lieber, C. M. *J. Am. Chem. Soc.* **2003**, *125*, 11498. (b) Dick, K. A.; Deppert, K.; Larsson, M. W.; Martensson, T.; Seifert, W.; Wallenberger, L. R.; Samuelson, L. *Nature Mater.* **2004**, *3*, 380. (c) Lao, J.; Huang, J.; Wang, D.; Ren, Z. *Adv. Mater.* **2004**, *16*, 65.
- (a) Kan, S.; Mokari, T.; Rothenberg, E.; Banin, U. *Nature Mater.* **2003**, *2*, 155. (b) Ahrenkiel, S. P.; Micic, O. I.; Miedaner, A.; Curis, C. J.; Nedeljkovic, J. M.; Nozik, A. J. *Nano Lett.* **2003**, *3*, 833. (c) Nedeljkovic, J. M.; Micic, O. I.; Ahrenkiel, S. P.; Miedaner, A.; Nozik, A. J. *J. Am. Chem. Soc.* **2004**, *126*, 2632.
- (a) Martin, C. R. *Acc. Chem. Res.* **1995**, *28*, 61. (b) Zach, M. P.; Nag, K. H.; Penner, R. M. *Science* **2000**, *290*, 2120. (c) Yin, Y.; Lu, Y.; Sun, Y.; Xia, Y. *Nano Lett.* **2002**, *2*, 427.
- (a) Zhang, Z.; Kotov, N. A.; Giersig, M. *Science* **2002**, *297*, 237. (b) Pacholski, C.; Kornowski, A.; Weller, H. *Angew. Chem. Int. Ed.* **2002**, *41*, 188. (c) Penn, R. L.; Banfield, J. F. *Science* **1998**, *281*, 969–971.

One-dimensional (1D) nanostructures based on rods, wires, belts, and tubes, as well as their related three-dimensional

- (a) Le, S.-M.; Cho, S.-N.; Cheon, J. *Adv. Mater.* **2003**, *15*, 441. (b) Peng, X. *Adv. Mater.* **2003**, *15*, 459. (c) Manna, L.; Scher, E. C.; Alivisatos, A. P. *Clusters Sci.* **2002**, *13*, 521. (d) Peng, X. *Chem.—Eur. J.* **2002**, *8*, 335.
- (a) Ahmadi, T. S.; Wang, Z. L.; Green, T. C.; Henglein, A.; El-Sayed, M. A. *Science* **1996**, *272*, 1924. (b) Murphy, C. J.; Jana, N. R. *Adv. Mater.* **2002**, *14*, 82. (c) Huang, L.; Wang, H.; Wang, Z.; Wang, A.; Mitra, A.; Bozhilov, K. N.; Yan, Y. *Adv. Mater.* **2002**, *14*, 61.
- (a) Monge, M.; Kahn, M. L.; Maisonnat, A.; Chaudret, B. *Angew. Chem., Int. Ed.* **2003**, *115*, 5749. (b) Cozzoli, P. D.; Kornowski, A.; Weller, H. *J. Am. Chem. Soc.* **2003**, *125*, 14539.
- (a) Peng, X.; Manna, L.; Yang, W.; Wickham, J.; Scher, E.; Kadavanich, A.; Alivisatos, A. P. *Nature* **2000**, *404*, 59. (b) Manna, L.; Scher, E. C.; Alivisatos, A. P. *J. Am. Chem. Soc.* **2000**, *122*, 12700. (c) Peng, Z. A.; Peng, X. *J. Am. Chem. Soc.* **2001**, *123*, 1389. (d) Peng, Z. A.; Peng, X. *J. Am. Chem. Soc.* **2002**, *124*, 3343. (e) Peng, X.; Wickham, J.; Alivisatos, A. P. *J. Am. Chem. Soc.* **1998**, *120*, 5343.
- (a) Peng, Z. A.; Peng, X. *J. Am. Chem. Soc.* **2001**, *123*, 183. (b) Manna, L.; Milliron, D. J.; Meisel, A.; Scher, E. C.; Alivisatos, A. *Nature Mater.* **2003**, *2*, 382. (c) Yang, Q.; Tang, K.; Wang, C.; Qian, Y.; Zhang, S. *J. Phys. Chem. B* **2002**, *106*, 9227. (d) Yu, S.-H.; Wu, Y.-S.; Yang, J.; Han, Z.-H.; Xie, Y.; Qian, Y.-T.; Liu, X.-M. *Chem. Mater.* **1998**, *10*, 2309. (16) Yu, W. W.; Wang, Y. A.; Peng, X. *Chem. Mater.* **2003**, *15*, 4300.
- (a) Jun, Y.-W.; Lee, S.-M.; Kang, N.-J.; Cheon, J. *J. Am. Chem. Soc.* **2001**, *123*, 5150. (b) Gao, F.; Lu, Q.; Xie, Q.; Zhao, D. *Adv. Mater.* **2002**, *14*, 1537. (c) Yang, J.; Xue, C.; Yu, S.-H.; Zeng, J.-H.; Quian, Y.-T. *Angew. Chem., Int. Ed.* **2002**, *41*, 4697. (d) Li, Y.-D.; Liao, H.-W.; Ding, Y.; Qian, Y.-T.; Yang, L.; Zhou, G.-E. *Chem. Mater.* **1998**, *10*, 2301.
- (a) Lee, S.-M.; Jun, Y.-W.; Cho, S.-N.; Cheon, J. *J. Am. Chem. Soc.* **2002**, *124*, 11244.
- (a) Chen, X.; Xu, H.; Xu, N.; Zhao, F.; Lin, W.; Lin, G.; Fu, Y.; Huang, Z.; Wang, H.; Wu, M. *Inorg. Chem.* **2003**, *42*, 3100. (b) Zhao, Y.; Zhang, Y.; Zhu, H.; Hadjipanayis, G. C.; Xiao, J. Q. *J. Am. Chem. Soc.* **2004**, *126*, 6874. (c) Li, Y.; Li, X.; Yang, C.; Li, Y. *J. Phys. Chem. B* **2004**, *108*, 16002.
- (a) Kim, Y.-H.; Jun, Y.-W.; Jun, B.-H.; Lee, S.-M.; Cheon, J. *J. Am. Chem. Soc.* **2002**, *124*, 13656.
- (a) Jun, Y.-W.; Jung, Y.-Y.; Cheon, J. *J. Am. Chem. Soc.* **2002**, *124*, 615.
- (a) Park, J.; Koo, B.; Hwang, Y.; Bae, C.; An, K.; Park, J.-G.; Park, H. M.; Hyeon, T. *Angew. Chem. Int. Ed.* **2004**, *43*, 2282. (b) Qian, C.; Kim, F.; Ma, L.; Tsui, F.; Yang, P.; Liu, J. *J. Am. Chem. Soc.* **2004**, *126*, 1195.
- (a) Cheon, J.; Kang, N.-J.; Lee, S.-M.; Lee, J.-H.; Yoon, J.-H.; Oh, S. J. *J. Am. Chem. Soc.* **2004**, *126*, 1950.

## Shape- and Phase-Controlled ZnSe Nanocrystals

organization, have become the focus of intensive research. Studies on these materials aim both to assess the foundations of physical laws at the nanoscale and to pave the way to practical applications. 1D structures represent ideal systems to investigate the dependence of optical, electrical transport, and mechanical properties on dimensionality.<sup>2</sup> In addition, they are expected to play an important role as functional units in devices and processes.<sup>3</sup> Demonstrated examples include the observation of linearly polarized emission<sup>2a–b</sup> and lasing from quantum rods,<sup>2c</sup> improved photochemical performances in hybrid nanocrystal–polymer solar cells,<sup>3c</sup> and shape-dependent catalytic activity.<sup>4</sup>

In comparison with quantum dots and wells, the advancement of 1D materials has been slow until very recently, as it was hindered by the difficulties associated with the synthesis of nanostructures with well-controlled dimensions, morphology, phase purity, and chemical composition. 1D materials can now be prepared using a variety of techniques, although their development into straightforward, low-cost practical routes to large quantities of 1D nanostructures still requires great ingenuity. Modern approaches based on chemical synthesis<sup>5–9</sup> are emerging as viable strategies for the large-scale production of a diversified range of 1D materials. These methods involve: (i) The exploitation of a unique direction in the crystal structure<sup>5</sup> of certain materials as a possible source of anisotropic growth; (ii) The introduction of a solid–liquid interface that reduces the symmetry of the nascent seeds, as in the vapor–liquid–solid (VLS)<sup>6</sup> and in the solution–liquid–solid (SLS)<sup>7</sup> growth mechanisms; (iii) The use of suitable templates with 1D morphologies;<sup>8</sup> (iv) The self-assembly of zero-dimensional (0D) nanostructures driven by a variety of mechanisms, such as dipole–dipole interactions or oriented attachment;<sup>9</sup> (v) The control of supersaturation in solution by means of surfactants.<sup>10–12</sup>

The advantages of colloidal methods over other approaches rely on the ease of manipulation and processability of ligand-coated nanocrystals, which make these materials more suitable for integration with the existing technologies. Moreover, colloidal chemistry provides easy and accessible tools for systematic and detailed studies on the growth mechanisms of nanocrystals, which should be useful for understanding crystallization in general.

Despite of the wealth of recent progress in the control of the size, shape, and crystal structure of many colloidal semiconductor (CdSe,<sup>10b–d,13</sup> CdTe,<sup>9a,14</sup> CdS,<sup>15</sup> PbS,<sup>16</sup> ZnS,<sup>17</sup> InAs,<sup>7a</sup> InP,<sup>7b–c</sup> GaP,<sup>18</sup> ZnO,<sup>9b,12a</sup> and TiO<sub>2</sub><sup>12b</sup>), magnetic (Cd<sub>1-x</sub>Mn<sub>x</sub>S,<sup>19</sup> Fe<sub>2</sub>P,<sup>20a</sup> FeP,<sup>20b</sup> Fe<sub>2</sub>O<sub>3</sub>,<sup>21</sup> and transition elements<sup>22</sup>) and noble metal<sup>11</sup> nanocrystals, the explicit growth mechanism of anisotropic nanocrystals remains somewhat controversial, being limited to specific materials and morphologies.<sup>10</sup> This lack of knowledge is primarily related to the difficulty of applying the classic theories of crystallization<sup>25</sup> to nanocrystals, whose shape evolution can occur far from the thermodynamic equilibrium.<sup>10b–d,13</sup>

(22) (a) Puntes, V. F.; Krishnan, K. M.; Alivisatos, A. P. *Science* **2001**, *291*, 2115. (b) Park, J.; Kim, S.; Lee, S.; Khim, Z. G.; Char, K.; Hyeon, T. *J. Am. Chem. Soc.* **2000**, *122*, 8581.  
 (23) Murray, C. B.; Norris, D. J.; Bawedin, M. G. *J. Am. Chem. Soc.* **1993**, *115*, 8706.  
 (24) Yeh, C.-Y.; Lu, Z. W.; Froyen, S.; Zniger, A. *Phys. Rev. B* **1992**, *46*, 10086.

## Chem. Mater., Vol. 17, No. 6, 2005 1297

It is generally accepted that some surfactants (such as phosphonic acids, amines, and carboxylic acids, depending on the system) play a key role in governing morphological changes of colloidal nanocrystals under suitable reaction conditions.<sup>13–23</sup> It was initially suggested<sup>13a–b</sup> that different ligands selectively adhering to specific crystal facets are intrinsically required to achieve anisotropic crystal growth. It is now clear that that shape modulation is the result of selective adhesion of only one surfactant species to the various facets of the growing nanocrystals (as for instance the phosphonic acid<sup>13c–d,14</sup> in the case of CdSe nanocrystals) and that anisotropic growth is usually driven by high monomer activity.<sup>10b,13–17</sup> Also, it has been rationalized that the crystalline phase of the clusters formed at the nucleation stage is critical for directing the intrinsic growth of nanocrystals.<sup>10a,15a–b,16,19</sup> In materials exhibiting polytypism,<sup>24</sup> this concept is illustrated by the possibility to adjust the chemical environment in such a way that the relative stability of one phase over another can be reversed<sup>17–19</sup> at nucleation or during growth to yield complex rod-based architectures.<sup>13b,d,14b,e,15a–b,25</sup> On the basis of this model, elaborate shape control has been achieved also for materials with symmetric crystal structure through switching the growth of the seeds from a thermodynamic regime to a kinetically limited one.<sup>16</sup>

The present study extends the scenario of systematic shape modulation of colloidal nanocrystals to the case of zinc selenide. The interest toward ZnSe, a II–VI semiconductor with a room temperature bulk band gap of 2.7 eV, is strongly justified by the still comparatively poorer availability of materials emitting in the UV-blue region for optoelectronic devices. To date, a few solution-based routes have been reported for nearly spherical zinc blend (ZB)<sup>26–29</sup> ZnSe nanocrystals. Examples of 1D nanostructures based on ZnSe are nanowires grown by catalytic VLS,<sup>6a,32</sup> by electrochemical deposition,<sup>33</sup> and by other physical techniques.<sup>34,35</sup> Solution-based approaches have also been reported, including solvothermal,<sup>15c,33</sup> micellar,<sup>31a</sup> and surfactant-based methods.<sup>31b</sup>

(25) (a) Milliron, D. J.; Hughes, S. M.; Cui, Y.; Manna, L.; Li, J.; Wang, L.-W.; Alivisatos, A. P. *Nature* **2004**, *430*, 190. (b) Mokari, T.; Rothenberg, E.; Popov, I.; Costi, R.; Banin, U. *Science* **2004**, *304*, 1787.  
 (26) Hines, M. A.; Guyot-Sionnest, P. *J. Phys. Chem. B* **1998**, *102*, 3655.  
 (27) Cumberland, S. L.; Hanif, K. M.; Javier, A.; Khitrov, G. A.; Strouse, G. F.; Woessner, S. M.; Yun, C. S. *Chem. Mater.* **2002**, *14*, 1576.  
 (28) Shavel, A.; Gaponik, N.; Eychmuller, A. *J. Phys. Chem. B* **2004**, *108*, 5905.  
 (29) (a) Karanikolos, G. N.; Alexandridis, P.; Itskos, G.; Petrou, A.; Mountzaris, T. *J. Langmuir* **2004**, *20*, 5550. (b) Zhu, J.; Koltypin, Y.; Gedanken, A. *Chem. Mater.* **2000**, *12*, 73.  
 (30) (a) Deng, Z.-X.; Wang, C.; Sun, X.-M.; Li, Y.-D. *Inorg. Chem.* **2002**, *41*, 869. (b) Wang, W.; Geng, Y.; Yan, P.; Liu, F.; Xie, Y.; Qian, Y. *Inorg. Chem. Comm.* **1999**, *2*, 83.  
 (31) (a) Lv, R.; Cao, C.; Zhai, H.; Wang, D.; Liu, S.; Zhu, H. *Solid State Commun.* **2004**, *130*, 241. (b) Li, L. S.; Pradhan, N.; Wang, Y.; Peng, X. *Nano Lett.* **2004**, *4*, 2261.  
 (32) (a) Jiang, Y.; Meng, X.-M.; Liu, W.-C.; Liu, J.; Ding, J.-X.; Lee, J.-X.; Lee, S.-T. *J. Phys. Chem. B* **2004**, *108*, 2784. (b) Xiang, B.; Zhang, H. Z.; Li, G. H.; Yang, F. H.; Su, F. H.; Wang, R. M.; Xu, J.; Lu, G. W.; Sun, X. C.; Zhao, Q.; Yu, D. P. *Appl. Phys. Lett.* **2003**, *82*, 3330. (c) Zhu, Y.-C.; Bando, Y. *Chem. Phys. Lett.* **2003**, *377*, 367. (d) Li, Q.; Gong, X.; Wang, C.; Wang, J.; Ip, K.; Hak, S. *Adv. Mater.* **2004**, *16*, 1436.  
 (33) Koulkin, N.; Menon, L.; Wong, A. Z.; Thompson, D. W.; Woollam, J. A.; Williams, P. F.; Bandyopadhyay, S. *Appl. Phys. Lett.* **2001**, *79*, 4423.

These routes, however, yield either wurtzite (WZ)<sup>17c,32a–c</sup> or ZB<sup>30b,31,32d</sup> ZnSe nanocrystals, frequently insoluble, in the exclusive rodlike morphology and with dimensions well beyond the quantum confinement regime.

In this contribution, the synthesis of quantum-sized colloidal ZnSe nanocrystals in a variety of morphologies (rods, polypods, and multiple branched particles) has been realized by means of continuous addition of diethylzinc and selenium precursors into a hot mixture of a long-chain alkylamine and an alkylphosphine. Control over the injection rate and temperature modulation allows the nucleation, as well as the growth of ZnSe nanocrystals, to switch between the WZ and the ZB structures, so that the nanocrystal morphologies can vary from a spherical shape to a range of complex architectures based on rods connected through branching points. The as-prepared ZnSe nanocrystals exhibit distinguishable shape-dependent optical properties in the UV-blue region that make them potentially appealing for a variety of optoelectronic applications. The proposed method offers a simple approach to phase/shape modulation that can provide the existing models of colloidal nanocrystal growth with further useful shape-guiding criteria.

## 2. Experimental Section

**2.1. Materials.** Diethylzinc ( $Zn(C_2H_5)_2$ , 97%), selenium (Se, 99.999%), *n*-octadecylamine ( $NC_{18}H_{39}$  or ODA, 97%), and tri-*n*-butylphosphine ( $P(C_4H_9)_3$  or TBP, 97%) were purchased from Aldrich. *n*-Hexadecylamine ( $NC_{16}H_{35}$  or HDA, 99%) was purchased from Fluka. Tri-*n*-octylphosphine ( $P(C_8H_{17})_3$  or TOP, 97%) was purchased from Strem. All solvents used were anhydrous, purchased from Aldrich and used without any further purification.  $Zn(C_2H_5)_2$  was vacuum distilled and stored at  $-20^{\circ}C$  under nitrogen in a glovebox.

**2.2. Synthesis of ZnSe Nanocrystals.** All manipulations were performed using standard air-free techniques. Stock precursor solutions were all freshly prepared at room temperature by codissolving the zinc and selenium precursors in TOP or TBP under the inert atmosphere of a glovebox. Typically, the Zn:Se molar ratio was kept close to 1 with the precursor concentration being in the range 0.1–0.7 M. For the synthesis of the nanocrystals, the stock solution was injected, under  $N_2$ , via a syringe, into a three-neck flask containing either hot, vigorously stirred HDA or ODA and connected to a Schlenk line. The growth stage was monitored by measuring the UV–vis absorption and PL emission spectrum of small aliquots of the reaction mixture withdrawn by a syringe and then diluted with chloroform. Unless otherwise stated, the above techniques were used in all of the following syntheses.

**2.2.1. Synthesis of Spherical ZnSe Nanocrystals.** Spherical ZnSe nanocrystals were prepared according to a previously reported procedure with minor changes.<sup>26</sup> Briefly, 7 g of HDA (or ODA) was degassed under vacuum at  $130^{\circ}C$  for 1 h, after which it was

(34) (a) Solanki, R.; Huo, J.; Freeouf, J. L.; Miner, B. *Appl. Phys. Lett.* **2002**, *81*, 3864. (b) Stifter, D.; Heiss, W.; Bonanni, A.; Prechtl, G.; Schmid, M.; Hingerl, K.; Seringer, H.; Sitter, H.; Liu, J.; Gornik, E.; Toth, L.; Barna, C. *J. Cryst. Growth* **1998**, *184–185*, 347. (c) Peck, J.; Mountzaris, T. J.; Stoltz, S.; Petrou, A.; Mattocks, P. G. *J. Cryst. Growth* **1997**, *184–185*, 347.

(35) (a) Schreder, B.; Materny, A.; Kiefer, W.; Bacher, G.; Forchel, A.; Landwehr, G. *J. Raman Spectrosc.* **2000**, *31*, 959. (b) Ikada, H.; Saito, T.; Takahashi, N.; Shibata, K.; Sato, T.; Chen, Z.; Souma, I.; Oka, Y. *Physica E* **2001**, *10*, 373. (c) Bacher, G.; Illing, M.; Spiegel, R.; Kummel, T.; Herz, K.; Forchel, A.; Jobst, B.; Hommel, D.; Landwehr, G. *J. Cryst. Growth* **1996**, *159*, 455.

heated under  $N_2$  flow. Zn/Se precursor solution (2.5 mL, 0.32 M) was then manually (in 0.1 s) added to HDA at  $T_{inj} = 300^{\circ}C$ . Upon injection, the temperature dropped to  $T_{gr} \approx 265^{\circ}C$  and was maintained at this level throughout the entire synthesis. To grow monodisperse ( $\sigma \approx 5\%$ ) ZnSe nanocrystals with diameter in the 3–5-nm range, additional injections of precursors were performed in a dropwise fashion at a rate of about 0.2 mL/min to sustain nanocrystal growth. The reaction could be stopped (generally after 3–5 h) when the desired particle size was reached by removing the heating source. By application of a similar procedure, larger nanocrystals ( $d \leq 7$ –8 nm) could be grown by using stock solutions with higher concentration of the Zn/Se precursors. ZnSe quantum dots could be also grown at much faster rate in ODA by performing the first injection at  $T_{inj} \approx 300$ –340 °C and allowing further growth at  $T_{gr} \approx 265$ –320 °C with several monomer additions. However, nearly spherical or oval nanocrystals with a broader size distribution ( $\sigma = 15\%$ ) were obtained in this case.

**2.2.2. Synthesis of ZnSe Nanocrystals of Various Morphologies.** In general, shape control of ZnSe nanocrystals was achieved by using a syringe pump to adjust the rate of precursor supply to the reaction vessel at a considerably lower level, as compared to that used for the preparation of spherical nanocrystals. The temperature was maintained almost constant (within  $\pm 2^{\circ}C$ ) during precursor addition. The morphology of the nanocrystals was dependent on the injection rate, on the concentration, on the total volume of the stock solution, and on the reaction temperature. Controlled syntheses, performed in amine/TOP (or TBA) as the starting mixtures, allowed us to exclude that the time-dependent content of phosphine ligands during the dropwise addition modality altered the final particle shape appreciably, as compared to the one-pot injection modality.

(a) *Injection Volume Experiments.* All injection volume experiments were performed by quickly injecting a 0.35 M Zn/Se stock solution either at  $290^{\circ}C$  in HDA or close to the boiling point of ODA ( $\sim 345^{\circ}C$ ). To provide enough nanocrystals for analysis, a scaled-up synthesis was implemented. For this purpose, 28 g of amine was weighed in the flask, while 8, 2, 1, and 0.4 mL of stock solution were injected in less than 0.4 s in four independent experiments, respectively. The reaction was allowed to proceed for 2 min, after which the heating source was promptly removed and cold TOP (5 mL) was injected to further quench growth.

(b) *ZnSe Nanorods.* A fixed volume (1–2 mL) of a 0.32 M Zn/Se solution was injected dropwise into 14 g of ODA at  $345^{\circ}C$ . The aspect ratio of the nanorods could be varied from 2–3 to 7–8 by changing the injection rate from  $\sim 0.20$  mL/min to  $\sim 0.05$  mL/min. Alternatively, when the injection rate was kept fixed, an increase in the precursor volume led to higher aspect ratio nanorods. To avoid the development of branched nanostructures during growth, no more than 2 mL were added when injecting dropwise at  $\sim 0.20$  mL/min, whereas up to 5–6 mL could be used when operating at an injection rate of  $\sim 0.05$  mL/min. After the addition was completed, the flask was allowed to cool to room temperature.

(c) *Branched ZnSe Nanocrystals.* Polypods were obtained by injecting a 0.32 M Zn/Se precursor solution into 14 g of ODA at lower temperatures ( $330$ – $290^{\circ}C$ ) and at an injection rate of  $\sim 0.40$ – $0.30$  mL/min. Injection of relatively small precursor volumes (2.5 mL) led to tetra- and tripods with equally short arms as the major product. Polypods with longer and dissimilar arms were prepared by injecting 5–7 mL of the same solution. Nanocrystals with multiple branching points were obtained by injecting 5–7 mL of a 0.64 M Zn/Se precursor solution into 14 g of ODA (or of HDA) at  $290$ – $270^{\circ}C$ . After the injection was completed, the reaction was stopped by removing the heating source. Notably, branching could be also achieved by applying the

*Shape- and Phase-Controlled ZnSe Nanocrystals*

same conditions used for growing rods (temperature and injection rate) except that the total volume of injected precursors was drastically increased. However, a broader range of nanoparticle typologies was obtained in this case.

**2.3. Extraction Procedures.** Butanol (3–4 mL) and 3–4 mL of chloroform were added to the reaction vessel at  $\sim 60$  °C in order to prevent solidification of the mixture. Subsequently, methanol was added to flocculate the nanocrystals. They were immediately separated by centrifugation to avoid massive contamination by the amine that started precipitating at temperatures below 40–50 °C. Cleaning was carried out by repeatedly (three times) by redissolving the nanocrystals in a minimum volume of  $\text{CHCl}_3$  and by reprecipitating them by  $\text{CH}_3\text{OH}$  addition. The purified nanocrystals, regardless of their morphologies, were highly soluble in a variety of nonpolar solvents (chloroform, hexane, toluene, etc.).

**2.4. Characterization.** *UV-vis Absorption Spectroscopy.* To monitor nanocrystal growth, UV-vis absorption spectra were recorded with an Ocean Optics UV-vis diode array spectrophotometer equipped with an optical fiber, a deuterium lamp, and a tungsten–halogen lamp. UV-vis absorption spectra of the extracted nanocrystals were measured with Cary 5 Varian UV-vis/near-IR spectrophotometer. Photoluminescence (PL) emission spectra were measured with a Cary Eclipse spectrofluorimeter. The PL quantum yields (QY) were evaluated by comparing the integrated emission intensity with the integrated PL of a Stilbene solution in ethanol. The nanocrystal and dye solutions were both excited at the wavelength where their absorption spectra intersected. The samples were maintained under  $\text{N}_2$  and diluted to an optical density of between 0.1 and 0.3 at the excitation wavelength (350 nm) to minimize self-absorption effects. For PL measurements, only freshly prepared samples dissolved in anhydrous oxygen-free solvents were used, as the emission from the nanocrystals was rapidly quenched upon exposure to air (in 1–2 h).

*Powder X-ray Diffraction (XRD).* XRD measurements were performed with a D8 Discover-Bruker diffractometer equipped with a 3-kW ceramic tube with a copper anode, a Goebel type parabolic mirror and two-bounces monochromator (V Groove) as primary optics, and a NaI(Tl) scintillator detector. A coupled  $\theta$ – $2\theta$  movement was chosen for data collection. Concentrated nanocrystal solutions were spread on top of a silicon substrate. The sample was allowed to dry and was measured in reflection geometry.

*Transmission Electron Microscopy.* Low-resolution transmission electron microscopy (TEM) investigation was performed using a JEOL JEM-1011 microscope operated at 100 kV. High-resolution images (HR-TEM) were recorded on a Philips EM 430 microscope (TEM) operating at 300 kV. The samples for the analysis were prepared by injection of dilute solutions of ZnSe nanocrystals onto 400-mesh carbon-coated copper grids and leaving the solvent to dry. The samples were stable under the electron beam within the typical observation times.

### 3. Results

In this work, the influence of the reaction conditions on the crystalline phase and on the shape of ZnSe nanoparticles was investigated by manipulating their growth kinetics in the high-temperature organometallic approach originally developed to prepare highly luminescent organic-capped ZB ZnSe quantum dots.<sup>26</sup> Because this investigation was intended to understand the nucleation and growth processes related to the formation of shape-controlled nanocrystals, no size/shape sorting was performed for all the products obtained from the syntheses discussed below.

*Chem. Mater., Vol. 17, No. 6, 2005 1299*

**3.1. Morphological Characterization.** (a) *ZnSe Quantum Dots.* The growth of spherical ZnSe nanocrystals was carried out by means of the classical hot-injection technique based on initial rapid addition of a relatively large volume of  $\text{Zn}(\text{C}_2\text{H}_5)_2\text{:Se:TOP}(\text{or TBP})$  solution into hot alkylamine at  $T_{\text{inj}} \approx 300$ –340 °C. Further growth of the formed nuclei was then accomplished at lower temperatures ( $T_{\text{gr}} \approx 265$ –290 °C), while performing additional precursor injections to “refocus” the size distribution.<sup>13e</sup> The entire process could be easily followed by monitoring the temporal evolution of the ZnSe absorption and emission spectrum (Supporting Information, Figures 1S–2S). Monodisperse ZnSe nanocrystals with mean particle diameter tuneable in the 3–5-nm range could be obtained within typical reaction times on the order of 4–5 h in HDA (Supporting Information Figure 3Sa). The use of an amine with a longer alkyl chain, ODA, allowed us to grow larger ZnSe nanocrystals at comparatively higher temperature (Supporting Information, Figure 2S). However, even with additional injections, the size distribution remained broad (Supporting Information, parts b and c of Figure 3S). The largest ZnSe nanocrystals that could be grown by the hot-injection method in HDA possessed narrow exciton absorption and luminescence peaks at around  $\sim 425$  and  $\sim 434$  nm, respectively, while nanoparticles grown in ODA exhibited an absorption onset red-shifted up to  $\sim 455$  nm with a corresponding broad luminescence band at  $\sim 465$  nm. These optical features reflected the attained size-distributions.

(b) *Injection Volume Experiments.* These experiments shed light onto the process of nanocrystal shape evolution at the early stages of growth following nucleation. The variation of the precursor volume (or, alternatively, of the precursor concentration at a fixed volume) in the fast-injection technique was actually found to be rather critical in order to produce systematic changes in the mean particle shape. The reaction was allowed to proceed only for a brief period (2 min) to minimize shape variation that would occur over long growing times. The use of ODA allowed us to inject the precursors solution at temperatures as high as 345 °C. In the scaled-up synthesis adapted for the purpose of this investigation, the overall growth kinetics remained practically unaffected. Very large injection volumes (5–8 mL) corresponded to the same general conditions adopted to nucleate spherical nanocrystals, as previously reported. In this case, only very small ZnSe clusters (excitonic peak at  $\lambda < 350$  nm) were present in the final solution after quenching the growth. These particles could not be seen under TEM. Conversely, a decrease of the injection volume below 3 mL produced larger nanocrystals that could be clearly detected by TEM, as illustrated in Figure 1 and as further supported by the corresponding absorption and emission spectra (Supporting Information, Figure 4S). When related to the short reaction time, this fact undoubtedly pointed to a faster crystal growth. More importantly, the morphological inspection of the samples revealed that the ZnSe nanocrystals gradually changed from moderately monodisperse spherical particles (Figure 1a) to slightly elongated objects with irregular profiles (Figure 1b) to polydisperse rods with aspect ratios in the range of 2–5 (Figure 1c). Notably, such particle shape modulation appeared accentuated by increasing temperature,

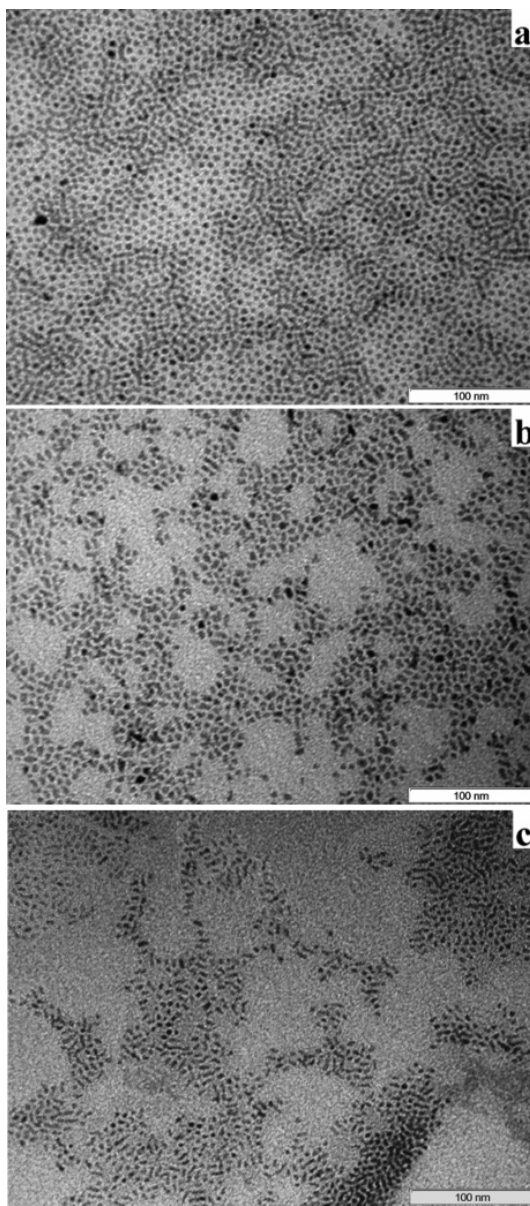


**Figure 1.** TEM images relative to the single injection volume experiments. Separate syntheses were carried out by rapidly injecting (a) 2 mL; (b) 1 mL; (c) 0.4 mL of a 0.35 M Zn/Se stock solution into 28 g of ODA at 345 °C. Growth was quenched after 2 min.

even though in a relatively narrow range (300–345 °C). Similar results were obtained by performing the injection of a fixed volume of stock solution with proportionally decreased precursor concentration, which additionally excluded that shape changes were due to the variation in the phosphine content in the final mixture.

(c) *ZnSe Nanorods*. The above observations suggested that reducing monomer supersaturation in the reaction vessel could lead to anisotropic crystal growth. This hypothesis was actually verified by experiments demonstrating exclusive rod formation upon dropwise addition of the stock precursor solution at ~340 °C. The rod aspect ratio could be systematically increased either by decreasing the injection

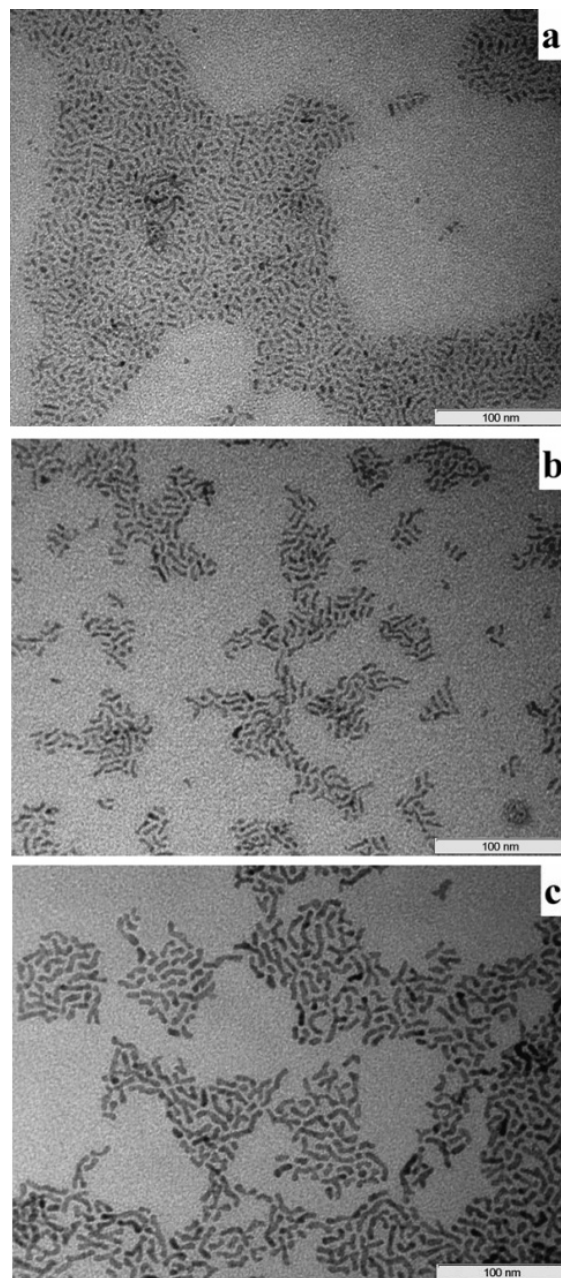


**Figure 2.** TEM overview of rodlike ZnSe nanocrystals of different aspect ratio prepared in ODA at 340 °C.

rate of a fixed moderate precursor volume (less than 2 mL) from ~0.20 to ~0.05 mL/min or by increasing the total injected volume at a constant injection rate. In this latter mode, the rod morphology was maintained, provided that the larger injection volumes were associated with relatively lower injection rates. The low-resolution TEM images in Figure 2 demonstrate the degree of control over rod length and aspect ratio achievable by this procedure. In general, the nanoparticles exhibited uniform diameters (within ~5%), although with a relatively broader length distribution. In addition, a minor (5–15%) presence of morphologies deviating from the pure rodlike, such as arches, zigzag-segments,

## Shape- and Phase-Controlled ZnSe Nanocrystals

Chem. Mater., Vol. 17, No. 6, 2005 1301

bipods (V-shaped), and tripods with dissimilar arms (Y-shaped) could be observed in the samples containing larger particles (parts b and c of Figure 2), i.e., those grown upon injection of more concentrated stock solutions and/or larger precursor volumes.

(d) **Branched ZnSe Nanocrystals.** Further manipulation of the growth kinetics led to the formation of more complex 1D-based nanostructures, although branched and multiarmed nanocrystals could not be completely excluded from the growth of the longest rods. As compared to the rod-generating synthesis conditions, branching could be generally introduced by increasing either the total volume of injected precursors or the injection rate to  $\sim 0.40$ – $0.30$  mL/min and/or at comparatively lower temperatures (340–270 °C). However, only the latter procedure could guarantee a sufficiently narrow shape distribution. Some representative examples are shown in Figure 3. Nanocrystals with a single branching point (i.e., polypods) were easily obtained by injecting increasing amounts of the stock solution (parts a and b of Figure 3). As a general feature, tetra- and tripods represented the major product, with the distribution of diameters of the rodlike branches appearing rather uniform. However, the length of the arms became less uniform when the average nanocrystal size increased (Figure 3b) due to deviation from a rigorously straight geometry.

Nanocrystals with multiple branching points were obtained by employing more concentrated precursor solutions in combination with lower temperatures. Such typology could also be found as a side product in the samples containing larger polypods (as in Figure 3b). In such shaped nanoparticles (Figure 3c), a dendritic or a comblike structural pattern developed as a result of multiple branching points, while the individual arms retained the rodlike morphology.

**3.2. Structural Characterization.** As a representative example, the evolution of the powder XRD profiles for ZnSe nanorods with varying aspect ratio is shown in Figure 4. Similar patterns were measured for the branched nanocrystals with increasing arm length. In all cases, the characteristic line broadening pointed to nanosized crystal domains. The spherical nanocrystals (Figure 4a) exhibited XRD diffraction peaks that could be indexed by the known diffraction pattern of the ZB phase of ZnSe without any other feature. As opposed, a WZ structure could be generally assigned to the nanorods (parts b–d of Figure 4), although the coexistence of the ZB phase could not be excluded.

The XRD of the elongated nanocrystals indicated an extended crystalline domain along the *c* axis of the WZ lattice. This attribution was supported by the observation of an increasingly intense and sharp (002) WZ peak, asymmetrically broadened by the convolution with the (100) and (101) WZ reflexes. The suppression of the (102) and the strong attenuation of the (103) peak could be explained by the presence of stacking faults along the (002) direction.<sup>13a–b,14e,25a,36</sup> Accordingly, such lattice imperfections are known to cause further broadening and/or shape modification of the XRD peaks,<sup>36c</sup> thus explaining the discrepancy between the mean particle length that could be estimated from fitting the XRD and that measured directly by TEM.

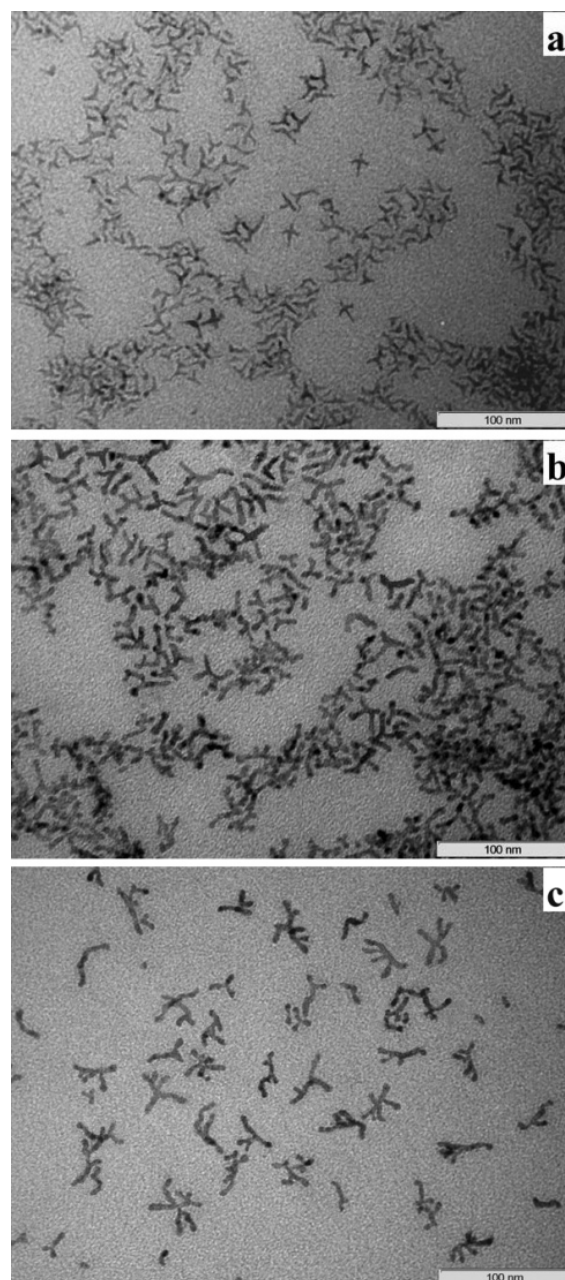


**Figure 3.** TEM overview of ZnSe polypods and multibranched nanocrystals.

Detailed HRTEM studies on the samples provided a deeper insight into the formation of the diverse range of nanostructures observed by the present synthetic approach. Figure 5 presents an overview of the structural details relative to the principal particle morphologies. The measured interplanar distance for the 3–7 nm nearly spherical nanoparticles (parts a and b of Figure 5) matched the *d* spacing values of the ZB

(36) (a) Murray, C. B.; Kagan, C. R.; Bawendi, M. G. *Annu. Rev. Mater. Sci.* **2000**, *30*, 545. (b) Talapin, D. V.; Koeppen, R.; Gotzinger, S.; Kornowski, A.; Lupton, J. M.; Rogach, A. L.; Benson, O.; Feldmann, J.; Weller, H. *Nano Lett.* **2003**, *3*, 1677. (c) Guinier, A. *X-ray Diffraction in Crystals, Imperfect Crystals, and Amorphous Bodies*; Dover: New York, 1994.

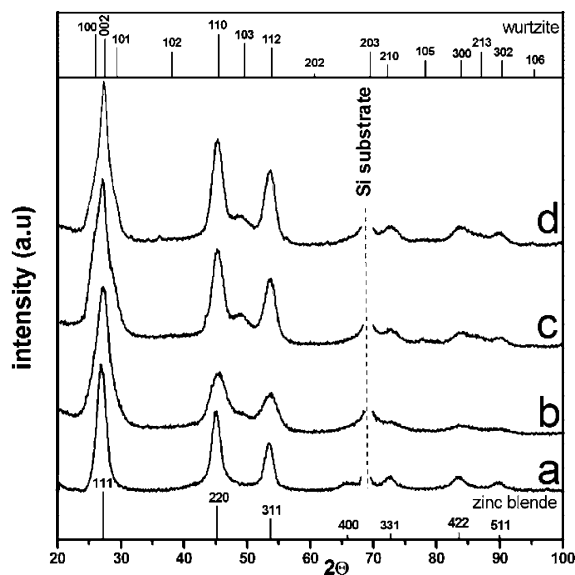


**Figure 4.** Powder XRD pattern of (a) spherical ZnSe nanoparticles and (b–d) ZnSe nanorods with aspect ratios of 3, 6, and 8, respectively.

phase, in agreement with the relative XRD pattern. In contrast, in all anisotropic ZnSe nanostructures, both the WZ and the ZB phase coexisted, and their combination in turn determined the overall crystal morphology.

The case of the lowest aspect ratio rods (parts c–f of Figure 5) is representative of the genesis of all anisotropic particles in general. Even among these nanoparticles, a variety of structurally heterogeneous nanocrystals could be found. Rods in the exclusive WZ phase, being distinguishable by the characteristic ziz-zag behavior when viewed down the (100) direction (Figure 5c), were dominant in the synthesis designed to yield the lowest aspect ratio nanorods. Mixed-phase, elongated particles (parts d–f of Figure 5) could be more commonly encountered at the early stages of the growth of high aspect ratio nanorods and branched nanocrystals. They comprised ZB tetrahedral crystals that coherently continued in the WZ phase (parts d–f of Figure 5), thus generating stacking faults. In the HRTEM of longer rods (parts g and h of Figure 5), stacking faults were more frequently observed.

The occurrence of the ZB phase provided also the basic structural motif for potentially introducing unusual rod-based 3D organization, as previously observed for a number of semiconductors exhibiting ZB–WZ polytypism.<sup>13–17</sup> The close similarity between the WZ and the ZB structures can be easily grasped by observing that the  $\pm(111)$  facets of the ZB structure are atomically identical to the polar (001) and (001) facets of the WZ structure. In this notation, we are assuming that the “+” sign refers to the four equivalent polar (111) facets of ZB that expose cations with one dangling bond each (here the Zn atoms), which are equivalent to the unique (001) polar facet in WZ. The “–” sign refers to the ZB facets exposing anions with one dangling bond (Se in our case), which are equivalent to the (001) polar facet in WZ. Polypods, as well as the observed rods with one ZB cluster on one rod tip, are originated when WZ arms grow on one or more  $\pm(111)$  facets of a ZB nanocrystal (parts

h–l of Figure 5). The maximum observed number of branches departing from a ZB nucleus is four, and this indicates that of the two possible groups of equivalent facets of ZB, the  $+(111)$  and the  $-(111)$  ones, only one group is most likely responsible for branching. An interesting example is represented by sequential arrangement of ZB and WZ structures, which can ultimately result in the development of nanocrystal curvature (Figure 5i). The details of such combined structures can be more easily observed in nanoparticles, such as bipods (Figure 5h) and tripods (Figure 5l), that are missing of one or more branches.

**3.3. Optical Characterization.** The various nanocrystal shapes exhibited unique spectroscopic features. The UV–vis absorption and PL spectra of ZnSe nanocrystals with different morphologies are compared in Figure 6. The spherical particles (Figure 6a) exhibit up to three resolved electronic transitions and PL peak widths as narrow as  $\sim 17$  nm with a QY of  $\sim 20$ –40%. A broadening of both the first excitonic peak and the related PL emission with increasing aspect ratio of the rods was typically observed. Such a broadening reflects the contribution from the confinement along the *c* axis of the nanorods, for which a substantial distribution of lengths was observed. In addition, the Stokes shift was progressively larger for nanocrystals with increasing rod length (see also Figure 4S in the Supporting Information). This behavior is indicative of a length dependence of the electronic structure in nanorods, as previously reported for similar systems.<sup>7,13a,19</sup> The smaller overlap area between the absorption and the emission spectra is particularly desirable in optoelectronic applications, such as light-emitting diodes, where reabsorption would reduce the total efficiency of the device.

In all samples, a red-shift of the band gap in longer nanorods, or in general in branched nanostructures with long rod sections, was generally accompanied by a significant decrease in the PL QY, which could be much lower than 1% for branched structures. Atomistic pseudopotential calculations<sup>37</sup> of the simplest and most symmetric branched structure (a tetrapod made of four WZ rods joined to a central ZB core) have shown that electrons localize in the ZB core while the holes delocalize in the WZ rods. When an electron–hole pair is created in a branched nanostructure, the two carriers can separate at the interface between a hexagonal branch and a cubic section (the branching point). The carriers are then likely to delocalize into two distinct branches. Because of this intrinsic charge-separation property of branched nanostructures, their fluorescence efficiency is significantly lower than in the case of rods or spherical nanocrystals. This feature can be appealing for the realization of semiconductor-based photovoltaic devices, in which long-range charge separation is required.

#### 4. Discussion

In the present work, shape and phase control of ZnSe nanocrystals has been achieved without changing the nature of the ligands. Furthermore, the results of our experiments exclude a primary role of the phosphine in governing the

(37) Li, J.; Wang, W. *Nano Lett.* **2003**, 3, 1357.

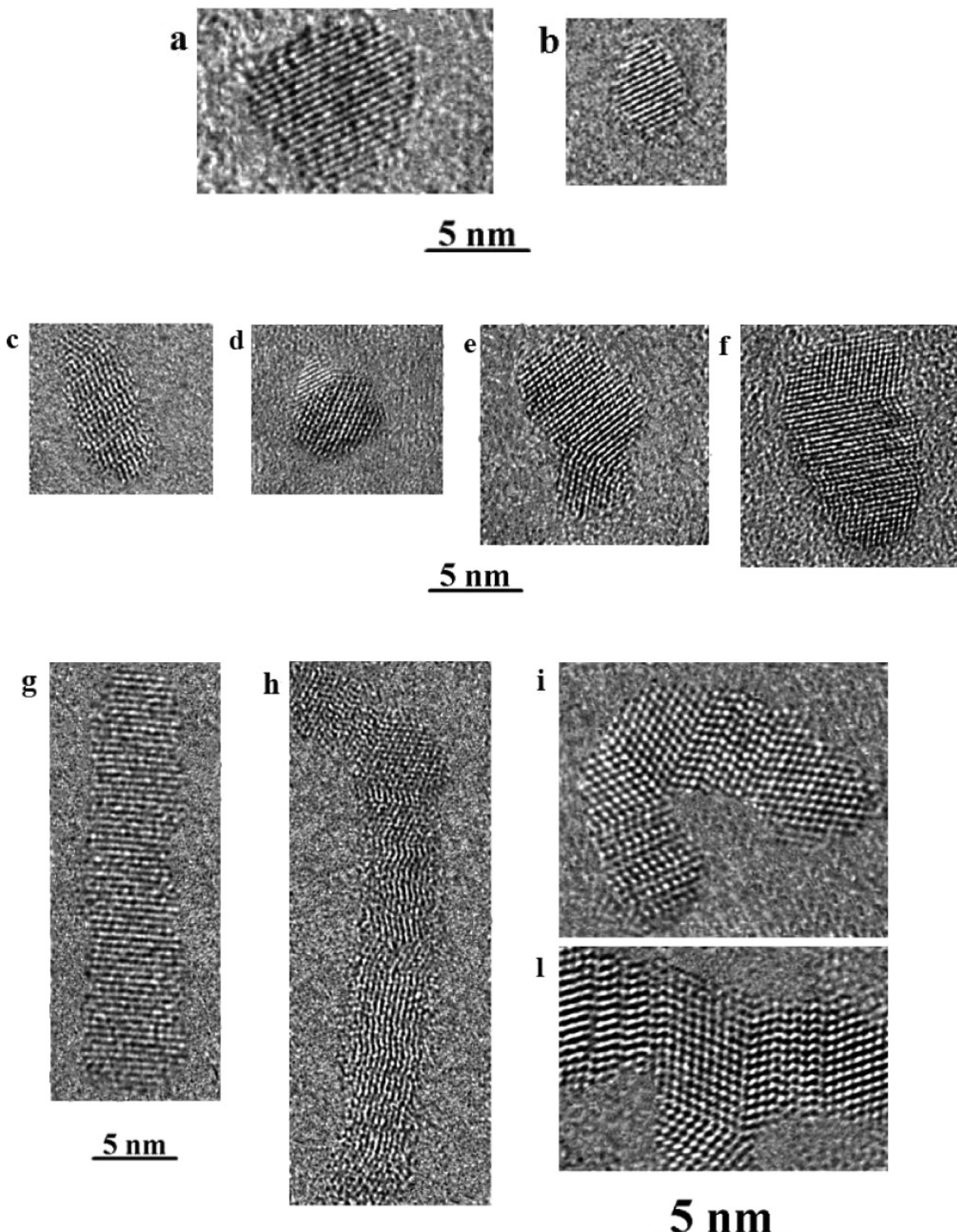


**Figure 5.** HRTEM images of variously shaped ZnSe nanocrystals: (a–b) ZB spherical dots; (c) short WZ rod; (d–f) elongated particles with both ZB and WZ regions; (g) long WZ rod; (h) WZ bipod with stacking faults and a ZB region at the curvature point; (i) U-shaped particle; (l) tripod with a ZB branching point and WZ arms with several stacking faults.

shape and phase evolution of ZnSe nanocrystals. Therefore, the binary amine/TOP system can be simply treated as a monosurfactant system<sup>15a,19</sup> in which the influence of experimental conditions on the nanocrystal growth can be

ultimately traced to the chemical potential of the monomer species in solution. A major role in tailoring nanoparticle shape and structure was played by the temporal variation of precursor supply in combination with temperature modula-

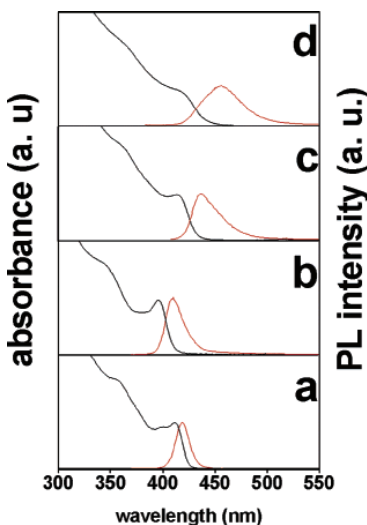


**Figure 6.** UV-vis absorption (left side) and PL emission (right side) spectra of ZnSe spherical (a) and elongated nanocrystals (b-d) nanorods with aspect ratios of 3, 6, and 8, respectively.

tion. The injection of large volumes of stock solution yielded spherical particles in the exclusive cubic ZB structure. In contrast, slow, dropwise addition of the same stock solution promoted the formation of complex 3D architectures in which the rodlike sections (branches) occurred mainly in the WZ phase, while the ZB structure was located at the branching points and/or curvatures.

The microscopic mechanism and the kinetics of nucleation in colloidal nanoparticles is a complex topic of study. The classical nucleation theory (CNT)<sup>38</sup> provides the two following expressions for the crystal nucleation rate per unit volume,  $J_N$ , and for the activation energy for homogeneous nucleation,  $\Delta G^N$ <sup>39,40</sup>

$$J_N = B_N \exp(-\Delta G^N/RT) \quad (1)$$

$$\Delta G^N = 16\pi\gamma^3 V_m^2 / (3|\Delta\mu|^2) \quad (2)$$

In the expressions above,  $R$  is the gas constant,  $T$  is the absolute temperature,  $\gamma$  is the solid–liquid interfacial tension (henceforth referred to as “surface energy” for the case of nanocrystals),  $V_m$  is the molar volume of the corresponding bulk solid and  $\Delta\mu$  ( $<0$ ) is the difference between the chemical potential of the component species in the crystal and that of the corresponding species in the bulk solution (the monomers), and  $B_N$  is a kinetic prefactor that depends on several parameters (e.g., desolvation of species and so forth). In the discussion, we will address the significance of these two equations with respect to the various growth regimes for ZnSe nanocrystals.

Spherical ZnSe nanocrystals were prepared via the “fast-injection” technique. As  $\Delta G_N$  is much higher than the activation energy for particle growth,<sup>39</sup> the temperature drop that follows the rapid injection reduces the rate of homogeneous nucleation significantly but affects much less the

growth rate. This simple technique provides a means of separating the nucleation and growth stages in time and leads to monodisperse ZnSe spheres, provided that the solution is continuously fed with fresh monomers, which keep the growth in the “size-focusing” regime<sup>13e</sup> (Supporting Information Figures 1S–3S). Size control of spherical ZnSe nanocrystals depends on the relative balance between monomer depletion during the nucleation and the growth stages. This balance can be adjusted further by tuning the stability of the Zn–amine complex, by varying, for instance, the chain length of the amine, or the injection/growth temperature. The fast-injection method is not a convenient approach to promote anisotropic growth, unless the absolute amounts of Zn and Se precursors are reduced considerably, as shown in the injection volume experiments of Figure 1. High monomer supersaturation inevitably favored both nucleation and growth in the ZB structure, which is more symmetric than the WZ structure and does not have a single preferential direction of growth.

Shape and limited phase control was easily achieved through slow, dropwise addition of monomers, a technique that allowed to keep the temperature constant throughout the synthesis. In such case, the control over the temporal variation of monomer concentration provided the potential for generating the entire variety of shapes. These results indicated that an extremely low monomer concentration was the stringent requirement to promote the exclusive formation of ZnSe WZ seeds but also to guarantee WZ growth on ZB seeds. Therefore, the solution supersaturation clearly dictated the phase that nucleated and that grew preferentially. At the temperature at which the syntheses are carried out, this phase is not necessarily the most thermodynamically stable one in the bulk (the ZB to WZ transition occurs at about 1420 °C for ZnSe<sup>41</sup>). A similar behavior is observed in other materials that exhibit polytypism<sup>13b,d,14b,c,15a–b,25</sup> or that can be trapped in the high-temperature stable polymorph under remarkably mild solution conditions.<sup>15c,17,20b</sup>

Overall, the variety of the observed shapes arises from the delicate phase balance between the nucleation and the growth steps.<sup>13–16,19</sup> A plausible growth mechanism for the ZnSe system under study should consider the nucleation as the process that governs the overall shape evolution. The monomers left, after the nucleation event is completed, would dictate the fate of the initially formed nuclei. Such nanocrystal nuclei could reasonably be “magic-size” clusters with a peculiar electronic configuration and ZB structure,<sup>42</sup> in analogy with other semiconductor systems.<sup>10b,13d,14e</sup> These clusters should have an exceptionally high stability, as for the case of “magic” metal clusters generated in the gas

(40) (a) Auer, S.; Frenkel, D. *Nature* **2001**, *409*, 1020. (b) Zhang, K.-Q.; Liu, X. Y. *Nature* **2004**, *429*, 739. (c) Gasser, U.; Weeks, E. R.; Schofield, A.; Pusey, P. N.; Weitz, D. A. *Science* **2001**, *292*, 258.

(41) (a) Okada, H.; Kawanaka, T.; Ohmoto, S. *J. Cryst. Growth* **1996**, *165*, 31. (b) Okada, H.; Kawanaka, T.; Ohmoto, S. *J. Cryst. Growth* **1997**, *172*, 361. (c) Kulakov, M. P.; Kulakovskii, V. D.; Savchenko, I. B.; Fadeev, A. V. *Sov. Phys. Solid State* **1976**, *18*, 526.

(42) (a) Kasuya, A.; Sivamohan, R.; Barnakov, Y. A.; Dmitruk, I. M.; Nirasawa, T.; Romanyuk, V. R.; Kumar, V.; Mamykin, S. U.; Tohji, K.; Jeyadevan, B.; Shinoda, K.; Kudo, T.; Terasaki, O.; Liu, Z.; Belosludov, R. V.; Sundararajan, V.; Kamazoe, Y. *Nature* **2004**, *399*, 99. (b) Soloviev, V. N.; Eichhofer, A.; Fenske, D.; Banin, U. *J. Am. Chem. Soc.* **2000**, *122*, 2673.

(38) Mullin, J. W. *Crystallization*, 3rd ed; Butterworth-Heinemann: Oxford, 1997.

(39) Sugimoto, T. *Monodisperse Particles*; Elsevier: Amsterdam, 2001.

## Shape- and Phase-Controlled ZnSe Nanocrystals

phase.<sup>43</sup> In our experiments, very high solution supersaturation kinetically froze the ZnSe system in the ZB phase at nucleation and during growth. The isotropic growth entirely in this phase yielded nearly spherical nanocrystals. Very low supersaturation, on the other hand, allowed the nanocrystal to grow under quasiequilibrium conditions that favored the WZ phase, which should be stable only at high temperatures. Whenever this occurred, the nanocrystals grew anisotropically due to the unique *c* axis of the WZ structure.

These results can be rationalized by considering that, in a nanocluster, the contribution of the surface energy to the total energy is much more influent than in a macroscopic solid, for which the chemical potential of the elemental components is practically the only relevant term.<sup>44</sup> This is also predicted by theoretical calculations, which emphasize the size dependence of the structural metastability at the nanoscale.<sup>45</sup> It is plausible that nanocrystals can form in a phase that is unstable in the bulk, if the growth in this phase minimizes the overall surface energy significantly.<sup>44</sup> In solution, the dynamic binding of monomers and surfactants to nanocrystals can influence dramatically the relative stabilities of the various facets, through steric and electronic effects. The results of growing ZnSe nanocrystals in alkylamines through low supply of monomers, suggest that these surfactants can stabilize more efficiently the facets of WZ ZnSe nanocrystals than the facets of the ZB structure when near-equilibrium conditions are established. In addition, the rod morphology of WZ branches in the ZnSe rods and polypods indicates that the most developed facets, hence, the most stable ones, are the nonpolar (100) and (110) facets of the WZ structure. These facets have no equivalents in the cubic ZB structure. Therefore, the surface energy term can revert the stability between the ZB and WZ phases at the nanoscale, rendering nanocrystals more stable in the WZ rather than in the ZB structure.

While we can rationalize the preference for growth in the WZ structure under suitable conditions, a less straightforward explanation is possible for which phase is preferred at nucleation. The WZ phase can originate from three possible paths: (i) ZB–WZ transition; (ii) direct WZ nucleation; and (iii) WZ growth on ZB. ZB–WZ transition has been observed on nanocrystals at room temperature upon surface restructuring with the assistance of ligands or of the solvent.<sup>46</sup> Additional studies suggest that magic clusters of II–VI semiconductors may undergo a sudden transformation to the WZ structure once they reach a critical size.<sup>13d,15e</sup> In principle,

## Chem. Mater., Vol. 17, No. 6, 2005 1305

the remarkable influence of the surfactant on the average surface energy,  $\gamma_{\text{ZB}}$  and  $\gamma_{\text{WZ}}$ , for the ZB and WZ phases, would differentiate the corresponding values of  $\Delta G^{\text{N}}$  in eq 2 for the two phases, to the point of making homogeneous nucleation possible in the WZ phase. These considerations, however, do not take into account that magic clusters are intrinsically stable and very likely have a low energetic barrier of formation. Consequently, eqs 1–2 should not be applicable to describe their formation and/or their successive evolution. Magic clusters might simply nucleate at much faster rate, even at modest temperature.

The conditions promoting thermodynamic control of the growth (low supersaturation and high temperature) can be expected to give enough time to the system so that equilibrium is reached between the ZB magic clusters and the monomers, as well as between the monomers and nuclei in the WZ phase. Under this growth regime, hexagonal nuclei, when they are formed, are likely to develop into larger particles, as these would be more stable than the corresponding ZB nanocrystals originating from further growth of magic clusters. As opposed, at low growth temperatures and at high supersaturation, as for the fast injection approach, quasiequilibrium conditions cannot set in, and the growth is kinetically controlled. In this case, the high chemical potential of the monomers remaining in the solution will not allow the ZB nuclei to reconvert to the initial monomers, and such clusters would be forced to grow fast, retaining their original ZB phase. One additional possibility for initially formed ZB nanocrystals to increase in size further, while keeping their surface energy low, is to continue to grow in WZ structure. This is realized if hexagonal arms develop from the  $\pm(111)$  facets of the ZB nanocrystals, leading to branched structures.

Alternation of WZ and ZB was also observed during growth. Whenever growth alternated from WZ to ZB and back, deviations from a linear rod geometry were observed, such as particle curvature or branching (Figure 5), as the ZB section could act as a new branching point from which up to three new WZ arms could develop (Figure 3). The possibility for the nanocrystals to easily switch between the two phases is due to the relatively small difference in the total energy between the two phases (5.3 meV/atom)<sup>24</sup> and is the main reason why only a limited phase control, hence, shape control, could be achieved in this work. In general, faster injection rates, therefore higher levels of supersaturation, led to nanocrystal morphologies characterized by a progressively higher number of branches (rods, bi-, tri-, and tetrapods), up to nanocrystals having multiple branching points. The statistical probability of growth continuation in either the ZB or WZ phase scales with the injection rate and/or the concentration of precursor stock solution, as observed for the homogeneous nucleation. A comparatively higher chemical potential is also beneficial to sustain anisotropic growth, according to the shape order seen above.

The temperature dependence of the formation of the branched nanocrystals can be ultimately traced to monomer concentration effects.<sup>13d,15a</sup> In general, the depletion of monomers in the nucleation process and the number of nuclei formed should decrease at lower temperatures. This would keep the monomer chemical potential in the solution at a

- (43) Deheer, W. A. The Physics of Simple Metal-Clusters - Experimental Aspects and Simple-Models. *Rev. Mod. Phys.* **1993**, *65*, 611–676.
- (44) (a) Chen, C.-C.; Herhold, A. B.; Johnson, C. S.; Alivisatos, A. P. *Science* **1997**, *276*, 398. (b) Jacobs, K.; Zaziski, D.; Scher, E.; Herhold, A. B.; Alivisatos, A. P. *Science* **2001**, *293*, 1803. (c) Qadri, S. B.; Skelton, E. F.; Hsu, D.; Dinsmore, A. D.; Yang, J.; Gray, H. F.; Ratna, B. R. *Phys. Rev. B* **1999**, *60*, 9191.
- (45) (a) Belloni, J.; Pernot, P. *J. Phys. Chem. B* **2003**, *107*, 7299. (b) Joswig, J.-O.; Springborg, M.; Seifert, G. *J. Phys. Chem. B* **2000**, *104*, 2617. (c) Joswig, J.-O.; Roy, S.; Sarkar, P.; Springborg, M. *Chem. Phys. Lett.* **2002**, *365*, 75.
- (46) (a) Zhang, H.; Gilbert, B.; Huang, F.; Banfield, J. F. *Nature* **2003**, *424*, 1025. (b) Murakoshi, K.; Hosokawa, H.; Tanaka, N.; Saito, M.; Wada, Y.; Sakata, T.; Mori, H.; Yanagid, S. *Chem. Commun.* **1998**, 321–322. (c) Rockenberger, J.; Troger, L.; Kornowski, A.; Vossmeyer, T.; Eychmuller, A.; Feldhaus, J.; Weller, H. *J. Phys. Chem. B* **1997**, *101*, 2691.

relatively higher level, so that the formation of the branched nanocrystals can be promoted.

The rod-generating synthesis conditions (low injection rates and high temperature) can be taken as an example that illustrates the general size/shape guiding mechanisms. The rate of injection is critical in governing the overall aspect ratio of the rods as it regulates the nucleation event. At low injection rates, a few WZ nuclei are initially formed. These nuclei are then fed by the continuous supply of monomers and can evolve into long rods. At higher injection rates, on the other hand, a larger number of WZ nuclei are formed. These nuclei then have to compete more for the monomers delivered and, therefore, can evolve only into short rods. A similar trend is observed when varying the total injected volume at a fixed injection rate. A remarkable aspect of the slow injection technique is that no additional nuclei are formed during the injection after the initial nucleation event, even when fast injection rates are devised. This guarantees a reasonably narrow distribution of rod lengths. Apparently, the continuously replenished monomers are rapidly consumed to feed the nanocrystals already existing in solution, and the nucleation threshold is not reached again.

## 5. Conclusions

The synthesis of quantum-sized colloidal ZnSe nanocrystals in a variety of morphologies (spheres, rods, and branched

structures) with peculiar shape-dependent optical properties has been demonstrated by proper manipulation of particle growth kinetics using an organometallic approach. Control over the injection rate of the precursors demonstrated to be an advantageous general method for controlling the production of the two crystalline polymorphs either separately (ZB spheres and WZ rods) or combined in multibranched structures. The proposed method offers the potential for generating elaborate morphologies by proper modification of the synthesis conditions.

**Acknowledgment.** The authors thank Dr. Danièle Laub (EPFL-CIME-Centre Interdisciplinaire de Microscopie Electronique, Batiment MXC, 1015 Lausanne, Switzerland) for HR-TEM studies and Dr. Roberto Lassandro for assistance in XRD measurements. The partial support of the EC-funded project NaPa (Contract No. NMP4-CT-2003-500120) is gratefully acknowledged.

**Supporting Information Available:** Growth kinetics of spherical ZnSe nanocrystals followed by UV-vis absorption and PL emission measurements, TEM images of spherical ZnSe nanocrystals, and absorption and PL spectra of the ZnSe samples obtained by the injection volume experiments (PDF). This material is available free of charge via the Internet at <http://pubs.acs.org>.

CM047874V

## Supporting Information

### Shape and Phase Control of Colloidal ZnSe Nanocrystals

*P. Davide Cozzoli,<sup>a\*</sup> Liberato Manna,<sup>b</sup> M. Lucia Curri,<sup>c</sup> Stefan Kudera,<sup>d</sup> Cinzia Giannini,<sup>e</sup> Marinella Striccoli<sup>c</sup> and Angela Agostiano<sup>a,c</sup>*

<sup>a</sup> Dipartimento di Chimica, Università di Bari, Via Orabona 4, 70126 Bari, Italy

<sup>b</sup> National Nanotechnology Laboratory of INFM, Via Arnesano Km 5, 73100 Lecce, Italy

<sup>c</sup> CNR-Istituto per i Processi Chimico-Fisici (IPCF), sez. Bari, via Orabona 4, 70126 Bari, Italy

<sup>d</sup> Center for Nanoscience, Ludwig Maximilians Universität München, Munich, Germany

<sup>e</sup> CNR-Istituto di Cristallografia (IC), via Amendola 122/O, 70126 Bari, Italy

Corresponding author: d.cozzoli@ba.ipcf.cnr.it

### Growth kinetics of spherical ZnSe nanocrystals

**Fig. 1S** reports a typical ZnSe growth kinetics in HDA. Soon after the first injection, ultratin TEM-invisible clusters with a well-defined exciton peak (at  $\sim$ 325 nm) were generated, which were usually nonemitting. Subsequently, a progressive red-shift of the excitonic absorption and of the related intense band-edge emission peak indicated the slow growth of regularly-sized luminescent nanoparticles at the expense of the reactive monomers present in the solution. However, as the system early entered a size “defocusing” growth regime, a broadening of both peaks could be observed. Additional precursor injections were therefore required in order to replenish the concentration of reactive monomers in solution, ultimately yielding monodisperse ZnSe nanocrystals (**Fig. 3S-a**).

The use of an amine with a longer alkyl chain, ODA, allowed to grow larger ZnSe nanocrystals. The synthesis could be carried out also at comparatively higher temperature in ODA. With this solvent, an increase in the growth rate was observed in the initial period (**Fig. 2S**). However, additional injections demonstrated to be poorly useful to improve the size-distribution which, in fact, inevitably tended to broaden, ultimately comprising faceted, oval and slightly elongated nanoparticles (**Fig. 3S b-c**).

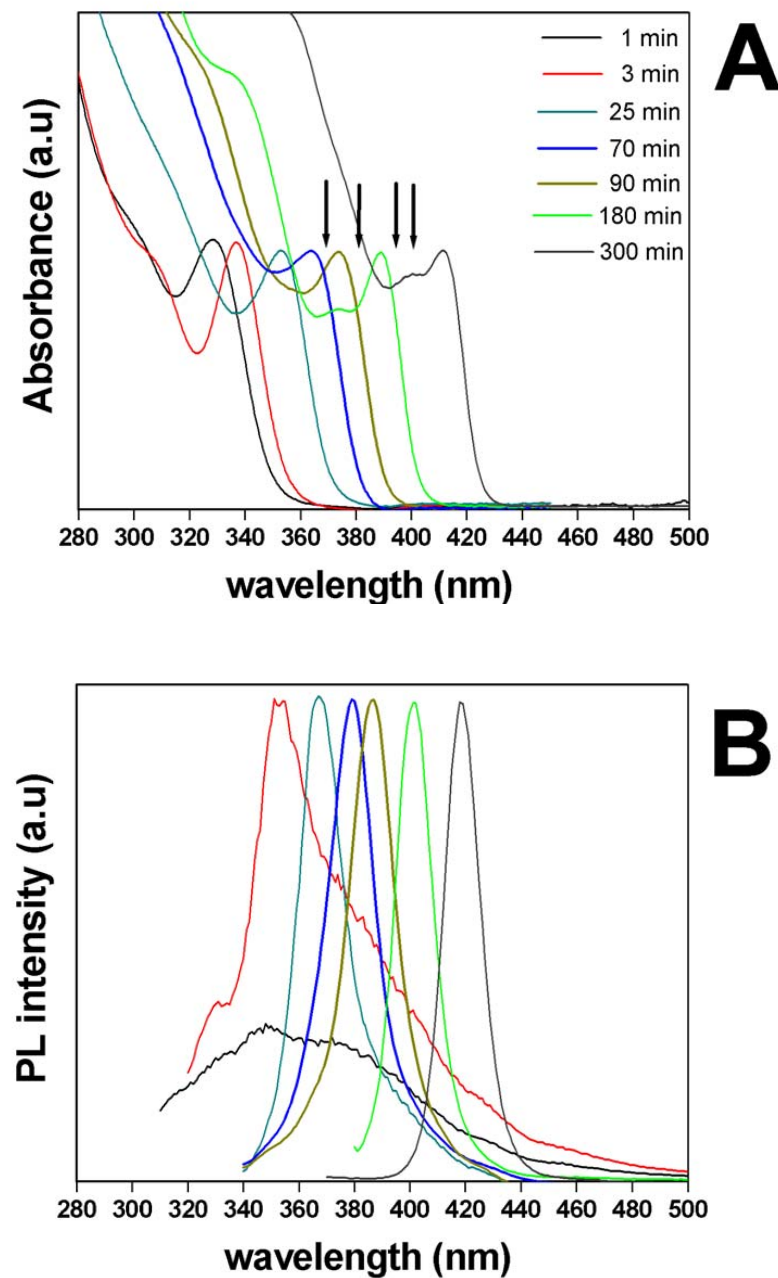


**Figure 1S** Typical growth kinetics of spherical ZnSe nanocrystals in HDA, followed by monitoring the temporal evolution of their UV-vis absorption (A) and PL emission spectra (B). The reaction was initiated by rapidly injecting 2.5 mL of a 0.32 M Zn/Se stock solution into 7g HDA at 300°C. Growth was then allowed at 270°C and sustained by additional dropwise (at 0.2 mL/min) injections of 1 mL, 2 mL, 3 mL and 3 mL of the same stock solution after 1h15min, 2h, 3h40min, 4h20min reaction time, respectively (indicated by the arrows in A). Growth was stopped after 5h.

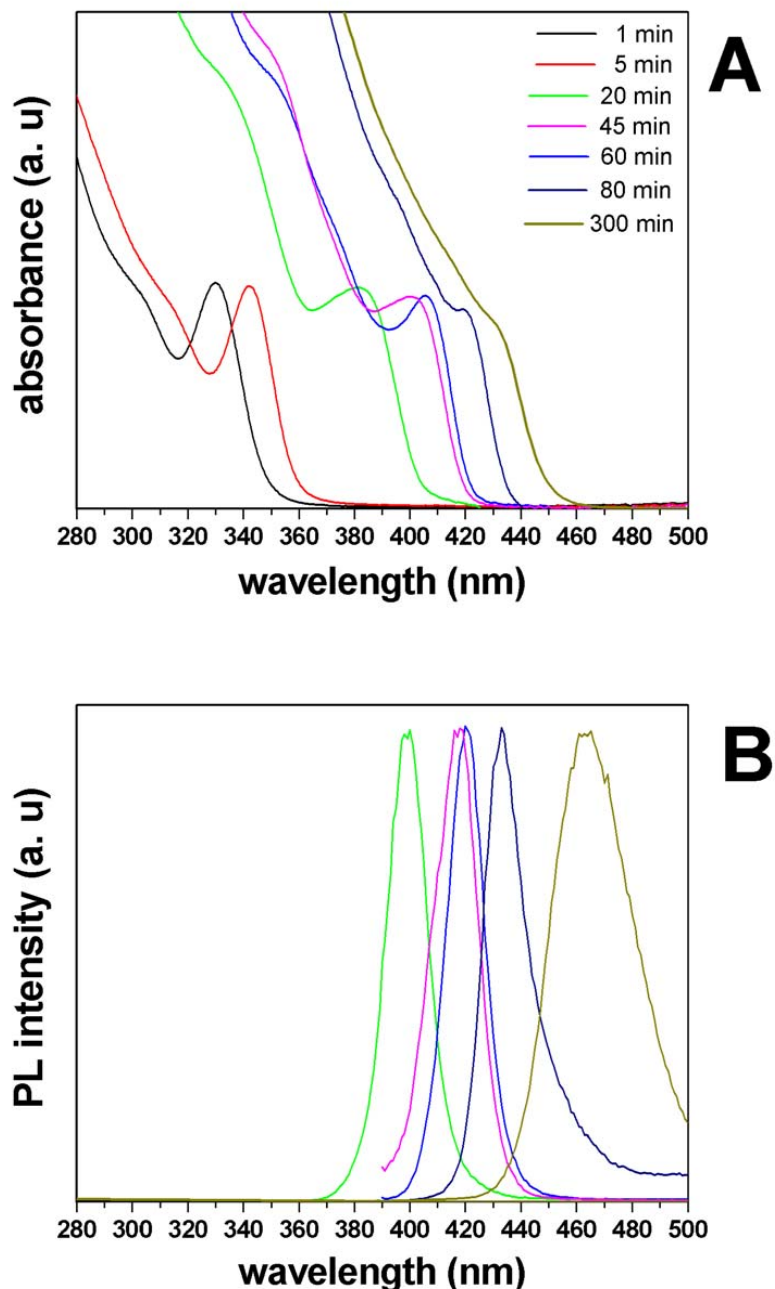


**Figure 2S** Typical growth kinetics of spherical ZnSe nanocrystals in ODA, followed by monitoring the temporal evolution of their UV-vis absorption (A) and PL emission spectra (B). The reaction was initiated by rapidly injecting 2.5 mL of a 0.32 M Zn/Se stock solution into 7g ODA at 340°C. Growth was then allowed at 300°C and sustained by additional dropwise (at 0.2 mL/min) injections of 1 mL, 2 mL, 3 mL and 3 mL of the same stock solution after 30min, 1h10min, 2h, 3h30min reaction time, respectively. Growth was stopped after 5h.

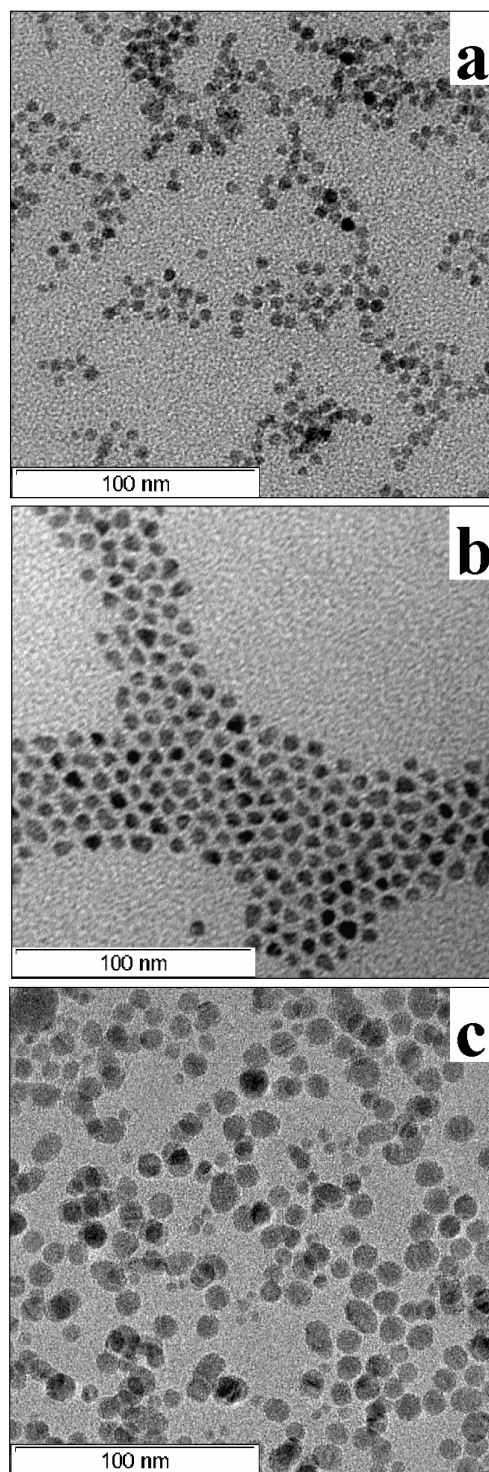


**Figure 3S** Low resolution TEM images of spherical ZnSe nanocrystals grown: (a) in HDA with  $T_{inj} \sim 300^\circ\text{C}$  and at  $T_{gr} \sim 270^\circ\text{C}$ ; (b) in ODA with  $T_{inj} \sim 320^\circ\text{C}$  and at  $T_{gr} \sim 290^\circ\text{C}$ ; and (c) in ODA with  $T_{inj} \sim 340^\circ\text{C}$  and at  $T_{gr} \sim 310^\circ\text{C}$ .

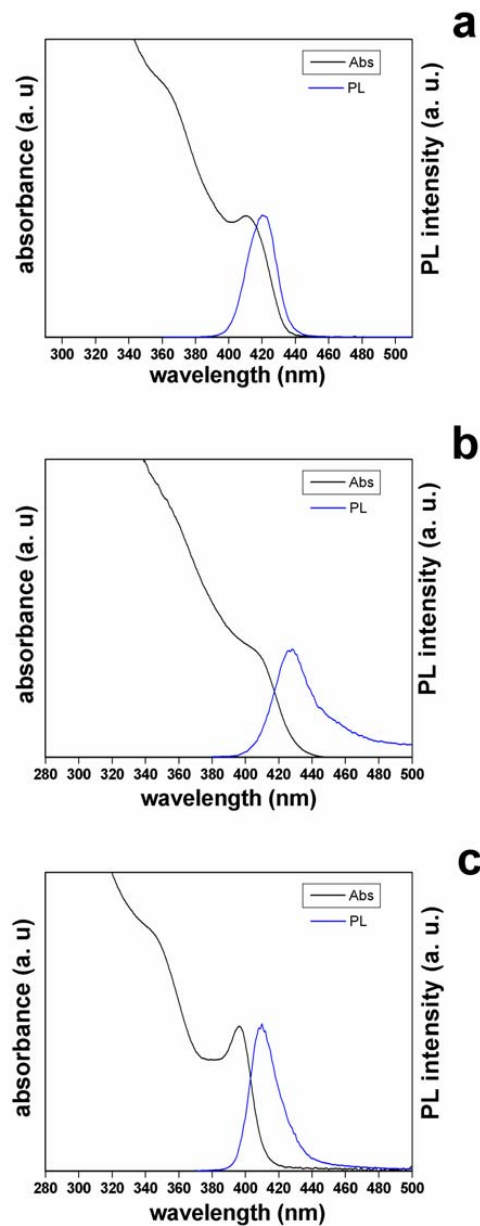


**Figure 4S** Absorption and PL emission spectra of the ZnSe nanocrystals obtained by the injection volume experiments shown in Fig. 1a-c, respectively.

### B.3 Optical properties of tetrapod-shaped CdTe nanocrystals

D. TARÌ, M. DE GIORGI, F. DELLA SALA, L. CARBONE, R. KRAHNE, L. MANNA,  
R. CINGOLANI, S. KUDERA, W.J. PARAK

*Appl. Phys. Lett.* **87**(22), pp. 224101, 2005

We studied the carrier confinement in tetrapod-shaped colloidal CdTe nanocrystals by means of absorption, photoluminescence, and photoluminescence excitation spectroscopy at room and cryogenic temperatures. The spectra show features characteristic of the tetrapod shape together with a clear dependence on the dominant confinement parameter, i.e., the diameter of the tetrapod arm. Theoretical calculations based on an envelope-function approximation and using the exact tetrapod shape have been performed to assign the observed spectral features. Oscillator strength and size dependence of the transitions energy have been calculated showing a direct correlation between the oscillator strength and the nanocrystal shape.

## Optical properties of tetrapod-shaped CdTe nanocrystals

Davide Tari,<sup>a)</sup> Milena De Giorgi, Fabio Della Sala, Luigi Carbone, Roman Krahne, Liberato Manna, and Roberto Cingolani

*National Nanotechnology Laboratory of INFM c/o Istituto Superiore Universitario di Formazione Interdisciplinare, Università di Lecce, Via per Arnesano, 73100 Lecce, Italy*

Stefan Kudera and Wolfgang J. Parak  
*Center for Nanoscience, Ludwig Maximilians Universität München, Munich, Germany*

(Received 24 May 2005; accepted 19 September 2005; published online 21 November 2005)

We studied the carrier confinement in tetrapod-shaped colloidal CdTe nanocrystals by means of absorption, photoluminescence, and photoluminescence excitation spectroscopy at room and cryogenic temperatures. The spectra show features characteristic of the tetrapod shape together with a clear dependence on the dominant confinement parameter, i.e., the diameter of the tetrapod arm. Theoretical calculations based on an envelope-function approximation and using the exact tetrapod shape have been performed to assign the observed spectral features. Oscillator strength and size dependence of the transitions energy have been calculated showing a direct correlation between the oscillator strength and the nanocrystal shape. © 2005 American Institute of Physics.

[DOI: 10.1063/1.2130727]

In recent years, there has been a remarkable advancement in the ability to grow anisotropic nanocrystals, such as rods,<sup>1–3</sup> tetrapods,<sup>4</sup> and nanocrystals with even more complex branched shapes.<sup>5</sup> The influence of the geometric shape on the electronic structure of the nanocrystals is of great interest, since it modifies their optical and electrical properties. Hu and co-workers, for instance,<sup>3</sup> have shown that colloidal quantum rods exhibit linearly polarized light emission. Therefore, the opportunity to tune the nanocrystal shape paves the way to new properties stemming from the peculiar geometry of these structures. This has a great impact in different fields of nanotechnology, such as biological tagging, photovoltaics, electronics and light-emitting diodes (LEDs). An intriguing nanocrystal shape is the tetrapod [Fig. 1(a)], in which four rod-shaped arms branch with a wurtzite crystal structure from a central zinc blende core.<sup>4</sup>

In this letter, we study the electronic structure of CdTe tetrapods as a function of the length and diameter of the arms. Linear absorption spectra, photoluminescence excitation (PLE), and fluorescence experiments at room and low temperatures together with theoretical calculations were performed on samples of different geometrical dimensions. The tetrapods exhibit a remarkable fluorescence yield with well resolved multifold splitting of the spectra originating from the electron quantization in the arms of the nanostructure, as confirmed by theoretical calculations.

The tetrapod samples were grown according to the protocol described by Manna and co-workers.<sup>4</sup> Figure 1(a) shows a schematic illustration of the tetrapod shape and sketches the band offset between the zinc blende core and the wurtzite arms.<sup>6</sup> Structural information about tetrapod samples has been obtained by transmission electron measurements (TEM). In this letter, we discuss the properties of a set of tetrapods (labeled as *T1*, *T2*, and *T3*) whose geometrical dimensions were assessed by wide-field TEM images [Figs. 1(b)–1(d)]. The tetrapod samples have a good homogeneity

in shape and a rather narrow distribution of arm diameters (*d*) and lengths (*l*), whose average values have been found to be equal to: *d*=7 nm and *l*=60 nm for the sample *T1*, *d*=5.7 nm and *l*=30 nm for *T2* and finally, *d*=4.7 nm and *l*=25 nm for *T3*.

Figures 2(a)–2(c) shows the linear absorption and the fluorescence spectra of the three tetrapod samples recorded at room temperature in solution. In all absorption spectra, quantum confinement causes the lowest energy peak to blueshift with respect to the bulk CdTe value (1.50 eV at *T*=300 K), and a series of overlapping peaks appears at higher energies due to high-index exciton states. As a general trend, the absorption features of the tetrapods are size-dependent. In smaller tetrapods the lowest exciton state occurs at higher energy (1.81 eV for sample *T3*) compared with the larger tetrapods (1.715 eV for sample *T1*), and the energy spacing

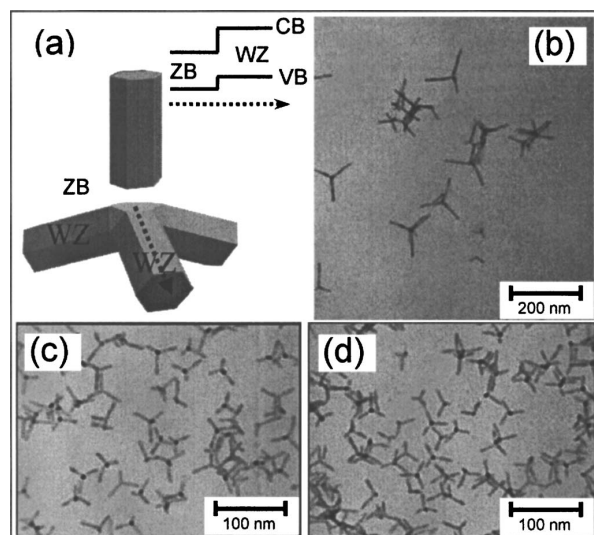


FIG. 1. (a) An illustration of a tetrapod. (b)–(d) TEM of three CdTe tetrapod samples.

<sup>a)</sup>Author to whom correspondence should be addressed; electronic mail: davide.tari@unile.it

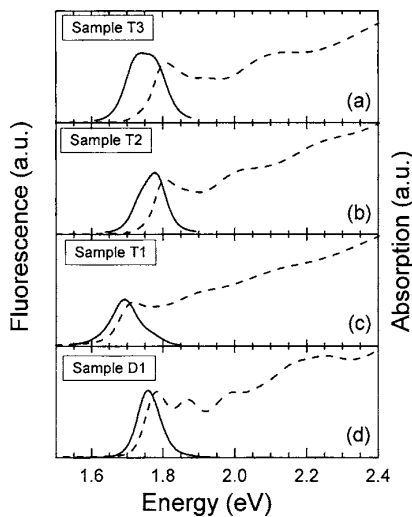


FIG. 2. Absorption (dashed line) and fluorescence spectra (solid line) taken at room temperature of (a)–(c) tetrapods and (d) dot samples.

between the various exciton states increases when the dimensions are reduced.

In order to understand the effect of the tetrapod shape on its overall electronic structure, it is useful to compare these nanostructures with nanospheres, widely studied in the last years. The absorption and emission spectra from spherical CdTe nanocrystals (sample D1), emitting in a comparable spectral range, are displayed in Fig. 2(d). The absorption spectra of the tetrapods are less distinct than in spheres, and this can be explained by the effect of the more elaborate geometry of the tetrapods on their electronic structure. Although the confinement in tetrapods depends more strongly on the diameter of the arms than on their length, the smaller degree of exciton confinement in the arms and their lower symmetry lead to a multitude of exciton states separated by comparatively smaller energy gaps.

By looking at the emission spectra from the tetrapods we clearly observe a double-peak structure in smaller tetrapods (samples T2 and T3), whereas in larger tetrapods (sample T1) the second peak can be better resolved after a careful deconvolution of the spectrum. A detailed analysis of the emission spectra shows that a decrease in arm width of the tetrapods leads to an increase both in energy spacing between the two peaks and of the intensity of the high-energy peak. Moreover, in the tetrapod spectra displayed in Figs. 2(a)–2(c), the Stokes shift increases with decreasing size, in analogy with spherical nanocrystals,<sup>7</sup> but it stays remarkably large (about 100 meV for smaller tetrapods). For comparison, in spherical nanocrystals of diameter around 5 nm, the Stokes shift is rather small (about 50 meV). The large Stokes shift observed in the tetrapods could partly result from the larger size distribution compared to dots<sup>8</sup> and partly from the shape anisotropy, as observed in rods.<sup>3</sup>

Figures 3(a)–3(c) shows the room temperature PLE spectra of the three tetrapod samples. If the detection energy is tuned over the full spectral width of the fluorescence signal, no significant change in the characteristic features is observed. This proves that the double-peak structure in emission [resolved also in the PLE spectra, as indicated by the small arrows in Figs. 3(b) and 3(c)] originates from the same class of nanocrystals, i.e., the tetrapods. In the intermediate

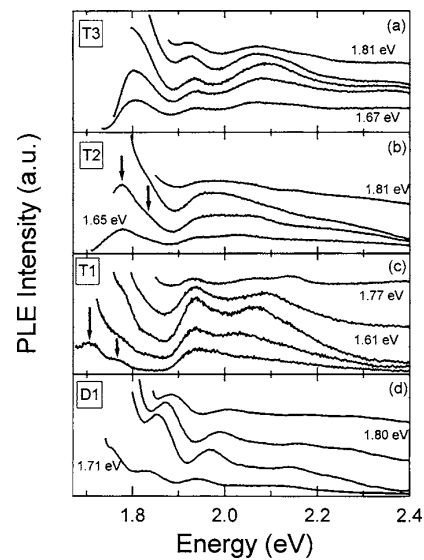


FIG. 3. Photoluminescence excitation spectra of (a)–(c) tetrapods and (d) dots at different detection energies for each sample. The small peak at 2 eV that shifts with the detection energy is an artefact of the solvent.

detection energy range, the PLE signal results from two transitions, namely coming from the two peaks observed in fluorescence. This effect, together with the size distribution and the elaborate geometry of the tetrapods<sup>8</sup> leads to an inhomogeneous broadening of the features, which prevents us from observing photoselection of nanocrystals with different sizes as normally observed in dot samples [like the one shown in Fig. 3(d)], where a blueshift of about 60 meV of the higher energy states is observed when increasing the detection energy.

Measurements at cryogenic temperatures were performed by depositing a drop of nanocrystal solution on SiO<sub>2</sub>

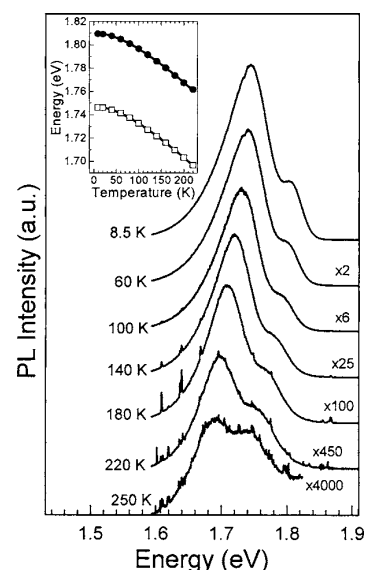


FIG. 4. Temperature-dependent PL spectra of the sample T2. The different curves are shifted for clarity (corresponding magnification is indicated). The inset shows the peak positions fitted by the Varshni function for both transitions observed in the PL spectra.

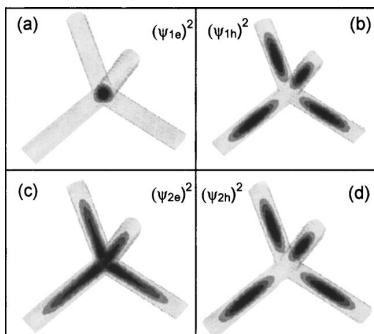


FIG. 5. Three-dimensional view of the isosurfaces of  $\Psi^2$  of the electron (a) and hole (b) ground state and of the first electron (c) and hole (d) excited state calculated for the T2 tetrapod.

substrates. Figure 4 shows PL spectra of the sample T2 recorded in a temperature range between 8.5 and 250 K. The ratio between the intensity of the high energy peak and the low energy peak varies significantly with increasing temperature,<sup>9</sup> while the overall intensity of the signal decreases due to the increased rate of nonradiative processes. This behavior can be correlated with the thermal filling of the electronic levels due to a rise of the Fermi level at higher temperatures. Both peaks show a redshift with increasing temperature. In the inset of Fig. 4 we report the peak position of the two observed transitions as a function of the temperature. The experimental points for both transitions follow the Varshni equation<sup>10</sup>

$$E_g(T) = E_g(0) - \frac{\alpha T^2}{\beta + T}, \quad (1)$$

where  $E_g$  is the energy gap of material,  $T$  is the temperature, and  $\alpha$  and  $\beta$  are Varshni's coefficients.

For a more complete understanding of the optical properties of the tetrapods, we performed preliminary theoretical calculations of the electronic structure, based on the envelope-function approximation, and using the geometrical dimensions (arm lengths and diameters) derived from the TEM measurements. We modeled the tetrapod shape, by considering a zinc blende (ZB) octahedron as the core and four wurtzite (WZ) hexagonal prisms as the arms and by solving numerically the three-dimensional single-particle effective-mass Schrödinger equations.<sup>11</sup> We also assumed that the electrons are confined by a potential barrier whose height is equal to the electron affinity of CdTe<sup>12</sup> whereas the holes are confined by an infinite potential barrier. In the following, we discuss the results for the sample T2.

For the T2 sample, the calculated excitation energies for the ground (GS) and the first excited (EX) states (GS = 1.674 eV and EX = 1.747 eV, respectively) agree well with the PL experimental peak. The squared wave functions of the first two confined electron and hole states for the T2 sample are shown in Fig. 5. We found that the ground state of the electrons has a  $A_1$  symmetry, with the electron density mostly localized in the core of the tetrapod [Fig. 5(a)], whereas the wave function of the ground state of the holes has a  $T_2$  symmetry and spreads into the arms [Fig. 5(b)]. On the other hand, both the electron and hole wave functions of the first excited state have  $T_2$  symmetry, with the carriers completely localized in the arms [Figs. 5(c) and 5(d)]. As a

result of the different electron-hole overlap, the oscillator strength for the transition between the ground state levels is much smaller (0.52) than that between the first excited states (1.76), i.e., the probability that the excited state recombines radiatively is increased. In addition, due to the different symmetry of the two electron states, the probability of an intraband transition which leads the carrier from the first excited state to the ground state is reduced. Thus the two peaks observed in the fluorescence spectra can be ascribed to the transition of the two lowest confined electron and hole states. The peak at lower energy should be correlated to the transition between the ground state in conduction band and to the ground state in valence band ( $E_{1e} \rightarrow E_{1h}$ ), whereas the peak at higher energy to the transition between the first excited states in conduction and valence band ( $E_{2e} \rightarrow E_{2h}$ ).

In conclusion, we investigated the photoluminescence properties of tetrapod-shaped nanocrystals as a function of their size. We observed that the absorption, PL, and PLE spectra show also features peculiar of their complex shape. A theoretical calculation which takes into account the exact shape of the tetrapods and based on the envelope-function approximation made possible to understand the origin of these features and to assign the observed experimental energy transitions.

The authors gratefully acknowledge the useful discussion from Dr. Marco Anni and P. Pompa for the PLE measurements. They also thank the expert technical help of P. Cazzato. This work has been partially supported by the SANANO European project Contract No. STRP013698, MIUR-FIRB project, the Deutscher Akademischer Austauschdienst (DAAD) and the Vigoni Foundation.

<sup>1</sup>X. G. Peng, L. Manna, W. D. Yang, J. Wickman, E. Scher, A. Kadavanich, and A. P. Alivisatos, *Nature (London)* **404**, 59 (2000).

<sup>2</sup>T. Mokari and U. Banin, *Chem. Mater.* **15**, 3955 (2003); C. Pacholski, A. Kornowski, and H. Weller, *Angew. Chem., Int. Ed.* **41**, 1188 (2002).

<sup>3</sup>J. T. Hu, L. S. Li, W. D. Yang, L. Manna, L. Wang, and A. P. Alivisatos, *Science* **292**, 2060 (2001).

<sup>4</sup>L. Manna, D. J. Milliron, A. Meisel, A. Scher, and A. P. Alivisatos, *Nat. Mater.* **2**, 382 (2003).

<sup>5</sup>D. J. Milliron, S. M. Hughes, Y. Cui, L. Manna, J. Li, L. W. Wang, and A. P. Alivisatos, *Nature (London)* **430**, 190 (2004); K. A. Dick, K. Deppert, M. W. Larsson, T. Martensson, W. Seifert, L. R. Wallenberg, and L. Samuelson, *Nat. Mater.* **3**, 380 (2004).

<sup>6</sup>M. Nirmal, D. J. Norris, M. Kuno, and M. G. Bawendi, *Phys. Rev. Lett.* **75**, 3728 (1995); A. L. Efros, M. Rosen, M. Kuno, M. Nirmal, D. J. Norris, and M. Bawendi, *Phys. Rev. B* **54**, 4843 (1996); Z. H. Yu, J. B. Li, D. B. O'Connor, L. W. Wang, and P. F. Barbara, *J. Phys. Chem. B* **107**, 5670 (2003).

<sup>7</sup>D. J. Norris, A. L. Efros, M. Rosen, and M. Bawendi, *Phys. Rev. B* **53**, 16347 (1996).

<sup>8</sup>The peak around 2 eV has been attributed to the solvent by performing PLE measurements on the solution in the absence of nanocrystals.

<sup>9</sup>By a rough fit of the ratio between the intensity of the two PL peaks as a function of the temperature and considering one Arrhenius plot we obtain an activation energy which falls within the 10% margin of error of the energy spacing between the two states, as measured from the PL spectra.

<sup>10</sup>J. Perez-Conde, A. K. Bhattacharjee, M. Chamorro, P. Lavallard, V. D. Petrikov, and A. A. Lipoovskii, *Phys. Rev. B* **64**, 113303 (2001).

<sup>11</sup>I. Calderon-Hernandez, edited by M. C. Tamargo (New York, 2001); F. Long, W. E. Hagston, P. Harrison, and T. Stirner, *J. Appl. Phys.* **82**, 3414 (1997); Y. Yan, M. M. Al-Jassim, K. M. Jones, S. H. Wei, and S. B. Zang, *Appl. Phys. Lett.* **77**, 1461 (2000); S. H. Wei and S. B. Zhang, *Phys. Rev. B* **62**, 6944 (2000).

<sup>12</sup>I. Visoly-Fisher, A. Sitt, M. Wahab, and D. Cahen, *ChemPhysChem* **6**, 277 (2005).

## B.4 Electron-Hole Dynamics in CdTe Tetrapods

S. MALKMUS, S. KUDERA, L. MANNA, W. J. PARAK, M. BRAUN  
*J. Phys. Chem. B* **110**(35), pp. 17334–17338, 2006

We present transient absorption studies with femtosecond time resolution on the electron-hole dynamics in CdTe tetrapod nanostructures. Electron-hole pairs are generated by optical excitation in the visible spectral range, and an immediate bleach and induced absorption signal are observed. The relaxation dynamics to the lowest excitonic state is completed in about 6 ps. Experiments with polarized excitation pulses give information about the localization of the excited-state wave functions. The influence of the nanocrystal shape on the optical properties of CdTe nanoparticles is discussed.

## Electron–Hole Dynamics in CdTe Tetrapods

Stephan Malkmus,<sup>†</sup> Stefan Kudera,<sup>‡,§</sup> Liberato Manna,<sup>§</sup> Wolfgang J. Parak,<sup>‡</sup> and Markus Braun<sup>\*,†</sup>

BioMolekulare Optik, Department für Physik, Ludwig-Maximilians-Universität, Oettingenstr. 67, D-80538 München, Germany, Center for Nanoscience (CENS), Department für Physik, Ludwig-Maximilians-Universität, Amalienstr. 54, D-80799 München, Germany, and National Nanotechnology Laboratory of CNR–INFM c/o Istituto Superiore Universitario di Formazione Interdisciplinare, Università di Lecce, Via per Arnesano, 73100 Lecce, Italy

Received: March 13, 2006; In Final Form: July 11, 2006

We present transient absorption studies with femtosecond time resolution on the electron–hole dynamics in CdTe tetrapod nanostructures. Electron–hole pairs are generated by optical excitation in the visible spectral range, and an immediate bleach and induced absorption signal are observed. The relaxation dynamics to the lowest excitonic state is completed in about 6 ps. Experiments with polarized excitation pulses give information about the localization of the excited-state wave functions. The influence of the nanocrystal shape on the optical properties of CdTe nanoparticles is discussed.

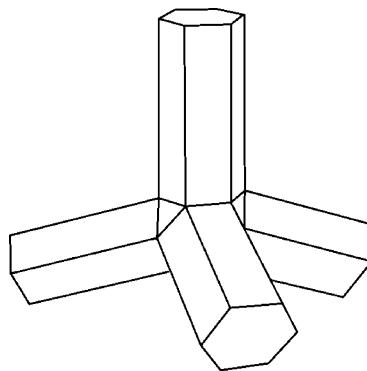
### Introduction

Colloidal nanocrystals of II–VI semiconductors such as CdSe and CdTe have been intensively investigated over recent years, not only because of the interesting, fundamental physics of confined charge carriers,<sup>1–10</sup> but also concerning their potential use for biological and technical applications. The energy of the lowest excitonic state in these materials can be blue-shifted just by decreasing the size of the crystals into the range of a few nanometers due to the quantum confinement effect. This tunability of their color combined with a high fluorescence quantum yield at room temperature make these materials promising candidates for emitters in displays, lasers, or biological labeling.<sup>11–16</sup>

Meanwhile, synthesis conditions were developed that allow for the reproducible fabrication of strongly luminescent, colloidal nanocrystals with a well-defined size and narrow size distribution.<sup>6,17–19</sup> Also the synthesis of well-defined composite materials and nanocrystal shapes such as dots, disks, rods, teardrops, or tetrapods were demonstrated.<sup>19–25</sup> This large flexibility in size, shape, and composition facilitates the tailoring of colloidal nanostructures in order to realize new materials with distinct functionalities. Therefore detailed knowledge on the fundamental electronic processes in these nanomaterials such as charge-carrier dynamics as a function of their shape is required.

Transient absorption (TA) experiments using time-resolved pump–probe spectroscopy are a perfect tool to investigate the ultrafast electron–hole dynamics in semiconductor nanoparticles. Optical pulses on the femtosecond time scale are available nowadays from the UV to the IR spectral range from Ti: sapphire-based tabletop laser systems with parametric frequency conversion stages. Tunable multi-color experiments with a temporal resolution of better than 20 fs are feasible using

### CHART 1



noncollinear optical parametric amplifiers (NOPA) and pulse compression techniques.<sup>26–28</sup> This allows us to study the spectrally broad bleach dynamics in semiconductor nanocrystals with highest temporal resolution.

Many time-resolved investigations on the electron–hole dynamics in colloidal II–VI semiconductor nanoparticles are found in the literature.<sup>2–5,8–10,29–32</sup> These studies give a deeper insight into the nonradiative intraband and interband relaxation mechanisms, charge-carrier trapping, and the cooling dynamics due to the solvent. The preferred object of interest for those investigations are spherical CdSe and CdTe nanocrystals. Only little is known about the ultrafast charge-carrier dynamics of nanocrystals with different shapes, that is, nanorods.<sup>29–33</sup> CdTe tetrapod-shaped nanocrystals (see Chart 1) are quite complex, as they consist of four nanorodlike arms with wurtzite structure grown on a tetrahedron-shaped nanocrystal core.<sup>21</sup> Only a few studies using optical spectroscopy were performed for this type of nanocrystal.<sup>21,34,35</sup>

In this work we present femtosecond time-resolved transient absorption studies on CdTe tetrapod nanocrystals. The ultrafast bleach dynamics in the visible spectral range is discussed and compared to results on spherical nanocrystals and nanorods. Also, polarization-dependent bleach dynamics on the tetrapod is presented. The observed bleach dynamics monitors the charge-

\* Corresponding author. Tel.: ++49/89/2180 9215. Fax.: ++49/89/2180 9202. E-mail: markus.braun@physik.uni-muenchen.de.

<sup>†</sup> BioMolekulare Optik, Department für Physik, Ludwig-Maximilians-Universität.

<sup>‡</sup> Center for Nanoscience (CENS), Department für Physik, Ludwig-Maximilians-Universität.

<sup>§</sup> National Nanotechnology Laboratory of CNR–INFM c/o Istituto Superiore Universitario di Formazione Interdisciplinare, Università di Lecce.

## Electron–Hole Dynamics in CdTe Tetrapods

carrier relaxation to the electronic states near the band gap in the range of a few picoseconds. Evaluation of the polarized signals allows us to assign the observed optical transitions to charge carriers localized at an arm or the central core of the tetrapod nanocrystal.

## Materials and Methods

Tetrapods of CdTe were prepared following the procedure described in the literature,<sup>21</sup> with further modifications.<sup>36</sup> The synthesis of CdTe dots<sup>37</sup> follows a similar procedure, which is still unpublished.

The tetrapod and spherical CdTe nanoparticles were characterized by transmission electron microscopy (TEM), shown as insets in Figure 1. The arms of the tetrapod nanocrystals were determined to have a length of  $(25 \pm 6)$  nm and a width of  $(6.8 \pm 0.6)$  nm; the diameter of the spherical nanocrystals is  $(5.9 \pm 0.8)$  nm according to the TEM measurement and 5.4 nm as determined by UV/vis spectroscopy.<sup>38</sup>

TEM images of the investigated tetrapod sample show that a large fraction of the branched tetrapod nanocrystals are not perfect. About 34% of the sample are branched nanocrystals with one arm broken, about 20% have two broken arms, and also unbranched nanorods are observed. Spherical nanocrystals are not observed in the sample. Taking into account the TEM measurements and the amount of CdTe unit cells for the different types of nanocrystals, we can state that the optical absorption of branched nanocrystals (perfect tetrapods or tetrapods with broken arms) is about 95% of the overall sample. Therefore, unbranched nanocrystals play a minor role for the transient absorption data. Nevertheless, one should keep in mind that other spectroscopic methods (e.g., fluorescence) would require a much higher degree of purity.

The laser system for the TA measurements<sup>39</sup> consists of a home-built Ti:sapphire oscillator (100-MHz repetition rate, 20-fs pulse duration, 10-nJ pulse energy) and a regenerative amplifier (1-kHz repetition rate, 80-fs pulse duration, 350- $\mu$ J pulse energy) at a central wavelength of 800 nm. The output of the laser is used as the pump source for two NOPAs (noncollinear optical parametric amplifier) that deliver pump and probe pulses for the TA measurements in the visible spectral range. Pump pulses at a wavelength of 480 nm and spectrally broad probe pulses (about 200 nm) with unstructured spectral profiles were achieved by the proper choice of collinear angles in the NOPA process. The pulses were compressed by a quartz prism compressor to 50 fs (pump pulse) and 22 fs (probe pulse), respectively. The pulses were characterized by measuring their spectrum (Figure 1c) and auto-correlation.

For the measurement of the TA signal the output of one NOPA was split in two parts, the probe pulse and a reference pulse. Both pulses pass the sample at the same position under a small angle. A fixed delay line ensures that the reference pulse travels through the sample about 1 ns in advance of the probe pulse and never interacts with the pump pulse. The transmitted light of both pulses is spectrally resolved by two identical spectrometers. The spectra are recorded with two photodiode arrays (42 elements each) that are read out with 1-kHz repetition rate in order to facilitate single-pulse detection. The sample is photoexcited by the output of the second NOPA. The delay between pump and probe pulse is varied by a mechanical delay stage. For each delay time the TA signal is recorded by averaging over about 500 laser shots.

The sample concentration of tetrapod nanocrystals in chloroform was adjusted to yield an optical transmission of 10% at 480 nm in a quartz cuvette of thickness 500  $\mu$ m. Three different samples of CdTe tetrapod nanoparticles from independent

*J. Phys. Chem. B*, Vol. 110, No. 35, 2006 17335

synthesis runs with identical size parameters were investigated. Time constants and decay-associated spectra from the TA measurements were reproduced for all samples.

## Results

Steady-state absorption spectra of CdTe tetrapods and spherical dots in chloroform are presented in Figure 1. The excitonic absorption peak of lowest energy is situated at 690 nm (CdTe bulk band gap: 830 nm) for the dot and the tetrapod sample. Weak maxima in the absorption spectrum are found at 695, 650, 595, and 520 nm for the tetrapod sample (Figure 1a) and at 695, 655, 615, 555, and 490 nm for the dot sample (Figure 1b). These spectral positions are also visualized by plotting the second derivative of the absorption spectrum for both samples. This shows that even though the lowest excitonic peak of both samples is identical, the complete excitonic structure differs explicitly due to the shape of the nanoparticles.

To learn about the ultrafast electron–hole dynamics in CdTe tetrapods after optical excitation, spectrally resolved pump–probe spectroscopy in the visible spectral range is performed. The pump pulse optically excites electrons and holes in the nanocrystal and therefore alters the occupation of the energy states. This leads to a change in the optical absorption of the sample, which is monitored by the probe pulse. The dynamics due to the relaxation of electrons and holes is visualized by taking the optical absorption spectrum of the sample for several delay times between pump and probe pulse. The measurements were performed for parallel and perpendicular orientation of the polarization between pump and probe beam. The spectra of pump (solid line) and probe (dotted line) pulses are plotted for comparison in Figure 1c. The pump pulse at 480 nm excites the tetrapod sample in a high-energy excitonic state, and the probe pulse covers the spectral range where bleach, induced absorption, and stimulated emission signals are expected.

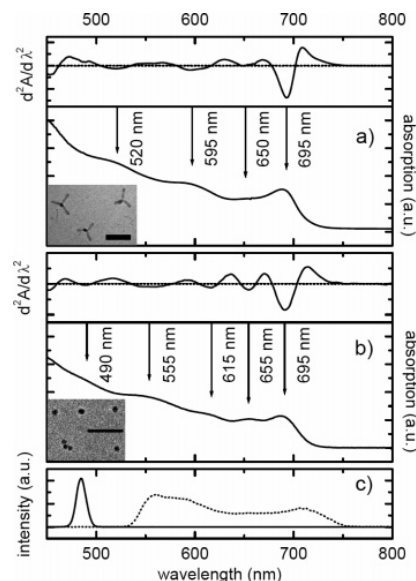


**Figure 1.** (a) Steady-state absorption spectrum of tetrapod-shaped CdTe nanocrystals. Also plotted is the second derivative of the spectrum for better visualization of the broad absorption maxima at 520, 595, 650, and 695 nm (TEM picture of the sample is shown as inset, length of the bar: 50 nm). (b) Steady-state absorption of spherical CdTe nanocrystals. Absorption maxima are observed at 490, 555, 615, 655, and 695 nm (TEM picture of the sample is shown as inset, length of the bar: 50 nm). (c) Spectrum of the pump (solid line) and probe pulses (dotted line) used for the femtosecond time-resolved transient absorption experiment.

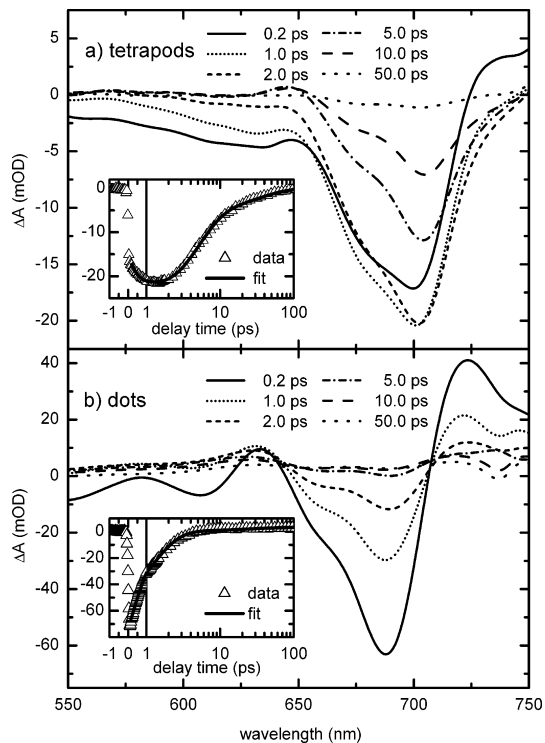


**Figure 2.** Transient absorption spectra for colloidal CdTe nanocrystals in chloroform at different delay times (0.2, 1.0, 2.0, 5.0, 10.0, and 50.0 ps) under magic angle conditions. The transient absorption signal for the lowest excitonic state (triangles) and a theoretical fit (line) is shown as inset. (a) Tetrapod-shaped nanocrystals, the transient absorption signal shown as inset, were recorded at 700 nm. (b) Spherical nanocrystals (dots), the transient absorption signal shown as inset, were recorded at 680 nm.

In Figure 2a, chirp-corrected time slices of the TA spectrum under magic angle conditions are shown for delay times at 0.2, 1.0, 2.0, 5.0, 10, and 50 ps. The time slice at 0.2 ps represents the instantaneous TA signal. It consists of a bleach over the whole measured absorption range and a small induced absorption signal centered at about 740 nm. After about 2.0 ps the induced absorption signal at 740 nm and the bleach signal in the wavelength range between 530 and 570 nm has vanished completely, whereas the bleach between 570 and 650 nm remains nearly unchanged and the strong bleach signal at 700 nm is increased to its maximum value. After about 5.0–10 ps the bleach signal between 570 and 650 nm is recovered completely and the bleach signal at 700 nm is strongly reduced. The remaining bleach signal at 700 nm decays with a time constant of several tens of picoseconds.

For comparison of the ultrafast dynamics observed for different nanocrystal shapes the transient absorption of spherical CdTe nanocrystals is shown in Figure 2b. We present chirp-corrected time slices for several delay times. Similar to the tetrapod sample we observe a strong bleach in the spectral range of the steady-state absorption spectrum and induced absorption at about 740 nm. The dominant transient absorption signal at 680 nm shows an initial rise with a time constant of about 300 fs and decays biexponentially with a dominant decay time of 1.0 ps (see inset in Figure 2b) and 25 ps. The differences in the ultrafast dynamics observed for spherical and tetrapod-shaped nanocrystals will be discussed below.

To obtain time constants for the observed electron–hole dynamics of the tetrapod sample the time-resolved absorption

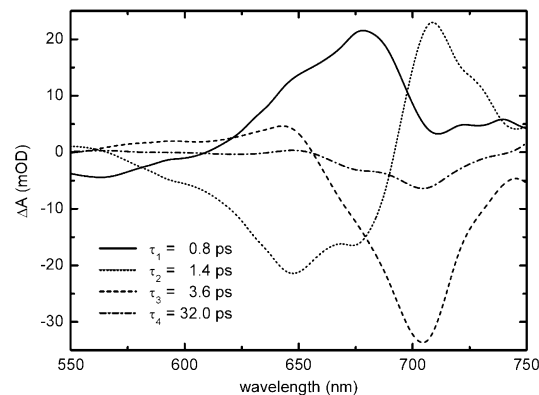


**Figure 3.** Decay-associated spectra for the transient absorption data of the tetrapod sample (shown in Figure 2a). An exponential model with four time constants 0.8, 1.4, 3.6, and 32 ps was used to yield a satisfactory fit of the data.

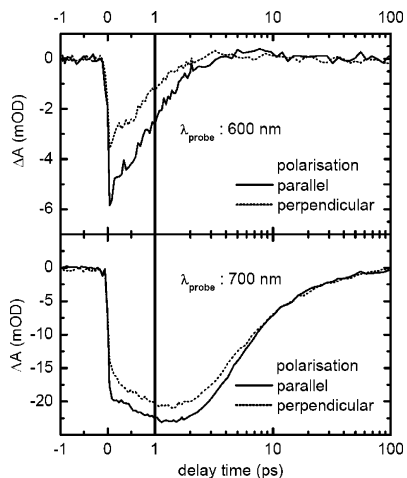
data are fitted by a multiexponential model using a simultaneous fitting procedure for all probe wavelengths. Four time constants of 0.8, 1.4, 3.6, and 32 ps can be extracted to yield a satisfactory fit for the experimental data (as an example, see Figure 2a, inset). The amplitudes connected to a distinct time constant are determined by the fitting routine for all probe wavelengths, and this yields the so-called decay-associated spectrum (DAS). The superposition of the four DAS reproduces the original time-resolved data. Decay-associated spectra for these time constants are shown in Figure 3. The DAS for the 0.8-ps time constant shows a negative amplitude between 530 and 600 nm indicating the decay of a bleach signal in this spectral range. The positive amplitude between 600 and 700 nm is associated with the rise of a bleach signal in this spectral range, and the positive amplitude between 700 and 750 nm reflects the fast decay of the instantaneous induced absorption signal. The DAS for the 1.4-ps time constant consists of a bleach decay at 640 nm (negative amplitude) and the rise of a bleach signal at 700 nm (positive amplitude). The DAS for the time constants of 3.6 and 32 ps both show the decay of the dominant bleach signal at 700 nm.

The TA was recorded for parallel and perpendicular orientation of the polarization between pump and probe pulse. In Figure 4 the polarization-dependent TA signal is shown for probe wavelengths of 600 and 700 nm as an example. Polarization anisotropy is observed immediately after photoexcitation and vanishes after about 6 ps. The evaluation of the complete data sets (analogue to Figure 2 and Figure 3) using a multiexponential model shows that the DAS for the 0.8-, 1.4-, and 3.6-ps time constants exhibit a polarization anisotropy, but the 32-ps component is completely isotropic. (See Figure 5.)

## Discussion

Transient absorption (TA) spectroscopy is a powerful tool for the investigation of ultrafast charge-carrier relaxation processes in colloidal nanocrystal solutions. The main features observed in TA spectra of semiconductor nanocrystals are due to state-filling and the carrier-induced Stark effect.<sup>2,5</sup> The strength of the TA signal due to the state-filling mechanism is proportional to the occupation of the electron and hole states  $n_e$  and  $n_h$ , involved in the probed excitonic transitions. In this case the induced TA signal is observed as a bleaching of these transitions. The Stark effect leads to an energetic shift of excitonic transitions and can also modify the selection rules. Therefore, this effect can lead to bleaching and induced absorption.

## Electron–Hole Dynamics in CdTe Tetrapods

*J. Phys. Chem. B*, Vol. 110, No. 35, 2006 17337

**Figure 4.** Polarization-dependent transient absorption data recorded at probe wavelength of 600 and 700 nm. Anisotropy between parallel (solid lines) and perpendicular (dotted lines) orientation of pump and probe pulse is observed for several picoseconds. After about 6 ps the behavior is isotropic.

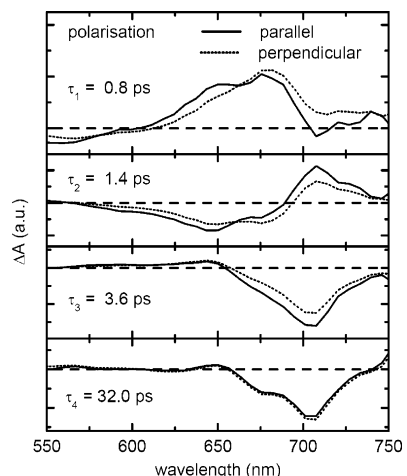


**Figure 5.** Decay-associated spectra (DAS) for the transient absorption experiment as a function of the polarization. The data sets for parallel (solid lines) and perpendicular (dotted lines) polarization between pump and probe pulse are fitted with identical time constants 0.8, 1.4, 3.6, and 32 ps. Anisotropy is found for the DAS of the time constants 0.8, 1.4, and 3.6 ps. The DAS for the time constant 32 ps are identical for parallel and perpendicular polarization.

The presented TA data of CdTe tetrapods show that the relaxation of the photoexcited holes and electrons to the lowest excitonic state occurs on a picosecond time scale. The bleach signal probed at high energetic excitonic transitions and the induced absorption at 740 nm decay with time constants of 0.8, 1.4, and 3.6 ps, and only a bleach signal at the excitonic transition at 700 nm persists for longer delay times. This signal probed at the lowest energetic exciton transition decays with a time constant of 32 ps. The three fast time constants 0.8, 1.4, and 3.6 ps are related to decay-associated spectra (see Figure 3) which describe the decay of bleach signals with the central wavelength of 570, 650, and 700 nm. That means that the bleach signals at longer wavelength decay with longer decay times. This behavior is due to the fast relaxation of excited electrons and holes to energetic states near the band gap. The bleach spectrum is red-shifted, mostly due to the relaxation of the electrons, which dominate the bleach signal.

The TA data of spherical CdTe nanocrystals show qualitatively a behavior very similar to that of the tetrapod sample. The bleach and induced absorption signals decay on a picosecond time scale with time constants of 0.3, 1.0, and 25 ps. The ultrafast bleach decay with the dominant time constant of 1.0 ps is in accordance with the literature.<sup>40</sup> The spherical dotlike sample is confined in three dimensions, and therefore the resulting energy level structure is discrete. In contrast to the tetrapod sample, the charge-carrier relaxation for spherical nanocrystals described by the obtained time constants is faster. The confinement for the tetrapod sample is very similar to that for nanorods, where along the axis of the arms a one-dimensional degree of freedom will induce additional energy levels in the conduction or valence bands. If a charge-carrier relaxation mechanism via LO phonons is assumed as the dominant process as in bulk semiconductor, one would expect a faster cooling rate for the less-confined tetrapod nanocrystal. This effect known as “phonon bottleneck” was investigated intensively for spherical nanocrystals.<sup>2</sup> According to our results, it can be concluded that emission of LO phonons is not the dominant process responsible for the ultrafast charge-carrier relaxation in tetrapod-shaped nanocrystals. This observation was also made for other nanocrystal systems as spherical nanocrystals of different size<sup>2</sup> and nanorods.<sup>31</sup>

From nanocrystal samples of various size and shape it is known from literature that the ultrafast electron–hole dynamics due to intraband transitions typically occurs on a subpicosecond to picosecond time scale.<sup>2,30</sup> The relaxation of electrons and holes at the band gap is mostly dominated by surface or interface states. Therefore, it might be possible to draw a similar picture of the charge-carrier relaxation also for the investigated tetrapod sample. Nevertheless, one has to keep in mind that the CdTe tetrapod-shaped nanocrystal consists of four rodlike arms connected to a tetrahedron-shaped nanocrystal core. The exact structure of the tetrapods core is currently under investigation. One common model<sup>21</sup> of the tetrapod takes into account the polytypism of CdTe (zinc blende and wurtzite phase), and the other model<sup>36</sup> describes the core as a set of eight wurtzite nuclei that are joined by twin interfaces. Branches of the tetrapod grow only out of four of these nuclei. In both cases, the interfaces between the building blocks, that is, the boundaries between the zinc blende core and the wurtzite branches or the twin boundaries, and charge-carrier localization have to be considered by analyzing the electron–hole dynamics. The additional defect sites induced by the formation of the complex tetrapod nanostructure could be the reason for the slower charge-carrier relaxation compared to that of spherical nanocrystals.

From polarization-dependent emission studies on single nanocrystals at room temperature it is known that the emission of spherical nanodots is isotropic whereas nanorods exhibit a polarized emission with a polarization ratio of up to 86%.<sup>41</sup> This strong polarization anisotropy is observed even for nanorods with low aspect ratios as 1:1.25. Similar results on the polarization dependence are obtained also by ultrafast pump probe methods.<sup>42</sup> These studies show that polarization anisotropy on semiconductor nanocrystals is strongly related to the symmetry of the investigated system. The tetrapod nanostructure can be described by a symmetric combination of four nanorods that are connected to a central tetrahedron-shaped nanodot. Therefore polarization-dependent measurements can give direct information if the probed excited level is distributed symmetrically over the nanostructure or if it is localized at one of the four asymmetric rodlike arms. For excited states that are symmetrically distributed no anisotropy signal is expected, and

for excited-states localized at one of the four pods a polarization anisotropy should be observed.

For the investigated tetrapod samples polarization anisotropy of the TA signal is measured for the decay components at 0.8, 1.4, and 3.6 ps. This anisotropy has to be correlated to the symmetry of the probed electronic states. Therefore, a large fraction of the excited states probed at the high energetic excitonic transitions between 530 and 700 nm are attributed to states localized at the pods. For the slow decay component at 32 ps a zero anisotropy was found in the experiment. From these data it can be concluded that several picoseconds after photoexcitation the probed excitonic transition is due to a relaxed isotropic state.

Another possible depolarization mechanism for tetrapod nanocrystals in solution is due to their rotational movement. The rotational correlation time  $\Phi$  for this process can be estimated by the Stokes–Einstein equation  $\Phi = (V\eta)/(kT)$ , where  $V$  is the particle volume (four arms of radius 2 nm and arm length of 20 nm),  $\eta$  is the viscosity of the solvent (chloroform at 293 K: 0.58 mPa s), and  $T$  is the temperature (293 K). For the tetrapod nanocrystal this yields a correlation time  $\Phi$  of 140 ns. Due to its nonspherical shape the tetrapod nanocrystal is expected to rotate even more slowly. Therefore, the observed ultrafast depolarization after several picoseconds has to be attributed to inner-particle relaxation mechanisms.

Theoretical calculations for the wave functions of the electron and hole in tetrapod nanocrystals show that the electron state of lowest energy is localized at the center of the nanocrystal, where the four arms are connected to each other.<sup>43,44</sup> This result is also supported experimentally as the optical absorption shows no dependence on the arm length of various tetrapod samples.<sup>21</sup> Therefore, this state is highly symmetric and should not lead to an anisotropy signal. The higher energetic electron and hole states are described by wave functions that are localized at the arms of the nanocrystal. This means that the behavior is similar to that of nanorods, and a high anisotropy is expected in this case. This theoretical finding fits very well to the observed ultrafast polarization anisotropy in tetrapod nanocrystals. For excited electron–hole pairs polarization anisotropy is found, whereas the lowest excitonic state is found to be completely symmetric. Therefore, the localization process of electron and hole into the center of the tetrapod nanocrystal has to be taken into account by the intraband electron–hole relaxation process.

We have performed transient absorption experiments with femtosecond time-resolution on branched CdTe nanocrystals in solution. Ultrafast electron–hole dynamics is observed that reflects the relaxation of excited electrons and holes to the lowest energetic excitonic state. The relaxation occurs in the temporal range of several picoseconds. Polarization-dependent experiments reveal an ultrafast decay of the anisotropy signal in about 6 ps. The transient absorption signal of the lowest energetic exciton that decays with a time constant of 32 ps is completely isotropic in polarization. This is explained by the localization of the lowest energetic exciton in the center of the nanocrystal.

**Acknowledgment.** The authors thank W. Zinth and R. Cingolani for fruitful discussion and support. This project was funded by the Deutsche Forschungsgemeinschaft (Emmy-Noether/Parak). S.M. and S.K. contributed equally to this study.

## References and Notes

- (1) Alivisatos, A. P. *J. Phys. Chem.* **1996**, *100*, 13226.
- (2) Klimov, V. I. *J. Phys. Chem. B* **2000**, *104*, 6112.
- (3) Klimov, V. I.; McBranch, D. W.; Leatherdale, C. A.; Bawendi, M. G. *Phys. Rev. B* **1999**, *60*, 13740.
- (4) Guyot-Sionnest, P.; Hines, M. A. *Appl. Phys. Lett.* **1998**, *72*, 686.
- (5) Woggon, U.; Giessen, H.; Gindele, F.; Wind, O.; Fluegel, B.; Peyghambarian, N. *Phys. Rev. B* **1996**, *54*, 17681.
- (6) Murray, C. B.; Norris, D. J.; Bawendi, M. G. *J. Am. Chem. Soc.* **1993**, *115*, 8706.
- (7) Norris, D. J.; Bawendi, M. G. *Phys. Rev. B* **1996**, *53*, 16338.
- (8) Landes, C. F.; Braun, M.; El-Sayed, M. A. *J. Phys. Chem. B* **2001**, *105*, 10554.
- (9) Landes, C.; Burda, C.; Braun, M.; El-Sayed, M. A. *J. Phys. Chem. B* **2001**, *105*, 2981.
- (10) Burda, C.; Link, S.; Mohamed, M.; El-Sayed, M. A. *J. Phys. Chem. B* **2001**, *105*, 12286.
- (11) Parak, W. J.; Gerion, D.; Pellegrino, T.; Zanchet, D.; Micheel, C.; Williams, S. C.; Boudreau, R.; Le Gros, M. A.; Larabell, C. A.; Alivisatos, A. P. *Nanotechnology* **2003**, *14*, R15.
- (12) Huynh, W. U.; Dittmer, J. J.; Alivisatos, A. P. *Science* **2002**, *295*, 2425.
- (13) Gerion, D.; Pinaud, F.; Williams, S. C.; Parak, W. J.; Zanchet, D.; Weiss, S.; Alivisatos, A. P. *J. Phys. Chem. B* **2001**, *105*, 8861.
- (14) Colvin, V. L.; Schlamp, M. C.; Alivisatos, A. P. *Nature* **1994**, *370*, 354.
- (15) Mattossi, H.; Mauro, J. M.; Goldman, E. R.; Anderson, G. P.; Sundar, V. C.; Mikulec, F. V.; Bawendi, M. G. *J. Am. Chem. Soc.* **2000**, *122*, 12142.
- (16) Parak, W. J.; Pellegrino, T.; Plank, C. *Nanotechnology* **2005**, *16*, R9.
- (17) Talapin, D. V.; Rogach, A. L.; Kornowski, A.; Haase, M.; Weller, H. *Nano Lett.* **2001**, *1*, 207.
- (18) Hines, M. A.; Guyot-Sionnest, P. *J. Phys. Chem.* **1996**, *100*, 468.
- (19) Chen, C. C.; Chao, C. Y.; Lang, Z. H. *Chem. Mater.* **2000**, *12*, 1516.
- (20) Bunge, S. D.; Krueger, K. M.; Boyle, T. J.; Rodriguez, M. A.; Headley, T. J.; Colvin, V. L. *J. Mater. Chem.* **2003**, *13*, 1705.
- (21) Manna, L.; Milliron, D. J.; Meisel, A.; Scher, E. C.; Alivisatos, A. P. *Nat. Mater.* **2003**, *2*, 382.
- (22) Manna, L.; Scher, E. C.; Alivisatos, A. P. *J. Am. Chem. Soc.* **2000**, *122*, 12700.
- (23) Shieh, F.; Saunders, A. E.; Korgel, B. A. *J. Phys. Chem. B* **2005**, *109*, 8538.
- (24) Peng, X. G.; Manna, L.; Yang, W. D.; Wickham, J.; Scher, E.; Kadavich, A.; Alivisatos, A. P. *Nature* **2000**, *404*, 59.
- (25) Kudera, S.; Carbone, L.; Casula, M. F.; Cingolani, R.; Falqui, A.; Snoeck, E.; Parak, W. J.; Manna, L. *Nano Lett.* **2005**, *5*, 445.
- (26) Baum, P.; Lochbrunner, S.; Riedle, E. *Appl. Phys. B* **2004**, *79*, 1027–1032.
- (27) Wilhelm, T.; Piel, J.; Riedle, E. *Opt. Lett.* **1997**, *22*, 1494.
- (28) Riedle, E.; Beutter, M.; Lochbrunner, S.; Piel, J.; Schenkl, S.; Sporlein, S.; Zinth, W. *Appl. Phys. B* **2000**, *71*, 457.
- (29) Landes, C. F.; Link, S.; Mohamed, M. B.; Nikoobakht, B.; El-Sayed, M. A. *Pure Appl. Chem.* **2002**, *74*, 1675.
- (30) Mohamed, M. B.; Burda, C.; El-Sayed, M. A. *Nano Lett.* **2001**, *1*, 589.
- (31) Yu, P. R.; Nedeljkovic, J. M.; Ahrenkiel, P. A.; Ellingson, R. J.; Nozik, A. J. *Nano Lett.* **2004**, *4*, 1089.
- (32) Link, S.; El-Sayed, M. A. *J. Appl. Phys.* **2002**, *92*, 6799.
- (33) Hu, M.; Wang, X.; Hartland, G. V.; Mulvaney, P.; Juste, J. P.; Sader, J. E. *J. Am. Chem. Soc.* **2003**, *125*, 14925.
- (34) De Giorgi, M.; Tari, D.; Manna, L.; Krahne, R.; Cingolani, R. *Microelectron. J.* **2005**, *36*, 552.
- (35) Peng, P.; Milliron, D. J.; Hughes, S. M.; Johnson, J. C.; Alivisatos, A. P.; Saykally, R. J. *Nano Lett.* **2005**, *5*, 1809.
- (36) Carbone, L.; Kudera, S.; Carlino, E.; Parak, W. J.; Giannini, C.; Cingolani, R.; Manna, L. *J. Am. Chem. Soc.* **2006**, *128*, 748.
- (37) Peng, Z. A.; Peng, X. G. *J. Am. Chem. Soc.* **2001**, *123*, 183.
- (38) Yu, W. W.; Qu, L. H.; Guo, W. Z.; Peng, X. G. *Chem. Mater.* **2003**, *15*, 2854.
- (39) Baigar, E.; Braun, M.; Peine, A.; Konjaev, V.; Zinth, W. “Convenient tunability of sub-10 fs-pulses in the visible range”; *Ultrafast Phenomena*, 2002, Vancouver.
- (40) Barbosa, L. C.; Reynoso, V. C. S.; dePaula, A. M.; deOliveira, C. R. M.; Alves, O. L.; Craievich, A. F.; Marotti, R. E.; Cruz, C. H. B.; Cesar, C. L. *J. Non-Cryst. Solids* **1997**, *219*, 205.
- (41) Hu, J. T.; Li, L. S.; Yang, W. D.; Manna, L.; Wang, L. W.; Alivisatos, A. P. *Science* **2001**, *292*, 2060.
- (42) Ispasoiu, R. G.; Lee, J.; Papadimitrakopoulos, F.; Goodson, T. *Chem. Phys. Lett.* **2001**, *340*, 7.
- (43) Li, J. B.; Wang, L. W. *Nano Lett.* **2003**, *3*, 1357.
- (44) Tari, D.; De Giorgi, M.; Della Sala, F.; Carbone, L.; Krahne, R.; Manna, L.; Cingolani, R.; Kudera, S.; Parak, W. J. *Appl. Phys. Lett.* **2005**, *87*, 224101.

Malkmus et al.

## **B.5 Confinement Effects on Optical Phonons in Polar Tetrapod Nanocrystals Detected by Resonant Inelastic Light Scattering**

R. KRAHNE, G. CHILLA, G., C. SCHÜLLER, L. CARBONE, S. KUDERA, G. MAN-  
NARINI, L. MANNA, D. HEITMANN, R. CINGOLANI  
*Nano Letters* **6**(3), pp. 478–482, 2006

We investigated CdTe nanocrystal tetrapods of different sizes by resonant inelastic light scattering at room temperature and under cryogenic conditions. We observe a strongly resonant behavior of the phonon scattering with the excitonic structure of the tetrapods. Under resonant conditions we detect a set of phonon modes that can be understood as confined longitudinal-optical phonons, surface-optical phonons, and transverse-optical phonons in a nanowire picture.

NANO  
LETTERS2006  
Vol. 6, No. 3  
478–482

# Confinement Effects on Optical Phonons in Polar Tetrapod Nanocrystals Detected by Resonant Inelastic Light Scattering

Roman Krahne,<sup>\*,†</sup> Gerwin Chilla,<sup>‡</sup> Christian Schüller,<sup>‡,§</sup> Luigi Carbone,<sup>†</sup> Stefan Kudera,<sup>†</sup> Gianandrea Mannarini,<sup>†</sup> Liberato Manna,<sup>†</sup> Detlef Heitmann,<sup>‡</sup> and Roberto Cingolani<sup>†</sup>

*National Nanotechnology Laboratory of CNR-INFM c/o Istituto Superiore Universitario di Formazione Interdisciplinare, Università di Lecce, Via per Arnesano, 73100 Lecce, Italy, and Institute of Applied Physics, University of Hamburg, 20355 Hamburg, Germany*

Received December 12, 2005; Revised Manuscript Received January 13, 2006

## ABSTRACT

We investigated CdTe nanocrystal tetrapods of different sizes by resonant inelastic light scattering at room temperature and under cryogenic conditions. We observe a strongly resonant behavior of the phonon scattering with the excitonic structure of the tetrapods. Under resonant conditions we detect a set of phonon modes that can be understood as confined longitudinal-optical phonons, surface-optical phonons, and transverse-optical phonons in a nanowire picture.

Recently, chemical synthesis has made remarkable advances in controlling the shape of colloidal nanocrystals leading to spheres,<sup>1,2</sup> rods,<sup>3–5</sup> and branched nanostructures.<sup>6,7</sup> The tetrapod (TP) represents an intriguing nanostructure where four nanorods branch out at tetrahedral angles from a central region.<sup>6</sup> The specific geometry of the tetrapods has already demonstrated new properties in charge transport<sup>8</sup> and photoluminescence.<sup>9</sup>

Optical phonons in confined nanostructures have been studied experimentally and theoretically in a variety of semiconductor nanocrystals such as spheres<sup>10,11</sup> and rods.<sup>12–16</sup> In nanocrystal dots the general picture is that the phonons couple to the optical excitations via the Förmlich interaction.<sup>11,17–20</sup> In spherical nanocrystals the confinement leads to a red shift and broadening of the LO phonon mode<sup>21</sup> and to the observation of surface optical (SO) phonons.<sup>10,22</sup> Nanorods instead can be regarded as nanowaveguides and are an especially interesting system for the study of phonons because of their uniaxial anisotropy both in shape and in crystal lattice.<sup>5</sup> An experimental and theoretical study of SO

phonons in nanorods has shown that the SO phonon excitation depends on the nanowire shape,<sup>16,23</sup> and Raman scattering experiments on nanorods have shown splittings of the phonon modes that originate from the lateral confinement.<sup>12–15</sup> In this Letter we report the observation of confined phonons by resonant Raman scattering in tetrapod-shaped nanocrystals. We employ a nanowire picture to interpret the TP data (since TPs consist of joined nanorods) and find good agreement with the predicted splittings of the LO and TO phonons, as well as for the energy of the SO phonon.

CdTe TPs of different sizes were fabricated by chemical synthesis as reported in refs 6 and 24 and dissolved in a solvent, typically chloroform. Figure 1 shows transmission electron microscope (TEM) images of two TP samples: (a) T1 with large and (b) T2 with small arm diameter and length. We investigated a series of tetrapod samples with arm diameter and length ranging from 5 to 12 nm and 18–80 nm, respectively. The solution containing the nanocrystals was drop-casted onto the surface of a silicon substrate, and the solvent was allowed to evaporate under soft nitrogen flow. The samples were then mounted in an optical cryostat, and the Raman experiments were performed using a tunable Ti:sapphire laser (700–850 nm). The excitation light (laser power 30 mW) was focused onto the samples on a spot of 50  $\mu\text{m}$  diameter, and the signal was collected by an

\* Corresponding author: roman.krahne@unile.it; tel, +39 0832 298 209; fax, +39 0832 298 238

† National Nanotechnology Laboratory of CNR-INFM c/o Istituto Superiore Universitario di Formazione Interdisciplinare, Università di Lecce.

‡ Institute of Applied Physics, University of Hamburg.

§ Present address: Institute of Experimental and Applied Physics, University of Regensburg, 93040 Regensburg, Germany.

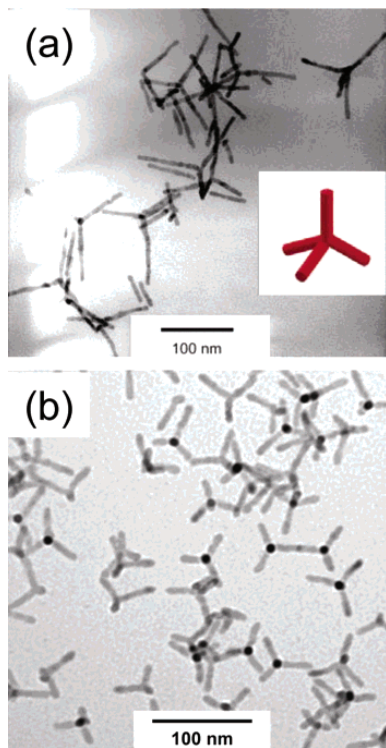


**Figure 1.** TEM images of CdTe tetrapods with different size: (a) large TPs with 12 nm/80 nm arm diameter and length; (b) small TPs with 7 nm/30 nm arm diameter and length. The inset shows a schematic drawing of a tetrapod.

achromatic lens and detected by a triple Raman spectrometer (DILOR XY) and a CCD camera.

Figure 2a shows resonant Raman spectra of large tetrapods (arm diameter = 12 nm and length = 80 nm, see Figure 1a) at room temperature. The laser excitation energy was varied from 1.678 to 1.755 eV, and the spectra were normalized with respect to the amplitude of the Si substrate phonon. The resonant behavior of the LO phonon, and of its second-order scattering mode, 2LO, is clearly observed, and the extracted amplitudes of the excitations are reported in Figure 2c. A spectrum at maximum resonance is shown in Figure 2b, and the positions of the observed peaks are evaluated by Lorentz fits. We find the TP LO phonon at 168.6 cm<sup>-1</sup> and its second-order scattering at 335.5 cm<sup>-1</sup>. Another weak excitation can be identified at 307 cm<sup>-1</sup>, which most likely results from higher order scattering. Interestingly, the energy of this mode matches almost exactly the sum of the measured LO phonon and the bulk value of the TO phonon<sup>25</sup> (168 cm<sup>-1</sup> + 140 cm<sup>-1</sup> = 308 cm<sup>-1</sup>).

We now focus on the resonant behavior of the phonon excitations and plot the amplitude of the phonons with respect to the laser excitation energy in Figure 2c. For comparison, we show also the emission and absorption of this sample (taken from ref 9). We find the resonance maximum of the LO phonon at 1.715 eV, slightly blue shifted with respect

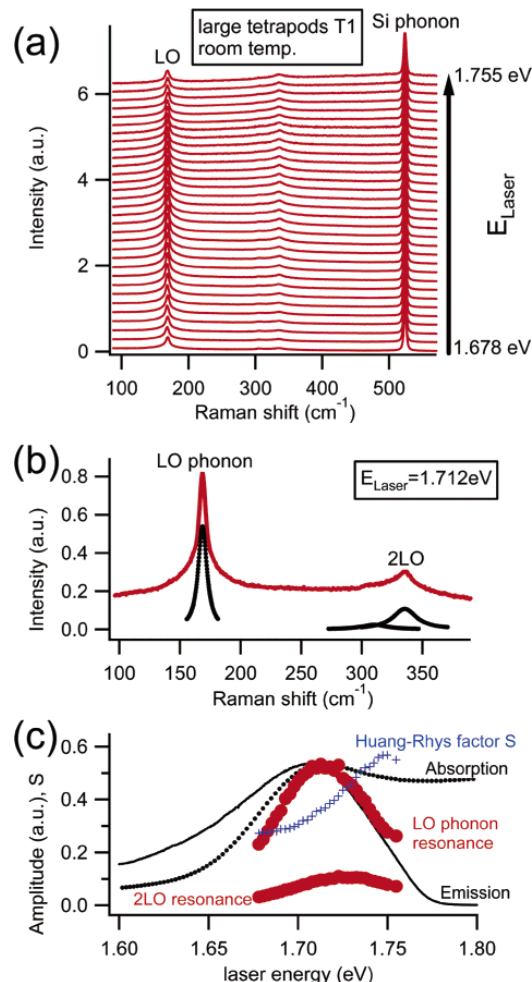


**Figure 2.** Resonant Raman spectra of the large CdTe TPs at room temperature. (a) The TP LO phonon is observed at 168.6 cm<sup>-1</sup> and its second-order scattering at 335.5 cm<sup>-1</sup>. The resonance of the LO phonon with respect to the laser excitation energy is clearly visible. The spectra are normalized with respect to the Si phonon intensity and have been shifted vertically for clarity. (b) Raman spectrum from (a) at resonance maximum. Lorentz fits (black dotted lines) yield as peak positions for LO 168.6 cm<sup>-1</sup>, for 2LO 335.5 cm<sup>-1</sup>, and a third small peak can be identified at 307 cm<sup>-1</sup>. (c) TP LO and 2LO phonon intensity (red thick dots) plotted versus laser energy. The room-temperature absorption and emission spectra are shown in black dotted and continuous lines, respectively. Blue markers show the experimental Huang–Rhys factor derived from the ratio of the first- and second-order scattering of the LO phonon mode.

to the energy of the first absorption peak. This is consistent with the expectation of a strong resonance maximum at one phonon energy above the exciton energy for the so-called outgoing resonance. The outgoing resonance, which should occur at exactly the exciton ground-state energy plus one phonon energy, has been shown for bulk samples to be much stronger than the incoming resonance.<sup>26–28</sup> We think that due to broadening the incoming and outgoing resonance maxima,

which should differ by one LO phonon energy, are not individually resolved in Figure 2c. Due to a much stronger outgoing resonance, however, the maximum of the observed phonon resonance is slightly shifted to higher energies as compared to the absorption maximum (in small TPs this shift is more evident, see Figure S 1b in Supporting Information).

We note that a double-peak structure is observed in the emission of tetrapods, which becomes more evident in smaller tetrapods, and at low temperatures (see Figure S 2b in Supporting Information). Theory showed that the high-energy peak in emission can be correlated to transitions from first excited states of electrons and holes that are mainly localized in the tetrapod arms, whereas the low-energy peak originates from exciton ground state transitions where the electrons are localized mainly in the tetrapod core.<sup>9</sup> The onset of the LO phonon resonance at low temperatures and in small TPs (see Figures S 1 and S 2 in Supporting Information) occurs clearly at higher energies than the exciton ground-state emission, and therefore we conclude that the phonon resonance can be correlated to transitions from excited states that are localized in the TP arms. By comparing the resonance maxima of the first- and of the second-order scattering (at 1.715 and 1.730 eV, respectively) we find that the 2LO phonon resonance maximum occurs at a higher laser excitation energy of approximately 15 meV (almost the phonon energy), which further supports the above conclusion that the observed resonances are outgoing resonances.

The Huang–Rhys factor  $S$ , which is identified with the exciton–phonon coupling in the Franck–Condon model, can be used as a fitting parameter for the relative intensities of different scattering orders. From the data reported in Figure 2 we can calculate  $S$  from the first- and the second-order scattering amplitudes and we plot its dependence on the exciting laser energy, i.e., on the resonance conditions, shown by the blue markers in Figure 2c. We find a significant dependence of  $S$  on the exciting laser energy that results from different maxima positions of the scattering orders discussed above. The absolute values of the Huang–Rhys factor in Figure 2c are of the same order as those reported by Krauss et al.,<sup>29</sup> although they are much larger than those calculated for spherical CdSe nanocrystals.<sup>30</sup> The general understanding is that the Franck–Condon model does not adequately describe the exciton–phonon coupling and that additional, nonadiabatic effects have to be taken into account. In particular, multiphonon scattering has been discussed experimentally and theoretically for spherical nanocrystals by Cardona and co-workers<sup>31</sup> and by Pokatilov et al.<sup>32</sup> Their calculations show that the discrepancy between experiment and theory can be removed, if band mixing of the exciton states is taken into account and if additional scattering channels are allowed for the higher order processes. The relative intensities of the different scattering orders in our experiments are very similar to the “strong confinement” condition of Pokatilov et al.<sup>32</sup> which implies also strong band mixing.

To resolve the phonon excitations in more detail, we performed resonant Raman scattering at low temperatures.

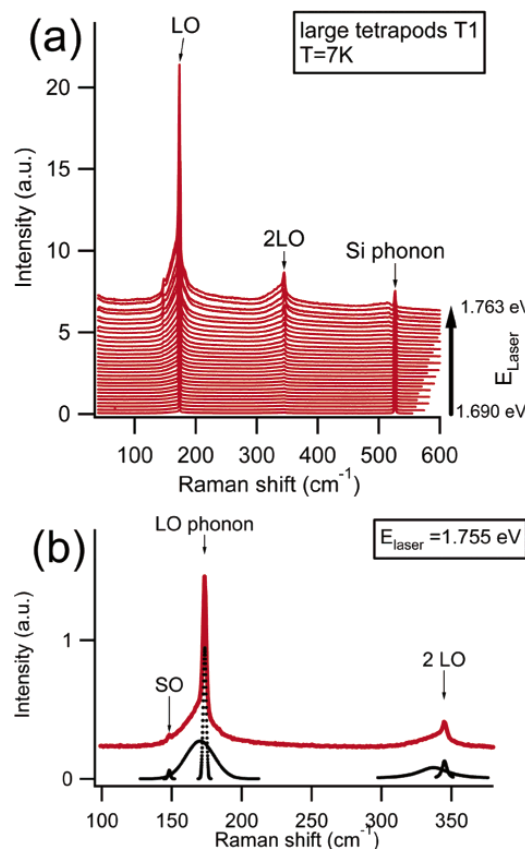


**Figure 3.** (a) Resonant Raman spectra of large CdTe tetrapods at  $T = 7$  K. (b) A spectrum in resonant condition (red line) and Lorentz fits to the data (black dotted lines). We observe a mode at  $148\text{ cm}^{-1}$  (fwhm =  $1.2\text{ cm}^{-1}$ ), a mode at  $173.5\text{ cm}^{-1}$  (fwhm =  $1.5\text{ cm}^{-1}$ ), and a broad underlying signal that was fitted with a peak at  $170\text{ cm}^{-1}$  (fwhm =  $14\text{ cm}^{-1}$ ). Experimental spectra have been shifted for clarity.

Figure 3a shows resonant Raman spectra of large tetrapods (sample T1) at a temperature of  $T = 7$  K. We observe a rich phonon excitation spectrum and find strong resonant enhancement by tuning the laser energy toward the exciton transitions of the tetrapods. We find a small peak at  $148\text{ cm}^{-1}$  that becomes clearly observable under strong resonant conditions. A sharp phonon mode is identified at  $173.5\text{ cm}^{-1}$  (not broadened significantly with respect to the CdTe bulk LO phonon, see Figure 4), and two higher order scattering orders of this mode are found at  $343$  and  $515\text{ cm}^{-1}$ . For further discussion of the first- and second-order scattering peaks, we plot a spectrum in strong resonance in Figure 3b. In addition to the above-mentioned peaks at  $148$ ,  $173.5$ , and  $343\text{ cm}^{-1}$ , Lorentz fits to the data evidence another broad excitation at  $170\text{ cm}^{-1}$  and its second-order scattering at  $337\text{ cm}^{-1}$ .

To understand the physical origin of the phonon modes, we regard the arms of the large tetrapods as nanowires with  $12\text{ nm}$  diameter and  $80\text{ nm}$  length. Focusing on the mode at

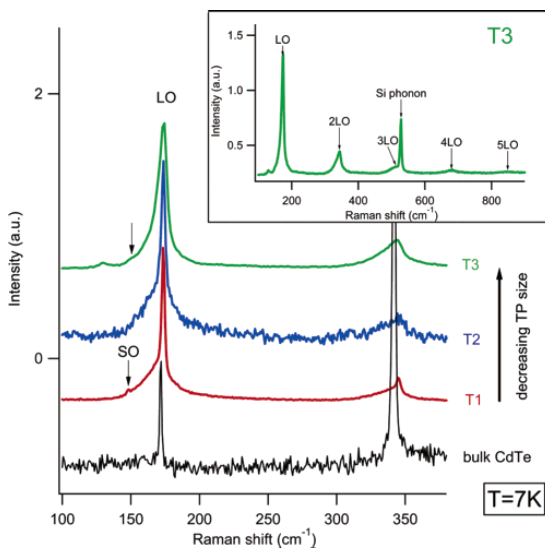


**Figure 4.** Raman spectra of large (T1, red), small (T2, blue), and very small (T3, green) tetrapods and of bulk CdTe (black) at  $T = 7\text{ K}$ . All TP spectra show the broad peak at the low energy shoulder of the  $\text{LO}_z$  phonon excitation. The SO phonon can be clearly identified in the large TPs T1, and can be identified as the small feature indicated by the arrow for T3. As a trend we observe that the intensity of second-order scattering increases with decreasing TP dimension. Spectra are normalized with respect to the LO phonon amplitude and have been shifted vertically for clarity. The inset shows a larger range of the T3 spectrum where up to five scattering orders are detected. The laser excitation energy for the bulk and samples T1, T2 is  $1.755\text{ eV}$  and for sample T3 is  $2.33\text{ eV}$ . The excitation at  $129\text{ cm}^{-1}$  of sample T3 is due to Te residues.<sup>34,35</sup>

$148\text{ cm}^{-1}$ , we follow the theory of Gupta and co-workers<sup>16</sup> for SO phonons in nanowires which yields

$$\omega_{\text{SO}}^2 = \omega_{\text{TO}}^2 + \frac{\varpi_p^2}{\epsilon_{\infty} + \epsilon_m f(x)}$$

$$x = qr$$

where  $\varpi_p^2 = \epsilon_{\infty}(\omega_{\text{LO}}^2 - \omega_{\text{TO}}^2)$  is the screened ion-plasma frequency,  $f(x) = (I_0(x)K_1(x)/I_1(x)K_0(x))$  (with  $I$  and  $K$  Bessel functions) and  $\epsilon_{\infty}$  and  $\epsilon_m$  are the bulk CdTe high-frequency and surrounding medium dielectric constants, respectively. For our tetrapod sample T1 we can take the length ( $l = 80\text{ nm}$ ) as the longitudinal symmetry breaking mechanism that leads to  $q = 2\pi/l$ ,  $r = 6\text{ nm}$  is the arm radius which yields  $x = 0.47$ . With  $\epsilon_m = 6.5$  (average silicon/vacuum) and  $\epsilon_{\infty} = 7$  and  $\epsilon_0 = 10$ , we obtain  $\omega_{\text{SO}} = 146\text{ cm}^{-1}$ , which is in good agreement with the peak at  $148\text{ cm}^{-1}$  in Figure 3b.

The effect of the nanowire shape on the LO and TO phonons in polar nanocrystals has been investigated by Mahan and co-workers.<sup>13</sup> They predicted a significant splitting of the Raman-active TO and LO phonons in large polar nanowires ( $5\text{ }\mu\text{m}$  maximum diameter) due to long-range dipolar interactions. The bulk TO and LO phonon frequencies are still observed as the  $z$ -mode of the phonons

and additional modes appear because of the lateral constriction of the wire geometry ( $z$ -direction is along and  $x$ -direction is perpendicular to the wire axis). In particular, the predicted values for CdTe wires are  $\text{TO}_z = \text{TO}_{\text{bulk}} = 140\text{ cm}^{-1}$ ,  $\text{TO}_x = 167.3\text{ cm}^{-1}$ ,  $\text{LO}_z = \text{LO}_{\text{bulk}} = 171\text{ cm}^{-1}$ , and  $\text{LO}_x = 172.4\text{ cm}^{-1}$ . The predicted splitting of the LO phonon is probably too small to be resolved experimentally, in particular if one of the modes is more intense in the spectrum than the other. In general, we would expect the  $z$ -modes to be more sharp due to their bulklike character and the  $x$ -confined modes to be broad since they should be sensitive to fluctuations in the nanocrystal size (in arm diameter). For example, the confined acoustic phonons in Si nanocrystal spheres reported in ref 33 show line width comparable to the broad mode at  $170\text{ cm}^{-1}$ . This makes us confident that the sharp phonon excitation at  $173.5\text{ cm}^{-1}$  can be attributed to the  $\text{LO}_z$  mode and that the broad excitation at  $170\text{ cm}^{-1}$  comes from the  $\text{TO}_x$  phonon mode. The fact that the excitations are observed at slightly higher energies than predicted can be explained by the finite  $z$ -confinement.

Figure 4 plots the low-temperature Raman spectra of large tetrapods (same as in Figure 3b), of two smaller TP samples T2 and T3 (arm diameter and length  $7\text{ nm}/30\text{ nm}$  and  $5\text{ nm}/18\text{ nm}$ , respectively), and of bulk CdTe. The LO phonon of bulk CdTe is detected at  $172\text{ cm}^{-1}$ , and we find the dominant mode in the TP spectra slightly blue-shifted and slightly broadened at  $173.5\text{ cm}^{-1}$ , and the broad mode at  $170\text{ cm}^{-1}$ . We remark that the fitting in this energy range with two peaks (at  $170$  and  $173.5\text{ cm}^{-1}$ ) can be applied to all our TP spectra at low temperature, independent of size and laser energy. In the experimental spectra, the SO phonon mode is clearly observed in the large TPs T1 and can be weakly noted in the spectrum of T3 (see the arrow). By calculating the SO phonon energy for the small TPs T2 and T3 in the same nanowire framework as for T1, with  $l = 30\text{ nm}$ ,  $r = 3.5\text{ nm}$  (for T2) and  $l = 18\text{ nm}$ ,  $r = 2.5\text{ nm}$  (for T3), we obtain  $\text{SO}(\text{T2}) = 148\text{ cm}^{-1}$  and  $\text{SO}(\text{T3}) = 149\text{ cm}^{-1}$ . We note that for sample T1 we observe the SO phonon only in strong resonant conditions (Figure 3a) and point out that for sample T3 the exciting laser energy of  $2.33\text{ eV}$  also meets good vibronic coupling conditions, indicated by the large number of higher order scattering modes (see inset in Figure 4). However, in sample T2 we do not observe an excitation near  $148\text{ cm}^{-1}$ , due to the nonresonant conditions. By analyzing the first and second-order scattering of TPs with different dimensions, we find that, as a trend, the Huang–Rhys factor  $S$  increases with decreasing TP size, namely,  $S(\text{T1}) = 0.17$ ,  $S(\text{T2}) = 0.18$ , and  $S(\text{T3}) = 0.23$  for the sharp LO phonon. We remark that this conclusion is weakened by the fact that we do not have similar resonance conditions for this comparison. However, we also observe first- and second-order scattering for the broad peaks with the same trend:  $S_{\text{broad}}(\text{T1}) = 0.45$ ,  $S_{\text{broad}}(\text{T2}) = 0.46$ , and  $S_{\text{broad}}(\text{T3}) = 0.62$ . This behavior is in agreement with a systematic study on CuCl nanocrystal spheres, where also the increase of the Huang–Rhys factor  $S$  with decreasing nanocrystal size was observed.<sup>36</sup>

In conclusion, we observe strongly resonant phonon excitations that can be assigned to confined optical phonon

modes in a nanowire picture. We map in detail the resonance behavior of the phonons with respect to the exciting laser energy and we find that LO and 2LO phonon excitations are resonant with different exciton levels.

**Acknowledgment.** The authors gratefully acknowledge the support by the SA-NANO European project (Contract No. STRP013698), by the MIUR-FIRB and MIUR 297 (Contract No. 13587) projects, and by the German Science Foundation through SFB 508.

**Supporting Information Available:** Resonant Raman spectra of tetrapods with small arms (sample T2) at room temperature and at  $T = 7$  K. This material is available free of charge via the Internet at <http://pubs.acs.org>.

## References

- (1) Alivisatos, A. P. *Science* **1996**, *271* (16 February), 933–937.
- (2) Alperson, B.; Rubinstein, I.; Hodes, G. *Phys. Rev. B: Condens. Matter Mater. Phys.* **2001**, *63*(8) (081303).
- (3) Kan, S.; Mokari, T.; Rothenberg, E.; Banin, U. *Nat. Mater.* **2003**, *2* (3), 155–158.
- (4) Hu, J. T.; Li, L. S.; Yang, W. D.; Manna, L.; Wang, L. W.; Alivisatos, A. P. *Science* **2001**, *292* (5524), 2060–2063.
- (5) Manna, L.; Scher, E. C.; Li, L. S.; Alivisatos, A. P. *J. Am. Chem. Soc.* **2002**, *124* (24), 7136–7145.
- (6) Manna, L.; Milliron, D. J.; Meisel, A.; Scher, E. C.; Alivisatos, A. P. *Nat. Mater.* **2003**, *2* (6), 382–385.
- (7) Dick, K. A.; Deppert, K.; Larsson, M. W.; Martensson, T.; Seifert, W.; Wallenberg, L. R.; Samuelson, L. *Nat. Mater.* **2004**, *3* (6), 380–384.
- (8) Cui, Y.; Banin, U.; Bjork, M. T.; Alivisatos, A. P. *Nano Lett.* **2005**, *5* (7), 1519–1523.
- (9) Tari, D.; De Giorgi, M.; Della Sala, F.; Carbone, L.; Krahne, R.; Manna, L.; Cingolani, R.; Kudera, S.; Parak, W. J. *Appl. Phys. Lett.* **2005**, *87*, 224101.
- (10) dePaula, A. M.; Barbosa, L. C.; Cruz, C. H. B.; Alves, O. L.; Sanjurjo, J. A.; Cesar, C. L. *Appl. Phys. Lett.* **1996**, *69* (3), 357–359.
- (11) Chamberlain, M. P.; Trallero-Giner, C.; Cardona, M. *Phys. Rev. B: Condens. Matter Mater. Phys.* **1995**, *51* (3), 1680–1693.
- (12) Thonhauser, T.; Mahan, G. D. *Phys. Rev. B: Condens. Matter Mater. Phys.* **2004**, *69* (7), Art. No. 075213.
- (13) Mahan, G. D.; Gupta, R.; Xiong, Q.; Adu, C. K.; Eklund, P. C. *Phys. Rev. B: Condens. Matter Mater. Phys.* **2003**, *68* (7), Art. No. 73402.
- (14) Thonhauser, T.; Mahan, G. D. *Phys. Rev. B: Condens. Matter Mater. Phys.* **2005**, *71* (8), Art. No. 081307.
- (15) Xiong, Q. H.; Gupta, R.; Adu, K. W.; Dickey, E. C.; Lian, G. D.; Tham, D.; Fischer, J. E.; Eklund, P. C. *J. Nanosci. Nanotechnol.* **2003**, *3* (4), 335–339.
- (16) Gupta, R.; Xiong, Q.; Mahan, G. D.; Eklund, P. C. *Nano Lett.* **2003**, *3* (12), 1745–1750.
- (17) Roca, E.; Trallero-Giner, C.; Cardona, M. *Phys. Rev. B: Condens. Matter Mater. Phys.* **1994**, *49* (19), 13704–13711.
- (18) Yu, P.; Cardona, M. *Fundamentals of Semiconductors*, 2 ed.; Springer: Berlin, 1999.
- (19) Shiang, J. J.; Goldstein, A. N.; Alivisatos, A. P. *J. Chem. Phys.* **1990**, *92* (5), 3232–3233.
- (20) Shiang, J. J.; Risbud, S. H.; Alivisatos, A. P. *J. Chem. Phys.* **1993**, *98* (11), 8432–8442.
- (21) Alim, K. A.; Fonoberov, V. A.; Balandin, A. A. *Appl. Phys. Lett.* **2005**, *86* (5), Art. No. 053103.
- (22) Roy, A.; Sood, A. K. *Phys. Rev. B: Condens. Matter Mater. Phys.* **1996**, *53* (18), 12127–12132.
- (23) Xiong, Q. H.; Wang, J. G.; Reese, O.; Voon, L. C. L. Y.; Eklund, P. C. *Nano Lett.* **2004**, *4* (10), 1991–1996.
- (24) Carbone, L.; Kudera, S.; Carlino, E.; Parak, W. J.; Giannini, C.; Cingolani, R.; Manna, L. *J. Am. Chem. Soc.* **2006**, *128* (3), 748–755.
- (25) Landolt-Bornstein, Springer-Verlag GmbH: Berlin, 1999; Vol. 41.
- (26) Cantarero, A.; Trallero-Giner, C.; Cardona, M. *Phys. Rev. B: Condens. Matter Mater. Phys.* **1989**, *40* (18), 12290–12295.
- (27) Cantarero, A.; Trallero-Giner, C.; Cardona, M. *Phys. Rev. B: Condens. Matter Mater. Phys.* **1989**, *39* (12), 8388–8397.
- (28) Belitsky, V. I.; Cantarero, A.; Pavlov, S. T.; Cardona, M.; Lang, I. G.; Prokhorov, A. V. *Phys. Rev. B: Condens. Matter Mater. Phys.* **1995**, *52* (16), 11920–11926.
- (29) Krauss, T. D.; Wise, F. W. *Phys. Rev. B: Condens. Matter Mater. Phys.* **1997**, *55* (15), 9860–9865.
- (30) Nomura, S.; Kobayashi, T. *Phys. Rev. B: Condens. Matter Mater. Phys.* **1992**, *45*, 1305.
- (31) Rodriguez-Suarez, R.; Menendez-Proupin, E.; Trallero-Giner, C.; Cardona, M. *Phys. Rev. B: Condens. Matter Mater. Phys.* **2000**, *62* (16), 11006–11016.
- (32) Pokatilov, E. P.; Klimin, S. N.; Fomin, V. M.; Devreese, J. T.; Wise, F. W. *Phys. Rev. B: Condens. Matter Mater. Phys.* **2002**, *65* (7), Art. No. 075316.
- (33) Fujii, M.; Kanzawa, Y.; Shinji, H.; Keiichi, Y. *Phys. Rev. B: Condens. Matter Mater. Phys.* **1996**, *54* (12), R8373–R8376.
- (34) Freire, P. T. C.; Silva, M. A. A.; Reynoso, V. C. S.; Vaz, A. R.; Lemos, V. *Phys. Rev. B: Condens. Matter Mater. Phys.* **1997**, *55* (11), 6743–6746.
- (35) Islam, S. S.; Rath, S.; Jain, K. P.; Abbi, S. C.; Julien, C.; Balkanski, M. *Phys. Rev. B: Condens. Matter Mater. Phys.* **1992**, *46* (8), 4982–4985.
- (36) Baranov, A. V.; Yamauchi, S.; Matsumoto, Y. *Phys. Rev. B: Condens. Matter Mater. Phys.* **1997**, *56* (16), 10332–10337.

NL0524492

Confinement effects on optical phonons in polar  
tetrapod nanocrystals detected by resonant inelastic  
light scattering

*Roman Krahne<sup>a\*</sup>, Gerwin Chilla<sup>b</sup>, Christian Schüller<sup>b+</sup>, Luigi Carbone<sup>a</sup>, Stefan Kudera<sup>a</sup>,*

*Gianandrea Mannarini<sup>a</sup>, Liberato Manna<sup>a</sup>, Detlef Heitmann<sup>b</sup>, Roberto Cingolani<sup>a</sup>,*

<sup>a</sup>National Nanotechnology Laboratory of CNR-INFN c/o Istituto Superiore Universitario di  
Formazione Interdisciplinare, Università di Lecce, Via per Arnesano, 73100 Lecce, Italy

<sup>b</sup>Institute of Applied Physics, University of Hamburg, 20355 Hamburg, Germany

<sup>+</sup> present address: Institute of Experimental and Applied Physics, University of Regensburg, 93040  
Regensburg, Germany

[roman.krahne@unile.it](mailto:roman.krahne@unile.it)

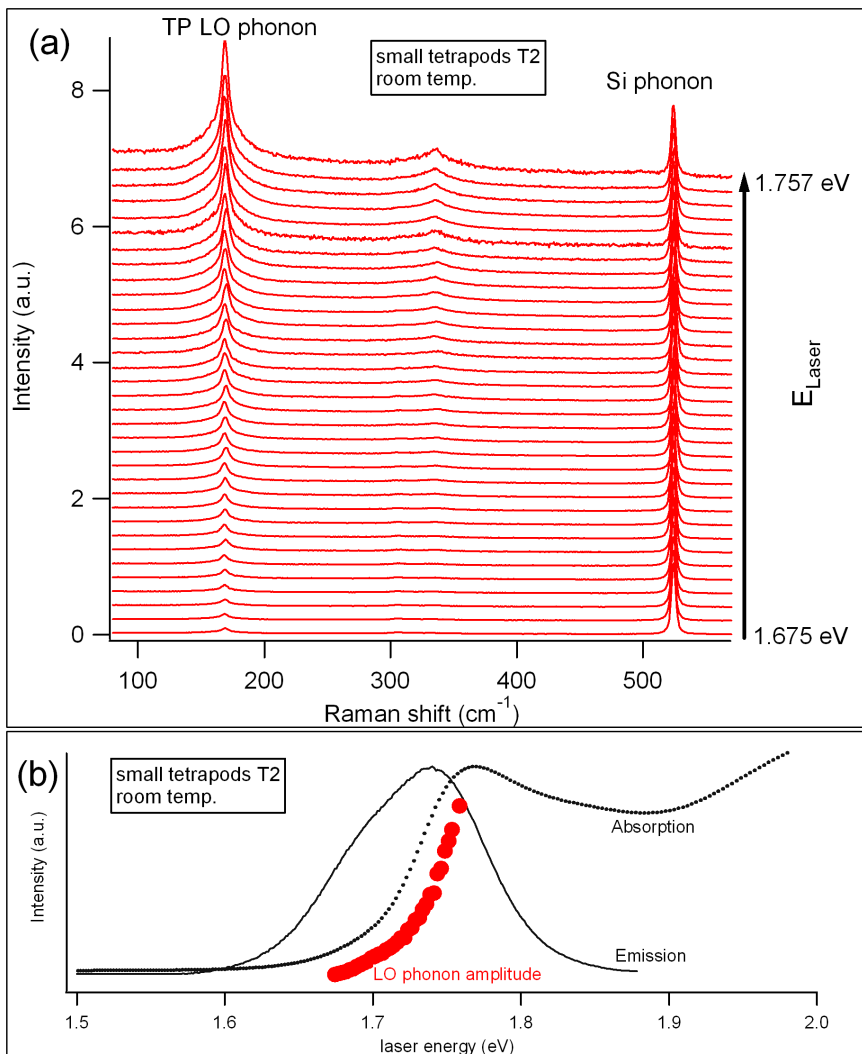
**RECEIVED DATE (to be automatically inserted after your manuscript is accepted if  
required according to the journal that you are submitting your paper to)**

\*Corresponding author:

[roman.krahne@unile.it](mailto:roman.krahne@unile.it); tel. +39 0832 298 209; fax +39 0832 298 238

**Supplementary information**

Resonant Raman Spectra of tetrapods with small arms (sample T2) at room temperature. Resonant  
Raman Spectra of tetrapods with small arms (sample T2) at T = 7 K.

**Supporting information:**

**Figure S1:** (a) Resonant Raman spectra of the small TPs T2 at room temperature. The CdTe phonon is observed at 168.5 cm<sup>-1</sup>. The laser energy range is not sufficient to map the resonance maximum. The spectra are normalized with respect to the Si phonon intensity and shifted vertically for clarity; (b) TP LO phonon amplitude (red dots) and optical emission and absorption plotted versus the excitation laser energy. The phonon resonance is blue-shifted by roughly 20 meV (the LO phonon energy) with respect to the absorption curve.

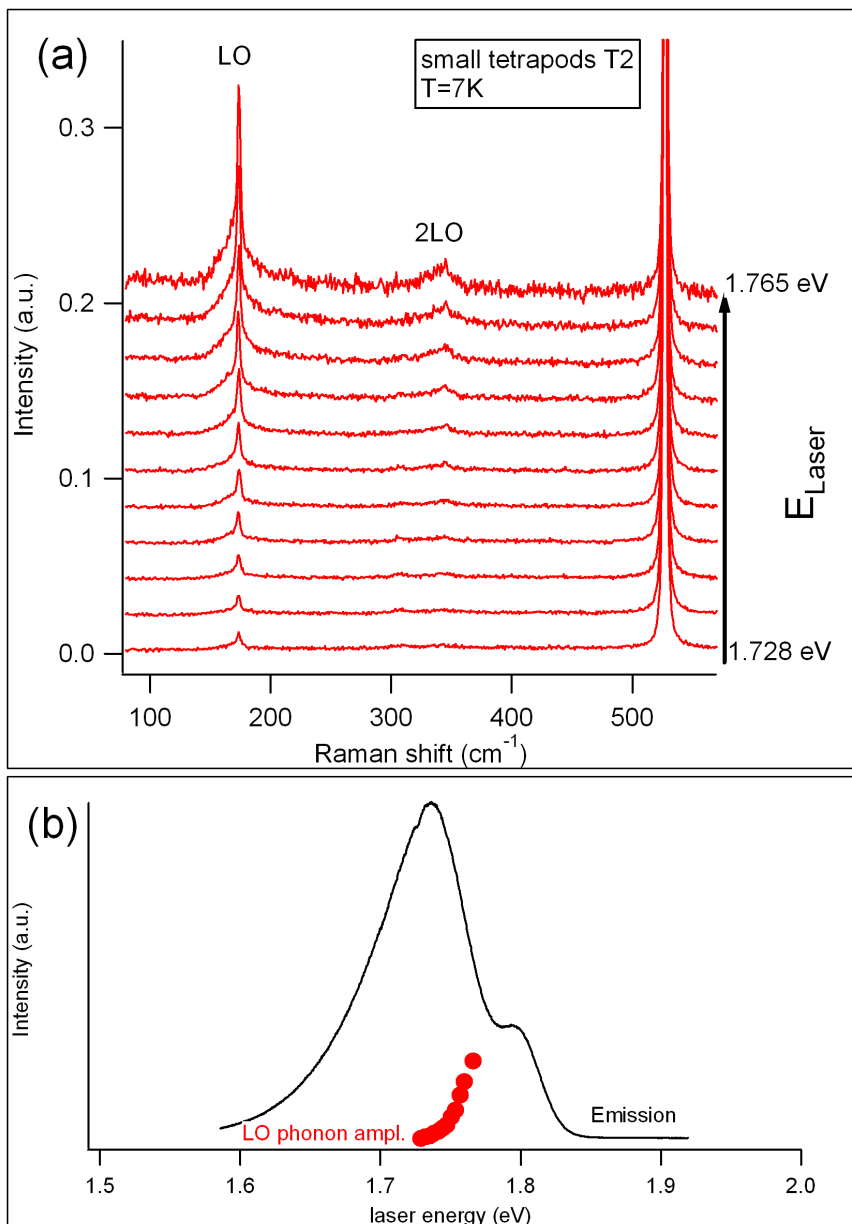


**Figure S2:** Resonant Raman spectra of the small TPs T2 at T = 7 K. The laser energy range is not sufficient to map the resonance maximum. The spectra are normalized with respect to the Si phonon intensity and shifted vertically for clarity; (b) phonon amplitude and emission at T = 7 K. Here the double peak in TP emission is clearly evident (emission spectrum from Ref. <sup>9</sup>).

## B.6 Shape Dependence of the Scattering Processes of Optical Phonons in Colloidal Nanocrystals Detected by Raman Spectroscopy

R. KRAHNE, G. CHILLA, C. SCHÜLLER, S. KUDERA, D. TARÌ, M. DE GIORGI, D. HEITMANN, R. CINGOLANI, L. MANNA  
*J. Nanoelectron. Optoelectron.* **1**(1), pp. 104–107, 2006

We investigated by Raman spectroscopy optical phonon excitations in colloidal CdTe nanocrystals of different shapes. The phonon spectra at excitation energies slightly below the absorption onset showed a strong dependence on the nanocrystal shape. For spherical nanocrystals, we detected broad longitudinal-optical phonon-scattering peaks that were blue shifted from the longitudinal-optical phonon bulk energy by the exciton resonant Stokes shift. These are reminiscent of the phonon replicas reported in fluorescence line-narrowing experiments. Tetrapod-shaped nanocrystals, on the other hand, showed a sharp LO phonon peak that was only slightly blue shifted by confinement effects on the phonon excitations. We propose that the localization of the carriers in the optical excitations is responsible for the different phonon spectra in tetrapods.



## **Shape Dependence of the Scattering Processes of Optical Phonons in Colloidal Nanocrystals Detected by Raman Spectroscopy**

Roman Krahne<sup>1,\*</sup>, Gerwin Chilla<sup>2</sup>, Christian Schüller<sup>2,3</sup>, Stefan Kudera<sup>1</sup>, Davide Tari<sup>1</sup>, Milena De Giorgi<sup>1</sup>, Detlef Heitmann<sup>2</sup>, Roberto Cingolani<sup>1</sup>, and Liberato Manna<sup>1</sup>

<sup>1</sup>*National Nanotechnology Laboratory of CNR-INFM c/o Istituto Superiore Universitario di Formazione Interdisciplinare, Università di Lecce, 73100 Lecce, Italy*

<sup>2</sup>*Institute of Applied Physics, University of Hamburg, 20355 Hamburg, Germany*

<sup>3</sup>*Present address: Institute of Experimental and Applied Physics, University of Regensburg, 93040 Regensburg, Germany*

(Received 02 February 2006; accepted 23 February 2006)

We investigated by Raman spectroscopy optical phonon excitations in colloidal CdTe nanocrystals of different shapes. The phonon spectra at excitation energies slightly below the absorption onset showed a strong dependence on the nanocrystal shape. For spherical nanocrystals, we detected broad longitudinal-optical phonon-scattering peaks that were blue shifted from the longitudinal-optical phonon bulk energy by the exciton resonant Stokes shift. These are reminiscent of the phonon replicas reported in fluorescence line-narrowing experiments. Tetrapod-shaped nanocrystals, on the other hand, showed a sharp LO phonon peak that was only slightly blue shifted by confinement effects on the phonon excitations. We propose that the localization of the carriers in the optical excitations is responsible for the different phonon spectra in tetrapods.

State-of-the-art chemical synthesis has achieved remarkable control over the size and shape of colloidal nanocrystals leading to spheres,<sup>1,2</sup> rods,<sup>3–5</sup> and branched nanostructures.<sup>6–8</sup> The shape of colloidal nanocrystals has strong effects on their optical and electronic properties. In spherical nanocrystals, the electronic band gap, the resonant Stokes shift, and the optical phonon excitation energies depend on the nanocrystal diameter. Rod-shaped nanocrystals provide a uniaxial symmetry that leads to polarized emission,<sup>4</sup> as well as to laterally and longitudinally confined vibronic excitations.<sup>9–11</sup> Tetrapods represent an even more complex geometry in which four arms branch out from a central core. The peculiar symmetry of tetrapods has demonstrated novel properties in electronic and optical experiments.<sup>12–14</sup>

Phonon excitations in colloidal nanocrystals have been studied by Raman spectroscopy and fluorescence line-narrowing (FLN) experiments.<sup>15,16</sup> (For a review, see Ref. 17, chapters 2 and 3.) The coupling of the optical phonons to the photo-excited carriers is mediated by the Froehlich interaction.<sup>18–22</sup> In Raman experiments on nanocrystal spheres, the confinement leads to a red shift and broadening

of the longitudinal-optical (LO) phonon mode<sup>23</sup> and to the observation of surface optical (SO) phonons.<sup>24,25</sup> In FLN experiments on spherical nanocrystals, in which the nanocrystal ensemble is excited on the red edge of its absorption spectrum, phonon replicas are observed at the low-energy shoulder of the luminescence signal due to recombination from the dark state by LO phonon-assisted transitions. In this article, we report a strong dependence of these phonon-assisted transitions on the nanocrystal shape. In particular, in tetrapod-shaped nanocrystals the localization of the carriers in the arms leads to an increased direct recombination of the excited exciton, thereby suppressing the phonon replicas on the red edge of the photoluminescence signal.

Colloidal nanocrystals of different shapes and sizes were fabricated by chemical synthesis.<sup>6,8,26</sup> Figure 1 shows transmission electron microscopy images of spherical nanocrystals (Fig. 1a), tetrapods with very short arms (Fig. 1b), and tetrapods with arm length much larger than arm diameters (Fig. 1c). Absorption and luminescence spectra of spherical (dots) and tetrapod-shaped nanocrystals of different sizes recorded at room temperature in solution are plotted in Figure 2a–2c.

In the absorption spectra of the dots (Fig. 2a, 2b), we observe a series of well-defined peaks resulting from the

\*Author to whom correspondence should be addressed.

level structure of the confined excitons in the nanocrystal dots. The fluorescence peak is red shifted from the lowest absorption peak by the Stokes shift,<sup>15,16</sup> which increases with decreasing nanocrystal size. The tetrapods (Fig. 2c–2d) display absorption spectra with overlapping peaks that originate from the more complex electronic structure.<sup>13</sup> In particular, the luminescence signal of larger tetrapods (TP2) consists of a double-peak structure that can be clearly resolved at low temperatures (Fig. 2e), whereas the dots show only a single peak with slight asymmetric broadening on the low-energy shoulder. For the low-temperature measurements, the solution containing the nanocrystals was drop-casted onto the surface of a silicon substrate, the solvent was allowed to evaporate under soft nitrogen flow, and the samples were mounted in an optical cryostat.

The Raman experiments were performed using a tunable Ti-Sa laser (700–850 nm) and a semiconductor diode laser (532 nm wavelength). The excitation light (30 mW laser power) was focused onto the samples on a spot with a 50- $\mu$ m diameter, and the signal was collected by an achromatic lens and detected by a triple Raman spectrometer (DILOR XY) and a charge-coupled device (CCD) camera. Figure 3a shows Raman spectra of large (D1: 6 nm diameter) and small (D2: 4 nm diameter) dots and of two tetrapod samples with different arm lengths (TP1: approximately 3 nm arm length and diameter; TP2: 30 nm arm length, 7 nm arm diameter) at  $T = 15$  K with a laser excitation energy of 2.33 eV, which is well above the band gap of the nanocrystals (see dashed vertical line in Fig. 2). At this excitation energy, we observe the LO phonon at  $170\text{ cm}^{-1}$  and its second scattering order at  $340\text{ cm}^{-1}$ . The LO phonon excitation is slightly red shifted and broadened with respect to the bulk value ( $172\text{ cm}^{-1}$ ), as expected for nanocrystal dots.<sup>19,25</sup>

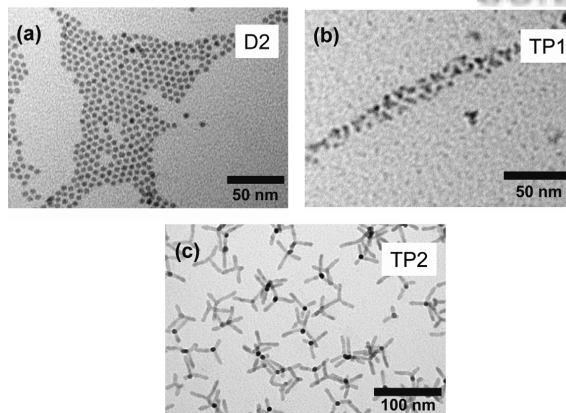


**Fig. 1.** Transmission electron microscopy images of nanocrystals with different shapes: (a) spherical nanocrystals with 4-nm diameter; (b) tetrapod-shape nanocrystals with very short arms (arm length of approximately 3 nm is comparable to arm diameter); (c) tetrapods with well-developed arms (arm length and diameter are 30 and 7 nm, respectively).

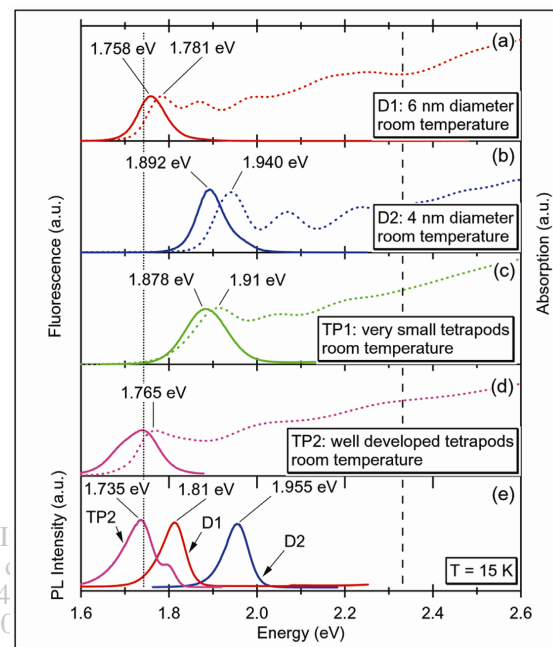


**Fig. 2.** (a)–(d) Fluorescence (solid lines) and absorption (dotted lines) spectra of spherical and tetrapod-shaped CdTe nanocrystals at room temperature; (e) photoluminescence of large (D1) and small (D2) nanocrystal dots and tetrapods (TP2) at low temperature ( $T = 15$  K). The tetrapod luminescence of TP2 shows a double peak, whereas on spherical nanocrystals only a single peak is observed. For the low-temperature measurements, the nanocrystals were drop-casted on a Si substrate. The dotted lines show the laser excitation energies for the Raman scattering experiments reported in Fig. 3.

In the spectra of the spherical nanocrystals, we can identify the SO phonon at  $147\text{ cm}^{-1}$  on the low-energy side of the LO phonon. The SO phonon energy can be calculated as the sphere-surface ground mode using the dielectric continuum model of Ruppin and Englman<sup>27</sup>:

$$\omega_{SO}^2 = \omega_{TO}^2 \frac{\varepsilon_0 + 2\varepsilon_m}{\varepsilon_\infty + 2\varepsilon_m}$$

which yields  $149\text{ cm}^{-1}$  as SO phonon energy if  $\varepsilon_m$  (surrounding medium dielectric constant) is taken as 6.5 (average of vacuum and Si).  $\varepsilon_\infty$  and  $\varepsilon_0$  are the bulk CdTe high-frequency and static dielectric constants, respectively, and  $\omega_{TO}$  is the frequency of the transverse-optical phonon.<sup>28</sup> For a sample with a high density of nanocrystals (as is the case in our experiments),  $\varepsilon_m$  can be assumed larger ( $\varepsilon_m = 10$ ), which reduces the theoretical value for the SO phonon to  $147\text{ cm}^{-1}$ , leading to even better agreement with our experimental value.

In Figure 3b, we plot the Raman spectra of dots and tetrapods measured with a laser excitation energy on the red edge of their respective first absorption peak at  $T = 15$  K (see dotted vertical line in Fig. 2). In this energy range, the exciting laser energy is selectively exciting classes of

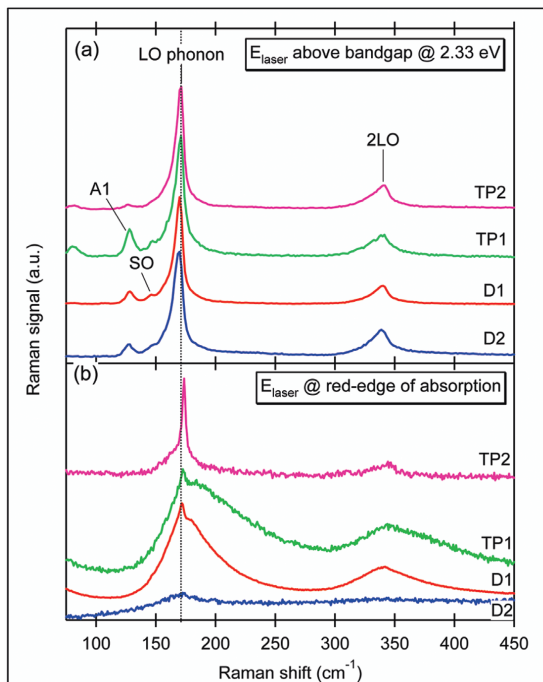


**Fig. 3.** Raman spectra of small (blue: 4 nm diameter) and large (red: 6 nm diameter) nanocrystal dots and tetrapods (TP1, green; TP2, magenta) at  $T = 15$  K. (a) Laser excitation energy above the band gap; (b) laser excitation energy on the low-energy side of their photoluminescence signal. The peak labeled A1 in (a) at  $128\text{ cm}^{-1}$  originates most likely from tellurium formed by photococrystallization, and the sharp excitation in (b) at the LO bulk frequency,  $172\text{ cm}^{-1}$ , originates from CdTe aggregates formed by laser illumination. The spectra have been shifted vertically for clarity, and the vertical gray line is a guide to the eye indicating the bulk CdTe LO phonon energy.

nanocrystals that absorb at the same energy. For the large dots D2, we observe broad peaks at  $177\text{ cm}^{-1}$  (full width at half maximum [FWHM] =  $23\text{ cm}^{-1}$ ) and  $347\text{ cm}^{-1}$  (FWHM =  $20\text{ cm}^{-1}$ ) that are blue shifted with respect to the LO phonon energy of  $170\text{ cm}^{-1}$  found in Figure 2a. These broad peaks are reminiscent of phonon replicas that were reported in FLN experiments on nanocrystal dots,<sup>15,16</sup> in which the nanocrystals are also excited with the laser energy on the red edge of the first absorption peak. In FLN spectra, the energy difference between the excitation laser and the position of the  $n$ th LO phonon replica consists of the resonant Stokes shift ( $\sim 8\text{ cm}^{-1}$  for nanocrystal dots with 6 nm diameter) plus  $n$  times the LO phonon energy.

The phonon spectrum of very short tetrapods TP1 (arm length comparable to arm diameter) also shows broad phonon replica (at  $180$  and  $353\text{ cm}^{-1}$ ) that are blue shifted from the bulk phonon energy. This energy difference of the LO phonon replica in Figure 3b to the LO phonon excitation in Figure 3a of  $10\text{ cm}^{-1}$  can be regarded as the resonant Stokes shift and is slightly larger than the Stokes shift observed in the case of the large dots D2 due to shape

asymmetry. Otherwise, sample TP1 can be treated as a deformed dot in which the carriers are mostly localized in and near the core.

The LO phonon excitations of tetrapods with arm lengths much larger than their arm diameter<sup>14</sup> that are observed with laser energies at the band edge differ significantly from the signal obtained from spherical nanocrystals. The spectrum of sample TP2 in Figure 3b shows a sharp peak at  $173.5\text{ cm}^{-1}$  and a broad signal at its low-energy shoulder that originate from phonon excitations in the TP arms. These phonon excitations that are observed in larger tetrapods<sup>14</sup> are dominated by the shape of the tetrapod arms and can be modeled in a nanowire picture.<sup>9,11</sup>

To gain more insight into the difference of the phonon excitations of dots and tetrapods at laser energies near the band gap, we discuss the scattering processes for the phonon excitations. In Raman scattering with laser energies above the band gap, an incoming photon is absorbed instantaneously by the nanocrystal into a virtual or real exciton state. The exciton transfers part of its energy to the crystal lattice, creating a phonon, and recombines under photon emission.

Figure 4a illustrates the phonon-scattering process in FLN experiments, in which the lowest optically allowed state, the bright exciton, is excited by the incoming laser light. Then, the bright state relaxes nonradiatively into the dark state (mediated by acoustic phonons), and the dark state recombines by LO phonon-assisted transitions.<sup>16</sup> In this scattering process, the LO phonon replica line shape is dominated by inhomogeneous broadening of the excited class of nanocrystals, leading to a FWHM of  $14\text{ cm}^{-1}$ . The key difference between spherical nanocrystals and tetrapods is that in tetrapods the electron and hole wave functions of first excited exciton states and the ground exciton state have a different spatial distribution.<sup>13,29</sup> In particular, the electrons and holes of the first excited states are localized in the arms, which leads to stronger coupling to the phonons and to an increased radiative recombination probability (illustrated in Fig. 4b). We think that the phonon replicas that originate from ground exciton state transitions are suppressed in tetrapods due to the localization of the carriers. This interpretation is supported by the fact that the main contribution of the phonon excitation comes from the arm regions (if only by the ratio of arms to core volume). In the sample TP1, the arms are too short (see Fig. 1b) to have a significant impact on the phonon excitations, whereas in TP2 and larger tetrapods the phonon spectrum is dominated by the arms.

In conclusion, we have measured the optical phonon excitations of spherical and tetrapod-shape nanocrystals with laser energies above the band gap and on the red edge of their absorption spectrum. For tetrapods with well-defined arms, we find that the phonon-assisted transitions from the exciton ground state are suppressed, and we observe the LO phonon excitation with narrow line width. We propose the carrier localization of the first excited exciton states in the tetrapod

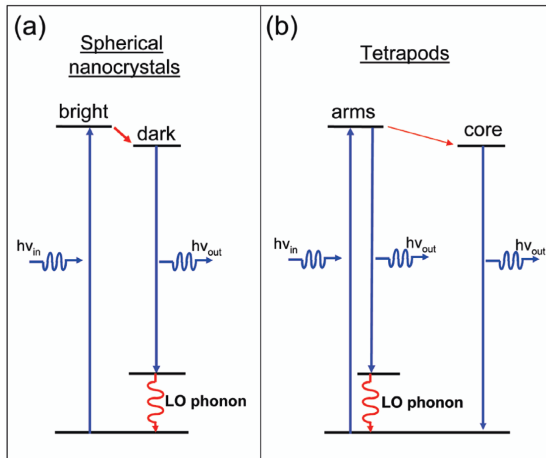


**Fig. 4.** Schematics of the scattering processes for LO phonons. (a) In spherical nanocrystals, the excitation on the red edge of the luminescence peak probes the bright exciton state, followed by a relaxation into the dark exciton state. The dark state recombines by phonon-assisted emission. The relaxation of the excited state leads to inhomogeneous broadening of the LO phonon replica; (b) in tetrapods, the electrons and holes of the first excited states are localized in the arms and therefore are spatially separated from the carriers in the exciton ground state in the core. This leads to an increased radiative recombination probability, assisted by phonon scattering, of the first excited states.

arm as the origin for the absence of broad phonon replicas, which are observed for spherical nanocrystals at such laser excitation energies.

**Acknowledgments:** We gratefully acknowledge the support by the SA-NANO European project (contract STRP013698), by the MIUR-FIRB and MIUR 297 (contract 13587) projects, and by the German Science Foundation through SFB 508.

## References

1. A. P. Alivisatos. *Science*, 271, 933–937 (1996).
2. B. Alperson, I. Rubinstein, and G. Hodes. *Phys. Rev. B*, 6308, 081303 (2001).
3. S. Kan, T. Mokari, E. Rothenberg, and U. Banin. *Nat. Mater.*, 2, 155–158 (2003).
4. J. T. Hu, L. S. Li, W. D. Yang, L. Manna, L. W. Wang, and A. P. Alivisatos. *Science*, 292, 2060–2063 (2001).
5. L. Manna, E. C. Scher, L. S. Li, and A. P. Alivisatos. *J. Am. Chem. Soc.*, 124, 7136–7145 (2002).
6. L. Manna, D. J. Milliron, A. Meisel, E. C. Scher, and A. P. Alivisatos. *Nat. Mater.*, 2, 382–385 (2003).
7. K. A. Dick, K. Deppert, M. W. Larsson, T. Martensson, W. Seifert, L. R. Wallenberg, and L. Samuelson. *Nat. Mater.*, 3, 380–384 (2004).
8. L. Carbone, S. Kudera, E. Carlini, W. J. Parak, C. Giannini, R. Cingolani, and L. Manna. *J. Am. Chem. Soc.*, 128, 748–755 (2006).
9. G. D. Mahan, R. Gupta, Q. Xiong, C. K. Adu, and P. C. Eklund. *Phys. Rev. B*, 68, 73402 (2003).
10. R. Gupta, Q. Xiong, G. D. Mahan, and P. C. Eklund. *Nano Lett.*, 3, 1745–1750 (2003).
11. Q. H. Xiong, J. G. Wang, O. Reese, L. C. L. Y. Voon, and P. C. Eklund. *Nano Lett.*, 4, 1991–1996 (2004).
12. Y. Cui, U. Banin, M. T. Bjork, and A. P. Alivisatos. *Nano Lett.*, 5, 1519–1523 (2005).
13. D. Tarì, M. De Giorgi, F. Della Sala, L. Carbone, R. Krahne, L. Manna, R. Cingolani, S. Kudera, and W. J. Parak. *Appl. Phys. Lett.*, 87, 224101 (2005).
14. R. Krahne, G. Chilla, C. Schüller, L. Carbone, S. Kudera, G. Mananirini, L. Manna, D. Heitmann, and R. Cingolani. *Nano Lett.*, 6(3), 478–482 (2006).
15. M. Nirmal, D. J. Norris, M. Kuno, M. G. Bawendi, A. Efros, and M. Rosen. *Phys. Rev. Lett.*, 75, 3728–3731 (1995).
16. A. L. Efros, M. Rosen, M. Kuno, M. Nirmal, D. J. Norris, and M. Bawendi. *Phys. Rev. B Condens. Matter*, 54, 4843–4856 (1996).
17. V. Klimov., Semiconductor and Metal Nanocrystals, Marcel Dekker, New York (2004).
18. E. Roca, C. Tralleroginer, and M. Cardona. *Phys. Rev. B*, 49, 13704–13711 (1994).
19. M. P. Chamberlain, C. Tralleroginer, and M. Cardona. *Phys. Rev. B*, 51, 1680–1693 (1995).
20. P. Yu and M. Cardona. Fundamentals of Semiconductors, 2nd ed., Springer, New York (1999).
21. J. J. Shiang, A. N. Goldstein, and A. P. Alivisatos. *J. Chem. Phys.*, 92, 3232–3233 (1990).
22. J. J. Shiang, S. H. Risbud, and A. P. Alivisatos. *J. Chem. Phys.*, 98, 8432–8442 (1993).
23. K. A. Alim, V. A. Fonoberov, and A. A. Balandin. *Appl. Phys. Lett.*, 86, 053103 (2005).
24. A. Roy and A. K. Sood. *Phys. Rev. B*, 53, 12127–12132 (1996).
25. A. M. dePaula, L. C. Barbosa, C. H. B. Cruz, O. L. Alves, J. A. Sanjurjo, and C. L. Cesar. *Appl. Phys. Lett.*, 69, 357–359 (1996).
26. L. Manna, E. C. Scher, and A. P. Alivisatos. *J. Cluster Sci.*, 13, 521–532 (2002).
27. R. Rupp and R. Englman. *Rep. Prog. Phys.*, 33, 149 (1970).
28. Landolt-Börnstein—Group III. Condensed Matter, II-VI and I-VII Compounds, Volume 41, Subvolume B. Springer, Berlin/Heidelberg (1999).
29. J. B. Li and L. W. Wang. *Nano Lett.*, 3, 1357–1363 (2003).

## **B.7 Confinement effects on optical phonons in spherical, rod- and tetrapod-shaped nanocrystals detected by Raman spectroscopy**

C. NOBILE, S. KUDERA, A. FIORE, L. CARBONE, G. CHILLA, T. KIPP, D. HEITMANN, CINGOLANI, L. MANNA, R. KRAHNE  
*Phys. stat. sol. (a)* **204**(2), pp. 483–486, 2007

Spherical, rod- and tetrapod shaped CdSe nanocrystals are investigated by Raman spectroscopy and the longitudinal-optical and surface optical phonons are observed. We find that the position of the longitudinal-optical phonon slightly red-shifts with decreasing diameter, whereas the position of the surface optical phonon depends significantly on diameter and length of the rods or the tetrapod arms.

Original  
Paper

phys. stat. sol. (a) **204**, No. 2, 483–486 (2007) / DOI 10.1002/pssa.200673223

## Confinement effects on optical phonons in spherical, rod-, and tetrapod-shaped nanocrystals detected by Raman spectroscopy

Concetta Nobile<sup>1</sup>, Stefan Kudera<sup>1</sup>, Angela Fiore<sup>1</sup>, Luigi Carbone<sup>1</sup>, Gerwin Chilla<sup>2</sup>, Tobias Kipp<sup>2</sup>, Detlef Heitmann<sup>2</sup>, Roberto Cingolani<sup>1</sup>, Liberato Manna<sup>1</sup>, and Roman Krahne<sup>\*1</sup>

<sup>1</sup> National Nanotechnology Laboratory of CNR-INFM, Via per Arnesano km5, 73100 Lecce, Italy

<sup>2</sup> Institute of Applied Physics, University of Hamburg, 20355 Hamburg, Germany

Received 30 July 2006, revised 7 November 2006, accepted 13 November 2006

Published online 6 February 2007

PACS 63.22.+m, 71.35.Ji, 73.22.-f, 78.30.Fs, 78.67.Bf

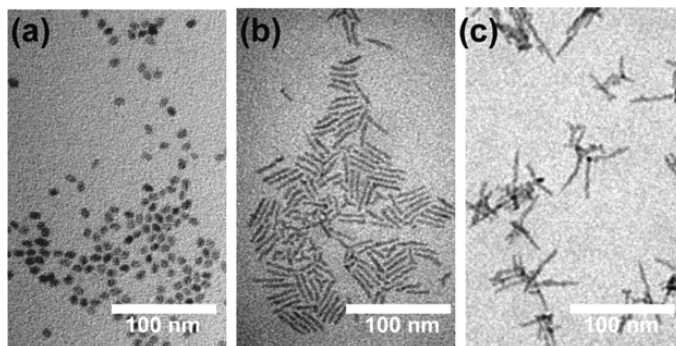
Spherical, rod- and tetrapod shaped CdSe nanocrystals are investigated by Raman spectroscopy and the longitudinal-optical and surface optical phonons are observed. We find that the position of the longitudinal-optical phonon slightly red-shifts with decreasing diameter, whereas the position of the surface optical phonon depends significantly on diameter and length of the rods or the tetrapod arms.

© 2007 WILEY-VCH Verlag GmbH & Co. KGaA, Weinheim

Chemical synthesis has achieved remarkable control over the size and shape of colloidal nanocrystals leading to spheres [1], rods [2–4], and branched nanostructures [5–7]. The shape of colloidal nanocrystals has strong effects on their optical and electronic properties, for example, in spherical nanocrystals the electronic bandgap, the resonant Stokes shift, and the optical phonon excitation energies depend on the nanocrystal diameter. Rod-shaped nanocrystals provide a uniaxial symmetry that leads to laterally and longitudinally confined vibronic excitations [8–10]. Tetrapods represent an even more complex geometry where four arms branch out from a central core that results in novel electronic and optical properties [11–13]. Optical phonons in nanocrystal spheres and rods have been studied experimentally and theoretically [14–18]. In spherical nanocrystals the confinement leads to a red-shift and broadening of the longitudinal-optical (LO) phonon mode [19], and to the observation of surface-optical (SO) phonons [20, 21]. Phonon excitations in nanorods and tetrapods can be treated in a nanowire picture [8, 9, 13, 22–25] where the confinement depends on the length and diameter of the nanocrystal structure.

Colloidal CdSe nanospheres, nanorods, and tetrapods in wurtzite crystalline structure were fabricated by chemical synthesis in a hot mixture of surfactants following a published approach [4, 5, 7, 26]. The unique axis of the wurtzite crystalline structure enables anisotropic growth due to the different chemical reactivity and growth rate of the lateral and longitudinal crystal facets. The transmission electron microscopy images of the three samples with different shapes that will be investigated in the following are shown in Fig. 1. The Raman experiments were performed using a diode laser at 532 nm wavelength that was coupled into an optical microscope setup and detected by a triple Raman spectrometer (Dilor XY) and a charge coupled device camera. The nanocrystals were casted from solution onto a Si substrate, dried under nitrogen flow and mounted into an optical cryostat.

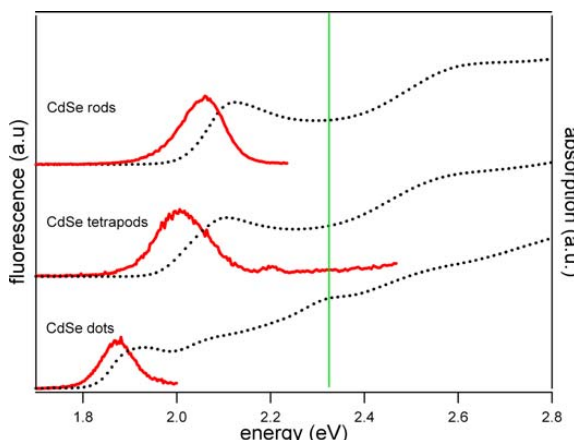
\* Corresponding author: e-mail: roman.krahne@unile.it



**Fig. 1** Transmission electron microscopy images of CdSe (a) dots with 8 nm diameter, (b) rods with 5/25 nm diameter/length and (c) tetrapods with 6/40 nm arm diameter and length.

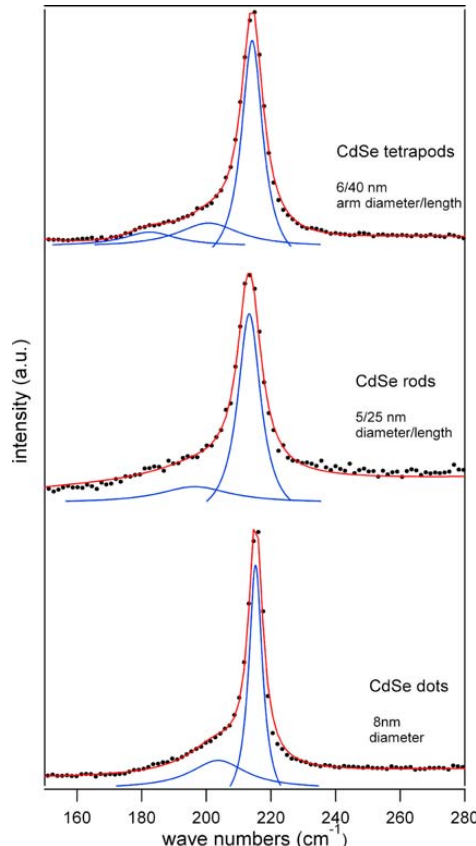
Figure 2 shows the absorption and luminescence spectra of the three samples that are displayed in Fig. 1, recorded at room temperature and in solution. The well defined level structure in the dots leads to a series of distinct peaks in the absorption spectrum. In rods and tetrapods the more complicated electronic structure results in overlapping peaks in their absorption spectra. The fluorescence peaks show a blue-shift with decreasing diameter of the nanocrystals, confirming that the diameter is the dominant parameter for the optical excitations. The fluorescence peaks are red shifted from the lowest absorption peaks by the Stokes shift, which increases with decreasing nanocrystal diameter and rising nanocrystal shape complexity. The particular geometry of the tetrapods leads to a double peak structure in their fluorescence [12, 27]. Here we observe a large peak at 2 eV that results from recombination of the exciton ground state and a small peak at the high energy side at 2.2 eV peak that we believe originates from recombination of the first excited exciton state.

Figure 3 shows Raman spectra of the dots, tetrapods and rods recorded at  $T = 13$  K with a power density of  $1 \text{ mW}/\mu\text{m}^2$ . We observe an asymmetric excitation and its higher scattering orders (not shown) for



**Fig. 2** (online colour at: [www.pss-a.com](http://www.pss-a.com)) Fluorescence (solid lines) and absorption spectra (dashed lines) of the dot, rod, and tetrapod samples under investigation. The fluorescence of the tetrapods shows a second peak (at 2.2 eV), whereas in the case of dots and rods only a single peak is observed. The green vertical line marks the laser excitation energy for the Raman experiments.

Original  
Paper



**Fig. 3** (online colour at: [www.pss-a.com](http://www.pss-a.com)) Raman spectra of nanocrystals with different shape. We observe the LO phonon modes at  $215\text{ cm}^{-1}$  for dots,  $213\text{ cm}^{-1}$  for rods and  $214\text{ cm}^{-1}$  for tetrapods, showing a trend that a decreasing nanocrystal diameter leads to an increasing red shift of the LO phonon frequency. The SO phonon modes at the low energy side of the LO phonon peak are sensitive to the aspect ratio of the nanocrystal shape. The thin solid lines show best Lorentzian fits to the data.

all nanocrystal shapes. The high energy peaks of this excitation can be attributed to the LO phonon scattering. The Lorentzian fits to the data reveal well defined peaks at  $215\text{ cm}^{-1}$  for dots,  $214\text{ cm}^{-1}$  for tetrapods and  $213\text{ cm}^{-1}$  for rods showing a trend that the LO phonon shifts to lower energy with decreasing nanocrystal diameter, as it was observed in experiments on spheres with different diameters. The low energy side of the excitation can be fitted with peaks at  $203\text{ cm}^{-1}$  for dots,  $196\text{ cm}^{-1}$  for rods, and for tetrapods with a double peak located at  $185$  and  $200\text{ cm}^{-1}$ . The low energy peak values can be modeled by the SO phonon energies for the respective geometries. To calculate the SO phonon energies of spherical nanocrystals we apply the dielectric continuum model of Ruppin and Englman [28]

$$\omega_{\text{SO}}^2 = \omega_{\text{TO}}^2 \frac{\varepsilon_0 + \varepsilon_M(l+1)/l}{\varepsilon_\infty + \varepsilon_M(l+1)/l}; \quad l=1, 2, 3 \dots,$$

where  $\varepsilon_M = 1$  (surrounding medium dielectric constant) for vacuum,  $\varepsilon_\infty$  and  $\varepsilon_0$  are the bulk CdSe high frequency and static dielectric constants, respectively, and  $\omega_{\text{TO}} = 173\text{ cm}^{-1}$  is the frequency of the transverse-optical phonon. This approach yields for the SO phonon ground mode ( $l=1$ ) of CdSe spheres  $\omega_{\text{SO}} = 205\text{ cm}^{-1}$ , in good agreement with the low energy peak of the dot sample located at  $203\text{ cm}^{-1}$ .



For the rods and tetrapods we follow the approach of Gupta and coworkers [9] for surface optical (SO) phonons in nanowires [13]:

$$\omega_{\text{SO}}^2 = \omega_{\text{TO}}^2 + \frac{\sigma_p^2}{\epsilon_{\infty} + \epsilon_M f(x)}; \quad x = q \cdot d / 2,$$

where  $\sigma_p^2 = \epsilon_{\infty} (\omega_{\text{LO}}^2 - \omega_{\text{TO}}^2)$  is the screened ion-plasma frequency,  $f(x) = (I_0(x) K_1(x)) / (I_1(x) K_0(x))$  (with  $I$  and  $K$  Bessel functions), and  $d$  is the rod (or tetrapod arm) diameter. We can take the length of the rods (or the tetrapod arms) as the longitudinal symmetry breaking mechanism that leads to  $q = 2\pi/l$ . For the tetrapod samples the SO phonon is calculated at  $\omega_{\text{SO}} = 185 \text{ cm}^{-1}$  (5/40 nm diameter/length), and for the rods  $\omega_{\text{SO}} = 195 \text{ cm}^{-1}$  (5/22 nm diameter/length), also in very good agreement with our data. The signal that we observe in the tetrapods in the regime between the SO and the LO phonon could be due to higher harmonics of the surface modes, or could originate from LO or TO phonon mode splittings due to the wire geometry [13].

In conclusion, we measured the LO and SO phonons in CdSe nanocrystals with different shapes. We find that the LO phonon frequency depends dominantly on the nanocrystal diameter, whereas the SO phonon is also sensitive on the length of the nanocrystal rods.

**Acknowledgements** The authors gratefully acknowledge the support by the SA-NANO European project (Contract No. STRP013698), by the MIUR-FIRB and MIUR 297 (Contract No. 13587) projects.

## References

- [1] A. P. Alivisatos, *Science* **271**, 933 (1996).
- [2] S. Kan, T. Mokari, E. Rothenberg et al., *Nature Mater.* **2**, 155 (2003).
- [3] J. T. Hu, L. S. Li, W. D. Yang et al., *Science* **292**, 2060 (2001).
- [4] L. Manna, E. C. Scher, L. S. Li et al., *J. Am. Chem. Soc.* **124**, 7136 (2002).
- [5] L. Manna, D. J. Milliron, A. Meisel et al., *Nature Mater.* **2**, 382 (2003).
- [6] K. A. Dick, K. Deppert, M. W. Larsson et al., *Nature Mater.* **3**, 380 (2004).
- [7] L. Carbone, S. Kudera, E. Carlini et al., *J. Am. Chem. Soc.* **128**, 748 (2006).
- [8] G. D. Mahan, R. Gupta, Q. Xiong et al., *Phys. Rev. B* **68**, 73402 (2003).
- [9] R. Gupta, Q. Xiong, G. D. Mahan et al., *Nano Lett.* **3**, 1745 (2003).
- [10] Q. H. Xiong, J. G. Wang, O. Reese et al., *Nano Lett.* **4**, 1991 (2004).
- [11] Y. Cui, U. Banin, M. T. Bjork et al., *Nano Lett.* **5**, 1519 (2005).
- [12] D. Tari, M. De Giorgi, F. Della Sala et al., *Appl. Phys. Lett.* **87**, 224101 (2005).
- [13] R. Krahne, G. Chilla, C. Schüller et al., *Nano Lett.* **6**, 478 (2006).
- [14] E. Roca, C. Trälleroginer, and M. Cardona, *Phys. Rev. B* **49**, 13704 (1994).
- [15] M. P. Chamberlain, C. Trälleroginer, and M. Cardona, *Phys. Rev. B* **51**, 1680 (1995).
- [16] V. A. Fonoberov and A. A. Balandin, *Phys. Rev. B* **70**, 233205 (2004).
- [17] V. A. Fonoberov and A. A. Balandin, *J. Phys.: Condens. Matter* **17**, 1085 (2005).
- [18] V. A. Fonoberov and A. A. Balandin, *J. Nanoelectron. Optoelectron.* **1**, 19 (2006).
- [19] K. A. Alim, V. A. Fonoberov, and A. A. Balandin, *Appl. Phys. Lett.* **86**, 053103 (2005).
- [20] A. Roy and A. K. Sood, *Phys. Rev. B* **53**, 12127 (1996).
- [21] A. M. dePaula, L. C. Barbosa, C. H. B. Cruz et al., *Appl. Phys. Lett.* **69**, 357 (1996).
- [22] Q. H. Xiong, G. Chen, J. D. Acord et al., *Nano Lett.* **4**, 1663 (2004).
- [23] Q. H. Xiong, R. Gupta, K. W. Adu et al., *J. Nanosci. Nanotechnol.* **3**, 335 (2003).
- [24] T. Thonhauser and G. D. Mahan, *Phys. Rev. B* **69**, 075213 (2004).
- [25] T. Thonhauser and G. D. Mahan, *Phys. Rev. B* **71**, 081307 (2005).
- [26] Z. A. Peng and X. G. Peng, *J. Am. Chem. Soc.* **123**, 183 (2001).
- [27] R. Krahne, G. Chilla, C. Schüller et al., *J. Nanoelectron. Optoelectron.* **1**, 104 (2006).
- [28] R. Ruppin and R. Englman, *Rep. Prog. Phys.* **33**, 149 (1970).

## B.8 Confined Optical Phonon Modes in Aligned Nanorod Arrays Detected by Resonant Inelastic Light Scattering

C. NOBILE, V.A. FONOBEROV, S. KUDERA, A. DELLA TORRE, A. RUFFINO, G. CHILLA, T. KIPP, D. HEITMANN, L. MANNA, R. CINGOLANI, A.A. BALANDIN, R. KRAHNE

*Nano Letters* **7**(2), pp. 476–479, 2007

We investigated the optical phonon excitations of laterally aligned nanorod arrays by resonant Raman scattering. We observed a strong suppression of the surface-optical phonon modes in the closely packed aligned arrays and a small asymmetry in the longitudinal-optical phonon peak with respect to the rod alignment orientation. These observations can be explained by the spatial distribution of the potential of the different phonon modes derived from the first principles calculations.

# Confined Optical Phonon Modes in Aligned Nanorod Arrays Detected by Resonant Inelastic Light Scattering

Concetta Nobile,<sup>†</sup> Vladimir A. Fonoberov,<sup>‡</sup> Stefan Kudera,<sup>†</sup> Antonio Della Torre,<sup>†</sup> Antonio Ruffino,<sup>†</sup> Gerwin Chilla,<sup>§</sup> Tobias Kipp,<sup>§</sup> Detlef Heitmann,<sup>§</sup> Liberato Manna,<sup>†</sup> Roberto Cingolani,<sup>†</sup> Alexander A. Balandin,<sup>‡</sup> and Roman Krahne<sup>\*,†</sup>

National Nanotechnology Laboratory of CNR-INFM, Via per Arnesano, 73100 Lecce, Italy, Department of Electrical Engineering, University of California—Riverside, Riverside, California 92521, Institute of Applied Physics, University of Hamburg, 20355 Hamburg, Germany

Received December 2, 2006; Revised Manuscript Received January 10, 2007

## ABSTRACT

We investigated the optical phonon excitations of laterally aligned nanorod arrays by resonant Raman scattering. We observed a strong suppression of the surface-optical phonon modes in the closely packed aligned arrays and a small asymmetry in the longitudinal-optical phonon peak with respect to the rod alignment orientation. These observations can be explained by the spatial distribution of the potential of the different phonon modes derived from the first principles calculations.

The chemical synthesis of colloidal semiconductor nanorods allows one to control the length and diameter and thereby provides the possibility to tune their optical and electronic properties. For this reason, nanorods have emerged as a very interesting material for both fundamental studies<sup>1,2</sup> and for optical<sup>3</sup> and electronic applications.<sup>4</sup> In particular, the uniaxial symmetry in shape and crystal structure of wurtzite nanorods has strong effects on their electronic level structure and optical excitations.<sup>5–8</sup> This results, for example, in the emission of linearly polarized light from CdSe nanorods.<sup>9</sup> Spectral hole-burning experiments on CdSe/ZnS nanorods have revealed a difference in decoherence rate for rods and spherical nanocrystals by investigating the zero-phonon line line width.<sup>10</sup> Raman spectroscopy has proven to be a powerful tool for the investigation of lattice vibrations,<sup>11,12</sup> and confined optical phonon excitations in nanorods and nanowires have been studied experimentally<sup>13–19</sup> and were described by different theoretical models.<sup>20–25</sup> Recently, efforts toward the self-assembly of nanorods and nanowires into ordered arrays, for example, by electric field mediated alignment, have been reported.<sup>26–29</sup> This technique can be exploited to realize ordered arrays of nanorods on the scale

of some microns, which is comparable with the spatial resolution of optical spectroscopy and thereby enables optical spectroscopy studies of orientation-dependent properties on large ensembles of nanorods.

In this letter, we present a detailed comparison between experiments and first principles theory on optical phonon excitations in CdSe nanorods. We report Raman experiments that probe the optical lattice vibrations in ordered arrays of CdSe nanorods, which were assembled on a substrate surface by electric-field-induced alignment. We found that the lateral packing of nanorods into dense arrays leads to the suppression of the surface optical phonon modes. In the LO phonon peak, we observe a fine structure that depends on the relative orientation of the nanorods with respect to the incident and detected light polarization. We compare the experimental data with first principles calculations on corresponding nanostructures, which reveal the symmetry of the phonon potentials of the Raman active modes and provide a qualitative explanation of the experimental spectra.

Colloidal wurtzite CdSe nanorods were fabricated by chemical synthesis in a hot mixture of surfactants following a published approach.<sup>30</sup> The nanorods samples were inspected by transmission electron microscope imaging, and fluorescence and absorption spectra were recorded at room temperature in solution (see Supporting Information). For random orientation experiments, the nanorods were drop-casted from solution on a Si substrate and dried by nitrogen flow.

\* Corresponding author. E-mail: roman.krahne@unile.it. Telephone: +39 0832 298 209. Fax: +39 0832 298 238.

<sup>†</sup> National Nanotechnology Laboratory of CNR-INFM.

<sup>‡</sup> Department of Electrical Engineering, University of California—Riverside.

<sup>§</sup> Institute of Applied Physics, University of Hamburg.

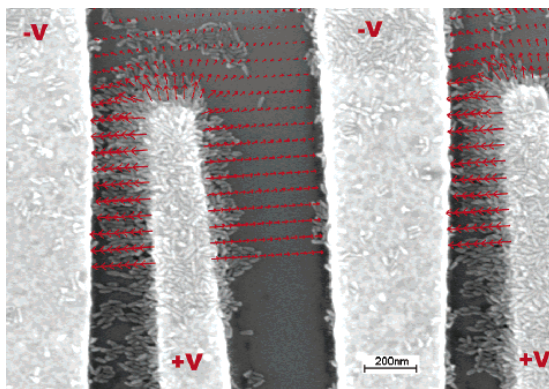


**Figure 1.** Scanning electron microscope image of laterally aligned nanorods in between interdigitated electrodes defined by electron-beam lithography. The red arrows show the calculated electric field for bias  $\pm V$  applied to neighboring electrodes (as was the case during alignment). In the lower part of the image, the electric field lines are not shown in order to enhance the visibility of the nanorods. We find that the rods accumulate in the regions of strongest electric field and observe excellent alignment with the electric field.

To laterally align nanorods, we fabricated interdigitated electrode structures with electrode distances of the order of some microns by optical lithography and metal evaporation (Cr/Au) onto a Si/SiO<sub>2</sub> substrate (see schematics in Figure 2). A quantity of typically 50 microliters of nanorod solution (nanorods were dispersed in either chloroform or toluene) was drop-casted onto the electrode device, and an ac electric field of  $10^5$  V/cm at a frequency of 10 MHz was applied during solvent evaporation. The use of alternating electric fields for the alignment avoids charging effects and accumulation of the nanorods on the electrodes. After the alignment process, the electrode devices were inspected by scanning electron microscopy (SEM) imaging (see Figure 1) and the regions of best alignment were identified for the Raman measurements. We worked with relatively large rods with 10 nm diameter and 50 nm length in order to increase their visibility in the SEM imaging. To reduce contamination of the rods due exposure to the electron beam during imaging, we worked with short exposure times and at comparatively low accelerating voltages (10 kV or lower). We did not observe any influence of the SEM imaging on the line-shape of the phonons.

The samples were mounted into an optical cryostat, cooled to  $T = 15$  K, and the Raman experiments were performed using a diode-pumped solid-state laser at 532 nm wavelength that was coupled into an optical microscope setup with an 80 $\times$  objective lens, which focused the light on a spot with approximately 1  $\mu\text{m}$  diameter. The signal was detected by the same optical path and analyzed by a triple Raman spectrometer (Dilor XY) and a charge-coupled device camera.

Figure 3a shows Raman spectra of randomly oriented (blue-dotted) and closely packed laterally aligned (red-solid) nanorods with 10/50 nm diameter/length that were taken on regions outside and within the interdigitated electrodes, respectively, on the same sample. In the spectrum of the

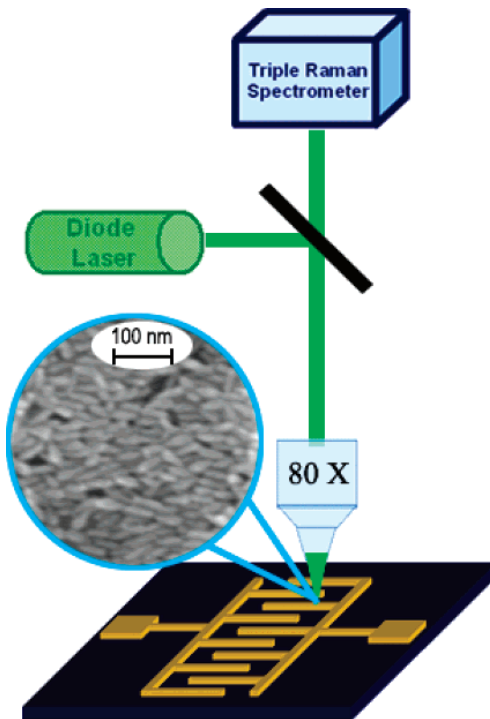


**Figure 2.** Schematic illustration of the experimental setup. A diode-pumped solid-state laser (wavelength 532 nm) was focused by an optical microscope using an 80 $\times$  objective on a region of aligned nanorods in between the interdigitated electrodes. The zoom shows a SEM image of an array of aligned nanorods.

randomly oriented rods, we observe the LO phonon at 214  $\text{cm}^{-1}$ , and at the low-energy side, a broad peak centered around 185  $\text{cm}^{-1}$  originating from the SO phonon modes. The spectrum of the laterally aligned nanorods (with *c*-axis perpendicular to the incident light polarization) shows a very small blue-shift of the LO phonon peak and a significant decrease in the SO phonon intensity. In the following, we will compare the experimental Raman spectra with first principles calculations on nanorods with corresponding aspect ratio.

The phonon modes in CdSe nanorods were calculated according to a theory developed by Fonoferov and Balandin in refs 23, 24 for spheroidal nanocrystals with wurtzite crystal lattice. It is convenient to use cylindrical coordinates ( $\rho, \phi, z$ ) for a spheroidal nanorod with semi-axes *a* and *c* and the dispersions of the anisotropic dielectric function  $\epsilon_{\perp}(\omega)$  and  $\epsilon_c(\omega)$  in the following denotations:

$$\begin{aligned} \epsilon_1 &= \frac{\epsilon_c(\omega)}{\epsilon_{\perp}(\omega)}; & g_2 &= 1; & f_n &= c^2 - g_n a^2 \\ p_n &= f_n + z^2 + g_n \rho^2; & t_n &= \sqrt{p_n^2 - 4f_n z^2} \\ \xi_n &= |z| \sqrt{\frac{2}{p_n - t_n}}; & \eta_n &= \text{sign}(z) \sqrt{\frac{p_n - t_n}{2f_n}} \end{aligned}$$

We describe the phonon potential inside (in) and outside (out)

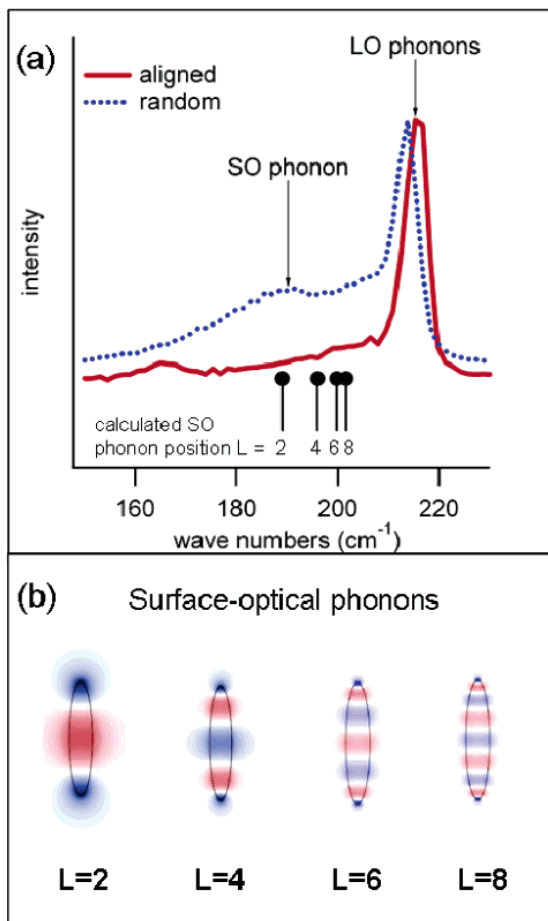


**Figure 3.** (a) Resonant Raman spectra of randomly oriented (blue dotted line) and laterally aligned (solid red line) nanorods at  $T = 15$  K recorded in parallel polarization with respect to incident and detected light. The laser energy and power density were 2.33 eV and  $2.4 \text{ mW}/\mu\text{m}^2$ , respectively. The Raman signal was normalized with respect to the LO phonon peak. The black bars indicate the calculated energies for the first four Raman active SO phonon modes. (b) Cross sections of the calculated phonon potential for the SO modes with  $M = 0$  and different angular momentum. Only SO phonon modes with even quantum number  $L$  are Raman active. Note that the  $L = 2$  mode has significant phonon potential outside the nanorod surface.

of the nanorod as

$$V_{L,M,\omega}^{(\text{in})}(\rho, \phi, z) = \frac{P_L^M(\xi_1)}{P_L^M(c/\sqrt{f_1})} P_L^M(\eta_1) e^{iM\phi}$$

$$V_{L,M,\omega}^{(\text{out})}(\rho, \phi, z) = \frac{Q_L^M(\xi_2)}{Q_L^M(c/\sqrt{f_2})} P_L^M(\eta_2) e^{iM\phi}$$

Here  $P_L^M$  and  $Q_L^M$  are associated Legendre functions of the first and second kind, respectively. The integers  $L$  ( $L \geq 1$ ) and  $M$  ( $|M| \leq L$ ) are quantum numbers of the phonon mode, and the eigenfrequencies  $\omega$  of the phonon modes are defined from the secular eq 25 of ref 24. In the calculation, the aspect

ratio  $c/a$  of CdSe nanorods was taken to be 5, and the material parameters of wurtzite CdSe were taken from ref 31. The theory predicts that only phonon modes with even  $L$  and with  $M = 0$  can be active in a resonant Raman spectrum.

Figure 3b shows the calculated potential of the SO phonon modes with  $M = 0$  and even angular quantum numbers  $L$  according to the formalism reported above. The energy of these modes is depicted in Figure 3a by the black bars with full heads (energy is increasing with higher angular momentum number). We find excellent agreement of the calculated Raman active energies with the data obtained from the randomly oriented rods. In Figure 3b, we see that the phonon potentials of the SO modes with low  $L$  extend significantly outside of the rod surface. The surface or interface phonon modes are stimulated by the change in dielectric medium at the interface. In a close-packed 2D array of nanorods, the space adjacent to the rods is occupied by other nanorods, and therefore, the dielectric medium surrounding the individual rods is severely modified, leading to the observed suppression of the SO phonon modes. The fact that SO phonon modes with higher angular momentum extend less outside the rod region accounts for the low-energy shoulder of the LO phonon peak around  $200 \text{ cm}^{-1}$ .

Figure 4 shows spectra of aligned arrays of nanorods in which the  $c$ -axis of the rods was oriented parallel or perpendicular to the incident laser polarization, as illustrated by the insets. Incident laser polarization and detection were in parallel configuration. We find that the signal of the rods parallel to the laser polarization can be accurately fitted with a single Lorentz peak centered at  $216 \text{ cm}^{-1}$ . However, in the perpendicular configuration, we observe an asymmetric peak that has to be fitted with two Lorentz peaks centered at  $213.5$  and  $216.2 \text{ cm}^{-1}$ . Theory can provide a qualitative explanation for this effect: the phonon potential for the LO modes displayed in Figure 4b shows that, for  $L = 2$  ( $214.9 \text{ cm}^{-1}$ ) and  $L = 4$  ( $214.9 \text{ cm}^{-1}$  [the second mode in the  $L = 4$  pair]), the symmetry is high in both directions. Thus, such modes with high frequency are observed in both parallel and perpendicular configurations. On the other hand, lower-frequency modes like  $L = 4$  ( $214.6 \text{ cm}^{-1}$ ) and  $L = 6$  ( $214.1 \text{ cm}^{-1}$ ) [the first modes of  $L = 4$  and  $L = 6$  sets in Figure 4b] have high symmetry only in the direction perpendicular to the nanorod axis. Therefore, these low-frequency LO modes have significant Raman intensity only when excited in the perpendicular configuration and are not observed in the top spectrum in Figure 4a. Calculations of LO modes with higher  $L$  show that the splitting in energy between the low- and high-energy modes increases with increasing  $L$ ; for example, the left bar in Figure 4a indicates the energy of the low-frequency mode for  $L = 8$  at  $213.2 \text{ cm}^{-1}$ , and the bar on the right shows the energy of the  $L = 2$  ( $214.9 \text{ cm}^{-1}$ ) mode, which is at the same energy as the high-energy mode for  $L = 8$ . The quantitative difference between theory and experiment can be attributed to the large nanorod size that was used in the experiment in order to enhance the visibility in SEM verification of the achieved alignment. In larger nanorods, bulk effects could still contribute to the

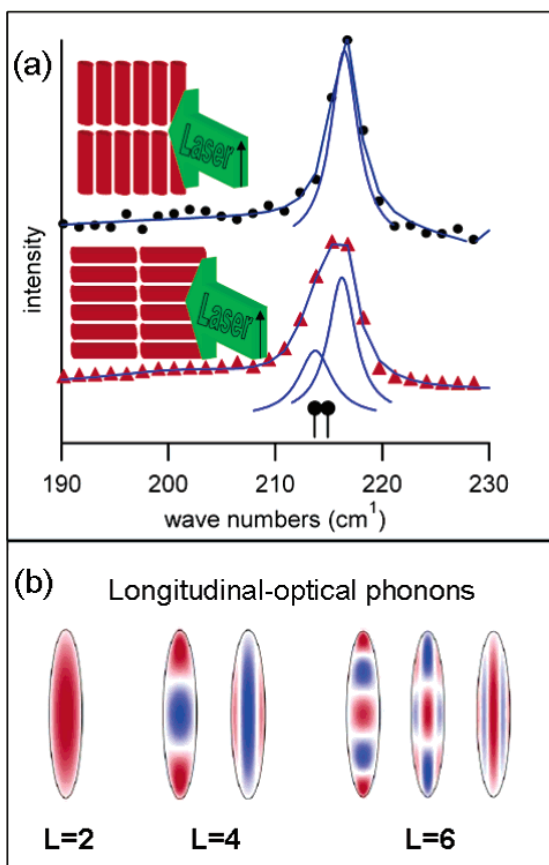


**Figure 4.** (a) Resonant Raman spectra of laterally aligned nanorods oriented parallel (black dots) and perpendicular (red triangles) to the incident laser polarization (as illustrated by the schematic insets where the black arrow indicates the laser polarization). The blue lines show Lorentz fits to the data and their resulting spectra. The black bars indicate the maximum splitting for  $L = 8$  between the low- and high-energy mode. (b) Cross sections of the calculated phonon potential for the LO Raman-active modes with  $M = 0$  and different angular momentum  $L$ . There are  $n$  Raman active LO modes for each  $L = 2n$ .

signal (in CdSe bulk the energy difference between the LO phonon along and perpendicular to the wurtzite  $c$ -axis was found to be as large as  $8\text{ cm}^{-1}$ ).<sup>31</sup> Therefore, bulk effects can be accounted for the large experimentally observed splitting between the low- and high-frequency modes.

In conclusion, we compared the experimental optical phonon excitations in aligned nanorod arrays with the results of first principles calculations. The observed SO and LO phonon energies are in good agreement with the theoretical predictions. In particular, the calculations yield high- and low-energy LO phonon modes that provide a qualitative explanation of the observed asymmetry in the experimental spectra with respect to the long axis orientation of the nanorods.

**Acknowledgment.** We gratefully acknowledge the support by the SA-NANO European project (contract no. STRP013698), by the MIUR-FIRB and MIUR 297 (contract

no. 13587) projects, and by the German Science Foundation through SFB 508. The work at UCR has been supported, in part, by the UCR-UCLA-UCSB Center for Nanoscience Innovations for Defense (CNID) and NSF award to A.A.B.

**Supporting Information Available:** Fluorescence and absorption spectra of the nanorods. Experimental data in parallel and crossed polarization with respect to incident and detected light. This material is available free of charge via the Internet at <http://pubs.acs.org>.

## References

- Li, L. S.; Hu, J. T.; Yang, W. D.; Alivisatos, A. P. *Nano Lett.* **2001**, *1*, 349–351.
- Li, L. S.; Alivisatos, A. P. *Phys. Rev. Lett.* **2003**, *90*, 097402.
- Becker, K.; Lupton, J. M.; Muller, J.; Rogach, A. L.; Talapin, D. V.; Weller, H.; Feldmann, J. *Nat. Mater.* **2006**, *5*, 777–781.
- Gudiksen, M. S.; Maher, K. N.; Ouyang, L.; Park, H. *Nano Lett.* **2005**, *5*, 2257–2261.
- Katz, D.; Wizansky, T.; Millo, O.; Rothenberg, E.; Mokari, T.; Banin, U. *Phys. Rev. Lett.* **2002**, *89*, 086801.
- Millo, O.; Katz, D.; Steiner, D.; Rothenberg, E.; Mokari, T.; Kazes, M.; Banin, U. *Nanotechnology* **2004**, *15*, R1–R6.
- Millo, O.; Steiner, D.; Katz, D.; Aharoni, A.; Kan, S.; Mokari, T.; Banin, U. *Physica E* **2005**, *26*, 1–8.
- Rothenberg, E.; Mokari, T.; Kazes, M.; Banin, U.; Katz, D.; Steiner, D.; Millo, O. *Isr. J. Chem.* **2004**, *44*, 391–400.
- Hu, J. T.; Li, L. S.; Yang, W. D.; Manna, L.; Wang, L. W.; Alivisatos, A. P. *Science* **2001**, *292*, 2060–2063.
- Tavernier-Kruger, S.; Park, Y. S.; Lonergan, M.; Woggon, U.; Wang, H. L. *Nano Lett.* **2006**, *6*, 2154–2157.
- Roca, E.; Trälleroginer, C.; Cardona, M. *Phys. Rev. B* **1994**, *49*, 13704–13711.
- Chamberlain, M. P.; Trälleroginer, C.; Cardona, M. *Phys. Rev. B* **1995**, *51*, 1680–1693.
- Teredesai, P. V.; Deepak, F. L.; Govindaraj, A.; Sood, A. K.; Rao, C. N. R. *J. Nanosci. Nanotechnol.* **2002**, *2*, 495–498.
- Gupta, R.; Xiong, Q.; Mahan, G. D.; Eklund, P. C. *Nano Lett.* **2003**, *3*, 1745–1750.
- Piscanec, S.; Cantoro, M.; Ferrari, A. C.; Zapien, J. A.; Lifshitz, Y.; Lee, S. T.; Hofmann, S.; Robertson, J. *Phys. Rev. B* **2003**, *68*, 241312.
- Xiong, Q. H.; Chen, G.; Acord, J. D.; Liu, X.; Zengel, J. J.; Gutierrez, H. R.; Redwing, J. M.; Voon, L. C. L. Y.; Lassen, B.; Eklund, P. C. *Nano Lett.* **2004**, *4*, 1663–1668.
- Krahne, R.; Chilla, G.; Schüller, C.; Carbone, L.; Kudera, S.; Mannarini, G.; Manna, L.; Heitmann, D.; Cingolani, R. *Nano Lett.* **2006**, *6*, 478–482.
- Krahne, R.; Chilla, G.; Schüller, C.; Carbone, L.; Kudera, S.; Tari, D.; De Giorgi, M.; Heitmann, D.; Cingolani, R.; Manna, L. *J. Nanoelectron. Optoelectron.* **2006**, *1*, 104–107.
- Nobile, C.; Kudera, S.; Fiore, A.; Carbone, L.; Chilla, G.; Kipp, T.; Heitmann, D.; Cingolani, R.; Manna, L.; Krahne, R. *Phys. Status Solidi A* **2007**, <http://dx.doi.org/10.1002/pssa.200673223>.
- Mahan, G. D.; Gupta, R.; Xiong, Q.; Adu, C. K.; Eklund, P. C. *Phys. Rev. B* **2003**, *68*, 73402.
- Thonhauser, T.; Mahan, G. D. *Phys. Rev. B* **2004**, *69*, 075213.
- Thonhauser, T.; Mahan, G. D. *Phys. Rev. B* **2005**, *71*, 081307.
- Fonoferov, V. A.; Balandin, A. A. *Phys. Rev. B* **2004**, *70*, 233205.
- Fonoferov, V. A.; Balandin, A. A. *J. Phys.: Condens. Matter* **2005**, *17*, 1085–1097.
- Fonoferov, V. A.; Balandin, A. A. *J. Nanoelectron. Optoelectron.* **2006**, *1*, 19–38.
- Harnack, O.; Pacholski, C.; Weller, H.; Yasuda, A.; Wessels, J. M. *Nano Lett.* **2003**, *3*, 1097–1101.
- Ghezelbash, A.; Koo, B.; Korgel, B. A. *Nano Lett.* **2006**, *6*, 1832–1836.
- Hu, Z. H.; Fischbein, M. D.; Querner, C.; Drndic, M. *Nano Lett.* **2006**, *6*, 2585–2591.
- Ryan, K. M.; Mastrianni, A.; Stancil, K. A.; Liu, H. T.; Alivisatos, A. P. *Nano Lett.* **2006**, *6*, 1479–1482.
- Manna, L.; Scher, E. C.; Alivisatos, A. P. *J. Cluster Sci.* **2002**, *13*, 521–532.
- Landolt-Boernstein; Springer-Verlag GmbH: Berlin, 1999; Vol. 41.

NL062818+

# Confined optical phonon modes in aligned nanorod arrays detected by resonant inelastic light scattering

*Concetta Nobile<sup>a</sup>, Vladimir A. Fonoberov<sup>b</sup>, Stefan Kudera<sup>a</sup>, Antonio Della Torre<sup>a</sup>, Gerwin Chilla<sup>c</sup>,  
Tobias Kipp<sup>c</sup>, Detlef Heitmann<sup>c</sup>, Liberato Manna<sup>a</sup>, Roberto Cingolani<sup>a</sup>, Alexander A. Balandin<sup>b</sup>, and  
Roman Krahne<sup>a\*</sup>,*

<sup>a</sup>National Nanotechnology Laboratory of CNR-INFM, Via per Arnesano, 73100 Lecce, Italy

<sup>b</sup>Department of Electrical Engineering, University of California – Riverside, Riverside, CA 2521 USA

<sup>c</sup>Institute of Applied Physics, University of Hamburg, 20355 Hamburg, Germany

[roman.krahne@unile.it](mailto:roman.krahne@unile.it)

## RECEIVED DATE

\*Corresponding author:

[roman.krahne@unile.it](mailto:roman.krahne@unile.it); tel. +39 0832 298 209; fax +39 0832 298 238

## Supporting information

Fluorescence and absorption spectra of the nanorods

Experimental data in parallel and crossed polarization with respect to incident and detected light.

**Supporting information:**

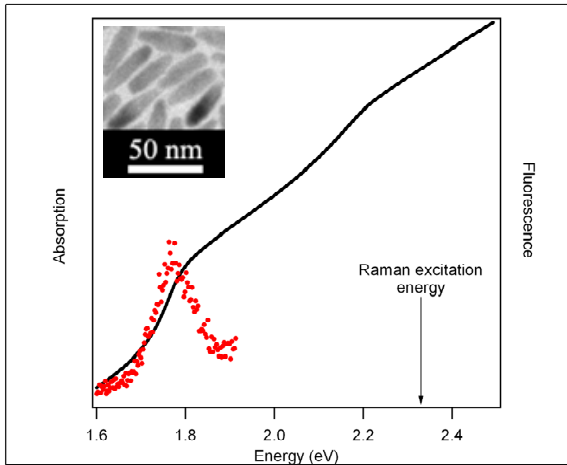


Figure S1: Absorption (solid black line) and fluorescence (red dots) spectra of nanorods with 50 nm length and 10 nm diameter, recorded in solution at room temperature. The inset show a transmission electron microscope image of the nanorods.

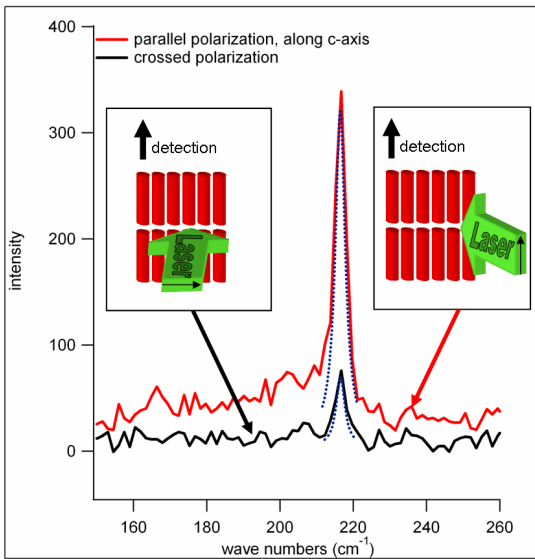
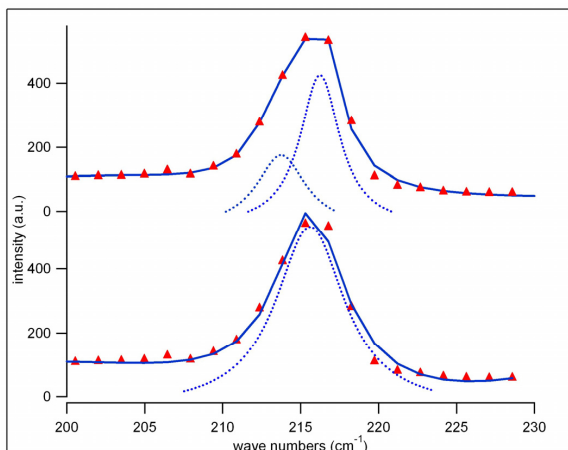


Figure S2: Raman spectra of an array of aligned nanorods in parallel and crossed polarization. The insets illustrate the incident laser polarization with respect to the nanorod orientation and the polarization of the detection gratings (solid black arrow). We observe no shift in energy with respect to the polarization of the incident laser. The signal ratio between crossed and parallel polarization is 21%, in good agreement with our theory that predicts 20%.



*Fig. S3: The Raman spectrum of laterally aligned nanorods oriented perpendicular (red triangles) to the incident laser polarization that is displayed in Fig. 4a, fitted with one Lorentz peak (bottom) and two Lorentz peaks (top). The solid blue lines are the result of the fitting with a linear base line. We find that fitting with one Lorentz peak is not sufficient to describe the line shape, in particular the high energy shoulder of the peak.*



# C Hybrid Colloidal Nanocrystals

## C.1 Selective Growth of PbSe on One or Both Tips of Colloidal Semiconductor Nanorods

S. KUDERA, L. CARBONE, M.F. CASULA, R. CINGOLANI, A. FALQUI, E. SNOECK, W.J. PARAK, L. MANNA  
*Nano Letters* **5**(3), pp. 445–449, 2005

PbSe nanocrystals with rock-salt structure are grown on the tips of colloidal CdS and CdSe nanorods. The facets of wurtzite rods provide a substrate with various degrees of reactivity for the growth of PbSe. The presence of dangling Cd bonds may explain subtle differences between nonequivalent facets resulting in the selective nucleation of PbSe only on one of the two tips of each CdS rod. This approach has the potential to facilitate the fabrication of heterostructures with tailored optical and electronic properties.

# Selective Growth of PbSe on One or Both Tips of Colloidal Semiconductor Nanorods

NANO  
LETTERS

2005  
Vol. 5, No. 3  
445–449

Stefan Kudera,<sup>†</sup> Luigi Carbone,<sup>‡</sup> Maria Francesca Casula,<sup>§</sup> Roberto Cingolani,<sup>‡</sup>  
Andrea Falqui,<sup>§</sup> Etienne Snoeck,<sup>||</sup> Wolfgang J. Parak,<sup>\*,†</sup> and Liberato Manna<sup>\*,‡</sup>

Center for Nanoscience, Ludwig Maximilians Universität München, Munich, Germany,  
National Nanotechnology Laboratory of INFM, Via Arnesano Km 5,  
73100 Lecce, Italy, Dipartimento di Scienze Chimiche, Università di Cagliari,  
09042 Monserrato, Cagliari, Italy, and CEMES/CNRS, 29 Rue Jeanne Marvig,  
31055 Toulouse, France

Received November 23, 2004; Revised Manuscript Received January 13, 2005

## ABSTRACT

PbSe nanocrystals with rock-salt structure are grown on the tips of colloidal CdS and CdSe nanorods. The facets of wurtzite rods provide a substrate with various degrees of reactivity for the growth of PbSe. The presence of dangling Cd bonds may explain subtle differences between nonequivalent facets resulting in the selective nucleation of PbSe only on one of the two tips of each CdS rod. This approach has the potential to facilitate the fabrication of heterostructures with tailored optical and electronic properties.

Architectures based on inorganic materials, such as self-assembled quantum dots,<sup>1</sup> nanowires,<sup>2</sup> and nanowire superlattices,<sup>3,4</sup> arise from the delicate balance, at the nanoscale, of parameters such as strain, surface and interfacial energy, and solubility. An increasing degree of complexity is being achieved in such structures, as they start incorporating multiple materials linked together in a programmed way.<sup>5</sup> Likewise, research on colloidal nanocrystals has moved from the synthesis of simple structures, such as spherical nanoparticles, to more elaborate shapes such as rods,<sup>6,7</sup> stars,<sup>8</sup> disks,<sup>9</sup> branched nanocrystals<sup>10–12</sup> and recently to nanostructures based on inorganic sections interconnected without the need of organic linkers.<sup>13–15</sup> Recent examples are inorganically coupled quantum rods and dots connected epitaxially at branched and linear junctions within single colloidal nanocrystals,<sup>13</sup> metal-tipped semiconductor nanorods,<sup>14</sup> and nanocrystal heterodimers based on magnetic and fluorescent nanoparticles.<sup>15</sup>

Nanocrystal heterostructures represent a convenient approach to the development of nanoscale building blocks,<sup>11</sup> as they group inorganic sections with different functionalities in the same particle. Sections based on semiconductor nanorods, for instance, will emit linearly polarized light,<sup>16,17</sup> will

exhibit lower lasing threshold,<sup>18</sup> and will result in improved power conversion efficiency in solar cells.<sup>19</sup> Gold or magnetic tips on rods or on nanocrystals with other shapes<sup>14,15</sup> can serve as preferential anchoring points for connecting nanocrystals to substrates, for their organization in solution into superstructures via linkage with molecules, or for their orientation under external biases.

The simplest heterostructure is the one based on the so-called core/shell system. In core/shell nanocrystals, an additional inorganic material is uniformly grown around a nanocrystal core, for disparate purposes. It can be used, for instance, to increase the robustness and the fluorescence efficiency of semiconductor nanocrystals,<sup>20–23</sup> to create prototype quantum-confined structures as the quantum dot/quantum well system,<sup>24</sup> to tune the magnetic properties of the overall nanocrystal,<sup>25</sup> or to provide a surface to which molecules can be attached easily.<sup>26</sup> The design of more elaborate inorganic heterostructures, in which a second material is grown only on certain facets of a starting nanocrystal, requires a more accurate knowledge of the mechanism of growth under the various conditions. Cadmium chalcogenide nanocrystals can grow anisotropically in rods or in more complex shapes.<sup>6,10,11,27–29</sup> When these materials form in the wurtzite structure in the presence of suitable surfactants, the lateral, nonpolar facets can have much lower growth rates than the basal, polar facets, and therefore the nanocrystals can develop preferentially along their unique *c* axis. The higher reactivity of the tips of such anisotropic

\* Corresponding authors: Wolfgang.Parak@physik.uni-muenchen.de; tel. +49 (0)89 21801438; fax +49 (0)89 21802050. liberato.manna@unile.it; tel. +39 0832 298 207; fax +39 0832 298 238.

<sup>†</sup> Ludwig Maximilians Universität München.

<sup>‡</sup> National Nanotechnology Laboratory of INFM.

<sup>§</sup> Università di Cagliari.

<sup>||</sup> CEMES/CNRS.

nanocrystals opens up the possibility to nucleate a second material exclusively at these locations.<sup>13,14</sup>

In the wurtzite structure, the absence of a plane of symmetry perpendicular to the *c* axis implies that the 001 and the 001̄ facets are never equivalent. In CdSe, the 001 facet exposes either Cd atoms with one dangling bond, or Se atoms with three dangling bonds, while the opposite is true for the 001̄ facet. We can therefore expect significant differences between the growth along the 001 and the 001̄ directions. This diversity was highlighted in the synthesis of arrow- and tadpole-shaped CdSe nanocrystals<sup>27,28</sup> and in the lateral growth of sections of a semiconductor material on a starting semiconductor nanorod.<sup>13</sup> Recent *ab initio* pseudopotential calculations on small CdSe wurtzite clusters suggest that the differences in reactivity among the various facets, even between the two polar facets perpendicular to the *c* axis, can be related to differences in the passivating strength of surfactant molecules.<sup>30</sup> In principle, it would be possible to exploit this concept to allow for the nucleation of a second material only on one polar facet of a wurtzite nanocrystal. In this communication, we report the selective growth of spherical PbSe nanocrystals on the tips of CdSe and CdS nanorods. The remarkable difference in reactivity among the various facets of the rods is clearly demonstrated for CdS as PbSe can be grown either on both tips of a rod or just on one tip, by carefully adjusting the synthesis conditions.

Nanorods of CdSe and CdS were prepared using octadecylphosphonic acid as promoter of anisotropic growth, according to the procedure of Peng and co-workers, although with minor changes (see Supporting Information).<sup>27,29</sup> Sulfur or selenium were supplied to the reaction flask as trioctyl phosphine sulfide and trioctylphosphine selenide, respectively. After the synthesis, the rods were precipitated from the solution by the addition of methanol. This procedure yielded nanorods mixed with a gel due to unreacted Cd-phosphonate precursor. The separation of the nanorods from this gel is described in detail in the Supporting Information. The selective growth of PbSe nanocrystals on the nanorods was carried out by first dissolving the nanorods in diphenyl ether. To this solution a stock solution was injected which contained trioctylphosphine selenide, lead acetate, oleic acid, and diphenyl ether. These conditions were similar to those employed by Wehrenberg and co-workers to prepare monodisperse PbSe nanocrystals,<sup>31</sup> although lower temperatures and lower concentrations of PbSe precursors were used here.

The selective growth of PbSe on both tips of CdSe nanorods (Figure 1a) was relatively straightforward. It was achieved by keeping the reaction temperature at 130 °C and by injecting dropwise the stock solution of the PbSe precursors. This procedure yielded dumbbell-shaped, PbSe–CdSe–PbSe hybrid nanocrystals (Figure 1b) and almost no isolated PbSe nanocrystals. Higher temperature decreased the selectivity in the end-growth since, under this circumstance, PbSe started forming also on the lateral facets of the rods.

The above conditions were extended to CdS nanorods (Figure 2a). In this case, only the homogeneous nucleation of PbSe nanocrystals in solution was observed, with no growth at all on the preformed semiconductor rods. Selective

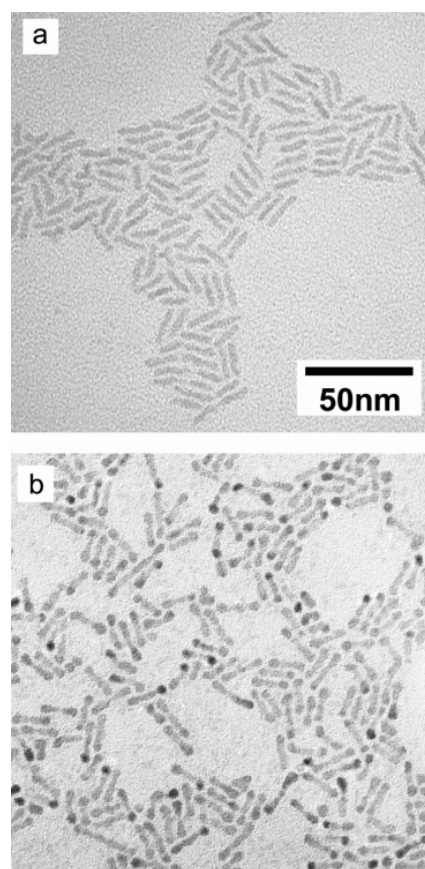


**Figure 1.** Low-resolution transmission electron microscopy (TEM) images of CdSe nanorods (a) and of dumbbell shaped PbSe–CdSe–PbSe nanocrystal heterostructures (b).

growth of PbSe on CdS nanocrystals required both higher temperature and a fast injection of PbSe precursors (the injection temperature was 190 °C, the growth temperature was 150 °C), while growth on the lateral facets was never observed. These stronger conditions required to form PbSe–CdS–PbSe dumbbells always led to the additional nucleation of isolated PbSe nanocrystals, from which dumbbells could be isolated via size-selective precipitation. In the final sample, the yield of dumbbells, estimated as the fraction of dumbbells with respect to other structures from statistical analysis of TEM images, was larger than 55%. A lower concentration of PbSe precursors, delivered in the fast injection, reduced the nucleation of isolated nanocrystals drastically and promoted the preferential growth of PbSe on only one tip of the CdS rods (Figure 2b,c). In this case, at least 60–65% of the sample consisted of heterostructures showing a PbSe dot just at one tip of the CdS rod, and the remaining nanocrystals were mostly “asymmetric” dumbbells, in which one PbSe domain at one tip of the rods was usually much larger than the PbSe domain at the other tip.

Powder X-ray diffraction<sup>32</sup> of spherical PbSe nanocrystals, CdS nanorods and PbSe–CdS–PbSe dumbbells are reported in Figure 3. The spectrum of the CdS nanorod sample indicates the presence of the hexagonal wurtzite structure.

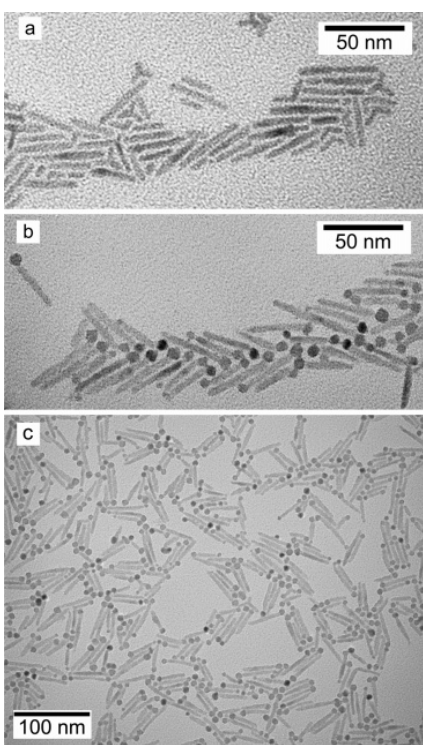


**Figure 2.** Low-resolution TEM images of CdS nanorods (a) and CdS–PbSe heterostructures with PbSe preferentially grown on one tip of the rods (b, c).

The comparison with the diffraction pattern of bulk CdS shows a high degree of distortion of the intensity ratios due to shape anisotropy,<sup>6</sup> which results in an enhancement of the reflections associated with crystalline domains along the *c* axis. The spectrum of isolated dots indicates, on the other hand, that PbSe crystallizes in its typical rock-salt structure. The representative diffraction spectra for CdS-based dumbbells present only peaks which can be attributed either to the PbSe rock salt or to the CdS wurtzite structures. Therefore we conclude that PbSe grows on the nanorod tips in the rock-salt structure.

High-resolution TEM<sup>33</sup> of CdSe- and CdS-based dumbbells (Figure 4) shows that in both cases PbSe crystallizes in the rock-salt structure on the tips of wurtzite nanorods, in agreement with the XRD results. The formation of nanocrystal heterostructures, with sections having remarkably different crystal structures, was shown recently for the case of gold tipped nanorods and tetrapods.<sup>14</sup> Gold domains were reported to grow with no preferential crystallographic orientation with respect to the underlying wurtzite lattice. In our case, however, PbSe domains show a preferential orientation with respect to the substrate. In the majority of heterostructures based on CdS or on CdSe, the 002 planes of PbSe rock salt were aligned with the 100 planes of CdS or CdSe wurtzite (Figure 4a,b).

The structure of the interface between PbSe and CdSe or between PbSe and CdS is not clear. Certainly, we cannot expect perfect epitaxial growth of a rock-salt island on top

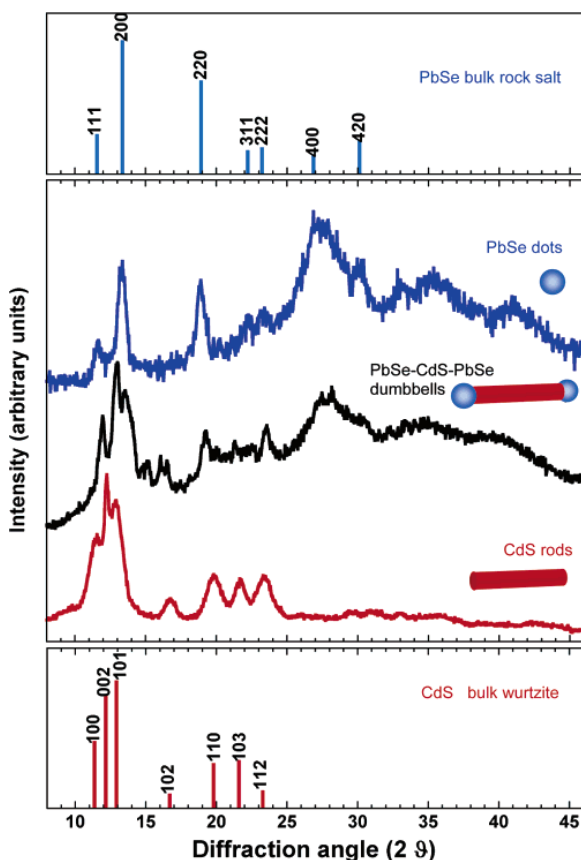


**Figure 3.** XRD spectra of PbSe dots, CdS rods, and PbSe–CdS–PbSe dumbbells are compared with the diffraction pattern of bulk rock-salt PbSe and wurtzite CdS.

of a wurtzite substrate, and therefore this interface should be highly defective, with considerable strain developing and with unsaturated dangling bonds left. The tips of the rods, prior to PbSe end-growth, do not show a sharp 001 or 00̄1 termination (Figures 1a and 2a). Consequently, the wurtzite–rock-salt interface does not develop just along two facets, for instance between the 00̄1 facet of wurtzite and the 100 facet of rock salt, but between several couples of facets between the two phases. This more complex interface might provide pathways for releasing and/or compensating the strain that can develop locally along a specific couple of facets.

The reasons underlying the large differences in reactivity among the various facets of the wurtzite structure, which allow for the selective growth on the tips of the rods, are still under investigation. So far, the indication is that this is driven by the difference in the binding energy of the surfactant molecules to the different facets.<sup>29,30</sup> The results of our experiments do not allow us to recognize whether the 001 or the 00̄1 facet is the most reactive. There is, however, evidence that the surfactants that are almost exclusively bound to the surface of nanocrystals are those that form strong complexes with Cd<sup>2+</sup> ions in the growth solution but not with Se or S (for instance phosphonates<sup>29</sup> or carboxylates<sup>12</sup>). Moreover, in semiconductors, as a

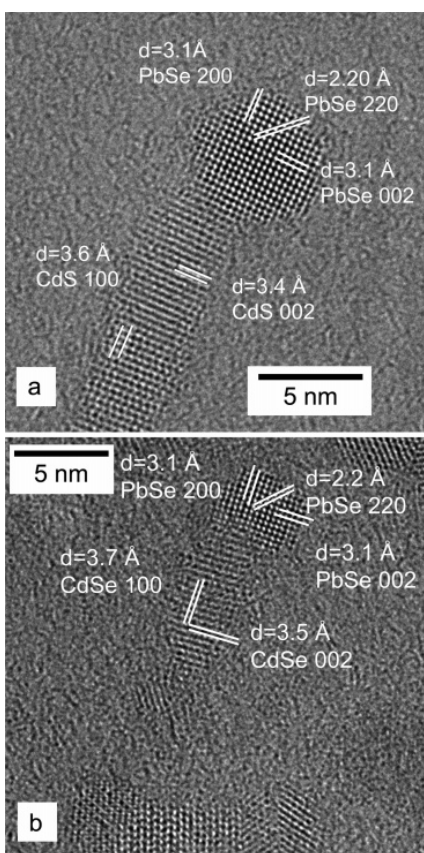


**Figure 4.** High-resolution TEM images of PbSe–CdS–PbSe (a) and PbSe–CdSe–PbSe dumbbells (b) with the corresponding interplanar distances. Image analysis shows that cubic PbSe dots grow at the tips of the CdS or CdSe hexagonal rods. HRTEM observations rule out heteroepitaxial growth of PbSe on the lateral facets of the rods.

consequence of surface reconstruction,<sup>34</sup> the dangling bonds of surface cations (Cd) are empty whereas the dangling bonds of surface anions (S, Se) are filled. If this concept is extended to the surface atoms of nanocrystals, one can argue that these Lewis base surfactants should bind exclusively to electron deficient surface Cd atoms and leave the surface S or Se atoms unpassivated. Therefore, we can speculate that incomplete or weak passivation of surface Cd atoms on a given facet is the main cause of instability for that facet, resulting in higher reactivity. Based on this assumption, the  $00\bar{1}$  facet is the most reactive one as it can expose Cd atoms with three dangling bonds each. On this facet, it is unlikely for all these dangling bonds to be passivated efficiently by bulky surfactant molecules, and therefore some of these bonds can serve as active sites for further growth.

Nanocrystal heterostructures represent unique systems in which the optical and electronic properties can be tuned by varying the chemical composition of their components and their mutual distance. Dumbbell-shaped nanocrystals, as the ones reported in this work, are composed of two PbSe quantum dots separated by a large potential barrier (either the CdSe or the CdS rod section). The height of this barrier

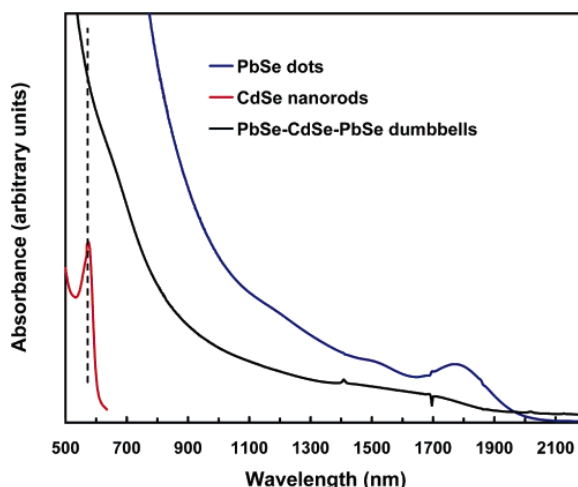


**Figure 5.** Optical absorption spectra of CdSe nanorods (red line), of spherical PbSe dots (blue line) and of PbSe–CdSe–PbSe dumbbells (black line), respectively.

can be adjusted by varying the diameter and the length of the rod. In Figure 5, the absorption spectra of a sample of CdSe nanorods, of a sample of spherical PbSe nanocrystals and of a corresponding PbSe–CdSe–PbSe dumbbell sample are shown, respectively. The exciton peak from the CdSe section is absent in the dumbbell spectrum, as the PbSe tips significantly modify the electronic structure of the starting rods. Although the carriers can be photogenerated over the whole dumbbell structure, we can expect that they are mainly localized at the PbSe tips. This peculiar property could be exploited, for instance, to align dumbbells under electric fields while they are photoexcited. The electric field would help to localize the photogenerated electrons and holes in the opposite PbSe tips, resulting in a large dipole moment that would help to align the rod under the field.

A heterostructure consisting of a nanorod with a single nanosphere attached to one tip (as the one reported in Figure 2) provides a particularly appealing structure. The potential exists for the tip of a magnetic material to act as a preferential anchoring point for the nanorod to a substrate, or as a “navigation” sensor.

This work shows that the development of approaches for the controlled growth of nanocrystalline heterostructures may significantly expand the range of applications of colloidal nanocrystals. The ease of fabrication of large amounts of nanocrystalline heterostructures by means of solution procedures fulfills an important requirement for their use as building blocks in nanotechnology.

**Acknowledgment.** This work was funded by the German research foundation (DFG, Emmy Noether program), the Deutscher Akademischer Austauschdienst (DAAD, Vigoni Funds), the Fonds der Chemischen Industrie, and by the Italian MIUR (FIRB and Vigoni Funds). We thank Dr. Mauro Lomascolo for helpful discussions.

**Supporting Information Available:** Description of the various nanocrystal syntheses, XRD characterization of the

intermediate heterostructure with PbSe dots only at one tip of a CdS rod, low resolution TEM image of PbSe–CdS–PbSe dumbbells, and optical spectra of CdS–PbSe heterostructures. This material is available free of charge via the Internet at <http://pubs.acs.org>.

## References

- Priester, C.; Lannoo, M. *Phys. Rev. Lett.* **1995**, 75(1), 93–96.
- Morales, A. M.; Lieber, C. M. *Science* **1998**, 279(5348), 208–211.
- Duan, X. F.; Lieber, C. M. *Adv. Mater.* **2000**, 12(4), 298–302.
- Bjork, M. T.; Ohlsson, B. J.; Sass, T.; Persson, A. I.; Thelander, C.; Magnusson, M. H.; Deppert, K.; Wallenberg, L. R.; Samuelson, L. *Nano Lett.* **2002**, 2(2), 87–89.
- Dick, K. A.; Deppert, K.; Larsson, M. W.; Martensson, T.; Seifert, W.; Wallenberg, L. R.; Samuelson, L. *Nature Mater.* **2004**, 3(6), 380–384.
- Peng, X. G.; Manna, L.; Yang, W. D.; Wickham, J.; Scher, E.; Kadavanich, A.; Alivisatos, A. P. *Nature* **2000**, 404(6773), 59–61.
- Kim, Y. H.; Jun, Y. W.; Jun, B. H.; Lee, S. M.; Cheon, J. W. *J. Am. Chem. Soc.* **2002**, 124(46), 13656–13657.
- Lee, S. M.; Jun, Y. W.; Cho, S. N.; Cheon, J. *J. Am. Chem. Soc.* **2002**, 124(38), 11244–11245.
- Puntes, V. F.; Zanchet, D.; Erdonmez, C. K.; Alivisatos, A. P. *J. Am. Chem. Soc.* **2002**, 124(43), 12874–12880.
- Jun, Y. W.; Lee, S. M.; Kang, N. J.; Cheon, J. *J. Am. Chem. Soc.* **2001**, 123(21), 5150–5151.
- Manna, L.; Milliron, D. J.; Meisel, A.; Scher, E. C.; Alivisatos, A. P. *Nature Mater.* **2003**, 2(6), 382–385.
- Yu, W. W.; Wang, Y. A.; Peng, X. G. *Chem. Mater.* **2003**, 15(22), 4300–4308.
- Milliron, D. J.; Hughes, S. M.; Cui, Y.; Manna, L.; Li, J. B.; Wang, L. W.; Alivisatos, A. P. *Nature* **2004**, 430(6996), 190–195.
- Mokari, T.; Rothenberg, E.; Popov, I.; Costi, R.; Banin, U. *Science* **2004**, 304(5678), 1787–1790.
- Gu, H. W.; Zheng, R. K.; Zhang, X. X.; Xu, B. *J. Am. Chem. Soc.* **2004**, 126(18), 5664–5665.
- Hu, J. T.; Li, L. S.; Yang, W. D.; Manna, L.; Wang, L. W.; Alivisatos, A. P. *Science* **2001**, 292(5524), 2060–2063.
- Rothenberg, E.; Ebenstein, Y.; Kazes, M.; Banin, U. *J. Phys. Chem. B* **2004**, 108(9), 2797–2800.
- Kazes, M.; Lewis, D. Y.; Ebenstein, Y.; Mokari, T.; Banin, U. *Adv. Mater.* **2002**, 14(4), 317–321.
- Huynh, W. U.; Dittmer, J. J.; Alivisatos, A. P. *Science* **2002**, 295(5564), 2425–2427.
- Hines, M. A.; Guyot-Sionnest, P. *J. Phys. Chem.* **1996**, 100(2), 468–471.
- Dabbousi, B. O.; Rodriguez-Viejo, J.; Mikulec, F. V.; Heine, J. R.; Mattoussi, H.; Ober, R.; Jensen, K. F.; Bawendi, M. G. *J. Phys. Chem. B* **1997**, 101(46), 9463–9475.
- Peng, X. G.; Schlamp, M. C.; Kadavanich, A. V.; Alivisatos, A. P. *J. Am. Chem. Soc.* **1997**, 119(30), 7019–7029.
- Cao, Y. W.; Banin, U. *J. Am. Chem. Soc.* **2000**, 122(40), 9692–9702.
- Eychmuller, A.; Mews, A.; Weller, H. *Chem. Phys. Lett.* **1993**, 208(1–2), 59–62.
- Zeng, H.; Li, J.; Wang, Z. L.; Liu, J. P.; Sun, S. H. *Nano Lett.* **2004**, 4(1), 187–190.
- Cao, Y. W.; Jin, R.; Mirkin, C. A. *J. Am. Chem. Soc.* **2001**, 123(32), 7961–7962.
- Peng, Z. A.; Peng, X. G. *J. Am. Chem. Soc.* **2001**, 123(7), 1389–1395.
- Manna, L.; Scher, E. C.; Alivisatos, A. P. *J. Am. Chem. Soc.* **2000**, 122(51), 12700–12706.
- Peng, Z. A.; Peng, X. G. *J. Am. Chem. Soc.* **2002**, 124(13), 3343–3353.
- Puzder, A.; Williamson, A. J.; Zaitseva, N.; Galli, G.; Manna, L.; Alivisatos, A. P. *Nano Lett.* **2004**, 4(12), 2361–2365.
- Wehrenberg, B. L.; Wang, C. J.; Guyot-Sionnest, P. *J. Phys. Chem. B* **2002**, 106(41), 10634–10640.
- XRD spectra were collected using a D500 Siemens diffractometer equipped with Mo K $\alpha$  radiation and a graphite monochromator on the diffracted beam. Phase identification was performed according to the Powder Diffraction File database [PDF-2 File, JCPDS International Center for Diffraction Data, 1601 Park Lane, Swarthmore, PA 1998].
- HRETEM measurements were performed at the CEMES/CNRS Laboratory in Toulouse on a FEI SACTEM microscope, equipped with a field emission electron source operating at 200 kV and with a spherical aberration corrector.
- Duke, C. B. *Chem. Rev.* **1996**, 96, 1237–1259.

NL048060G

# Selective growth of PbSe on one or on both tips of colloidal semiconductor nanorods

*Stefan Kudera<sup>a</sup>, Luigi Carbone<sup>b</sup>, Maria Francesca Casula<sup>c</sup>, Roberto Cingolani<sup>b</sup> Andrea Falqui<sup>c</sup>, Etienne Snoeck<sup>d</sup>, Wolfgang J. Parak<sup>a\*</sup> and Liberato Manna<sup>b\*</sup>*

<sup>a</sup> Center for Nanoscience, Ludwig Maximilians Universität München, Munich, Germany

<sup>b</sup> National Nanotechnology Laboratory of INFM, Via Arnesano Km 5, 73100 Lecce, Italy

<sup>c</sup> Dipartimento di Scienze Chimiche, Università di Cagliari, 09042 Monserrato, Cagliari, Italy

<sup>d</sup> CEMES/CNRS, 29 Rue Jeanne Marvig, 31055 Toulouse, France

Corresponding authors: [Wolfgang.Parak@physik.uni-muenchen.de](mailto:Wolfgang.Parak@physik.uni-muenchen.de),  
[liberato.manna@unile.it](mailto:liberato.manna@unile.it)

## Supplementary information

### General

TOPO (trioctylphosphine oxide, technical grade, Product number #089793) was purchased from Alfa Aesar. ODPA (octadecylphosphonic acid) was purchased from

PolyCarbon Industries. Selenium (99.99%, #34-0090), Cadmium oxide (CdO, 99.999%, #48-0800), TOP (trioctylphosphine, 97%, #15-6655) and TBP (tributylphosphine, 99%, #15-5800) were purchased from Strem. Diphenyl ether (99+, #24,083-4), oleic acid (90%, #36,452-5), Pb(II)acetate trihydrate (#46,786-3), nonanoic acid (97+, #N5502) were purchased from Sigma-Aldrich. All syntheses were carried out in standard air-free conditions.

### Synthesis and purification of nanorods of CdSe

Nanorods of CdSe and CdS were prepared following the procedure of Peng and coworkers,<sup>1, 2</sup> with minor changes. For the synthesis of CdSe nanorods, 4.2g TOPO, 1.56g ODPA and 0.297g CdO were mixed in a 50mL flask, degassed for 10-20 minutes and heated to 320°C under nitrogen. At this temperature, the CdO decomposed after several minutes, and the solution turned completely transparent only after the addition of 1 g of TOP. After the temperature had stabilized at 320°C, a mixture of 2.095g of TOP, 0.51g of toluene and 0.391g of Se:TBP (25% selenium in weight) was injected into the solution, causing a temperature drop to around 250°C. The rods nucleated and were allowed to grow at 250°C for 20 minutes, whereupon the reaction was stopped by removing the heating mantle. In order to separate the nanorods from the growth solution, toluene was added to the solution before it solidified, along with a few mL of nonanoic acid. The resulting solution was heated until it turned clear ( $\approx$ 100°C), whereupon it was allowed to cool down to room temperature. Finally, this solution was centrifuged for some minutes, yielding a gel as precipitate, which clearly had engulfed also nanocrystals. However, a large fraction of nanocrystals remained in the supernatant from which they could be extracted by precipitation with methanol. More particles were extracted from the gel by repeating the cycle of addition of toluene and nonanoic acid, heating, centrifugation and purification of the clear supernatant.

### Synthesis and purification of nanorods of CdS

For the synthesis of CdS nanorods, 6.64g TOPO, 0.816g ODPA and 0.105g CdO were mixed in a 50mL flask, degassed for 10-20minutes and heated to 320°C under nitrogen. After a clear and colorless solution had formed, 1.5g TOP were injected. As the

temperature of the solution stabilized, 0.5g of TOP:S (6% sulfur in weight) were injected. After approximately one minute a color change was observed, indicating the nucleation of CdS nanocrystals. The rods were allowed to grow for 8 minutes, whereupon the heating mantle was removed. When the solution reached a temperature of 100°C, 3-5mL toluene were injected to prevent solidification. The CdS nanorods were precipitated by addition of methanol, after the solution had cooled down to room temperature. In some cases, a gel-like precipitate formed also in this synthesis. The nanorods could be separated from the gel either by following the same procedure as had been used for CdSe rods, or by an alternative approach (which also worked for CdSe rods). Briefly, the gel was suspended in chloroform through vigorous shaking. After the solution was at rest for some hours, two phases formed. The upper phase contained the gel engulfing the nanorods, whereas the lower phase contained only the nanorods in chloroform. The two phases could be separated with a separation funnel. By addition of chloroform to the remaining gel in the funnel additional nanorods could be extracted.

### **Synthesis of PbSe nanocrystals**

PbSe particles were prepared following the procedure employed by Wehrenberg and coworkers.<sup>3</sup> Lead(II)acetate (654 mg), Oleic Acid (1.5 mL), Diphenyl Ether (2 mL) and TOP (8 mL) were loaded into a 50mL flask (flask I). A second flask with 10mL Diphenyl Ether was prepared (flask II). Both flasks were heated to  $\approx$ 100°C and degassed for one hour. Flask I was then cooled to room temperature under nitrogen and flask II was heated to 180°C. 1.5mL of 1M Se:TOP (8.6% selenium in weight) were added to flask I and the whole content of flask I was quickly injected into Flask II. The temperature dropped to 110°C and raised again to 150°C after 2-3 minutes. The reaction was allowed to proceed at this temperature for additional 2-3 minutes, for an overall reaction time of 5-6 minutes. After the synthesis, the particles were extracted and purified by repeated precipitation with methanol and dissolution in chloroform.

### **Selective growth of PbSe on nanorods**

Selective growth of PbSe on CdSe and CdS nanorods was carried out with minor modifications of the protocol followed to grow PbSe nanocrystals. In flask I, all

chemicals as in the synthesis of PbSe nanocrystals were added, except for TOP. In flask II, the diphenyl ether was first degassed, then a solution of nanorods in chloroform was injected into it under nitrogen. The chloroform was evaporated by pumping the solution to vacuum for a few minutes.

When CdSe nanorods were used, the fast injection of the PbSe precursors led to the formation of free PbSe particles, in addition to selective growth on the rod tip. Moreover, the final sample contained also a small percentage of the original CdSe rods with no PbSe on their tips. A uniform sample was obtained by slowly injecting the PbSe precursors. Slow injections of 1mL of precursors were performed over a period of 1-2 minutes, separated by a waiting period of 3 minutes, within which the precursors injected were allowed to react. This procedure led to a uniform sample that contained mostly PbSe-CdSe-PbSe dumbbells. A detailed protocol of a typical synthesis is as follows: Flask I was loaded with 2 mL diphenyl ether, 1.5mL oleic acid and 0.657g Lead(II)acetate. Flask II was loaded with 10 mL diphenyl ether. After degassing both flasks at 100°C, flask I was cooled down to room temperature and 1.33g of 1M TOP:Se (8.6% selenium in weight) was injected into it. A solution of CdSe nanorods (2.2mL) in chloroform was injected into flask II, the chloroform was evaporated, and the temperature of the flask was set to 130°C. Then the PbSe-precursors from flask I were slowly injected into flask II. An estimate of the actual amount of CdSe nanorods injected was given by optical absorption, as the experiments were performed with a solution of CdSe nanorods that contained a residual gel (Complete purification of the rods from the gel was difficult to achieve). The optical density at the first exciton peak (590nm) of the CdSe nanorods used was 0.12 in a 1cm cuvette, when the original solution was diluted by a factor of 40. Assuming that the extinction coefficient of rods is comparable to that of dots having the same diameter as the rods,<sup>4</sup> the amount of rods used could be estimated as 40nmol.

In the case of PbSe-CdS-PbSe particles, a slow injection led to the formation of mostly free PbSe particles and almost no PbSe growth on the rods was observed. Better results were achieved with fast injections. The particles shown in Figure 2 of the paper were synthesized according to the following protocol: Flask I was loaded with 0.330g lead(II)acetate, 2 mL diphenyl ether and 1.5mL oleic acid. After dissolving the lead acetate, degassing the solution, and cooling it to room temperature under nitrogen,

0.85mL of 1M TOP:Se (8.6% selenium in weight) was injected into this flask. Flask II contained 10mL diphenyl ether. Half of the product of one CdS synthesis was later injected into the diphenyl ether (approximately 50mg). Flask I, containing Pb and Se precursors was injected into flask II at 190°C, and during the reaction the temperature of solution stayed at 150°C.

A statistical analysis was performed on TEM images to determine the relative concentration of PbSe-CdS matchstick structures and of PbSe-CdS-PbSe dumbbells structures. More than 600 particles of each sample were analyzed. With the described synthesis, more than 60% of the CdS-rods were modified with PbSe spheres only on one of their tips. Most of the remaining CdS-rods had PbSe spheres on both tips, and only few rods without any PbSe attached were found. In Figure S1 we report the XRD spectrum of the sample consisting mainly of CdS-PbSe matchsticks. As discussed for the XRD spectrum of the CdS-PbSe-CdS dumbbells sample, we observe both peaks due to PbSe rock salt nanocrystals and to CdS wurtzite crystalline domains (elongated along the *c*-axis).

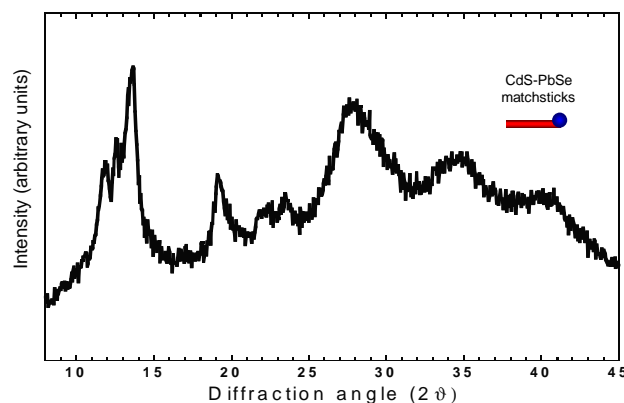


**Figure S1.** XRD spectrum of the CdS-PbSe sample where rock salt PbSe dots mainly grow only on one tip of the CdS rods.

When the amount of Pb- and Se-precursors was doubled without changing the other conditions, the synthesis favored slightly the generation of PbSe-CdS-PbSe dumbbell-structures. In this case, less than 45% of the particles formed the PbSe-CdS matchstick-

structure. A typical low-resolution TEM image of a sample of PbSe-CdS-PbSe dumbbell nanocrystals is reported in Figure S2.

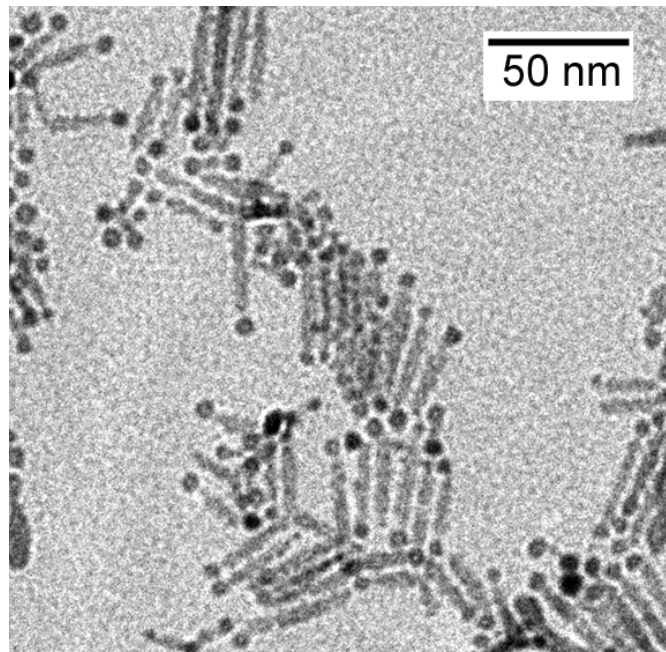


**Figure S2.** Low resolution TEM of PbSe-CdS-PbSe dumbbell nanocrystals.

The optical features of the parent CdS rods and PbSe dots and of the corresponding matchstick and dumbbell heterostructures have been investigated by optical absorption. In Figure S3 we report the optical absorption spectra of CdS nanorods and PbSe spherical dots (a), and of PbSe-CdS-PbSe dumbbells and PbSe-CdS matchsticks (b). As expected, the spectra of the matchstick and dumbbell heterostructures are very similar and they substantially differ from those of the isolated PbSe dots and CdS rods, as discussed for the CdSe-based structures.

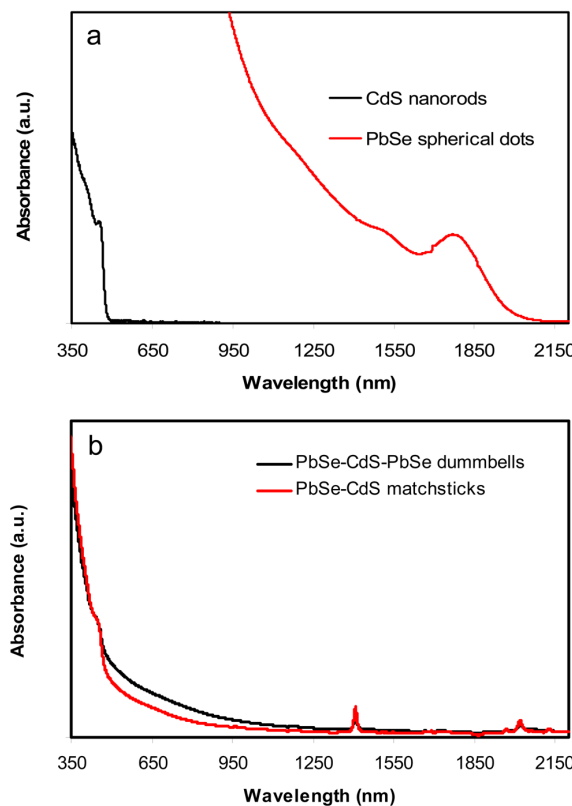


**Figure S3.** Optical absorption spectra of CdS nanorods and PbSe spherical dots (a), and of PbSe-CdS-PbSe dumbbells and PbSe-CdS matchsticks (b).

## References

1. Peng, Z. A.; Peng, X. G., Mechanisms of the shape evolution of CdSe nanocrystals. *Journal of the American Chemical Society* **2001**, 123, (7), 1389-1395.
2. Peng, Z. A.; Peng, X. G., Nearly monodisperse and shape-controlled CdSe nanocrystals via alternative routes: Nucleation and growth. *Journal of the American Chemical Society* **2002**, 124, (13), 3343-3353.
3. Wehrenberg, B. L.; Wang, C. J.; Guyot-Sionnest, P., Interband and intraband optical studies of PbSe colloidal quantum dots. *Journal of Physical Chemistry B* **2002**, 106, (41), 10634-10640.
4. Yu, W. W.; Qu, L. H.; Guo, W. Z.; Peng, X. G., Experimental determination of the extinction coefficient of CdTe, CdSe, and CdS nanocrystals. *Chemistry of Materials* **2003**, 15, (14), 2854-2860.

## C.2 Selective reactions on the tips of colloidal semiconductor nanorods

L. CARBONE, S. KUDERA, C. GIANNINI, G. CICCARELLA, R. CINGOLANI, P.D. COZZOLI, L. MANNA

*J. Mater. Chem.* **16**(40), pp. 3952–3956, 2006

A strategy to access several types of Au- tipped dumbbell- like nanocrystal heterostructures is presented, which involves the selective oxidation of either PbSe or CdTe sacrificial domains, initially grown on CdSe and CdS nanorods, with a Au(III): surfactant complex. The formation of gold patches is supported by TEM, XRD and elemental analysis. This approach has allowed us to grow Au domains onto specific locations of anisotropically shaped nanocrystals for which direct metal deposition is unfeasible, as for the case of CdS nanorods. We believe that this strategy may be of general utility to create other types of complex colloidal nanoheterostructures, provided that a suitable sacrificial material can be grown on top of the starting nanocrystal seeds.

## Selective reactions on the tips of colloidal semiconductor nanorods†

Luigi Carbone,<sup>a,b</sup> Stefan Kudera,<sup>a</sup> Cinzia Giannini,<sup>c</sup> Giuseppe Ciccarella,<sup>a</sup> Roberto Cingolani,<sup>a</sup> Pantaleo Davide Cozzoli\*<sup>a</sup> and Liberato Manna\*<sup>a</sup>

Received 22nd May 2006, Accepted 21st June 2006  
First published as an Advance Article on the web 6th July 2006  
DOI: 10.1039/b607217h

A strategy to access several types of Au-tipped dumbbell-like nanocrystal heterostructures is presented, which involves the selective oxidation of either PbSe or CdTe sacrificial domains, initially grown on CdSe and CdS nanorods, with a Au(III) : surfactant complex. The formation of gold patches is supported by TEM, XRD and elemental analysis. This approach has allowed us to grow Au domains onto specific locations of anisotropically shaped nanocrystals for which direct metal deposition is unfeasible, as for the case of CdS nanorods. We believe that this strategy may be of general utility to create other types of complex colloidal nanoheterostructures, provided that a suitable sacrificial material can be grown on top of the starting nanocrystal seeds.

### 1. Introduction

Colloidal inorganic nanocrystals (NCs) represent a class of materials which is under intensive investigation in various fields of nanoscience. Advances in the fabrication methods of such nanoscale objects have led to systematic tuning of their size and shape for a wide range of materials<sup>1–3</sup> and, recently, to fine topological control over their composition.<sup>4–12</sup> Hybrid NCs formed by sections of two or more materials joined in a unique particle would be technologically advantageous, because they could perform multifunctional tasks based on the specific properties (such as, for instance, fluorescence and magnetism) which are characteristic of each domain. Examples of these novel nanostructure types are heterodimers made of spherical domains of two materials (for instance CdS and FePt,<sup>4</sup> CoPt<sub>3</sub> and Au,<sup>5</sup>  $\gamma$ -Fe<sub>2</sub>O<sub>3</sub> and Au, Ag and Au,<sup>6</sup> Fe<sub>3</sub>O<sub>4</sub> and Au,<sup>7</sup> and so on), linear and branched junctions of two different types of semiconductors,<sup>8</sup> dumbbell-like<sup>9,10</sup> and matchstick-shaped NCs,<sup>10–12</sup> in which domains of a metal or a semiconductor are grown on one or both tips of a starting semiconductor nanorod. In the latter cases, selective growth of the second material on such locations is possible, as the basal facets are not as efficiently passivated by surfactant molecules as the lateral facets of the rods.<sup>9–12</sup> Recently reported examples are nanodumbbells in which the starting rod is either CdS or CdSe and the domains at the tips are either Au<sup>9,12</sup> or PbSe.<sup>10</sup> The presence of Au patches on NCs is especially desirable because such domains can be used as preferential anchoring points onto which organic molecules or biomolecules can be selectively attached.<sup>6,9</sup> Unfortunately, it is not easy to grow Au domains on any type of nanocrystal. While, for instance, this

has been demonstrated for CdSe nanorods<sup>9,12</sup> and for roughly spherical CoPt<sub>3</sub>,<sup>5</sup> Ag<sup>6</sup> and iron oxide NCs,<sup>6,7</sup> on other types of nanocrystals such growth still represents an open challenge. As an example, we have tried in our labs to grow Au directly onto CdS nanorods using these established approaches,<sup>5–7,9</sup> however with no success. Here, we report a method by which Au can be grown on both CdSe and CdS nanorods, by performing a two-step reaction. First, a sacrificial material, that can be either PbSe or CdTe, is nucleated on the tips of the rods. Later, these domains are oxidized by means of a Au(III) : surfactant complex, which partially replaces them, leading to the formation of Au patches on the rod terminations. The structure of the hybrid nanocrystals was verified by a combination of low resolution Transmission Electron Microscopy (TEM) investigation, Powder X-ray Diffraction (XRD) measurements, and Inductively Coupled Plasma Atomic Emission Spectroscopy (ICP-AES) elemental analysis.

### 2. Experimental

All syntheses were carried out in a standard Schlenk line set-up under nitrogen flow. Gold growth on the dumbbells was carried out in a glove-box under nitrogen atmosphere. The samples were washed and stored in the glove-box.

#### 2.1. Chemicals

Cadmium oxide (CdO, 99.999%), tri-n-octylphosphine oxide (TOPO, 99%), tri-n-octylphosphine (TOP, 97%), tri-n-butylphosphine (TBP, 97%), tellurium powder (99.999%), sulfur powder (99%), selenium powder (99.99%) and hydrogen tetrachloroaurate(III) hydrate (HAuCl<sub>4</sub>, 99.9%) were purchased from Strem Chemicals. n-Octadecylphosphonic acid (ODPA, 99%) and n-hexadecylphosphonic acid (HPA, 99%) were purchased from Polycarbon Industries. Lead(II) acetate trihydrate (99.95%), diphenyl ether (99%), oleic acid (90%), n-dodecylamine (DDA, 98%) and didodecyldimethyl-ammonium bromide (DDAB, 98%) were purchased from Sigma Aldrich. All solvents, such as toluene or chloroform, were anhydrous and purchased from Aldrich.

<sup>a</sup>National Nanotechnology Laboratory of CNR-INFM, Distretto Tecnologico ISUFI, 73100, Lecce, Italy. E-mail: davide.cozzoli@unile.it; liberato.manna@unile.it

<sup>b</sup>Istituto Superiore Universitario Formazione Interdisciplinare, ISUFI, Via Per Arnesano, 73100, Lecce, Italy

<sup>c</sup>CNR-Istituto di Cristallografia (IC), via Amendola 122/O, 70126, Bari, Italy

† This paper is part of a *Journal of Materials Chemistry* theme issue on Anisotropic Nanomaterials. Guest editor: Luis Liz-Marzan.

Stock precursor solutions of Te:TOP (10% wt), S:TOP (6% wt) and Se:TBP (8% wt) were freshly prepared in a glovebox before use.

## 2.2. Synthesis of semiconductor nanodumbbells

**PbSe–CdSe–PbSe nanodumbbells.** These nanodumbbells were prepared by a two-step synthesis as described in ref. 10, with minor modifications. For the preparation of the CdSe nanorods, a mixture of TOPO (3 g), ODPA (0.430 g), HPA (0.130 g) and CdO (0.160 g) was heated to 350 °C in a flask under inert atmosphere. Then, 2.5 g of the Se:TBP stock solution was added rapidly to the hot surfactant mixture under vigorous stirring and the temperature was kept at 280 °C for 6 min. After the synthesis, the flask was cooled to room temperature, and methanol was added to induce the precipitation of the CdSe nanorods. The CdSe precipitate was collected by centrifugation, then washed twice, and finally solubilized in 10 mL of toluene. PbSe–CdSe–PbSe nanocrystal dumbbells were synthesized by growing PbSe tips selectively onto the basal facets of the CdSe nanorods in a subsequent synthesis step. For this purpose, 1 mL of the purified CdSe nanorod solution described above was diluted with 10 mL of previously degassed diphenyl ether and heated to 130 °C. Then, a Pb–Se precursor solution consisting of oleic acid (1.5 mL), diphenyl ether (2 mL), lead acetate (0.660 g), and Se:TOP (1.3 g) was injected dropwise over a period of 10 min.

After the synthesis the reaction mixture was cooled to room temperature, and the PbSe–CdSe–PbSe nanodumbbells were extracted and purified as described above for the CdSe nanorods.

**CdTe–CdS–CdTe nanodumbbells.** These nanodumbbells were prepared following the one-pot approach described in ref. 8. CdS nanorods were grown in a mixture of TOPO (3 g), ODPA (0.385 g), CdO (0.050 g) and TOP (1.5 mL) at 360 °C. The synthesis was started by rapid injection of 0.600 g of the S:TOP stock solution into the vigorously stirred surfactant mixture. After 1 min of reaction, the heat source was removed temporarily and the solution was allowed to cool and stabilize at 320 °C. To grow CdTe tips onto the CdS nanorods, 0.180 g of Te:TOP stock solution was rapidly injected into the flask and allowed to react for an additional 5 min.

After the synthesis, the reaction mixture was cooled to room temperature, and the CdTe–CdS–CdTe nanodumbbells were extracted and purified as described above.

## 2.3. Deposition of metallic gold onto the tips of the nanocrystal dumbbells

A Au(III) : surfactant stock solution was prepared as follows: HAuCl<sub>4</sub> (0.011 g), DDA (0.078 g) and DDAB (0.034 g) were co-dissolved in 7 mL of toluene by sonication. During this process, the colour of the solution changed from orange to pale yellow. 0.5–2 mL of this stock solution was added dropwise to a vigorously stirred diluted solution of nanocrystal dumbbells (roughly 5 mg of dumbbells in 3 mL of toluene) at a rate of 0.2 mL min<sup>−1</sup>. The formation of metallic gold was accompanied by a progressive darkening of the solution which occurred in 1–5 min. After Au(III) addition, the mixture was

allowed to react for an additional 5 min, after which the nanocrystals were precipitated with methanol, washed once, and finally redispersed in toluene.

## 2.4. Characterization

**Transmission electron microscopy (TEM).** Samples for TEM were prepared by dropping dilute solutions of nanocrystals onto carbon coated copper grids and leaving the solvent to evaporate. TEM images were recorded on a JEOL Jem 1011 microscope operating at 100 kV.

**Powder X-ray diffraction (XRD) analysis.** XRD measurements were performed with a NONIUS KappaCCD single crystal diffractometer equipped with a 3 kW generator molybdenum tube, a high precision four circle goniometer, and a low noise and high sensitivity CCD detector. Folding of the images into powder diffraction patterns was done using the FIT2D software<sup>13</sup> after calibrating the detector with Si-NIST (640c) powder standard. The samples were measured in Debye–Scherrer configuration using Lindemann capillaries (0.5 mm diameter) that were filled with dried NC powder.

**Elemental analysis.** ICP-AES analysis was performed with a Varian Vista AX spectrometer. Samples were dissolved in HCl–HNO<sub>3</sub> 3 : 1 (v/v) by using a CEM “MARS 5” microwave digester.

## 3. Results and discussion

Representative TEM images of different types of nanodumbbells are shown in Fig. 1 and 2. Fig. 1 displays an overview of: starting CdSe nanorods (Fig. 1a), PbSe–CdSe–PbSe dumbbells synthesized from these nanorods before and after reaction with the Au(III) solution (Fig. 1b and c, respectively). Fig. 2 reports representative images of: initial CdS nanorods (Fig. 2a), CdTe–CdS–CdTe dumbbells grown from these rods before and after reaction with Au(III) (Fig. 2b and c, respectively). In PbSe–CdSe–PbSe and CdTe–CdS–CdTe dumbbell samples, the formation of the PbSe and CdTe domains, respectively, can be inferred from both the small increase in the rod length (Fig. 1b and 2b) and the slightly different image contrast observable at the nanorod terminations.<sup>10</sup> When the dumbbells reacted with the Au(III) solution (approximately 1 mL of the above described solution was used), Au patches appeared to partially replace the original PbSe (or CdTe) domains at the tips of the rods. The metallic domains can be distinguished clearly at this stage as they exhibit a higher TEM contrast than that of the rod sections (Fig. 1c and Fig. 2c).

A comparison between the TEM images of samples taken before and after the reaction with Au(III) indicated that the mean length of the dumbbells as well as their diameter were reduced to some extent, an effect that was previously observed in the case of the direct Au growth on CdSe nanorods and ascribed to dissolution induced by the DDA and DDAB surfactants used to dissolve the gold salt in toluene.<sup>8,11</sup> However, when the amount of Au(III) added was increased even more, additional topological changes were observed. A representative example of such a growth regime is reported in

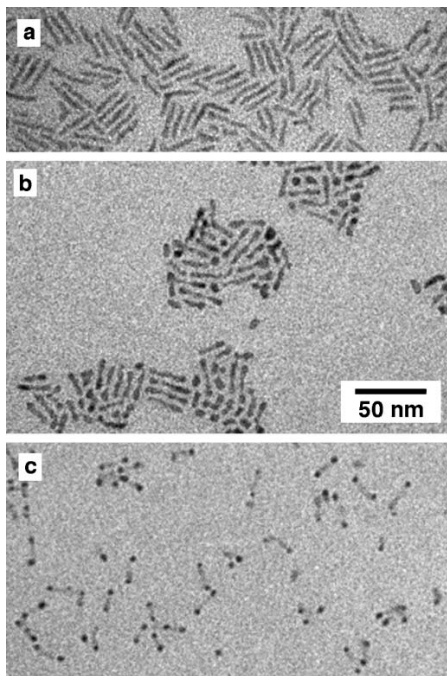


**Fig. 1** TEM images of dumbbell-like nanocrystals synthesized from CdSe nanorods (a); PbSe–CdSe–PbSe dumbbells before (b) and after Au(III) reaction on their tips (c).

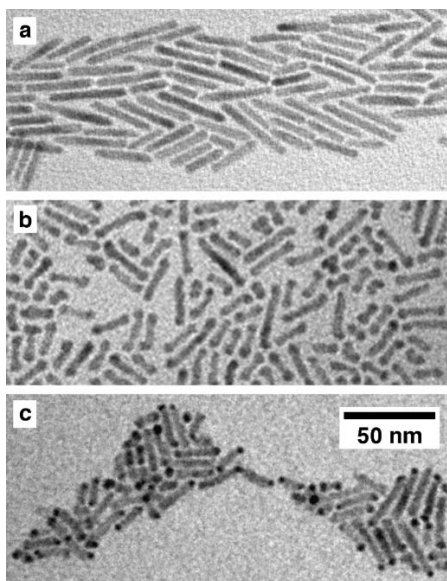


**Fig. 2** TEM images of dumbbell-like nanocrystals prepared from CdS nanorods (a); CdTe–CdS–CdTe dumbbells before (b) and after Au deposition on their tips (c).

Fig. 3 for the case of CdTe–CdS–CdTe nanodumbbells. Upon reaction with excess Au(III) stock solution (approximately 2 mL), the CdTe–CdS–CdTe structures evolved into remarkably thinner and shorter nanorods, most of which carried a

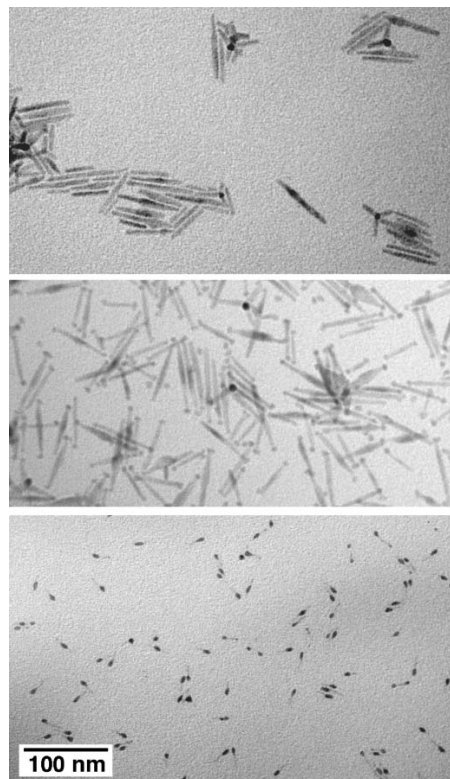


**Fig. 3** TEM images illustrating the formation of asymmetric semiconductor–gold heterostructures at the expense of initial CdTe–CdS–CdTe nanodumbbells upon reaction with Au(III). Onto CdS rods (top), CdTe tips were first grown (middle), and then exposed to a excess quantity (2 mL) of Au(III) precursors (bottom).

single Au domain that was mainly located on one side of the rod section. These findings closely resembled the two-side to one-side Au tip growth reported for bare CdSe nanorods.<sup>12</sup> In agreement with this previous study, in our case it could be assumed that the initially formed symmetric Au–CdS–Au dumbbells (such as those shown in Fig. 2c) underwent a transformation into asymmetric CdS–Au matchstick-like nanocrystals when an excess of Au(III) species was present in the solution. Under such conditions, the difference in the chemical potential between Au tips of dissimilar sizes can sustain an intra-particle Ostwald ripening mechanism that can lead to the dissolution of the most unstable metal patches.<sup>12</sup>

XRD patterns provided further structural and compositional information on the various samples, as shown in Fig. 4 for the case of CdTe–CdS–CdTe heterostructures. In the original CdTe–CdS–CdTe dumbbells, a prominent peak at a low angles can be attributed to either the (111) planes of the cubic sphalerite structure or eventually to the (002) planes of the wurtzite structure of CdTe. Notably, this peak is asymmetrically broadened, due to its convolution with CdS wurtzite reflections, and is slightly shifted to higher angles (smaller *d* spacings) with respect to its bulk position. It is known that, for linear and branched NC heterojunctions based on CdS, CdSe and CdTe, the growth of one material on the

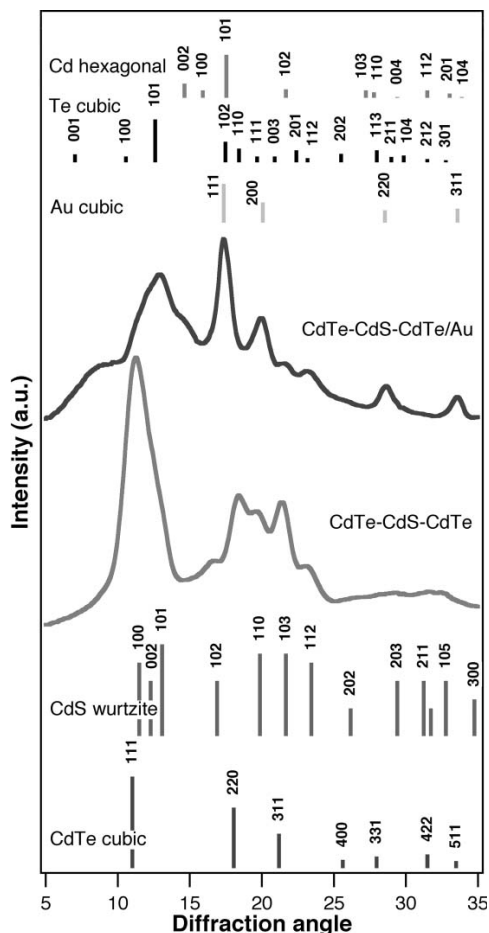


**Fig. 4** XRD patterns of CdTe–CdS–CdTe dumbbells (lower spectrum) and CdTe–CdS–CdTe/Au dumbbells (upper spectrum). For comparison, the reference peaks of bulk wurtzite CdS, cubic CdTe, fcc gold, cubic Te, and hexagonal Cd are displayed.

top of the other occurs epitaxially.<sup>8</sup> Therefore, the observed CdTe peak shift may be due either to a compressive strain of the CdTe domain, or to the presence of an interfacial region in which CdS and CdTe form an alloy.<sup>14</sup> After the dumbbells reacted with the Au(III) solution (upper spectrum in Fig. 4), the CdTe reflection vanished almost completely, and the CdS contribution was clearly disclosed. More importantly, new distinguishable signals appeared, which confirmed the presence of fcc metallic gold in the final heterostructures. Furthermore, a tiny contribution from metallic Cd and Te can be also noted.

Further support to the TEM observations was provided by ICP-AES elemental analysis. As a representative case, we discuss the experiments on the CdSe rod-based samples

in Fig. 1. The measured concentrations ( $\text{mol L}^{-1}$ ) of the individual species are reported in Table 1 for a sample of PbSe–CdSe–PbSe dumbbells before and after reaction with the Au(III) stock solution. In the initial CdSe nanorod sample, we measured a Cd : Se ratio of 1.14, which is in agreement with surface enrichment with Cd atoms, as ascertained earlier for CdSe nanocrystals.<sup>15–17</sup> Similarly, in the PbSe–CdSe–PbSe dumbbells, the cations (Cd + Pb) were found to be in stoichiometric excess relative to the anions (Se). The ratio ( $[\text{Cd}] + [\text{Pb}]$ ) : [Se] was, however, found to be as high as 1.4. For isolated PbSe nanocrystals, a  $[\text{Pb}]$  : [Se] molar ratio of about 1.3 was usually measured, which allowed us to conclude that the unusually high ( $[\text{Cd}] + [\text{Pb}]$ ) : [Se] molar ratio in the PbSe–CdSe–PbSe dumbbells could indeed result from the presence of the PbSe domains in the nanostructures.

Upon Au(III) reaction, a simultaneous decrease in the  $[\text{Cd}] + [\text{Pb}]$  and in the [Se] concentrations was detected. As the gold reduction yield could be easily explained by oxidation of only a small fraction of the total  $\text{Se}^{2-}$  anions lost, major consumption of the CdSe and PbSe materials could arise from the surfactant-driven nanocrystal dissolution, as detected by TEM (Fig. 1–3). Interestingly, the net amount of Cd removed was almost two orders of magnitude smaller than the Pb loss, so that it could be presumed that the Au growth mainly proceeded at the expense of PbSe. This was consistent with the TEM observations, which indeed showed Au patches forming almost exclusively at the dumbbell terminations.

At present, the mechanism of Au formation is only partially understood. Control experiments in the absence of DDA revealed that the sole Au(III):DDA complex could react efficiently with both the PbSe and CdTe sacrificial domains, leading to Au metal deposition. However, under these circumstances, nanocrystal precipitation was prone to occur. TEM investigation showed that the latter event proceeded through the formation of a disordered network of nanorod chain-like segments, in which individual dumbbells fused with each other *via* their gold terminations. An example is reported in Fig. 5. This evidence suggested that, unlike the bare CdSe nanorod system,<sup>9</sup> DDA did not serve as a reducing agent for Au(III), but was necessary as a surface stabilizer for the gold patches. Therefore, other chemical species should be responsible for the reduction of the Au(III) precursor.

The formation of complexes with the surfactants and size-dependent variation of the redox power of nanoscale materials<sup>12,18–20</sup> can be expected to alter the absolute values of the electrochemical potentials of the chemical species in our system. Nevertheless, at a first approximation, one can assume that the relative scale of the standard redox potentials, measured in aqueous media, is still applicable to the species involved in the present system.<sup>18–21</sup> Therefore, from the electrochemical potential point of view, Au(III) reduction to Au(0) could occur directly through oxidation of  $\text{Te}^{2-}$  in CdTe

**Table 1** ICP-AES elemental analysis of nanocrystal dumbbells ( $\text{mol L}^{-1}$ )

	Au	Cd	Pb	Se
PbSe–CdSe–PbSe (initial)				
PbSe–CdSe–PbSe (after reaction with Au <sup>III</sup> )	$7.41 \times 10^{-7}$	$4.37 \times 10^{-7}$ $1.30 \times 10^{-7}$	$1.06 \times 10^{-5}$ $3.61 \times 10^{-6}$	$7.87 \times 10^{-6}$ $2.66 \times 10^{-6}$

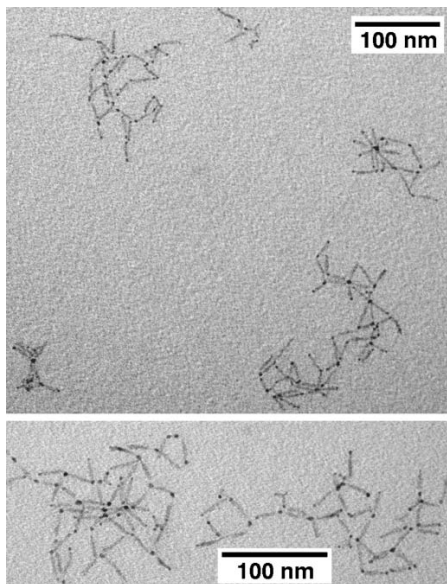


**Fig. 5** Examples of aggregates formed by Au-tipped CdSe nanorods fused with each other through their Au terminations.

domains to Te(0) (or of Se<sup>2-</sup> in PbSe).<sup>21</sup> This would actually agree with both the TEM and ICP-AES analyses, thus further corroborating the hypothesis that the PbSe and CdTe tips were sacrificially consumed during Au metal production. However, while the formation of Te(0) could be rationalized by these arguments, it remains unclear how the reduction of Cd<sup>2+</sup> to Cd was also triggered. One possibility could be that the formed Au patches themselves acted as efficient redox catalysts<sup>19,20</sup> for electron transfer to Cd<sup>2+</sup> ions. Experiments are currently under way to elucidate the nature of the various chemical processes that accompany gold deposition on the nanocrystal dumbbells under the present reaction conditions.

#### 4. Conclusions

The possibility to perform selective chemical reactions on the tips of CdSe and CdS nanorods has been demonstrated. The developed method involves the growth of additional semiconductor domains on the tips of the rods and subsequent selective oxidation reaction of only these materials. This approach has allowed us to grow Au domains onto specific locations of rod-shaped CdS NCs for which direct metal deposition is unfeasible. We believe that this strategy may be of general utility to create other types of complex colloidal

nanoheterostructures, provided that a suitable sacrificial material can be purposely grown on top of the starting nanocrystals.

#### Acknowledgements

This work was supported by the European projects SA-NANO (contract number STRP 013698) and by the Italian projects MIUR 297 (contract number 13587).

#### References

- 1 X. Peng, L. Manna, W. Yang, J. Wickham, E. Scher, A. Kadanich and A. P. Alivisatos, *Nature*, 2000, **404**, 59.
- 2 H. Yan, R. He, J. Pham and P. Yang, *Adv. Mater.*, 2003, **15**, 402.
- 3 P. D. Cozzoli, L. Manna, M. L. Curri, S. Kudera, C. Giannini, M. Striccoli and A. Agostiano, *Chem. Mater.*, 2005, **17**, 1296.
- 4 H. W. Gu, R. K. Zheng, X. X. Zhang and B. Xu, *J. Am. Chem. Soc.*, 2004, **126**, 5664.
- 5 T. Pellegrino, A. Fiore, E. Carlino, C. Giannini, P. D. Cozzoli, G. Ciccarella, M. Respaud, L. Palmirotta, R. Cingolani and L. Manna, *J. Am. Chem. Soc.*, 2006, **128**, 6690.
- 6 H. W. Gu, Z. M. Yang, J. H. Gao, C. K. Chang and B. Xu, *J. Am. Chem. Soc.*, 2005, **127**, 34.
- 7 H. Yu, M. Chen, P. M. Rice, S. X. Wang, R. L. White and S. Sun, *Nano Lett.*, 2005, **5**, 379.
- 8 D. J. Milliron, S. M. Hughes, Y. Cui, L. Manna, J. Li, L.-W. Wang and A. Paul Alivisatos, *Nature*, 2004, **430**, 190.
- 9 T. Mokari, E. Rothenberg, I. Popov, R. Costi and U. Banin, *Science*, 2004, **304**, 1787.
- 10 S. Kudera, L. Carbone, M. F. Casula, R. Cingolani, A. Falqui, E. Snoeck, W. J. Parak and L. Manna, *Nano Lett.*, 2005, **5**, 445.
- 11 C. Pacholski, A. Kornowski and H. Weller, *Angew. Chem., Int. Ed.*, 2004, **43**, 4774.
- 12 T. Mokari, C. G. Szturz, A. Salant, E. Rabani and U. Banin, *Nat. Mater.*, 2005, **4**, 855.
- 13 A. P. Hammersley, S. O. Svensson, M. Hanfland, A. N. Fitch and D. Häusermann, *High Pressure Res.*, 1996, **14**, 235.
- 14 R. E. Bailey and S. Nie, *J. Am. Chem. Soc.*, 2003, **125**, 7100.
- 15 J. Taylor, T. Kippens and S. J. Rosenthal, *J. Cluster Sci.*, 2001, **12**, 571.
- 16 H. Borchert, D. V. Talapin, N. Gaponik, C. McGinley, S. Adam, A. Lobo, T. Möller and H. Weller, *J. Phys. Chem. B*, 2003, **107**, 9662.
- 17 H. Borchert, D. V. Talapin, C. McGinley, S. Adam, A. Lobo, A. R. B. de Castro, T. Möller and H. Weller, *J. Chem. Phys.*, 2003, **119**, 1800.
- 18 C. Burda, X. Chen, R. Narayan and M. A. El-Sayed, *Chem. Rev.*, 2005, **105**, 1025.
- 19 (a) T. Ung, L. M. Liz-Marzan and P. Mulvaney, *J. Phys. Chem. B*, 1999, **103**, 6770; (b) N. R. Jana, T. K. Sau and T. Pal, *J. Phys. Chem. B*, 1999, **103**, 115; (c) T. K. Sau, A. Pal and T. Pal, *J. Phys. Chem. B*, 2001, **105**, 9266.
- 20 (a) P. D. Cozzoli, M. L. Curri and A. Agostiano, *Chem. Commun.*, 2005, 3186; (b) P. D. Cozzoli, E. Fanizza, R. Comparelli, M. L. Curri, A. Agostiano and D. Laub, *J. Phys. Chem. B*, 2004, **108**, 9623.
- 21 D. C. Harris, *Quantitative Chemical Analysis*, W. H. Freeman & Company, New York, 6th edn., 2002.

### C.3 Synthesis and Micrometer-Scale Assembly of Colloidal CdSe/CdS Nanorods Prepared by a Seeded Growth Approach

L. CARBONE, C. NOBILE, M. DE GIORGI, F. DELLA SALA, G. MORELLO, P. POMPA, M. HYTCH, E. SNOECK, A. FIORE, I.R. FRANCHNI, M. NADASAN, A.F. SILVESTRE, L. CHIODO, S. KUDERA, R. CINGOLANI, R. KRAHNE, L. MANNA  
*Nano Letters* 7(10), pp. 2942–2950, 2007

Key limitations of the colloidal semiconductor nanorods that have been reported so far are a significant distribution of lengths and diameters as well as the presence of irregular shapes produced by the current synthetic routes and, finally, the poor ability to fabricate large areas of oriented nanorod arrays. Here, we report a seeded-growth approach to the synthesis of asymmetric core-shell CdSe/CdS nanorods with regular shapes and narrow distributions of rod diameters and lengths, the latter being easily tunable up to 150 nm. These rods are highly fluorescent and show linearly polarized emission, whereby the emission energy depends mainly on the core diameter. We demonstrate their lateral alignment as well as their vertical self-alignment on substrates up to areas of several square micrometers.

# Synthesis and Micrometer-Scale Assembly of Colloidal CdSe/CdS Nanorods Prepared by a Seeded Growth Approach

Luigi Carbone,<sup>†,‡</sup> Concetta Nobile,<sup>†,‡</sup> Milena De Giorgi,<sup>‡</sup> Fabio Della Sala,<sup>‡</sup> Giovanni Morello,<sup>‡</sup> Pierpaolo Pompa,<sup>‡</sup> Martin Hytch,<sup>§</sup> Etienne Snoeck,<sup>§</sup> Angela Fiore,<sup>‡</sup> Isabella R. Franchini,<sup>‡</sup> Monica Nadasan,<sup>‡</sup> Albert F. Silvestre,<sup>‡</sup> Letizia Chiodo,<sup>‡</sup> Stefan Kudera,<sup>‡</sup> Roberto Cingolani,<sup>‡</sup> Roman Krahne,<sup>‡</sup> and Liberato Manna<sup>\*,‡</sup>

NNL-National Nanotechnology Laboratory of CNR-INFM and IIT Research Unit, via per Arnesano, km 5, 73100 Lecce, Italy, and CEMES-CNRS, 29 rue Jeanne Marvig, B.P. 94347, F-31055 Toulouse Cedex, France

Received July 20, 2007

## ABSTRACT

Key limitations of the colloidal semiconductor nanorods that have been reported so far are a significant distribution of lengths and diameters as well as the presence of irregular shapes produced by the current synthetic routes and, finally, the poor ability to fabricate large areas of oriented nanorod arrays. Here, we report a seeded-growth approach to the synthesis of asymmetric core–shell CdSe/CdS nanorods with regular shapes and narrow distributions of rod diameters and lengths, the latter being easily tunable up to 150 nm. These rods are highly fluorescent and show linearly polarized emission, whereby the emission energy depends mainly on the core diameter. We demonstrate their lateral alignment as well as their vertical self-alignment on substrates up to areas of several square micrometers.

Ordered assemblies of nanorods are important both in fundamental research, as they present new systems on which chemical and physical interactions among nanocrystals can be investigated, and for practical applications, as they provide the basis to the engineering of new materials and the fabrication of devices. Significant progress has been made recently both on the synthesis of nanorods of different materials<sup>1–3</sup> as well as on understanding and mastering their assembly.<sup>4,5</sup> This can be mediated for instance by external fields,<sup>6–10</sup> by interparticle interactions as well as rod solubility in a binary solvent/nonsolvent liquid mixture,<sup>11–13</sup> by controlling the rod interfacial energy, by slow solvent evaporation on a liquid–solid–air interface,<sup>14</sup> by solvent fluidics and the presence of liquid–air interface in the deposition of a lyotropic phase from a drying solution,<sup>15</sup> by a Langmuir–Blodgett approach,<sup>16</sup> or by unidirectional alignment through attachment of nanorods to the surface of a single cleaved semiconductor monolayer.<sup>17</sup> Important requirements for

organizing nanorods in ordered close-packed arrays over significantly large areas are, however, a high homogeneity of shapes and, in the case of alignment assisted by external biases, the ability of nanorods to respond to such biases effectively.

We have developed a new, seeded-type growth approach to fabricate colloidal nanorods, which we have successfully applied to the synthesis of mixed CdSe/CdS nanorods with narrow distributions of rod lengths and diameters. Our CdSe/CdS nanorods present the appealing characteristics of strong and tunable light emission from green to red, they spontaneously self-assemble on substrates, and can be easily organized in close-packed ordered arrays over large areas. The synthesis is based on the co-injection of appropriate precursors and preformed spherical CdSe nanocrystal seeds (nearly monodisperse in size) in a reaction flask that contains a mixture of hot surfactants suited for the anisotropic growth of CdS nanocrystals. In a typical synthesis of nanorods reported in this work, CdO is decomposed in the presence of a mixture of trioctylphosphine oxide, hexylphosphonic acid, and octadecylphosphonic acid in relative ratios that have been carefully optimized (see Supporting Information for details). The resulting solution is heated to 350–380 °C (depending

\* Corresponding author. E-mail: liberato.manna@unile.it. Telephone: +39 0832 298 207. Fax: +39 0832 298 238.

† These authors have contributed equally to this work.

‡ NNL-National Nanotechnology Laboratory of CNR-INFM and IIT Research Unit.

§ CEMES-CNRS.

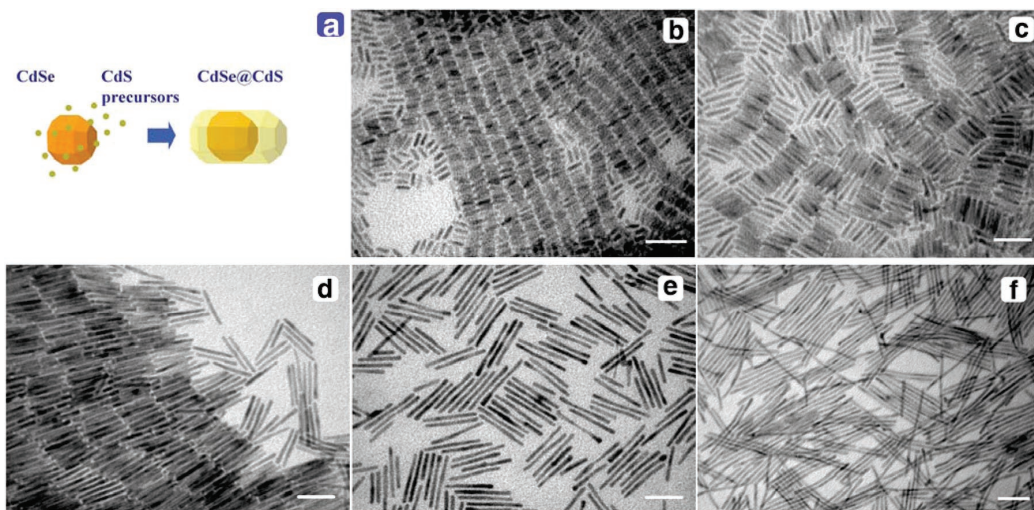


**Figure 1.** Evaporation-mediated self-assembly of CdSe/CdS nanorods prepared by seeded growth. (a) Sketch of the seeded growth approach. (b–f) Transmission electron micrographs of self-assembled CdSe/CdS nanorods. As soon as the solvent, in which the CdSe/CdS are dissolved (toluene), is allowed to evaporate from the grid on which the drop of solution is deposited, the nanorods start self-assembling. Short aspect ratio (rod length/rod diameter, AR) rods (b–d) tend to form locally ordered 2D smectic phases, while longer rods tend to form either disordered assemblies, ribbons, or locally ordered 2D nematic phases. A similar AR dependence on the assembly was reported for instance for Ag and Au nanorods<sup>4</sup> and pencil-shaped CoO nanocrystals.<sup>20</sup> Average rod diameter and length, as determined by HRTEM, are respectively: (b)  $4.9 \pm 0.7$  nm and  $19 \pm 1$  nm; (c)  $4.2 \pm 0.4$  nm and  $35 \pm 2$  nm; (d)  $3.9 \pm 0.2$  nm and  $53 \pm 4$  nm; (e)  $3.8 \pm 0.3$  nm and  $70 \pm 4$  nm; (f)  $3.8 \pm 0.3$  nm and  $111 \pm 10$  nm. The conditions at which the various nanorod samples are grown are reported in Table 1 of the Supporting Information. In general, the mean rod diameter is dictated not only by the diameter of the seeds but also by the growth temperature, which can control the thickness of the shell (higher temperatures promote the formation of a thicker shell). The rod length on the other hand can be varied not only by the amount of precursors and/or seeds added but also by the growth temperature and/or reaction time. Also, the amount and the size of the added seeds has an influence on the overall length of the rods. Large seeds, for instance, tend to promote the formation of short (and fat) rods (b), while small seeds tend to form long (and thin) rods (f). All scale bars are 50 nm long.

on the synthesis) under inert atmosphere. Separately, a solution is prepared by dissolving sulfur in trioctylphosphine and by adding to it either CdS or CdSe nanocrystals (previously prepared, purified, and solubilized in TOP). This solution is quickly injected in the flask, after which the temperature of the flask is allowed to recover to its pre-injection value and the synthesis is kept running for several minutes before stopping it by removing the heating mantle. Immediately after injection, CdS starts growing preferentially on the CdSe seeds rather than forming separate nuclei in solution because the activation energy for heterogeneous nucleation is much lower than that for homogeneous nucleation.<sup>18</sup> As the homogeneous nucleation is bypassed by the presence of the seeds, all nanocrystals undergo almost identical growth conditions and therefore they maintain a narrow distribution of lengths and diameters during their evolution. The synthesis is rather flexible, as there are various parameters that can be tuned in order to control the morphology of the resulting nanorods such as the diameter of the seeds, the growth temperature, and the amount of precursors and seeds added (see Figure 1). When no CdSe seeds are co-injected, CdS nanorods start nucleating only several seconds after the injection, and the final sample is characterized by large distributions of rod lengths and diameters. Also, the range of aspect ratios (rod length/rod diameter, ARs) of the rods attainable with the present synthesis (up to 30:1) is much wider than that attainable with the synthesis scheme reported by Talapin and co-workers

for asymmetric CdSe/CdS core–shell nanorods, which was based on an extension of the traditional synthesis of core–shell nanocrystals (for which the maximum AR reported was 4:1).<sup>19</sup> The power of the seeded-growth approach carried out at high temperatures in suitable surfactant mixtures is therefore that large AR rods can be synthesized that still preserve regular shapes and show no tendency to aggregate, all features that are not achievable with lower-temperature shell-growth approaches.

A key issue of this type of synthesis approach is whether the original seed is preserved in the final rod structure and also which is the location of the seed along the rod. This can be partly elucidated by carrying out geometric phase analysis (GPA),<sup>21</sup> which is a quantitative high-resolution transmission electron microscopy (HRTEM) technique. It allows detection of variations in the periodicities of the HRTEM contrast via analysis of the local components in the Fourier transform of the image. Possible deformations and strains of the 2D-projected lattice can be deduced with respect to an “unstrained” area within the HRTEM image taken as reference. This method was applied to HRTEM images recorded on CdSe/CdS nanorods (Figure 2a) and also on “CdS-only” nanorods that were grown using spherical CdS seeds (Figure 2b). The images were taken on a 200 kV TEM-FEG microscope (F-20 FEI) fitted with a spherical aberration corrector (CEOS). In the corresponding “mean dilatation” (i.e., the average of the 2D lattice deformation) image of a CdSe/CdS nanorod of Figure 2c,

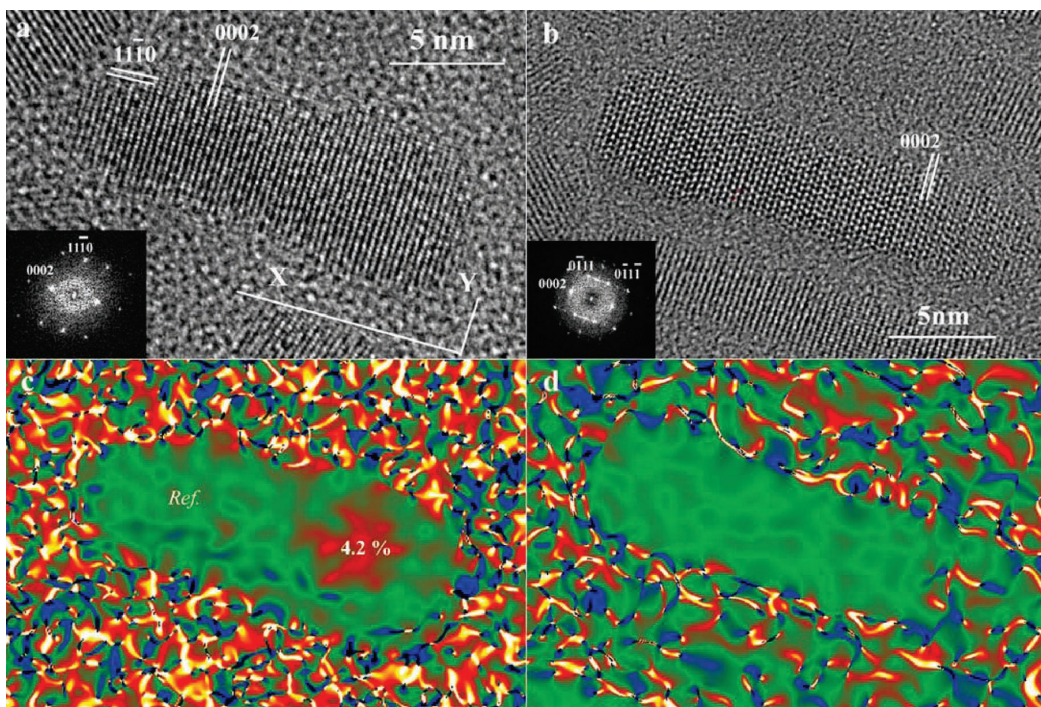


**Figure 2.** Structural analysis of seeded-grown nanorods. HRTEM images of nanorods grown using either CdSe (a) or CdS (b) as seeds. The nanorods show little occurrence of stacking faults over the entire structure due to the high temperature at which they are grown. (c,d) Corresponding “mean dilatation” images. This technique allows a mean dilatation mapping from high-resolution electron microscope images or indeed any type of lattice image. It uses a color scale for displaying variation in the periodicity of the HRTEM contrast. Areas of the same color are regions with the same periodicity. The mean dilatation image of the CdSe/CdS rod (c) shows an area with lattice parameters altered by 4.2% with respect to the reference area, situated at the opposite tip of the rod. For comparison, the same analysis is performed on “CdS-only” rods, and no variation of the lattice parameters over the whole length of the nanorod can be observed (d).

for instance, it is possible to recognize at the right side of the nanorod a region with a lattice constant different from that of a reference area at the opposite tip. This region should correspond to the original CdSe seed, and this is supported by the quantitative measurement of the relative dilatation (4.2%), which is almost equal to the misfit between bulk CdS and CdSe (i.e., +4%). As a control, the deformation image of a CdS-only rod (Figure 2d) shows an undistorted lattice across the whole rod. In the large AR rods that it is possible to synthesize with the present approach, quantitative HRTEM analysis is less straightforward. Nevertheless, it shows that the CdSe region is rarely localized near the tips of the rods nor at their center, but in most cases in a region between  $\frac{1}{3}$  and  $\frac{1}{4}$  of their overall length (see Supporting Information). This is consistent with a fast growth rate of the rods along the unique *c*-axis of their wurtzite structure, the growth along one direction of this axis being faster than along the opposite direction, as observed previously<sup>3</sup> and also as predicted theoretically for wurtzite-type nanorods.<sup>22</sup> An additional advantage of the present synthetic approach is that it yields rods that have few structural defects, as can be inferred by the low density of stacking faults along the rod structure.

Optical absorption and photoluminescence (PL) spectra of CdSe/CdS nanorods in solution show a considerable red-shift with respect to the corresponding spectra of the starting

CdSe seeds (Figure 3a,b). In samples of large AR rods, the absorption spectra are characterized by well-resolved peaks appearing at higher energies with respect to the lowest energy peak (Figure 3a). Theoretical absorption spectra (Figure 3a, dashed lines) were calculated using the envelope function approximation<sup>23</sup> (see also Supporting Information). The nanorods were modeled as a CdSe sphere inside a CdS hexagonal prism. The three-dimensional single-band effective mass Hamiltonian was solved on a Cartesian grid, using the parameters taken from Müller et al.<sup>24</sup> (i.e.  $m_e = 0.13$ ,  $m_h = 0.45$ , for CdSe;  $m_e = 0.2$ ,  $m_h = 0.70$  for CdS; zero conduction band-offset) and bulk energy gaps at room temperature from Landolt–Börnstein<sup>25</sup> (i.e., 1.75 eV for CdSe and 2.5 eV for CdS). The theoretical absorption spectrum shown in Figure 3a is obtained by considering transitions in the single-particle approximation from the highest 50 hole levels to the lowest 50 electron levels and applying a Gaussian broadening ( $\sigma = 50$  meV) to each exciton level. The calculated spectra are in good agreement with the experimental data. On the basis of the results of the calculations, the high-energy peaks in the absorption spectra can be ascribed to the absorption from CdS, while the lowest energy peak is due to electronic transitions from holes confined in the CdSe core to electrons delocalized throughout the whole nanocrystal structure as a consequence of the negligible conduction band offset between CdSe and CdS.<sup>26</sup> This

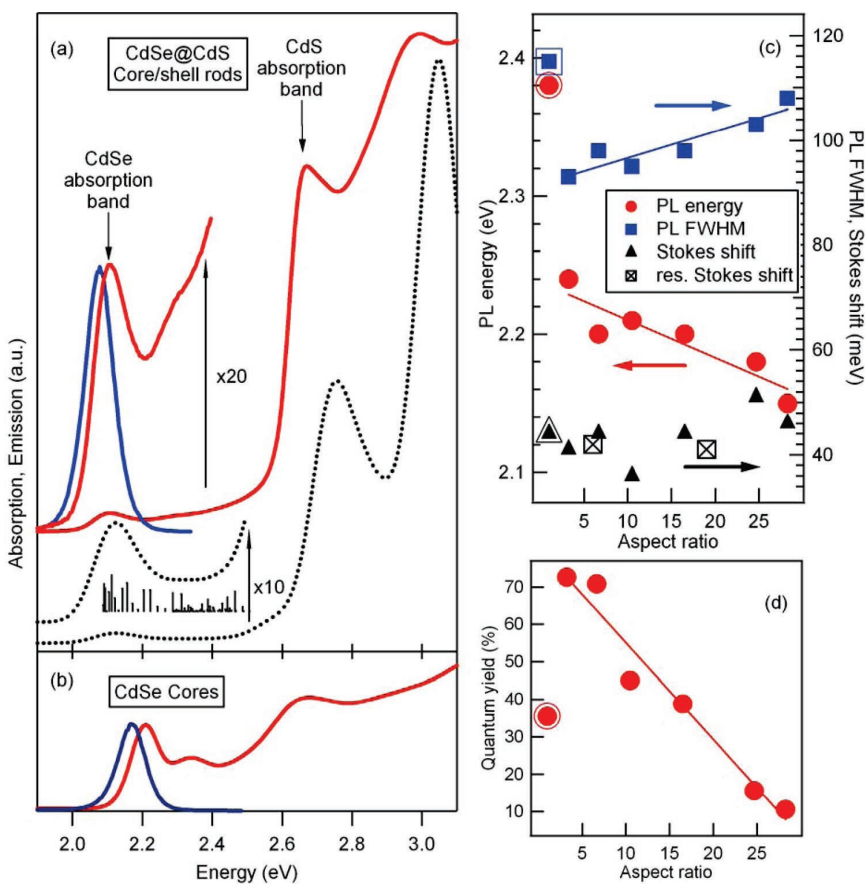


**Figure 3.** Measured and modeled optical parameters of CdSe/CdS nanorods. (a) Optical absorption and photoluminescence (PL) spectra of a typical sample of CdSe/CdS nanorods dissolved in toluene (continuous lines). The rods have an average length of 51 nm and average diameter of 3.9 nm. They were prepared from CdSe seeds with a diameter of 3.2 nm. The corresponding theoretical absorption spectrum is shown in dotted lines.<sup>23</sup> Vertical bars in the  $\times 10$  magnification of the low-energy side of calculated spectrum indicate the energy position and oscillator strength of the first few exciton levels, which represent transitions from the hole 1S level of the CdSe sphere to the electron nS levels of the CdS rod. The absorption and PL spectra of the starting spherical CdSe nanocrystal sample are shown in (b). Spectra of core-shell samples show always a considerable red-shift with respect to the corresponding spectra of the starting CdSe seeds. (c) Nonresonant Stokes shifts (labeled “Stokes shift” in the legend), full width at half-maximum, and PL peak energy for different samples of CdSe/CdS nanorods prepared from the same batch of CdSe seeds (which had a diameter of 2.3 nm). The corresponding values of the starting CdSe seeds are indicated by outlined markers, and the resonant Stokes shifts obtained from PLE experiments at  $T = 10$  K are indicated with crossed box markers. In going from the nanorods with the smallest AR to those with the largest AR, the average diameter of the rods varies from 3.5 to 5 nm, and their average length varies from 10 to 130 nm, respectively. Straight lines are inserted as a guide to the eye. (d) Quantum yields of the same nanorods samples as in (c).

behavior has been already observed in both spherical and asymmetric core-shell CdSe/CdS nanocrystals but grown at much lower temperatures (120–150 °C).<sup>19,26</sup>

The full widths at half-maximum of the PL peaks for all our rods remain relatively narrow even in large AR rods (Figure 3c) and therefore are indicative of the high homogeneity in shape of our samples and of the limited occurrence of graded composition (a graded shell) at the CdSe/CdS core-shell interface. Also, it is remarkable that even growth temperatures as high as those at which our nanorods are synthesized (350–380 °C) are not able to cause alloying of the CdSe core with the growing CdS shell, a situation that would lead instead to a blue-shift in the optical absorption and emission spectra of the resulting  $\text{CdSe}_x\text{S}_{1-x}$  alloy

nanorods with respect to those of the starting CdSe seeds.<sup>27</sup> The nonresonant Stokes shifts for the nanorods (i.e., shifts between the emission peak and the lowest energy peak in absorption, see plot of Figure 3c) range from 40 to 50 meV and are not much different from those of the starting CdSe seeds. In addition, such shifts show a negligible dependence on the AR of the rods, differently from what had been reported earlier on CdSe/CdS nanorods prepared by Talapin and co-workers at much lower temperatures, for which much bigger and strongly AR-dependent Stokes shifts were observed.<sup>19</sup> Such reduced Stokes shifts confirm the size homogeneity and low interdiffusion of chemical species in our nanostructures. Also resonant Stokes shifts, determined by low-temperature PLE measurements (Figure 3c and

Supporting Information) are not dependent on the AR of the rods, provided that the latter are all prepared starting from the same CdSe seeds.

PL quantum yields (QYs) from core–shell rods in solution are of the order of 70–75% for short AR rods and decay to about 10% in the largest AR rods that we could synthesize (Figure 3d). The relatively high QYs of the short AR nanorod samples, which are comparable to those of spherical or asymmetric core–shell nanocrystals reported earlier,<sup>19,26</sup> point to a homogeneous shell growth, with little presence of defects in the core–shell interfacial region, even under the fast growth rates taking place in our syntheses. For ARs larger than 10, the decrease in QY can be due to an increasing number of surface trap states arising from the CdS region. Such decrease of QY, together with a more delocalized electron wave function (which therefore has a smaller overlap with the hole wave function), results in increased radiative decay times in longer rods (i.e., they vary from 13.5 ns in rods with AR equal 3, to 164 ns in rods with AR equal to 28, see Supporting Information for more details).

The CdSe/CdS nanorods reported here start self-assembling on substrates as soon as the solvent in which they are dissolved is allowed to evaporate, forming long-range ordered assemblies that are reminiscent of liquid-crystalline phases (Figure 1). The formation of these types of assemblies is entropically driven and has been observed already in several colloidal nanorod solutions.<sup>4,11,13,20</sup> Also, ordered arrays of close-packed, vertically aligned nanorods can be obtained by evaporation-mediated self-assembly of nanorods on substrates from more concentrated nanorod solutions. We have observed the formation of small areas of vertically oriented nanorods already when a drop of solution is deposited on the carbon support film of TEM grids, similar to those seen by Li and Alivisatos.<sup>14</sup> However, larger areas, often of the order of several square micrometers, can be achieved when the process is carried out on the surface of water.<sup>7</sup> As an example, we let the solvent evaporate from a concentrated solution of nanocrystals in toluene that had been deposited on the surface of water in a glass beaker, and we then collected part of the floating nanocrystal film with a carbon-coated TEM grid. Some regions of this film are shown in Figure 4a–c. Regular patterns of vertically stacked nanorods are seen, which are organized either in hexagonally close-packed monolayers (Figure 4b) or in ordered multilayer structures (Figure 4a, bottom right, and Figure 4c). In general, interfacial self-segregation of nanoparticles leads to a reduction of interfacial energy, and for instance, the segregation of TOPO-coated spherical CdSe nanocrystals at the water–toluene interface has been observed recently.<sup>28</sup> It is likely that vertical assembly of nanorods in our experiments leads to a lower interfacial energy than for a lateral close-packed or disordered assembly at the interface, as in this configuration each nanorod has one of its polar facets (which are also less passivated with surfactants than its nonpolar facets and are likely to carry residual charges) closer to the water–toluene interface. In addition, such arrangement maximizes the hydrophobic interactions among nanorods, at least in monolayer structures. Evaporation-mediated assembly on

warm (50–60 °C) water led to the most reproducible results, as higher temperature improves rod solubility and should help the system to reach such lower energy configuration, in analogy with the conditions recently found for the formation of complex binary superlattices of spherical nanoparticles.<sup>29</sup>

We also observed the formation of large vertically aligned nanorod arrays when the evaporation-mediated assembly took place on TEM grids that had been placed on electrostatically charged surfaces or, with a higher degree of control, by using planar electrodes separated by some tens of micrometers distance (see Figure 4d). For the latter experiments, we used silicon nitride membrane window grids with a nitride thickness of 100 nm on which we evaporated a 10 nm Ti gate from the back side for the vertical alignment of nanorods. A standard carbon-coated TEM grid placed on top of the membrane during solvent evaporation served as a counter electrode. We used a voltage of 32 V, while the nanorod solution and its container were heated to 45 °C. Also, in this case, we find that temperature has a significant influence on the alignment because, under the same conditions, but with solution and container at 20 °C (instead of 45 °C for successful vertical alignment), we observed mainly lateral alignment in ribbon structures (see Figure 4e) and only few and very small areas of vertically aligned rods. We attribute the dominant driving forces for this alignment to a combination of the interaction of the rods with the electric field via their intrinsic dipoles,<sup>7,30</sup> and thermal effects like conductivity and convective flow of the liquid in the evaporation process.<sup>14</sup> A similar degree of assembly could not be achieved for instance with CdS-only rods or with CdSe rods prepared by any of the synthetic routes reported so far, most likely because of their comparatively broader size distributions.

Also the lateral alignment of nanorods can be extended over larger areas and controlled in direction if the evaporation-mediated assembly is influenced by an external perturbation like an electric field.<sup>7–10</sup> As an example, we exploited the presence of a significant dipole in this type of nanorods<sup>30</sup> to laterally align them on planar surfaces using external electric fields. In this case, we used interdigitated electrode devices (electrode separation 4 μm, electrode length 600 μm), which were fabricated by optical lithography and subsequent metal evaporation (500 nm Al) on Si/SiO<sub>2</sub> (100 nm oxide thickness) substrates. A quantity of typically 50 μL of nanorod solution (nanorods were dispersed in toluene, the optical density of the solution at 595 nm was equal to 0.05) was drop-casted onto the electrode device under ambient conditions, and a dc electric field of 2.5 10<sup>5</sup> V/cm was applied during solvent evaporation (typically 2 min). After the alignment process, the electrode devices were inspected by scanning electron microscopy (SEM) imaging. The rods aligned uniformly over areas on the scale of several tens of square micrometers by following the field streamlines throughout the electrode gap (Figure 5a and Supporting Information). Magnifications of randomly picked areas in between the electrodes showed indeed an almost perfect lateral alignment of rods in monolayers or multilayered

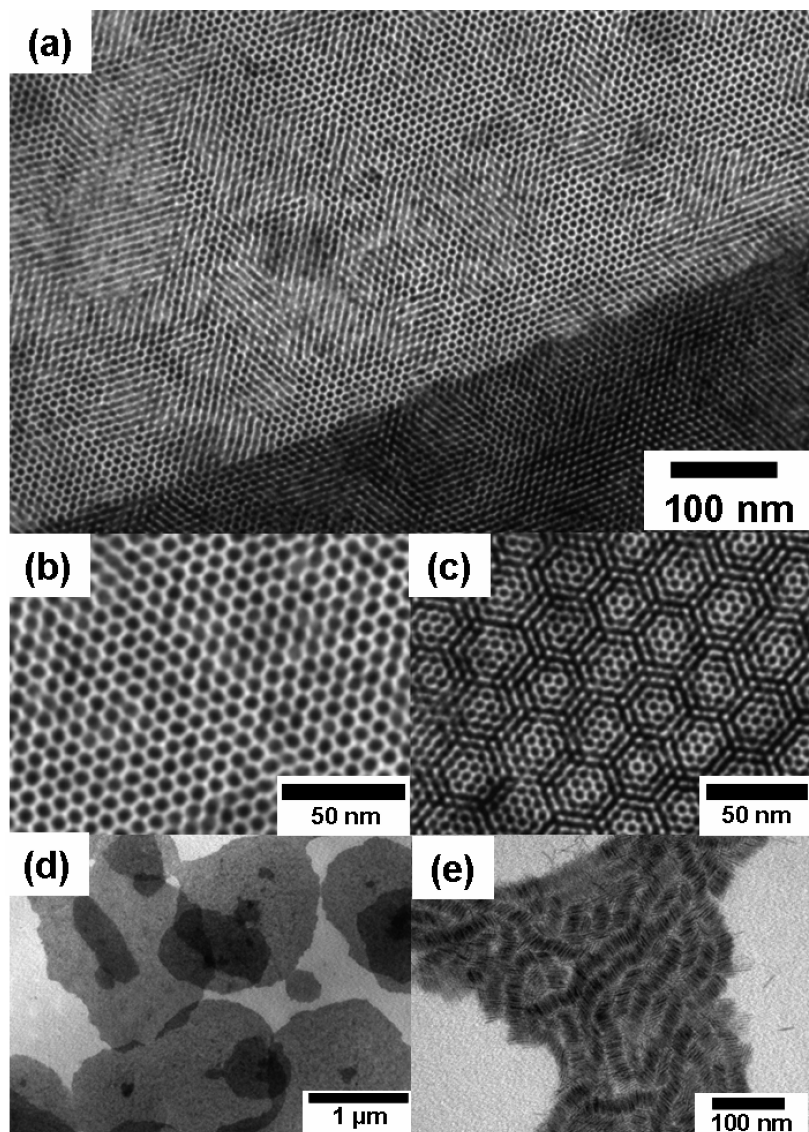


**Figure 4.** TEM images of ordered nanorod arrays obtained by evaporation-mediated self-assembly. (a) Micrometer size closely packed layers of vertically stacked rods obtained upon evaporation of toluene on top of water. (b–c) Higher magnification imaging revealed regular patterns of vertically stacked nanorods, which are organized either in hexagonally closed packed monolayers (b) or in multilayer structures (a, bottom right, and c). (d) Micrometer size plaques of vertically aligned rods obtained by an electric field in vertical direction. (e) Lateral ribbon structures that consist of a few multilayers of nanorods.

structures, with a type of organization that resembles either the nematic (Figure 5b) or the smectic liquid-crystal phases (Figure 5c). The polarized emission from the regions of aligned nanorods under ambient conditions was recorded with a conventional microphotoluminescence setup. The sample was excited by a circularly polarized He–Cd laser at 325 nm. The emitted light was collected by a objective lens (20 $\times$  magnification, NA = 0.4) and detected by a 0.33 m monochromator equipped with an Andor CCD camera. The emission polarization was analyzed with a linear polarizer in combination with a  $\lambda$ -half plate, placed in front of the monochromator to correct the polarization-dependent response of both the monochromator and the detector (see

illustration in Figure 4d). Figure 5d(ii) shows the fluorescence emission spectra recorded from a micrometer size region of aligned nanorods under ambient conditions. The PL of such large arrays of oriented nanorods is strongly polarized along the alignment direction. The integrated PL intensity dependence on the polarizer angle can be fitted nicely to a  $\cos^2$  function as shown in Figure 5d(iii). Polarization ratios as high as 45% were observed on such micrometer size oriented ensembles for rods that had an AR of 10. As a control experiment, we performed the same measurements after rotating the sample by 90° and obtained the same results shifted by 90°. Also, control experiments performed on

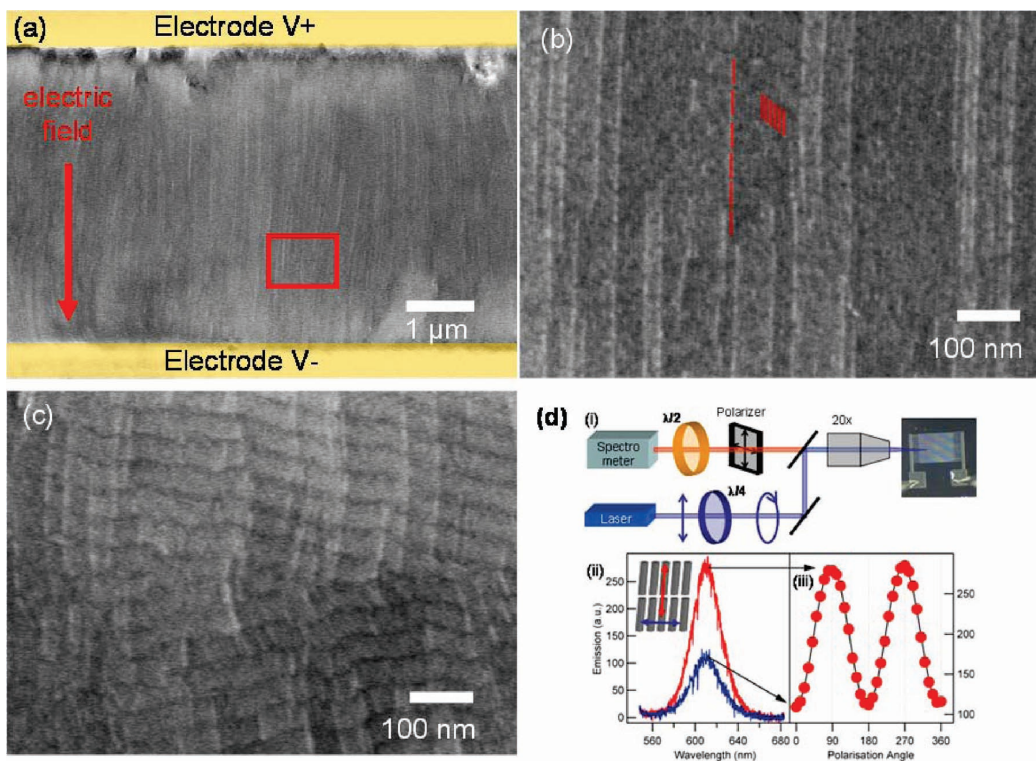


**Figure 5.** Lateral alignment of nanorods with electric fields and polarized emission from aligned nanorods. (a–c) SEM images showing aligned arrays of nanorods with an aspect ratio of 10. The red arrow indicates the direction of the electric field that was applied during the evaporation of the nanorod solution, and the red square marks the region that is displayed in (b). (b) Micrometer size area where the individual rods can be resolved. Some rods are highlighted in red as a guide to the eye. (c) Zoom that displays an area of nanorods assembled in ribbonlike structures. (d) (i) Schematic illustration of the experimental setup. (ii) Nanorod emission spectra, recorded from the micrometer size regions of aligned nanorods under ambient conditions, polarized parallel (red) and perpendicular (blue) to the long axis of the nanorods, as illustrated by the schematic inset. (iii) Red dots show the PL intensity dependence on the polarization angle and can be fitted to a  $\cos^2$  function (black line). From the data a polarization ratio of 45% can be calculated as  $(I_{||} - I_{\perp})/(I_{||} + I_{\perp})$ . Here,  $I_{||}$  and  $I_{\perp}$  are the emission intensities parallel and perpendicular to the long axis of the rods, respectively.

regions of randomly oriented nanorods did not show any significant polarization of the fluorescence emission.

Figure 6 shows spatially resolved PL spectra that were collected with a confocal system (Olympus FV1000) in epilayer configuration (with a spatial resolution of 200 nm) from different regions of substrates on which nanorods exhibited the following different types of alignment: densely packed hexagonal arrays of vertically aligned rods, laterally aligned ribbon-like assemblies, and disordered assemblies (see insets of Figure 6). The samples were excited by an UV diode laser ( $\lambda = 405$  nm) through an objective lens 60 $\times$  oil with a numerical aperture of NA = 1.40. The emission from areas with 300–500 nm diameter, which were selected with the confocal system, was detected by a 0.32 m monochromator equipped with a nitrogen-cooled CCD camera that was coupled to the confocal head (the spectral resolution of the whole system is 0.5 nm). The nanorod samples were deposited on a substrate consisting either of a carbon-coated TEM grid or of a 100 nm thick silicon nitride membrane. Measurements on several arrays of nanorods with also different ARs show that the regions of vertically oriented rods are almost non emissive (Figure 6) and their PL spectrum is slightly blue-shifted with respect to that from areas of

disordered nanorods. Areas of ribbonlike assemblies of nanorods are characterized by strong PL emission, which is significantly blue-shifted (up to 30 meV) with respect to the PL from areas of disordered nanorods. The difference in PL intensity between ribbonlike and vertically aligned nanorod arrays could be due to the spatial anisotropy of the optical dipole emission field of elongated nanorods. The emission from such nanocrystals, in which the transition dipole is parallel to the nanorod long axis, is expected to be maximal in the plane perpendicular to the dipole and minimal in the direction of the nanorod long axis. The blue-shift observed in emission could be related to the screening of the internal (piezo)electric field present in each nanorod that is induced by the photogenerated charge distributions in neighboring rods, which should be more efficient in ordered assemblies than in disordered aggregates. Förster resonance energy transfer, which should lead to a red-shift in the PL of close-packed assemblies of nanorods,<sup>31</sup> is not observed here probably due to the nearly monodisperse size distribution of such nanorods. Wave function delocalization and the formation of minibands, which should also cause a red-shift of the PL spectrum,<sup>32</sup> can be theoretically estimated to be

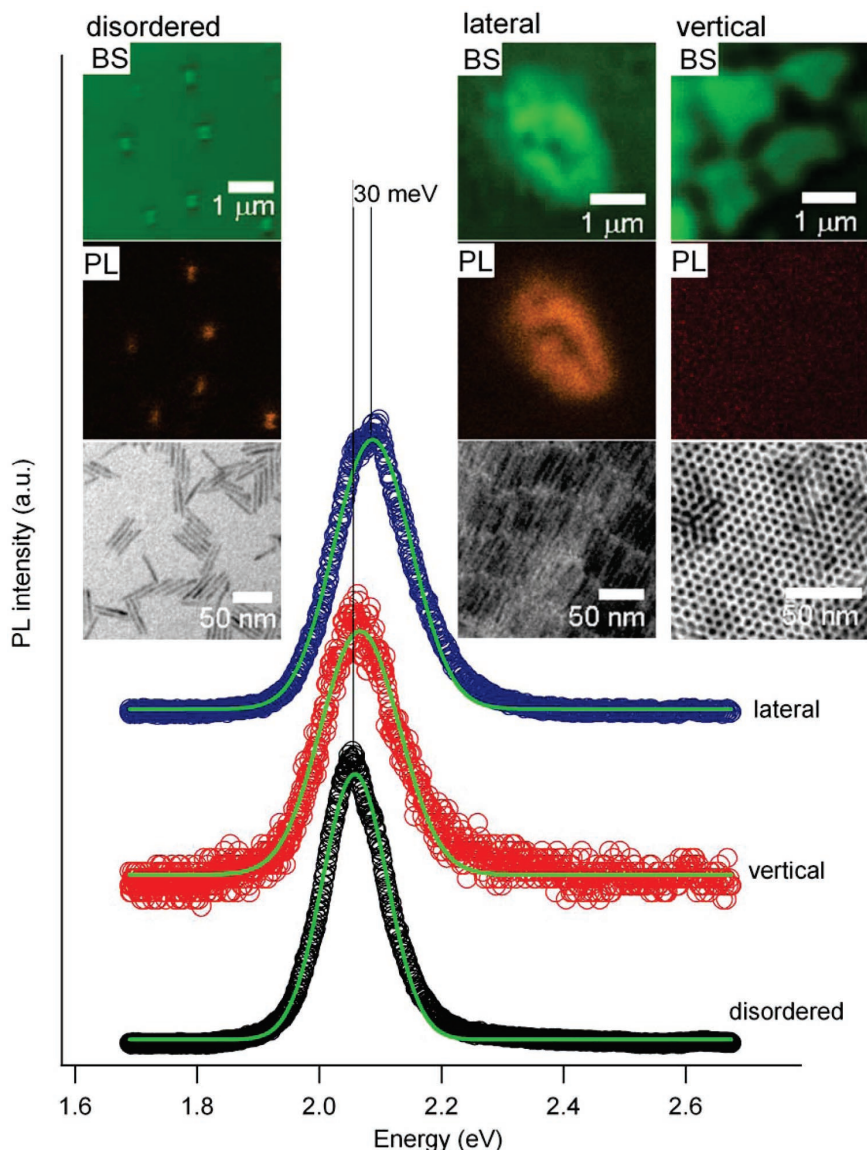


**Figure 6.** PL from different types of nanorod assemblies. PL spectra of regions of laterally, vertically aligned, and disordered nanorods with AR = 10 are marked by the open circles. The Gaussian fits of the data shown by solid green lines give 2.06, 2.07, and 2.09 eV as energy peak position for disordered ensemble, vertical arrays, and lateral arrays, respectively. The PL spectra were normalized with respect to their amplitude and shifted vertically for clarity. The insets show corresponding images of the laser backscattering (BS) and photoluminescence (PL) intensity of regions consisting of disordered, vertically, and laterally aligned nanorod arrays recorded with the confocal setup, and representative TEM images taken from the respective regions (various regions of self-assembled vertically and laterally aligned nanorods were mapped by inspecting the substrate under low magnification TEM). Large areas of vertically aligned nanorods (with respect to the substrate) were observed that could also be spotted under the confocal microscope, as they showed a characteristic “globular” and often faceted shape (see Figure 4d). The bright areas in the backscattering images originate from the nanorod ensembles.

of the order of 0.7 meV (see Supporting Information) and is therefore negligible.

The ability to fabricate ordered, large-scale assemblies of colloidal semiconductor nanorods as those reported here should strengthen the studies on physical properties arising from superstructure organization and coupling effects among nanorods. Also, it should promote further exploitation of these materials into functional, nanocrystal-based devices such as solar cells, solar concentrators, light-emitting diodes,

and field effect transistors. In addition, the seeded-growth method is easily extendible to other combinations of materials, and as a proof of concept, we demonstrate here its viability to the synthesis of tetrapod-shaped ZnTe/CdS and ZnSe/CdS nanocrystals (see Supporting Information). In this case, the starting ZnTe or ZnSe seeds have a cubic zinc-blende structure, which leads to the concerted growth of four CdS arms on top of such seeds. In particular, for the case of ZnTe seeds, the resulting ZnTe/CdS tetrapods too have a

significantly narrow distribution of arm lengths and diameters (see Supporting Information), which should lead to further exploitation also of colloidal nanocrystal tetrapods in self-assembled functional materials and devices.

**Acknowledgment.** This work was supported by the European projects ESTEEM (contract no. 026019), SANANO (contract no. 013698), and NANOTAIL (contract no. 042459), and by the Italian Ministry of Research (contract nos. RBLA03ER38 and RBIN048TSE). We thank Dr. Elvio Carlini and Dr. Davide Cozzoli for useful discussions.

**Supporting Information Available:** Detailed description of the syntheses of nanorods and tetrapods of various materials by seeded growth, structural analysis on long aspect ratio rods, additional details on electric field alignment of nanorods, theoretical calculations on isolated nanorods and on close-packed, vertically aligned nanorod assemblies, time-resolved optical measurements, and low-temperature PLE measurements. This material is available free of charge via the Internet at <http://pubs.acs.org>.

## References

- (1) Hao, E.; Schatz, G. C.; Hupp, J. T. *J. Fluoresc.* **2004**, *14*, 331–341.
- (2) Jun, Y. W.; Lee, J. H.; Choi, J. S.; Cheon, J. *J. Phys. Chem. B* **2005**, *109*, 14795–14806.
- (3) Kumar, S.; Nann, T. *Small* **2006**, *2*, 316–329.
- (4) Jana, N. R. *Angew. Chem., Int. Ed.* **2004**, *43*, 1536–1540.
- (5) Ghezelbash, A.; Koo, Koergel, B. A. *Nano Lett.* **2006**, *6*, 1832–1836.
- (6) Harnack, O.; Pacholski, C.; Weller, H.; Yasuda, A.; Wessels, J. M. *Nano Lett.* **2003**, *3*, 1097–1101.
- (7) Ryan, K. M.; Mastrianni, A.; Stancil, K. A.; Liu, H. T.; Alivisatos, A. P. *Nano Lett.* **2006**, *6*, 1479–1482.
- (8) Gupta, S.; Zhang, Q.; Emrick, T.; Russell, T. P. *Nano Lett.* **2006**, *6*, 2066–2069.
- (9) Hu, Z.; Fischbein, M. D.; Querner, C.; Drndić, M. *Nano Lett.* **2006**, *6*, 2585–2591.
- (10) Nobile, C.; Fonoberov, V. A.; Kudera, S.; Della Torre, A.; Ruffino, A.; Chilla, G.; Kipp, T.; Heitmann, D.; Manna, L.; Cingolani, R.; Balandin, A. A.; Krahne, R. *Nano Lett.* **2007**, *7*, 476–479.
- (11) Li, L. S.; Walda, J.; Manna, L.; Alivisatos, A. P. *Nano Lett.* **2002**, *2*, 557–560.
- (12) Dumestre, F.; Chaudret, B.; Amiens, C.; Respaud, M.; Fejes, P.; Renaud, P.; Zurcher, P. *Angew. Chem., Int. Ed.* **2003**, *42*, 5213–5216.
- (13) Talapin, D. V.; Shevchenko, E. V.; Murray, C. B.; Kornowski, A.; Forster, S.; Weller, H. *J. Am. Chem. Soc.* **2004**, *126*, 12984–12988.
- (14) Li, L. S.; Alivisatos, A. P. *Adv. Mater.* **2003**, *15* (5), 408–411.
- (15) Sun, B. Q.; Sirringhaus, H. *J. Am. Chem. Soc.* **2006**, *128*, 16231–16237.
- (16) Kim, F.; Kwan, S.; Akana, J.; Yang, P. D. *J. Am. Chem. Soc.* **2001**, *123*, 4360–4361.
- (17) Artemyev, M.; Moller, B.; Woggon, U. *Nano Lett.* **2003**, *3*, 509–512.
- (18) Markov, I. V. *Crystal Growth for Beginners: Fundamentals of Nucleation, Crystal Growth, and Epitaxy*; World Scientific: Singapore, 2003.
- (19) Talapin, D. V.; Koeppe, R.; Gotzinger, S.; Kornowski, A.; Lupton, J. M.; Rogach, A. L.; Benson, O.; Feldmann, J.; Weller, H. *Nano Lett.* **2003**, *3*, 1677–1681.
- (20) An, K.; Lee, N.; Park, J.; Kim, S. C.; Hwang, Y.; Park, J. G.; Kim, J.-Y.; Park, J.-H.; Han, M. J.; Yu, J.; Hyeon, T. *J. Am. Chem. Soc.* **2006**, *128*, 9753–9760.
- (21) GPA Phase plug-in for DigitalMicrograph (Gatan) available from HREM Research Inc.: <http://www.hremresearch.com>.
- (22) Rempel, J. Y.; Trout, B. L.; Bawendi, M. G.; Jensen, K. F. *J. Phys. Chem. B* **2005**, *109*, 19320–19328.
- (23) Bastard, G., *Wave Mechanics Applied to Semiconductor Heterostructures*; John Wiley & Sons: New York, 1991.
- (24) Müller, J.; Lupton, J. M.; Lagoudakis, P. G.; Schindler, F.; Koeppe, R.; Rogach, A. L.; Feldmann, J.; Talapin, D. V.; Weller, H. *Nano Lett.* **2005**, *5*, 2044–2049.
- (25) *Landolt-Börnstein, New Series, Group III, Vol. 17b*; Springer: New York, 1982.
- (26) Peng, X. G.; Schlamp, M. C.; Kadavanich, A. V.; Alivisatos, A. P. *J. Am. Chem. Soc.* **1997**, *119*, 7019–7029.
- (27) Swafford, L. A.; Weigand, L. A.; Bowers, M. J.; McBride, J. R.; Rapaport, J. L.; Watt, T. L.; Dixit, S. K.; Feldman, L. C.; Rosenthal, S. J. *J. Am. Chem. Soc.* **2006**, *128*, 12299–12306.
- (28) Lin, Y.; Skaff, H.; Emrick, T.; Dinsmore, A. D.; Russell, T. P. *Science* **2003**, *299*, 226–229.
- (29) Shevchenko, E. V.; Talapin, D. V.; O'Brien, S.; Murray, C. B. *J. Am. Chem. Soc.* **2005**, *127*, 8741–8747.
- (30) Li, L. S.; Alivisatos, A. P. *Phys. Rev. Lett.* **2003**, *90*, 097402.
- (31) Kagan, C. R.; Murray, C. B.; Bawendi, M. G. *Phys. Rev. B* **1996**, *54*, 8633–8643.
- (32) Artemyev, M. V.; Woggon, U.; Jaschinski, H.; Gurinovich, L. I.; Gaponenko, S. V. *J. Phys. Chem. B* **2000**, *104*, 11617–11621.

NL0717661

# Synthesis and micrometer-scale assembly of colloidal CdSe/CdS nanorods prepared by a seeded growth approach

*Luigi Carbone<sup>1†</sup>, Concetta Nobile<sup>1†</sup>, Milena De Giorgi<sup>1</sup>, Fabio Della Sala<sup>1</sup>, Giovanni Morello<sup>1</sup>, Pierpaolo Pompa<sup>1</sup>, Martin Hytch<sup>2</sup>, Etienne Snoeck<sup>2</sup>, Angela Fiore<sup>1</sup>, Isabella R. Franchini<sup>1</sup>, Monica Nadasan<sup>1</sup>, Albert F. Silvestre<sup>1</sup>, Letizia Chiodo<sup>1</sup>, Stefan Kudera<sup>1</sup>, Roberto Cingolani<sup>1</sup>, Roman Krahne<sup>1</sup> and Liberato Manna<sup>1\*</sup>*

<sup>1</sup> NNL-National Nanotechnology Laboratory of CNR-INFM and IIT Research Unit, 73100 Lecce, Italy

<sup>2</sup> CEMES-CNRS, 29 rue Jeanne Marvig, B.P. 94347, F-31055 Toulouse Cedex, France

<sup>†</sup> These authors have contributed equally to this work

\* Correspondence should be addressed to Liberato Manna (liberato.manna@unile.it)

## Supporting Information

\*Corresponding author:

liberato.manna@unile.it; tel. +39 0832 298 207; fax +39 0832 298 238

### **Synthesis of CdSe/CdS and CdS-only nanorods**

#### **Chemicals**

Trioctylphosphine oxide (TOPO 99%), Trioctylphosphine (TOP, 97%), Tributylphosphine, (TBP, 97%), Sulfur (99%), Tellurium (Te, 99,999%), Selenium (Se, 99,99%) diethylzinc ( $\text{Et}_2\text{Zn}$ , 97%) were purchased from Strem Chemicals. Octadecylphosphonic acid (ODPA, 99%) and hexylphosphonic acid (HPA, 99%) were purchased from Polycarbon Industries. Cadmium Oxide (CdO, 99.5%), octadecylamine (ODA 97%), 1-octadecene (ODE 90%), hexadecylamine (HAD, 98%) were purchased from Sigma-Aldrich.

#### **Synthesis of CdSe seeds**

TOPO (3.0g), ODPA (0.280g) and CdO (0.060g) are mixed in a 50mL flask, heated to ca. 150°C and exposed to vacuum for ca. 1 hour. Then, under nitrogen, the solution is heated to above 300°C to dissolve the CdO until it turns optically clear and colorless. At this point, 1.5g of TOP is injected in the flask and the temperature is allowed to recover to the value required for the injection of the Se:TOP solution (0.058g Se + 0.360g TOP). The injection temperature and the reaction time are modified in order to synthesize CdSe dots of different sizes. As an example, for the synthesis of green fluorescent CdSe dots the Se:TOP solution is injected at 380°C and the heating mantle is removed immediately after the injection. On the other hand, red fluorescent CdSe dots can be synthesized by injecting the Se:TOP at 370°C and stopping the reaction only after 3 minutes. After the synthesis, the nanocrystals are precipitated with methanol, they are washed by repeated re-dissolution in toluene and precipitation with the addition of methanol, and they are finally dissolved in TOP.

#### **Synthesis of CdS seeds**

TOPO (3.299g), ODPA (0.603g) and CdO (0.100g) are mixed in a 50mL flask, heated to ca. 150°C and exposed to vacuum for ca. 1 hour. Then, under nitrogen, the solution is heated to above 300°C to dissolve the CdO until it turns optically clear and colorless. The temperature is stabilized at 320°C and a mixture of  $(\text{TMS})_2\text{S}$  (0.170g) and TBP (3g) is injected swiftly. The heat-controller is set to 250°C and the nanocrystals are allowed to grow at this temperature for several minutes, depending on the final desired size. As an example, a reaction time of 7 minutes leads to nanocrystals with an average diameter of 3.5 nm. After the synthesis, the nanocrystals are precipitated with methanol, they are washed by repeated re-dissolution in toluene and precipitation with the addition of methanol, and they are finally dissolved in TOP.

#### **Synthesis of CdSe/CdS nanorods and CdS-only nanorods**

In a typical synthesis of CdSe/CdS nanorods *via* seeded growth, CdO is mixed in a flask together with TOPO, ODPA and HPA (see Tables S1, S2 for amounts). After pumping the flask to vacuum for about 1 hour at 150°C, the resulting solution is heated to 350-380°C, depending on the synthesis (see Tables S1, S2), under nitrogen. At this step 1.5 g of TOP is injected, after which the temperature is allowed to recover to the value required for the injection of the solution of sulphur precursor + nanocrystals. Such solution is prepared by dissolving S in TOP (see Table 1 and Table 2 for amounts) and adding to this 200  $\mu\text{l}$  of a solution of readily prepared CdSe dots or CdS dots dissolved in TOP (the concentration of dots in the TOP solution was always 400  $\mu\text{M}$ ). The resulting solution is quickly injected in the flask. After injection, the temperature drops to 270-300°C and it recovers within two minutes to the pre-injection temperature. The nanocrystals are allowed to grow for about 6-8 minutes after the injection (see Table 1 and Table 2), after which the heating mantle is removed. There are several parameters that can be varied in order to control the morphology of the resulting nanorods. Fig. 1 of the paper reports for instance the results of syntheses of CdSe/CdS

nanorods using CdSe seeds and carried out under different conditions. Such conditions are reported in Table 1.

**Table 1.**

This table lists all the parameters used for the syntheses of CdSe/CdS nanorods that are shown in Figure 1 of the paper, and prepared according to the procedure described above. Nanorods of similar morphology can be prepared also under different conditions. In Table 2 such alternative set of conditions is reported. The conditions that vary from Table 1 to Table 2 are marked in red.

Type of nanorod	CdSe/CdS Fig. 1 (b)	CdSe/CdS Fig. 1 (c)	CdSe/CdS Fig. 1 (d)	CdSe/CdS Fig. 1 (e)	CdSe/CdS Fig. 1 (f)
<b>Nanorod length (nm)</b>	19 $\pm$ 1	35 $\pm$ 2	53 $\pm$ 4	70 $\pm$ 4	111 $\pm$ 10
<b>Diameter (nm)</b>	4.9 $\pm$ 0.7	4.2 $\pm$ 0.4	3.9 $\pm$ 0.2	3.8 $\pm$ 0.3	3.8 $\pm$ 0.3
<b>TOPO (g)</b>	3	3	3	3	3
<b>ODPA (g)</b>	0.290	0.290	0.290	0.290	0.290
<b>HPA (g)</b>	0.080	0.080	0.080	0.080	0.080
<b>CdO (g)</b>	0.057	0.086	0.091	0.060	0.090
<b>S+TOP (g)</b>	0.120+1.5	0.120+1.5	0.120+1.5	0.120+1.5	0.060+1.5
<b>Core diameter (nm)</b>	3.5	3.3	3.2	2.3	2.3
<b>T<sub>injection</sub> (°C)</b>	350°	350°	350°	380°	350°
<b>Time of growth (min)</b>	8'	8'	8'	8'	8'

**Table 2.**

Type of nanorod	CdSe/CdS	CdSe/CdS	CdSe/CdS	CdSe/CdS	CdSe/CdS
<b>Nanorod length (nm)</b>	19 $\pm$ 1	32 $\pm$ 2	44 $\pm$ 3	66 $\pm$ 7	130 $\pm$ 10
<b>Diameter (nm)</b>	5.0 $\pm$ 0.5	4.8 $\pm$ 0.5	4.3 $\pm$ 0.2	4.0 $\pm$ 0.7	3.8 $\pm$ 0.3
<b>TOPO (g)</b>	3	3	3	3	3
<b>ODPA (g)</b>	0.290	0.290	0.290	0.290	0.290
<b>HPA (g)</b>	0.080	0.080	0.080	0.080	0.080
<b>CdO (g)</b>	0.060	0.086	0.060	0.090	0.093
<b>S+TOP (g)</b>	0.070+1.5	0.120+1.5	0.200+2.3	0.120+1.5	0.120+1.5
<b>Core diameter (nm)</b>	3.3	2.7	3.6	3	2.3
<b>T<sub>injection</sub> (°C)</b>	380°	350°	350°	350°	350°
<b>Time of growth (min)</b>	8'	6'	8'	8'	8'

**Structural Analysis on long aspect ratio nanorods**

**Figure S1. (Left panel):** High-resolution transmission electron microscopy (HRTEM) image of small aspect ratio CdSe/CdS nanorods. TEM samples were prepared by dropping a dilute solution of nanocrystals in toluene on carbon-coated copper grids and by letting the solvent evaporate. The nanorods have a mean diameter of  $4.9 \pm 0.7$  nm and mean length of  $19 \pm 1$  nm. The **right panel** shows a series of “mean dilatation” images of various rods from the same sample, obtained carrying out a quantitative analysis on their respective HRTEM images. Note that on average the area of lattice deformation (red region) is localized at about  $\frac{1}{4}$  of the rod length. The length of the scale-bars is 5 nm.

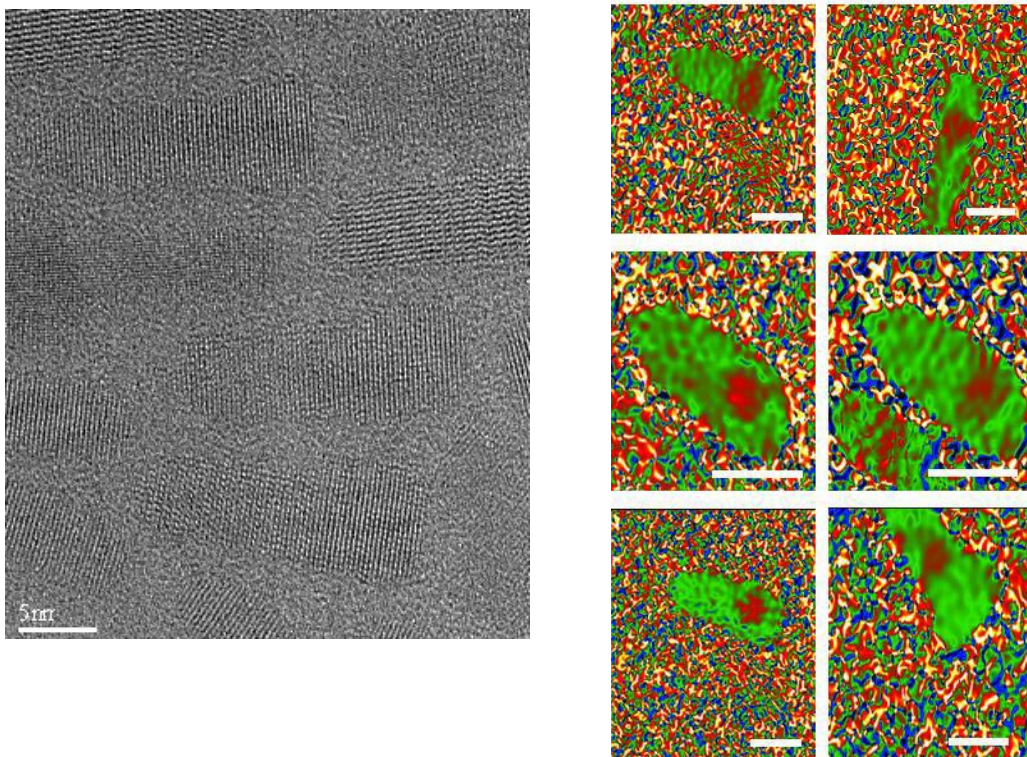


**Figure S2. (Left panel):** HRTEM image of CdSe/CdS nanorods with aspect ratio higher than those shown in Figure S1. The nanorods have a mean diameter of  $4.2 \pm 0.4$  nm and mean length of  $35 \pm 2$  nm. The **right panel** shows a series of “mean dilatation” images of various rods from the same sample, obtained carrying out a quantitative analysis on their respective HRTEM images. Note that on average the area of lattice deformation (red region) is localized at about 1/3-1/4 of the rod length.

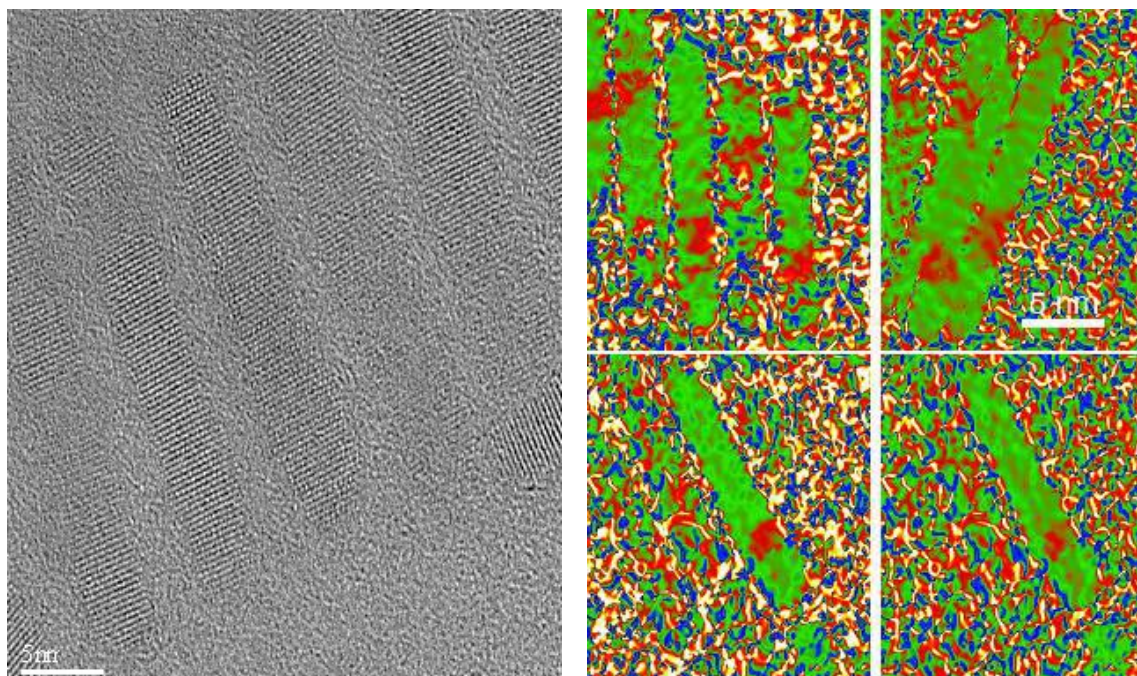
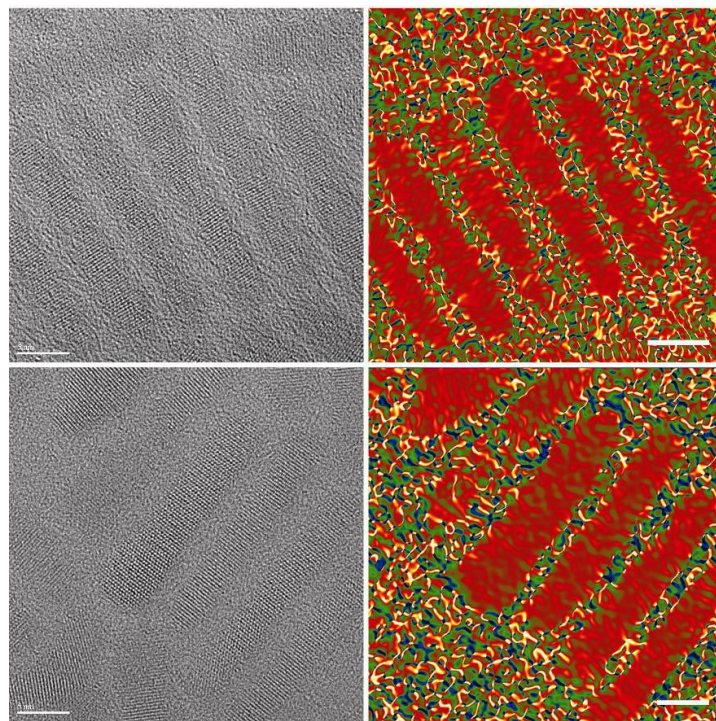


**Figure S3.** (Left panel): HRTEM image of CdS rods (average diameter  $4 \pm 1$  nm and average length  $29 \pm 2$  nm) which were grown starting from spherical CdS seeds. (Right panel) Mean dilatation images of the respective HRTEM images. No regions of significant lattice distortion can be found on these rods.



**Electric Field Alignment**

**Figure S4(i).** Scanning Electron Microscopy (SEM) images of CdSe/CdS nanorods (aspect ratio of 10) laterally aligned under the assistance of electric fields ( $10^5$  V/cm). (a) Low magnification image showing wide areas (several tens of square microns) of aligned nanorod arrays in within the gaps of an interdigitated electrode device (electrodes appear as white horizontal stripes). (b) Higher magnification image of a micron size area in between the electrodes, where the nanorods are laterally aligned in a multilayered structure. The orientation of nanorod alignment follows the applied field streamlines. (c) Area of nanorod arrays in proximity of the tip of one electrode finger, where the field lines are oriented radially. As it can be recognized in the magnified areas (d-e), nanorods are arranged parallel to the electric field.

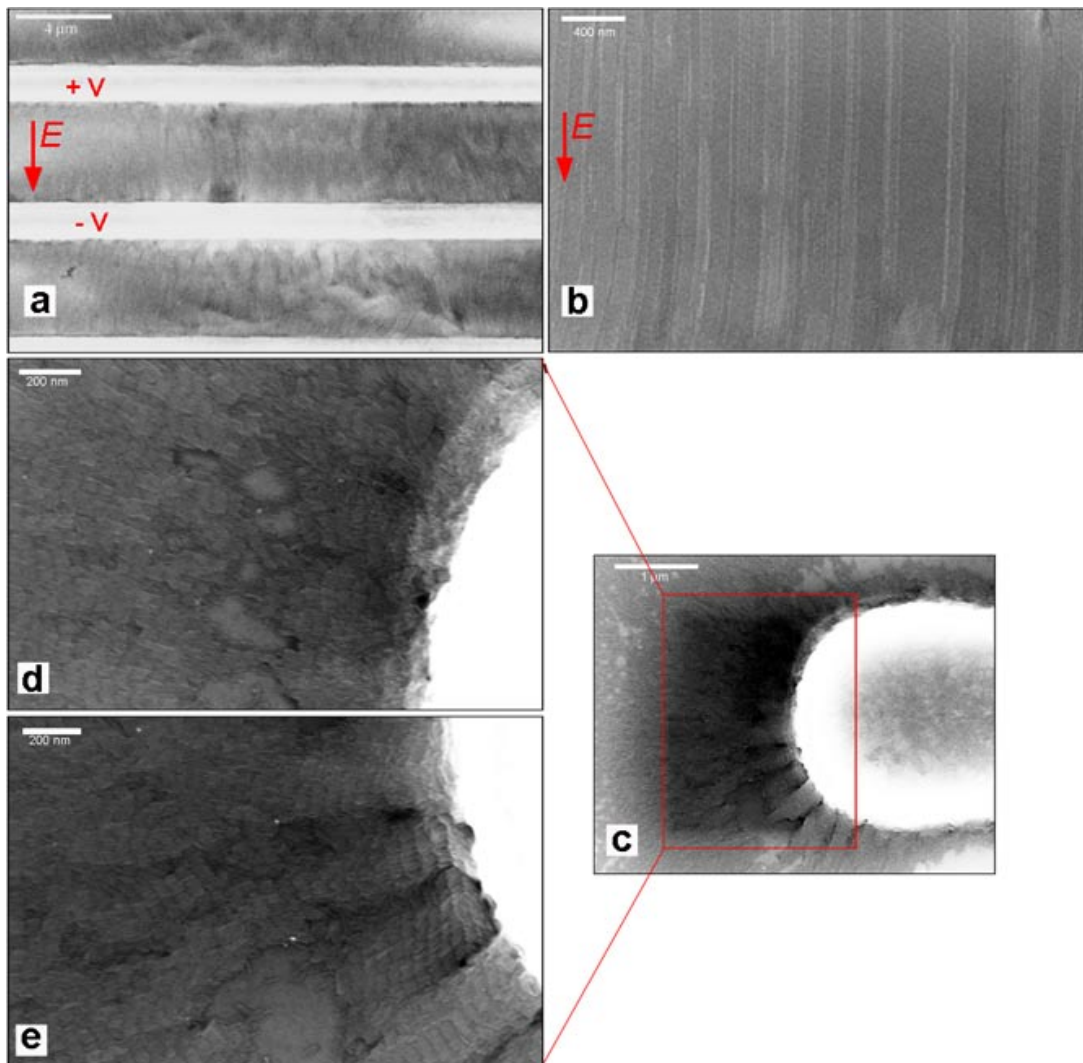


**Figure S4(ii):** Vertical nanorod structures obtained by placing the TEM grid on an electrostatically positive substrate during the evaporation of the nanorod solution.

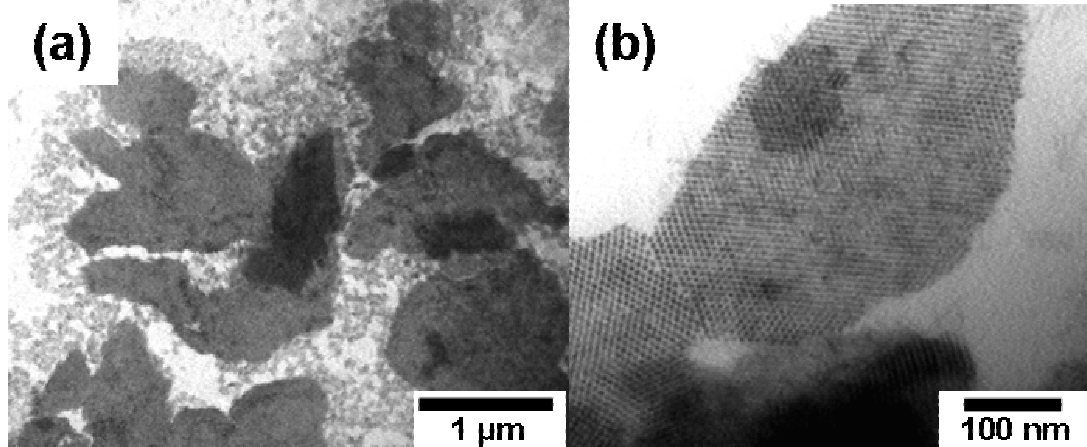
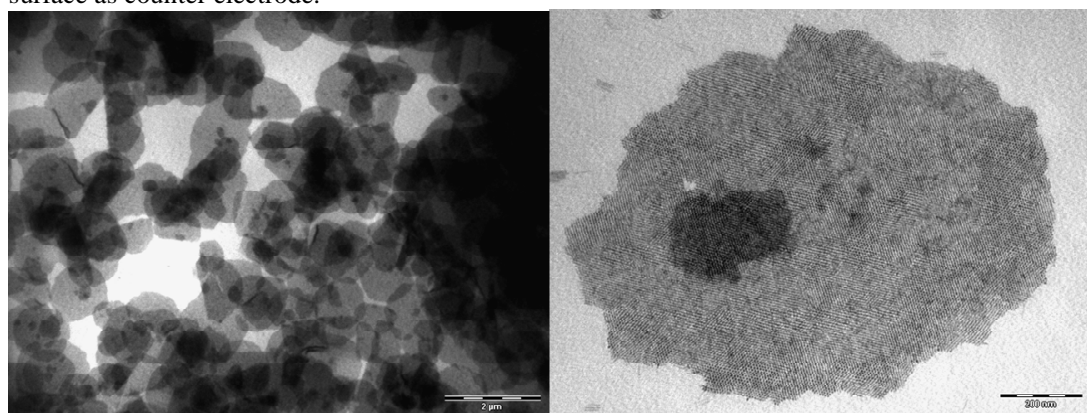


**Figure S4(iii):** Vertical nanorod structures obtained by applying a voltage of  $V=32V$  to the planar gate electrode on the back side of the membrane and a TEM grid placed on top of the sample surface as counter electrode.



### Theoretical Calculations

**Isolated Nanorods.** We modeled the asymmetric nanorod as a CdSe sphere of radius  $R_c$  inside a CdS hexagonal prism of length  $L$  and radius  $R$ . The centre of the CdSe sphere is located at a distance  $D$  from the hexagonal basis (see Figure S5).

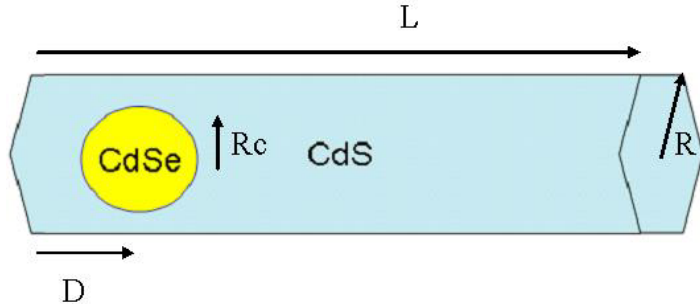


**Figure S5.** Geometrical parameters which describe the asymmetric nanorod.

In Figure S6 we report the lowest part of the absorption spectrum of a CdSe/CdS rod ( $R_c=1.5\text{nm}$   $R=2.25\text{nm}$ ,  $L=29\text{nm}$ ) calculated using the single particle approximation, including perturbatively Coulomb corrections and solving the full excitonic problem (i.e. Configuration Interaction with Single excitation, CIS). The absorption spectra are obtained using a gaussian broadening of  $50\text{meV}$  for each exciton level. Due to the electron-hole separation the Coulomb interaction is quite small, thus all the spectra are quite similar to each other. This allowed us to use the less expensive single particle approximation for the computation of electronic spectra.

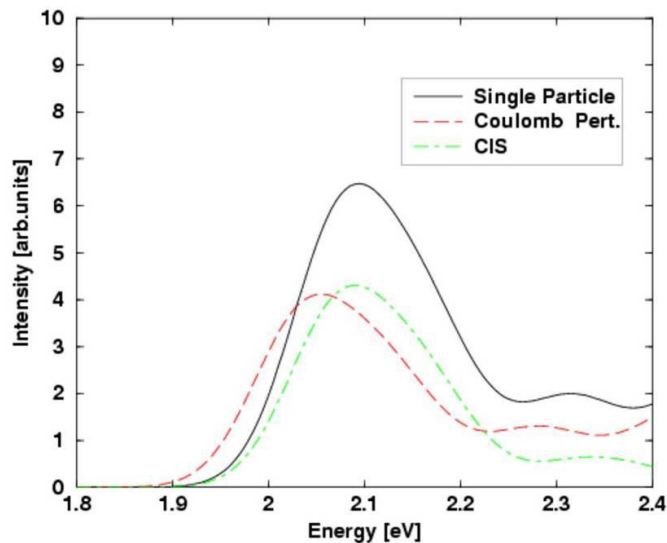


**Figure S6.** Computed absorption spectra using different approach (see text for details).

In Figure S7 we report the lowest part of the absorption spectrum of a CdSe/CdS rod ( $R_{\text{core}}=1.6\text{nm}$ ,  $R=2.5\text{nm}$ ,  $L=51\text{nm}$ ) for two different positions of the CdSe sphere. Vertical bars indicate the energy position and oscillator strength of the single exciton levels. The first 16 levels represent electronic transitions from the first  $1S$  hole level to the various electron states delocalized

over the whole systems. Using different values of  $D$ , the energy positions of the exciton levels remain constant but the oscillator strengths strongly change due to the different overlap between the hole and the electron wavefunctions. However, the final broadened absorption spectra are very similar to each other.

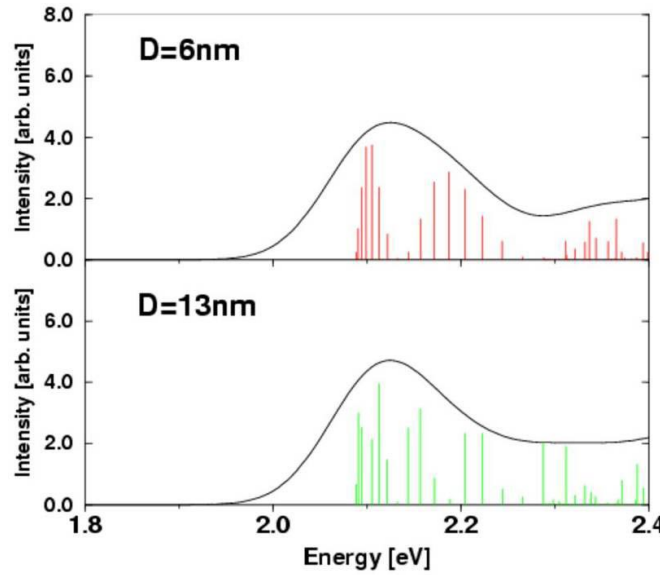


**Figure S7.** Computed absorption spectra for different position ( $D$ ) of the CdSe sphere.

**Nanorod Assemblies.** We modeled the vertically aligned nanorod assemblies ( $L=50\text{nm}$ ,  $R=2\text{nm}$ ,  $R_c=1.6\text{nm}$ ) as a two-dimensional hexagonal superlattice, as shown in Figure S8.

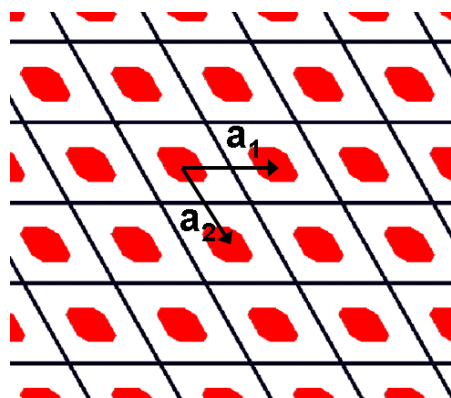


**Figure S8.** Top view of the hexagonal superlattice that models the interacting rods array.  $a_1$  and  $a_2$  denote the vectors of the unit cell.

As extrapolated from TEM analysis, the inter-rod lateral distance was set to 1.8 nm. We implemented the effective mass approximation into a modified version of the plane-wave PWSCF

code [Baroni, S.; Dal Corso, A.; de Gironcoli, S.; Giannozzi, P., available online at <http://www.pwscf.org/>]. The confining potentials applied to model the hexagonal prism for the electrons, and the sphere inside this prism for the holes, are the same as those used in the description of the isolated rod (see previous section). A kinetic energy cutoff of 1.0 Ryd. for the electrons and 5.0 Ryd. for the holes was required to ensure convergence of the electron and of the hole eigenvalues. We computed the electronic and the hole band-structure for rods at the experimental inter-rod distance (i.e. 1.8 nm) and at much larger distance (i.e. 5 nm) where the interaction between rods is expected to vanish. The computed electronic band-structure for the lowest two levels are shown in Fig. S9.

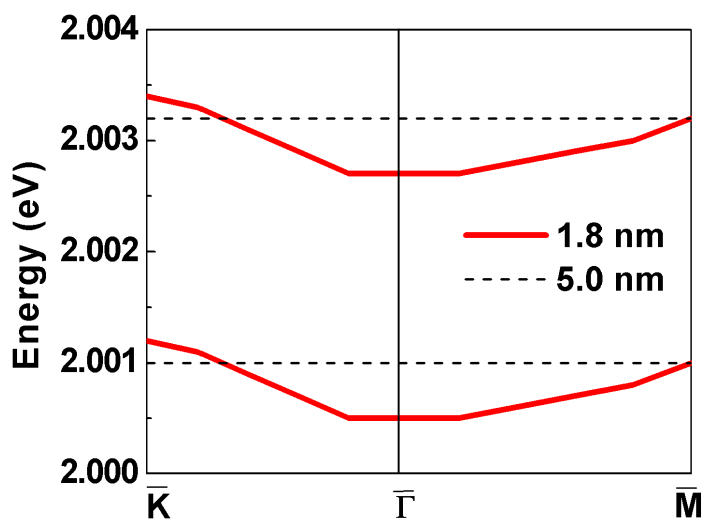


**Figure S9.** Band structure of the electronic levels for interacting nanorods, at 1.8 nm and 5.0 nm of inter-rod spacing. The high symmetry directions of the hexagonal Surface Brillouin Zone are reported.

The band-width is 0.7 meV along the  $\overline{\Gamma K}$  direction of the hexagonal Surface Brillouin Zone, for rods at 1.8 nm distance, while bands are completely flat for an inter-rod distance of 5.0 nm. The first electronic level red shifts by 0.5 meV going from a distance of 1.8 nm to 5 nm. The corresponding red shift for the first hole level is found to be much smaller (0.02 meV) due to the larger effective mass and because the hole wavefunction is completely confined in the CdSe sphere. These results show that in the vertical aligned assemblies very small (less than 1 meV) electronic coupling between rods is expected.

**Time resolved optical measurements**

Time-correlated single photon counting measurements were performed on colloidal CdSe/CdS nanorods, dissolved in toluene solution, on the nanosecond time scale. The excitation sources consist of the pulsed diode laser (340 nm) with a duration of less than 1 ns and repetition rate of 1 MHz. The sample emission was dispersed by a spectrograph (0.35 m focal length).

A strong dependence of the exciton lifetime on the aspect ratio (AR) of the rods was found. The photoluminescence (PL) emission rate decreases with increasing AR and the decay is not mono-exponential. The best fit of the PL time trace at 1/50<sup>th</sup> of the higher emission intensity is obtained by a bi-exponential decay curve for which the extracted decay times  $\tau_1^{\text{PL}}$  and  $\tau_2^{\text{PL}}$  are of the order of few ns and tens of ns, respectively. We correlated the first decay time ( $\tau_1^{\text{PL}}$ ) to the time of the intrinsic radiative emission, whereas  $\tau_2^{\text{PL}}$  can be related to recombination from surface trap states. This attribution is confirmed by a detailed time-resolved PL analysis performed on nanorods of different ARs as a function of the excitation density.

By estimating the radiative decay as  $\tau_{\text{R}}$  normalized to the PL quantum yield (QY), we found that it decreases by one order of magnitude by going from rods with AR equal to 3 to rods with AR equal to 28 (as shown in Fig S10). This behaviour is supported by theoretical calculations, which predicts for such nanorods that the electron is completely delocalized throughout the rod whereas the hole is localized in the CdSe core. In rods with larger AR the overlap of the electron-hole wave function decreases, and this leads to an increase of the intrinsic radiative decay time.

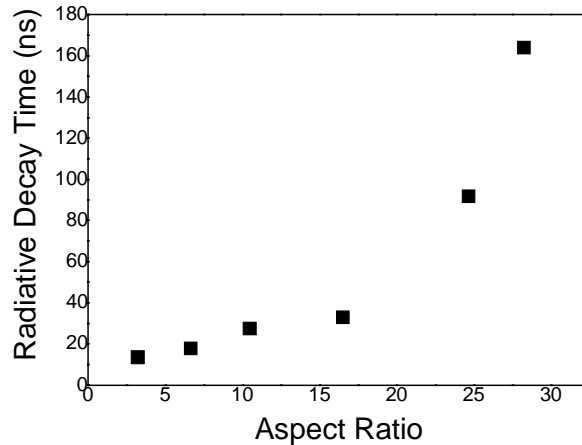


**Figure S10.** Radiative decay rate as a function of the AR for different samples of CdSe/CdS nanorods prepared from the same type of CdSe core (which had a diameter of 2.3 nm). In going from the nanorods with the smallest AR to those with the largest AR, the average diameter of the rods varies from 4 nm to 5 nm, and their average length varies from 10 nm to 130 nm, respectively.

### Low-temperature PLE measurements

Photoluminescence (PL) and photoluminescence excitation (PLE) measurements performed at low temperature (10 K) on two representative samples with different ARs (namely 6 and 19) are shown in figure S11. The detection energy was taken on the half maximum of the blue side of the PL spectrum for both samples. PLE spectra show two sharp peaks (*a* and *b*) which are attributed to the ground state resonance (*a*) and to the phonon replica (*b*). The Stokes shift estimated by the difference of the detection energy and the energy of feature *a* is about 41 meV for both samples. We note that the phonon replica lies approximately at 26 meV above the ground state energy. This value corresponds to the Longitudinal Optical phonon energy of CdSe, and it confirms that in these nanostructures the emission arises from the core.

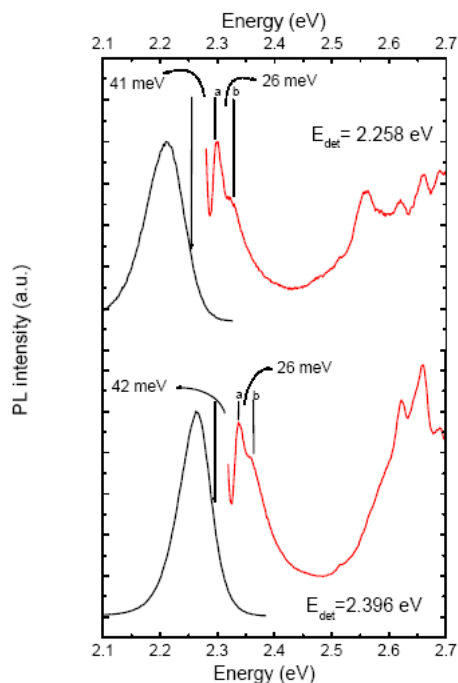


**Figure S11.** PL (black lines) and PLE (red lines) spectra for two representative samples, with ARs equal to 19 (top) and to 6 (bottom). The PLE detection energy is indicated by the arrows in the blue side of the PL spectra. The lowest resonances in the PLE spectra correspond to the ground state resonance (*a*) and its phonon replica (*b*), respectively. The peaks at higher energies are due to resonance with states in the CdS shell.

**Extension of the seeded growth approach to other materials: ZnSe/CdS and ZnTe/CdS tetrapods**

**Synthesis of ZnTe seeds**

ODA (1 g) and ODE (3 g) are mixed in a 50mL flask, heated to ca. 150°C and exposed to vacuum for ca. 1 hour. The solution is then heated to 280 °C under nitrogen flow. A solution of Te and Et<sub>2</sub>Zn in TOP (0.1 g Te + 0.096 g Et<sub>2</sub>Zn + 0.9 g TOP, molar ratio Te:Zn = 1:1) in TOP is injected quickly into the reaction flask. After the injection, the reaction temperature is set to 270 °C and the nanocrystals are allowed to grow for 3 minutes. After the synthesis, the nanocrystals are precipitated with butanol, they are washed by repeated re-dissolution in toluene and precipitation with butanol, and they are finally dissolved in TOP.

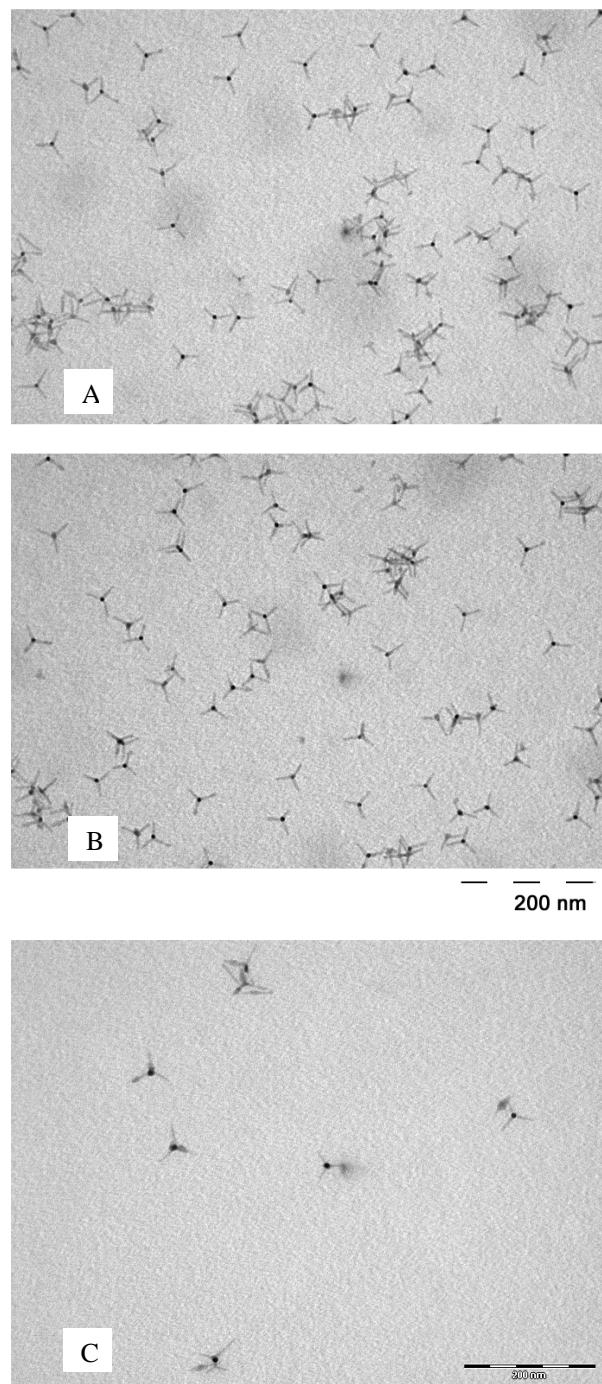
**Synthesis of ZnSe seeds**

ZnSe nanocrystals were prepared according to a previously reported procedure with minor changes. (Chem. Mater., 17, 6, 2005). In a three neck flask, HDA (6 g) was degassed under vacuum at 140 °C for 1 h, after which it was heated under N<sub>2</sub> flow. 2.5 ml of Zn/Se precursor solution (0.190 g of Se, 0.296 g of distilled ZnEt<sub>2</sub> and 6.220 g of TOP) were then quickly injected to HAD at 310 °C. Upon injection, the temperature dropped to 270 °C after which it was allowed to recover to 290 °C. To grow monodisperse ZnSe nanocrystals, additional injections of precursors were performed from time to time, in a drop-wise fashion (at a rate of about 0.2 mL/min). The reaction could be stopped (generally after 3 h) when the desired particle size was reached by removing the heating source. After the synthesis, the nanocrystals were precipitated by methanol, they were washed by repeated re-dissolution in toluene and precipitation with the addition of methanol, and they were finally dissolved in chloroform.

**Synthesis of ZnTe/CdS and of ZnSe/CdS tetrapods**

TOPO (3.0g), ODPA (0.280g), HPA (0.080g) and CdO (0.060g) are mixed in a 50mL flask. After pumping the flask to vacuum for about 1 hour at 150°C, the resulting solution is heated to 350 °C under nitrogen to dissolve the CdO until it turns optically clear and colorless. At this point, 1.5g of TOP is injected in the flask and the temperature is allowed to recover to the value required for the injection of the S:TOP+ZnTe (ZnSe) solution. This solution is prepared by dissolving S in TOP (0.120g S + 1.50g TOP) and adding to it 20  $\mu$ l of a solution of freshly prepared ZnTe (ZnSe) nanocrystal seeds dissolved in TOP (the concentration of dots in the TOP solution was set to 480 $\mu$ M). The solution is quickly injected in the flask, after which the temperature in the flask drops to 270-300°C and it recovers within two minutes to the pre-injection temperature. The resulting ZnTe/CdS (ZnSe/CdS) tetrapod-shaped nanocrystals are allowed to grow for about 3 minutes after the injection, after which the heating mantle is removed. The final sample is washed by repeated precipitation via addition of methanol as re-dissolution in toluene. Figure S1 reports low-magnification TEM images of ZnTe/CdS and ZnSe/CdS tetrapod-shaped nanocrystals prepared by this approach.

**Figure S12.** Transmission electron microscopy (HRTEM) images of ZnTe/CdS (a, b) and ZnSe/CdS (c) tetrapod-shaped nanocrystals.



# **D Reviews and Conference Proceedings**

## **D.1 On the Development of Colloidal Nanoparticles towards Multifunctional Structures and their Possible Use for Biological Applications**

T. PELLEGRINO, S. KUDERA, T. LIEDL, A. MUÑOZ JAVIER, L. MANNA, W.J. PARAK

*small* **1**(1), pp. 48–63, 2005

In this Review, we describe the synthesis of high-quality colloidal nanoparticles in organic solvents, the mechanisms by which they can be transferred into aqueous solution, and some of their applications in biology. In particular, we will place emphasis on the creation of multifunctional nanoparticles or nanoparticle assemblies.

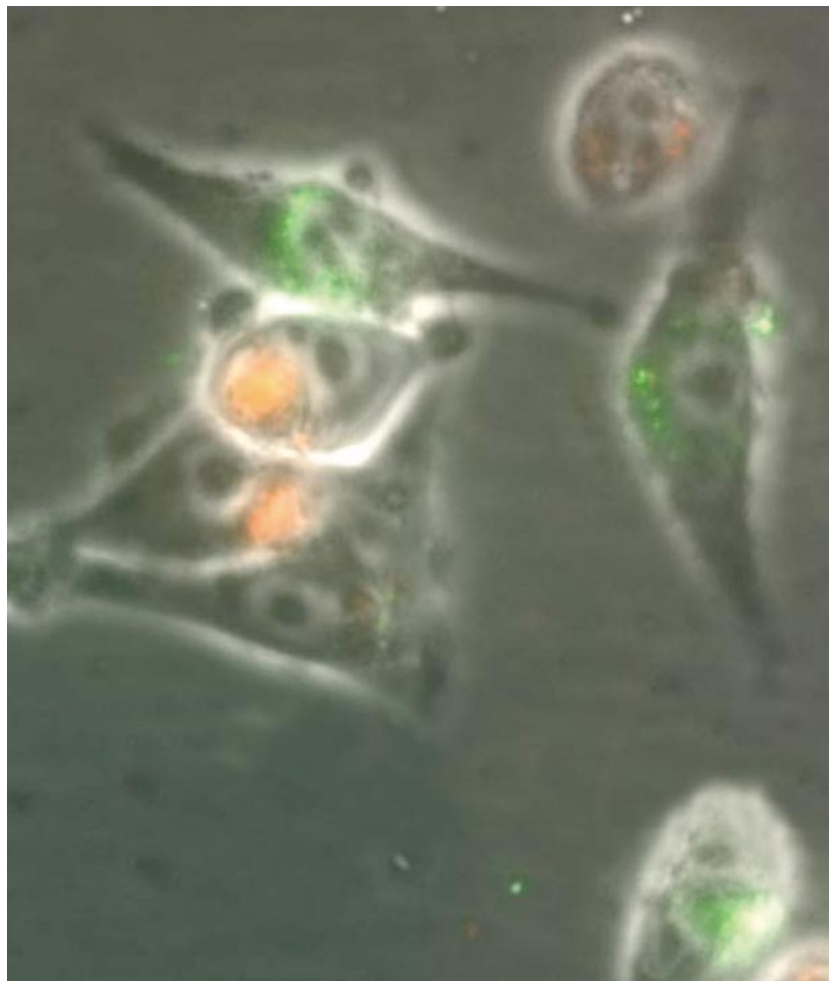
## reviews

L. Manna, W. J. Parak, et al.

## Nanoparticles in biology

## On the Development of Colloidal Nanoparticles towards Multifunctional Structures and their Possible Use for Biological Applications

Teresa Pellegrino, Stefan Kudera, Tim Liedl, Almudena Muñoz Javier, Liberato Manna,\* and Wolfgang J. Parak\*



Cancer cells imaged with red and green silica-coated CdSe/ZnS nanocrystals.

NANO MICRO  
small

### From the Contents

1. Introduction.....	49
2. Nanoparticle Synthesis in Organic Solvents.....	50
3. Transferring Nanoparticles into Aqueous Solution.....	54
4. DNA–Nanoparticle Conjugates.....	55
5. Nanoparticle Uptake by Living Cells.....	58
6. Outlook.....	60

### Keywords:

- biological systems
- colloids
- DNA
- hybrid materials
- nanoparticles

*In this Review, we describe the synthesis of high-quality colloidal nanoparticles in organic solvents, the mechanisms by which they can be transferred into aqueous solution, and some of their applications in biology. In particular, we will place emphasis on the creation of multifunctional nanoparticles or nanoparticle assemblies.*

## 1. Introduction

Nanocrystals represent one type of artificial nanostructure that can be designed to exhibit different properties. For example, semiconductor nanocrystals composed of materials such as CdSe, CdTe, and InP can be physically described as quantum dots,<sup>[1,2]</sup> which exhibit atom-like energy states that are a consequence of the confinement of carriers in three dimensions. Due to their particular electronic properties they can be used, for example, as active materials in single-electron transistors.<sup>[3]</sup> The atom-like energy states also contribute to special optical properties, such as a particle-size-dependent wavelength of fluorescence. Furthermore, nanocrystals composed of magnetic materials such as Co, CoPt<sub>3</sub>, and Fe<sub>2</sub>O<sub>3</sub> possess magnetic properties; each particle can be regarded as a single nanomagnet. Depending on their material and their shape, nanocrystals can possess many varied properties. Thus, we can consider nanocrystals as functional building blocks on the nanometer scale.

Such tiny building blocks are particularly interesting with regard to the construction of smaller and faster devices or multifunctional materials on the nanometer scale. However, each building block is itself isolated, thus to form a device or multifunctional entity the building blocks have to be arranged and connected. Since a large number of building blocks are required to form devices with reasonable complexity, the process of arranging them must be carried out in a parallel way, rather than in a sequential fashion. This is where biological molecules come into play. Certain biological molecules have two important properties: they are capable of molecular recognition and they can self-assemble. Molecular recognition is a "key/lock" principle realized on a molecular scale: Receptor molecules (the lock) recognize certain ligand molecules (the "key") with very high selectivity. Thus, only the appropriate ligand will bind to its receptor. Several important classes of receptor-ligand pairs exist, such as oligonucleotides and their complementary counterpart, antibodies and antigens, and the biotin/avidin system.<sup>[4]</sup>

The self-assembly process dictates that molecules find their appropriate positions without any external driving force. The idea is to harness these properties of biological molecules to control the arrangement of building blocks on the nanometer scale. For this purpose, each building block has to be functionalized with ligand molecules. The building block-ligand conjugates will now bind to positions where corresponding receptor molecules are present (see Figure 1). In this way the following three types of applications are possible: 1) The assembly of receptor-ligand-medi-

ated groupings of building blocks<sup>[5-7]</sup> to form new multifunctional building blocks, 2) the arrangement of ligand-modified building blocks on a surface that is patterned with receptor molecules,<sup>[8-15]</sup> and 3) the labeling of specific receptors in a cell with ligand-modified building blocks.<sup>[16-18]</sup>

- 1) The first application will allow for the creation of new materials with multifunctional properties.<sup>[19]</sup> Let us assume that we have two types of building blocks characterized by different properties. In order to combine both properties, each building block of one type must be functionalized with one ligand molecule, and each building block of the other type must be functionalized with the corresponding receptor molecule. If the two different building blocks are mixed together, they will recognize each other and bind to form a new entity that combines the properties of both starting blocks. It should be pointed out that the processes described here are solution-based and can occur in parallel for a large number of building blocks. Despite its simplicity, the assembly is precisely controlled at the nanometer scale.
- 2) One example for the second application is the assembly of single-electron transistors on a substrate to designated positions. Although problems concerning the arrangement of the components of a nanocircuit could be solved in this way, the problem of connecting or wiring the individual components remains. However, solutions for this problem based on biological molecules have also been demonstrated. With the same principles of molecular recognition and self-assembly, individual building blocks can be connected with DNA molecules. Upon metallization, the DNA molecules become conductive and can act as molecular wires.<sup>[20-23]</sup>
- 3) The labeling of cellular structures with antibodies that specifically recognize a designated structure is a common method in cell biology.<sup>[24]</sup> Typically, antibodies

[\*] T. Pellegrino, S. Kudera, T. Liedl, A. Muñoz Javier, Dr. L. Manna, Dr. W. J. Parak  
Center for Nanoscience, Ludwig Maximilians Universität München, Munich (Germany)  
Fax: (+49) 89-2180-2050  
E-mail: Liberato.Manna@unile.it  
Wolfgang.Parak@physik.uni-muenchen.de  
Dr. L. Manna  
National Nanotechnology Lab of INFM, Lecce (Italy)  
Fax: (+39) 0832-298-238

## reviews

L. Manna, W. J. Parak, et al.

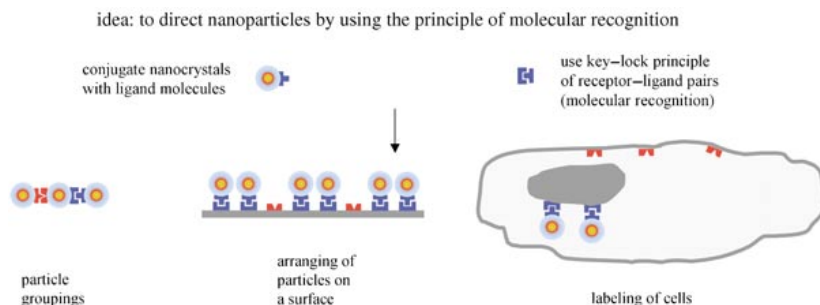


**Figure 1.** Nanocrystals can be functionalized with ligand molecules that specifically bind to certain receptor molecules. The ligand-modified nanocrystals can be directed to positions where corresponding receptor molecules are present. This strategy facilitates three different applications: 1) If one particle is functionalized with a “red” and a “blue” receptor molecule, a particle functionalized with a corresponding red (or blue) ligand will bind to its red (or blue) receptor. Thus, the controlled formation of particle groupings is possible; 2) A surface is modified with “red” and “blue” receptor molecules. Nanocrystals modified with blue ligands will selectively bind to the positions covered by the blue receptor. In this way nanoparticles can be arranged along a surface; 3) Nanocrystals with a “blue” ligand, which binds to certain blue receptor molecules present on the nuclear membrane, will bind to the nuclear membrane, but not to the plasma membrane, where only “red” receptors are present. Thus, certain parts of cells can be selectively stained with nanocrystals. If the nanocrystals are fluorescent, staining can be observed by fluorescence microscopy.

are conjugated to an organic fluorophore, so that the labeled structure can be visualized by fluorescence microscopy. Instead of conjugating the antibodies to organic fluorophores, they can be conjugated to any nanoscale building block. Depending on the properties of this building block, improved and different ways of visualizing the labeled structures are possible.<sup>[25,26]</sup>

In this article, we will describe colloidal inorganic nanocrystals as a versatile example of nanoscale building blocks. In most cases, these building blocks are synthesized most successfully in organic surfactants. As a consequence of this synthetic approach, they are often hydrophobic. There are methods for transferring these nanocrystals into aqueous solution, which will be reviewed herein. As a next step, the nanocrystals have to be functionalized with biological molecules; an example of how small groupings of nanoparticles

can be formed using these conjugates will be provided. Finally, a discussion on the uptake of colloidal nanocrystals by living cells is given, as well as an outlook on future possibilities, in particular the creation of multifunctional structures.

## 2. Nanoparticle Synthesis in Organic Solvents

Our groups use inorganic colloidal nanocrystals as one possible type of nanoscale building block. Colloidal nanocrystals are crystalline clusters of a few hundreds up to a few thousands of atoms, which are dispersed in a solvent. In other words, each colloidal nanocrystal is an individual, freestanding nanoparticle in solution. Inorganic colloidal nanocrystals can be prepared from many different materials, including metals, semiconductors, and insulators (Figure 2).



Liberato Manna graduated in chemistry at the University of Bari, Italy (1996) and received his PhD (2001) from the same university. From 1999–2003 he worked in the group of Prof. Paul Alivisatos (University of California, Berkeley) first as a visiting scientist, then as a postdoctoral fellow. He then joined the National Nanotechnology Lab of INFM, Lecce (Italy) as a staff scientist. He has pioneered the field of shape control of II–VI nanocrystals (e.g., CdSe rods and CdTe tetrapods), the study of light emission, the self-assembly of rods, and the growth of colloidal nanocrystal heterostructures containing nanosized heterojunctions with linear and branched topology. He has been awarded various national and international awards and holds six patents and patent applications in nanotechnology. He also has been scientific consultant to several companies and institutions.



Wolfgang Parak graduated in physics at the Technische Universität München, Germany (1997) working in the group of Prof. Hermann Gaub on hybrid structures between living cells and semiconductor devices. He continued this research in the same group, now at the Ludwig Maximilians Universität, München (Germany) and obtained his PhD in 1999. From 2000–2003 he worked as a postdoctoral fellow in the group of Prof. Paul Alivisatos (University of California, Berkeley), where he started working on the biological applications of colloidal nanoparticles. Since 2003 has held a position of Assistant Professor at the Ludwig Maximilians Universität, where he leads a junior research group, which is funded by the Deutsche Forschungsgemeinschaft (Emmy Noether program).

Synthesizing Colloidal Nanoparticles

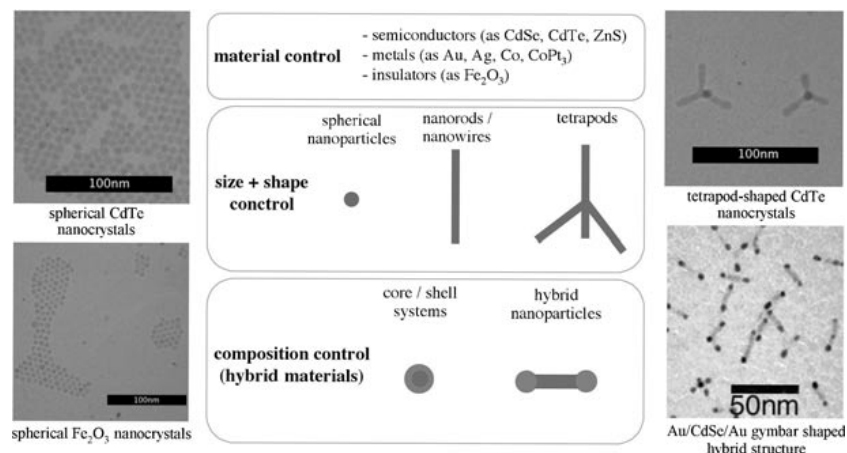


**Figure 2.** High-quality colloidal nanocrystals of various materials can be synthesized in hot organic solvents. This route typically yields roughly spherical nanoparticles with a diameter of a few nanometers. For many systems (such as the CdTe and Fe<sub>2</sub>O<sub>3</sub> nanocrystals shown), spherical nanoparticles with a well-defined size distribution can be obtained. TEM images were prepared by placing a drop of the colloidal particle solution on a TEM grid and evaporating the solvent before TEM imaging. Each dark spot corresponds to an individual nanocrystal (only the inorganic cores have enough contrast to be visualized by TEM). The stabilizing molecules (not seen by TEM) are responsible for the surface-to-surface distance between the individual inorganic nanoparticles. For many materials, the size and shape of the nanoparticles can be controlled; in the case of CdTe, spherical, rod-, and tetrapod-shaped nanocrystals can be grown. Even the composition of nanocrystals can be controlled: Either a shell of one material can be grown around a particle of another material, or nanoparticles of one material can be grown on selected positions on nanoparticles of another material (see the TEM image of Au nanoparticles grown on the end of CdSe rods, bottom right; image courtesy of U. Banin et al.<sup>[134]</sup>).

A large variety of methods exist for growing nanocrystals in aqueous solution, and as such those methods deliver nanocrystals that are hydrophilic and water-soluble. However, growth in a specific organic medium that acts as a stabilizer in the absence of water is often preferred. Such organic media are called surfactants and are composed of molecules that exhibit a polar head group and one or more hydrocarbon chains, which constitute the hydrophobic part of the molecule. One important advantage of growing nanocrystals directly in organic surfactants is that several surfactants can be heated well above 100°C (the boiling point of water). The use of high temperatures and the absence of water expands the range of materials that can be synthesized, and indeed, the optimal combination of surfactants and reaction temperatures suitable for growing a given material can be ascertained, as explained in more detail below. In addition, various defects in the crystal lattice of nanoparticles, which can form during synthesis, can be annealed out easily at higher temperatures.

Surfactants are crucial for the controlled growth and stability of nanocrystals. In the case of nanoparticles directly grown in organic surfactants, each nanocrystal is coated with a monolayer of surfactant molecules, which are bound to the surface of the nanocrystal via their polar head groups, while exposing their hydrophobic tails to the outer environment (see Figure 5). This outer layer of surfactants effectively renders the nanocrystals hydrophobic, and as such they can be easily dissolved in a wide range of nonpolar or moderately polar organic solvents. Van der Waals interactions would favor interparticle aggregation, however, the presence of the stable organic coating prevents the inorgan-

ic cores of neighboring nanocrystals from touching each other, thus resulting in a solution of well-dispersed particles. This can be deduced easily by observing a monolayer of surfactant-coated nanocrystals deposited on a suitable substrate, viewed under a transmission electron microscope (TEM, see the left column of Figure 2). This image shows a sample of nanocrystals that were prepared by casting a drop of solution containing the nanocrystals on a thin film of amorphous carbon and by allowing the solvent to evaporate. Here a gap can be seen between adjacent nanoparticles, which is due to the presence of the organic coating layers that act as spacers between adjacent nanocrystal cores. Due to intrinsic limitations of the TEM technique, these layers cannot be seen directly in the image, and the corresponding region appears as transparent.

Some basic principles of nanocrystal growth can be described by referring to a well-studied case, the growth of CdSe nanocrystals. The discussion, however, will sacrifice some details and peculiarities that are particular to other systems. For a typical synthesis of CdSe nanocrystals,<sup>[27]</sup> a mixture of surfactants is heated at temperatures of around 250–300°C. The surfactants usually chosen to grow CdSe nanocrystals are a mixture of trioctylphosphine oxide (TOPO) and a phosphine, such as tributyl- or trioctylphosphine. This mixture can also be more complex, and include alkyl amines, phosphonic acids, or carboxylic acids. The atomic species that will form the nanoparticles are added to this solution in the form of precursor molecules. One possible precursor for Cd atoms is dimethyl cadmium, [Cd(CH<sub>3</sub>)<sub>2</sub>], which is a liquid at room temperature.<sup>[131]</sup> When dimethyl cadmium is injected into the mixture of sur-

## reviews

L. Manna, W. J. Parak, et al.

factants, it decomposes and Cd atoms are released. In a similar way, Se atoms are introduced through complexation with a phosphine. At high temperature this complex dissociates to release the Se atoms. Recent advances in the synthesis of CdSe nanocrystals have led to less-hazardous precursors for Cd, such as a complex between Cd<sup>2+</sup> ions and an organic acid, such as an alkylphosphonic or carboxylic acid.<sup>[132,133]</sup> This precursor can be formed directly in the reaction flask by heating together cadmium oxide (or other cadmium salt) with the organic acid.

The surfactant molecules play a key role in the synthesis. They bind to the surface of the growing crystals and, in addition, they form complexes with the atomic species in solution, thus controlling the reactivity and the diffusion of the elemental species to the surface of the growing nanocrystals. Without them, the Cd and Se species would bind rapidly to each other, resulting in uncontrolled growth of CdSe crystals. A common feature of the surfactants used in the synthesis is that their polar head groups are functional moieties capable of donating electron pairs. Hence all of these surfactants can be defined as Lewis bases and the overall influence in controlling the growth of nanocrystals is mainly dictated by their ability to form complexes with the free Cd species in solution and to their binding ability to the Cd atoms on the surface of the nanocrystals.

The stability of the complexes formed in solution between the surfactants and the atomic species, their diffusion coefficients, as well as the binding strength of the surfactants to the nanocrystal surface, are all parameters that vary with temperature. Low temperatures lead to high complex stabilities, low diffusion, and higher surface coordinating strength, all factors that limit or even hinder nucleation and crystal growth. On the other hand, too high a temperature can also lead to uncontrolled growth. Thus choosing an appropriate temperature range is key to the control of particle growth; once a desired average crystal size is reached, the growth can be stopped by simply cooling down the reaction flask below the temperature range at which growth is possible.

The growth of nanocrystals depends on a number of parameters, such as the surface energy of the nanocrystal, the concentration of free species in solution, and the nanocrystal size, and thus nanocrystal growth can be controlled by considering these parameters. During the growth of CdSe particles, there is a thermodynamic equilibrium between the Cd and Se atoms assembled on the nanocrystal surface and the corresponding free species in solution. This means that Cd and Se atoms are continuously binding and unbinding to the particles surface, and consequently the nanocrystals, at a given time, are either growing or dissolving. One important parameter to consider in the growth process is the surface-to-volume ratio of the nanocrystals, which dictates their overall reactivity. The smaller the nanocrystals, the higher their surface tension is. As a matter of fact, smaller nanocrystals are thermodynamically less stable than larger ones, because they have a higher ratio of surface to bulk atoms. In the presence of a high concentration of free atomic species in solution (a situation usually encountered at the early stages of the growth), smaller crystals grow faster than

larger crystals, since they are more reactive and tend to incorporate the incoming free species more rapidly, which in turn lowers the ratio of surface to bulk atoms. In this case, the starting distribution of sizes narrows over time, a situation defined as a “focusing regime”. Over time, however, the concentration of free species in solution drops, and fresh monomers, which need to diffuse from the bulk of the solution to the surface of the growing nanocrystals, are not able to sustain the fast growth of the smaller particles. The growth rate of the large particles then becomes higher than that of the smaller particles, and the size distribution begins to broaden (the “defocusing regime”). Finally, when the concentration of free species in solution drops further, small particles, which are highly reactive, start dissolving and release free atomic species back into the solution. These species then feed the larger crystals, which are more stable, and the overall size distribution broadens much faster over time, a phenomenon known as “Ostwald ripening”.

Once the parameters affecting growth are well understood, manipulation of the growth kinetics can lead to the formation of nearly monodisperse nanocrystals of any desired size. In order to keep the system in the focusing regime for a long time, it is possible to nucleate just a few nanocrystals, so that they will compete less with the remaining free species in solution, which will then be depleted over a much longer timeframe. Alternatively, it is possible to perform additional slow injections of precursors during the growth, effectively keeping the concentration of free species in solution above a critical threshold. Based on these principles, high-quality spherical nanoparticles of a large variety of semiconductor materials, in addition to CdSe, are now produced routinely, such as CdS, CdTe,<sup>[27,28]</sup> InAs, InP<sup>[29,30]</sup> and Ge.<sup>[31]</sup>

Recently, the synthetic methods described above have been used to synthesize relatively monodisperse nanocrystals of oxides (such as Fe<sub>2</sub>O<sub>3</sub>,<sup>[32]</sup> Fe<sub>3</sub>O<sub>4</sub>, CoFe<sub>2</sub>O<sub>4</sub>, MnFe<sub>2</sub>O<sub>4</sub>,<sup>[33]</sup>) and of metals and metal alloys (such as FePt,<sup>[34]</sup> Co,<sup>[35-37]</sup> and CoPt<sub>3</sub>,<sup>[38,39]</sup> see Figure 2).

Crystals are intrinsically anisotropic objects and the assumption that various nanocrystal facets will have similar surface energies under given reaction conditions is a rough approximation. In a crystal, different facets have different arrangements and densities of atoms, polarity, and number of dangling bonds. Consequently, the ability of a surfactant to coordinate surface atoms will vary face-by-face. In addition, a surfactant can be multidentate, and so its ability to bind to multiple surface atoms can be enhanced or limited by specific surface stereochemistry requirements. The combination of these factors leads to differences in surface energies and therefore in growth rates of the various facets. Frequently, the growth of colloidal nanocrystals is isotropic, which indicates that the influence of these factors is not so relevant. However, several research groups in the last few years have exploited this fact and have proposed various approaches aimed at synthesizing colloidal nanocrystals with anisotropic shapes. It is now possible to synthesize nanocrystals of various materials that have rod-like, disk-like, or even more complex shapes, such as the tetrapods.<sup>[40]</sup>

Synthesizing Colloidal Nanoparticles

Recently, shape-controlled growth has been demonstrated for a wide range of materials, such as  $\text{TiO}_2$ ,<sup>[41]</sup>  $\text{Co}$ ,<sup>[42]</sup>  $\text{CdSe}$ ,<sup>[40,43]</sup>  $\text{CdTe}$ ,<sup>[44]</sup>  $\text{ZnTe}$ ,<sup>[45]</sup> and  $\text{Ni}$ .<sup>[46]</sup> A detailed review about the shape-controlled growth of nanocrystals has been reported elsewhere.<sup>[47]</sup>

At the next level of complexity, nanocrystals of one material can be embedded in a shell of another material, and in some cases epitaxial growth is even possible. For example, the growth of epitaxial shells of  $\text{ZnS}$  around spherical<sup>[48,49]</sup> and rod-shaped  $\text{CdSe}$  nanoparticles is well established.<sup>[50,51]</sup> Other examples for core/shell systems include  $\text{CdSe}/\text{CdS}$ ,<sup>[52,53]</sup>  $\text{CdTe}/\text{CdSe}$  and  $\text{CdSe}/\text{ZnTe}$ ,<sup>[54]</sup>  $\text{InAs}/\text{InP}$  and  $\text{InAs}/\text{CdSe}$ ,<sup>[55]</sup>  $\text{FePt}/\text{Fe}_3\text{O}_4$ ,<sup>[56]</sup>  $\text{Pt}/\text{Co}$ ,<sup>[57]</sup> and  $\text{Ag}/\text{Co}$ .<sup>[58]</sup> In these cases the system as a whole is still highly symmetric, however, it is also possible to grow one material in an asymmetric fashion onto another one. Such heterostructures have been demonstrated for  $\text{CdSe}-\text{CdS}$ ,<sup>[59]</sup>  $\text{CdS}-\text{FePt}$ ,<sup>[60]</sup> and  $\text{CdSe}-\text{Au}$ <sup>[134]</sup> (Figure 2).

Colloidal nanocrystals can possess a variety of physical properties. For example,  $\text{Fe}_2\text{O}_3$  and  $\text{CoPt}_3$  nanoparticles exhibit superparamagnetic behavior, while semiconductor nanoparticles such as  $\text{CdSe}$  are fluorescent materials. Compared to organic fluorophores, colloidal semiconductor nanocrystals have peculiar fluorescence properties.<sup>[16]</sup> They have a continuous absorption spectrum, symmetric and narrow emission, and reduced photobleaching (Figure 3). Most important, the wavelength of fluorescence depends on

the particle size.<sup>[2]</sup> In this way all fluorescence colors (wavelengths) spanning from the infrared to the ultraviolet can be obtained by selecting the appropriate semiconductor material and by tuning the particle size. Particle shape is also a key factor (in contrast to spherical  $\text{CdSe}$  nanoparticles, rod-shaped  $\text{CdSe}$  nanoparticles have a polarized emission).<sup>[61]</sup>

By combining different materials in one entity nanoparticles with several properties, such as fluorescence and certain magnetic behavior, can be obtained.<sup>[60]</sup> The synthesis of colloidal nanoparticles of different materials and shape is already highly advanced and synthesis protocols for many systems have been published. However, the synthetic creation of nanohybrid materials with controlled composition is still in its infancy and exciting future developments in this direction can be expected.

As already stated, the nanoparticles are coated with hydrophobic stabilizing molecules, which renders them insoluble in aqueous solution; this effect can be used to select nanoparticles by size. The principle of the so-called "size-selective precipitation" is easy to understand (Figure 4): If a polar solvent (such as methanol) is added to a solution of hydrophobically capped nanoparticles dissolved in an organic solvent (such as toluene), the nanoparticles start to precipitate. Since larger nanoparticles are dispersed in a less stable way than smaller ones, the larger nanoparticles precipitate first. Thus, a polar solvent can be added until the first nanoparticles begin to precipitate. The solution is then centrifuged, whereby the larger nanoparticles settle down as a pellet and the smaller ones stay as a supernatant in solution. The pellet can then be redissolved in the organic solvent so that this solution contains the fraction of the largest nanoparticles. This process can be repeated in an iterative way, so that fractions containing different nanoparticle sizes can be obtained. This procedure is very important to obtain homogeneous products. As a further example, it is possible that a synthesis of  $\text{CdSe}$  tetrapods may also generate  $\text{CdSe}$  spheres. By using size-selective precipitation, the smaller spheres can be separated from the larger tetrapods and a pure sample of tetrapods can be obtained.<sup>[44]</sup>

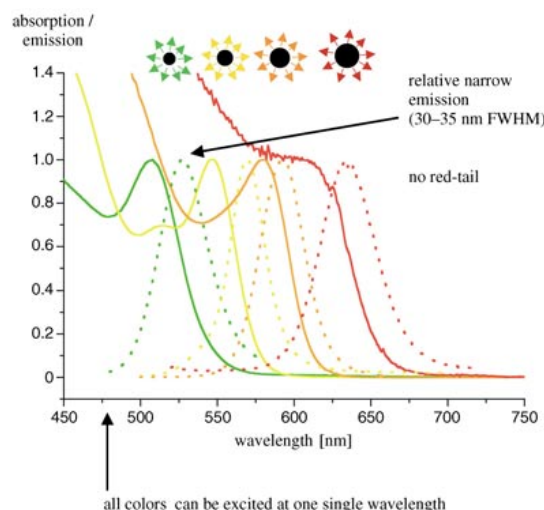


**Figure 3.** The optical properties of colloidal  $\text{CdSe}$  nanocrystals strongly depend on their size. The smaller the nanoparticle, the more blue-shifted its fluorescence is. The absorption and emission spectra of four different samples of  $\text{CdSe}$  nanocrystals with different sizes are shown. The absorption spectra of the nanoparticles are continuous in the UV region and have a peak whose position is shifted to shorter wavelength as they reduce in size. The fluorescence emission of the nanoparticles is fairly symmetric and narrow (30–35 nm full width at half maximum) and peaks at a wavelength that is a few nanometers red-shifted compared to their absorption peak. Because of the continuous absorption spectrum in the UV region, all nanoparticles of different color can be excited at one single wavelength. One particularity of  $\text{CdSe}$  nanocrystals is their reduced tendency to photobleach compared to typical organic fluorophores (upper right: nanoparticles of different sizes in solution; lower right: fluorescence of these solutions under illumination with a hand-held UV lamp).



## reviews

L. Manna, W. J. Parak, et al.

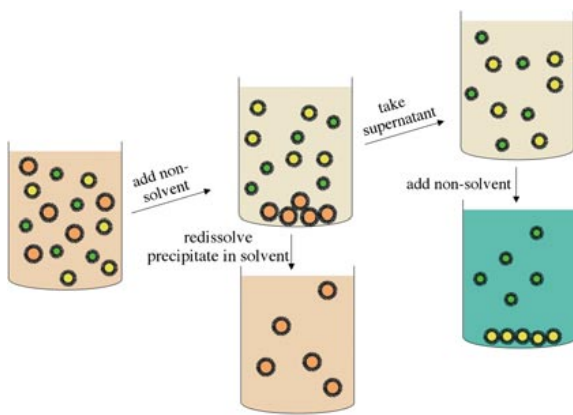


**Figure 4.** The colloidal stability of nanoparticles depends on their size. Fluorescent CdSe nanoparticles of different sizes (smallest: green, medium-sized: yellow, largest: orange) capped with hydrophobic stabilizing molecules (black) and dissolved in toluene (brown) are illustrated. If a (more polar) non-solvent (e.g., methanol; drawn in blue) is added, the solubility of the nanoparticles decreases. Larger nanoparticles are more prone to lose their colloidal stability. Thus the largest nanoparticles with orange fluorescence precipitate first. When the precipitate is isolated and organic solvent is added the nanoparticles will be redispersed. Adding further non-solvent can then separate the yellow particles. Hence, nanoparticles can be sorted by their size by this method.

### 3. Transferring Nanoparticles into Aqueous Solution

In order to use hydrophobic nanoparticles for biological applications, they first have to be transferred into aqueous solution. Figure 5 provides a general scheme for the conversion of hydrophobic nanoparticles into hydrophilic species. Stabilizing molecules coordinate with the surface of the nanoparticle; this binding procedure, and the stabilizing molecule, has to be chosen carefully for every nanoparticle material. Thiols, for example, are known to bind well to gold surfaces,<sup>[62]</sup> whereas amines bind to cobalt surfaces.<sup>[63]</sup> Therefore, alkyl chains with either thiol or amino groups are appropriate stabilizing molecules for gold and cobalt nanoparticles, respectively. The alkyl chains point away from the particle surface (Figure 5a), which means that the inorganic nanoparticles cannot touch each other; they are stabilized by the steric repulsion of the hydrophobic chains. If nanoparticles of a highly concentrated solution are immobilized on a surface by evaporation of the solvent, they can form tightly packed arrays, which can be seen by TEM analysis (left column of Figure 2). However, the minimum distance between the surfaces of two inorganic cores is typically found to be smaller than two times the length of the stabilizing molecules, which means that the shells of organic stabilizing molecules can partially penetrate each other.<sup>[64,65]</sup>

In general, there are two strategies to stabilize nanoparticles in aqueous solution. The first is based on the introduction of charge. Nanoparticles of similar charge repel each other and thus aggregation is prevented. However, in electrolytic solution charges are screened by counterions and the electrostatic repulsion is weakened, which at sufficiently

high salt concentrations finally can yield to particle aggregation. Thus, particle stabilization by electrostatic repulsion is only possible for moderate salt concentrations. Furthermore, the charge of stabilizing molecules depends on the pH value of the solution. For pH values above 5–6 carboxy (COOH) groups become negatively charged (COO<sup>−</sup>), whereas they are neutral for pH values below 5–6. Nanoparticles stabilized by the charge of carboxy groups are therefore only stable under neutral and alkaline pH conditions.

An alternative method of stabilization is through steric repulsion. Here, the ligand molecules form hydrophilic “brushes” around the nanoparticle surface. These brushes prevent inorganic particle cores from coming into contact. Typical molecules used for this purpose are polyethylene glycol (PEG)<sup>[66]</sup> and dextrane.<sup>[67]</sup> By these methods, nanoparticles can be made water-soluble by providing them with a hydrophilic coating, which is either charged or consists of polymer brushes. The next challenge is how to coat initially hydrophobic nanoparticles with such a hydrophilic shell.

The most straightforward way to achieve such coatings is via ligand exchange, where the hydrophobic stabilizing molecules are exchanged by hydrophilic ones.<sup>[68–71]</sup> Although this method is simple and direct, there are certain disadvantages involved with it. One site of the stabilizing molecule has to be able to strongly coordinate to the surface of the inorganic nanoparticle. This

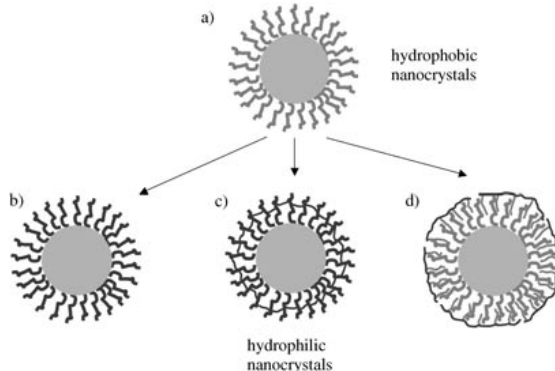


**Figure 5.** a) Hydrophobic nanoparticles (inorganic part: light-gray sphere) are stabilized by hydrophobic stabilizing molecules (medium-gray lines), which coordinate at one end to the particle surface; different nanoparticle materials require different head groups to be used; b) the easiest strategy to transfer such nanoparticles into polar solvent is to exchange hydrophobic for hydrophilic stabilizing molecules (dark-gray lines). Again, the hydrophilic stabilizing molecules need one site that can coordinate to the particle surface; c) cross-linking after ligand exchange yields a more stable shell; d) an amphiphilic polymer is wrapped around the nanoparticle, whose hydrophobic chains intercalate the hydrophobic stabilizing molecules bound to the particle, whereas the hydrophilic parts of the polymer endow water-solubility.

Synthesizing Colloidal Nanoparticles

site has to be individually chosen for every nanoparticle material. Therefore, no general procedure that works for all nanoparticle materials exists. In addition, there exists for many materials no site that strongly coordinates to the particle surface. For example, thiols (-SH) are typically used to bind to the surface of fluorescent CdSe/ZnS nanoparticles. The hydrophilic head group of such stabilizing molecules is often a carboxy (electrostatic stabilization) or a polyethylene glycol (steric stabilization) group. Since the binding affinity of thiols to ZnS surfaces is only moderate, these nanoparticles are not stable in aqueous solution for long periods.<sup>[72]</sup> Eventually the thiol-ZnS bonds are broken and the stabilizing molecules are removed from the particle surface (this can occur either because the thiol groups are hydrolyzed or photo-oxidized). If, for example, mercaptopropionic acid (HS-CH<sub>2</sub>-CH<sub>2</sub>-COOH) stabilized CdSe/ZnS nanoparticles are dialyzed against an aqueous solution, the nanoparticles start to precipitate after some hours. This is because through dialysis there are no excess mercaptopropionic acid molecules in solution, and those molecules initially bound to the particle surface unbind after a certain period of time and cannot rebind. Although still frequently used, simple ligand exchange of the stabilizing molecules is not optimal for the water-solubilization of nanoparticles. Advanced performance can be obtained with stabilizing molecules that have more than one site that coordinates to the inorganic particle surface.<sup>[73,74,135]</sup>

More elaborate protocols are still based on ligand exchange of the stabilizing molecules, but with the possibility of cross-linking the shell of the stabilizing molecules. Even if the bond between one stabilizing molecule and the particle surface breaks, this molecule is still kept in place by cross-linking to neighboring stabilizing molecules. Again the hydrophilic part of the stabilizing molecules can be either charged or consist of a polymer brush. An advanced method using such a protocol is surface silanization: First, the original hydrophobic ligand shell is replaced by a layer of silane molecules. On one of their end groups, the silane molecules are modified with a group that binds to the particle surface, such as thiol groups to bind to ZnS surfaces. Silane molecules include silanol groups, which can cross-link through the formation of siloxane bonds. In this way, stabilizing shells with more than one layer can also be created. Added silane molecules are incorporated in such a layer under the formation of siloxane bonds. When the outer shell consists of hydrophilic silanes (either with a charged or polymer-based tail group), the resulting nanoparticles are stable in water. Surface silanization has been successfully employed for many different nanoparticle materials.<sup>[63,66,75-80]</sup> The use of cross-linked ligand shells improves water stability, however, ligand exchange is still involved, and therefore the silane molecules that bind to certain particle surfaces have to be chosen individually.

In contrast to the two methods described above, there are further strategies that do not involve ligand exchange. These methods are based on the addition of an extra layer around the original hydrophobic layer of stabilizing molecules. The additional layer can be stabilized by hydrophobic interactions: The hydrophobic part of amphiphilic molecules

coordinates to the hydrophobic stabilizing shell around the nanoparticles, whereas their hydrophilic part points outwards into the solution, and thus facilitates water solubility. This concept can be used to form water-soluble hydrophobic nanoparticles in a very general way and has been already applied to membrane proteins<sup>[81]</sup> and different types of nanoparticles (see Figure 6).<sup>[82-84]</sup> The great advantage of this concept is that it does not involve ligand exchange.

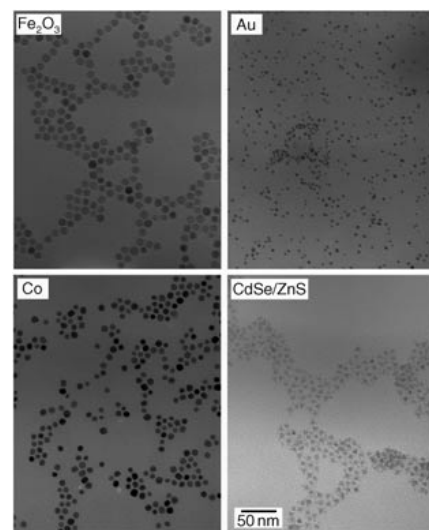


**Figure 6.** Transmission electron microscope (TEM) images of water-soluble polymer-coated nanoparticles of different materials (left to right: CoPt, Au, Fe<sub>2</sub>O<sub>3</sub>, and CdSe/ZnS).

Therefore, the same procedure can be applied to almost any hydrophobically capped particle, regardless of the material of the inorganic core. However since multiple shells are involved, the overall size of the nanoparticles will certainly be larger in comparison with nanoparticles solubilized by direct exchange to a hydrophilic monolayer shell. On the other hand, a large variety of amphiphilic polymers can be used, which allows for the direct incorporation of different functionalities directly into the shell. These functionalities can then be used to link the nanocrystals to biological molecules.

#### 4. DNA–Nanoparticle Conjugates

Many groups<sup>[85,86]</sup> have reported the attachment of biological molecules to water-soluble nanocrystals. From the conceptual point of view there are two possibilities: First, biological molecules that are modified with a chemical group that is reactive towards the nanoparticle surface can be directly attached to the nanoparticle surface. This involves a ligand exchange in which part of the stabilizing molecules are replaced by the biological molecules. For example, biological molecules with thiol groups can react with the surface of gold<sup>[85,87]</sup> and CdSe/ZnS<sup>[88-90]</sup> nanocrystals by

## reviews

L. Manna, W. J. Parak, et al.

partially replacing the phosphine and mercaptopropionic acid stabilizing shells around the Au and CdSe/ZnS nanoparticles, respectively. Second, the biological molecules can be bound to the stabilizing shell around the inorganic nanocrystal core.<sup>[86]</sup>

Several types of interaction can be used to attach biological molecules to nanoparticles. In the most primitive case the molecules are simply adsorbed either directly to the nanoparticle surface or to the shell of stabilizing molecules around the nanoparticles.<sup>[91,92]</sup> Better stability can be obtained through electrostatic interactions between biological molecules that are oppositely charged to the nanoparticles.<sup>[73,93]</sup> The most elegant method, however, is via the formation of chemical bonds between the biological molecules and the stabilizing shell around the nanoparticles.<sup>[18,66,86]</sup> Nanocrystal-biomolecule conjugates have already successfully been employed for various applications such as sensors for the detection of molecules<sup>[94–96]</sup> or the labeling of cells.<sup>[18,97,98]</sup>

This Review will focus on one example, that is, the conjugation of Au nanoparticles with single-stranded oligonucleotides. Certainly this is one of the easiest systems to produce, but because of its simplicity many concepts can be described in a straightforward way. Gold nanoparticles can be stabilized in aqueous solution by using charged phosphine molecules. The phosphine moiety coordinates to the Au surface, while the charged group (e.g., -SO<sub>3</sub>) points towards the solution and thus renders the particle hydrophilic.<sup>[99]</sup> As already pointed out, thiol groups can bind to Au surfaces in a quasi-covalent manner. Thus, for the bioconjugation of Au nanoparticles with oligonucleotides, it is straightforward to simply add thiol-modified oligonucleotides to a solution of phosphine-stabilized nanoparticles. The oligonucleotides will partly replace the phosphine-stabilizing shell and bind strongly to the Au surface via the thiol group. This standard procedure has also routinely been employed to functionalize citrate-stabilized Au nanoparticles with oligonucleotides.<sup>[107]</sup>

From a conceptual viewpoint, it would be ideal to control the number of oligonucleotides attached per nanoparticle. This is of particular importance for the construction of DNA-mediated particle groupings. Let us assume that a DNA-mediated nanoparticle trimer is desired, in which two small Au nanoparticles should be attached to one large Au nanoparticle. For this purpose, a large nanoparticle with exactly two strands of DNA, and two small nanoparticles with exactly one strand of complementary DNA is required. If the large Au particle had three strands of DNA attached to which three small Au nanoparticles could bind, a particle tetramer would be obtained instead. Therefore, for the creation of defined building blocks the number of DNA molecules per particle has to be controlled. Unfortunately no easy direct synthesis to obtain nanoparticles with an exact DNA-molecule-to-particle ratio exists; if thiol-modified DNA and nanoparticles are mixed in a 1:1 ratio, a stoichiometric distribution will always be obtained. This means that besides nanoparticles with one DNA unit per particle, the reaction mixture will also contain nanoparticles without DNA and nanoparticles with two DNA molecules per particle. For this reason a method has to be found to extract the

Au nanoparticles with the desired number of attached DNA molecules from the reaction mixture.

One possibility to achieve this goal is through the use of gel electrophoresis. A gel is basically a porous matrix of a polymer to which an electric voltage can be applied. Charged nanoparticles can move through the electric field within the gel, and their speed of migration depends on the degree of charge associated with the nanoparticle (the higher the charge, the more rapid the migration). The polymer matrix hinders the flux of the nanoparticles; the larger the nanoparticles, the harder for them it is to squeeze through the pores and the slower the speed of migration will be. Thus, gel electrophoresis is sensitive to both particle charge and size. Both phosphine-stabilized Au nanoparticles and DNA are negatively charged. It can therefore be assumed that the total change in surface charge density of the Au nanoparticles upon conjugation with DNA is of minor importance. On the other hand, the attachment of DNA certainly increases the total size of the Au-DNA conjugate; the more DNA that is attached, the larger the total diameter of the conjugate becomes. This assumption corresponds well with our experimental findings.<sup>[87]</sup> Conjugation of nanoparticles with DNA decreases the speed of migration on the gel, which corresponds to an increase in conjugate diameter. The addition of charge, on the other hand, should increase the speed of migration, which cannot be observed in experiments. Thus, gel electrophoresis can be employed to sort DNA-Au conjugates by their size, and in parallel, by the number of DNA molecules attached per particle.<sup>[100]</sup> An example of such discrimination is shown in Figure 7b. Indeed, discrete bands corresponding to nanoparticles with zero, one, two, three, and four DNA molecules per Au particle can be resolved. The DNA-particle conjugates can be extracted from these bands of the gel<sup>[7]</sup> and used for further experiments. A similar gel-sorting concept has also been applied for different types of nanoparticles.<sup>[101]</sup> Unfortunately gel-sorting requires very good size and charge distributions of the unconjugated nanoparticles to afford good resolution of discrete bands.<sup>[66]</sup>

It should be noted that sorting by charge is also possible through gel electrophoresis techniques. For uncharged unconjugated nanoparticles, the conjugation with DNA primarily increases the surface-charge density. Therefore, these conjugates migrate faster as more DNA is attached.<sup>[66]</sup> Recently more direct concepts for the creation of nanoparticles with a controlled number of attached biological molecules have been reported that do not require gel sorting.<sup>[102]</sup>

Once DNA-particle conjugates with a controlled number of DNA molecules per particle are available, DNA-mediated particle groupings can be formed. For the creation of particle dimers, two types of nanoparticles each bearing complementary strands of oligonucleotides are required. When both DNA-particle conjugates are brought together under suitable buffer conditions the complementary strands of DNA start to hybridize and thus link the two nanoparticles together. So far this method has been successfully employed for the creation of DNA-mediated dimers and trimers of Au nanoparticles (Figure 7c).<sup>[7]</sup> To date, no larger structures with controlled composition have been reported.

Synthesizing Colloidal Nanoparticles

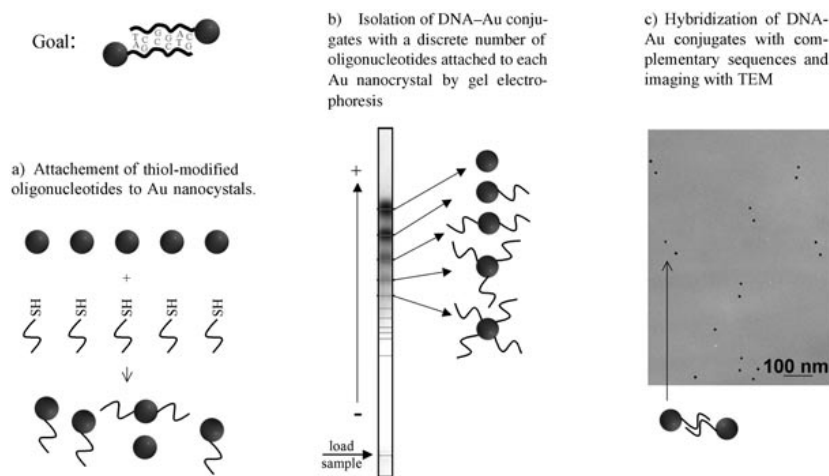


**Figure 7.** Forming DNA-mediated dimers of Au nanoparticles requires each nanoparticle to be functionalized with one oligonucleotide, with both oligonucleotides being complementary to each other. a) When phosphine- (or citric acid) stabilized Au nanoparticles and thiol-modified oligonucleotides react, DNA binds with its thiol group to the Au surface. However, even for 1:1 mixtures of DNA and Au, Au nanoparticles with more or less than one bound oligonucleotide will result; b) Au nanoparticles with a different number of DNA molecules bound per particle can be sorted by gel electrophoresis (image adapted from ref. [87]). Individual bands of nanoparticles with a discrete number of DNA molecules per particle can be observed and extracted from the gel; c) Au nanoparticles with one DNA molecule can be mixed with another solution of Au nanoparticles modified with a complementary DNA sequence. The single-stranded DNA molecules hybridize to a double strand, thus connecting the Au nanoparticles. The resulting dimers can be observed by TEM imaging (the Au-nanoparticle dimers shown comprise two 10-nm-diameter Au nanocrystals; the DNA molecules cannot be seen by TEM). Image courtesy of D. Zanchet et al.<sup>[7]</sup>

This is mainly due to the fact that the hybridization efficiency of DNA attached to Au nanoparticles is impaired. Part of the oligonucleotide can bind to the particle surface in a nonspecific way and is therefore only partly accessible for hybridization.

For some systems the number of attached DNA molecules per particle is yet to be controlled. However, such systems provide many possible applications, mainly in the area of biosensing. The group of Mirkin has developed very elaborate protocols to use DNA-modified Au nanoparticles (with many DNA molecules per particle) for the detection of DNA-sequences.<sup>[103,104]</sup> By using aptamer sequences as DNA, even molecules other than DNA can be detected with this universal method.<sup>[105]</sup> In addition, DNA-modified semiconductor nanoparticles have been used as fluorescent labels for DNA chips.<sup>[14]</sup>

So far, DNA-particle conjugates either with a small, discrete, and controllable number of DNA molecules per particle have been discussed as well as those with an uncontrolled number of DNA molecules per particle. However, there must be a limit to the number of DNA molecules that can be attached, a point where the particle surface will be completely saturated with DNA. This situation can be observed very well with gel electrophoresis. Once the Au particle is completely loaded with DNA the speed of migration reaches saturation.<sup>[87]</sup> In the case of 13 and 15.7-nm-diameter Au nanoparticles, a maximum of 115 and 157 single-stranded oligonucleotides of 12 bases could be bound per nanoparticle, respectively.<sup>[106,107]</sup> Further, it could be shown that the short oligonucleotides are fully stretched.<sup>[87]</sup> Upon the addition of more and more DNA the effective particle diameter

becomes larger and larger; for steric reasons, when the particle is fully loaded with DNA the oligonucleotides point outward, fully extended along its contour length (see Figure 8a). Therefore, the total conjugate diameter is two

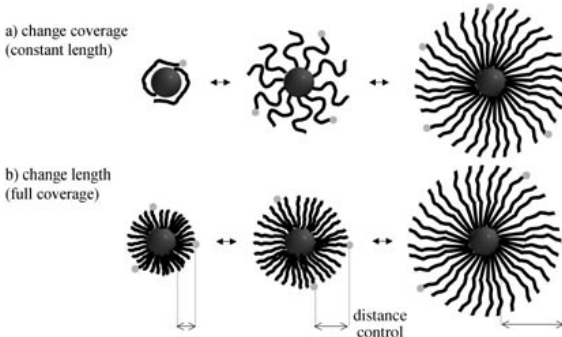


**Figure 8.** Single-stranded DNA is attached via a thiol group to the nanoparticle surface. a) As more DNA of the same length (black lines) is bound to the nanoparticles (light-gray spheres), the DNA molecules become elongated until they are fully stretched to their contour length. If a fluorescent dye (small medium-gray spheres) is attached to the free end of the DNA molecule, the distance between this dye and the Au surface increases as more DNA is adsorbed by the particle; b) When Au nanoparticles are saturated with (relatively short) DNA molecules, the DNA is fully stretched to its contour length;<sup>[87]</sup> the more bases the DNA is composed of, the longer its contour length. Thus, the distance between a dye molecule and a Au surface can be tuned by saturating Au nanoparticles with single-stranded DNA of an appropriate number of bases.

## reviews

L. Manna, W. J. Parak, et al.

times the contour length of the DNA molecules plus the diameter of the Au particle.

The ability to fully stretch short DNA molecules provides the possibility of creating a spacer on the nanometer scale. One interesting photophysical problem is the quenching of fluorescence in the vicinity of gold surfaces. For detailed studies of this phenomenon, it would be desirable to precisely control the distance between the fluorescence dye and the gold surface. DNA-saturated Au nanoparticles seem to be a promising system for such studies. The fluorescent dye could be covalently attached on one end of the oligonucleotide, whose other end would be modified with a thiol group to bind to the gold surface. By using gel electrophoresis the saturation of the Au nanoparticles with DNA can be controlled. Since the DNA is fully stretched at full saturation, the distance between the fluorescence dye and the Au surface would be the contour length of the oligonucleotide (Figure 8b). By using DNA of different lengths, separations between 1 and 10 nm could be generated,<sup>[87]</sup> a respective study is under way.

Although this report is limited to the modification of Au nanoparticles with DNA, other particle materials and other biological molecules have also been used. In the future, such systems will allow for the controlled production of hybrid materials on the nanometer scale; many reports in these fields are predicted.

## 5. Nanoparticle Uptake by Living Cells

Colloidal semiconductor nanocrystals can emit fluorescence, which is suggestive of their use for the fluorescence labeling of cells. Compared to organic fluorophores they suffer less from photobleaching and easily allow for multiplexing (one excitation source, many channels of different colors). Soon after high-quality nanocrystals could be transferred to aqueous solution, the first labeling experiments of cells were reported.<sup>[16,86]</sup> These experiments were based on the conjugation of nanoparticles with biological ligands that specifically bind against certain cellular structures or compartments. In one of the original papers, CdSe/ZnS nanocrystals were modified with phalloidin, which triggered specific binding of these conjugates to the actin network of fibroblasts.<sup>[16]</sup> Since then, the multicolor labeling of different structures of fixed and living cells has been reported.<sup>[17,18]</sup> Recently, nanoparticles have been modified with biological molecules to facilitate the binding of conjugates to membrane-bound receptors.<sup>[98]</sup>

Because of reduced photobleaching the diffusion pathway of the receptor molecules within the cell membrane could be recorded over extended periods of time. It is predicted that the main labeling applications of fluorescent nanoparticles will be found in this field of single-molecule tracing. For a more detailed overview about labeling experiments with nanocrystals we refer the reader to already published reviews.<sup>[108–111]</sup>

In this review, the focus is towards another direction. Besides the labeling of cellular structures it has been also observed that living cells ingest colloidal nanocrystals. If

cells are exposed to a culture medium that contains nanocrystals, they start to uptake the nanoparticles by endocytosis.<sup>[86,112,115–115]</sup> Nanoparticles are then transported to vesicular compartments around the nucleus of the cell where they remain.<sup>[91,112,115–117]</sup> Some authors have claimed receptor-mediated uptake,<sup>[97,114]</sup> whereas others report nonspecific uptake. As mentioned above there are several ways to transfer nanoparticles into aqueous solution, and certainly the ingestion of the nanoparticles might well depend on the particular protocol. In Figure 9 the distribution of CdSe/ZnS

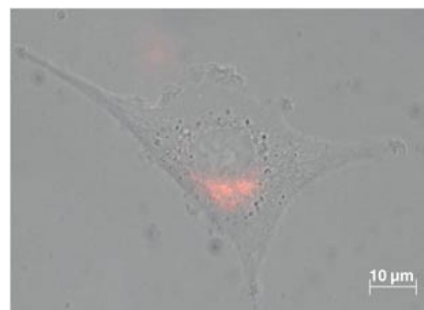


**Figure 9.** MDA-MB-435s cells incubated with red-fluorescent silanized CdSe/ZnS nanocrystals: After some hours the cells incorporate a significant amount of nanocrystals, so that microscopy is possible. The overlay of the phase contrast and fluorescence images is shown (For the experimental procedure see ref. [112]).

nanoparticles that were incorporated into a cell is shown. The effect of particle uptake can be used to label cells and follow their pathway or fate. Let us assume the following situation: Two different types of cells have to be cultured in parallel. With phase-contrast microscopy it is often not possible to determine the type of a cell, since the shapes of many cells can vary dramatically. Certainly, cells of one type can be stained specifically with a fluorescence-labeled antibody, which only binds to this particular type of cell. However, such staining impairs the cells and is thus not appropriate for following the fate of individual cells. Labeling with nanocrystals could be an interesting alternative. If cells of type A are incubated with green fluorescent nanoparticles, and cells of type B in another flask with red fluorescent nanoparticles, the cells ingest the respective nanoparticles. Thus cells of type A show green fluorescence and cells of type B exhibit red fluorescence. If both types of cells are finally seeded in co-culture on the same substrate, each type of cell can be identified by its color of fluorescence (Figure 10).

Nanocrystals are suitable labels for several reasons: First, they have a reduced tendency to photobleach. Second, they are relatively biocompatible.<sup>[114]</sup> Third, upon cell division the nanoparticles are passed to both daughter cells and therefore the label is not lost.<sup>[91,112,116,118]</sup> These facts facilitate long-term observation of the fate of individual cells. With this technique the fate of a subpopulation of dictyostelium cells within a whole population could be traced.<sup>[115]</sup> In another experiment nanocrystals were microinjected into

Synthesizing Colloidal Nanoparticles

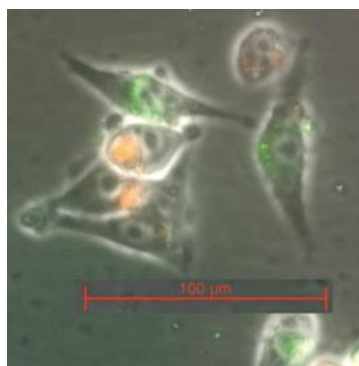


**Figure 10.** MDA-MB-435s and MCF-7 cells were fed with green and red fluorescent silica-coated CdSe/ZnS nanocrystals, respectively, in separate culture flasks. Both types of cells were then mixed and seeded on the same substrate. The overlay of the phase contrast and fluorescence images is shown after some hours of incubation. Each cell can now be identified by the color of its fluorescence.

fluorescence. The fluorescence image of the culture substrate thus resembles a blueprint of the migration pathway of the cells.<sup>[112]</sup> The speed and pattern of migration differs from cell type to cell type.

The phagokinetic track technique is a convenient method to determine the migration properties of cells. The more cells migrate, the larger the area cleared of nanocrystals per cell will be. This procedure could be highly automated; with fluorescence microscopy, intensity levels can be observed. One can observe the homogenous fluorescence of the undistorted layer, enhanced fluorescence within the cells that have accumulated the nanoparticles, and no fluorescence at positions that have been traversed by cells. The nonfluorescent area around each cell is characteristic for different types of cells.<sup>[122]</sup> It has been demonstrated that for different cell types derived from breast tissue the area cleared of nanoparticles per cell is higher where the metastatic potential of the cells is at its highest.<sup>[122]</sup> This might be the basis of a test for the metastatic potential of living cells.

specific cells of Xenopus embryos to follow their development.<sup>[118]</sup> Due to their particular properties, an increased use of fluorescent nanoparticles in this kind of fate-mapping study is expected.

Alternatively, the fate of individual cells on a cell culture substrate can be followed by using the so-called phagokinetic track method;<sup>[119–121]</sup> the principle is illustrated in Figure 11. Let us assume a cell culture substrate is homogeneously coated with red fluorescent nanoparticles. Under the fluorescence microscope the substrate will appear simply red. Cells will then be cultured on the nanoparticle-coated substrate; the cells will start to ingest the nanoparticles. Compared to nanoparticles dissolved in solution the uptake of nanoparticles adsorbed to a surface is more efficient. The issue of three-dimensional diffusion of a dissolved particle into a cell now is reduced to a two-dimensional one for adsorbed nanoparticles. Adherent cells can migrate along the culture substrate. Wherever the cell moves, it ingests the nanoparticles of the underlying particle layer and stores the nanoparticles around its nucleus. This means that along the pathway of every cell the particle layer has been removed. Due to this phenomenon, the migration pathway of every cell appears dark under the fluorescence microscope, whereas areas where no cells have passed still exhibit homogeneous

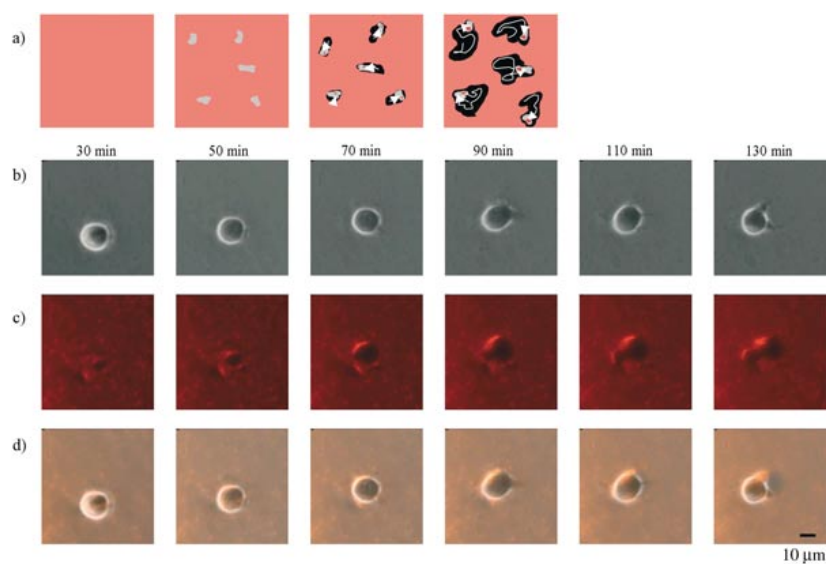


**Figure 11.** Phagokinetic tracks: a) Cells (gray) seeded on top of a collagen layer mixed with fluorescent nanocrystals (red), start to ingest the nanocrystals while they crawl along the layer (white arrows indicate the direction of cell movement). The ingested nanocrystals are stored inside the cells (red spot inside the cell). Areas of the layer that have been cleared of nanocrystals no longer fluoresce (black areas). The longer the incubation time, the more the cells move and the larger the non-fluorescent areas become.<sup>[112,122]</sup> b–d) phase-contrast, fluorescence, and overlay images of a time series of phagokinetic tracks; the phase-contrast image shows the cell, while the fluorescence image displays the nanocrystal layer. The images were recorded for MCF-7 breast cancer cells seeded on top of a collagen layer infiltrated with silica-coated red fluorescent CdSe/ZnS nanocrystals.<sup>[112,122]</sup> The images were recorded 30–130 min after seeding the cells on the layer; the hole in the layer clearly becomes larger with time. The fluorescence of nanocrystals accumulated inside the cells cannot be seen in these fluorescence images because the focus of the microscope was adjusted to the layer surface and not on the middle of the cells.

## reviews

L. Manna, W. J. Parak, et al.

## 6. Outlook

In this review, we have described some biological applications of colloidal nanocrystals, in particular of fluorescent semiconductor nanoparticles. Besides labeling applications, nanocrystals have also been used for other purposes. The use of magnetic nanoparticles in drug delivery is particularly worthy of mention.<sup>[123]</sup> Drugs can be immobilized on the surface of magnetic nanocrystals and the resulting drug–nanocrystal assemblies can be directed with magnetic fields to the target tissue.<sup>[124]</sup> Typically, however, each particle material exhibits only one “feature”: Semiconductor nanoparticles are fluorescent and some metal and metal oxide nanoparticles are magnetic. For many applications, it would be desirable to have a material that combined these properties. The combination of a fluorescent and a magnetic particle to one material would allow for visualization by fluorescence and manipulation in magnetic fields. It is therefore proposed that the creation of materials on the nanometer scale with several properties will have a large future. The following section discusses several strategies as to how such nanohybrid materials could be obtained (see Figure 12).

Nanohybrid particles could be directly obtained through chemical synthesis by selectively growing one material on top of certain positions of another. The growth of ZnS

shells around CdSe cores was demonstrated several years ago.<sup>[48]</sup> Nowadays fluorescent nanoparticles can also be directly grown on to magnetic ones.<sup>[60]</sup> This is an excellent demonstration of the combination of two properties in one particle. The clear advantage of this method is that when nanoparticles are grown on top of each other there is a negligible space between the domains. This should facilitate experiments in which the coupling between the different domains in hybrid nanoparticles is to be investigated. No energy transfer or tunneling is possible when nanoparticles are further apart than a few nanometers. Also the connection between the individual domains should be very stable. However, the large disadvantage of this method is that it will almost certainly be limited to relatively primitive structures. One could, for example, imagine spheres of one material grown on the ends of a tetrapod shaped nanoparticle of another material. However, it does not seem feasible to grow more than a few materials in one hybrid system.

Larger structures could be obtained through linkage with biological molecules. Almost 10 years ago, the first examples of DNA-mediated particle assemblies were reported.<sup>[85, 88, 125]</sup> However, the obtained assemblies were more like aggregates than well-defined structures. Today, much effort is invested in the assembly of exactly defined structures. Such examples have already been demonstrated with the

construction of DNA-mediated particle groupings.<sup>[6, 7]</sup> This method in principle would allow for the construction of complex structures composed of multiple nanoparticles of different materials. Some work in this direction has already been reported.<sup>[126]</sup> The use of DNA as a linker offers the ability to precisely program the linkage by selecting appropriate sequences of complementary oligonucleotides.

Unfortunately there are also some conceptual disadvantages involved with this technique. First, the biological molecules that are employed to link the nanoparticles act as a spacer between the nanoparticles. Thus, there always will be a gap between the individual nanoparticles within one particular grouping. Second, the biological molecules and especially their linkage to the nanoparticles are not stiff, but rather flexible. Such flexibility suggests that the nanoparticles will not be linked in a rigid assembly, but rather the whole construct

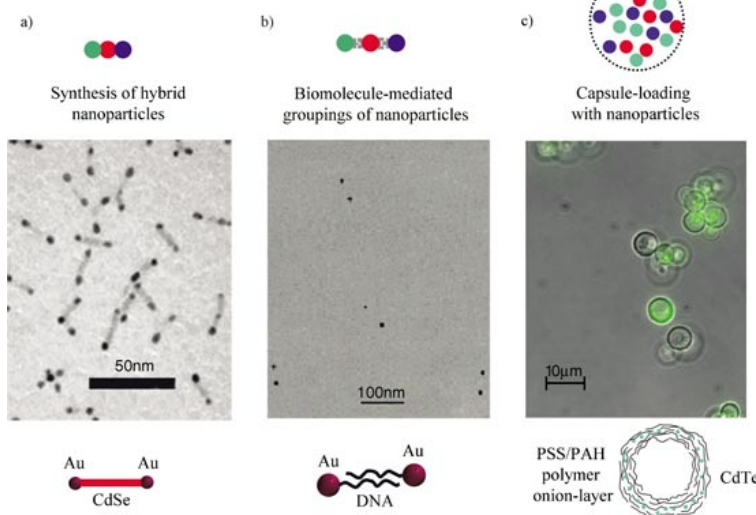


**Figure 12.** One goal of nanotechnology is the construction of materials with new properties, for example the combination of magnetic and fluorescent properties in one material. Hybrid structures comprising three different materials are systematically sketched (drawn in green, red, and blue). a) Different materials can be grown directly on each other. This elegant and stable method will be limited to small structures (the growth of Au nanoparticles at the end of CdSe rods is shown; image courtesy of U. Banin et al.<sup>[124]</sup>); b) nanoparticles of different materials can be grown separately and then linked by biological molecules. These systems will be more general, but less stable because the linker-molecules keep individual nanoparticles further apart (the DNA-mediated linkage of Au nanoparticles is shown; image courtesy of D. Zanchet et al.<sup>[7]</sup>); c) a straightforward approach is to load containers with nanoparticles of different materials. Such hybrid systems are larger but much easier to prepare (polymer capsules containing fluorescent CdTe nanoparticles are shown; image courtesy of G. Sukhorukov, A. Rogach, and B. Zebli<sup>[129]</sup>).

Synthesizing Colloidal Nanoparticles

will be flexible and the distance between the nanoparticles within the assembly will fluctuate. For example, a three-dimensional construct in solution might collapse to two dimensions once it is adsorbed and dried on a surface. Third, the stability of the linkage is limited. Biological molecules are bound by certain conditions. DNA-mediated particle groupings certainly will not be able to withstand high temperatures ( $\geq 100^\circ\text{C}$ ) at which biological molecules start to degrade. There also exists possibilities of destruction in solution. For example, enzymes might digest part of the linker molecules. With DNA the linkage can also be broken by increasing the temperature or by decreasing the salt concentration, that is, by reducing the melting temperature. Although these factors limit stability, they could also be used for the controlled release of nanoparticles from the particle assembly.

Maybe the easiest way to combine nanoparticles of different functionality is to simply pack them in one container. Such an assembly will typically have dimensions on the microscale rather than the nanoscale, but certainly they would offer the possibility of combining as many different materials as desired. One example in this direction is the incorporation of nanoparticles in hollow polymer capsules. Such capsules are assembled layer by layer.<sup>[127,128]</sup> First a charged template, for example a microsphere, is required. Then polymer molecules of opposite charge are added that bind electrostatically to the template. Unbound excess polymer is removed, then a polymer of opposite charge to the first polymer layer is added, which adsorbs by electrostatic interaction. The excess polymer is then removed. These steps are iterated and a multilayer construct like an onion of many successive polymer layers of opposite charge is formed. Finally the template is dissolved and a hollow sphere composed of polyelectrolyte multilayers is obtained. Nanoparticles can be introduced in two different ways. By controlling the pH- and salt conditions the mesh size of the capsule walls can be controlled. In this way the nanoparticles can be introduced since the capsule walls are permeable, and can then be trapped inside the capsule by rendering the capsule wall impermeable. Alternatively, nanoparticles can be incorporated into the capsule walls. When the outer layer of the capsules is positively charged, then negatively charged nanoparticles will adsorb to this layer. Unbound nanoparticles are removed and positively charged polymer is added. In this way nanoparticles of different functionality can be incorporated at different layers of the capsule wall. The groups of Sukhorukov and Rogach have demonstrated the construction of magnetic and fluorescent capsules by incorporating magnetic and fluorescent nanoparticles to the capsule walls.<sup>[129]</sup> Such constructs hold great promise in many biological applications, such as drug delivery.<sup>[130]</sup>

To conclude this Review, it should be pointed out that the synthesis of colloidal nanocrystals and their modification with biological molecules is already highly advanced. Research on such nanoparticles has changed from development and characterization to real applications. Nevertheless, it is predicted that efforts in particle synthesis will shift towards the construction of heterostructured nanoparticles that combine multiple functionalities.

**Acknowledgement**

*This project was supported by the Deutsche Forschungsgemeinschaft (DFG, Emmy Noether grant WP), by the Deutscher Akademischer Austauschdienst (DAAD, Vigoni Project), and by the Fonds der Chemischen Industrie. The authors are grateful to Prof. U. Banin and Drs. G. Sukhorukov and A. Rogach for providing images of their work for this Review. Many of the ideas described in this Review are based on work initiated in the group of Prof. A. P. Alivisatos, in whose groups some of the authors have worked previously.*

- [1] A. L. Efros, M. Rosen, *Annu. Rev. Mater. Sci.* **2000**, *30*, 475–521.
- [2] W. J. Parak, L. Manna, F. C. Simmel, D. Gerion, A. P. Alivisatos in *Nanoparticles—From Theory to Application* (Ed.: G. Schmid), Wiley-VCH, Weinheim, **2004**, pp. 4–49.
- [3] D. L. Klein, R. Roth, A. K. L. Lim, A. P. Alivisatos, P. L. McEuen, *Nature* **1997**, *389*, 699–701.
- [4] V. B. Alberts, D. Bray, J. Lewis, M. Raff, K. Roberts, J. D. Watson, *Molecular biology of the cell*, 3rd ed., Garland Publishing, New York, **1994**.
- [5] R. C. Mucic, J. J. Storhoff, C. A. Mirkin, R. L. Letsinger, *J. Am. Chem. Soc.* **1998**, *120*, 12674–12675.
- [6] C. J. Loweth, W. B. Caldwell, X. G. Peng, A. P. Alivisatos, P. G. Schultz, *Angew. Chem.* **1999**, *111*, 1925–1929; *Angew. Chem. Int. Ed.* **1999**, *38*, 1808–1812.
- [7] D. Zanchet, C. M. Micheel, W. J. Parak, D. Gerion, S. C. Williams, A. P. Alivisatos, *J. Phys. Chem. B* **2002**, *106*, 11758–11763.
- [8] E. Winfree, F. R. Liu, L. A. Wenzler, N. C. Seeman, *Nature* **1998**, *394*, 539–544.
- [9] S. J. Xiao, F. R. Liu, A. E. Rosen, J. F. Hainfeld, N. C. Seeman, K. Musier-Forsyth, R. A. Kiehl, *J. Nanopart. Res.* **2002**, *4*, 313–317.
- [10] T. A. Taton, R. C. Mucic, C. A. Mirkin, R. L. Letsinger, *J. Am. Chem. Soc.* **2000**, *122*, 6305–6306.
- [11] C. M. Niemeyer, *Curr. Opin. Chem. Biol.* **2000**, *4*, 609–618.
- [12] C. M. Niemeyer, B. Ceyhan, S. Gao, L. Chi, S. Peschel, U. Simon, *Colloid Polym. Sci.* **2001**, *279*, 68–72.
- [13] D. Gerion, W. J. Parak, S. C. Williams, D. Zanchet, C. M. Micheel, A. P. Alivisatos, *J. Am. Chem. Soc.* **2002**, *124*, 7070–7074.
- [14] D. Gerion, F. Q. Chen, B. Kannan, A. H. Fu, W. J. Parak, D. J. Chen, A. Majumdar, A. P. Alivisatos, *Anal. Chem.* **2003**, *75*, 4766–4772.
- [15] I. Willner, F. Patolsky, J. Wasserman, *Angew. Chem.* **2001**, *113*, 1913–1916; *Angew. Chem. Int. Ed.* **2001**, *40*, 1861–1864.
- [16] M. Bruchez, M. Moronne, P. Gin, S. Weiss, A. P. Alivisatos, *Science* **1998**, *281*, 2013–2016.
- [17] S. Pathak, S. K. Choi, N. Arneheim, M. E. Thompson, *J. Am. Chem. Soc.* **2001**, *123*, 4103–4104.
- [18] X. Y. Wu, H. J. Liu, J. Q. Liu, K. N. Haley, J. A. Treadway, J. P. Larson, N. F. Ge, F. Peale, M. P. Bruchez, *Nat. Biotechnol.* **2003**, *21*, 41–46.
- [19] J. J. Storhoff, C. A. Mirkin, *Chem. Rev.* **1999**, *99*, 1849–1862.
- [20] E. Braun, Y. Eichen, U. Sivan, G. Ben-Yoseph, *Nature* **1998**, *391*, 775–778.
- [21] M. Mertig, L. C. Ciacchi, R. Seidel, W. Pompe, A. De Vita, *Nano Lett.* **2002**, *2*, 841–844.
- [22] F. Patolsky, Y. Weizmann, O. Lioubashevski, I. Willner, *Angew. Chem.* **2002**, *114*, 2321–2325; *Angew. Chem. Int. Ed.* **2002**, *41*, 2323–2327.
- [23] K. Keren, R. S. Berman, E. Buchstab, U. Sivan, E. Braun, *Science* **2003**, *302*, 1380–1382.

## reviews

L. Manna, W. J. Parak, et al.

[24] A. Miyawaki, A. Sawano, T. Kogure, *Nat. Cell Biol.* **2003**, *5*, S1–S7.

[25] A. Watson, X. Wu, M. Bruchez, *Biotechniques* **2003**, *34*, 296–303.

[26] T. M. Jovin, *Nat. Biotechnol.* **2003**, *21*, 32–33.

[27] C. B. Murray, D. J. Norris, M. G. Bawendi, *J. Am. Chem. Soc.* **1993**, *115*, 8706–8715.

[28] W. W. Yu, X. Peng, *Angew. Chem.* **2001**, *114*, 2474–2477; *Angew. Chem. Int. Ed.* **2001**, *41*, 2368–2371.

[29] A. A. Guzelian, J. E. B. Katari, A. V. Kadavanich, U. Banin, K. Hamad, E. Juban, A. P. Alivisatos, R. H. Wolters, C. C. Arnold, J. R. Heath, *J. Phys. Chem. B* **1996**, *100*, 7212–7219.

[30] D. Battaglia, X. Peng, *Nano Lett.* **2002**, *2*, 1027–1030.

[31] D. Gerion, N. Zaitseva, C. Saw, M. F. Casula, S. Fakra, T. Van Buuren, G. Galli, *Nano Lett.* **2004**, *4*, 597–602.

[32] T. Hyeon, S. S. Lee, J. Park, Y. Chung, H. Bin Na, *J. Am. Chem. Soc.* **2001**, *123*, 12798–12801.

[33] S. H. Sun, H. Zeng, D. B. Robinson, S. Raoux, P. M. Rice, S. X. Wang, G. X. Li, *J. Am. Chem. Soc.* **2004**, *126*, 273–279.

[34] S. H. Sun, C. B. Murray, D. Weller, L. Folks, A. Moser, *Science* **2000**, *287*, 1989–1992.

[35] V. F. Puntes, K. Krishnan, A. P. Alivisatos, *Top. Catal.* **2002**, *19*, 145–148.

[36] V. F. Puntes, K. M. Krishnan, A. P. Alivisatos, *Science* **2001**, *291*, 2115–2117.

[37] V. F. Puntes, K. M. Krishnan, P. Alivisatos, *Appl. Phys. Lett.* **2001**, *78*, 2187–2189.

[38] E. V. Shevchenko, D. V. Talapin, A. L. Rogach, A. Kornowski, M. Haase, H. Weller, *J. Am. Chem. Soc.* **2002**, *124*, 11480–11485.

[39] E. V. Shevchenko, D. V. Talapin, H. Schnablegger, A. Kornowski, O. Festin, P. Svedlindh, M. Haase, H. Weller, *J. Am. Chem. Soc.* **2003**, *125*, 9090–9101.

[40] L. Manna, E. C. Scher, A. P. Alivisatos, *J. Am. Chem. Soc.* **2000**, *122*, 12700–12706.

[41] Y.-w. Jun, M. F. Casula, J. H. Sim, S. Y. Kim, J. Cheon, A. P. Alivisatos, *J. Am. Chem. Soc.* **2003**, *125*, 15981–15985.

[42] V. F. Puntes, D. Zanchet, C. K. Erdonmez, A. P. Alivisatos, *J. Am. Chem. Soc.* **2002**, *124*, 12874–12880.

[43] X. G. Peng, L. Manna, W. D. Yang, J. Wickham, E. Scher, A. Kadavanich, A. P. Alivisatos, *Nature* **2000**, *404*, 59–61.

[44] L. Manna, D. J. Milliron, A. Meisel, E. C. Scher, A. P. Alivisatos, *Nat. Mater.* **2003**, *2*, 382–385.

[45] Y.-w. Jun, C. S. Choi, J. Cheon, *Chem. Commun.* **2001**, 101–102.

[46] N. Cordente, M. Respaud, F. Senocq, M. J. Casanove, C. Amiens, B. Chaudret, *Nano Lett.* **2001**, *1*, 565–568.

[47] L. Manna, E. C. Scher, A. P. Alivisatos, *J. Cluster Sci.* **2002**, *13*, 521–532.

[48] B. O. Dabbousi, J. RodriguezViejo, F. V. Mikulec, J. R. Heine, H. Mattoussi, R. Ober, K. F. Jensen, M. G. Bawendi, *J. Phys. Chem. B* **1997**, *101*, 9463–9475.

[49] D. V. Talapin, A. L. Rogach, A. Kornowski, M. Haase, H. Weller, *Nano Lett.* **2001**, *1*, 207–211.

[50] L. Manna, E. C. Scher, L. S. Li, A. P. Alivisatos, *J. Am. Chem. Soc.* **2002**, *124*, 7136–7145.

[51] T. Mokari, U. Banin, *Chem. Mater.* **2003**, *15*, 3955–3960.

[52] X. Peng, M. C. Schlamp, A. V. Kadavanich, A. P. Alivisatos, *J. Am. Chem. Soc.* **1997**, *119*, 7019–7029.

[53] I. Mekis, D. V. Talapin, A. Kornowski, M. Haase, H. Weller, *J. Phys. Chem. B* **2003**, *107*, 7454–7462.

[54] S. Kim, B. Fisher, H. J. Eisler, M. Bawendi, *J. Am. Chem. Soc.* **2003**, *125*, 11466–11467.

[55] Y.-W. Cao, U. Banin, *Angew. Chem.* **1999**, *111*, 3913–3916; *Angew. Chem. Int. Ed.* **1999**, *38*, 3692–3694.

[56] H. Zeng, J. Li, Z.-L. Wang, J. P. Liu, S. H. Sun, *Nano Lett.* **2004**, *4*, 187–190.

[57] N. S. Sobal, U. Ebels, H. Möhwald, M. Giersig, *J. Phys. Chem. B* **2003**, *107*, 7351–7354.

[58] N. S. Sobal, M. Hilgendorff, H. Möhwald, M. Giersig, M. Spasova, T. Radetic, M. Farle, *Nano Lett.* **2002**, *2*, 621–624.

[59] D. V. Talapin, R. Koeppe, S. Gotzinger, A. Kornowski, J. M. Lupton, A. L. Rogach, O. Benson, J. Feldmann, H. Weller, *Nano Lett.* **2003**, *3*, 1677–1681.

[60] H. W. Gu, R. K. Zheng, X. X. Zhang, B. Xu, *J. Am. Chem. Soc.* **2004**, *126*, 5664–5665.

[61] J. T. Hu, L. S. Li, W. D. Yang, L. Manna, L. W. Wang, A. P. Alivisatos, *Science* **2001**, *292*, 2060–2063.

[62] M. Brust, M. Walker, D. Bethell, D. J. Schiffrin, R. Whyman, *J. Chem. Soc. Chem. Commun.* **1994**, 801–802.

[63] Y. Kobayashi, M. Horie, M. Konno, B. Rodriguez-Gonzalez, L. M. Liz-Marzan, *J. Phys. Chem. B* **2003**, *107*, 7420–7425.

[64] J. Fink, C. J. Kiely, D. Bethell, D. J. Schiffrin, *Chem. Mater.* **1998**, *10*, 922–926.

[65] A. Kumar, H. Joshi, R. Pasricha, A. B. Mandale, M. Sastry, *J. Colloid Interface Sci.* **2003**, *264*, 396–401.

[66] W. J. Parak, D. Gerion, D. Zanchet, A. S. Woerz, T. Pellegrino, C. Michelet, S. C. Williams, M. Seitz, R. E. Bruehl, Z. Bryant, C. Bustamante, C. R. Bertozi, A. P. Alivisatos, *Chem. Mater.* **2002**, *14*, 2113–2119.

[67] C. Wilhelm, C. Billotey, J. Roger, J. N. Pons, J. C. Bacri, F. Gazeau, *Biomaterials* **2003**, *24*, 1001–1011.

[68] A. C. Templeton, W. P. Wuelfing, R. W. Murray, *Acc. Chem. Res.* **2000**, *33*, 27–36.

[69] Y. Chen, T. Ji, Z. Rosenzweig, *Nano Lett.* **2003**, *3*, 581–584.

[70] S. F. Wuister, I. Swart, F. van Driel, S. G. Hickey, C. D. Donega, *Nano Lett.* **2003**, *3*, 503–507.

[71] K. S. Mayya, F. Caruso, *Langmuir* **2003**, *19*, 6987–6993.

[72] J. Aldana, Y. A. Wang, X. Peng, *J. Am. Chem. Soc.* **2001**, *123*, 8844–8850.

[73] H. Mattoussi, J. M. Mauro, E. R. Goldman, G. P. Anderson, V. C. Sundar, F. V. Mikulec, M. G. Bawendi, *J. Am. Chem. Soc.* **2000**, *122*, 12142–12150.

[74] S. Kim, M. G. Bawendi, *J. Am. Chem. Soc.* **2003**, *125*, 14652–14653.

[75] M. Alejandro-Arellano, T. Ung, A. Blanco, P. Mulvaney, L. M. Liz-Marzan, *Pure Appl. Chem.* **2000**, *72*, 257–267.

[76] M. A. Correa-Duarte, M. Giersig, L. M. Liz-Marzán, *Chem. Phys. Lett.* **1998**, *286*, 497–501.

[77] D. Gerion, F. Pinaud, S. C. Williams, W. J. Parak, D. Zanchet, S. Weiss, A. P. Alivisatos, *J. Phys. Chem. B* **2001**, *105*, 8861–8871.

[78] L. M. Liz-Marzán, A. P. Philipse, *J. Colloid Interface Sci.* **1995**, *176*, 459–466.

[79] A. Schroedter, H. Weller, *Angew. Chem.* **2002**, *114*, 3346–3350; *Angew. Chem. Int. Ed.* **2002**, *41*, 3218–3221.

[80] A. Schroedter, H. Weller, R. Eritja, W. E. Ford, J. M. Wessels, *Nano Lett.* **2002**, *2*, 1363–1367.

[81] C. Tribet, R. Audebert, J.-L. Popot, *Proc. Natl. Acad. Sci. USA* **1996**, *93*, 15047–15050.

[82] X. Y. Wu, H. J. Liu, J. Q. Liu, K. N. Haley, J. A. Treadway, J. P. Larson, N. F. Ge, F. Peale, M. P. Bruchez, *Nat. Biotechnol.* **2003**, *21*, 452 (corrigendum).

[83] M. A. Petruska, A. P. Bartko, V. I. Klimov, *J. Am. Chem. Soc.* **2004**, *126*, 714–715.

[84] T. Pellegrino, L. Manna, S. Kudera, T. Liedl, D. Koktysh, A. L. Rogach, S. Keller, J. Radler, G. Natile, W. J. Parak, *Nano Lett.* **2004**, *4*, 703–707.

[85] C. A. Mirkin, R. L. Letsinger, R. C. Mucic, J. J. Storhoff, *Nature* **1996**, *382*, 607–609.

[86] W. C. W. Chan, S. Nie, *Science* **1998**, *281*, 2016–2018.

[87] W. J. Parak, T. Pellegrino, C. M. Michelet, D. Gerion, S. C. Williams, A. P. Alivisatos, *Nano Lett.* **2003**, *3*, 33–36.

[88] G. P. Mitchell, C. A. Mirkin, R. L. Letsinger, *J. Am. Chem. Soc.* **1999**, *121*, 8122–8123.

[89] M. E. Akerman, W. C. W. Chan, P. Laakkonen, S. N. Bhatia, E. Ruoslahti, *Proc. Natl. Acad. Sci. USA* **2002**, *99*, 12617–12621.

[90] S. J. Rosenthal, A. Tomlinson, E. M. Adkins, S. Schroeter, S. Adams, L. Swafford, J. McBride, Y. Q. Wang, L. J. DeFelice, R. D. Blakely, *J. Am. Chem. Soc.* **2002**, *124*, 4586–4594.

[91] K. Hanaki, A. Momo, T. Oku, A. Komoto, S. Maenosono, Y. Yamaguchi, K. Yamamoto, *Biochem. Biophys. Res. Commun.* **2003**, *302*, 496–501.

[92] R. Mahtab, H. H. Harden, C. J. Murphy, *J. Am. Chem. Soc.* **2000**, *122*, 14–17.

[93] H. Matoussi, J. M. Mauro, E. R. Goldman, T. M. Green, G. P. Anderson, V. C. Sundar, M. G. Bawendi, *Phys. Status Solidi B* **2001**, *224*, 277–283.

[94] R. Elghanian, J. J. Storhoff, R. C. Mucic, R. L. Letsinger, C. A. Mirkin, *Science* **1997**, *277*, 1078–1081.

[95] B. M. Lingerfelt, H. Matoussi, E. R. Goldman, J. M. Mauro, G. P. Anderson, *Anal. Chem.* **2003**, *75*, 4043–4049.

[96] E. R. Goldman, A. R. Clapp, G. P. Anderson, H. T. Uyeda, J. M. Mauro, I. L. Medintz, H. Matoussi, *Anal. Chem.* **2004**, *76*, 684–688.

[97] D. S. Lidke, P. Nagy, R. Heintzmann, D. J. Arndt-Jovin, J. N. Post, H. E. Grecco, E. A. Jares-Erijman, T. M. Jovin, *Nat. Biotechnol.* **2004**, *22*, 198–203.

[98] M. Dahan, S. Levi, C. Luccardini, P. Rostaing, B. Riveau, A. Triller, *Science* **2003**, *302*, 442–445.

[99] G. Schmid, A. Lehner, *Angew. Chem.* **1989**, *101*, 773–774; *Angew. Chem. Int. Ed. Engl.* **1989**, *28*, 780–781.

[100] D. Zanchet, C. M. Micheel, W. J. Parak, D. Gerion, A. P. Alivisatos, *Nano Lett.* **2001**, *1*, 32–35.

[101] S. D. Jhaveri, E. E. Foos, D. A. Lowy, E. L. Chang, A. W. Snow, M. G. Ancona, *Nano Lett.* **2004**, *4*, 737–749.

[102] K. M. Sung, D. W. Mosley, B. R. Peele, S. G. Zhang, J. M. Jacobson, *J. Am. Chem. Soc.* **2004**, *126*, 5064–5065.

[103] J. J. Storhoff, R. Elghanian, R. C. Mucic, C. A. Mirkin, R. L. Letsinger, *J. Am. Chem. Soc.* **1998**, *120*, 1959–1964.

[104] T. A. Taton, C. A. Mirkin, R. L. Letsinger, *Science* **2000**, *289*, 1757–1760.

[105] J. W. Liu, Y. Lu, *J. Am. Chem. Soc.* **2003**, *125*, 6642–6642.

[106] P. Sandström, M. Boncheva, B. Åkerman, *Langmuir* **2003**, *19*, 7537–7543.

[107] L. M. Demers, C. A. Mirkin, R. C. Mucic, R. A. Reynolds, R. L. Letsinger, R. Elghanian, G. Viswanadham, *Anal. Chem.* **2000**, *72*, 5535–5541.

[108] W. C. W. Chan, D. J. Maxwell, X. H. Gao, R. E. Bailey, M. Y. Han, S. M. Nie, *Curr. Opin. Biotechnol.* **2002**, *13*, 40–46.

[109] A. J. Sutherland, *Curr. Opin. Solid State Mater. Sci.* **2002**, *7*, 365–370.

[110] X. Gao, S. Nie, *Trends Biotechnol.* **2003**, *21*, 371–374.

[111] P. Alivisatos, *Nat. Biotechnol.* **2004**, *22*, 47–51.

[112] W. J. Parak, R. Boudreau, M. Le Gros, D. Gerion, D. Zanchet, C. M. Micheel, S. C. Williams, A. P. Alivisatos, C. Larabell, *Adv. Mater.* **2002**, *14*, 882–885.

[113] M. Dahan, T. Laurence, F. Pinaud, D. S. Chemla, A. P. Alivisatos, M. Sauer, S. Weiss, *Opt. Lett.* **2001**, *26*, 825–827.

[114] A. M. Derfus, W. C. W. Chan, S. N. Bhatia, *Nano Lett.* **2004**, *4*, 11–18.

[115] J. K. Jaiswal, H. Matoussi, J. M. Mauro, S. M. Simon, *Nat. Biotechnol.* **2003**, *21*, 47–51.

[116] L. C. Mattheakis, J. M. Dias, Y. J. Choi, J. Gong, M. P. Bruchez, J. Q. Liu, E. Wang, *Anal. Biochem.* **2004**, *327*, 200–208.

[117] C. Y. Zhang, H. Ma, S. M. Nie, Y. Ding, L. Jin, D. Y. Chen, *Analyst* **2000**, *125*, 1029–1031.

[118] B. Dubertret, P. Skourides, D. J. Norris, V. Noireaux, A. H. Briand, A. Libchaber, *Science* **2002**, *298*, 1759–1762.

[119] G. Albrecht-Buehler, *Cell* **1977**, *12*, 333–339.

[120] G. Albrecht-Buehler, *J. Cell Biol.* **1977**, *72*, 595–603.

[121] G. Albrecht-Buehler, *Cell* **1977**, *11*, 395–404.

[122] T. Pellegrino, W. J. Parak, R. Boudreau, M. A. Le Gros, D. Gerion, A. P. Alivisatos, C. A. Larabell, *Differentiation* **2003**, *71*, 542–548.

[123] Q. A. Pankhurst, J. Connolly, S. K. Jones, J. Dobson, *J. Phys. D* **2003**, *36*, R167–R181.

[124] C. Alexiou, W. Arnold, R. J. Klein, F. G. Parak, P. Hulin, C. Bergemann, W. Erhardt, S. Wagenpfeil, A. S. Lubbe, *Cancer Res.* **2000**, *60*, 6641–6648.

[125] A. P. Alivisatos, K. P. Johnsson, X. G. Peng, T. E. Wilson, C. J. Loweth, M. P. Bruchez, P. G. Schultz, *Nature* **1996**, *382*, 609–611.

[126] D. S. Wang, J. B. He, N. Rosenzweig, Z. Rosenzweig, *Nano Lett.* **2004**, *4*, 409–413.

[127] E. Donath, G. B. Sukhorukov, F. Caruso, S. A. Davis, H. Möhwald, *Angew. Chem.* **1998**, *110*, 2324–2327; *Angew. Chem. Int. Ed.* **1998**, *37*, 2202–2205.

[128] G. B. Sukhorukov, E. Donath, S. Davis, H. Lichtenfeld, F. Caruso, V. I. Popov, H. Möhwald, *Polym. Adv. Technol.* **1998**, *9*, 759–767.

[129] N. Gaponik, I. L. Radtchenko, G. B. Sukhorukov, A. L. Rogach, *Langmuir* **2004**, *20*, 1449–1452.

[130] G. B. Sukhorukov, A. L. Rogach, B. Zebli, T. Liedl, A. G. Skirtach, K. Köhler, A. A. Antipov, N. Gaponik, A. S. Susha, M. Winterhalter, W. J. Parak, *Small* **2004**, in press.

[131] X. Peng, J. Wickham, A. P. Alivisatos, *J. Am. Chem. Soc.* **1998**, *120*, 5343–5344.

[132] W. W. Yu, Y. A. Wang, X. Peng, *Chem. Mater.* **2003**, *15*, 4300–4308.

[133] Z. A. Peng, X. Peng, *J. Am. Chem. Soc.* **2001**, *123*, 183–184.

[134] T. Mokari, E. Rothenburg, I. Popov, R. Costi, U. Banin, *Science* **2004**, *304*, 1787–1790.

[135] F. Pinaud, D. King, H.-P. Moore, S. Weiss, *J. Am. Chem. Soc.* **2004**, *126*, 6115–6123.

Received: September 8, 2004

## D.2 Synthesis and perspectives of complex crystalline nano-structures

S. KUDERA, L. CARBONE, M. ZANELLA, R. CINGOLANI, W.J. PARAK, L. MANNA  
*Phys. stat. sol. (a)* **203**(6), pp. 1329–1336, 2006

Research on inorganic colloidal nanocrystals has moved from the synthesis of simple structures, such as spherical nanoparticles, to more elaborate particles with shapes such as rods, stars, discs, and branched nanocrystals, and recently to nanoparticles that are composed out of sections of different materials. Nanocrystal heterostructures represent a convenient approach to the development of nanoscale building blocks, as they merge sections with different functionality in the same particle, without the need of inorganic cross-linkers. The present article gives an overview of synthesis strategies to complex nanocrystals and will highlight their structural properties, as well as discuss some envisaged applications.

## Synthesis and perspectives of complex crystalline nano-structures

Stefan Kudera<sup>\*, 1, 2</sup>, Luigi Carbone<sup>1</sup>, Marco Zanella<sup>2</sup>, Roberto Cingolani<sup>1</sup>,  
Wolfgang J. Parak<sup>2</sup>, and Liberato Manna<sup>1</sup>

<sup>1</sup> National Nanotechnology Laboratories of INFM-CNR, Via Arnesano (km 5), 73100 Lecce, Italy

<sup>2</sup> Center for Nanoscience, Ludwig-Maximilians-Universität, Amalienstr. 54, 80799 München, Germany

Received 17 October 2005, revised 26 February 2006, accepted 26 February 2006

Published online 3 May 2006

PACS 81.07.Be

Research on inorganic colloidal nanocrystals has moved from the synthesis of simple structures, such as spherical nanoparticles, to more elaborate particles with shapes such as rods, stars, discs, and branched nanocrystals, and recently to nanoparticles that are composed out of sections of different materials. Nanocrystal heterostructures represent a convenient approach to the development of nanoscale building blocks, as they merge sections with different functionality in the same particle, without the need of inorganic cross-linkers. The present article gives an overview of synthesis strategies to complex nanocrystals and will highlight their structural properties, as well as discuss some envisaged applications.

© 2006 WILEY-VCH Verlag GmbH & Co. KGaA, Weinheim

### 1 Introduction

Synthesis techniques for colloidal nanocrystals have seen a fast development over the last years. In the nanometer size-regime the particles of some materials experience already quantum confinement effects. Therefore, by simply varying the size of a particle one can tune its properties over a considerable range, especially in the case of fluorescent semiconductor nanoparticles [1]. The relative ease of fabrication and manipulation combined with the flexibility offered by the possible tuning of their physical properties makes nanomaterials an appealing tool for many applications. This ranges from the development of LEDs [2] solar cells [3–5], lasers [6, 7], to biological tagging with semiconductor particles [8–10] and to biomedical applications of magnetic nanoparticle [11, 12] and also to future electronic devices [13–17].

A recent direction in the field of nanocrystal research is the development of synthetic techniques that allow for controlling the shape of the nanoparticles [18, 19]. Shape-controlled nanoparticles are promising candidates for several new applications. It has been proven for example that semiconductor nanorods enhance the efficiency of solar cells compared to spherical nanocrystals [5]. There are also several fundamental studies on the electronic behavior of semiconductor nanorods [20] and tetrapods [21] as these possess more intriguing shapes with respect to spherical nanocrystals, which might prove advantageous in displays, solar cells, field emitters and in nano-transistors. In addition, by introducing nanoparticles with a complex three-dimensional shape into composite materials, one can expect a strong influence on the materials' mechanical behavior.

The next step in complexity of nanoparticles is the fabrication of hybrid structures. The motivation for research in this direction is clear, as by merging different materials into a single nano-object, such object

\* Corresponding author: e-mail: stefan.kudera@physik.uni-muenchen.de



might exhibit multiple functionalities. First results have been demonstrated in this field, namely in the fabrication of hybrid materials. In this review we will focus on inorganic colloidal nanocrystals synthesized in hot organic solvents (200–400 °C).

## 2 Synthesis of spherical nanocrystals

Generally, the synthesis at high temperatures offers the advantage that defects are easily annealed from the crystal lattice. In addition, the nucleation and growth stages can be controlled and tuned easily. The reaction of the particles is started by injecting molecular precursors (which contain the atoms out of which the particle will be made) into a mixture of different organic molecules at a given temperature. These molecules have multiple roles. First, they serve as a solvent for the growing particles. Therefore, they have to support the high temperature without degradation and with negligible evaporation. Second, they also act as surfactants. At the high temperatures of the growth, they bind dynamically to the surface of the particles and by this they control the growth kinetics. When the synthesis is stopped by lowering the reaction temperature, such molecules form a stable monolayer around the particles. For a general overview on synthesis techniques we refer to various reviews [22, 23]. In a very simplified model, the surfactant molecules bind to and unbind from the surface of the nanoparticles, whereby the rates of these two processes are controlled by the temperature. Whenever there is a free site on the surface of a nanocrystal, the surfactants have to compete with the ions/atoms coming from the bulk of the solution for attachment to this site. In order to have a sufficient control on the dynamics of the growth, the surfactants must not bind too strongly to the particle surface, as this would suppress the crystals growth. On the other hand they should not bind too weakly, as otherwise the growth would be uncontrollably fast. This ultimately would result in the formation of large clusters and aggregates of clusters. The surfactant molecules most frequently used for such purpose are for instance phosphine oxides (tri-n-octylphosphine oxide) [1, 24], phosphines (e.g. tri-n-butylphosphine) [1, 24], phosphonic acids [25], amines [24, 26], and carboxylic acids [27]. In general, nanocrystals of different materials require different surfactants to be grown in a controlled and reproducible way. CdSe, for instance, is frequently grown in a mixture of tri-n-octylphosphine oxide and tri-n-octylphosphine [1], whereas CoPt<sub>3</sub> is grown in a mixture of amines, carboxylic acid and hexadecanol [26], and Fe<sub>2</sub>O<sub>3</sub> in oleic acid [27]. At the end of the growth process, when the temperature of the reactor is lowered to room temperature, unreacted excess precursors can be removed by subsequent precipitation and re-dissolution of the particles, by adding solvents to which the surfactant-coated nanocrystals are not soluble. The resulting nanoparticles are hydrophobic because of the monolayer of surfactants bound to their surface. These particles are soluble in many organic solvents and can be also stored as a powder and re-dissolved at whish.

Spherical nanoparticles can be grown for a large variety of different materials. Due to their electronic structure semiconductor materials (such as CdSe, CdS, ZnSe, InAs, CdTe, etc.) are of special interest [28]. These nanoparticles show a size-dependent narrow fluorescence peak. In the case of CdSe, for instance, such peak can be centered anywhere within the visible range from 450 nm to 650 nm, depending on the particle size. Semiconductor nanocrystals also exhibit a size-dependent, continuous absorption spectrum, which is blue-shifted with respect to their bulk counterpart. This clearly distinguishes them from organic dyes, which possess a narrow absorption band at energies slightly higher with respect to their emitted energies. These optical properties and also their superior lifetime [29] compared to fluorescent dyes make semiconductor nanoparticles an attractive tool in fluorescent labeling techniques [30] [31, 32], as they render it easier to observe simultaneously different colours with only one excitation wavelength [8, 10]. Recently, even smaller particles of CdSe have been produced [33, 34] that emit in the blue range. Besides fluorescent, also magnetic particles as CoPt<sub>3</sub> [26, 35] or Fe<sub>2</sub>O<sub>3</sub> [27] are interesting for many technical applications, such as drug targeting [36, 37] and magnetic storage devices [17].

A more detailed understanding of the growth mechanism of nanocrystals can be obtained in the general framework of the diffusion-controlled growth model [38, 39]. Nanocrystals are crystals and therefore possess facets. One can show that the dynamics of the growth depends on the surface energy of the different crystalline facets onto which new atoms are deposited [40, 41]. In the simplest case, we can

assume that the surface energy for all facets is nearly the same, and in most cases this is a reasonable assumption, as usually the nanocrystals grow isotropically (they have a rather spherical shape). In the theory of colloidal growth one can derive a key parameter, namely the “critical particle size”, which is inversely proportional to the concentration of monomers in solution. A particle that has exactly such critical size is in equilibrium with the bulk solution of monomers, therefore monomers unbind and bind at the same rate on it, and thus this particle is not growing nor shrinking. Particles smaller than this critical size exhibit a negative growth rate (they tend to dissolve), whereas particles larger than the critical size are continuously growing. A general equation describing the distribution of growth rate versus size shows a maximum in growth rate for particles which are twice as big as the critical size. Therefore, during the synthesis one should try to arrange the distribution of sizes and the critical size in such a way that even the smallest particles present are significantly larger than the critical size. In this case the smaller particles grow faster than the bigger particles, resulting in a focusing of the size distribution over time [42].

One major complication is that, while the synthesis of nanocrystals is proceeding, the monomers in solution are consumed. This leads to an increase in the critical size and the reaction can ultimately shift into the so-called Ostwald-ripening [43] regime. Here the size distribution is such that the smallest particles present are smaller than the critical size. As soon as these small particles dissolve, they free monomers that can be incorporated into the bigger particles. This regime is characterized therefore by a fast broadening of the size distribution. For this reason, the critical size should be kept always small in order to obtain a narrow distribution of sizes in the final sample. One possibility is to stop the synthesis well before it enters into the broadening regime. Another possibility is to continuously add monomers to the solution [1, 42].

### 3 Shape control

The assumption of equal surface energies for all facets is most certainly an oversimplified model. For II–VI semiconductor nanoparticles in wurtzite structure, for instance, it has been proven experimentally [44] and theoretically [40, 41] that the different facets exhibit distinguishably different binding strengths for certain surfactant molecules. Especially phosphonic acids are strongly binding to the lateral facets of the wurtzite crystals CdSe, CdS and CdTe, whereas their binding efficiency to the basal facets, that is the (0001) and the (000 $\bar{1}$ ) facets, is much lower. Therefore, the basal facets are more unstable than the prismatic facet and these two types of facets will grow at different rates, depending on the monomer concentration in solution. If the concentration of monomers in the growth environment is high, the basal facets will grow faster, and a rod shape will develop [45]. On the other hand, if the system is in the Ostwald ripening regime (monomer concentration is low) and the nanocrystal is shrinking, the basal facets will dissolve at a higher rate than the lateral facets. The synthesis of the rod-shape is well controlled in the case of CdSe, CdS and CdTe. One additional point about the wurtzite structure is that there is also a remarkable difference between the (0001) and (000 $\bar{1}$ ) facets. In the first case the cations expose three dangling bonds, in the second case only one (the opposite is true for the anions). Therefore the two facets are chemically different and have different growth rates [46].

A more complex shape is the tetrapod [19]. In this structure four rods are assembled into one three-dimensional object. A variety of materials may be grown in this shape, e.g. ZnO [47], ZnSe [48], CdS [49], CdSe [50] or CdTe [19, 51]. For type II–VI semiconductors there are two different crystallographic models that can rationalize this structure. In both cases the arms are described as rods that are growing in wurtzite structure. The two models differ in the way they describe the core out of which the arms are growing. The first model relies on the polymorphism of the material, most II–VI and some III–V semiconductors can grow both in the sphalerite and in wurtzite phase [52]. In this model the core consists of a sphalerite particle. The arms, which are in hexagonal phase, branch out of this core through a transition from the cubic to the hexagonal phase. The cubic core has four equivalent (111) facets that are chemically identical to the (0001) facets of the hexagonal phase. Therefore, through generation of a stacking fault the growth can shift from the cubic to the hexagonal phase. Growth along the (0001) direction is

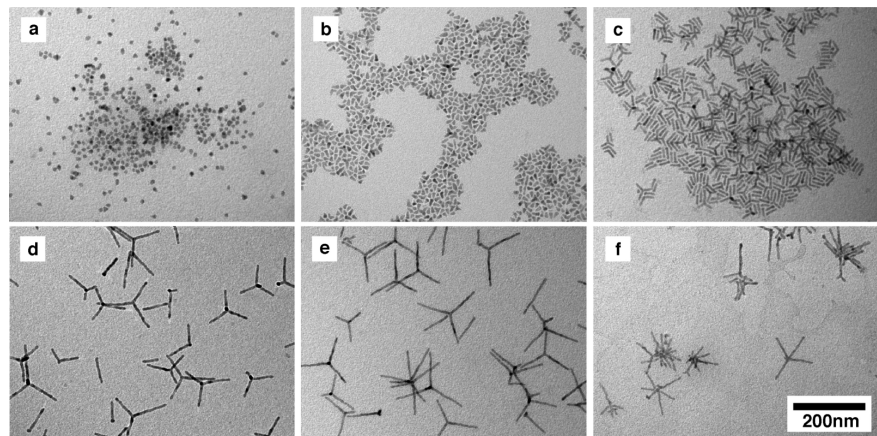


**Fig. 1** Transmission electron microscopy (TEM) images of CdTe nanoparticles with different shape.

suppressed due to the better passivation of this facet. The second model describes tetrapods as completely grown in the hexagonal phase, as each couple of arms is interconnected through two twin boundaries to another wurtzite domain located in the core of the tetrapod. In this model the tetrapods core can be considered as an assembly of eight building blocks that are connected to each other through twin boundaries. In the literature on ZnO tetrapods this model is known as the octatwin model [53].

Which of the two mechanism is operative in II–VI nanocrystals is object of investigation in our groups. In the case of CdTe nanocrystals, we are now able to tune the various reaction conditions so that we can synthesize nanocrystals having a variety of different shapes, ranging from spheres to rods, to nanocrystals that are progressively more branched (see Fig. 1). This controlled synthesis has also shed a light on the mechanism of branching in nanocrystals [54].

In a more elaborate approach to nanocrystal synthesis, starting from shape controlled CdSe, CdS or CdTe particles, nanocrystals of other materials, having the same shape or at least a similar shape can be obtained. This is possible for instance through a cation exchange reaction [55], which is even reversible. One demonstrated example is the replacement of Cd<sup>2+</sup> ions in CdSe rods by Ag<sup>+</sup> ions to form Ag<sub>2</sub>Se nanoparticles.

#### 4 Synthesis of hybrid materials

The combination of different inorganic materials in one particle is desirable, as the resulting new material exhibits the properties of both constituents. Inorganic colloidal particles can be connected with organic, biological molecules in a post-synthesis step. Here the key-lock principle is exploited by binding one type of molecule to the first particle and the complementary molecule to the second type of particles. This technique has been demonstrated for the formation of DNA-connected gold particles of different size [57, 58]. Unfortunately, these structures are very sensitive to environmental changes. DNA linkers are for example not stable against heat, as the double strand would break open. Biological linkers are typically also floppy. In order to get more stable and rigid hybrid materials it is preferable to epitaxially link different materials together.

The most symmetric example of inorganic hybrid materials is the core-shell structure. In this system one particle is embedded into a shell of a different material. For instance fluorescent semiconductor particles can be surrounded by a shell of a semiconducting material with a higher band gap. In the case of CdSe nanoparticles, the growth of a ZnS shell enhances the fluorescence properties of the material and the quantum yield can be increased by more than a tenfold [59].

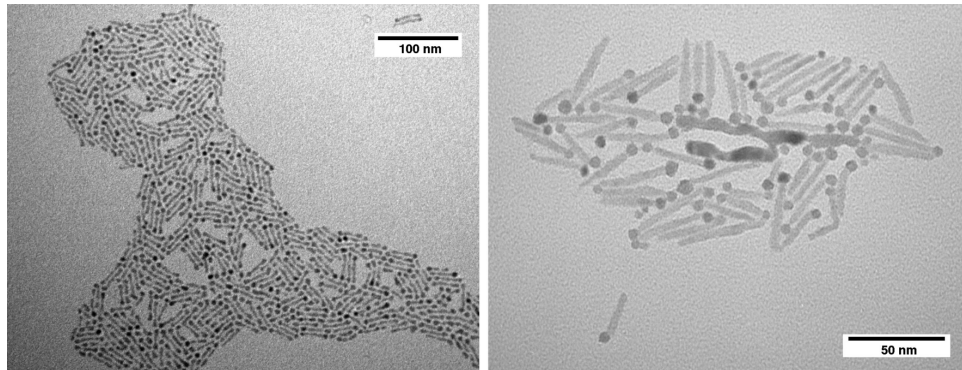


**Fig. 2** TEM images of dumbbell and matchstick structures. The left image shows a sample of CdSe rods with PbSe spheres on their tips. The right image shows a sample of CdS rods with a PbSe sphere mainly only on one of their tips. All experimental procedures are reported in Ref. [60].

Other examples of heterostructures are based on nanorods. As discussed above, in the case of rod growth different facets of the crystals have different reactivities. The higher reactivity of the tips or the better passivation of the lateral facets give rise to the possibility to nucleate another material only on the tips of the rods. This scheme can be exploited to grow dumbbell-shaped structures. As an example recently reported by our groups [60] and by the group of Banin [61], first rods of CdSe or CdS can be synthesized and purified. Then, in the presence of these particles, the synthesis of a second material is performed. When the concentration of the monomers of the second material is sufficiently low, the new material nucleates only on the tips of the rods. It seems that stress that is provoked by the lattice mismatch between the two materials does not suppress the formation of such structures. Gold tipped CdSe rods [61] can be produced according to this technique as well as PbSe dots may be grown onto CdSe or CdS rods (see Fig. 2) [60]. In the later case, even the number of dots per particle can be controlled. Instead of dumbbells with two dots, matchsticks with only one dot can be synthesized. With a slightly different approach, ZnO–Ag heterostructures can be produced [62]. Also in this case a two step synthesis is necessary. First the ZnO nanorods are synthesized, then Ag is deposited onto these particles through a photocatalytic reaction. Upon strong UV irradiation, electron–hole pairs are generated in the ZnO rods, the electrons can then reduce the Ag-ions and so trigger the nucleation of Ag-particles on the surface of the rods.

In an *in-situ* approach it is possible to first synthesize rods of a cadmium-based semiconductor material and then grow from its tips linear sections of a different material (CdTe or CdSe). By carefully adjusting the experimental conditions also the shape of the central material (either rod or tetrapod) and the outer material (either linear or branched section) can be controlled [63].

A completely different approach to produce hybrid nanocrystals was followed by Gu and co-workers [64]. They reported the synthesis of hybrids with a CdS and a FePt section. Here, first an amorphous shell of CdS is grown onto FePt particles and then by annealing these samples, crystalline CdS domains form on one side of the FePt, due to a de-wetting process which minimizes the interfacial energy between the two materials.

## 5 Outlook

By carefully manipulating the thermodynamics and kinetics of crystal growth one can control both the shape and the composition of nanocrystals. It is now possible to grow several materials in complex shapes, such as for instance tetrapods. Starting from these structures, one can synthesize hybrid materials

by exploiting the different passivation efficiencies of surfactant molecules towards the various crystal facets.

These new materials are promising candidates for different applications. First, they might open new perspectives in self-assembly, as in the case of metal tipped semiconductor rods. Reactive groups such as thiols bind strongly to Au, but only relatively weakly to CdSe and CdS surfaces [61]. This facilitates site-selective surface functionalization by organic molecules. By simply exposing CdSe–Au dumbbell structures to biological molecules bearing free thiol-groups, selective attachment of these molecules at the gold-tip regions is expected. First demonstrations in this direction have been reported already for hybrid materials of bigger size [65], namely Au/Ni particles. It was demonstrated that different reactive groups bind selectively to certain domains of a nanocrystal. In particular, thiol-functionalised biomolecules were bound to the gold domains, carboxylic groups were bound to the Ni domain. Also for nanometer-sized CdSe–Au dumbbell structures size-selective surface functionalization has been reported [61]. By adding dithiols, CdSe–Au dumbbells are selectively connected at their Au-ends, which leads to the formation of nanorod chains [61]. Nevertheless, experiments in this direction are just in their infancy and still many questions, such as the role of non-specific interactions remain to be solved. Site-specific functionalization on just one tip of the rods would facilitate new possibilities of arranging particles on surfaces. For an example, by linking rod-shaped objects with their tip to a surface, a brush of vertically aligned particles could be formed (see Fig. 3). This structure would be of great interest for the fabrication of solar cells [5]. Certainly, the possibility to selectively functionalize specific regions of the particles with organic molecules will play an important role in the future for the generation of complex self-assembled structures with an improved degree of programmability.

Other possible applications of hybrid particles are expected in the field of electronics [14, 20]. Gold tipped nanocrystals may render it easier to form electronic contacts with the particles. This might for example help the design of nanocrystal-modified electrodes [66]. In addition, linear junctions of semiconductor particles may provide interesting electronic properties by themselves. The band structure of heterostructures of two types of semiconductor may open up new applications for this material. The reported PbSe–CdSe–PbSe heterostructure [60] could be considered as a light-controlled transistor. Here a high-band gap material (CdSe,  $E_g \approx 2$  eV) is situated between two sections of a material with smaller band gap (PbSe,  $E_g \approx 0.5$  eV). In this way, communication between the two PbSe sections only is possible when they are in an excited state, that is after the absorption of a photon.

All synthesis procedures and reactions reported so far are dependent on organic molecules bearing long alkyl chains (the surfactants) and therefore the as-grown nanoparticles are hydrophobic. Several methods are now available to transfer these particles to aqueous solution, which work by rendering the surface of these nanocrystals hydrophilic [29, 67]. Water-soluble particles offer a whole new direction of applications, especially in the field of life sciences. We refer here to recent review articles [31, 32, 68]. It is currently under discussion if nanoparticles are compatible with biological applications. There are several investigations on this subjects [69–71], but it seems that this question is not easy to address, as for



**Fig. 3** Selective functionalization may be used for the formation of complex architecture as shown in a sketch here. By functionalizing only the tips of the dumbbell structures it may be possible to form chains of these particles (left sketch). This has been demonstrated already [61] by carefully exposing gold tipped nanorods to hexane(1,6)dithiol. Providing functional pads (right sketch) on a substrate may enable the formation of brushes of rods. For this approach matchstick-shaped particles with only one functional domain could be of advantage.

instance in the case of gold-nanoparticle there is a strong, non-linear dependence of the toxicity on the size of the particles [72, 73]. Hybrid nanoparticles also open new perspectives in life science applications. Nanoparticles with combined magnetic and fluorescent properties [64] could be directed with magnetic field gradients and detected on a single-particle level by their fluorescence.

We believe that in future the synthesis of nanocrystals should evolve into the development of more complex nano-structures. An appealing field of research would be the synthesis of hybrid nano-materials with increased functionality.

**Acknowledgements** The authors would like to acknowledge funding by the European Union (SA-NANO STRP 013698), the Deutscher Akademischer Austauschdienst (DAAD) and the DFG Emmy Noether programme.

## References

- [1] C. B. Murray, D. J. Norris, and M. G. Bawendi, *J. Am. Chem. Soc.* **115**, 8706–8715 (1993).
- [2] N. Tessler et al., *Science* **295**(5559), 1506–1508 (2002).
- [3] B. O'Regan and M. Grätzel, *Nature* **353**(6346), 737 (1991).
- [4] M. Grätzel, *Nature* **414**(6861), 338 (2001).
- [5] W. U. Huynh, J. J. Dittmer, and A. P. Alivisatos, *Science* **295**(5564), 2425–2427 (2002).
- [6] H. J. Eisler et al., *Appl. Phys. Lett.* **80**(24), 4614–4616 (2002).
- [7] P. T. Snee et al., *Adv. Mater.* **17**(9), 1131–1136 (2005).
- [8] M. J. Bruchez et al., *Science* **281**, 2013–2016 (1998).
- [9] W. J. Parak et al., *Adv. Mater.* **14**(12), 882–885 (2002).
- [10] W. C. W. Chan and S. Nie, *Science* **281**, 2016–2018 (1998).
- [11] Q. A. Pankhurst et al., *J. Phys. D, Appl. Phys.* **36**(13), R167–R181 (2003).
- [12] C. C. Berry, *J. Mater. Chem.* **15**(5), 543–547 (2005).
- [13] A. Bezryadin, C. Dekker, and G. Schmid, *Appl. Phys. Lett.* **71**(9), 1273 (1997).
- [14] D. L. Klein et al., *Nature* **389**(6652), 699 (1997).
- [15] R. Krahne et al., *Appl. Phys. Lett.* **81**(4), 730 (2002).
- [16] D. L. Feldheim et al., *J. Am. Chem. Soc.* **118**(32), 7640–7641 (1996).
- [17] D. Weller and A. Moser, *IEEE Trans. Magn.* **35**(6), 4423–4439 (1999).
- [18] X. Peng et al., *Nature* **404**(6773), 59–61 (2000).
- [19] L. Manna et al., *Nature Materials* **2**, 382–385 (2003).
- [20] O. Millo et al., *Nanotechnology* **15**(1), R1 (2004).
- [21] Y. Cui et al., *Nano Lett.* **5**(7), 1519–1523 (2005).
- [22] C. B. Murray, C. R. Kagan, and M. G. Bawendi, *Annu. Rev. Mater. Sci.* **30**(1), 545–610 (2000).
- [23] O. Masala and R. Seshadri, *Annu. Rev. Mater. Res.* **34**, 41–81 (2004).
- [24] P. Reiss, J. Bleuse, and A. Pron, *Nanoletters* **2**(7), 781–784 (2002).
- [25] Z. A. Peng and X. Peng, *J. Am. Chem. Soc.* **123**(1), 183–184 (2001).
- [26] E. V. Shevchenko et al., *J. Am. Chem. Soc.* **124**, 11480–11485 (2002).
- [27] T. Hyeon et al., *J. Am. Chem. Soc.* **123**, 12798–12801 (2001).
- [28] A. P. Alivisatos, *J. Phys. Chem.* **100**(31), 13226–13239 (1996).
- [29] D. Gerion et al., *J. Phys. Chem. B* **105**(37), 8861–8871 (2001).
- [30] W. J. Parak et al., *Nanotechnology* **14**, R15–R27 (2003).
- [31] X. Michalet et al., *Science* **307**(5709), 538–544 (2005).
- [32] I. L. Medintz et al., *Nature Materials* **4**(6), 435–446 (2005).
- [33] A. Kasuya et al., *Nature Materials* **3**, 99–102 (2004).
- [34] H. Z. Wang et al., *J. Mater. Res.* **19**(11), 3157–3161 (2004).
- [35] E. V. Shevchenko et al., *J. Am. Chem. Soc.* **124**, 11480–11485 (2003).
- [36] C. Alexiou et al., *Cancer Research* **60**(23), 6641–6648 (2000).
- [37] B. Zebli et al., *Langmuir* **21**(10), 4262–4265 (2005).
- [38] T. Sugimoto, *Adv. Colloid Interface Sci.* **28**, 65 (1987).
- [39] L. Manna et al., *Perspectives of Colloidal Nanocrystals in Nanoscience and Nanotechnology* (Enrico Fermi School, 2004).
- [40] A. Puzder et al., *Nanoletters* **4**(12), 2361–2365 (2004).
- [41] L. Manna et al., *J. Phys. Chem. B* **109**(13), 6183–6192 (2005).



[42] X. Peng, J. Wickham, and A. P. Alivisatos, *J. Am. Chem. Soc.* **120**(21), 5343–5344 (1998).

[43] J. A. Marques and J. Ross, *J. Chem. Phys.* **80**(1), 536–543 (1984).

[44] Z. A. Peng and X. G. Peng, *J. Am. Chem. Soc.* **123**, 1389–1395 (2001).

[45] Z. A. Peng and X. Peng, *J. Am. Chem. Soc.* **124**(13), 3343–3353 (2002).

[46] L. Manna, E. C. Scher, and A. P. Alivisatos, *J. Cluster Sci.* **13**(4), 521–532 (2002).

[47] K. Nishio et al., *Philos. Mag. A* **76**(4), 889–904 (1997).

[48] J. Hu, Y. Bando, and D. Golberg, *Small* **1**(1), 95–99 (2005).

[49] Y.-W. Jun et al., *J. Am. Chem. Soc.* **123**(21), 5150–5151 (2001).

[50] L. Manna, E. C. Scher, and A. P. Alivisatos, *J. Am. Chem. Soc.* **122**(51), 12700–12706 (2000).

[51] W. W. Yu, Y. A. Wang, and X. Peng, *Chem. Mater.* **15**, 4300–4308 (2003).

[52] C. Y. Yeh et al., *Phys. Rev. B: Condens. Matter* **46**, 10086–10097 (1992).

[53] H. Iwanaga, M. Fujii, and S. Takeuchi, *Phase Transit.* **66**, 147–165 (1998).

[54] L. Carbone, S. Kudera, E. Carlino, W. J. Parak, C. Giannini, R. Cingolani, and L. Manna, *J. Am. Chem. Soc.* **128**(3), 748–755 (2006).

[55] D. H. Son et al., *Science* **306**(5698), 1009–1012 (2004).

[56] F. Dumestre et al., *Angew. Chem., Int. Ed.* **41**(22), 4286–4289 (2002).

[57] R. C. Mucic et al., *J. Am. Chem. Soc.* **120**(48), 12674–12675 (1998).

[58] C. J. Loweth et al., *Angew. Chem.* **111**(12), 1925–1929 (1999).

[59] B. O. Dabbousi et al., *J. Phys. Chem. B* **101**(46), 9463–9475 (1997).

[60] S. Kudera et al., *Nanoletters* **5**(3), 445–449 (2005).

[61] T. Mokari et al., *Science* **304**, 1787–1790 (2004).

[62] C. Pacholski, A. Kornowski, and H. Weller, *Angew. Chem., Int. Ed.* **43**(36), 4774–4777 (2004).

[63] D. J. Milliron et al., *Nature* **430**(6996), 190–195 (2004).

[64] H. Gu et al., *J. Am. Chem. Soc.* **126**(18), 5664–5665 (2004).

[65] A. K. Salem, P. C. Searson, and K. W. Leong, *Nature Mater.* **2**(10), 668–671 (2003).

[66] C. Stoll et al., accepted by *Small* (2005).

[67] T. Pellegrino et al., *Nanoletters* **4**(4), 703–707 (2004).

[68] T. Pellegrino et al., *Small* **1**(1), 48–63 (2005).

[69] A. M. Derfus, W. C. W. Chan, and S. N. Bhatia, *Nano Lett.* **4**(1), 11–18 (2004).

[70] M. Green and E. Howman, *Chem. Commun.*, No. 1, 121–123 (2005).

[71] C. Kirchner et al., *Nanoletters* **5**(2), 331–338 (2005).

[72] E. E. Connor et al., *Small* **1**(3), 325–327 (2005).

[73] M. Tsoli et al., *Small* **1**(8/9), 841–844 (2005).

## D.3 Synthesis routes for the growth of complex nanostructures

S. KUDERA, L. CARBONE, E. CARLINO, R. CINGOLANI, P.D. COZZOLI, L. MANNA  
*Physica E* **37**(1–2), pp. 128–133, 2007

The interest in research on inorganic colloidal nanoparticles has moved to more complex structures, such as anisotropically shaped particles and branched objects. Recently, schemes for the synthesis of heterostructures have also been presented. In this article we discuss the synthesis conditions for spherical and branched nanoparticles. The influence of parameters as temperature and composition of the mixture of surfactants on the shape of the growing particles is discussed. Also, an overview on different approaches for the formation of heterostructures is presented briefly.



Available online at [www.sciencedirect.com](http://www.sciencedirect.com)



Physica E 37 (2007) 128–133

PHYSICA E

[www.elsevier.com/locate/physe](http://www.elsevier.com/locate/physe)

## Synthesis routes for the growth of complex nanostructures

Stefan Kudera<sup>a</sup>, Luigi Carbone<sup>a</sup>, Elvio Carlino<sup>b</sup>, R. Cingolani<sup>a</sup>,  
Pantaleo Davide Cozzoli<sup>a</sup>, Liberato Manna<sup>a,\*</sup>

<sup>a</sup>National Nanotechnology Laboratory of CNR-INFM, Via Arnesano (km 5), 73100 Lecce, Italy

<sup>b</sup>TASC-INFM-CNR National Laboratory, Area Science Park-Basovizza, 34012 Trieste, Italy

Available online 30 August 2006

### Abstract

The interest in research on inorganic colloidal nanoparticles has moved to more complex structures, such as anisotropically shaped particles and branched objects. Recently, schemes for the synthesis of heterostructures have also been presented. In this article we discuss the synthesis conditions for spherical and branched nanoparticles. The influence of parameters as temperature and composition of the mixture of surfactants on the shape of the growing particles is discussed. Also, an overview on different approaches for the formation of heterostructures is presented briefly.

© 2006 Elsevier B.V. All rights reserved.

PACS: 81.07.Bc

Keywords: Nanocrystals; Shape control; Nanostructures

### 1. Introduction

In the last few years the interest of research in the field of nanoparticle synthesis has moved to increasingly complex nanocrystal structures. Spherical nanoparticles [1] have proven their versatility in several applications, such as in the development of LEDs [2] or in biological tagging [3,4]. Shape-controlled nanocrystals [5,6], as for instance nanorods, are currently tested as active material in solar cells [7,8] or in electronic devices [9–11]. Recently the coupling of nanorods to photons in a microcavity has been also demonstrated [12], therefore paving a route towards applications in quantum information processing.

#### 1.1. General description of the synthesis technique

The nanoparticles described in this presentation are produced in a way similar to the route described in the classical literature on the synthesis of CdE (E = S, Se, Te) nanoparticles [13]. For a review on different protocols see,

for instance Refs. [1,14]. Generally the preparation schemes described in this article will focus on synthesis performed at high-temperatures in organic solvents. These conditions have the advantage that eventual nanocrystal defects occurring during the growth process can be annealed out. The organic solvents serve also as surfactant molecules to the particles. In this role they attach and detach dynamically to and from the growing nanocrystal, and therefore control the speed at which monomers can bind to the surface of the particle. In particular, for high temperature syntheses the choice of surfactants is restricted, as they should not evaporate from the growth solution, nor should degrade.

In a microscopic picture, the growth of colloidal particles [15,16] can be divided into two steps. First, the monomers have to reach the vicinity of the particle, and this occurs proceeds mainly through diffusion. Subsequently, the monomers have to react with crystal. In the most common situation, the so-called diffusion-controlled growth regime, the rate limiting factor is the diffusion of monomers towards the surface of the crystal, which is assumed to be slow compared to the reaction rate of monomers with the particle. Under these circumstances the growth rate of a particle depends on its size. This gives rise to two

\*Corresponding author.

E-mail address: [liberato.manna@unile.it](mailto:liberato.manna@unile.it) (L. Manna).

sub-regimes of diffusion-controlled growth, in which the size distribution either narrows or broadens. In the narrowing regime, the smaller particles grow faster than the larger ones. In contrast, in the broadening regime, the larger particles grow faster than the smaller particles. In an extreme case of the broadening regime the small particles eventually exhibit a negative growth rate and therefore they dissolve. In such case the large particles grow at the expense of the small particles and overall the concentration of particles is reduced over time. This is the so-called Ostwald ripening effect [17]. The actual state of the growth regime is dictated by the critical size [15], which determines the particle size that neither grows nor shrinks. This value depends on various parameters, among which the concentration of monomers in solution is the most critical [18]. To illustrate this dependence we consider a solution with a low monomer concentration. In this case the small particles become unstable and dissolve, as the critical size is large, whereas at a high monomer concentration even small particles are stable, as the critical size is comparatively small.

Additionally, the growth rate depends on the surface energy of the individual facets of the growing particle, as predicted by the Gibbs–Thompson–equation [19], which describes the solubility of a crystal as a function of its surface energy. There are different models that explain this behaviour [20]. One model takes into account the different binding affinities of the surfactants to the different crystal facets. As an example, the dependence of the binding affinity of various surfactants to the various crystalline facets of wurtzite CdSe nanocrystals has been highlighted in several experiments [21,22] and also studied theoretically [23,24].

The choice of proper surfactants for a nanocrystal synthesis is dictated by several factors, first of all the above mentioned suitability of the molecules in terms of physical stability. In general the synthesis of nanocrystals of different materials and with controlled shapes requires adequate surfactant/solvent mixtures. Currently, the most widely used classes of surfactants for the synthesis of CdSe nanoparticles include phosphine oxides [13,25], phosphines [13,25] and phosphonic acids [25,26], but also amines [25] and carboxylic acids [27]. Advances have been made towards the development of greener synthesis schemes [28]. The classical synthesis [13] of CdSe nanoparticles involves toxic and hazardous reactants. For instance it was demonstrated that the highly reactive dimethyl cadmium could be replaced by cadmium oxide [26], which is still toxic, but much easier to handle.

In the following Section 2.1 we will present a typical synthesis scheme for spherical particles of CdTe. Section 2.2 will highlight general issues of the shape control of nanocrystals, and in Section 2.3 branching in nanocrystals will be discussed in more detail. Finally, in Section 3 we will describe briefly the recent advances in the topological control of composition in colloidal nanocrystals.

## 2. Synthesis of nanoparticles of one material

### 2.1. Growth of spherical particles

In the simplest case of nanocrystal growth every nanocrystal facet experiences roughly the same growth rate, and therefore the particles will grow with a spherical shape. This is the case when surfactants show little or no selectivity in the binding to the various crystal facets. As an example describe here a synthesis of CdTe nanoparticles, in which the particles grow into an almost spherical shape with a narrow size distribution. In a typical synthesis protocol followed in our labs, CdO (0.051 g), octadecylphosphonic acid (ODPA) (0.280 g) and tri-n-octylphosphine oxide (TOPO) (3.77 g) are mixed in a three-neck flask, and degassed under vacuum at temperatures around 130–150 °C. Then the solution is heated to above 300 °C under an inert atmosphere until it turns from brown to transparent. This change in color indicates that CdO has reacted with the phosphonic acid, yielding a cadmium phosphonate complex. At this point 1 mL of tri-n-octylphosphine (TOP) is injected and the temperature is stabilized at 370 °C. Then a solution of Tellurium dissolved in tri-n-octylphosphine (TOP) (10 wt%, 0.55 g) is injected rapidly into the flask. Nucleation of CdTe occurs immediately after the injection, followed by the growth of the nanocrystals. The reaction is allowed to proceed up to 90 s, then the heating mantle is removed in order to stop the reaction by cooling. The average nanocrystal size is clearly dependent on the reaction time. If the same synthesis is carried out at a lower temperature nanocrystals with a slightly triangular or star-like shape are obtained (see Fig. 2a). This is due to the fact that at lower temperatures there is a higher selectivity in the binding affinity of the surfactants to the different facets and therefore the morphology of the nanocrystals deviates significantly from a spherical shape.

As concerns the fluorescence properties of the spherical particles produced under different conditions, the particles produced at higher temperature show in general a much higher fluorescence from band-edge states with respect to those synthesized at lower temperatures. This indicates that in nanocrystals prepared at higher temperatures the number of crystal defects is reduced.

In the case of CdTe nanocrystals the synthesis scheme reported above yields samples with a narrow size distribution, as deduced from the linewidth of the fluorescence signal. A typical fluorescence linewidth from CdTe nanocrystals in solution at room temperature is around 80–90 meV. Generally samples of CdTe nanocrystals extracted at progressively longer times during the synthesis show narrower fluorescence linewidths. As the width in the fluorescence signal can be correlated with the spread in the nanocrystal size distribution, this clearly indicated that the size distribution narrows over time. However, if syntheses are let to run for longer times (for instance for more than a few minutes), the size distribution starts

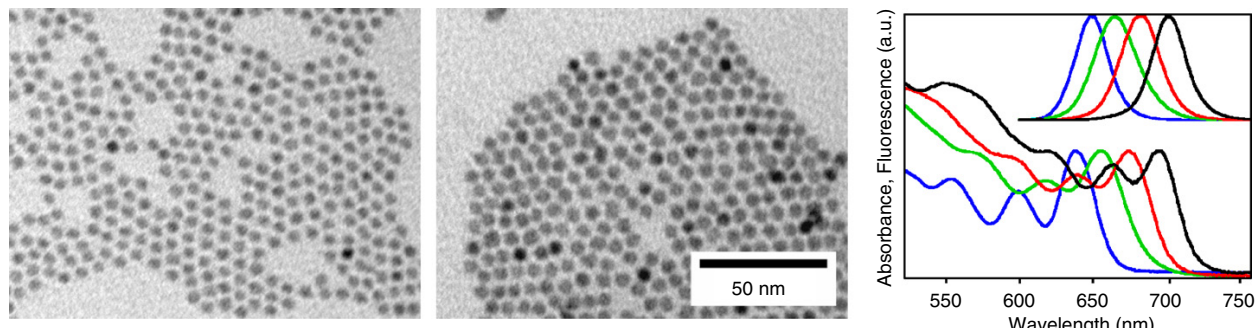


Fig. 1. Transmission Electron Microscopy (TEM) images of CdTe spherical dots and absorption and fluorescence spectra of CdTe dots of different sizes. For clarity the emission spectra are shifted upwards. The four spectra correspond to different sizes of the particle and also to different reaction times.

broadening at a certain point, as the concentration of monomers decreased below a critical value.

Apart from the example discussed above spherical nanocrystals are now produced from a wide variety of materials. Semiconductor materials are very appealing due to their electronic structure [29]. The band-edge emission of semiconductor nanoparticles is blue shifted with respect to their bulk counterpart, owing to the strong confinement of the exciton in the volume of the particles. Another key characteristic of semiconductor nanoparticles is their continuous absorption spectrum for energies higher than the bandgap (see Fig. 1), as opposed to organic fluorescent dyes that show a narrow absorption spectrum, only slightly blue shifted with respect to their fluorescence spectrum. This peculiar property, along with their longer fluorescence lifetime and much higher resistance to photodegradation as compared to organic fluorescent dyes [30] makes colloidal inorganic nanocrystals appealing as powerful fluorescent labels in biological applications [31–33]. Examples of colloidal semiconductor nanocrystals include CdSe [13,25,34], CdS [13,35,36], ZnSe [37,38], InP [39] etc. The interest in these nanoparticles arises from the possibility to easily tune their bandgap and therefore their fluorescence wavelength simply through the adjustment of their diameter. The fluorescence emission from colloidal CdSe nanocrystals, for instance, can be easily tuned all the way from about 450 nm (blue), to about 650 nm (red), depending on the nanocrystal diameter, therefore spanning all the visible region of the spectrum.

## 2.2. Shape control

In this section we will discuss briefly shape control of colloidal nanocrystals. In most cases, at the conditions under which syntheses are carried out surfactants do bind with different strengths to the various facets of the growing nanocrystals and therefore the overall nanocrystal morphology deviates significantly from the spherical shape. In addition, often nanocrystals have crystal phases with a unique axis of symmetry (such as the hexagonal wurtzite phase). In this latter case, when specific surfactants are present in the reaction environment the facets parallel to

the unique axis can exhibit growth rates that are significantly different with respect to those perpendicular to such axis. This leads to nanocrystal morphologies that are strongly anisotropic, such as rods or platelets. Apart from the different affinity of the surfactant to the individual facets of the particle, the anisotropic growth of nanocrystals that leads for instance to rods or platelet shaped nanocrystals must be kinetically favoured by a high flux of monomers, which enhances the differences in the growth rates of the various facets [40]. Consequently, the synthesis of shape-controlled nanocrystals is often carried out under conditions that ensure a high concentration of monomers. Among the various shape-controlled nanocrystals, perhaps CdSe nanorods are those for which the finest control over average rod length and diameter has been achieved so far. A similar fine control has been reported also for other materials, such as for instance gold [41], although in this latter case the growth mechanism differs significantly from the cases discussed so far and goes beyond the scope of this work.

A more intriguing shape often observed in micro- and nanocrystals of several materials, such as ZnO [42], ZnSe [38,43] and CdTe [6,44], is the tetrapod, a structural assembly of four rods connected together into a single object. Additionally to the effect of anisotropic growth, as discussed above, for the rod sections, also a branching event occurs in formation of these nanocrystals. Apparently, this is limited to early stages of the growth process, as the branching is restricted in general to the central region of the particle. In the case of tetrapod shaped CdTe nanocrystals synthesized in a mixture of TOPO, TOP and an alkyl phosphonic acid with a long hydrocarbon chain (such as octadecylphosphonic acid, ODPA), our groups recently found that the branching is actually controlled by the presence of an impurity in the composition of the surfactants [45,46]. In earlier works on CdTe tetrapods [6], OPDA, TOPO and TOP were used as a surfactant. At that time, commercially available OPDA contained a series of impurities, among them phosphonic acids with short alkylic chains. Since then, more refined synthesis schemes involving purer ODPA along with a controlled amount of propylphosphonic acid (PPA) [45] and methylphosphonic

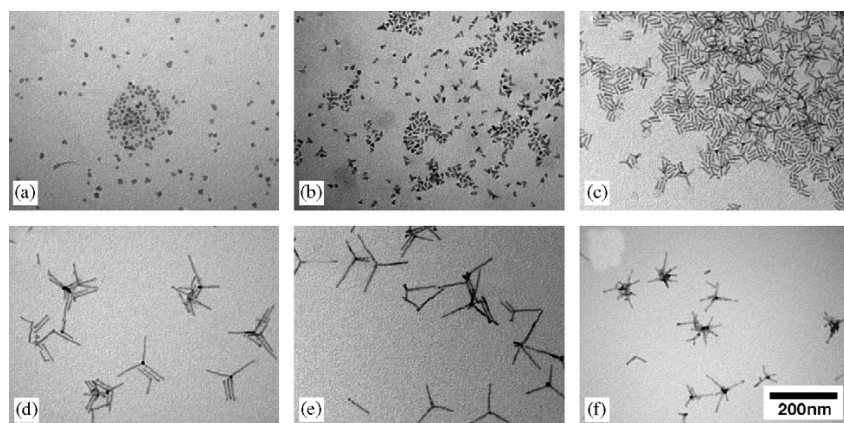


Fig. 2. CdTe samples with different shapes. The parameter varied in the different synthesis is the concentration of an impurity, namely methylphosphonic (MPA). The ratio of MPA to ODPA was adjusted as: (a) 0%, (b) 2.6%, (c) 5.3%, (d) 8.1%, (e) 9.3% and (f) 17.6%.

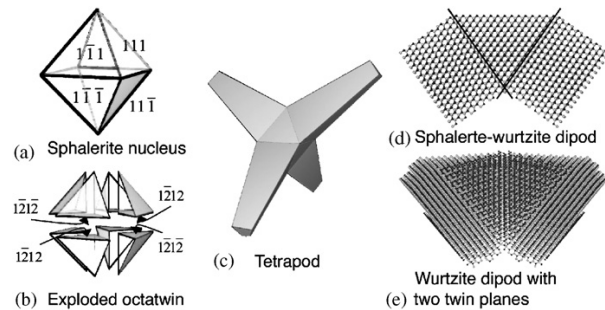


Fig. 3. Models that rationalize the shape of the tetrapod. The surface of an octahedral sphalerite nucleus (a) has the same arrangement of bonds as an octatwin (b). The tetrapod (c) can grow from both structures. In the right column atomic models of the junction between two arms are displayed. In the case of the sphalerite nucleus (d) the position of the stacking fault is marked. In (e) the core consists of just three domains. One can distinguish the intermediate pyramidal domain.

acid (MPA) [46] have been reported. In the case of MPA, our groups reported that only small amounts were needed to trigger both anisotropic growth and branching of CdTe nanocrystals, as displayed in Fig. 2. In order to prepare CdTe tetrapods, it was found that only a molar ratio MPA:ODPAE8–10% is needed. The contribution of MPA to the weight of the whole growth solution is below 1%.

### 2.3. Models of branching

The mechanism by which branching occurs is certainly interesting. There are at least two crystallographic models that rationalize the shape of the tetrapod (Fig. 3) in materials that can crystallize in both the wurtzite and sphalerite phases. In both cases the overall shape of the core is described as an octahedron. In case of cadmium chalcogenide tetrapods, on four of the eight facets of this octahedral core surface Cd atoms expose three dangling bonds. On the other four facets, surface Cd atoms expose just one dangling bond. These two families of facets have

different growth rates, also because surfactants should bind to them with different affinities [47,48]. It is likely that the group of facets in which Cd atoms expose three dangling bonds can be expected to be less efficiently passivated than the other group of facets. According to both models of branching the arms of the tetrapods are in the wurtzite phase and are grown on the top of the four weakly passivated facets of the nucleus. The two models differ only in the internal structure of the core. In one model the crystalline structure of the core is purely cubic sphalerite [6], whereas the second model describes this core as composed of eight wurtzite domains that share twin planes [46]. Thus the first model relies on the polymorphism of CdTe, which can grow both in the cubic sphalerite structure and in the hexagonal wurtzite structure. The difference in energy of formation of the two structures is relatively low for CdTe [49,50]. The transition from the cubic core to the hexagonal arm occurs through a stacking fault. In the second model of branching, the eight pyramidal domains are fused together through twin planes and each of the eight exposed facets of the octatwin is one of the two polar facets perpendicular to the unique *c*-axis in the wurtzite structure in each of the eight domains forming the nucleus. This mechanism has been observed and investigated extensively also in ZnO tetrapods [42,51,52]. In the wurtzite structure there are several types of twin boundaries that have a relatively low energy of formation. Among them, those that expose a head-to-tail arrangement in the polarity of the two domains are of special interest for the modelling of the crystal. In that case the *c*-axes of two adjacent wurtzite domains have a head to tail arrangement. Therefore the eight facets of the resulting octatwin show an alternating pattern of fast growing and slowly growing basal facets of the wurtzite structure.

There are several reports on branched micro- and nanocrystals in support of either the sphalerite-wurtzite or the multiple twin model. We recently found that the multiple twin model can explain the formation of CdTe tetrapods. First, the presence of twin planes was observed

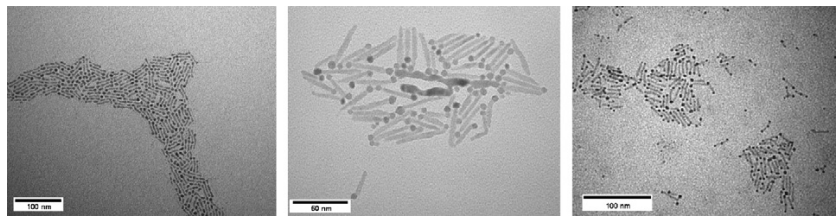


Fig. 4. Examples of different heterostructures: PbSe–CdSe–PbSe dumbbells (left panel). In the case of CdS–PbSe heterostructures, also the formation of matchstick-like objects is possible. The CdS rods are decorated with only one dot of PbSe [59], (middle panel) Au–CdSe–Au dumbbells (right panel).

directly in samples of CdTe nanocrystals [46] and also the occurrence of nanocrystals with a variable number of branches (such as dipods and tripods) supports the model in which the branching region is formed by several twins. In this context, the octatwin represents the maximum number of twins that can be assembled in the nucleus.

### 3. Hybrid materials

One step further in the complexity of nanomaterials can be achieved by the formation of hybrid structures, which are composed of sections of different materials. Development of these structures is motivated by the idea that the resulting particles should group in their structure the properties of the various materials. One approach to assemble nanoparticles of different materials and properties is to interconnect them through complex molecules in a post-synthesis step. A technique to achieve this has been demonstrated by attaching pair-wise complementary DNA-strands to two or more different materials [53,54]. In general, this technique is based on biomolecules and therefore requires water-soluble particles. Different approaches to render hydrophobic particles water soluble [30,55] open up the possibility to perform this task also on initially hydrophobic particles [56].

Nevertheless there is an interest to attach the different sections of the material stronger to each other by epitaxially growing one material on top of the other. In this scenario, one can regard the core-shell nanoparticles as the simplest example of such heterostructures [57]. A more elaborate shape is obtained when growing a second material only on specific regions of a starting nanocrystal. Again, this process can be triggered by the different reactivity of the individual facets. In the same way as the growth rate of some facets of a nanocrystal can be made extremely low, also the nucleation of a second material can be suppressed on them. One example is the growth of Au [58] or PbSe [59] sections onto CdSe rods. The resulting structures have the shape of dumbbells: the second material is deposited only on the tips of the rods as the other facets are passivated much stronger. Examples of these particles are displayed in Fig. 4.

The formation of heterostructures of other materials has been demonstrated. For instance, nanocrystal dimers formed by on FePt domain and on CdS domain joined together have been reported recently [60]. These hetero-

structures can possibly be localized with a strong magnetic field and in the same time be observed due to their fluorescence properties. A similar structure is a nanocrystal dimer made of CoPt<sub>3</sub> and Au [61]. Ideally, the magnetic properties of CoPt<sub>3</sub> should enable the localization of the particles, whereas the Au section can be easily functionalized with molecules/biomolecules, so that these hybrid nanocrystals can be used for delivery of molecules that are bound to the Au section.

### 4. Conclusion

The increase in the degree of structural complexity of solution-grown nanocrystals will certainly be one of the natural directions towards which materials science will increasingly orient. In this work we have briefly outlined recent innovative approaches to nanocrystals with size and shape control, up to nanocrystals made of inorganic materials with different properties in the same particle. These approaches will the way to the development of nanosized objects able to perform multiple technological tasks. An additional important point is a detailed understanding of the formation of branching in colloidal nanoparticles, which will trigger the development of branched structures for a wider variety of materials.

### References

- [1] C.B. Murray, C.R. Kagan, M.G. Bawendi, *Ann. Rev. Mater. Sci.* 30 (2000) 545.
- [2] N. Tessler, V. Medvedev, M. Kizes, S. Kan, U. Banin, *Science* 295 (2002) 1506.
- [3] M.J. Bruchez, M. Moronne, P. Gin, S. Weiss, A.P. Alivisatos, *Science* 281 (1998) 2013.
- [4] W.C.W. Chan, S. Nie, *Science* 281 (1998) 2016.
- [5] X. Peng, L. Manna, W. Yang, J. Wickham, E. Scher, A. Kadavanich, A.P. Alivisatos, *Nature* 404 (2000) 59.
- [6] L. Manna, D.J. Milliron, A. Meisel, E.C. Scher, A.P. Alivisatos, *Nat. Mater.* 2 (2003) 382.
- [7] W.U. Huynh, J.J. Dittmer, A.P. Alivisatos, *Science* 295 (2002) 2425.
- [8] I. Gur, N.A. Fromer, M.L. Geier, A.P. Alivisatos, *Science* 310 (2005) 462.
- [9] D.L. Klein, P.L. McEuen, J.E.B. Katari, R. Roth, A.P. Alivisatos, *Appl. Phys. Lett.* 68 (1996) 2574.
- [10] A. Bezryadin, C. Dekker, G. Schmid, *Appl. Phys. Lett.* 71 (1997) 1273.
- [11] O. Millo, D. Katz, D. Steiner, E. Rothenberg, T. Mokari, M. Kizes, U. Banin, *Nano technol.* 15 (2004) R1.

[12] N. LeThomas, U. Woggon, O. Schops, M.V. Artemyev, M. Kazes, U. Banin, *Nano Lett.* 6 (2006) 557.

[13] C.B. Murray, D.J. Norris, M.G. Bawendi, *J. Am. Chem. Soc.* 115 (1993) 8706.

[14] O. Masala, R. Seshadri, *Ann. Rev. Mater. Res.* 34 (2004) 41.

[15] T. Sugimoto, *Adv. Colloid Interface Sci.* 28 (1987) 65.

[16] X. Peng, J. Wickham, A.P. Alivisatos, *J. Am. Chem. Soc.* 120 (1998) 5343.

[17] J.A. Marqusee, J. Ross, *J. Chem. Phys.* 80 (1984) 536.

[18] L. Manna, M. De Giorgi, D. Tari, L. Carbone, R. Krahne, M. Anni, R. Cingolani, S. Kudera, W.J. Parak, *Enrico Fermi School* (2004).

[19] I.V. Markov, *Crystal Growth for Beginners*, World Scientific, Singapore, 2003.

[20] S. Kumar, T. Nann, *Small* 2 (2006) 316.

[21] L. Manna, E.C. Scher, A.P. Alivisatos, *J. Am. Chem. Soc.* 122 (2000) 12700.

[22] Z.A. Peng, X. Peng, *J. Am. Chem. Soc.* 124 (2002) 3343.

[23] A. Puzder, A.J. Williamson, N. Zaitseva, G. Galli, L. Manna, A.P. Alivisatos, *Nano lett.* 4 (2004) 2361.

[24] L. Manna, L.W. Wang, R. Cingolani, A.P. Alivisatos, *J. Phys. Chem. B* 109 (2005) 6183.

[25] P. Reiss, J. Bleuse, A. Pron, *Nano lett.* 2 (2002) 781.

[26] Z.A. Peng, X. Peng, *J. Am. Chem. Soc.* 123 (2001) 183.

[27] J. Jasieniak, C. Bullen, J. van Embden, P. Mulvaney, *J. Phys. Chem. B* 109 (2005) 20665.

[28] X. Peng, *Chem. Eur. J.* 8 (2002) 334.

[29] A.P. Alivisatos, *J. Phys. Chem.* 100 (1996) 13226.

[30] D. Gerion, F. Pinaud, S.C. Williams, W.J. Parak, D. Zanchet, S. Weiss, A.P. Alivisatos, *J. Phys. Chem. B* 105 (2001) 8861.

[31] R.E. Bailey, A.M. Smith, S. Nie, *Physica E* 25 (2004) 1.

[32] X. Michalet, F.F. Pinaud, L.A. Bentolila, J.M. Tsay, S. Doose, J.J. Li, G. Sundaresan, A.M. Wu, S.S. Gambhir, S. Weiss, *Science* 307 (2005) 538.

[33] I.L. Medintz, H.T. Uyeda, E.R. Goldman, H. Mattoussi, *Nat. Mater.* 4 (2005) 435.

[34] C.R. Bullen, P. Mulvaney, *Nano Lett.* 4 (2004) 2303.

[35] T. Vossmeyer, L. Katsikas, M. Giersig, I.G. Popovic, K. Diesner, A. Chemseddine, A. Eychmüller, H. Weller, *J. Phys. Chem.* 98 (1994) 7665.

[36] W.W. Yu, X. Peng, *Angew. Chem. Int. Ed.* 41 (2002) 2368.

[37] M.A. Hines, P. Guyot-Sionnest, *J. Phys. Chem. B* 102 (1998) 3655.

[38] P.D. Cozzoli, L. Manna, M.L. Curri, S. Kudera, C. Giannini, M. Striccoli, A. Agostiano, *Chem. Mater.* 17 (2005) 1296.

[39] A.A. Guzelian, J.E.B. Katari, A.V. Kadavanich, U. Banin, K. Hamad, E. Juban, A.P. Alivisatos, *J. Phys. Chem.* 100 (1996) 7212.

[40] Z.A. Peng, X.G. Peng, *J. Am. Chem. Soc.* 123 (2001) 1389.

[41] Y.Y. Yu, S.S. Chang, C.L. Lee, C.R.C. Wang, *J. Phys. Chem. B* 101 (1997) 6661.

[42] K. Nishio, T. Isshiki, M. Kitano, M. Shiojiri, *Philos. Mag. A* 76 (1997) 889.

[43] J. Hu, Y. Bando, D. Golberg, *Small* 1 (2005) 95.

[44] W.W. Yu, Y.A. Wang, X. Peng, *Chem. Mater.* 15 (2003) 4300.

[45] A.G. Kanaras, C. Sonnichsen, H. Liu, A.P. Alivisatos, *Nano Lett.* 5 (2005) 2164.

[46] L. Carbone, S. Kudera, E. Carlini, W.J. Parak, C. Giannini, R. Cingolani, L. Manna, *J. Am. Chem. Soc.* 128 (2006) 748.

[47] H. Borchert, D.V. Talapin, N. Gaponik, C. McGinley, S. Adam, A. Lobo, T. Moller, H. Weller, *J. Phys. Chem. B* 107 (2003) 9662.

[48] H. Borchert, D.V. Talapin, C. McGinley, S. Adam, A. Lobo, A.R.B. de Castro, T. Moller, H. Weller, *J. Chem. Phys.* 119 (2003) 1800.

[49] C.Y. Yeh, Z.W. Lu, S. Froyen, A. Zunger, *Phys. Rev. B* 46 (1992) 10086.

[50] Y.B. Ying-Chun Zhu, D.-F. Xue, D. Golberg, *J. Am. Chem. Soc.* 125 (2003) 16196.

[51] H. Iwanaga, M. Fujii, S. Takeuchi, *J. Cryst. Growth* 183 (1998) 190.

[52] Y. Yan, M.M. Al-Jassim, M.F. Chisholm, L.A. Boatner, S.J. Pennycook, M. Oxley, *Phys. Rev. B* 71 (2005) 041309.

[53] R.C. Mucic, J.J. Storhoff, C.A. Mirkin, R.L. Letsinger, *J. Am. Chem. Soc.* 120 (1998) 12674.

[54] C.J. Loweth, W.B. Caldwell, X. Peng, A.P. Alivisatos, P.G. Schultz, *Angew. Chem.* 111 (1999) 1925.

[55] T. Pellegrino, L. Manna, S. Kudera, T. Liedl, D. Koktysh, A.L. Rogach, S. Keller, J. Rädler, G. Natile, W.J. Parak, *Nano lett.* 4 (2004) 703.

[56] D. Gerion, W.J. Parak, S.C. Williams, D. Zanchet, C.M. Michelet, A.P. Alivisatos, *J. Am. Chem. Soc.* 124 (2002) 7070.

[57] B.O. Dabbousi, J. Rodriguez-Viejo, F.V. Mikulec, J.R. Heine, H. Mattoussi, R. Ober, K.F. Jensen, M.G. Bawendi, *J. Phys. Chem. B* 101 (1997) 9463.

[58] T. Mokari, E. Rothenberg, I. Popov, R. Costi, U. Banin, *Science* 304 (2004) 1787.

[59] S. Kudera, L. Carbone, M.F. Casula, R. Cingolani, A. Falqui, E. Snoeck, W.J. Parak, L. Manna, *Nano lett.* 5 (2005) 445.

[60] H. Gu, R. Zheng, X. Zhang, B. Xu, *J. Am. Chem. Soc.* 126 (2004) 5664.

[61] T. Pellegrino, A. Fiore, E. Carlini, C. Giannini, P.D. Cozzoli, G. Ciccarella, M. Respaud, L. Palmirotta, R. Cingolani, L. Manna, *J. Am. Chem. Soc.* 128 (2006) 6690.



# **E Water-Solubility, Applications and Further Characterisation**

## **E.1 Hydrophobic nanocrystals coated with an amphiphilic polymer shell: a general route to water soluble nanocrystals**

T. PELLEGRINO, L. MANNA, S. KUDERA, T. LIEDL, D. KOKTYSH, A.L. ROGACH,  
S. KELLER, J. RÄDLER, G. NATILE, W.J. PARAK  
*Nano Letters* 4(4), pp. 703–707, 2004

A general strategy is described which allows for transferring hydrophobically capped nanocrystals from organic to aqueous solution by wrapping an amphiphilic polymer around the particles. In particular, high quality CoPt<sub>3</sub>, Au, CdSe/ZnS, and Fe<sub>2</sub>O<sub>3</sub> nanocrystals have been water-solubilized in this way. Analysis with transmission electron microscopy, gel electrophoresis, and fluorescence correlation spectroscopy demonstrates that monodispersity of the particles is conserved upon phase transfer to aqueous solution.

NANO  
LETTERS2004  
Vol. 4, No. 4  
703–707

# Hydrophobic Nanocrystals Coated with an Amphiphilic Polymer Shell: A General Route to Water Soluble Nanocrystals

Teresa Pellegrino,<sup>†,‡</sup> Liberato Manna,<sup>\*,†,§</sup> Stefan Kudera,<sup>†</sup> Tim Liedl,<sup>†</sup> Dmitry Koktysh,<sup>†</sup> Andrey L. Rogach,<sup>†</sup> Simon Keller,<sup>†</sup> Joachim Rädler,<sup>†</sup> Giovanni Natile,<sup>‡</sup> and Wolfgang J. Parak<sup>\*,†</sup>

Department of Physics & Center for Nanoscience, Ludwig-Maximilians Universität München, München, Germany, Department of Chemistry and Pharmacology, University of Bari, Bari, Italy, and National Nanotechnology Lab of INFM, Via Arnesano, Lecce, Italy

Received December 12, 2003; Revised Manuscript Received February 9, 2004

## ABSTRACT

A general strategy is described which allows for transferring hydrophobically capped nanocrystals from organic to aqueous solution by wrapping an amphiphilic polymer around the particles. In particular, high quality  $\text{CoPt}_3$ , Au, CdSe/ZnS, and  $\text{Fe}_2\text{O}_3$  nanocrystals have been water-solubilized in this way. Analysis with transmission electron microscopy, gel electrophoresis, and fluorescence correlation spectroscopy demonstrates that monodispersity of the particles is conserved upon phase transfer to aqueous solution.

**Introduction.** Colloidal inorganic nanocrystals are promising materials because of their unique size-dependent properties.<sup>1–3</sup> For many materials nanocrystals can be either synthesized in aqueous solution (e.g., Au,<sup>4</sup> CdTe and CdSe,<sup>5</sup>  $\text{Fe}_3\text{O}_4$ <sup>6</sup>) or in organic solvents (e.g., Au,<sup>7</sup> CdTe and CdSe,<sup>8</sup>  $\text{Fe}_3\text{O}_4$ <sup>9</sup>). However, for some materials such as Co<sup>10</sup> or for improved shape control,<sup>11</sup> highly crystalline and monodisperse nanocrystals so far need to be synthesized in organic solvents at high temperature. This involves their surface to be coated with surfactants that render them hydrophobic.<sup>12</sup> Several methods exist for converting hydrophobic nanocrystals into hydrophilic particles, which is a prerequisite for biological applications.<sup>13–16</sup> Most methods rely on the exchange of the surfactant coating with ligand molecules that on one end carry a functional group that is reactive toward the nanocrystal surface and on the other end a hydrophilic group (see, for example, refs 13, 17–19). Appropriate ligand molecules have to be individually chosen for each material. Therefore, other strategies have been developed which, instead of exchanging the original hydrophobic surfactant layer with a hydrophilic one, are based on the addition of a second ligand layer. The second layer consists of amphiphilic molecules

that can intercalate the first hydrophobic surfactant layer with their hydrophobic portion and that ensure water solubility of the nanocrystal with their hydrophilic groups. Interdigitated bilayers have been formed, for instance, by the addition of *n*-alcanoic acids<sup>20</sup> or cetyltrimethylammonium bromide.<sup>21</sup> Alternatively, cyclodextrin has been used for the formation of the second ligand layer, whereby the hydrophobic cavity of the cyclodextrin is penetrated by the hydrophobic tails of the first layer and its hydrophilic surface is pointing toward the solution.<sup>22,23</sup> In these examples, the second layer is solely stabilized around the first layer by hydrophobic interactions. For improved stability a method has been suggested recently to coat hydrophobic CdSe/ZnS nanocrystals with a cross-linked amphiphilic polymer,<sup>24</sup> in which the hydrophobic tails of the polymer intercalate with the surfactant molecules of the nanocrystal and form an additional coating. The water solubility of the polymer-coated nanocrystals is ensured by the hydrophilic groups located on the outer region of the polymer shell. Finally, the polymer shell is stabilized by cross-linking.

Based on this scheme we have developed a simple and general strategy for decorating hydrophobic nanocrystals of various materials ( $\text{CoPt}_3$ ,<sup>25</sup> Au,<sup>7</sup> CdSe/ZnS,<sup>26</sup> and  $\text{Fe}_2\text{O}_3$ <sup>27</sup>) with a hydrophilic polymer shell by exploiting the nonspecific hydrophobic interactions between the alkyl chains of poly(maleic anhydride alt-1-tetradecene) and the nanocrystal

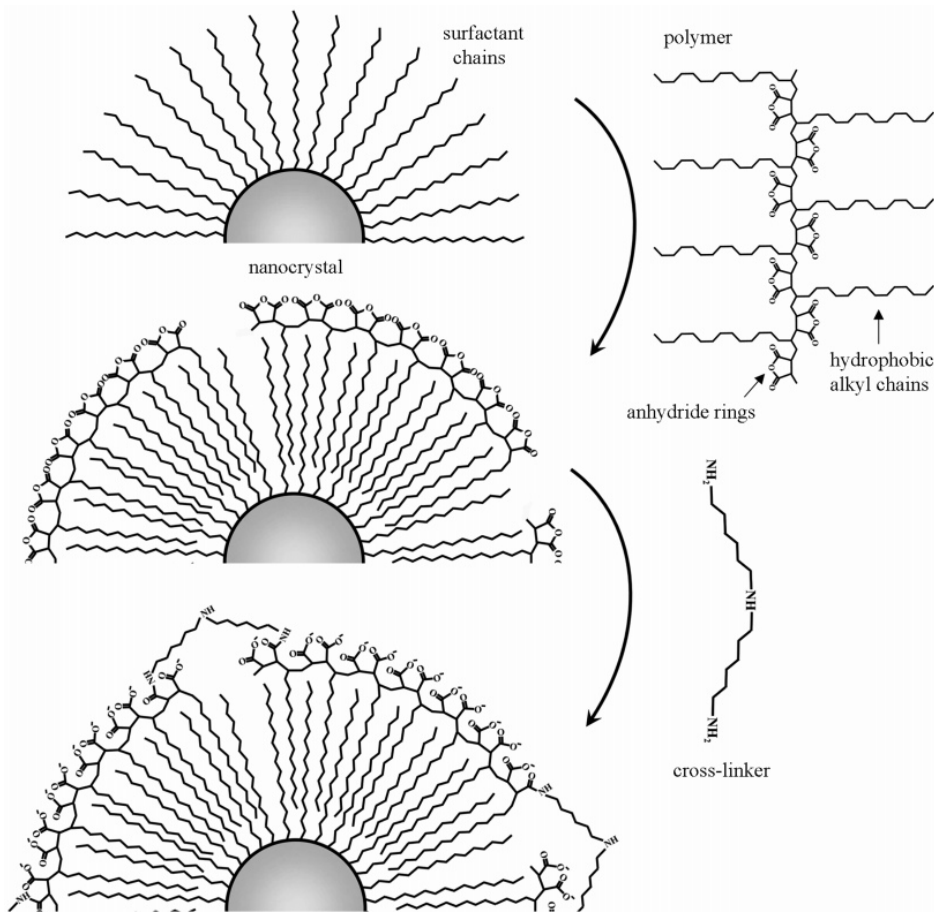
\* Corresponding authors. E-mail: liberato.manna@unile.it; wolfgang.parak@physik.uni-muenchen.de

<sup>†</sup> Ludwig-Maximilians Universität München, Germany.

<sup>‡</sup> University of Bari, Italy.

<sup>§</sup> National Nanotechnology Lab of INFM, Lecce, Italy.

**Scheme 1.** Polymer Coating of the Nanocrystals



Scheme of the polymer coating procedure. Several reports (e.g. ref 35) suggest that the surfactant chains for hydrophobically capped nanocrystals are pointing away from the nanocrystal surface, in a brush-like arrangement. The following plausible configuration is then assumed for the polymer coating process: The hydrophobic alkyl chains of the polymer intercalate with the surfactant coating. The anhydride rings are located on the surface of the polymer-coated nanocrystal. The amino end groups of the cross-linker molecule open the rings and link the individual polymer chains. The surface of the polymer shell becomes negatively charged, stabilizing the particles in water by electrostatic repulsion. A structural analysis aimed at determining the detailed conformation of the cross-linked polymer shell is in progress.

surfactant molecules. Addition of bis(6-aminohexyl)amine results in the cross-linking of the polymer chains around each nanoparticle (Scheme 1). The nanocrystals become soluble in water upon hydrolyzation of the unreacted anhydride groups (which effectively leads to an amphiphilic polymer shell) and can be further processed according to a universal protocol that relies solely on the chemistry of the outer polymer shell.

**Experimental Details.** Poly(maleic anhydride alt-1-tetradecene) was purchased from Aldrich and had a number average molecular weight ( $M_n$ )  $\sim 7300$ , corresponding to roughly 25 monomer units per polymer chain, and a monodispersity value ( $M_n/M_w$ ) equal to  $\sim 1.23$ , as declared by the vendor. Such polymer becomes amphiphilic upon hydrolyzation of the anhydride functional groups. A solution of poly(maleic anhydride alt-1-tetradecene) in chloroform and a solution of monodisperse nanocrystals in chloroform (100 polymer units per  $\text{nm}^2$  of nanocrystal surface) were

mixed and stirred for 2 h at room temperature. After evaporation of the solvent, bis(6-aminohexyl)amine in chloroform was then added to cross-link the polymer shell that had formed around each nanocrystal. The ratio of added cross-linker molecules to polymer units was 1:10. The solution was sonicated for 20 min, the solvent was evaporated again, and the solid was dissolved in a diluted TBE buffer solution (pH 8–9). After sonication for five minutes, the nanocrystals dissolved completely and the solution was filtered to remove the excess unbound polymer. The buffer was exchanged with water by two rounds of dilution and reconcentration through a centrifuge filter. Any residual unbound polymer was removed by two consecutive purification steps on a size-exclusion column. After purification the nanocrystals solutions were optically clear. The particles were characterized by transmission electron microscopy (TEM), gel electrophoresis, and fluorescence correlation spectroscopy (FCS). The solutions were stable for months (i.e., no

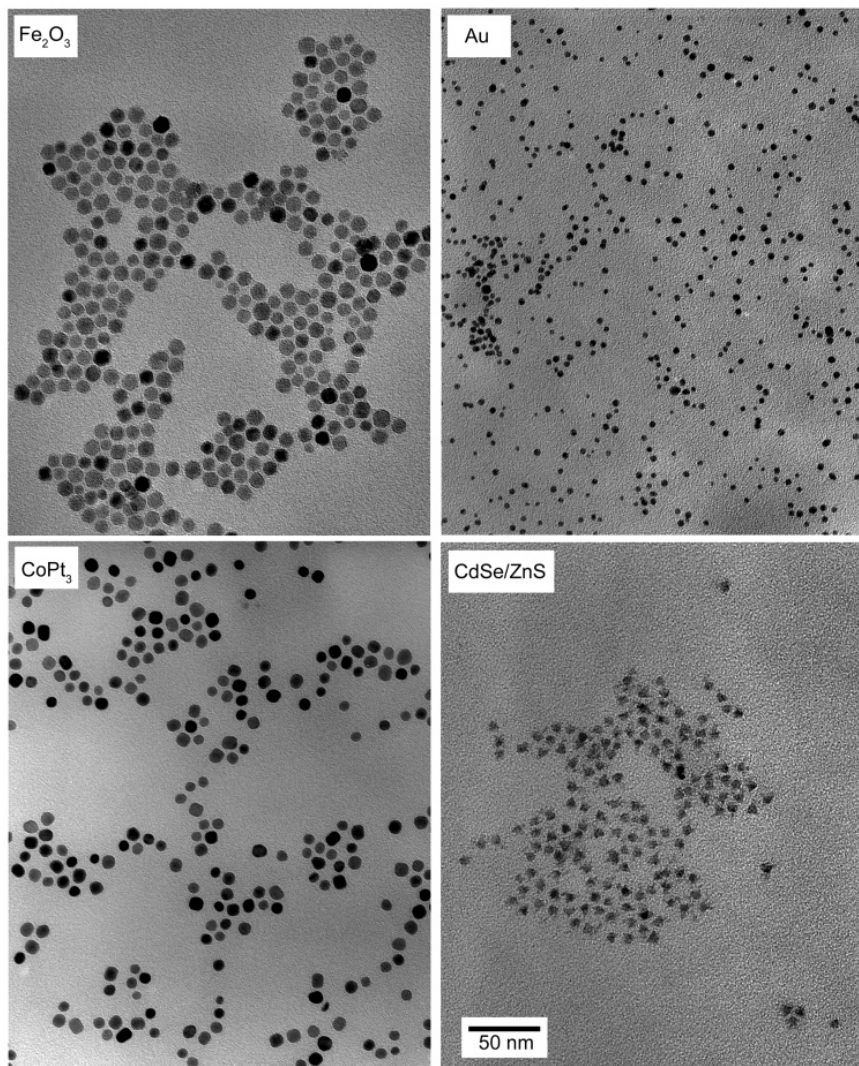


**Figure 1.** TEM images of polymer-coated nanocrystals of four different core materials:  $\text{Fe}_2\text{O}_3$  (9.2 nm average diameter), Au (4.0 nm),  $\text{CoPt}_3$  (8.0 nm), and  $\text{CdSe/ZnS}$  (7.0 nm) nanocrystals.

precipitation occurred and the bands during gel electrophoresis kept their narrow shape).

**Results and Discussions.** In water the nanocrystals retained their major physical properties (such as the fluorescence of  $\text{CdSe/ZnS}$  and the magnetic moment of  $\text{CoPt}_3$ ). TEM analysis (Figure 1) showed no large aggregates of particles, besides the formation of monolayers. Such patterns are due to particle–particle interactions (van der Waals, magnetic) and are also observed on grids prepared from solutions of hydrophobic nanocrystals. However, the presence of small aggregates, such as dimers and trimers, cannot be distinguished from such monolayers and so it cannot be excluded.

The polymer-coated nanocrystals were investigated with agarose gel electrophoresis<sup>28</sup> (Figure 2). The bands on the gels are remarkably narrow, and since the particle mobility on gels depends on both charge and size, we estimated that our polymer-coated particles have a rather homogeneous

distribution of sizes and charges. The mobility of the polymer-coated nanocrystals is comparable to that of phosphine stabilized Au particles,<sup>28</sup> indicating that there is no cross-linking between several particles. Any aggregates should in fact migrate much slower through the gel. We can estimate the sensitivity in assessing particle diameters by gel electrophoresis by devising a calibration curve of the particle mobility versus particle diameter, as reported in a previous study.<sup>29</sup> The study showed that the mobility of particles with diameters between 3 and 20 nm scaled roughly linearly with the particle diameter. In the present study, the band of 4.0 nm diameter polymer-coated gold nanoparticles (Figure 2) has a spread of  $\pm 0.03$  if the mobility of the middle of the band is normalized to 1, allowing us to distinguish between particles with mobility of 1.0 and 0.97 (or 1.0 and 1.03), respectively. From the calibration curve,<sup>29</sup> a decrease in

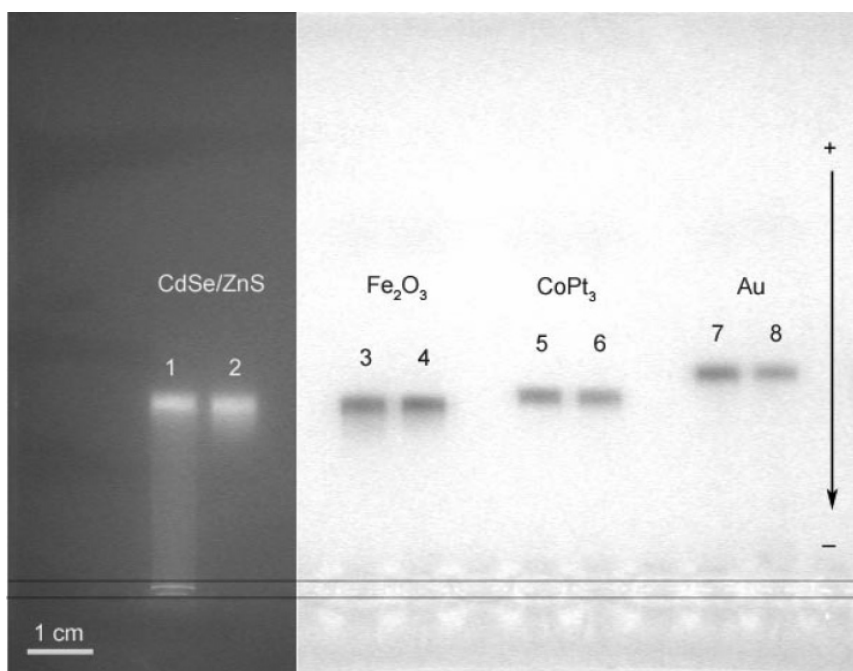


**Figure 2.** Gel electrophoresis of polymer-coated nanocrystals corresponding to the samples of Figure 1. The bands were observed either by their fluorescence (CdSe/ZnS) or by their absorption color. For each sample the left lane (lanes 1, 3, 5, 7) corresponds to particles as obtained after the last column purification step. The right lanes (lanes 2, 4, 6, 8) correspond to an additional purification step where the fastest migrating band of nanocrystals in a first gel run has been extracted.

mobility of 0.03 corresponds to an increase in effective particle diameter of only 1.2 nm, which cannot be due to an aggregation effect between particles having an average diameter of 4.0 nm. Any significant interparticle agglomeration, if present, would clearly cause a much larger band spread. We conclude then that no significant agglomerates are present. Only in the case of CdSe/ZnS nanocrystals could a small amount of aggregates be seen, since the gel electrophoresis bands showed slow migrating tails (Figure 2, lane 1). However, after extracting the fastest migrating band and rerunning it with gel electrophoresis, these aggregates were removed (Figure 2, lane 2). In the case of Fe<sub>2</sub>O<sub>3</sub>, CoPt<sub>3</sub>, and Au, no remarkable band tails were present already after the first run. It is worth noting that in this second run no stripping of the polymer shell from the particles was observed in any sample, since no tail of particles with reduced mobility was found. This is an indication that the polymer layer that formed around the nanocrystals is significantly stable.

To get an estimate of the effective particle diameter in solution we used fluorescence correlation spectroscopy (FCS)<sup>30,31</sup> (see Supporting Information). For green and red fluorescent hydrophobic CdSe/ZnS particles dissolved in chloroform, we obtained hydrodynamic diameters of  $5.7 \pm 0.5$  nm and  $11.6 \pm 2.8$  nm, respectively. After the polymer coating procedure, hydrodynamic diameters of  $19.2 \pm 2.0$  nm and  $23.6 \pm 2.0$  nm, respectively, were measured for the particles dissolved in water. Clearly an increase in size due to the formation of the polymer shell could be observed, but this is larger than expected if one considers only the

contribution from the polymer layer. The significant increase in the hydrodynamic diameter as determined from FCS measurements could partly result from the change in particle–solvent interaction, although the formation of small aggregates as dimers or trimers cannot be excluded.

Considering the TEM, gel electrophoresis, and FCS results, it seems that no significant interparticle cross-linking occurs during the synthesis. The minimization of interparticle aggregation during the polymer coating procedure has been achieved by working with enough diluted solutions (see Supporting Information).

**Conclusions.** The described procedure for transferring hydrophobic nanocrystals into aqueous solution should be extendable to any nanocrystal system in which hydrophobic tails are exposed to the external environment. For example, it has also been successfully applied to as complex objects as CdTe tetrapods<sup>32</sup> (data not shown). This method therefore is quite general and could be extended to systems for which phase transfer to aqueous solution has not been possible so far with other methods. In principle, the polymer shell could be further improved regarding its functional groups and its stability. Incorporation of poly(ethylene glycol) groups, for example, should improve the stability in electrolytic solution (such as making the solubility of nanocrystals less dependent on electrostatic repulsion) and should also minimize non-specific interactions.

One promising application of the polymer-coated nanocrystals could be the construction of DNA-mediated hybrid materials,<sup>33</sup> such as for instance the formation of dimers between fluorescent CdSe/ZnS and magnetic CoPt<sub>3</sub> nano-

crystals. One requisite for this goal is to precisely control the number of biological molecules (as oligonucleotides) that are attached per particle.<sup>28,34</sup>

The strategy described here yields particles with different intrinsic properties (such as fluorescence or magnetism) but identical surface chemistry and with good homogeneity in charge and size. These nanocrystals then should be promising candidates for the controlled fabrication of more sophisticated nanoscale structures.

**Acknowledgment.** The authors are grateful to Dr. Elena Shevchenko, Dr. David Gittins, and Eric Dulkeith for help with the cobalt–platinum and the gold syntheses, to Monika Rusp for the assistance in TEM measurements, and to Prof. Dr. Hermann Gaub, Dr. Markus Seitz, Prof. Dr. Jochen Feldmann, and Prof. Dr. Roberto Cingolani for helpful suggestions. This work was funded by the Emmy Noether program of the German research foundation DFG (W.J.P.), the Fonds der Deutschen Chemischen Industrie (W.J.P.), and was also supported by the Center for Nanoscience in Munich and by the Italian INFM-NNL and FIRB funds. T.P. is grateful to Marie Curie training program of the European Union, and D.K. is grateful to the Alexander von Humboldt Foundation. Travel costs between Germany and Italy were in part supported by the Vigoni foundation/Deutscher Akademischer Austauschdienst (DAAD).

**Supporting Information Available:** Description of the various nanocrystal syntheses and polymer coating procedures, gel electrophoresis, and fluorescence correlation spectroscopy setups. This material is available free of charge via the Internet at <http://pubs.acs.org>.

## References

- Alivisatos, A. P.; Barbara, P. F.; Castleman, A. W.; Chang, J.; Dixon, D. A.; Klein, M. L.; McLendon, G. L.; Miller, J. S.; Ratner, M. A.; Rossky, P. J.; Stupp, S. I.; Thompson, M. E. *Adv. Mater.* **1998**, *10*, 1297–1336.
- Efros, A. L.; Rosen, M. *Annu. Rev. Mater. Sci.* **2000**, *30*, 475–521.
- Moriarty, P. *Rep. Prog. Phys.* **2001**, *64*, 297–381.
- Schmid, G.; Lehnert, A. *Angew. Chem., Int. Ed. Engl.* **1989**, *28*, 780–781.
- Rogach, A. L.; Talapin, D. V.; Weller, H. Semiconductor Nanoparticles. In *Colloids and Colloid Assemblies*; Caruso, F., Ed.; Wiley-VCH: Weinheim, 2004; pp 52–95.
- Berger, P.; Adelman, N. B.; Beckman, K. J.; Campbell, D. J.; Ellis, A. B.; Lisensky, G. C. *J. Chem. Educ.* **1999**, *76*, 943–948.
- Fink, J.; Kiely, C. J.; Bethell, D.; Schiffrian, D. *J. Chem. Mater.* **1998**, *10*, 922–926.
- Peng, Z. A.; Peng, X. *J. Am. Chem. Soc.* **2001**, *123*, 183–184.
- Sun, S.; Zeng, H. *J. Am. Chem. Soc.* **2002**, *124*, 8204–8205.
- Puntes, V. F.; Krishnan, K. M.; Alivisatos, A. P. *Science* **2001**, *291*, 2115–2117.
- Manna, L.; Scher, E. C.; Alivisatos, A. P. *J. Am. Chem. Soc.* **2000**, *122*, 12700–12706.
- Trindade, T.; O'Brien, P.; Pickett, N. L. *Chem. Mater.* **2001**, *13*, 3843–3858.
- Chan, W. C. W.; Nie, S. *Science* **1998**, *281*, 2016–2018.
- Templeton, A. C.; Wuelfing, W. P.; Murray, R. W. *Acc. Chem. Res.* **2000**, *33*, 27–36.
- Parak, W. J.; Gerion, D.; Zanchet, D.; Woerz, A. S.; Pellegrino, T.; Micheel, C.; Williams, S. C.; Seitz, M.; Bruehl, R. E.; Bryant, Z.; Bustamante, C.; Bertozi, C. R.; Alivisatos, A. P. *Chem. Mater.* **2002**, *14*, 2113–2119.
- Potapova, I.; Mruk, R.; Prehl, S.; Zentel, R.; Basché, T.; Mews, A. *J. Am. Chem. Soc.* **2003**, *125*, 320–321.
- Gittins, D. I.; Caruso, F. *Angew. Chem., Int. Ed.* **2001**, *40*, 3001–3004.
- Gerion, D.; Pinaud, F.; Williams, S. C.; Parak, W. J.; Zanchet, D.; Weiss, S.; Alivisatos, A. P. *J. Phys. Chem. B* **2001**, *105*, 8861–8871.
- Kim, S.; Bawendi, M. G. *J. Am. Chem. Soc.* **2003**, *125*, 14652–14653.
- Shen, L.; Laibinis, P. E.; Hatton, T. A. *Langmuir* **1999**, *15*, 447–453.
- Swami, A.; Kumar, A.; Sastry, M. *Langmuir* **2003**, *19*, 1168–1172.
- Lala, N.; Lalbegi, S. P.; Adyanthaya, S. D.; Sastry, M. *Langmuir* **2001**, *17*, 3766–3768.
- Wang, Y.; Wong, J. F.; Teng, X.; Lin, X. Z.; Yang, H. *Nano Lett.* **2003**, *3*, 1555–1559.
- Wu, M. X.; Liu, H.; Liu, J.; Haley, K. N.; Treadway, J. A.; Larson, J. P.; Ge, N.; Peale, F.; Bruchez, M. P. *Nature Biotechnol.* **2003**, *21*, 41–46.
- Shevchenko, E. V.; Talapin, D. V.; Rogach, A. L.; Kornowski, A.; Haase, M.; Weller, H. *J. Am. Chem. Soc.* **2002**, *124*, 11480–11485.
- Dabbousi, B. O.; Rodriguez-Viejo, J.; Mikulec, F. V.; Heine, J. R.; Mattoussi, H.; Ober, R.; Jensen, K. F.; Bawendi, M. G. *J. Phys. Chem. B* **1997**, *101*, 9463–9475.
- Hyeon, T.; Lee, S. S.; Park, J.; Chung, Y.; Na, H. B. *J. Am. Chem. Soc.* **2001**, *123*, 12798–12801.
- Zanchet, D.; Micheel, C. M.; Parak, W. J.; Gerion, D.; Williams, S. C.; Alivisatos, A. P. *J. Phys. Chem. B* **2002**, *106*, 11758–11763.
- Parak, W. J.; Pellegrino, T.; Micheel, C. M.; Gerion, D.; Williams, S. C.; Alivisatos, A. P. *Nano Lett.* **2003**, *3*, 33–36.
- Schwille, P.; Bieschke, J.; Oehlenschläger, F. *Biophys. Chem.* **1997**, *66*, 211–228.
- Krichevsky, O.; Bonnet, G. *Rep. Prog. Phys.* **2002**, *65*, 251–297.
- Manna, L.; Milliron, D. J.; Meisel, A.; Scher, E. C.; Alivisatos, A. P. *Nature Materials* **2003**, *2*, 382–385.
- Mitchell, G. P.; Mirkin, C. A.; Letsinger, R. L. *J. Am. Chem. Soc.* **1999**, *121*, 8122–8123.
- Zanchet, D.; Micheel, C. M.; Parak, W. J.; Gerion, D.; Alivisatos, A. P. *Nano Lett.* **2001**, *1*, 32–35.
- Manna, L.; Scher, E. C.; Alivisatos, A. P. *J. Cluster Sci.* **2002**, *13*, 521–532.

NL035172J

**Hydrophobic nanocrystals coated with an amphiphilic polymer shell: a general route to water soluble nanocrystals**

Teresa Pellegrino<sup>1,2</sup>, Liberato Manna<sup>1,3,\*</sup>, Stefan Kudera<sup>1</sup>, Tim Liedl<sup>1</sup>,  
Dmitry Koktysh<sup>1</sup>, Andrey L. Rogach<sup>1</sup>, Simon Keller<sup>1</sup>, Joachim  
Rädler<sup>1</sup>, Giovanni Natile<sup>2</sup> and Wolfgang J. Parak<sup>1,\*</sup>

<sup>1</sup> *Department of Physics & Center for Nanoscience, Ludwig-Maximilians Universität München, München, Germany*

<sup>2</sup> *Department of Chemistry and Pharmacology, University of Bari, Bari, Italy*

<sup>3</sup> *National Nanotechnology Lab of INFM, Via Arnesano, Lecce, Italy*

**Supporting information**

**Materials and Methods**

All chemicals were purchased from the various vendors, they were degassed (when not shipped under inert gas by the vendor), stored in the glove box and used without any further purification. All solvents used for the synthesis and the purification of nanocrystals (except for gold) and prior to polymer coating were anhydrous. All syntheses and purifications of nanocrystals (except for gold) and prior to polymer coating were carried out under argon.

### Nanocrystal syntheses

Colloidal nanocrystals of different materials were synthesized according to standard procedures described in the literature (CoPt<sub>3</sub><sup>1</sup>, Au<sup>2</sup>, CdSe/ZnS<sup>3</sup>, and Fe<sub>2</sub>O<sub>3</sub><sup>4</sup>) with few changes.

#### Synthesis of colloidal CdSe/ZnS nanocrystals

CdSe nanocrystals of different sizes were synthesized according to the procedure described by Reiss and coworkers<sup>5</sup>, with minor changes. In a typical synthesis, 5.75 g of hexadecylamine (HDA, technical grade, Sigma-Aldrich #H7.40-8), 2.26 g of trioctylphosphine oxide (TOPO, 99%, Sigma-Aldrich #22.330-1), 2.20 g of dodecylphosphonic acid (DDPA 98%, Polycarbon Inc.) and 501 mg of CdO (99.99+%, Sigma-Aldrich #20.289-4) were mixed in a 50 ml 3-necked flask connected to an argon-vacuum line assembled in an argon glove-box. The mixture was degassed at 120 °C for 20 minutes and then heated to 300-320 °C until it turned clear and colorless. 1 ml of tributylphosphine (TBP, 99%, Strem #15-5800) was then injected in the flask and the temperature was lowered to 270 °C. In a vial, 320 mg of Se powder (99.99%, Sigma-Aldrich #22.986-5) were dissolved in 1.28 g of TBP under vigorous stirring and the resulting solution was injected in the flask. After injection, the temperature dropped by roughly 20 °C but was allowed to recover to 270 °C and was then maintained at this level throughout the synthesis. 3-5 minutes after the injection the color of the solution turned from colorless to yellow-orange, indicating the nucleation of CdSe nanocrystals. This color gradually turned to red, dark red and finally to brown 25-30 minutes after the injection (first exciton absorption peak at 620-630 nm). The reaction was monitored by taking aliquots during the growth, by diluting them in chloroform and by recording their UV-visible absorption spectra. The growth rate slightly varied from synthesis to synthesis, but it was always sufficiently low so that the synthesis could be stopped whenever the first exciton peak in the absorption spectrum reached a desired value, which could be easily correlated to the nanocrystal average size through calibration curves available from the literature<sup>6</sup>. The synthesis was stopped by removing the heating mantle and by rapidly cooling the flask. When nanocrystals with remarkably small average diameter were required (2 nm or less), the synthesis could be stopped few minutes after the injection, by quickly injecting 3-4 ml of toluene. However, the size distribution of these samples was always quite broad, and a size selective precipitation was required. The smallest, size-selected nanocrystal samples synthesized by this method had their first exciton absorption peak at around 480 nm.

After stopping the reaction, the flask was cooled to 100 °C and 20 ml of nonanoic acid (97%, Sigma-Aldrich #N5502) were added. The solution was stirred for additional 10-15 minutes at this temperature and then cooled to room temperature. The addition of an alkyl acid (carboxylic or phosphonic) avoided the formation of a gel when the original growth solution was cooled below 50 °C. This gel did not dissolve in any of the tested solvents (chloroform, toluene, methanol, hexane, tetrahydrofuran) at room temperature and practically made the nanocrystal-surfactant mixture intractable. Addition of 5-10 ml of methanol to the mixture of nonanoic acid and growth solution caused the flocculation of nanocrystals, which could be separated by centrifugation. The precipitate was then dissolved in 10 ml of toluene and the mixture was centrifuged for 30 minutes at 3000 rpm in a 20 ml vial to remove any residual gel present, which was collected at the bottom of the vial. The precipitate was discarded, and the supernatant was mixed with methanol to precipitate the nanocrystals. This precipitate was then redissolved in toluene, methanol was again added to it and the solution was centrifuged again. This step was repeated once more, after which the precipitate was dried under vacuum and stored as a powder in the dry box. This synthesis

usually yielded between 200 and 400 mg of nanocrystals in total, depending of the average nanocrystal size.

For the ZnS shell growth, 12 g of TOPO (technical grade, Alfa Aesar #14114) were weighted in a 50 ml 3-necked flask, pumped to vacuum at 120 °C for 20 minutes. One ml of Trioctylphosphine (technical grade, Sigma-Aldrich #11.785-4) was injected into the flask. 60 mg of a dry nanocrystal powder were dissolved in 3 ml of chloroform and the resulting solution was injected into the flask. The chloroform was removed by evacuating the flask for few minutes. The temperature of the mixture was then raised to 160 °C. The stock solution for the ZnS growth was freshly prepared by dissolving 0.647 g of a solution of diethylzinc ( $C_4H_{10}Zn$ , 1.0 M solution in heptane, Sigma-Aldrich #40.602-3) and 0.19 g of hexamethyldisilathiane ( $C_6H_{18}Si_2S$ ) (Aldrich #28.313-4) in 4.73 g of TBP. Several drop-wise injections of this solution were done (1 ml each) at 160 °C. The waiting time between injections was of the order of 5-10 minutes, during which it was assumed that the precursors injected had completely reacted. The injections were done drop-wise, to allow a slow and uniform shell growth and to prevent the nucleation of ZnS crystals. After each injection, a small aliquot (10-20  $\mu$ l) of solution was extracted via a syringe, dissolved in 2 ml of chloroform and its optical absorption and emission spectra were recorded. The optical densities of these aliquots were adjusted to 0.2 at the excitation wavelength, usually chosen in the 450-500 nm range. After the first few injections, the luminescence from the nanocrystals increased, indicating the growth of a ZnS shell. The luminescence then reached a maximum intensity, which was dependent on the particular nanocrystal size, and then it decreased upon additional injections. This decrease indicated that the shell grew over its optimal thickness and that it started developing defects. The optimal number of injections which maximized the final fluorescence quantum yield varied by synthesis, and ranged from 3-4 for the largest nanocrystal sizes to 6-7 for the smallest nanocrystals. After the injections were completed, the solution was cooled to 60 °C and 3 ml of butanol were added in order to avoid solidification and to quench the residual unreacted chemicals. The solution was then transferred into a vial and stored for the polymer coating experiments.

### **Synthesis of colloidal Au nanocrystals**

Colloidal Au nanocrystals were synthesized according to standard protocols<sup>2,7-9</sup>. All glassware was carefully cleaned in a KOH/isopropanol bath and carefully rinsed with water before use. All reactions were carried out at room temperature under ambient conditions. Briefly, 2.17 g of tetraoctylammonium bromide (TOABr, 98%, Sigma-Aldrich #29.413-6) were dissolved in 80 ml of HPLC grade toluene and 300 mg hydrogen tetrachloroaurate (III) (99.9%, Alfa Aesar #12325) were dissolved in 25 ml Millipore water to yield a yellow translucent solution. The two solutions were mixed in a 100 ml separation funnel and the funnel was shaken for about 5 minutes. During this time the initially colorless toluene phase (on the top) turned red and the initially yellow aqueous phase (on the bottom) turned colorless, indicating the formation of tetraoctylammonium-gold ion pairs. The aqueous phase was discarded and the toluene phase was transferred to a 100 ml round flask. In a beaker, 334 mg of sodium borohydride (98%, Sigma-Aldrich #45.288-2) were dissolved in 25 ml of Millipore water under vigorous stirring by means of a glass rod. This clear solution was then pipetted dropwise within one minute into the red solution of tetraoctylammonium-gold in toluene. Upon stirring for few seconds, the initial two phases started to mix and the color changed from red to red-violet. This color change indicates the nucleation of gold clusters mediated by sodium borohydride. The residual sodium borohydride in solution

reduces the remaining gold ions, providing additional monomers for the growth of the nuclei. The solution was stirred for 1 hour, then it was transferred to a clean separation funnel and 25 ml of 0.01 M HCl were added in order to remove the excess sodium borohydride. The funnel was shaken for 1 minute and the aqueous phase (on the bottom) was discarded. 25 ml of 0.01 M NaOH were added to the funnel to remove the excess acid and after shaking for 1 minute the aqueous phase was again discarded. Finally, 25 ml of Millipore water were added to remove excess ions, the funnel was shaken for 1 minute and the aqueous phase was discarded. This last washing step was repeated 4 more times. The final solution was then transferred to a 100 ml round flask and stirred for 1 day to allow the particles to Ostwald ripen to a thermodynamically stable average size and size distribution.

After the synthesis, a surfactant exchange procedure was carried out. Ten ml of 1-dodecanethiol (98%, Sigma-Aldrich #47,136-4) were added to the Au nanocrystals dissolved in toluene. The solution was heated to 65 °C and stirred for 2 hours. During this process the mercapto groups of the dodecanethiol molecules displace the Br<sup>-</sup> ions and yield dodecanethiol coated Au nanocrystals. The solution was then cooled to room temperature and the Au nanocrystals were precipitated by the addition of about 30 ml of methanol (methanol was added until the solution turned cloudy), followed by centrifugation. After discarding the supernatant, the precipitate was dissolved in 10 ml of toluene upon vigorous shaking, and the nanocrystals were precipitated again by the addition of about 4 ml of cold (-20°C) methanol (methanol was added until the solution turned cloudy) followed by centrifugation. The supernatant was discarded and the precipitate was redissolved in 2 ml of toluene. In order to improve the size distribution of the sample, a size selective precipitation was carried out. Addition of 20 µl of cold (-20°C) methanol, followed by centrifugation, caused the precipitation of only the largest nanocrystals from the solution. They were discarded and the supernatant was used as final solution. The average diameter of the Au nanocrystals was estimated by TEM (hence not considering the surfactant shell) and the particle concentration was determined by measuring the optical absorption of the nanocrystal solution. For Au nanocrystals with a core diameter of 4.0 nm we assumed an optical extinction coefficient of 8.7•10<sup>6</sup> M<sup>-1</sup> cm<sup>-1</sup> at their plasmon peak around 518 nm. The concentration of the resulting Au nanocrystal solution was typically in the µM range.

### Synthesis of colloidal CoPt<sub>3</sub> nanocrystals

CoPt<sub>3</sub> nanocrystals were synthesized according to the procedure described by Shevchenko and coworkers <sup>1</sup>. 0.033 g of Platinum (II) acetylacetone (98%, Strem #78-1400), 0.25 g of 1-adamantanecarboxylic acid (99+, Sigma-Aldrich #01823) and 0.13 g of 1,2-hexadecanediol (technical grade, Sigma-Aldrich #21.374-8) were dissolved in a mixture of hexadecylamine (4.0 g, technical grade, Sigma-Aldrich #H7.40-8) and diphenyl ether (2.0 ml, 99+, Sigma-Aldrich #24.083-4) and heated to 65 °C in a 50 ml three-necked flask. At this temperature the surfactants melted and the resulting clear, yellowish solution was degassed for several minutes. The stock solution for the cobalt precursor was prepared by mixing 0.015 g of Co<sub>2</sub>(CO)<sub>8</sub> (Strem #27-0400) with 0.7 ml of 1,2-dichlorobenzene (99%, Sigma-Aldrich #24.066-4) in a small vial. The reaction mixture was heated to 200 °C, and the stock solution for the cobalt precursor was injected into the flask through a syringe, under vigorous stirring. The solution was kept at 200 °C for 30 min, then at 290 °C for 30 min, and it was finally cooled to room temperature. Under these conditions relatively monodisperse CoPt<sub>3</sub> nanocrystals with an average diameter of 8.0 nm are formed. If

smaller particles are desired, a larger amount of  $\text{Co}_2(\text{CO})_8$  should be dissolved in the precursor stock solution and the injection should be performed at a lower temperature<sup>10</sup>.

#### **Synthesis of colloidal $\text{Fe}_2\text{O}_3$ nanocrystals**

$\gamma\text{-Fe}_2\text{O}_3$  nanocrystals were prepared according to the method described by Hyeon and coworkers<sup>4</sup>. Briefly, 10 ml of octyl ether (99%, Sigma-Aldrich #24.959-9) and 1.28 g of oleic acid (99+%, Sigma-Aldrich #75.090) were degassed in a 50 ml flask at 60 °C for 20 minutes. 0.29 ml of  $\text{Fe}(\text{CO})_5$  (99.999%, Sigma-Aldrich #48.171-8) were then added at 100 °C and the solution was heated up to refluxing temperature (~295-300 °C) for 1 hour. In case of insufficient cooling of the refluxing funnel oleic acid evaporated and the solution turned cloudy, which could be reverted by adding a small amount of oleic acid. This was especially problematic if the amount of iron precursor was too low. During the temperature rise the initial yellow-orange solution turned to pale yellow and sometimes to almost colorless. This color change was somehow different from what reported by Hyeon and coworkers and it initially induced us to believe that the synthesis was heading to failure. However, the solution almost suddenly turned to black during the refluxing, which was allowed to continue for the planned time (1 hour). The flask was then cooled down to room temperature, 0.34 g of  $(\text{CH}_3)_3\text{NO}$  (98%, Sigma-Aldrich #31.759-4) were added and the mixture was heated at 130 °C for two hours, during which time it turned to dark brown. The flask was heated again to refluxing temperature for 1 hour, after which the solution was cooled to room temperature. Methanol was added to precipitate the nanocrystals, which were recovered upon centrifugation and redissolution in toluene. This synthesis usually yielded nanocrystals with a residual distribution of sizes. The largest nanocrystals, scarcely soluble in toluene, were removed simply by centrifugation of the toluene solution at 3000 rpm for 30 minutes. The smallest nanocrystals were removed by size selective precipitation, by discarding the supernatant and by redissolving the precipitate in toluene. This size selective precipitation was quite easy since small nanocrystals hardly precipitated even upon the addition of several ml of methanol. The final, size-selected nanocrystals were redissolved in toluene and re-precipitated with methanol two additional times. This procedure helped to remove the excess surfactant and the residual  $(\text{CH}_3)_3\text{NO}$ . Removal of  $(\text{CH}_3)_3\text{NO}$  had to be carried out carefully, since the addition of large amounts of methanol to precipitate the nanocrystals from the toluene solution also caused the precipitation of the amine N-oxide.

### General description of the polymer coating procedure

Before undergoing the polymer coating procedure, the nanocrystals were cleaned by removing the excess unbound surfactant. This was done by precipitating the nanocrystals with the addition of an appropriate solvent, discarding the supernatant and redissolving the precipitate in chloroform. This precipitation/redissolution step was done twice for Au and three times for CoPt<sub>3</sub> and Fe<sub>2</sub>O<sub>3</sub>. For CdSe/ZnS and Au an additional round of precipitation/redissolution usually resulted in a significant loss of solubility of the nanocrystals in chloroform.

For each sample, the average diameter of the inorganic nanocrystal cores was determined by TEM analysis. The overall surface area of each nanocrystal was calculated by considering the effective nanocrystal diameter ( $d_{\text{eff}} \text{ (nm)} = d + 2$ ) as the sum of the diameter of its inorganic core ( $d$ ) plus the surfactant shell, which was assumed to be 1 nm in thickness. The concentration of the starting nanocrystal solution was determined either by gravimetric methods or by absorption measurements when extinction coefficients were available from the literature. In order to avoid cross-linking effects among nanocrystals, the concentration of the initial nanocrystal solution was always adjusted to 0.5 - 2  $\mu\text{M}$  by dilution with chloroform.

A solution of Poly(maleic anhydride alt-1-tetradecene) (Sigma-Aldrich #45.251-3) in chloroform (400mg/10ml, 0.136 M), henceforth referred to as “polymer solution”, a solution of Bis(6-aminohexyl)amine (Fluka #14506) in chloroform (43 mg/10 ml, 0.02 M), henceforth referred to as “cross-linker solution”, and a 0.5 x Tris-Borate-EDTA (TBE, Sigma-Aldrich #T-3913) buffer solution, henceforth referred to as “buffer solution”, were prepared and stored as stock solutions for all the polymer coating experiments. In poly(maleic anhydride alt-1-tetradecene) each polymer chain had an average length of 30 polymer units

The polymer solution was added to the nanocrystal solution. After stirring the resulting solution for 2 hours at room temperature, the chloroform solvent was slowly evaporated under reduced pressure by using a rotavapor system (Laborota 400, Heidolph). The cross-linker solution was then added to crosslink the polymer shell that had formed around each nanocrystal. The solution was then sonicated for 20 minutes, after which the solvent was slowly evaporated. The resulting powder was dissolved in the buffer solution to yield again a nanocrystal concentration in the range between 0.5 and 2  $\mu\text{M}$ . After sonication for five minutes, the polymer-coated nanocrystals dissolved completely in the buffer solution. A filtration through a syringe membrane filter (Roth #P818.1, 0.22  $\mu\text{m}$  pore size) helped to remove most of the excess of unbound polymer. The buffer was then exchanged with water by 2 rounds of dilution with water and re-concentration through a 100000 MWCO Centricon centrifuge filter (Millipore #4424). Periodically, the centrifugation was paused and the sample was mixed to accelerate the passage of water through the filter. Finally, the remaining unbound polymer was removed by 2 consecutive purifications steps on a size exclusion column (sephadex superfine G200, Sigma-Aldrich #84.961). Optionally, particles could be further purified by gel electrophoresis <sup>11</sup>.

Several polymer coating experiments have been performed. In these experiments the parameters that were varied are the number of polymer units per  $\text{nm}^2$  of nanoparticle surface and the ratio of polymer chains per cross-linker molecules (table 1). All experiments led to a successful transfer of the nanocrystals in water. We then decided to adopt a general protocol for the coating the nanocrystals, regardless of nanocrystal material. In this protocol the volumes of polymer and cross-linker solutions mixed with the nanocrystal solution are such that 100 polymer units are

added per nm<sup>2</sup> surface area of nanoparticles and the ratio of polymer chains to cross-linker is equal to 10. The application of this protocol is reported in detail for Fe<sub>2</sub>O<sub>3</sub>, Au, CdSe/ZnS, and CoPt<sub>3</sub> nanocrystals. Although the protocol worked satisfactorily for all the nanocrystal samples tested, it is likely that for each nanocrystal material and surfactant coating the parameters can be finely tuned to optimize the final sample quality.

In addition, control experiments were performed to confirm that indeed the combined effect of the polymer and of the cross-linker was responsible for the water solubility of the nanocrystals. Nanocrystals to which only the polymer solution was added, but which did not undergo the cross-linking step, did not dissolve in water. Likewise, nanocrystals to which only the cross-linker solution was added did not dissolve in water.

The choice of cross-linker molecule is not unique and we are confident that in principle a molecule carrying at least two amino groups, sufficiently separated from each other, can be a suitable candidate. When 1,4-diaminobutane was used for instance as cross-linker instead of bis(6-aminohexyl)amine, the nanocrystals could also be transferred in water. However in this case a drastic loss in the fluorescence quantum efficiency from the CdSe/ZnS nanocrystals was observed after the particles were run through the size exclusion column. A more systematic study of the cross-linker structural parameters influencing the nanocrystal solubility and their fluorescence efficiency (for semiconductors) is in progress.

### **Polymer coating of CdSe/ZnS nanocrystals**

The concentration of the CdSe/ZnS nanocrystal (7.0 nm) solutions was determined by absorption measurements. In the case of nanocrystals with an average diameter of 7.0 nm (first exciton peak at 641 nm in the absorption spectrum) an extinction coefficient of 1030000 M<sup>-1</sup> cm<sup>-1</sup> was assumed, as reported in the literature<sup>6</sup>. In order to precipitate the particles and to remove any excess surfactant, 10 ml of methanol were added to 600 µl of CdSe/ZnS nanocrystal solution (20 µM in chloroform). After centrifugation the supernatant was discarded. 2.24 ml of polymer solution and 3.76 ml of chloroform were added to the precipitate, resulting in a total volume of 6 ml. The concentration of nanocrystals in this solution was 2 µM, which was sufficiently low to avoid cross-linking effects among nanocrystals. After stirring for two hours, the solvent was slowly evaporated. 1.52 ml of cross-linker solution was added to the resulting powder and the solution was sonicated for 20 minutes. The solvent was again removed by evaporation, 5 ml of buffer solution were added to the solid and the sample was sonicated for 5 minutes. The solution was further diluted to 10 ml by the addition of water and filtered through a syringe filter. Before filtration the sample was cloudy, but after filtration it became optically clear. Ten additional ml of water were added and the solution was placed in a centricon centrifuge filter tube. The sample was then centrifuged until the volume was reduced to 5 ml. Additional water was added and the centrifuge step was repeated. When the volume of the sample was of the order of 2-4 ml, the sample was run twice on a size exclusion column. The final concentration of the sample could be finely adjusted by further centrifugation in a centricon tube.

### **Polymer coating of Au nanocrystals**

The concentration of colloidal gold nanocrystal solution (4.0 nm average diameter) was determined by UV-visible absorption measurements, assuming that gold particles with a diameter of 4 nm have an extinction coefficient of  $8.7 \times 10^6 \text{ M}^{-1} \text{ cm}^{-1}$  at their plasmon peak. 5 ml of cold methanol were added to 250  $\mu\text{l}$  of gold solution (11  $\mu\text{M}$ ), and the solution was centrifuged in order to precipitate the nanocrystals. The supernatant was discarded. 210  $\mu\text{l}$  of polymer solution were added to the precipitate and the solution was diluted to 5 ml volume by the addition of chloroform. The concentration of gold nanocrystals in this solution was 0.55  $\mu\text{M}$ , which was sufficiently low to avoid cross-linking effects among the particles. After stirring for two hours, the solvent was slowly evaporated. 140  $\mu\text{l}$  of cross-linker solution were added to the solid and the solution was sonicated for 20 minutes. The solvent was again removed by evaporation, 5 ml of buffer solution were added to the solid, and the solution was sonicated for 5 minutes. It was then further diluted to 10 ml by the addition of water and filtered through a syringe filter. After filtration, 10 additional ml of water were added and the solution was placed in a centricon tube. The sample was then centrifuged until the volume was reduced to 5 ml. Additional water was added and the centrifugation step was repeated. When the volume of the sample was of the order of 2 ml, it was removed from the tube and run twice on a size exclusion column. The final concentration of the sample could be finely adjusted by an additional centrifugation in a centricon centrifuge filter tube.

### **Polymer coating of CoPt<sub>3</sub> nanocrystals**

The concentration of the CoPt<sub>3</sub> nanocrystal solution was determined by gravimetric measurements. The number of nanoparticles in the solution was in fact estimated by evaluating the average weight of a single nanocrystal and the total amount of nanocrystals in the solution. The density of CoPt<sub>3</sub> is 18.86 g/cm<sup>3</sup> (as reported in the literature), so that the mass of a single CoPt<sub>3</sub> nanocrystals having a diameter of 8.0 nm was estimated to be  $5.43 \times 10^{-21}$  kg. This calculation does not take into account the surfactant coating, whose contribution however is considered to be negligible.

Ten ml of isopropanol were added to 3 ml of cobalt platinum solution (2  $\mu\text{M}$ ), and the solution was centrifuged in order to precipitate the nanocrystals. The supernatant was discarded. 1.44 ml of polymer solution was added to the precipitate and the volume was adjusted to 6 ml by the addition of chloroform. The concentration of CoPt<sub>3</sub> in this solution was 1  $\mu\text{M}$  and this was sufficiently low to avoid cross-linking effects among the particles. After stirring for two hours, the solvent was slowly evaporated under reduced pressure. To the resulting solid 0.98 ml of cross-linker solution was added and the sample was sonicated for 20 minutes. Shortly after, the solvent was again removed and 5 ml buffer solution were added to the solid. The sample was then sonicated for 5 min, it was further diluted with water to 10 ml and filtered through syringe filters. Ten additional ml of water were added and the solution was placed in a centricon tube. The sample was then centrifuged until the volume was reduced to 5 ml. Additional water was added and the centrifuge step was repeated. When the volume of the sample was of the order of 2-5 ml, the sample was run twice on a size exclusion column. The concentration of the sample could be adjusted by removing some of the solvent using centricon centrifuge tubes.

### **Polymer coating of $\text{Fe}_2\text{O}_3$ nanocrystals**

The concentration of the  $\gamma\text{-Fe}_2\text{O}_3$  nanocrystal solution (9.2 nm average diameter) was also determined by gravimetric measurements. The density of the  $\gamma\text{-Fe}_2\text{O}_3$  (maghemite) is  $5 \text{ g/cm}^3$ , so the mass of a single  $\gamma\text{-Fe}_2\text{O}_3$  nanocrystal was calculated to be  $1.91 \times 10^{-21} \text{ kg}$ . Once again, this calculation did not take into account the surfactant coating.

Six ml of methanol were added to 845  $\mu\text{l}$  of  $\gamma\text{-Fe}_2\text{O}_3$  solution (7.1  $\mu\text{M}$ ), and the solution was centrifuged in order to precipitate the nanocrystals. The supernatant was discarded. 1.68 ml of polymer solution (400 mg/10 ml) was added to the precipitate and the volume was adjusted to 6 ml by the addition of chloroform. The concentration of  $\gamma\text{-Fe}_2\text{O}_3$  nanocrystals in this solution was 1  $\mu\text{M}$ , sufficiently low to avoid cross-linking effects among the particles. After stirring for two hours the solvent was slowly evaporated under reduced pressure. 1.14 ml of cross-linker solution (43mg/10ml) was added to the solid and the resulting solution was sonicated for 20 minutes. Shortly after, the solvent was again removed by evaporation and 5 ml of buffer solution were added to the solid. The sample was sonicated for 5 min, it was further diluted with water to 10 ml and then filtered through syringe filters. Ten additional ml of water were added and the solution was placed in a centricon tube. The sample was then centrifuged until the volume was reduced to 5 ml. Additional water was added and the centrifugation step was repeated. When the volume of the sample was of the order of 2-5 ml, the sample was run twice on a size exclusion column. The concentration of the sample could be adjusted by removing some of the solvent using a centricon centrifuge filter tube.

**Transmission electron microscopy (TEM)**

Transmission electron microscope images were taken on a Philips CM 100 electron microscope operated at an accelerating voltage of 100 KV. The nanocrystals were deposited from a dilute solution onto a 3-4 nm thick film of amorphous carbon supported on a 400 mesh copper grid (Ted Pella Inc., # 01822-F). One drop of nanocrystal solution was deposited onto the grid and the solvent was evaporated. In the case of nanocrystals in water the grids were kept under ethanol vapors for 1-2 days prior to sample deposition. This treatment made the carbon film more hydrophilic and improved the adsorption of the nanocrystals on it. The microscope magnification was calibrated with a calibration grid (Grating Replica, Waffle, 2160 l/mm, on 3mm grid, Ted Pella Inc., # 607). The average sizes and size distributions of the various nanocrystal samples were estimated by analyzing the scanned TEM negatives with "ImageJ" image analysis software, freely available from <http://rsb.info.nih.gov/ij/>.

**Gel electrophoresis**

Gel electrophoresis was used to study the size and surface charge distribution of the polymer coated nanocrystals and to check for the presence of nanocrystal aggregates. The nanocrystals were diluted in a loading buffer containing glycerol (final glycerol concentration 5-10%) and were run in a 0.5 x TBE buffer on a 2 % agarose gel, at 100 V for 1 hour. In the case of CdSe/ZnS nanocrystals, the gel was illuminated with an ultraviolet trans-illuminator to image the fluorescence from the bands. In the case of CoPt<sub>3</sub>, Fe<sub>2</sub>O<sub>3</sub> and Au nanocrystals, the gels were imaged with a visible-light illuminator.

### Fluorescence Correlation Spectroscopy: theory and experiments

FCS was established by Madge et al. (1972)<sup>12</sup> as a way for measuring the diffusion constants of fluorescent particles dispersed in a solvent. From the diffusion constant of a particle it is possible to derive then its hydrodynamic radius through the Stokes-Einstein relation. Here, we first give a short overview of the FCS theory (details are discussed elsewhere<sup>13-15</sup>), and then we describe the experimental procedure for determining the average radius of the nanocrystals in the present work, using the FCS theory.

Let us assume that an excitation light source is focused on a tiny volume ( $V_{\text{eff}}$ ) of the solution containing the fluorescent particles. On average,  $\langle N \rangle$  particles will be sampled in this volume. However, the number of particles  $N(t)$  in this volume will fluctuate over time, because the particles can diffuse in and out of it. In the case of dilute solutions (so only few particles are present in the focus volume, on average), the fluctuation in the number of particles can be described by a Poisson distribution:

$$\sqrt{\frac{\langle (\delta N)^2 \rangle}{N}} = \frac{1}{\sqrt{N}} \quad (1)$$

$\delta N(t) = N(t) - \langle N \rangle$  is the fluctuation of the number of particles, and  $\langle N \rangle$  is the mean number of particles in the volume. Now, the concentration of the particles must be high enough to guarantee a good signal to noise ratio, but low enough to observe free particle diffusion. A good compromise would correspond roughly to 1 particle per femtoliter of the focus-volume  $V_{\text{eff}}$ . The FCS theory demonstrates that it is possible to derive the diffusion constant of the particles from  $\delta N(t)$ , and the principle can be understood in terms of a simple model. The time a particle needs to diffuse in and out of the focus volume depends indeed on its diffusion coefficient. The larger the diffusion coefficient, the faster the particles can diffuse in and out of the focus, and consequently faster time scale will characterize the fluctuations of the number of particles in  $V_{\text{eff}}$ . The analysis of the time scales involved in the fluctuations can be carried out by means of an autocorrelation function.

To a first approximation, we assume a constant value for the fluorescence emission from each particle inside the focus volume. In this simplified approach fluorescence fluctuations due to fluctuations in the absorption cross-section and in the quantum yield and blinking of the particles are neglected. Particles are also assumed to have a spherical shape.

The number of particles in the focus at a given time  $t$  can be experimentally determined by the total fluorescence  $F(t)$  collected. Since the excitation light is focused on a tiny volume  $V_{\text{eff}}$ , only the particles within this volume contribute to the fluorescence signal. The fluctuation  $\delta F(t) = F(t) - \langle F \rangle$  of the fluorescence signal is defined as the deviation from the mean fluorescence signal  $\langle F \rangle$ , which is given by:

$$\langle F \rangle = \frac{1}{T} \int_0^T F(t) dt \quad (2)$$

The number of particles  $N(t)$  in the focus can be written as an integral over the local particle concentration  $c(\underline{r}, t)$ :

$$N(t) = \int_{V_{\text{eff}}} c(\underline{r}, t) dV \quad (3)$$

We now assume that the fluctuations in the fluorescence signal are only due to local changes in the concentration  $\delta c(\underline{r}, t)$  in the effective focus-volume  $V_{\text{eff}}$ . In addition, we merge the spatial parameters of the illumination to a function  $W(\underline{r})$  that is written as:

$$W(\underline{r}) = e^{-2(x^2 + y^2)/r_0^2} \cdot e^{-2z^2/z_0^2} \quad (4)$$

$W(\underline{r})$  is the so called Molecule Detection Efficiency which gives the probability of exciting and detecting a fluorescent particle in the solution. It is therefore the product of the excitation profile of the focused laser and the spatial collection efficiency of the confocal detection optics. Under carefully chosen setup conditions  $W(\underline{r})$  can be approximated as a 3-dimensional Gaussian ellipsoid, as has been assumed in Equation (4).  $\underline{r} = (x, y, z)$  describes the coordinates in the three-dimensional space. Here  $r_0$  is the radius in the focal plane where the excitation intensity of the laser has dropped to  $1/e^2$  compared to the center. The parameter  $z_0$  gives the extension of the effective detection volume on the z-axis and is mainly determined by the used objective and the size of the pinhole.

The fluctuation of the fluorescence signal can then be written as:

$$\delta F(t) = \eta \int_{V_{\text{eff}}} W(\underline{r}) \cdot \delta c(\underline{r}, t) dV \quad (5)$$

The constant value  $\eta$  contains the quantum efficiency of the dye, detection efficiency and absorption cross-section. The normalized autocorrelation function  $G(\tau)$  for fluorescence fluctuations  $\delta F(t)$  is defined as:

$$G(\tau) = \frac{\langle \delta F(t) \cdot \delta F(t + \tau) \rangle}{\langle F(t) \rangle^2} \quad (6)$$

$G(\tau)$  is a measure of the self-similarity of the fluorescence signal after a delay-time  $\tau$ . Thus  $G(0)$  is the variance  $\langle \delta F(t)^2 \rangle / \langle F \rangle^2$ . By inserting equation (5) in equation (6) the autocorrelation function becomes:

$$G(\tau) = \frac{\int \int \int_{V V'} W(\underline{r}) \cdot W(\underline{r}') \cdot \langle \delta c(\underline{r}, 0) \cdot \delta c(\underline{r}', \tau) \rangle dV dV'}{\left( \langle c \rangle \int_{V'} W(\underline{r}) dV \right)^2} \quad (7)$$

Under the assumption that the particles can diffuse freely in all three spatial directions (Brownian diffusion), we can derive an expression for the concentration fluctuations  $\delta c(\underline{r}, t)$  if we solve the diffusion equation, where  $D$  is the diffusion coefficient.

$$\frac{\delta c(\underline{r}, t)}{\delta t} = D \nabla^2 \delta c(\underline{r}, t) \quad (8)$$

We can use the following expression for  $\delta c(\underline{r}, t)$ :

$$\delta c(\underline{r}, t) = \delta c(\underline{r}, 0) \cdot e^{-\underline{r}^2 / Dt} \quad (9)$$

The solution of the diffusion equation using (9) yields:

$$\langle \delta c(\underline{r}, 0) \delta c(\underline{r}', \tau) \rangle = \langle c \rangle \frac{1}{(4\pi D \tau)^{\frac{3}{2}}} \cdot e^{\frac{(\underline{r}-\underline{r}')^2}{4D\tau}} \quad (10)$$

Insertion of (10) into (7), followed by integration over the volume, finally leads to the autocorrelation function for freely diffusing particles (11).

$$G(\tau) = G_{\text{motion}}(\tau) = \frac{1}{V_{\text{eff}} \langle c \rangle} \cdot \frac{1}{(1 + \frac{\tau}{\tau_D})} \cdot \frac{1}{\sqrt{1 + \frac{\tau}{\tau_D \cdot s^2}}} \quad (11)$$

with the characteristic diffusion-time  $\tau_D$  given by

$$\tau_D = \frac{r_0^2}{4D} \quad (12)$$

and the structure parameter  $s$  given by

$$s = \frac{z_0}{r_0} \quad (13)$$

The effective focus volume  $V_{\text{eff}}$  is then defined as

$$V_{\text{eff}} = \frac{\left( \int_V W(\underline{r}) dV \right)^2}{\int_V W^2(\underline{r}) dV} = \frac{\left( \int e^{-\frac{2(x^2+y^2)}{r_0^2}} \cdot e^{-\frac{2z^2}{z_0^2}} dV \right)^2}{\int e^{-\frac{4(x^2+y^2)}{r_0^2}} \cdot e^{-\frac{4z^2}{z_0^2}} dV} = \pi^{\frac{3}{2}} \cdot r_0^2 \cdot z_0 \quad (14)$$

In a more advanced approach, the correlation function  $G_{\text{motion}}$  (which describes only changes in fluorescence due to the motion of the particles) is multiplied by a kinetic factor  $X(\tau)$

$$X(\tau) = \frac{1 - T_{\text{trip}} + T_{\text{trip}} e^{\tau/\tau_{\text{trip}}}}{1 - T_{\text{trip}}} \quad (15)$$

which accounts for blinking / flickering<sup>15,16</sup> in the fluorescence of the particles. The corrected autocorrelation function becomes then:

$$G_{\text{total}}(\tau) = G_{\text{motion}}(\tau) \cdot X(\tau) \quad (16)$$

The hydrodynamic radius  $r_h$  of the spherical particles can be obtained by inserting the diffusion constant  $D$  (from equation (12)) into the Stokes-Einstein-equation:

$$r_h = \frac{kT}{6\pi\eta D} \quad (17)$$

Having given a brief overview of the FCS theory, we now describe the experimental procedure followed for the determination of the average diameter of the polymer coated nanocrystals synthesized in the present work.

Figure 1 shows a sketch of the experimental setup. A laser beam is focused by an objective with a high numerical aperture. Fluorescent light that is collected by the same objective can pass through the dichroic mirror as it is slightly shifted to higher wavelengths compared to the excitation. A 50/50 beamsplitter gives half of the intensity to two independent detection channels. With the filters the desired detection wavelengths can be chosen. Behind the pinholes of variable size the photons are detected with avalanche photodiodes giving the intensity versus time  $F(t)$ . An autocorrelation of the signal is done by a correlator card attached to a computer.

The Experiments were performed with a Confocor2 FCS-setup from Zeiss™. The laser light from an Ar-ion-Laser (Lasos/Zeiss) was coupled into the system via a dichroic mirror and was focused with a Zeiss C-Apochromat water immersion objective (40x; numerical aperture: 1.2) to a small volume within the diluted sample. The fluorescence signal emitted from the particles passed through a dichroic mirror and the focal plane was selected by a pinhole with 70 µm diameter. The signal was split by a 50/50 beamsplitter and was collected by two Avalanche Photo Diodes (after passing appropriate filters).

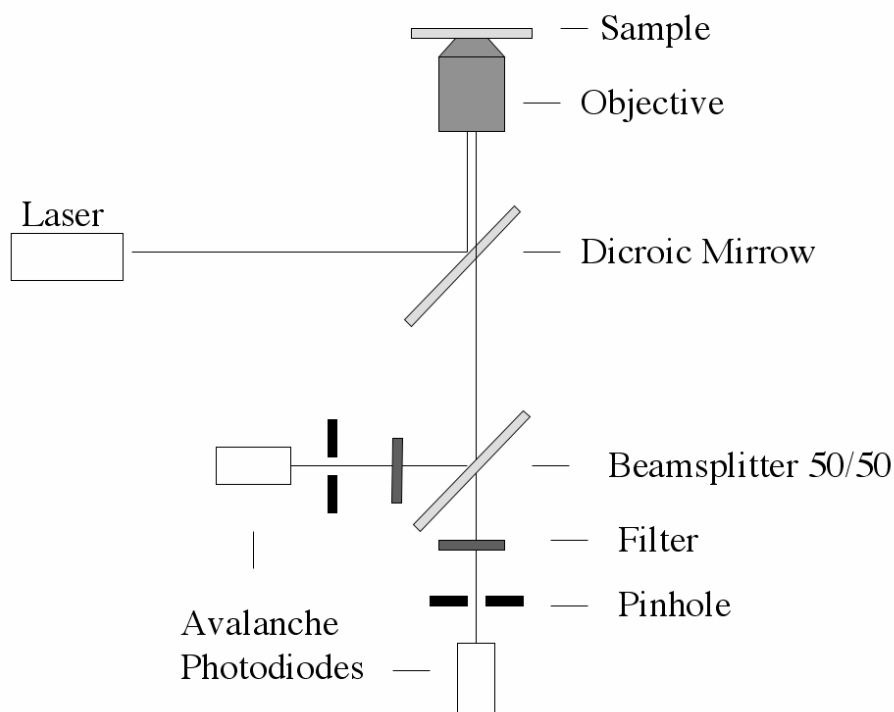


Figure 1. FCS setup. An Ar-ion-Laser (Lasos/Zeiss) was used, the cut-off wavelength of the dichroic mirror was 510 nm, and 510 nm longpass filters were used to observe the emitted fluorescence.

First of all, the system had to be calibrated. In particular the volume of the focus had to be determined experimentally. For this purpose fluorescent molecules with a known diffusion constant were used as calibration sample. We used a solution of Alexa488 dye (Molecular Probes, excitation maximum 493 nm, emission maximum 517 nm) dissolved in water (10 nM concentration). The time trace of the fluorescence signal  $F(t)$  from this sample was recorded 10 times, each time for 20 seconds (Figure 2). For each measurement, the autocorrelation function  $G(\tau)$  for the fluorescence fluctuations  $\delta F(t)$  was calculated by using equation (6) (Figure 3). The experimental data for the autocorrelation function were fitted with equations (11, 16), using the 5 fit parameters  $\tau_D$ ,  $s$ ,  $\langle N \rangle = V_{\text{eff}} \langle c \rangle$ ,  $T_{\text{trip}}$ , and  $\tau_{\text{trip}}$ . Since the diffusion constant for Alexa488 is known ( $D = 316 \mu\text{m}^2/\text{s}$ ), the focal radius  $r_0$  could be derived via (12) using for  $\tau_D$  the value obtained from the fit. Similarly,  $z_0$  could be derived via (13) by using the fit results for the structure parameter  $s$  and  $r_0$ . The mean values for  $r_0$  and  $z_0$  (and thus also for  $s$ ) obtained from the ten individual measurements were then used for all the measurements on nanocrystal samples. However, when other solvents than water were used, as in the case of nanocrystals dissolved in chloroform, the focal radius  $r_0$  had to be adjusted for changes in the refractive index  $n$  of the solvent:

$$r_0(\text{in H}_2\text{O}) \cdot n(\text{H}_2\text{O}) = r_0(\text{in chloroform}) \cdot n(\text{chloroform})$$

$$(n(\text{H}_2\text{O}) = 1.33, n(\text{chloroform}) = 1.45)$$

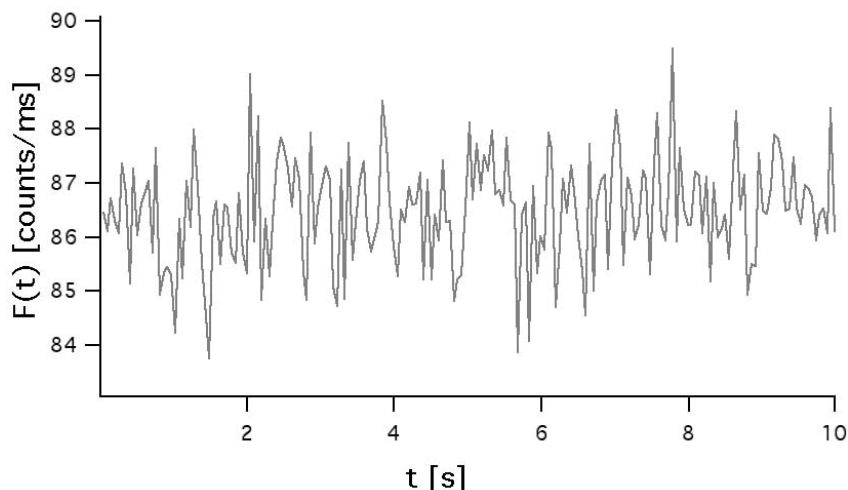


Figure 2: Time trace of the recorded fluorescence intensity  $F(t)$  of Alexa488 fluorescent dye.

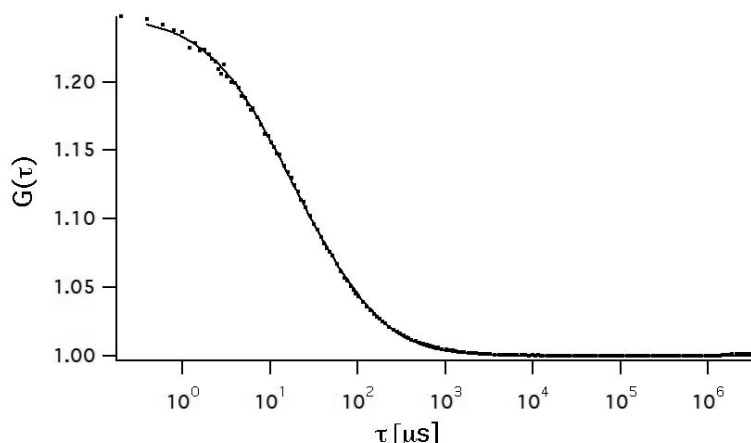


Figure 3: Autocorrelation function  $G(\tau)$  calculated from the  $F(t)$  data shown in Figure 2 (dotted line). The curve was fitted with the function given in equations (11, 16). The fit yielded the five fit parameters: characteristic diffusion time  $\tau_D = 26.6 \mu\text{s}$ , structure parameter  $s = 8.96$ , average number of dye molecules within the focal volume  $\langle N \rangle = V_{\text{eff}} \langle c \rangle = 4.7$ ,  $T_{\text{trip}} = 0.15$ , and  $\tau_{\text{trip}} = 4.7 \mu\text{s}$ . The focal radius  $r_0$  was calculated by means of (12), using the known diffusion-constant of Alexa488 ( $D = 316 \mu\text{m}^2/\text{s}$ ), and was equal to 183 nm.

For the measurements on the nanocrystal samples, nanocrystal solutions with a concentration of approximately 50 nM were deposited on a coverslip over the objective (the same as for the Alexa488 dye solution). The time trace of the fluorescence signal  $F(t)$  was recorded at least ten times, each time for 20 seconds. The corresponding autocorrelation functions  $G(\tau)$  were calculated using equation (6) and were fitted with (11) and (16). This time only four fit parameters were used:  $\tau_D$ ,  $\langle N \rangle = V_{\text{eff}} \langle c \rangle$ ,  $T_{\text{trip}}$ , and  $\tau_{\text{trip}}$ . The geometrical parameters for the focus volume ( $r_0$  and  $z_0$ , as well as  $s$ ) were in fact known from the previous calibration with the Alexa488 solution. The diffusion constant for the nanocrystals  $D$  could be calculated via (12), using the diffusion time  $\tau_D$ , as determined from the fit, and the known focal radius  $r_0$ . Finally, the hydrodynamic radius of the nanocrystals was calculated using the Stokes-Einstein-equation (17). For the samples dissolved in chloroform and for those dissolved in water the viscosities  $\eta_{\text{CHCl}_3} =$

0.57 mPa·s and  $\eta_{\text{water}} = 0.98 \text{ mPa}\cdot\text{s}$  respectively, were assumed at 20°C. At least 10 individual measurements were performed for each sample, and the resulting hydrodynamic radius was determined as the mean value of the measurements.

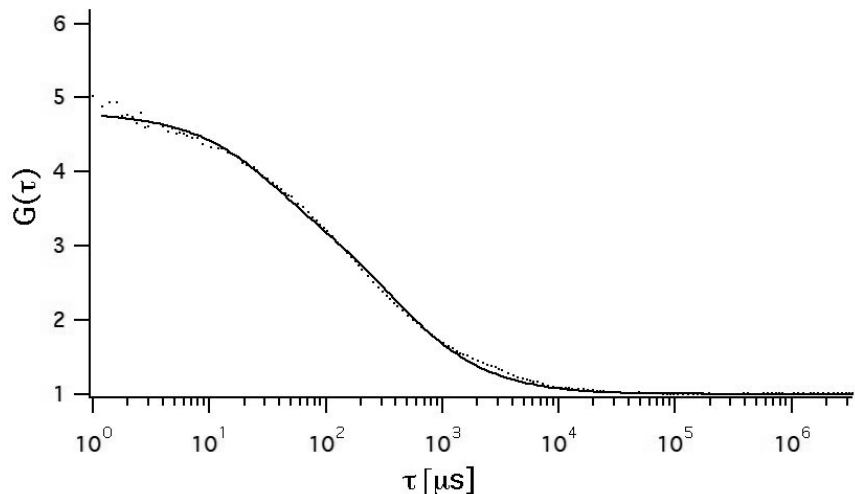


Figure 4: Autocorrelation function  $G(\tau)$  calculated from the  $F(t)$  data recorded on a sample of green fluorescent, polymer-coated CdSe/ZnS nanocrystals dissolved in water (dotted line). The curve was fitted with the function given in equation (11, 16), whereby the structure parameter (as determined from the calibration with Alexa488) was kept fixed at  $s = 7.6$ . This curve was actually recorded on a different day than the curve shown in Figure 3. Therefore a new calibration was necessary, and this yielded a structure parameter that was slightly different from the one reported in Figure 3. The fit yielded the following four free parameters: characteristic diffusion time  $\tau_D = 327.5 \mu\text{s}$ , average number of dye molecules within the focal volume  $\langle N \rangle = V_{\text{eff}} \langle c \rangle = 0.35$ ,  $T_{\text{trip}} = 0.34$  and  $\tau_{\text{trip}} = 30.1 \mu\text{s}$ . With the known value for  $r_0 = 167 \text{ nm}$  the diffusion constant was determined via (12) to be  $D = 21.3 \mu\text{m}^2/\text{s}$ .

**Table 1: Summary of all polymer coating experiments**

sample	polymer units		[polymer chains] [crosslinker]
	nm <sup>2</sup>	nanoparticle	
Fe <sub>2</sub> O <sub>3</sub>	93		13
Fe <sub>2</sub> O <sub>3</sub>	100		10
Fe <sub>2</sub> O <sub>3</sub>	182		13
Fe <sub>2</sub> O <sub>3</sub>	260		13
Fe <sub>2</sub> O <sub>3</sub>	519		10
Au	100		10
Au	92		10
Au	147		7
Au	295		7
Au	310		8
CdSe/ZnS	10		6
CdSe/ZnS	15		6
CdSe/ZnS	20		6
CdSe/ZnS	60		6
CdSe/ZnS	100		10
CoPt <sub>3</sub>	100		10

**References**

- (1) Shevchenko, E. V.; Talapin, D. V.; Rogach, A. L.; Kornowski, A.; Haase, M.; Weller, H. *JACS* **2002**, *124*, 11480-11485.
- (2) Fink, J.; Kiely, C. J.; Bethell, D.; Schiffrian, D. J. *Chem. Mat.* **1998**, *10*, 922-926.
- (3) Dabbousi, B. O.; Rodriguez-Viejo, J.; Mikulec, F. V.; Heine, J. R.; Mattoussi, H.; Ober, R.; Jensen, K. F.; Bawendi, M. G. *J. Phys. Chem. B* **1997**, *101*, 9463-9475.
- (4) Hyeon, T.; Lee, S. S.; Park, J.; Chung, Y.; Na, H. B. *J. Am. Chem. Soc.* **2001**, *123*, 12798-12801.
- (5) Reiss, P.; Bleuse, J.; Pron, A. *Nanoletters* **2002**, *2*, 781-784.
- (6) Yu, W. W.; Qu, L.; Guo, W.; Peng, X. *Chem. Mat.* **2003**, *15*, 2854-2860.
- (7) Leff, D. V.; O'Hara, P. C.; Heath, J. R.; Gelbart, W. M. *The Journal of Physical Chemistry* **1995**, *99*, 7036-7041.
- (8) Kiely, C. J.; Fink, J.; Zheng, J. G.; Brust, M.; Bethell, D.; Schiffrian, D. J. *Adv. Mater.* **2000**, *12*, 640-643.
- (9) Templeton, A. C.; Wuelfing, W. P.; Murray, R. W. *Accounts Chem. Res.* **2000**, *33*, 27-36.
- (10) Shevchenko, E. V.; Talapin, D. V.; Schnablegger, H.; Kornowski, A.; Festin, Ö.; Svedlindh, P.; Haase, M.; Weller, H. *JACS* **2003**, *125*, 9090-9101.
- (11) Zanchet, D.; Micheel, C. M.; Parak, W. J.; Gerion, D.; Williams, S. C.; Alivisatos, A. P. *J. Phys. Chem. B* **2002**, *106*, 11758-11763.
- (12) Magde, D.; Elson, E.; Webb, W. W. *Phys. Rev. Lett* **1972**, *29*, 705-708.
- (13) Eigen, M.; Rigler, R. *Proc. Natl. Acad. Sci. USA* **1994**, *91*, 5740-5747.
- (14) Schwille, P.; Bieschke, J.; Oehlenschläger, F. *Biophysical Chemistry* **1997**, *66*, 211-228.
- (15) Krichevsky, O.; Bonnet, G. *Rep. Prog. Phys.* **2002**, *65*, 251-297.
- (16) Amediek, A.; Haustein, E.; Scherfeld, D.; Schwille, P. *Single Molecules* **2002**, *3*, 201-210.

## **E.2 Cytotoxicity of Colloidal CdSe and CdSe/ZnS Nanoparticles**

C. KIRCHNER, T. LIEDL, S. KUDERA, T. PELLEGRINO, A. MUÑOZ JAVIER, H.E. GAUB, S. STÖLZLE, N. FERTIG, W.J. PARAK  
*Nano Letters* **5**(2), pp. 331–338, 2005

Cytotoxicity of CdSe and CdSe/ZnS nanoparticles has been investigated for different surface modifications such as coating with mercaptopropionic acid, silanization, and polymer coating. For all cases, quantitative values for the onset of cytotoxic effects in serum-free culture media are given. These values are correlated with microscope images in which the uptake of the particles by the cells has been investigated. Our data suggest that in addition to the release of toxic Cd<sup>2+</sup> ions from the particles also their surface chemistry, in particular their stability toward aggregation, plays an important role for cytotoxic effects. Additional patch clamp experiments investigate effects of the particles on currents through ion channels.

# Cytotoxicity of Colloidal CdSe and CdSe/ZnS Nanoparticles

Christian Kirchner,<sup>†</sup> Tim Liedl,<sup>†</sup> Stefan Kudera,<sup>†</sup> Teresa Pellegrino,<sup>†</sup> Almudena Muñoz Javier,<sup>†</sup> Hermann E. Gaub,<sup>†</sup> Sonja Stölzle,<sup>‡</sup> N. Fertig,<sup>‡</sup> and Wolfgang J. Parak<sup>\*,†</sup>

Center for Nanoscience, Ludwig Maximilians Universität München, Germany,  
Nanion Technologies GmbH, Pettenkoferstr. 12, 80336 Munich, Germany

Received December 3, 2004

## ABSTRACT

Cytotoxicity of CdSe and CdSe/ZnS nanoparticles has been investigated for different surface modifications such as coating with mercaptopropionic acid, silanization, and polymer coating. For all cases, quantitative values for the onset of cytotoxic effects in serum-free culture media are given. These values are correlated with microscope images in which the uptake of the particles by the cells has been investigated. Our data suggest that in addition to the release of toxic Cd<sup>2+</sup> ions from the particles also their surface chemistry, in particular their stability toward aggregation, plays an important role for cytotoxic effects. Additional patch clamp experiments investigate effects of the particles on currents through ion channels.

**Introduction.** Recent progress in nanotechnology allows for the creation of new materials with properties tunable on the nanometer scale. Currently, already first attempts to use the functionality of such “smart” nanomaterials in life sciences are reported. Applications range from using fluorescent nanoparticles as dyes for fluorescence labeling of cells<sup>1–3</sup> and for motility assays<sup>4</sup>, using gold nanoparticles for immunostaining<sup>5</sup> and gene delivery<sup>6</sup>, to using magnetic nanoparticles as contrast agents for magnetic resonance imaging<sup>7,8</sup> and for hypothermia.<sup>8,9</sup> In addition to working with cell cultures, nanoparticles have been successfully introduced in animal experiments as contrast agents,<sup>10,11</sup> and future use in clinical applications is envisioned.<sup>12</sup> It is evident that for any clinical application biocompatibility of the nanoparticles is crucial. Since nanoparticles are different from their respective bulk material due to their size, it is an obvious question to ask for potential dangers arising from their smallness.<sup>13</sup> We can think of at least three different pathways by which nanoparticles introduced into an organism could interfere with its function and finally lead to impairment. (1) Most evident, introduced nanoparticles can be composed of toxic materials. This is true, for example, for fluorescence CdSe as well as for magnetic Co particles. Upon corrosion inside the organism, toxic ions could be released which finally poison the cells. Cytotoxic effects of Cd<sup>2+</sup> (refs 14–18) and other metal ions<sup>19</sup> are well-known. Compared to the respective bulk material, partial decomposition and release

of ions is more likely for nanoparticles due to their enhanced surface-to-volume ratio. (2) There might be a negative effect of particles in general on cells, regardless of the material of the particles. It is known that particles can stick to the surface of cell membranes,<sup>20,21</sup> and particles are also known to be ingested by cells.<sup>4,21–23</sup> Mantling of the cell membrane and storage of particles inside cells might have impairing effects, even for absolutely inert particles that do not decompose or react. (3) There might be an effect caused by the shape of the (inert) particles. It has been reported for example, that carbon nanotubes can impale cells like needles.<sup>24,25</sup> Particles of the same material but in a different modification can have a different toxic effect on cells in this way: Carbon nanotubes that have reached the lung are significantly more toxic than carbon-black and graphite.<sup>24,25</sup> So far, most cytotoxicity studies on nanomaterials are focused on aerosols<sup>26</sup> and involve particle uptake by the lungs. Such studies are important for many technical devices, for example, regarding the output of platinum nanoparticles from the catalysts of cars which might potentially endanger people who inhale these particles.<sup>27,28</sup> In this study we focus on the toxic effects of colloidal nanoparticles dispersed in aqueous solution on cells. As already mentioned above, many different types of colloidal nanoparticles can be used for a broad variety of applications in life sciences and medicine. In this study we will focus on fluorescent CdSe and CdSe/ZnS nanoparticles.

To our knowledge, so far only two studies exist in which the cytotoxic effects of CdSe and CdSe/ZnS nanoparticles are investigated in detail. Derfus et al. have reported that

\* Corresponding author. E-mail: Wolfgang.Parak@physik.uni-muenchen.de.  
† Ludwig Maximilians Universität München.

‡ Nanion Technologies GmbH.

CdSe particles dissolved in aqueous solution release Cd<sup>2+</sup> ions<sup>29</sup> and that the concentration of the Cd<sup>2+</sup> ions directly correlates with cytotoxic effects. The same authors have demonstrated that ion release is enhanced by oxidation, either through exposure to air or UV irradiation, but is repressed by encapsulating the particles with appropriate shells, as with ZnS and an additional organic shell. Shiohara et al. have investigated the cytotoxic effects of CdSe/ZnS particles of different size on three different cell types.<sup>30</sup> The same group claims that for CdSe/ZnS particles the main source of cytotoxicity is not their cadmium content but rather the interaction of the particle surface with the cells.<sup>31</sup> In our work described here we want to extend these studies to investigate the effect of different organic shells on cytotoxicity. Also, quantitative values for the onset of cytotoxic effects are determined.

**Materials and Methods.** Several cell lines (NRK fibroblasts, MDA-MB-435S breast cancer cells, CHO cells, RBL cells) were grown on standard cell culture substrates (All Materials and Methods can be found in detail in the Supporting Information). Nanocrystals of different materials and different surface coatings dissolved in water were added at different concentrations to adherent cells. In particular, CdSe,<sup>32</sup> CdSe/ZnS,<sup>33</sup> and Au<sup>34</sup> nanocrystals coated with mercaptopropionic acid,<sup>35</sup> embedded in a silica shell<sup>35,36</sup> or embedded in an amphiphilic polymer shell,<sup>37</sup> were investigated. In a first set of experiments, uptake of the nanocrystals by cells was investigated. For this purpose, green and red fluorescent CdSe/ZnS nanocrystals with different surface coatings were added to the cells, and after 18 h incubation the nuclei of the cells were stained with DAPI.<sup>4</sup> Living cells were then imaged with differential interference contrast (DIC) and fluorescence microscopy. In this way the position of the nuclei and the ingested nanocrystals with two different surface coatings could be co-localized by their color of fluorescence (blue, green, red). In a second set of experiments, toxic effects of the ingested particles on the cells were investigated. From previous studies it is known that the adhesion behavior of NRK fibroblast is highly sensitive to toxic metal ions.<sup>38</sup> In the study described here, the proliferation of the adherent cells was blocked by exchanging the culture medium to SATO medium.<sup>39</sup> The number of adherent cells per labeled region on the cell culture substrate was counted and nanocrystals were then added at several concentrations. After 48 h of incubation, the nonadherent cells were removed by rinsing and the number of the adherent cells at the same region was counted. In this way the ratio  $R$  of the number of adherent cells after and before incubation with nanocrystals, detected at the identical position, could be derived. The more toxic the effect of the nanocrystals on the cells, the lower this value is expected to be. As control, the constituents of the nanocrystals as Cd<sup>2+</sup> and Se<sup>2-</sup> ions and mercaptopropionic acid were added to the cells. In addition, the viability of the adherent cells before and after incubation with the nanocrystals was measured with a commercially available test (L3224, Molecular Probes). As a third set of experiments, nanocrystals were added to cells expressing hERG ion channels, and the effect of the

nanocrystals on the ionic currents through these channels was investigated with an automated patch-clamp setup (Nanion<sup>40,41</sup>). This idea is similar to a previous study.<sup>42</sup> Uptake of nanocrystals by the cells was monitored by confocal microscopy.

**Results and Discussion. Uptake of CdSe/ZnS Nanocrystals by MDA-MB-435S Breast Cancer Cells.** In Figure 1 fluorescence and DIC images of MDA-MB-435S breast cancer cells that have been incubated for 18 h in serum-supplemented cell medium containing around c(CdSe/ZnS particles) = 2–10 nM water-soluble CdSe/ZnS nanocrystals are shown. For each experiment red and green fluorescent nanocrystals with different surface coatings were used simultaneously, and experiments were performed for all different combinations. In particular, particles coated with mercaptopropionic acid (MPA), a silica shell bearing phosphonate groups (phos-silane), a silica shell bearing polyethylene groups (PEG-silane), and an amphiphilic polymer (polymer) were used. From the images shown in Figure 1 it is evident that most of the different particles are ingested by the cells. By staining the nucleus with DAPI and manually changing the focus it could be shown that the ingested particles are stored in vesicular structures around the nucleus. For almost all combinations of particles with different surface coating, the ingested particles were stored in similar vesicular structures. Our data indicate that MPA, phos-silane, and polymer-coated particles are ingested by the cells in a very similar way, since these particles were found to co-localize inside the cells. However, different behavior was observed for PEG-silane coated particles. Whereas small green-fluorescent particles (hydrodynamic diameter of ~13 nm, unpublished results) were barely found inside the cells, bigger red-fluorescent particles (hydrodynamic radius of ~24 nm) could be detected inside the cells. These co-localization data demonstrate that water-soluble CdSe/ZnS particles are ingested by MDA-MB-435S cells in a nonspecific way, regardless of their size (in the range between 10 and 24 nm) and surface coating. Only for small PEG-silane coated particles uptake is significantly reduced. Nanocrystal uptake has also been demonstrated for other cell lines, such as NRK fibroblasts (data not shown).

**Detachment of NRK Fibroblast from the Cell Culture Substrate upon Incubation with Nanocrystals.** Since a previous study suggests that Cd<sup>2+</sup> ions released from the surface of Cd-containing nanocrystals are the main cause of toxic effects,<sup>29</sup> we converted the concentration of CdSe and CdSe/ZnS particles to the concentration of Cd atoms on the surface of the CdSe core (see Supporting Information). This means that, in the case of a 1 nM concentration of CdSe particles with 100 surface Cd-atoms per particle, the concentration of Cd surface atoms is 100 nM. Analogously, the concentration of Au particles was converted to the concentration of Au atoms on the surface of the Au particles. The study of Shiohara et al. showed that for the same mass concentration (mg/mL) of particles cytotoxic effects are higher for smaller particles.<sup>30</sup> Since for smaller particles the surface-to-volume ratio is higher, these findings support our idea to plot a “concentration parameter” proportional to the

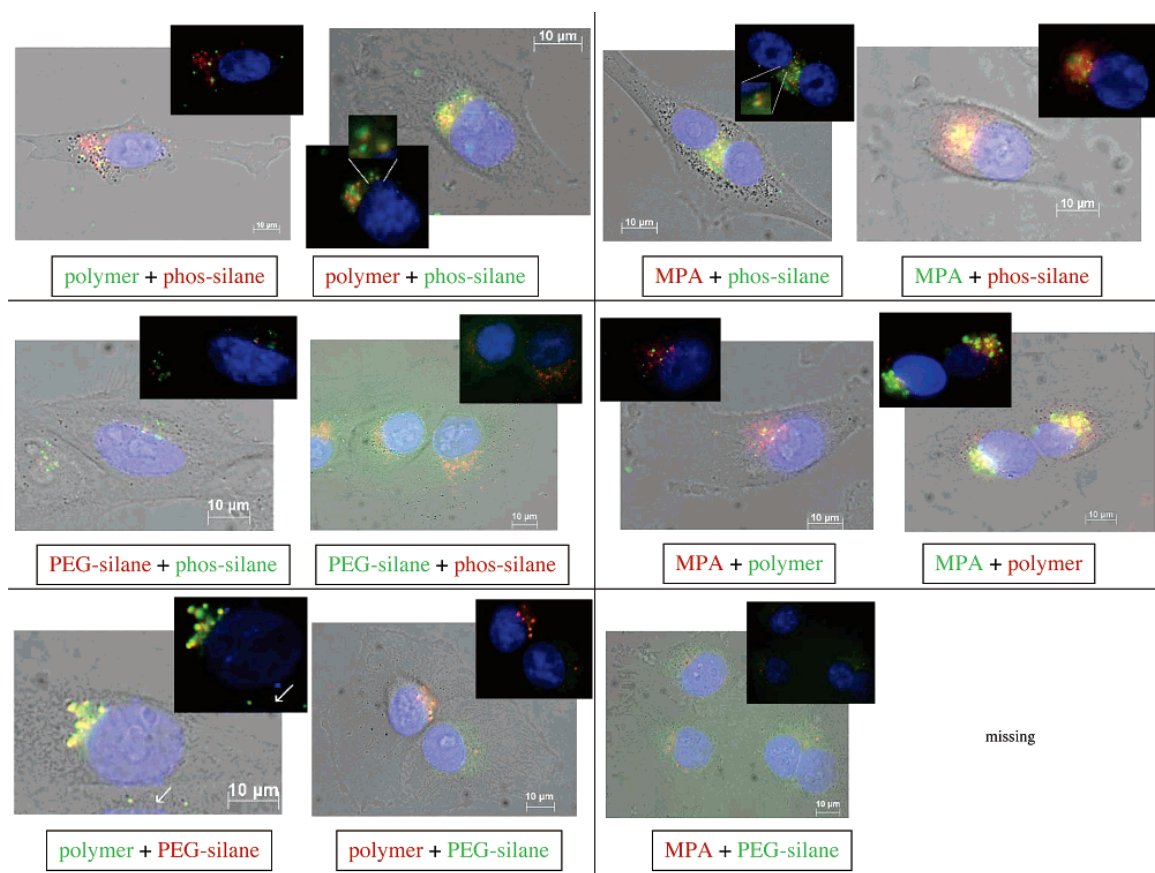


**Figure 1.** Red and green fluorescent CdSe/ZnS nanocrystals with different surface coatings have been ingested by MDA-MB-453S cells. Images of the cells were recorded with differential interference contrast (DIC) microscopy, and the nanocrystals and the DAPI-stained nuclei were recorded with fluorescence microscopy. For each experiment, always red and green fluorescent nanocrystals with different surface coatings were used so that their position within the cells can be resolved by their color of fluorescence. The DAPI-stained nuclei appear in blue. The big images contain the merged DIC and fluorescence images, the smaller images show only the fluorescence. All scale bars represent 10  $\mu$ m.

surface and not to the volume of the particles (i.e., to use the surface atom instead of the particle concentration). In Figure 2, the ratio  $R$  between the number of adherent cells after and before incubation with nanoparticles is shown. As reference, this ratio is shown also for the case of incubation with Cd salts.

As is seen in Figure 2a, the same characteristic tendency can be observed in Figure 2b. For low Cd concentrations,  $R$  adopts a constant value well below 1. With an increased number of Cd (surface) atoms,  $R$  first decreases to a minimum value and then increases again to a value that can be close to 1. Thus, we can divide these curves in three different concentration regions. In the first region, the concentration of Cd atoms is very low and cell viability tests showed that all attached cells were alive (see Supporting Information). Exchanging the serum-containing cell culture medium to serum-free SATO medium resulted in the detachment of a significant fraction of cells, i.e.,  $R < 1$  even for  $c(\text{Cd}) = 0$ . Therefore, we assume that there are no toxic effects due to Cd in the first region of low Cd concentration and that the value of  $R < 1$  can be simply explained by the effect of the SATO medium. In the second concentration

region,  $R$  drops. This means that more cells are detached due to the increased concentration of Cd (surface) atoms. Viability tests showed that attached cells in this region were still alive. For this reason we assume that in this region the viability of the cells is decreased due to poisoning by Cd<sup>2+</sup> ions in solution. Poisoned cells detach and therefore are not counted, which results in a decrease in  $R$ . We might refer to this effect as apoptosis. Upon further increment of the Cd concentration  $R$  raises again, even sometimes to values larger than the value for very low Cd concentrations. Viability tests showed that the attached cells in this region were dead. We therefore assume that the concentration of Cd<sup>2+</sup> ions in solution was sufficiently high to immediately poison the cells before they could start to detach. We might refer to this effect as necrosis. This differentiation is suggested by the detailed study of López et al., in which apoptosis and necrosis are reported to be the pathway for cell death for low and high cadmium concentrations, respectively.<sup>18</sup> The same authors also have shown that cytotoxic effects of Cd<sup>2+</sup> ions are more severe in serum-free medium compared to serum-containing medium. Therefore, our experimental conditions of serum-

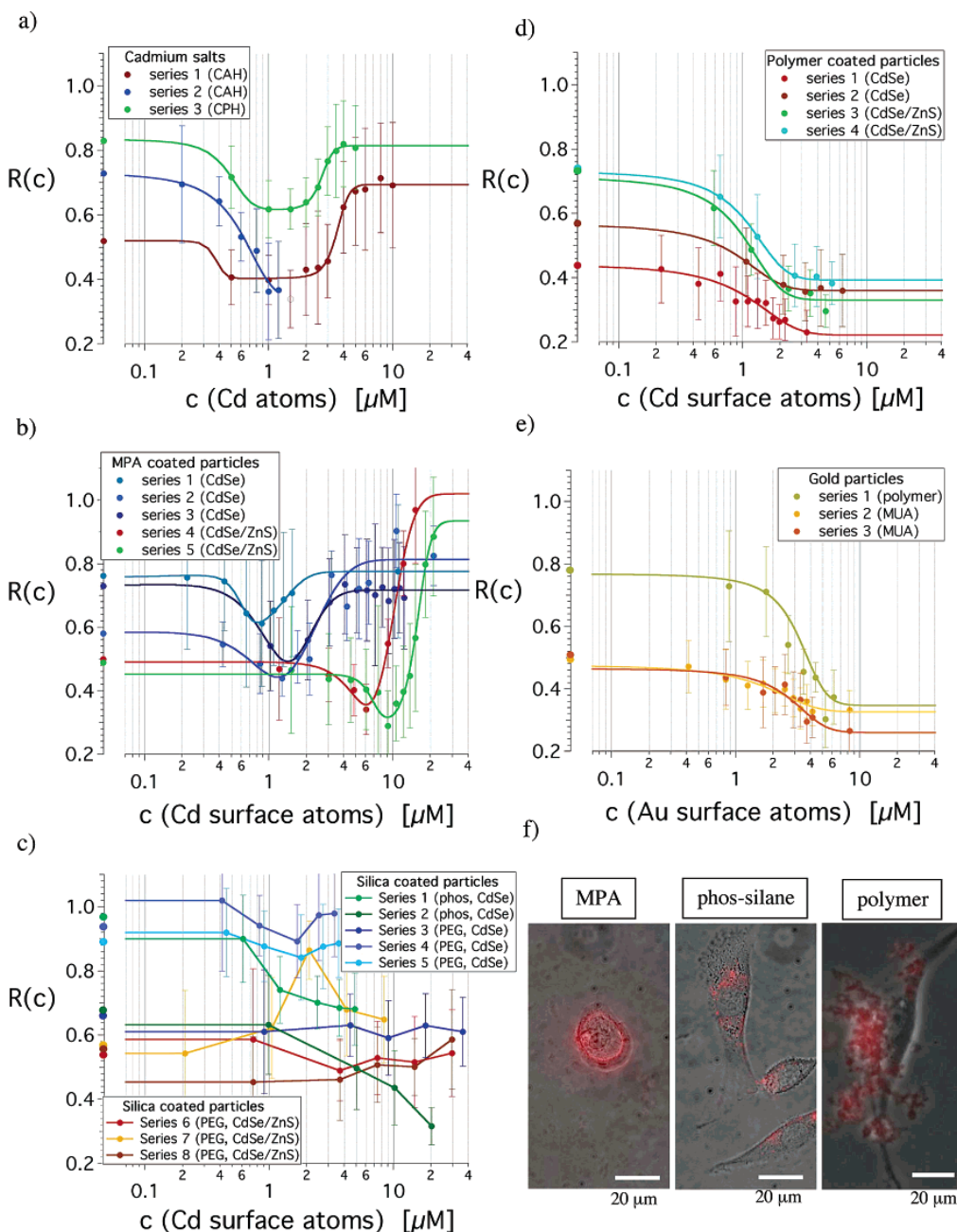


**Figure 2.** (a–e) Ratio  $R(c)$  of adherent cells after/before incubation with Cd salts, CdSe and CdSe/ZnS particles, and Au particles. NRK fibroblasts have been incubated with (a) cadmium acetate hydrate (CAH) and cadmium perchlorate hydrate (CPH), (b) mercaptopropionic acid coated CdSe- and CdSe/ZnS nanocrystals, (c) silica-coated CdSe and CdSe/ZnS nanocrystals, (d) polymer-coated CdSe and CdSe/ZnS nanocrystals, and (e) polymer and mercaptoundecanoic acid (MUA) coated Au nanocrystals. The Cd salts fully dissociate in aqueous solution. Therefore, in (a) the  $x$ -axis represents the concentration  $c$ (Cd atoms) of Cd atoms in solution. In (b–d) the  $x$ -axis represents the concentration  $c$ (Cd surface atoms) of all the Cd atoms that are on the surface of the nanoparticles (see the Supporting Information; there also the scaling factor between  $c$ (Cd surface atoms) and  $c$ (CdSe particles) is given), and in (e) the  $x$ -axis represents the concentration  $c$ (Au surface atoms) of all the Au atoms that are on the surface of the nanoparticles. In each case results are shown for at least three separate series. For each data point within each series around 20000 cells were analyzed. For practical reasons in each series only a limited number of data points could be recorded (due to the limited number of cells that could be analyzed under the same conditions). For this reason not all series span the whole concentration range. Therefore, to compare the separate series for similar tendencies, the data points of each series were fitted with a double sigmoidal curve:  $R(c) = a_1 - a_2/(1 + \exp((a_3 - c)/a_4)) + a_5/(1 + \exp(a_6 - c)/a_7))$  with seven fit parameters  $a_1$ – $a_7$ . The derived parameters for the respective series are enlisted in the table shown below. The value  $R(c = 0)$  represents the control sample to which no Cd, or CdSe or CdSe/ZnS nanoparticles have been added, but in which cell growth has been affected by changing the serum-containing medium to SATO medium. Due to a limited amount of nanocrystals, the accessible concentration range was limited. In

(a) and (b) clearly the double sigmoidal behavior of  $R(c)$  can be seen. As indicator for the concentration limit of the onset of cytotoxic effects we use the  $a_3$  parameter from the fits (a)  $\langle a_3 \rangle = <0.35, 0.60, 0.48> \mu\text{M} = 0.48 \pm 0.13 \mu\text{M}$ , (b)  $\langle a_3 \rangle = <0.58, 0.58, 0.79> \mu\text{M} = 0.65 \pm 0.12 \mu\text{M}$  for CdSe and (c)  $\langle a_3 \rangle = <4.9, 6.8> \mu\text{M} = 5.9 \pm 1.3 \mu\text{M}$  for CdSe/ZnS particles. In (c) no general tendency of  $R(c)$  can be seen for PEG-silica coated nanoparticles and  $R(c)$  seems to remain constant over the investigated concentration range. On the other hand,  $R(c)$  decreases for increased concentrations of phosphonate-silica coated nanoparticles. In (d) and (e) the shape of  $R(c)$  can be approximated with a sigmoidal curve with the  $a_3$  parameter from the fits as indicator for the concentration limit of the onset of cytotoxic effects: (d)  $\langle a_3 \rangle = <0.83, 0.77> = 0.80 \pm 0.04 \mu\text{M}$  for CdSe and  $\langle a_3 \rangle = <0.93, 1.0> \mu\text{M} = 0.98 \pm 0.07 \mu\text{M}$  for CdSe/ZnS particles, (e)  $\langle a_3 \rangle = 3.2 \mu\text{M}$  for polymer and  $\langle a_3 \rangle = <1.2, 2.7> \mu\text{M} = 2.0 \pm 1.1 \mu\text{M}$  for MUA-coated Au particles. In the case of CdSe and CdSe/ZnS particles  $\lambda_{\text{core}}$  denotes the wavelength of the first exciton peak of the CdSe core. In the case of Au and CdSe particles  $d_{\text{core}}$  denotes the diameter of the particles, and in the case of CdSe/ZnS particles  $d_{\text{core}}$  denotes the diameter of the CdSe core underneath the ZnS shell. The number of surface atoms per core in the case of CdSe, Au, and CdSe/ZnS particles is the number of Cd, Au, and Cd atoms on the surface of each CdSe particle, Au particle, and CdSe core underneath the ZnS shell, respectively. The terms  $a_1, a_2, a_3, a_4, a_5, a_6$ , and  $a_7$  are the resulting fit parameters for the function  $R(c) = a_1 - a_2/(1 + \exp((a_3 - c)/a_4)) + a_5/(1 + \exp(a_6 - c)/a_7))$ .  $R(c)$  describes a double sigmoidal curve. Sigmoid curves are typically used in toxicology to describe dose-response functions. All values of one sigmoidal curve are between two asymptotes, determined by  $a_1$  and  $a_1 + a_2$ . The parameter  $a_2/(4a_4)$  controls the slope in terms of a rate at the inflection point  $a_3$ , which is the response halfway between the baseline and the maximum, also called EC<sub>50</sub>. A double sigmoidal curve is the superposition of two single sigmoidal curves. (f) Overlay of phase-contrast and fluorescence image for NRK cells incubated for 48 h with CdSe/ZnS nanocrystals. The images of these cells correspond to the high concentration range shown in (b), (c), and (d). For MPA-coated CdSe/ZnS particles, cells incubated at high particle concentrations are dead, while the cell debris remains on the substrate. For silane coated particles no effect of the particles on the cells can be observed; even for high particle concentrations, the particles are ingested and stored around the nucleus and cells remain adherent. Polymer-coated particles at high concentrations tend to precipitate on the cell surface. Most cells detach from the surface, while the few still adherent cells are alive. Clearly different behavior dependent on the particle surface compared to the low concentration regime shown in Figure 1 can be seen.

fig.	series	salt/type of nanopart.			number of surface atoms per core							
			$\lambda_{\text{core}}$ [nm]	$d_{\text{core}}$ [nm]		$a_1$	$a_2$	$a_3$ [ $\mu\text{M}$ ]	$a_4$	$a_5$	$a_6$ [ $\mu\text{M}$ ]	$a_7$
a	1	CAH	-	-	-	0.52	0.12	0.35	0.042	0.29	3.6	0.43
a	2	CAH	-	-	-	0.76	0.42	0.60	0.22	0	-	-
a	3	CPH	-	-	-	0.61	-0.22	0.48	-0.11	0.20	2.7	0.31
b	1	CdSe	560	3.3	110	0.75	0.22	0.58	0.083	0.25	1.1	0.37
b	2	CdSe	599	4.5	213	-0.049	0.88	0.58	0.37	1.7	0.22	1.1
b	3	CdSe	599	4.5	213	0.52	1.6	0.79	0.39	1.8	0.80	0.63
b	4	CdSe/ZnS	508	2.4	61	0.47	0.60	4.9	1.4	1.2	8.5	2.4
b	5	CdSe/ZnS	508	2.4	61	0.45	0.18	6.8	0.88	0.66	16	2.1
c	1	CdSe (phos)	560	3.3	110	-	-	-	-	-	-	-
c	2	CdSe (phos)	560	3.3	110	-	-	-	-	-	-	-
c	3	CdSe (PEG)	560	3.3	110	-	-	-	-	-	-	-
c	4	CdSe (PEG)	560	3.3	110	-	-	-	-	-	-	-
c	5	CdSe (PEG)	560	3.3	110	-	-	-	-	-	-	-
c	6	CdSe/ZnS (PEG)	560	3.3	110	-	-	-	-	-	-	-
c	7	CdSe/ZnS (PEG)	510	2.4	62	-	-	-	-	-	-	-
c	8	CdSe/ZnS (PEG)	510	2.4	62	-	-	-	-	-	-	-
d	1	CdSe	560	3.3	110	0.51	-0.29	0.83	0.73	0	-	-
d	2	CdSe	599	4.5	213	0.61	-0.25	0.77	0.51	0	-	-
d	3	CdSe/ZnS	599	4.5	213	0.76	-0.43	0.93	0.45	0	-	-
d	4	CdSe/ZnS	510	2.4	62	0.77	-0.38	1.0	0.48	0	-	-
e	1	Au (polymer)	-	4.6	831	0.78	-0.43	3.22	0.93	0	-	-
e	2	Au (MUA)	-	4.6	831	0.53	-0.20	1.2	1.2	0	-	-
e	3	Au (MUA)	-	4.6	831	0.48	-0.22	2.7	1.1	0	-	-

free culture should allow for a very sensitive detection of cytotoxic effects.

In Figure 2a the concentration of Cd atoms is equal to the concentration of free Cd<sup>2+</sup> ions in solution because Cd was administered as salt. In Figure 2b the concentration of Cd is given as the concentration of Cd atoms on the surface of CdSe particles or on the surface of the CdSe core below the ZnS shell of CdSe/ZnS particles. Taking into account the findings of Derfus et al.,<sup>29</sup> who have shown by inductively coupled plasma optical emission spectroscopy (ICP/OES) measurements that free Cd<sup>2+</sup> ions are released by CdSe particles, we can assume that a part of the Cd surface atoms

is released to solution as Cd<sup>2+</sup> ions, which are, according to this study, primarily responsible for cytotoxic effects. Our data suggest that, for our conditions (serum-free medium, 48 h incubation time, NRK cells), toxic effects of Cd<sup>2+</sup> ions start at concentrations of about  $c(\text{Cd atoms}) = 0.48 \pm 0.13 \mu\text{M}$  (see Figure 2a). For CdSe and CdSe/ZnS particles, toxic effects start at concentrations of about  $c(\text{Cd surface atoms}) = 0.65 \pm 0.12 \mu\text{M}$  and  $5.9 \pm 1.3 \mu\text{M}$  Cd surface atoms (see Figure 2b). Within the hypothesis that Cd<sup>2+</sup> ions released into solution are the main source for cytotoxic effects, a comparison of these values suggests that a significant amount of the Cd atoms on the surface of CdSe particles is released

as  $\text{Cd}^{2+}$  ions into solution ( $\approx 0.48 \mu\text{M}/0.65 \mu\text{M} \approx 75\%$  as a very rough estimate), but that the mantling of CdSe with a ZnS shell drastically reduces this value to a rough estimate of  $0.48 \mu\text{M}/5.9 \mu\text{M} \approx 8\%$ . Here we want to point out again that both the CdSe and the CdSe/ZnS particles had the same surface chemistry, a ligand shell of mercaptopropionic acid. Therefore, this direct comparison is another indicator that in this case indeed the release of  $\text{Cd}^{2+}$  and not eventual effects of the surface chemistry is responsible for the cytotoxic effects.

We also tested the other constituent of mercaptocarbonic acid coated CdSe and CdSe/ZnS nanoparticles for cytotoxic effects. No cytotoxic effects of  $\text{Se}^{2-}$  (selenious acid) and  $\text{Zn}^{2+}$  (zinc chloride) ions could be observed up to concentrations of  $40 \mu\text{M}$  (we were not able to investigate higher ion concentrations). The ligands used to stabilize the particles in water, mercaptopropionic acid (MPA), led to cell detachment at concentrations between 1 and  $10 \text{ mM}$  (the same value was found for an alternative ligand, mercaptoacetic acid). Compared to the onset of cytotoxic effect of  $\text{Cd}^{2+}$  ions at concentrations of about  $0.48 \mu\text{M}$ , this suggests that cadmium is the main source of cytotoxic effects of mercaptopropionic acid stabilized CdSe and CdSe/ZnS nanocrystals (at most, one MPA molecule can be attached per Cd surface atom).

Instead of coating the nanocrystals with a monolayer ligand shell of mercaptopropionic acid, more stable coatings are also possible. First, we investigated the effect of embedding nanocrystals in a silica shell, which comprises many layers of cross-linked silane molecules. From Figure 2c it can be seen that a PEG-silica shell basically prevented toxic effects of particles on cells in the investigated concentration range. Even for PEG-silica coated CdSe nanoparticles, no clear toxic effects up to Cd surface atom concentrations of  $30 \mu\text{M}$  were found. On the other hand,  $R(c)$  decreased upon increasing the concentration of phosphonate-silica coated CdSe nanoparticles. Microscopy images showed reduced particle uptake for PEG-silica coated particles, whereas phosphonate-silica coated particles were ingested by the cells and stored around the nucleus even for high Cd concentrations (Figures 1 and 2f). Viability tests showed that as well for PEG-silica as for phosphonate-silica coated particles within the whole concentration region, all adherent cells were living. For phosphonate-silica coated CdSe particle  $R(c)$  started to decrease only at higher Cd surface atom concentrations than MPA coated CdSe particles. Therefore, we conclude that the cross-linked silica shell around the particles in general is a good barrier against the release of  $\text{Cd}^{2+}$  ions from the particle surface. In addition, embedding PEG-groups in the silica shell reduced the uptake of the particles (see microscopy images Figure 1), which resulted in reduced cytotoxicity (see the  $R(c)$  curves shown in Figures 2b and 2c). Since silica shells embedding PEG and phosphonate groups should prevent the release of  $\text{Cd}^{2+}$  ions, in the same way we can further conclude that not only is the absolute concentration of  $\text{Cd}^{2+}$  ions responsible for cytotoxic effects but also the location where the  $\text{Cd}^{2+}$  ions are released is very important. If particles are ingested by cells,  $\text{Cd}^{2+}$  can be released directly inside cells (e.g., for phosphonate-silica coating), which seems to

cause more severe cytotoxic effects than release of  $\text{Cd}^{2+}$  outside cells (e.g., for PEG-silica coating).

For polymer-coated CdSe and CdSe/ZnS nanocrystals, a gradual decrease of  $R$  upon increased Cd concentration was observed (Figure 2d). Viability tests showed that all adherent cells were living for all Cd surface atom concentrations, although there were basically no adherent cells left in the case of high Cd concentrations (right part of the curve in Figure 2d). Phase contrast and fluorescence microscopy analysis showed that, in the case of high concentrations, clouds of nanoparticles precipitated on the surface of the cells and on the cell culture substrate (Figure 2f). In the case of low concentrations no precipitation effects were observed, and it is important to point out that under these conditions polymer-coated particles were ingested by cells similar to silanized and mercaptopropionic acid coated ones (Figure 1). Reduction in the number of adherent cells already started at Cd surface atom concentrations of  $0.80 \pm 0.04 \mu\text{M}$  for CdSe and  $0.98 \pm 0.07 \mu\text{M}$  for CdSe/ZnS particles.

Most striking, for inert polymer-coated Au nanoparticles the same effects were observed as for polymer-coated CdSe and CdSe/ZnS nanoparticles (Figure 2e). This excludes the effect of  $\text{Cd}^{2+}$  ion release as the only source for poisoning of the cells in the case of polymer-coated particles. We therefore conclude that in the case of our polymer-coated particles the precipitation of the particles on the cells and not the release of  $\text{Cd}^{2+}$  atoms is the major factor for cell impairment. Again, we have to recall that for low particle concentration regular particle uptake by the cells has been observed and that therefore our polymer-coated particles are still useful for cellular labeling. Recently, other groups have reported a modified polymer coating procedure in which polyethylene groups are incorporated in the polymer shell,<sup>10</sup> which should make these particles more stable against precipitation. Also, for other systems such as  $\text{C}_{60}$  fullerenes, it has been observed that cytotoxicity correlates with water solubility and thus with the surface chemistry of the particles.<sup>43</sup>

*Impairment of Currents through Ion Channels upon Incubation of Cells with Nanocrystals.* Two cell lines (RBL and CHO) were investigated regarding changes in their morphology and their electrophysiological properties upon incubation with nanocrystals. The CHO cell line was stably transfected to express the hERG channel, and the used RBL cell line endogenously expressed an inward rectifying potassium channel. For CdSe/ZnS particle concentrations in the nM range and incubation times of up to 2 days in serum-containing medium, no morphological changes of the cells were identified using high magnification light microscopy (see Supporting Information), although uptake of the nanocrystals by the cells was clearly verified by fluorescence microscopy (Figure 3a). Patch-clamp recordings under identical experimental circumstances of untreated and incubated cells revealed no changes of ion channel function and characteristic electrophysiological properties of the cells. In Figures 3b and 3c, currents through the ion channels of RBL and CHO cells before and after incubation with nanocrystals are displayed. As ion channels play an important role in the

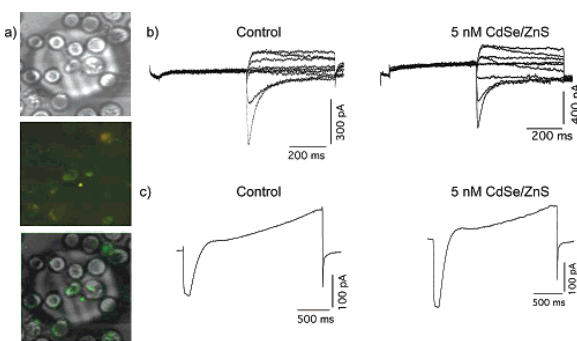


**Figure 3.** (a) RBL cells after 4 h incubation with  $c(\text{CdSe/ZnS particles}) = 10 \text{ nM}$  MPA-coated CdSe/ZnS particles on the patch-clamp chip (wavelength of the absorption peak of the CdSe core  $\lambda = 508 \text{ nm}$ , corresponding to a CdSe core diameter of  $d = 2.4 \text{ nm}$ ; 61 Cd surface atoms per nanoparticle). The bright field and fluorescence image as well as the overlay of both of them are shown. (b) hERG currents as obtained from one nontreated CHO cell and from one cell incubated 3 h in 5 nM MPA-coated CdSe/ZnS nanocrystals (wavelength of the absorption peak of the CdSe core  $\lambda = 508 \text{ nm}$ , corresponding to a CdSe core diameter of  $d = 2.4 \text{ nm}$ ; 61 Cd surface atoms per nanoparticle). (c) Endogenous  $\text{K}^+$  inward rectifier currents of RBL cells without treatment and 3 h after incubation in 5 nM MPA-coated CdSe/ZnS nanocrystals (wavelength of the absorption peak of the CdSe core  $\lambda = 508 \text{ nm}$ , corresponding to a CdSe core diameter of  $d = 2.4 \text{ nm}$ ; 61 Cd surface atoms per nanoparticle).

cells vitality and function, their characteristics and functionality are a subtle indicator of the condition and viability of the cells. We suggest that for our experimental conditions for concentrations sufficient for CdSe/ZnS fluorescence labeling of cells no impairment of the ion channels of the investigated cells is observable.

**Conclusions.** In addition to a previous study,<sup>29</sup> we have determined the concentration limits of mercaptopropionic acid coated CdSe and CdSe/ZnS nanocrystals in a more detailed and absolute way. Poisoning of NRK cells due to the release of  $\text{Cd}^{2+}$  ions starts at concentrations of  $0.65 \pm 0.12 \text{ } \mu\text{M}$  and  $5.9 \pm 1.3 \text{ } \mu\text{M}$  of surface Cd atoms for mercaptopropionic acid coated CdSe and CdSe/ZnS particles, respectively (Figure 2b). In agreement with previous studies<sup>29</sup> our data show that coating of CdSe particles with a ZnS shells increases the critical concentration up to which no toxic effects can be observed by almost a factor of 10. Since a ligand shell of mercaptopropionic acid around the particles is not very stable, such a shell cannot prevent the release of  $\text{Cd}^{2+}$  ions from the particle surface. On the other hand, embedding the particles in a stable ligand shell of cross-linked silica molecules dramatically reduces the release of  $\text{Cd}^{2+}$  ions. In the case of PEG-silica coated CdSe and CdSe/ZnS particles we could not observe any toxic effect up to concentrations of  $30 \text{ } \mu\text{M}$  Cd surface atoms (Figure 2c). We ascribe this to the fact of reduced uptake of these particles by cells. For polymer-coated nanocrystals, an additional pathway of poisoning was observed. For polymer-coated CdSe and CdSe/ZnS nanocrystals, cytotoxic effects started at concentrations of approximately  $0.80 \pm 0.04 \text{ } \mu\text{M}$  and  $0.98 \pm 0.07 \text{ } \mu\text{M}$  Cd surface atoms, respectively. These values seem to be independent of an optional ZnS shell around the

CdSe particles. Cytotoxic effects for polymer-coated particles start at slightly higher concentrations than for MPA-coated CdSe, but already at significantly lower concentrations than for MPA-coated CdSe/ZnS particles. These data suggest that the polymer shell rather than an MPA shell is a better diffusion barrier against the release of  $\text{Cd}^{2+}$  ions from CdSe surfaces. On the other hand, if  $\text{Cd}^{2+}$  is drastically hindered by a ZnS shell around the CdSe particles, cytotoxic effects are more severe for polymer- than for MPA-coated particles. This effect could be attributed to a precipitation of the polymer-coated particles on the cell surface (Figure 2f).

We conclude that, in addition to the release of  $\text{Cd}^{2+}$  ions from the surface of CdSe or CdSe/ZnS nanoparticles, cells can also be impaired if nanoparticles precipitate on the cell surface. Furthermore, cytotoxic effects are different in the case that particles are ingested by the cells compared to the case that particles are just present in the medium surrounding the cells. From this point of view it is important to correlate any study on the cytotoxicity of particles with a detailed microscopy analysis about the pathway of particle uptake. In accordance with another study,<sup>31</sup> our data indicate a massive influence of the surface chemistry of the particles on their cytotoxic behavior in addition to the release of toxic molecules. Certainly many aspects of particle cytotoxicity still have to be investigated, since effects strongly depend on many parameters such as surface chemistry, type of the cell line, incubation time, serum-containing/free medium, etc. Clearly, Cd-containing nanoparticles cannot be considered as 100% biocompatible, but depending on the experimental situation conditions can be found under which no cytotoxic effects occur.

**Acknowledgment.** This work was supported in part by the Emmy Noether Program of the Deutsche Forschungsgemeinschaft DFG (W.J.P.), the Volkswagen Stiftung (W.J.P.), the Sonderforschungsbereich SFB 486 of the DFG (H.E.G.), and the Excellence Network NanoBioTechnology ENNAB (W.J.P., N.F.). The authors are grateful to Michael George, Andrea Brüggemann, and Thomas Nicolaus for excellent technical support, and to Dr. Liberato Manna for helpful discussions.

**Supporting Information Available:** Details of Materials and Methods used in the study. This material is available free of charge via the Internet at <http://pubs.acs.org>.

## References

- Wu, M. X.; Liu, H.; Liu, J.; Haley, K. N.; Treadway, J. A.; Larson, J. P.; Ge, N.; Peale, F.; Bruchez, M. P. *Nature Biotechnol.* **2003**, *21*, 41–46.
- Dahan, M.; Levi, S.; Luccardini, C.; Rostaing, P.; Riveau, B.; Triller, A. *Science* **2003**, *302*, 442–445.
- Lidke, D. S.; Nagy, P.; Heintzmann, R.; Arndt-Jovin, D. J.; Post, J. N.; Grecco, H. E.; Jares-Erijman, E. A.; Jovin, T. M. *Nature Biotechnol.* **2004**, *22*, 198–203.
- Parak, W. J.; Boudreau, R.; Gros, M. L.; Gerion, D.; Zanchet, D.; Michelet, C. M.; Williams, S. C.; Alivisatos, A. P.; Larabell, C. A. *Adv. Mater.* **2002**, *14*, 882–885.
- Roth, J. *Histochem. Cell Biol.* **1996**, *106*, 1–8.
- Sanford, J. C.; Smith, F. D.; Russell, J. A. *Methods Enzymol.* **1993**, *217*, 483–509.
- Schulze, E.; Ferrucci, J. T.; Poss, K.; Lapointe, L.; Bogdanova, A.; Weissleder, R. *Invest. Radiol.* **1995**, *30*, 604–610.

(8) Pankhurst, Q. A.; Connolly, J.; Jones, S. K.; Dobson, J. *J. Phys. D* **2003**, *36*, R167–R181.

(9) Jordan, A.; Scholz, R.; Wust, P.; Fahling, H.; Felix, R. *J. Magn. Magn. Mater.* **1999**, *201*, 413–419.

(10) Ballou, B.; Lagerholm, B. C.; Ernst, L. A.; Bruchez, M. P.; Waggoner, A. S. *Bioconjugate Chem.* **2004**, *15*, 79–86.

(11) Kim, S.; Lim, Y. T.; Soltesz, E. G.; Grand, A. M. D.; Lee, J.; Nakayama, A.; Parker, J. A.; Mihaljevic, T.; Laurence, R. G.; Dor, D. M.; Cohn, L. H.; Bawendi, M. G.; Frangioni, J. V. *Nature Biotechnol.* **2004**, *22*, 93–97.

(12) Alivisatos, A. P. *Sci. Am.* **2001**, *285*(September), 59–65.

(13) Service, R. F. *Science* **2000**, *290*, 1526–1527.

(14) Kondoh, M.; Araragi, S.; Sato, K.; Higashimoto, M.; Takiguchi, M.; Sato, M. *Toxicol.* **2002**, *170*, 111–117.

(15) Limaye, D. A.; Shaikh, Z. A. *Toxicol. Appl. Pharmacol.* **1999**, *154*, 59–66.

(16) Rikans, L. E.; Yamano, T. *J. Biochem. Molec. Toxicol.* **2000**, *14*, 110–117.

(17) Santone, K. S.; Acosta, D.; Bruckner, J. V. *J. Toxicol. Environ. Health* **1982**, *10*, 169–177.

(18) López, E.; Figueroa, S.; Oset-Gasque, M. J.; Gonzalez, M. P. *Br. J. Pharmacol.* **2003**, *138*, 901–911.

(19) Goyer, R. A. *Am. J. Clin. Nutr.* **1995**, *61*, 646s–650s.

(20) Ghitescu, L.; Fixman, A. *J. Cell Biol.* **1984**, *99*, 639–647.

(21) Jordan, A.; Scholz, R.; Wust, P.; Schirra, H.; Schiestel, T.; Schmidt, H.; Felix, R. *J. Magn. Magn. Mater.* **1999**, *194*, 185–196.

(22) Wilhelm, C.; Billotey, C.; Roger, Pons, J. N.; Bacri, J.-C.; Gazeau, F. *Biomat.* **2003**, *24*, 1001–1011.

(23) Kloepfer, J. A.; Mielke, R. E.; Wong, M. S.; Nealson, K. H.; Stucky, G.; Nedeau, J. L. *Appl. Environ. Microbiol.* **2003**, *69*, 4205–4213.

(24) Lam, C.-W.; James, J. T.; McCluskey, R.; Hunter, R. L. *Toxicol. Sci.* **2004**, *77*, 126–134.

(25) Warheit, D. B.; Laurence, B. R.; Reed, K. L.; Roach, D. H.; Reynolds, G. A. M.; Webb, T. R. *Toxicol. Sci.* **2004**, *77*, 117–125.

(26) Videira, M. A.; Botelho, M. F.; Santos, A. C.; Gouveia, L. F.; Lima, J. J. P. d.; Almeida, A. J. *J. Drug. Target.* **2002**, *10*, 607–613.

(27) Artelt, S.; Creutzberg, O.; Kock, H.; Levsen, K.; Nachtigall, D.; Heinrich, U.; Ruhle, T.; Schlogl, R. *SCIENCE OF THE TOTAL ENVIRONMENT* **1999**, *228*, 219–242.

(28) Kanitsar, K.; Koellensperger, G.; Hann, S.; Limbeck, A.; Puxbaum, H.; Stinger, G. *J. Anal. Atomic Spectrom.* **2003**, *18*, 239–246.

(29) Derfus, A. M.; Chan, W. C. W.; Bhatia, S. N. *Nano Lett.* **2004**, *4*, 11–18.

(30) Shiohara, A.; Hoshino, A.; Hanaki, K.; Suzuki, K.; Yamamoto, K. *Microbiol. Immunol.* **2004**, *48*, 669–675.

(31) Hoshino, A.; Fujioka, K.; Oku, T.; Suga, M.; Sasaki, Y. F.; Ohta, T.; Yasuhara, M.; Suzuki, K.; Yamamoto, K. *Nano Lett.* **2004**, *4*, 2163–2169.

(32) Reiss, P.; Bleuse, J.; Pron, A. *Nano Lett.* **2002**, *2*, 781–784.

(33) Dabbousi, B. O.; Rodriguez-Viejo, J.; Mikulec, F. V.; Heine, J. R.; Mattoussi, H.; Ober, R.; Jensen, K. F.; Bawendi, M. G. *J. Phys. Chem. B* **1997**, *101*, 9463–9475.

(34) Fink, J.; Kiely, C. J.; Bethell, D.; Schiffrian, D. *J. Chem. Mater.* **1998**, *10*, 922–926.

(35) Gerion, D.; Pinaud, F.; Williams, S. C.; Parak, W. J.; Zanchet, D.; Weiss, S.; Alivisatos, A. P. *J. Phys. Chem. B* **2001**, *105*, 8861–8871.

(36) Parak, W. J.; Gerion, D.; Zanchet, D.; Woerz, A. S.; Pellegrino, T.; Michelet, C.; Williams, S. C.; Seitz, M.; Bruehl, R. E.; Bryant, Z.; Bustamante, C.; Bertozzi, C. R.; Alivisatos, A. P. *Chem. Mater.* **2002**, *14*, 2113–2119.

(37) Pellegrino, T.; Manna, L.; Kudera, S.; Liedl, T.; Koktysh, D.; Rogach, A. L.; Keller, S.; Rädler, J.; Natlie, G.; Parak, W. J. *Nano Lett.* **2004**, *4*, 703–707.

(38) Kirchner, C.; George, M.; Stein, B.; Parak, W. J.; Gaub, H. E.; Seitz, M. *Adv. Funct. Mater.* **2002**, *12*, 266–276.

(39) Barnes, D.; Sato, G. *Anal. Biochem.* **1980**, *102*, 255–270.

(40) Fertig, N.; Blick, R. H.; Behrends, J. C. *Biophys. J.* **2002**, *82*, 3056–3062.

(41) Brueggemann, A.; George, M.; Kla, M.; Beckler, M.; Steindl, J.; Behrends, J. C.; Fertig, N. *Curr. Drug Discovery Technol.* **2004**, *1*, 91–96.

(42) Rosenthal, S. J.; Tomlinson, I.; Adkins, E. M.; Schroeter, S.; Adams, S.; Swafford, L.; McBride, J.; Wang, Y.; DeFelice, L. J.; Blakely, R. D. *J. Am. Chem. Soc.* **2002**, *124*, 4586–4594.

(43) Sayes, C. M.; Fortner, J. D.; Guo, W.; Lyon, D.; Boyd, A. M.; Ausman, K. D.; Tao, Y. J.; Sitharaman, B.; Wilson, L. J.; Hughes, J. B.; West, J. L.; Colvin, V. L. *Nano Lett.* **2004**, *4*, 1881–1887.

NL047996M

### Supplementary Information

#### Cytotoxicity of colloidal CdSe and CdSe/ZnS nanoparticles

Christian Kirchner<sup>1</sup>, Tim Liedl<sup>1</sup>, Stefan Kudera<sup>1</sup>, Teresa Pellegrino<sup>1</sup>, Almudena Muñoz Javier<sup>1</sup>, Hermann E. Gaub<sup>1</sup>, Sonja Stölzle<sup>2</sup>, N. Fertig<sup>2</sup>, Wolfgang J. Parak<sup>1,\*</sup>

<sup>1</sup> Center for Nanoscience, Ludwig Maximilians Universität München, Germany

<sup>2</sup> Nanon Technologies GmbH, Pettenkoferstr. 12, 80336 Munich, Germany

\*To whom correspondence should be addressed:

Dr. Wolfgang J. Parak

Center for Nanoscience

Amalienstrasse 54

80799 München

Germany

Wolfgang.Parak@physik.uni-muenchen.de

#### **(I) Synthesis of the nanoparticles**

The synthesis of hydrophobic CdSe, CdSe/ZnS, and Au nanoparticles is described in detail in the supporting information of a previous paper<sup>1</sup>. We have followed these protocols without change. The hydrophobic particles were transferred to aqueous solution using three different protocols.

- 1) The silanization of CdSe/ZnS particles with phosphonate silane has been described by Gerion et al.<sup>2,3</sup> and the silanization of CdSe/ZnS particles with PEG silane has been performed as reported by Parak et al.<sup>3</sup>.
- 2) The polymer coating of Au and CdSe/ZnS particles has been described in detail by Pellegrino et al.<sup>1</sup>. We have followed these protocols without change. The same protocol was applied for the polymer coating of CdSe particles.
- 3) We have changed our previous protocol in which the transfer of particles to aqueous solution by ligand exchange with mercaptocarbonic acids is described<sup>2</sup>.

The protocols for ligand exchange with mercaptocarbonic acids as used in this study are reported below:

Coating of CdSe and CdSe/ZnS particles with mercaptopropionic acid

First, CdSe or CdSe/ZnS particles (as prepared in organic solvent as described above) were washed one time by precipitating them with methanol and redissolving them in chloroform. The particles were then precipitated by the addition of methanol and the sample was centrifuged and the supernatant discarded. The ligand exchange on the semiconductor particles was carried out by taking the wet precipitate (approximately 10 nmol of red fluorescent particles, or 40 nmol of green fluorescent particles) and adding 2 ml of anhydrous DMF (N,N-Dimethylformamide, purchased from Sigma, #22,705-6). A homogeneous distribution of the particles, which did not dissolve, was established by vortexing the sample. Then, equal molar amounts of mercaptopropionic acid (200  $\mu$ l, purchased from Sigma, #M580-1) and 2-mercaptopropanoic acid (160  $\mu$ l, purchased from Sigma, #56,867-2) were added. After vortexing the solution turned transparent in the case of CdSe/ZnS particles. The CdSe cores did not produce a clear solution. This product was stored in the dark at room temperature until actual experiments with the particles were scheduled. Then, the particles were precipitated by adding 2 ml of deionized water and centrifugation. The particles were resuspended in deionized water. The addition of 50-100  $\mu$ l Base (TMAH dissolved in methanol in a ratio of 1:3, tetramethylammonium hydroxide pentahydrate from Sigma, #T7505) yielded a clear solution with a pH of 10. The solution was then run through two NAP 25 gel columns (purchased from Amersham Biosciences, #17-0852-02) loaded with deionized water in order to neutralize the pH and to clean the product of remaining reactants.

Coating of Au particles with mercaptoundecanoic acid

Tetraoctylammonium bromide stabilized Au particles dissolved in toluene have been prepared according to standard protocols<sup>4,7</sup>. We have followed the detailed description of the gold synthesis reported by Pellegrino et al.<sup>1</sup>. In this report the tetraoctylammonium bromide ligands were then replaced by dodecanethiol ligands and the particles remained hydrophobic. Here we performed a ligand exchange to mercaptoundecanoic acid, which resulted in hydrophilic and thus water-soluble particles. For the ligand exchange with mercaptoundecanoic acid we followed the protocol of Mayya et al.<sup>8</sup>.

100 ml of tetraoctylammonium bromide stabilized Au particles dissolved in toluene as prepared by Pellegrino et al.<sup>1</sup> were heated to 65°C. A hot solution (65°C) of 5.8 g mercaptoundecanoic acid (MUA, Sigma #45.056-1) dissolved in 10 ml toluene was added. This corresponds to a thirty-fold molar excess of MUA over the initial amount of gold. The solution was kept at 65°C for 1 hour. Then it was stirred overnight at room temperature. The day after a precipitate had formed. The solution was then centrifuged, and the translucent supernatant was discarded. The precipitate was dissolved in 0.1M TRIS buffer and sonicated to obtain a homogeneous, clear, violet solution of mercaptoundecanoic acid stabilized water-soluble Au-particles.

**(II) Calculation of the number of surface atoms per nanoparticle and of the nanoparticle / surface atom concentrations**

1) Calculation of the number of Cd surface atoms per CdSe particle

Given a certain radius of the particles, the number of surface atoms could be calculated by comparing the spherical particles with a small, faceted nanorod with the same surface. We assume, that we find the same number of atoms on a rod as we would find on a spherical particle. A rod has six lateral and two basal facets, see Figure S1a. On the lateral (non-polar) facets of the rods one finds one Cd-Atom per  $30\text{ \AA}^2$ . This can be understood by looking at a unit cell of a wurtzite structure, see Figure S1b. The unit cell has the same shape as the rod; especially it also has the six lateral facets. Each of these facets contains one Cd-Atom. The area of one of these facets is  $a \cdot c$ , with  $a$  and  $c$  being the lattice constants of the CdSe-wurtzite structure. With  $a = 4.28\text{ \AA}$  and  $c = 7.01\text{ \AA}$ , one obtains  $30.00\text{ \AA}^2$  for the area occupied by one Cd-atom on the lateral facets. A rod can be constructed by adding an adequate number of layers of atoms onto one core unit cell.

On the hexagonal basal facets of the unit cell there are three atoms. This facet can be split into six equivalent triangles, each of them with an area of  $1/2 \cdot 3^{1/2}/2 \cdot a^2$ . So the total area per atom on this facet can be calculated to  $15.86\text{ \AA}^2$ . However, due to the intrinsic asymmetry of the wurtzite structure, and due to the growth mechanism, the (0001)-facet is only occupied by Cd atoms, whereas the opposing (000-1)-facet is composed exclusively of Se-atoms<sup>9</sup>, so that the overall density of atoms of one species on the basal facets, is one per  $31.72\text{ \AA}^2$ , which is roughly the same as on the lateral facets.

As the lateral facets mainly constitute the surface of the rod, a density of 1 atom per  $30\text{ \AA}^2$  surface area is a good approximation. Overall the number of Cd-atoms on the surface of a CdSe particle can be calculated as  $N = 4 \pi r^2/30\text{ \AA}^2$ , whereby  $r$  is the radius of the CdSe particle.

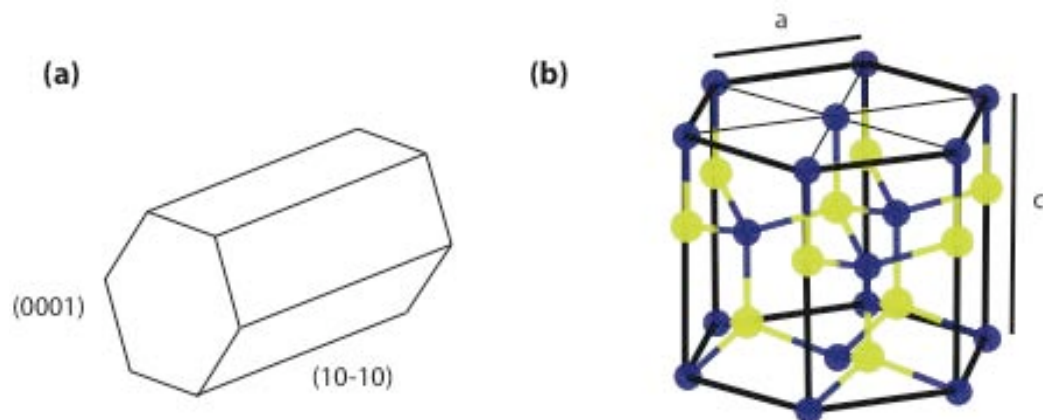


Figure S1: a) A schematic drawing of a rod. b) A unit cell of the wurtzite structure. Cd atoms are drawn in blue, Se atom in yellow. In each of the lateral facets there is one cadmium atom and one Selenium atom. Inner atoms are screened by atoms of the other species. From this picture one can also understand the difference between the two basal facets (0001) and (000-1). In this figure the Cd atoms have three bonds upwards, the selenium atoms only one. In the other direction the situation is contrary. From this derives the chemical difference of the two facets.

2) Calculation of the number of Cd atoms on the surface of the CdSe core of CdSe/ZnS particles

Since we identified Cd as the main source for cytotoxic effects, the ZnS shell around the CdSe cores rather has to be considered as a protection shell preventing the release of Cd atoms from the CdSe core than as an additional source of contamination. For this reason we consider the Cd atoms on the surface of the CdSe particle core as surface atoms, which are shielded by the ZnS shell. Thus, the number of Cd surface atoms for one CdSe/ZnS particle is  $N = 4 \pi r^2 / 30 \text{ \AA}^2$  (analogous to CdSe particles), whereby  $r$  is the radius of the CdSe core and not of the whole CdSe/ZnS particle.

3) Calculation of the number of Au atoms on the surface of Au particles

To estimate the number of atoms on the surface of Au particles a method similar to that used for the estimation of surface atoms of the CdSe particles is employed. First, we calculate a mean surface area  $A_{\text{Au}}$  per atom on a particle, then we calculate the number of atoms on the surface of a particle with given radius  $r$  as  $N = 4 \pi r^2 / A_{\text{Au}}$ . In the case of the gold particles we have to consider that gold grows in fcc-structure. We assume that the particles' surface is mainly constituted by (111) and (100) facets. They have a close packing, and therefore are very stable. On the (100) facet of the unit cell there are two atoms, so with a lattice constant of  $a = 4.08 \text{ \AA}$  we find a density of one atom per  $8.3 \text{ \AA}^2$ . On the (111) facet we find one atom per  $7.21 \text{ \AA}^2$ . This can be understood by looking at a cross section of the fcc unit cell perpendicular to the [111] axis as marked in figure S2b. We find a triangle with three atoms on each side. The side length is  $2^{1/2} \cdot a$ . One of these triangles contains 2 atoms. So we find a density of one atom per  $7.21 \text{ \AA}^2$  on the (111) facet. Looking at the model systems  $\text{Au}_{55}$  and  $\text{Au}_{147}$  (see Figure S2a and b), which have closed shells, one can easily see that their surface is mainly constituted by (100) facets. Therefore, as an approximation, we used the value of  $A_{\text{Au}} = 8 \text{ \AA}^2$  surface area per atom. Overall the number of Au atoms on the surface of an Au particle can be then calculated as  $N = 4 \pi r^2 / 8 \text{ \AA}^2$ , whereby  $r$  is the radius of the Au particle.

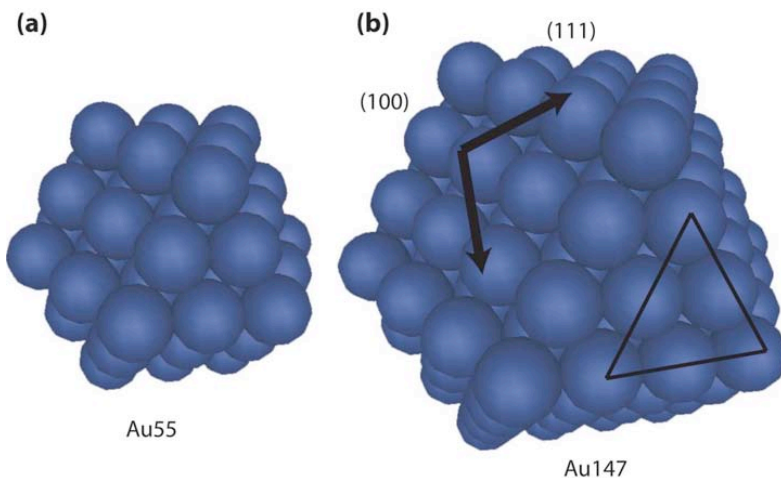


Figure S2: a) A model of  $\text{Au}_{55}$ . This cluster is obtained by covering one single Au atom with two closed layers of atoms. b) A model of  $\text{Au}_{147}$ . Marked with arrows on the (100) plane is one face of the cubic unit cell. On the (111) plane the triangle marks six atoms that can be assigned to one cubic unit cell.

#### 4) Determination of the concentration of CdSe particles and Cd surface atoms

##### Measurement of the CdSe particle concentration $c$ (CdSe particles):

The concentration of the CdSe nanocrystals is evaluated according to Yu et al.<sup>10</sup>. Here, absorption spectra of the cores in the range of 200-800 nm were measured with an UV/visible spectrophotometer (BIOCHROM Ultraspec 3100 pro). The absorption A at first exciton peak at wavelength  $\lambda_0$  is related to the particle concentration of the sample  $c_p = c$ (CdSe particles) by  $A = \frac{c_p \cdot \epsilon(\lambda_0)}{d}$ , where  $\epsilon(\lambda_0)$  is size-dependent the extinction coefficient<sup>10</sup>,  $d$  the pathlength of the cuvette, and  $d$  the dilution factor. Thus the particle concentration can be obtained from the absorption spectra.

##### Calculation of the concentration of cadmium atoms $c$ (Cd surface atoms) of the CdSe core surface in solution:

For the estimation of the number  $N_{Cd}$  of cadmium atoms on the surface of a CdSe core we calculate  $N_{Cd} = \frac{A_{core}(\lambda_0)}{A_{Cd}}$ , where  $A_{Cd} = 30 \text{ \AA}^2$  (see II.1) is the average area of one Cd atom and  $A_{core}(\lambda_0)$  the core surface area. The latter value is calculated by  $A_{core}(\lambda_0) = 4r(\lambda_0)^2 \cdot \lambda_0$ , where  $r_{core}(\lambda_0)$  is taken from Yu et al.<sup>10</sup>, in dependence of the wavelength  $\lambda_0$  of the first exciton peak. Thus the particle concentration  $c_p = c$ (CdSe particles) can be converted to a cadmium surface atom concentration  $c_N = c$ (Cd surface atoms) according to  $c_N = c_p \cdot N_{Cd}$ .

##### Calculation of the mass concentration of CdSe nanocrystals in solution:

The mass  $m_{NC}$  of one CdSe particle was calculated according to  $m_{NC} = m_{core} = d_{CdSe} \cdot V_{core}$ , using the particle volume  $V_{core} = \frac{4}{3} r_{core}^3 \cdot \lambda_0$  and the mass density of CdSe  $d_{CdSe} = 5.810 \frac{\text{g}}{\text{cm}^3}$  and ignoring the mass contribution of organic surface ligands. The mass concentration is  $c_m = c_p \cdot m_{NC} \cdot N_A$ , where  $N_A = 6.022 \cdot 10^{23} \text{ mol}^{-1}$  is the Avogadro constant.

#### 5) Determination of the concentration of CdSe/ZnS particles and Cd surface atoms

##### Measurement of the CdSe particle concentration:

In the case of CdSe cores with ZnS shell we assume the same extinction coefficient as for CdSe particles without shell to get the particle concentration. The extinction coefficient is taken from the data publishes by Yu et al.<sup>10</sup>. We neglect the fact that upon growing a ZnS shell the first exciton peak of CdSe/ZnS particles is shifted to higher wavelength by 5 to 15 nm compared to CdSe cores.

##### Calculation of the concentration of cadmium atoms $c$ (Cd surface atoms) of the CdSe core surface of CdSe/ZnS particles in solution:

For CdSe/ZnS particles we calculate the number of Cd surface atoms as the number of Cd atoms that lie on the surface of the CdSe core. For this purpose the first exciton peak of the CdSe cores has to be determined before growing the ZnS shell around them. From the wavelength of the first exciton peak the diameter of the CdSe core and thus the number of Cd atoms on the surface can be derived as described above for CdSe particles.

Calculation of the mass concentration of CdSe/ZnS nanocrystals in solution:

The mass  $m_{NC} = m_{core}$  of a CdSe particle without ZnS shell was calculated according to

$$m_{NC} = m_{core} = d_{CdSe} \cdot V_{core}, \text{ using } V_{core} = \frac{4}{3} \pi r_{core}^3$$

$d_{CdSe} = 5.810 \frac{g}{cm^3}$  by ignoring the mass contribution of organic surface ligands. In the case of an additional ZnS shell around the CdSe particles the mass  $m_{ZnS} = d_{ZnS} \cdot \frac{4}{3} \pi ((r_{core} + r_{shell})^3 - r_{core}^3)$  of the ZnS shell was added to the core mass  $m_{core}$  to

get  $m_{NC} = m_{core} + m_{ZnS}$ , where  $d_{ZnS} = 4.090 \frac{g}{cm^3}$  is the mass density of ZnS and

$r_{shell} = 0.75 \text{ nm}$  is an average empirical value for the thickness of a ZnS shell, derived from TEM measurements reported by Gerion et al.<sup>2</sup>. The mass concentration is  $c_m = c_p \cdot m_{NC} \cdot N_A$ , where  $N_A = 6.022 \cdot 10^{23} \text{ mol}^{-1}$  is the Avogadro constant and  $c_p$  the concentration of CdSe/ZnS particles in M.

## 6) Determination of the concentration of Au particles and Au surface atoms

Measurement of the Au particle concentration:

As in the case of CdSe particles absorption spectra of the Au particles in the range of 200-800 nm were measured with an UV/visible spectrophotometer (BIOCHROM Ultraspec 3100 pro).

The absorption A at the wavelength of the plasmon peak is  $A = \frac{c_p \cdot l \cdot \pi r_p}{d}$ , where  $\pi r_p = 1.29 \cdot 10^7 \text{ M}^{-1} \text{ cm}^{-1}$  is assumed as extinction coefficient for our gold particle with a radius of  $r_p = 2.3 \text{ nm}$ , l the pathlength of the cuvette, d the dilution factor, and  $c_p = c(\text{Au particles})$  the concentration of Au particles in the sample.

Calculation of the concentration of Au atoms located on the Au particle surface:

As in the case of CdSe particles, for the estimation of the number  $N_{Au}$  of Au atoms on the

surface of an Au particle we use  $N_{Au} = \frac{A_p(r_p)}{A_{Au}}$ , where  $A_{Au} = 8 \text{ \AA}^2$  (see II.3.) is the average

area of an Au atom and  $A_p(r_p)$  is the surface area of a particle with radius  $r_p$ . The latter value is calculated by  $A_p(r_p) = 4r_p^2 \pi$ , where all the Au particles used in this study had a radius of  $r_p = 2.3 \text{ nm}$  as determined by TEM. Thus the particle concentration  $c_p = c(\text{Au particles})$  was converted to an Au surface atom concentration  $c_N = c(\text{Au surface atoms})$  according to  $c_N = c_p \cdot N_{Au}$ .

## 7) Table of the used CdSe, CdSe/ZnS, and Au samples

In order to compare our results with the observations of other groups we give here a table in which the conversion between different ways of quantifying nanocrystal concentrations is given.

## CdSe nanocrystals

l [nm]	c(CdSe particles) [nM]	c(Cd surface atoms) [M]	c(CdSe particles) [g/ml]
560	10	1.1	0.63
599	10	2.1	1.7

$\lambda$  [nm] = wavelength of the first exciton peak in the absorption spectrum of the CdSe core particle

$c(\text{CdSe particles})$  [nM] = concentration of CdSe particles

$c(\text{Cd surface atoms})$  [ $\mu\text{M}$ ] = concentration of Cd atoms which are located on the surface of the CdSe particles

$c(\text{CdSe particles})$  [ $\mu\text{g/ml}$ ] = mass concentration of CdSe particles

#### CdSe/ZnS nanocrystals

$\lambda$ [nm]	$c(\text{CdSe/ZnS particles})$ [nM]	$c(\text{Cd surface atoms})$ [ $\mu\text{M}$ ]	$c(\text{CdSe/ZnS particles})$ [ $\mu\text{g/ml}$ ]
508	10	0.61	0.86
510	10	0.62	0.87
560	10	1.1	1.6
599	10	2.1	3.3

$\lambda$  [nm] = wavelength of the first exciton peak in the absorption spectrum of the CdSe core of the CdSe/ZnS particle (must have been determined before the growth of the ZnS shell)

$c(\text{CdSe/ZnS particles})$  [nM] = concentration of CdSe/ZnS core/shell particles

$c(\text{Cd surface atoms})$  [ $\mu\text{M}$ ] = concentration of Cd atoms which are located on the surface of the CdSe core of the CdSe/ZnS particles

$c(\text{CdSe/ZnS particles})$  [ $\mu\text{g/ml}$ ] = mass concentration of CdSe/ZnS particles

#### Au nanocrystals

$c(\text{Au particles})$ [nM]	$c(\text{Au surface atoms})$ [ $\mu\text{M}$ ]	$c(\text{Au particles})$ [ $\mu\text{g/ml}$ ]
10	8.31	5.92

$c(\text{Au particles})$  [nM] = concentration of Au particles

$c(\text{Au surface atoms})$  [ $\mu\text{M}$ ] = concentration of Au atoms which are located on the surface of the Au particles with a diameter of 4.6 nm

$c(\text{Au particles})$  [ $\mu\text{g/ml}$ ] = mass concentration of Au particles with a diameter of 4.6 nm

**(III) Uptake of CdSe/ZnS nanocrystals by MDA-MB-435S breast cancer cells**

MDA-MB-435S breast cancer cells were purchased from American Type Cell Culture (ATCC) and cultivated at 37°C and 5% CO<sub>2</sub> in the media proposed by ATCC. For uptake-experiments the adherent cells were rinsed twice with PBS without Ca<sup>++</sup> and Mg<sup>++</sup> (PBS, 9,55g/l, Biochrom AG, Germany) in order to reduce the concentration of adhesion-promoting Ca<sup>++</sup> and Mg<sup>++</sup>-ions inside the cells. The cells were then covered with Trypsin-EDTA-solution (Biochrom AG, Germany) and incubated at 37°C for 5 minutes. After incubation the now detached cells were diluted in PBS, filled into test tubes and centrifuged (5 min, 300g). The Trypsin-EDTA containing supernatant was removed and the cells were resuspended in media. The cells were diluted to a concentration of 7 \* 10<sup>4</sup> cells/ml. For all uptake-experiments 1 ml of cell-suspension was filled into a nunc-chamber® (Nalge, U.S.). To each chamber 10 µl of 2-10 nM solution of two types of different coated nanocrystals, fluorescing in red and green, respectively, were added. The final concentration of each type of nanocrystals in the serum-supplemented media was 2-10 nM. After 18 h of incubation at 37°C and 5% CO<sub>2</sub> the cells were rinsed twice with PBS and fresh medium was added. The cells were then incubated for additional 4 h to allow the cells to ingest the nanocrystals.

Before visualizing the cells their nucleus was stained with DAPI (Molecular Probes, U.S.) following the providers protocol for adherent cells. For visualizing the cells the nunc-chambers® were mounted onto a fluorescence microscope (Axiovert 200, Zeiss, Germany) using a 100x oil-immersion objective. For every image one channel in differential interference contrast mode (bw) and three individual channels in the fluorescence mode were recorded using the following filters: blue channel (DAPI): excitation: G 365, beamsplitter: FT 395, emission: BP 445/50; green channel (green nanocrystals): excitation: BP 450, beamsplitter: FT 480, emission: BP 535; red channel (red nanocrystals): excitation: BP 546, beamsplitter: FT 580, emission: LP 590. For excitation a 100 Watt Mercury lamp (HBO 100, Osram) was used at half power. The acquisition times varied between 100 and 500 ms for the different types of nanocrystals, as they have different quantum yields. Images were recorded with a Zeiss AxioCam CCD camera. The recorded channels were overlaid using the microscope software (Axiovision 4.1).

**(IV) Detachment of NRK fibroblast from the cell culture substrate upon incubation with nanocrystals****Chemicals**

Ultrapure water (MilliQ-grade) was used in all experiments. Octadecyltrichlorosilane (OTS) was obtained from ABCR, Karlsruhe, Germany. Hexadecane, hexane, chloroform, mercaptopropionic acid (MPA), cadmium acetate hydrate (CAH), cadmium perchlorate hydrate (CPH), selenious acid (SA), zincchloride (ZC) PBS (phosphate buffer saline), Penstrep solution (containing 10,000 units/ml Penicillin and 10 mg/ml streptomycin-sulfate, and 0.9% NaCl), Liquid Media Supplement (ITS) as well as trypsin were purchased from Sigma-Aldrich. Dulbecco's Modified Eagle Medium (DMEM, FG 0435), HAM'S F-12 Medium (FG 0815) and fetal bovine serum (FBS, S0115) were from Biochrom KG (Berlin, Germany). All chemicals were used as received.

**Cell culture**

Normal Rat Kidney (NRK)-fibroblasts (CRL-6509) were obtained from ATCC, Manassas, USA. As cell culture medium DMEM with 10% FBS (fetal bovine serum) and 1% Penstrep solution was used. During incubation with nanocrystals cells were cultivated in serum free SATO medium (HAMS F12 with 1% serum supplement ITS), which stopped cell proliferation. Measurements had to be performed in serum free medium since for our applied automated counting procedure (see below) it is important that cell do not proliferate and migrate too much. Otherwise it would be impossible to verify for each individual cell whether it is still adherent at the same place of whether it has detached from the surface.

NRK-fibroblasts were seeded in 6-wellplates (TPP, Switzerland; polyethylene, tissue culture treated) to a concentration of 3600 cells / cm<sup>2</sup>. Special care was taken to achieve a cell population of separated single cells, in order to get optimal conditions for the optical counting procedure. Adhesion of the cells was observed after 5 to 24 hours. After cell adhesion, the cell layer was gently rinsed three times with PBS buffer, and the adherent cells were counted in PBS buffer within 20 min. The buffer then was replaced by the incubation medium (SATO and the toxin, i.e. Cd salts or nanocrystals, in a target concentration). SATO treatment always caused a certain loss of cells by detachment, even without toxin. After 48 hours of incubation, cells were rinsed three times with PBS buffer, removing detached cells, while the residual adherent cells were counted again in PBS buffer within 20 min.

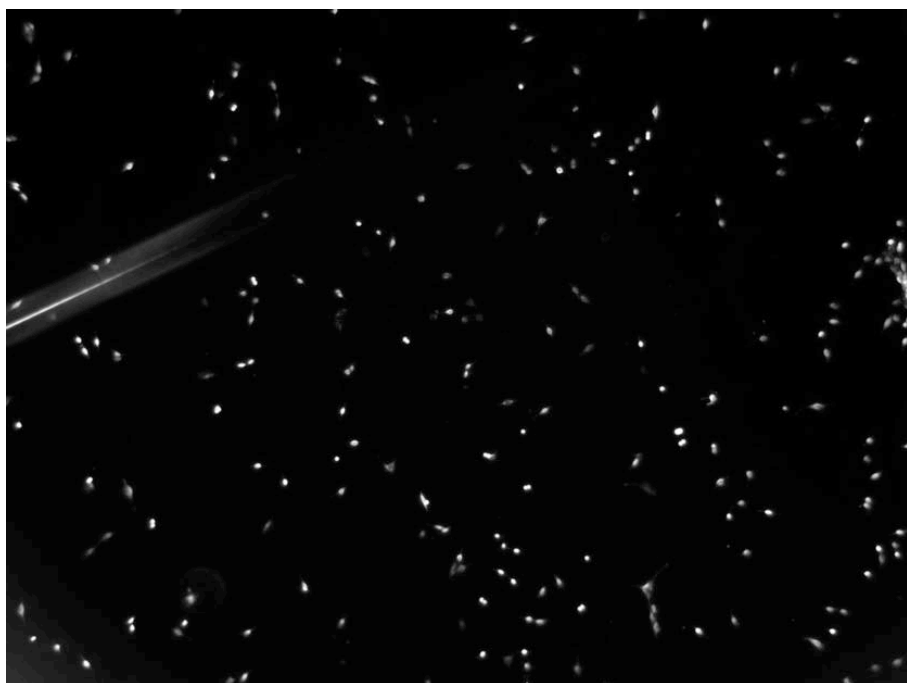
**Automated procedure to count adherent cells**

A computer based optical counting method was used to sensibly detect the effects of very low toxin concentrations to the adhesion behavior of living cells. Cells were counted on images recorded with a phase contrast microscope before and after incubation with the toxin, and the ratio R(c) of cells adherent to the surface after / before incubation versus the toxin concentration c is plotted. For this purpose for each individual cell which was adherent before incubation with the toxin, it was tested if the same cell is still adherent after incubation with the toxin. Therefore, the position of each cell within the wellplate had to be registered before incubation with the toxin and had to be found again after 48 hours incubation with the toxin. While the motorized xy-stage of the microscope allowed for a very precise repositioning of the wellplate holder, placing the wellplates led to an overall repositioning error of approx. 100  $\mu$ m. This contributes to the relative error of about 10% for the measured average ratios R. While a ratio R close to zero indicates the complete detachment of the cells from the surface, a ratio of R = 1 means that statistically every cell is found after the incubation time where it was seeded. The reference value R(c = 0) never is found to be = 1, because of the SATO medium. Changing the serum-containing medium to serum free SATO medium alone results in a detachment of some cells, even when no toxin is added (i.e. c = 0). Moreover, R(c) never

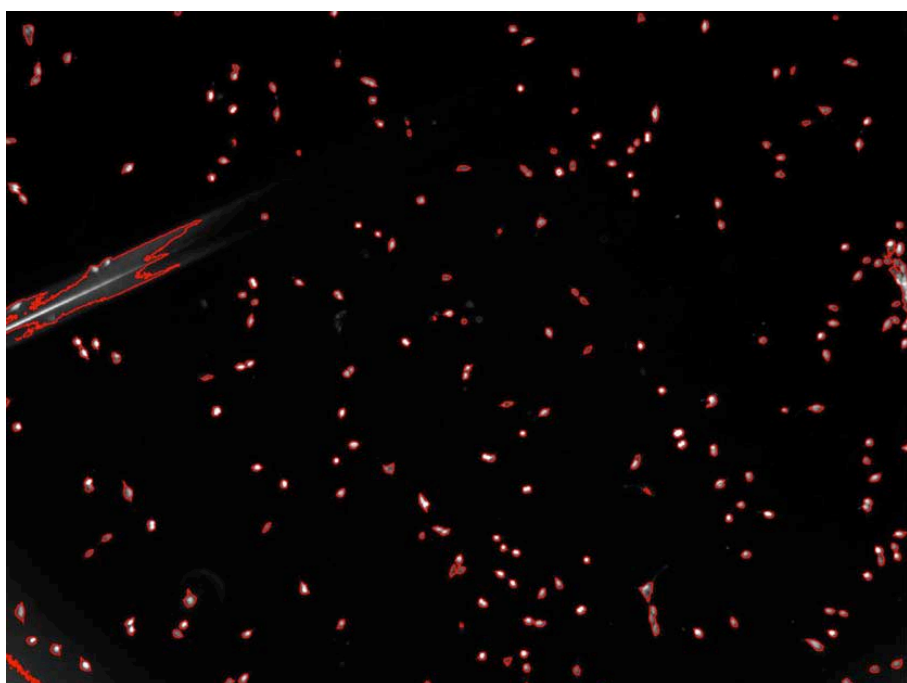
is found to be  $= 0$  since always a certain amount of dirt, dust particles, or cell debris is counted wrongfully as adherent cells. In the worst case this background noise in  $R(c)$  due to cell debris and other impurities could be as high as  $R(c) = 0.34$ . In the case of the polymer coated nanocrystals for high particle concentrations there are basically no adherent cells left and the constant  $R(c) > 0$  background level is due to impurities wrongfully counted as adherent cells. Therefore, for the interpretation of our data it is important to correlate the  $R(c)$  curve with microscopy images. Another important information additional to the  $R(c)$  curves is result of the viability tests performed for different concentrations. These data indicate whether the counted adherent cells are alive or dead.

In practice, for each toxin concentration approximately 20000 cells were monitored in 94 pictures taken from two wellplate chambers. This was done with an inverted optical microscope (Axiovert 200, Carl Zeiss, Jena) in phasecontrast mode with a 4x Achroplan objective. Hydrophobic circular glass cover slides (preparation see below) were placed to float on the buffer surface to avoid light scattering through the meniscus of the liquid at the chamber walls, which would result in a brightness gradient in the pictures. The pictures, taken with a Zeiss AxioCam HRm CCD camera, showed a surface area of  $2.6 \text{ mm} \times 3.5 \text{ mm}$  as a black background with the light spots of adherent cells (and dirt), see Figure S3. This high contrast and the low brightness variations of the background allowed for a computer based particle analysis with the data evaluation software Igor Pro 4.1, running on a Dual 2.0 GHz Macintosh PowerPC. Using the subroutine package of Igor Pro for image processing, it was possible to automate the cell counting. For particle analysis, a threshold in the grayscale was used for the particle detection based on the average brightness of a picture. The threshold and a minimum value for the spot size were the necessary parameters for a reliable counting of surface adherent particles.

a)



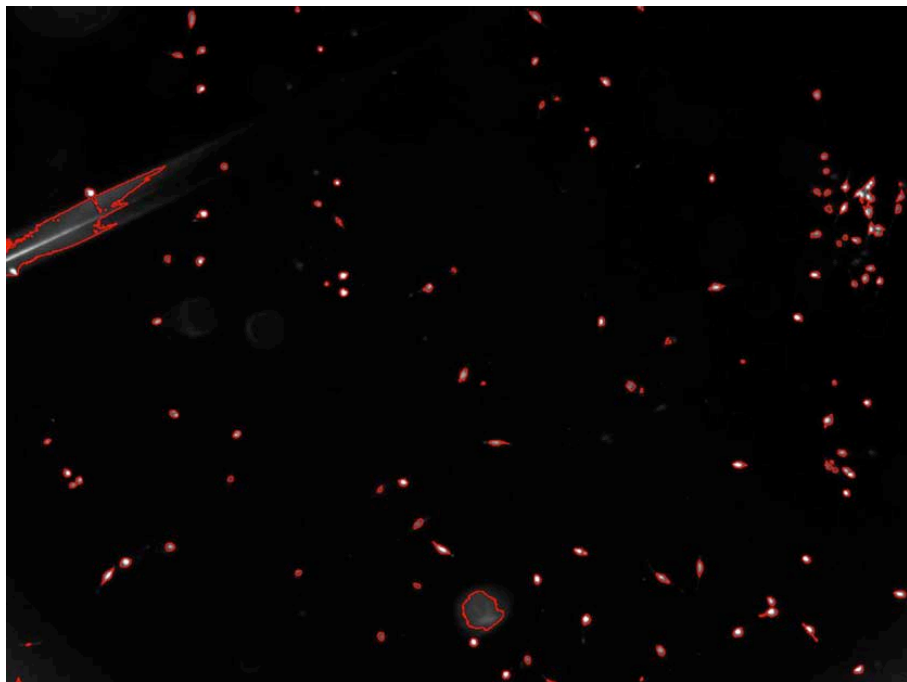
b)



c)



d)



e)

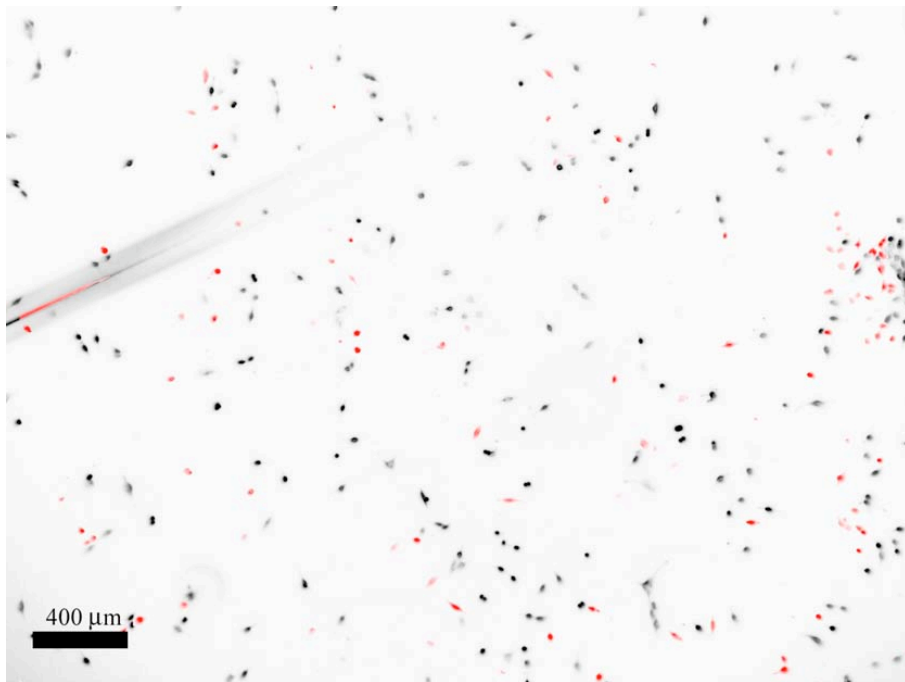
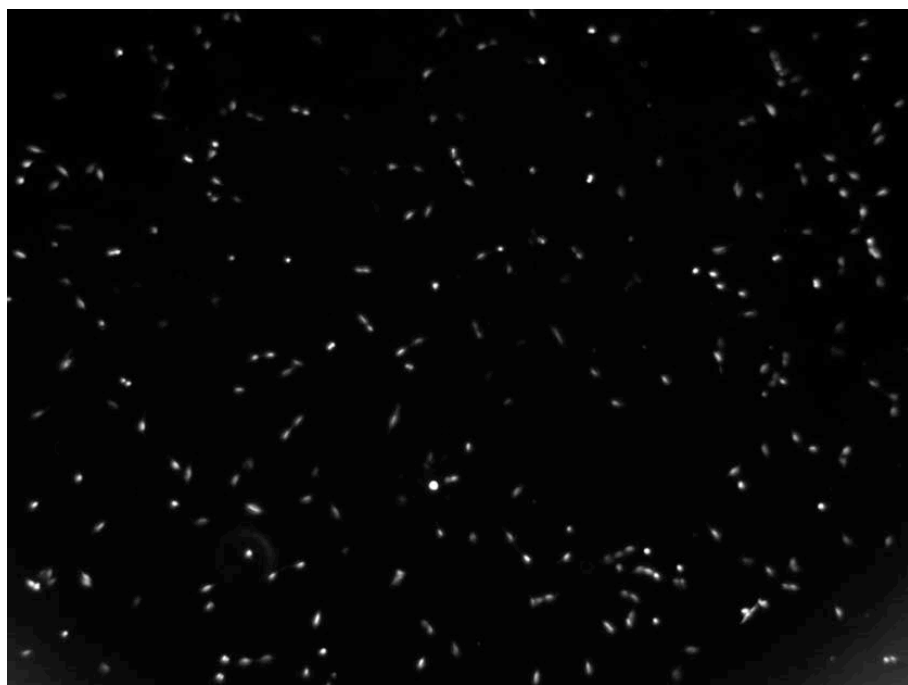
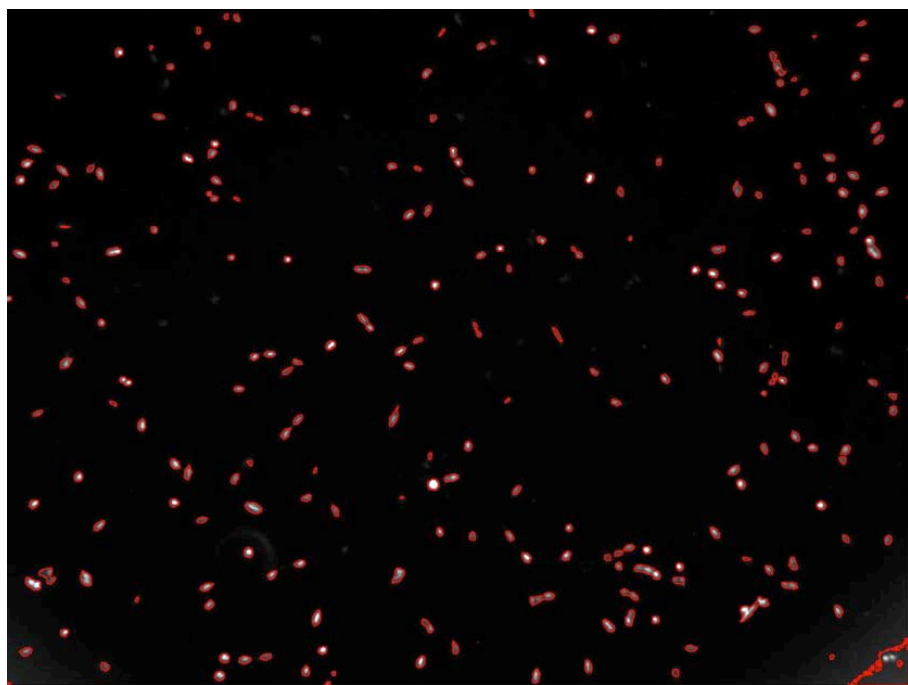


Figure S3.1: a) Phase contrast image of NRK fibroblasts in SATO medium, cultured for 24 hours, before the addition of nanocrystals. b) Same image with the  $N_A=198$  counted cells (marked in the image) that have been detected by the image analysis software. c) Phase contrast image of NRK fibroblasts after 48 hours of incubation in 50 nM MPA coated CdSe/ZnS nanocrystals (wavelength of the absorption peak of the CdSe core  $\lambda = 508$  nm, corresponding to a CdSe core diameter of  $d = 2.4$  nm; 61 Cd surface atoms per nanoparticle) in SATO medium. This image shows the same area of the cell culture substrate as shown in a) and b). The area could be identified by the scratch in the surface. d) Same image with  $N_B=108$  cells counted by the image analysis software (marked in the image). e) Overlay of image a) (black) and c) (red). This image compares the adherent cells before (a) and after (c) incubation with the nanocrystals. Note that a lot of cells detached from the surface upon incubation with the nanocrystals, while the still adherent cells moved during the 48 hours incubation time in SATO medium. They show a spindle-like shape and viability tests indicate that these cells are alive. The situation is typical for the intoxication of the NRK fibroblasts in serum free medium and for a low concentration of cadmium. The value  $R = \frac{N_B}{N_A}$  is taken for the same concentration from in total 94 positions (pictures). The averaged value is plotted in the diagrams R vs. concentration as one data point including the standard deviation of R as error bar.

a)



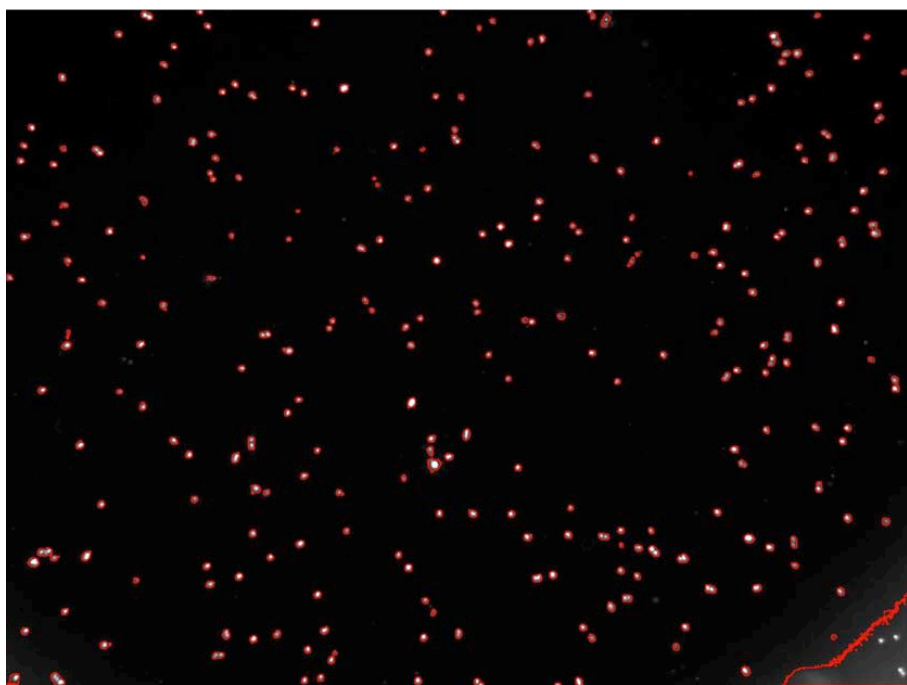
b)



c)



d)



e)

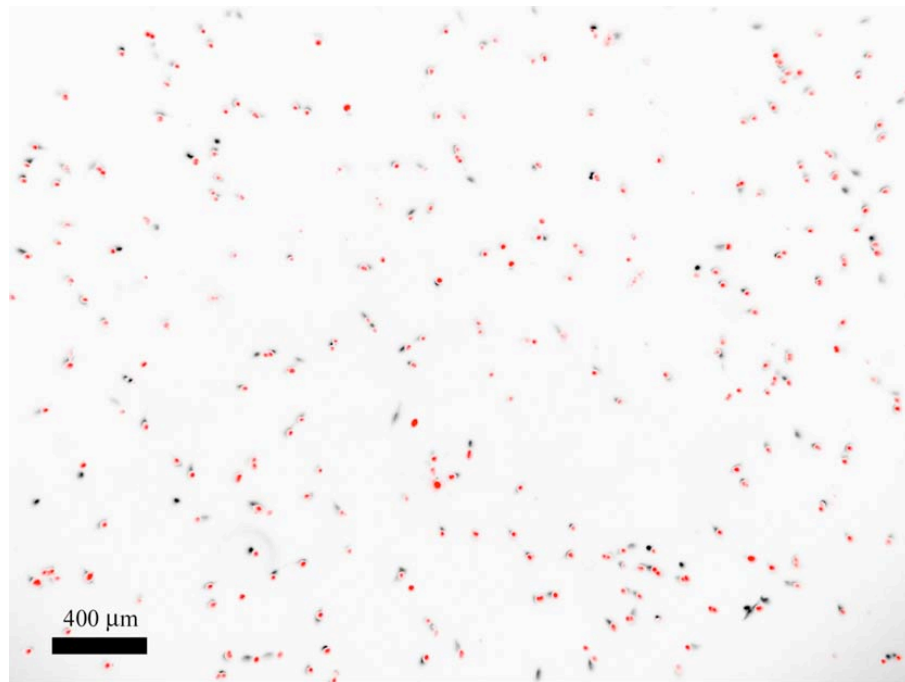


Figure S3.2: a) Phase contrast image of NRK fibroblasts in SATO medium, cultured for 24 hours, before the addition of nanocrystals. b) Same image with the  $N_A=228$  counted cells (marked in the image) that have been detected by the image analysis software. c) Phase contrast image of NRK fibroblasts after 48 hours of incubation in 325 nM MPA coated CdSe/ZnS nanocrystals (wavelength of the absorption peak of the CdSe core  $\lambda = 508$  nm, corresponding to a CdSe core diameter of  $d = 2.4$  nm; 61 Cd surface atoms per nanoparticle) in SATO medium. This image shows the same area of the cell culture substrate as shown in a) and b). d) Same image with  $N_B=225$  cells counted by the image analysis software (marked in the image). e) Overlay of image a) (black) and c) (red). This image compares the adherent cells before (a) and after (c) incubation with the nanocrystals. Note that almost no cells detached from the surface upon incubation with nanocrystals. Adherent cells did not move on the substrate during the 48 hours incubation in the SATO medium. They show a sphere-like shape and viability tests indicate that the cells are dead. The situation is typical for intoxication of the NRK fibroblasts in serum free medium at high concentration of cadmium. In general, non-adherent cells and dirt were suppressed by rinsing with PBS buffer prior to image capturing. The value  $R = \frac{N_B}{N_A}$  is taken for the same concentration from in total 94 positions (pictures). The averaged value is plotted in the diagrams R vs. concentration as one data point including the standard deviation of R as error bar.

Hydrophobic glass cover slides

A solution of 10 mM octadecyltrichlorosilane (OTS) in hexadecane was used to functionalize the surface of glass cover slides by dip coating for one hour. Finally the slides were rinsed with hexadecane, hexane and chloroform. The resulting surface showed advancing contact angles of approx. 92° for water.

Fluorescence microscopy to image the nanocrystals ingested by individual cells

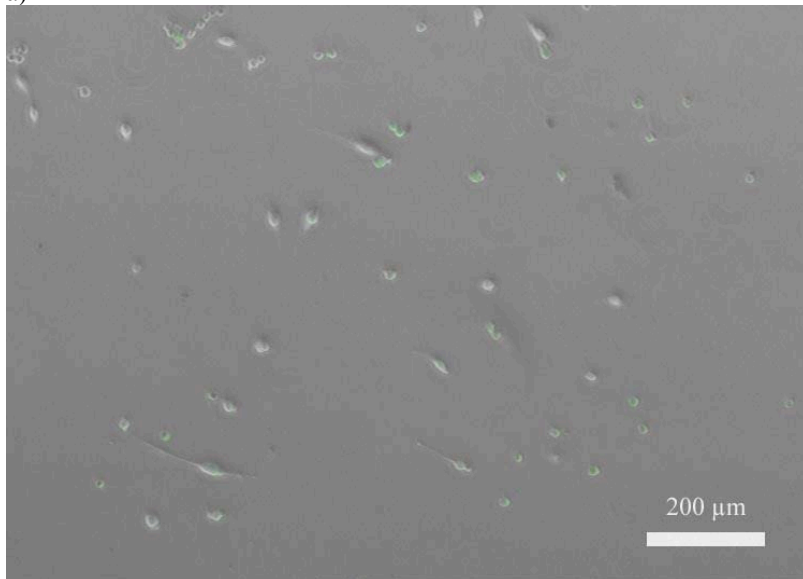
Fluorescence microscopy was performed on an inverted microscope (Axiovert 200 from Carl Zeiss) with a Carl Zeiss FluoArc system, using a mercury lamp HBO 100. The filters for the fluorescence detection of the nanocrystals were the Q-dot TM 500 LP from AHF, Germany, as well as the filter sets 15 and 49 from Carl Zeiss.

Viability test

The Viability Kit L3224 from Molecular Probes was applied to distinguish between living and dead cells. Esterase activity of living cells converts non-fluorescent calcein-AM to intensely green fluorescent calcein. The second agent of this kit, Ethidium homodimer-1, enters defect cell membranes of dead cells and shows a 40-fold enhanced red fluorescence when it binds to nucleic acids of the cytoplasm. Following the manufacturers instructions for this test, cells were rinsed thoroughly with PBS buffer and a 4 µM solution of the agents was applied for 45 min. The filter set 00 from Carl Zeiss was used to watch the red fluorescence, while a 31001 filter from Chroma was used for the green fluorescence. In Figure S4 an example of this viability test is shown.

Similar viability tests have been used by other groups to determine cytotoxic effects of Cd ions, and CdSe and CdSe/ZnS particles<sup>11-13</sup>. These tests are based on measuring metabolic activity of cells or on the staining of dead cells, and are from this point conceptually different from our experiments in which cell survival was measured in terms of cell adherence.

a)



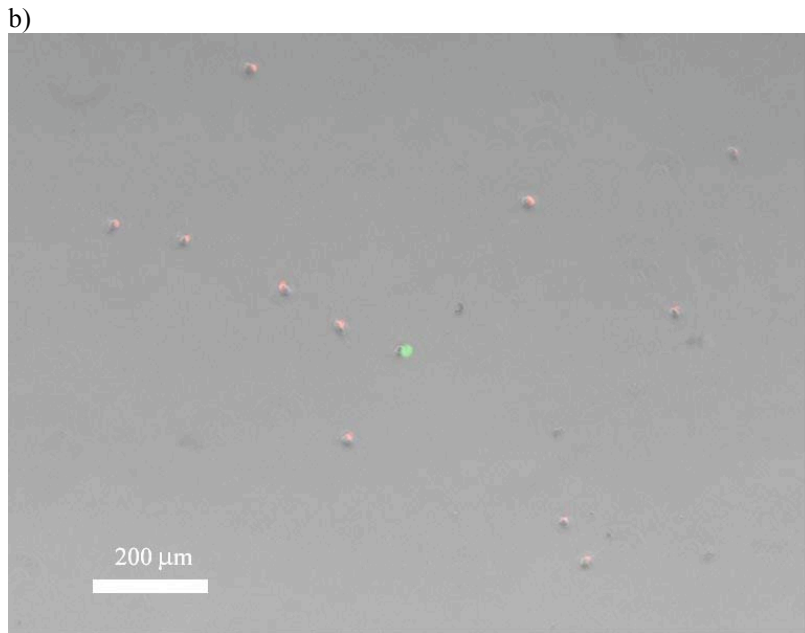


Figure S4: NRK fibroblasts were cultivated for 24 hours in DMEM cell medium with serum. After this incubation they were rinsed with PBS buffer. Further culture was performed in serum free SATO medium containing cadmium perchlorate hydrate as cadmium source. The viability test was applied. Pictures show an overlay of the phase contrast image and the images of green and red fluorescence. a) NRK fibroblasts after incubation in  $0.1 \mu\text{M}$  cadmium perchlorate hydrate. All adherent cells are marked as living (green color) and show a spindle like shape. b) NRK fibroblasts after incubation in  $5 \mu\text{M}$  of cadmium perchlorate hydrate. Almost all adherent cells are marked as dead (red color) and show a spherical shape.

#### (V) Patch clamp experiments

To further evaluate the biocompatibility of nanocrystals we conducted electrophysiological studies of cells incubated with nanocrystals using the planar patch clamp technique<sup>14</sup>. Two cell lines (RBL and CHO) were investigated in regard to changes in their morphology and their electrophysiological properties upon incubation with nanocrystals. The CHO cell line was stably transfected to express the hERG channel and the RBL cell line used endogenously expresses an inward rectifying potassium channel.

All cells were grown to 60-80% confluence in their standard serum-supplemented medium as described in the ATCC catalogue. The cells were incubated with nanocrystals at the desired concentration in their normal growth medium at 37 degrees Celsius and 5% CO<sub>2</sub> (several hours up to 2 days). After the incubation period, cells were isolated with a brief trypsin treatment. The resulting cell suspension was centrifuged twice at 1000 U/min for 2 minutes and the supernatant was pipetted off to remove cell fragments and debris. For resuspension the electrophysiological recording solutions were used. The cleaned cell suspension had a cell concentration of about one million cells per milliliter. Cells were examined with a confocal laser microscope to validate the quantum dot uptake by fluorescence measurements.

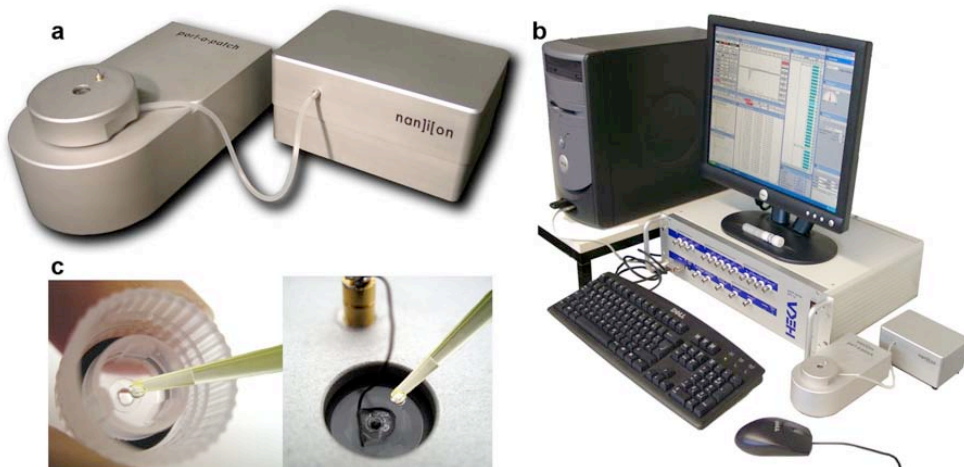


Figure S5: The Port-a-Patch electrophysiology workstation. In a) the chip mounting station and the software steered suction control unit are shown. The full Port-a-Patch system including amplifier and PC is depicted in b) and c) displays the micro structured borosilicate glass chips, which are glued onto small twist caps. The caps contain an O-ring and are screwed onto the holder in the chip mounting station to obtain an airtight arrangement for suction application. Electrolyte solutions and cell suspension is pipetted onto the backside and top of the chip with standard pipettes as shown. The solutions are electrically contacted via Ag/AgCl electrodes, which are implemented in the system.

Electrophysiological characterization and evaluation of cell function/viability of the cells ion channels were performed by whole cell recordings<sup>15</sup>. All measurement have been performed with the chip-based patch clamp technique<sup>14</sup> using the Port-a-Patch system by Nanion Technologies ([www.nanion.de](http://www.nanion.de))<sup>16</sup>. The system uses micro structured borosilicate glass chips for whole cell patch clamp assays in an automated format. The Port-a-Patch was used in conjunction with an EPC-10 patch clamp amplifier (HEKA, Lambrecht, Germany) and is shown in Figure S5.

Cells were positioned and sealed on a micron-sized aperture in the glass chips by feedback controlled suction application. Brief suction pulses were applied to rupture the cells membrane across the aperture to obtain access to the cells interior, e.g. getting into the whole cell configuration. In the whole cell configuration, the current through the complete ensemble of all ion channels in the cell membrane is recorded, allowing the investigation of the ionic current conducted by the entire cell.

The chips for the recordings had an open aperture resistance of 2-3 MΩ. The recorded data were filtered at 3 kHz and sampled at 10 kHz. The electrophysiological recording solutions had the following ionic compositions (mM): extracellular (top of chip): NaCl (140), KCl (3), MgCl<sub>2</sub> (1), CaCl<sub>2</sub> (1), HEPES (10), pH = 7.4, 270 mOsm; intracellular (underside of chip): for RBL cells: K-Aspartate (120), EGTA (10), HEPES (10), NaCl (10), pH=7.2; for CHO cells: KCl (120), NaCl (10), EGTA (10), Hepes (10), pH = 7.2. About 5 µl of cell suspension were pipetted onto the chip and standard suction protocols of the Port-a-Patch system were applied for cell positioning and achieving tight seal whole cell configurations. Standard voltage protocols were applied for the recordings of ionic currents.

After the electrophysiological characterization, the patch clamped cell on the aperture was examined with the confocal microscope to evaluate the fluorescence of nanocrystals inside the cell. In Figure S6, images of patch clamped cells on the chip are displayed, showing the fluorescence of the quantum dots inside the cell. Below the cell is the micron-sized aperture in the chip, which can be perceived as a small dot. The larger circle around aperture in the centre corresponds to the 3-D-microstructure in the chip. On the chip surface are more cells in the vicinity of the patch clamped cell and all show the characteristic fluorescence. By this procedure it was guaranteed, that all cells investigated had incorporated the nanocrystals.

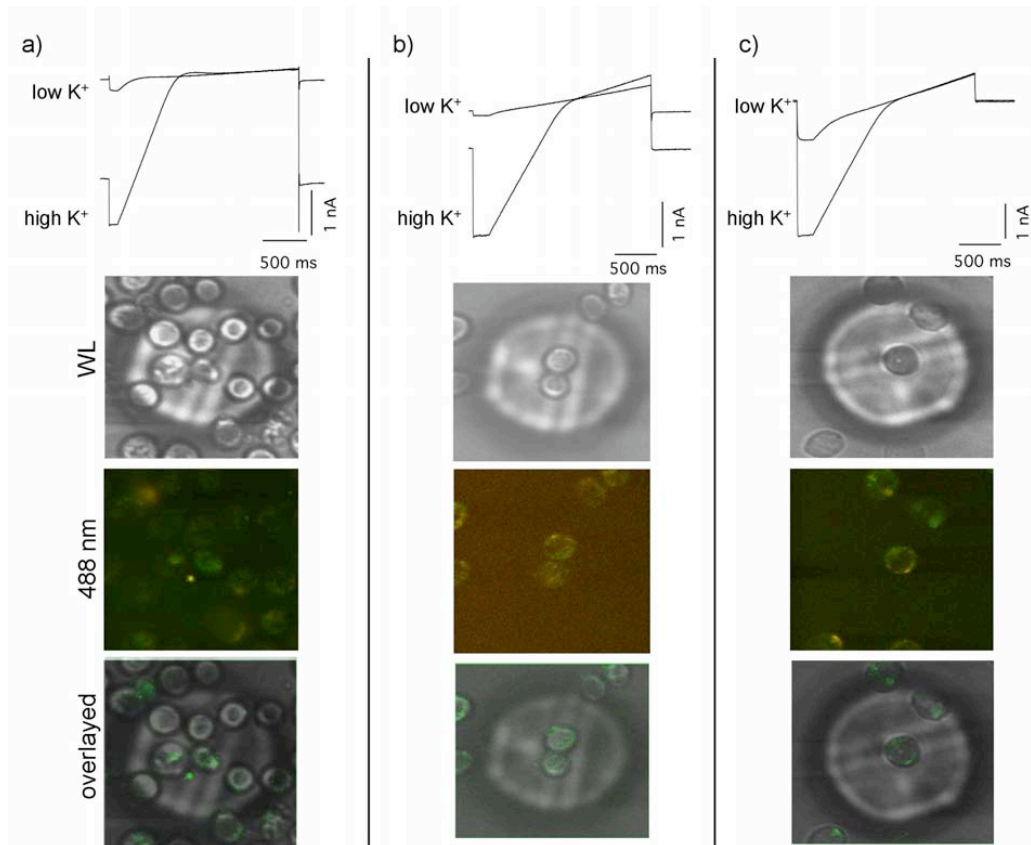


Figure S6: Electrical properties of RBL cells after 4 h incubation with MPA-coated CdSe/ZnS nanocrystals (wavelength of the absorption peak of the CdSe core  $\lambda = 508$  nm, corresponding to a CdSe core diameter of  $d = 2.4$  nm; 61 Cd surface atoms per nanoparticle). Top: Currents as obtained after incubation in 10 nM, 50 nM, and 100 nM CdSe/ZnS particles. Measurements were performed in two different external  $K^+$  concentrations showing the characteristic inward rectifying current of the fully functional potassium channels. The current at the higher potassium concentration is larger due to the abundance of permeating ions. Bottom: Each picture shows a cell positioned on the hole in the glass chip as seen under white light (WL, bright field) and as fluorescence while excitation with 488 nm laser light. The images at the bottom show an overlay of the bright field and fluorescence pictures.

In addition the cell morphology before and after incubation of the cells was investigated by optical microscopy (Figures S7, S8). No changes in cell morphology could be detected at the used concentrations and incubation time. Incubation with nanocrystals was performed for 4 hours in serum-supplemented medium.

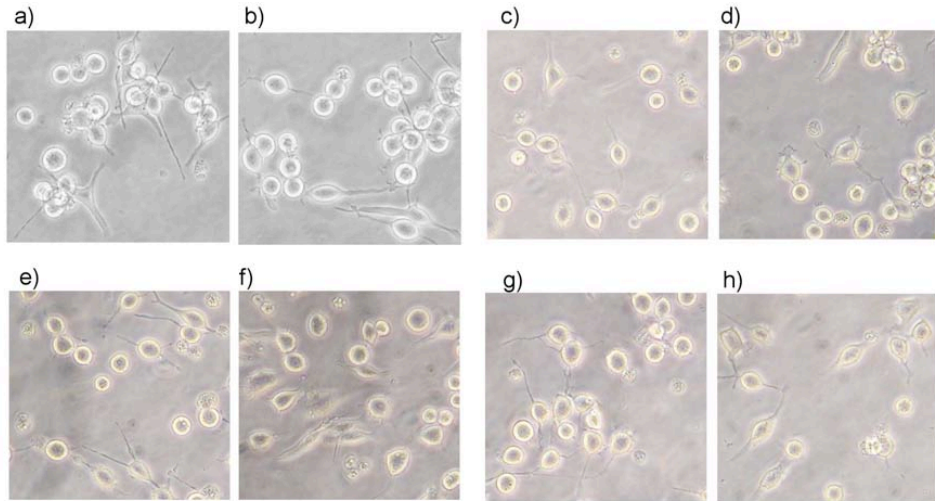


Figure S7: RBL cells before and after 3-4 h incubation with MPA-coated CdSe/ZnS nanocrystals (wavelength of the absorption peak of the CdSe core  $\lambda = 508$  nm, corresponding to a CdSe core diameter of  $d = 2.4$  nm; 61 Cd surface atoms per nanoparticle). The images show RBL cells before (a) and 3 h after (b) incubation in 5 nM CdSe/ZnS particles; RBL cells before (c) and 4 h after (d) incubation in 10 nM; before (e) and 4 h after (f) incubation in 50 nM; before (g) and 4 h after (h) incubation in 100 nM CdSe/ZnS particles.

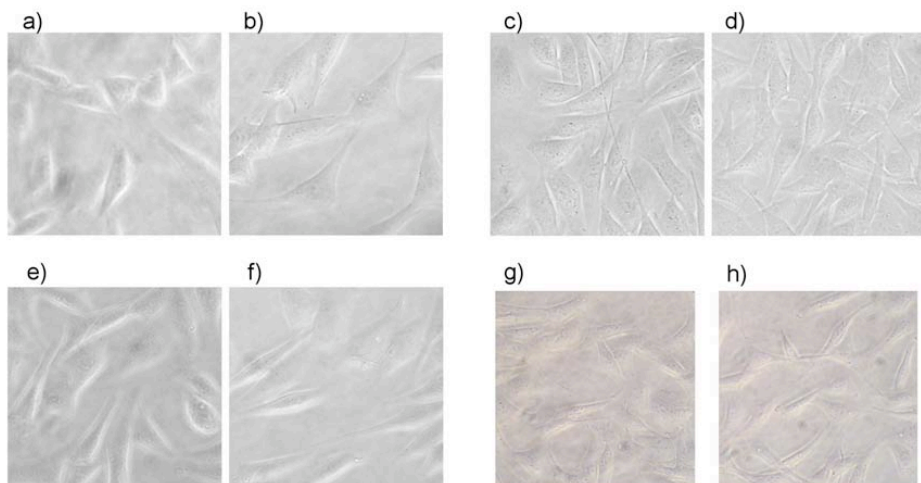


Figure S8: CHO cells expressing hERG before and after incubation with MPA-coated CdSe/ZnS nanocrystals. The images show cells before (a) and 3 h after (b) incubation in 5 nM nanocrystals (wavelength of the absorption peak of the CdSe core  $\lambda = 508$  nm, corresponding to a CdSe core diameter of  $d = 2.4$  nm; 61 Cd surface atoms per nanoparticle); before (c) and 3 h after (d) incubation in 5 nM nanocrystals (wavelength of the absorption peak of the CdSe core  $\lambda = 547$  nm, corresponding to a CdSe core diameter of  $d = 3.0$  nm; 92 Cd surface atoms per nanoparticle); before (e) and 3 h after (f) incubation in 200 nM nanocrystals (wavelength of the absorption peak of the CdSe core  $\lambda = 547$  nm, corresponding to a CdSe core diameter of  $d = 3.0$  nm; 92 Cd surface atoms per nanoparticle); before (g) and 10 h after (h) incubation in 200 nM (wavelength of the absorption peak of the CdSe core  $\lambda = 547$  nm, corresponding to a CdSe core diameter of  $d = 3.0$  nm; 92 Cd surface atoms per nanoparticle).

**(VI) References**

- (1) Pellegrino, T.; Manna, L.; Kudera, S.; Liedl, T.; Koktysh, D.; Rogach, A. L.; Keller, S.; Rädler, J.; Natile, G.; Parak, W. *J. Nanoletters* **2004**, *4*, 703-707.
- (2) Gerion, D.; Pinaud, F.; Williams, S. C.; Parak, W. J.; Zanchet, D.; Weiss, S.; Alivisatos, A. P. *J. Phys. Chem. B* **2001**, *105*, 8861-8871.
- (3) Parak, W. J.; Gerion, D.; Zanchet, D.; Woerz, A. S.; Pellegrino, T.; Micheel, C.; Williams, S. C.; Seitz, M.; Bruehl, R. E.; Bryant, Z.; Bustamante, C.; Bertozi, C. R.; Alivisatos, A. P. *Chem. Mat.* **2002**, *14*, 2113-2119.
- (4) Fink, J.; Kiely, C. J.; Bethell, D.; Schiffrin, D. *J. Chem. Mat.* **1998**, *10*, 922-926.
- (5) Kiely, C. J.; Fink, J.; Zheng, J. G.; Brust, M.; Bethell, D.; Schiffrin, D. *J. Adv. Mater.* **2000**, *12*, 640-643.
- (6) Templeton, A. C.; Wuelfing, W. P.; Murray, R. W. *Accounts Chem. Res.* **2000**, *33*, 27-36.
- (7) Leff, D. V.; O'Hara, P. C.; Heath, J. R.; Gelbart, W. M. *The Journal of Physical Chemistry* **1995**, *99*, 7036-7041.
- (8) Mayya, K. S.; Caruso, F. *Langmuir* **2003**, *19*, 6987-6993.
- (9) Scher, E. C.; Manna, L.; Alivisatos, A. P. *Phil. Trans. R. Soc. Lond. A* **2002**, *361*, 241-257.
- (10) Yu, W. W.; Qu, L.; Guo, W.; Peng, X. *Chem. Mat.* **2003**, *15*, 2854-2860.
- (11) López, E.; Figueroa, S.; Oset-Gasque, M. J.; Gonzalez, M. P. *Br. J. Pharmacol.* **2003**, *138*, 901-911.
- (12) Derfus, A. M.; Chan, W. C. W.; Bhatia, S. N. *NanoLetters* **2004**, *4*, 11-18.
- (13) Shiohara, A.; Hoshino, A.; Hanaki, K.; Suzuki, K.; Yamamoto, K. *MICROBIOLOGY AND IMMUNOLOGY* **2004**, *48*, 669-675.
- (14) Fertig, N.; Blick, R. H.; Behrends, J. C. *Biophys. J.* **2002**, *82*, 3056-3062.
- (15) Hamill, O. P.; Marty, A.; Neher, E.; Sakman, B.; Sigworth, F. J. *Pflügers Arch.* **1981**, *391*, 85 - 100.
- (16) Brueggemann, A.; George, M.; Klau, M.; Beckler, M.; Steindl, J.; Behrends, J. C.; Fertig, N. *Current Drug Discovery Technologies* **2004**, *1*, 91-96.

### **E.3 Quantum Dots on Gold: Electrodes For Photoswitchable Cytochrome c Electrochemistry**

C. STOLL, S. KUDERA, W.J. PARAK, F. LISDAT  
*small* **2**(6), pp. 741–743, 2006

**Protein chemistry**

DOI: [10.1002/smll.200500441](https://doi.org/10.1002/smll.200500441)

**Quantum Dots on Gold: Electrodes For Photoswitchable Cytochrome c Electrochemistry\*\***

*Christian Stoll, Stefan Kudera, Wolfgang J. Parak, and Fred Lisdat\**

Nanostructuring of surfaces has evolved as an interesting research target over the past decade. Electrochemical sensors have benefited from this new technology mainly due to modified diffusion characteristics, an increase in roughness, new electrocatalytic properties, and sensitivity enhancement.<sup>[1,2]</sup> For the application of proteins on electrodes, nanoparticles are particularly advantageous for the preservation of activity and signal amplification.<sup>[3-7]</sup>

The use of proteins in direct communication with an electrode provides the basis for constructing signal chains from reaction partners in solution towards the electrode, mainly for biosensor applications.<sup>[8-12]</sup> Cytochrome c is by far the most intensively investigated protein with respect to the heterogeneous electron transfer,<sup>[13-15]</sup> and was used as a model in the present study.

Recently it has been shown that semiconductor nanoparticles can not only be used as fluorescence labels for biomolecules<sup>[16-18]</sup> but can also be attached to metal electrodes for photoelectrochemical studies.<sup>[19,20]</sup> In this study, electron-hole pair generation within such particles is combined with a redox protein to obtain heterogeneous electron transfer after photoexcitation. This is an interesting feature since it is desirable to read out the electrochemical response of a protein on a certain area of an electrode, which cannot be achieved by the electrode potential only. Thus, the idea of a light-addressable sensor is envisaged.<sup>[21,22]</sup> Nanoparticles provide an additional advantage in this case since they allow a higher spatial resolution compared to a bulk semiconductor material.

In this study, it is shown that the application of quantum dots allows optical control of charge transfer from a protein to an electrode. For this purpose, CdSe/ZnS nanoparticles<sup>[23]</sup>

have been immobilized on gold electrodes using dithiane (Figure 1). The modified electrode was immersed in a phosphate buffer solution, light pulses of 5–20 s were applied (wavelengths within the absorption range of the particles

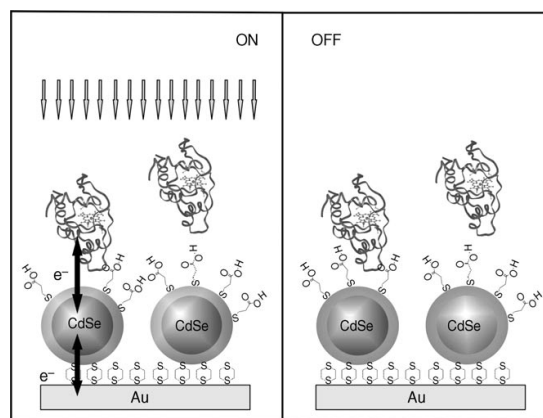


**Figure 1.** Schematic view of a system for photoswitchable electron transfer from an electrode via quantum dots towards the redox protein cytochrome c (in solution). After photoexcitation, a protein-dependent photocurrent can be detected (ON) whereas in the dark no electron transfer via the nanoparticles takes place (OFF). The CdSe/ZnS particles were fixed to the Au surface by using dithiane and modified with a promoter compound (e.g., mercaptopropionic acid).

$\lambda_{\text{max}}=525 \text{ nm}$ ), and the amperometric current response was recorded. A photocurrent at the nanoparticle-modified electrode was obtained, which resulted from electron–hole pair generation that followed the light absorption process and electron transfer between the nanoparticles and the gold surface (Figure 2 A). The direction of the current flow was found to depend on the applied electrode potential. Figure 3 illustrates this potential dependence within a range of  $-500 \text{ mV}$  to  $+500 \text{ mV}$  versus a  $\text{Ag}/\text{AgCl}$  electrode. A set of repetitive measurements ( $n=3$ ) at  $-250 \text{ mV}$  versus  $\text{Ag}/\text{AgCl}$  indicated good stability of the basic system (Au/dithiane/quantum dots) over several hours as only an average photocurrent decrease of  $1.5 \text{ nA}$  was observed (average starting value =  $8.5 \text{ nA}$ ). This also applies to dry storage at room temperature ( $1.4 \text{ nA}$  signal decrease after five days).

However, the layer of fixed CdSe nanoparticles was not only able to exchange electrons with the electrode but also with redox-active substances in solution.<sup>[23]</sup> In these cases an enhanced photocurrent was detected. For example, a light-induced reduction current was found at  $-250 \text{ mV}$  versus  $\text{Ag}/\text{AgCl}$  when hexacyanoferrate(III) ions were present in solution (Figure 2 B). Thus, an electron transfer from the electrode via the quantum dots to the ions in solution (acting as an electron acceptor) was achieved. As expected, no enhanced photocurrent was measurable at  $+250 \text{ mV}$  versus  $\text{Ag}/\text{AgCl}$ , since all the ions were already in the oxidized state and thus not able to transfer electrons towards the CdSe/ZnS nanoparticles. Hence, by applying a negative

[\*] Ch. Stoll, Prof. Dr. F. Lisdat  
University of Applied Sciences Wildau  
Biosystems Technology  
Bahnhofstrasse 1, 15745 Wildau (Germany)  
Fax: (+49)3375 508 578  
E-mail: [flisdat@igw.tfh-wildau.de](mailto:flisdat@igw.tfh-wildau.de)

S. Kudera, Dr. W. J. Parak  
Center for Nanoscience, Ludwig Maximilian University Munich  
Amalienstrasse 54, 80799 München (Germany)

[\*\*] Financial support by the “Ministerium für Wissenschaft, Forschung und Kultur Brandenburg” (Germany) is kindly acknowledged (24#2597-04/339; 2004).

Supporting information for this article is available on the WWW under <http://www.small-journal.com> or from the author.

## communications

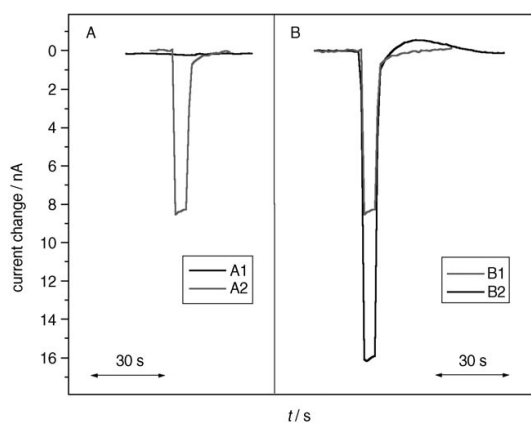


**Figure 2.** A) Current response in a 0.1 M phosphate buffer (pH 7.4) with A1) a dithiane-modified Au electrode and A2) a dithiane/quantum-dot-modified Au electrode; B) current response of a dithiane/quantum-dot-modified Au electrode in B1) 0.1 M phosphate buffer (pH 7.4) and B2) the same buffer containing 50  $\mu$ M hexacyanoferrate(III). Potential: -250 mV versus Ag/AgCl; pulse time: 6 s.

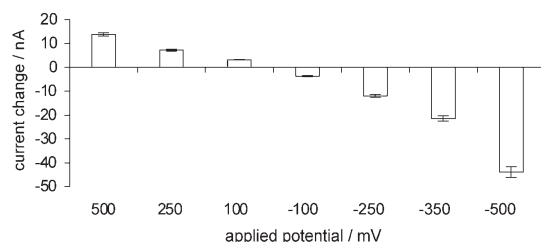


**Figure 3.** Dependence of the photocurrent of a quantum-dot-modified Au electrode on the applied potential (0.1 M phosphate buffer (pH 7.4), pulse time = 10 s, error bars indicate the variation found within six repeated measurements at each potential).

potential in combination with a light pulse it was possible to control the reduction of hexacyanoferrate(III) ions. It has to be mentioned that the basic current without illumination was also increased under these conditions, because the modification with dithiane and the nanoparticles did not completely block the surface for the small hexacyanoferrate ions. However, since only the photocurrent is evaluated, this does not limit the applicability of the measurement.

When the same electrode was used in a cytochrome c solution no photocurrent enhancement was found upon illumination. Clearly the CdSe/ZnS particles did not provide a suitable surface for efficient electron transfer to the heme protein. In order to decrease the hydrophobic properties of the particle surface, the original layer of hydrophobic surfactant molecules on their surface was converted to a hydrophilic one by ligand exchange using mercaptopropionic acid or mercaptosuccinic acid. As can be seen in the inset of Figure 4, the electrodes showed a completely different behavior. As cytochrome c has a redox potential at around 0 mV versus Ag/AgCl and the protein molecules are in an

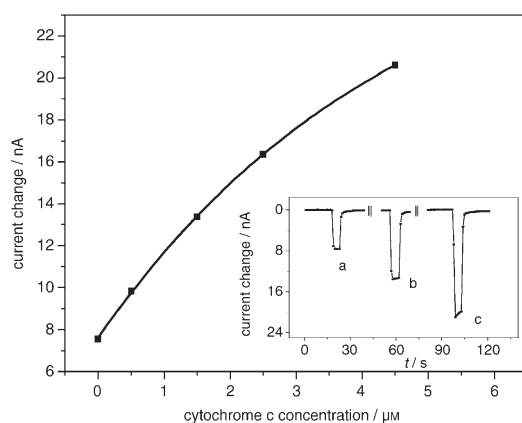


**Figure 4.** Dependence of the photocurrent on the concentration of cytochrome c detected at a Au electrode modified with quantum dots/mercaptosuccinic acid. The inset shows the change in current with time following a 5 s light pulse in a) 0.1 M phosphate buffer (pH 7.4), b) a 1.5  $\mu$ M cytochrome c solution, and c) a 4.5  $\mu$ M cytochrome c solution in the same buffer. Potential: -250 mV versus Ag/AgCl.

oxidized state, a negative electrode potential has been applied. An enhanced photocurrent was detected starting from protein concentrations of about 1  $\mu$ M. Advantageously, the basic current (without illumination) is only slightly influenced by the addition of cytochrome c to the solution (1 nA upon addition of 1.5  $\mu$ M cytochrome c). Thus, the nanoparticle modification provides a barrier for the electron transfer when the electrode is not photoexcited. The application of an electrode potential more positive than the redox potential (+250 mV) did not result in an enhanced photocurrent. These experiments prove that the quantum dot layer fixed to the gold electrode can work as a light-controlled switch for heterogeneous electron transfer to the redox protein cytochrome c. Investigations of the stability of the protein response showed the importance of a proper interface design. Several repeated measurements resulted in a gradual loss of the photocurrent. However, this instability probably originated from partial blocking of the surface by denatured protein as it could be circumvented by longer modification times of the nanoparticles within the promoter solution (mercaptopropionic or mercaptosuccinic acid).

The photocurrent was found to increase with the concentration of oxidized cytochrome c in the micromolar concentration range (Figure 4). Thus, the system allows not only detection of the redox state of the protein but also provides a basis for the detection of protein interactions with small analyte molecules such as superoxide radicals, which are able to reduce cytochrome c. In addition it may be valuable for the detection of analyte molecules that are converted by enzymes accepting cytochrome c as an electron donor or acceptor. The platform described here might be extended to other redox proteins by using different promoter molecules for modification of the nanoparticles and by immobilization of the proteins, thus providing the basis for use in a protein array. By immobilizing different proteins on

the same electrode surface and by addressing the respective readout with a light pulse, a new generation of protein arrays could evolve. In conclusion, we report that light-induced electron transfer from a modified electrode to the redox protein cytochrome c has been achieved.

**Keywords:**

cytochrome c • electrochemistry • gold • proteins • quantum dots

[1] A. N. Shipway, E. Katz, I. Willner, *ChemPhysChem* **2000**, *1*, 1–208.  
[2] B. Katz, I. Willner, J. Wang, *Electroanalysis* **2004**, *15*, 19–45.  
[3] J. J. Gooding, *Electrochim. Acta* **2005**, *50*, 3049–3060.  
[4] M. Zayats, E. Katz, R. Baron, I. Willner, *J. Am. Chem. Soc.* **2005**, *127*, 12 400–12 406.  
[5] F. Caruso, C. Schuler, *Langmuir* **2000**, *16*, 9595–9603.  
[6] C. M. Niemeyer, *Angew. Chem.* **2003**, *47*, 5974–5978; *Angew. Chem. Int. Ed.* **2003**, *115*, 5796–5800.  
[7] S. Q. Liu, D. Leech, H. X. Ju, *Anal. Lett.* **2003**, *36*, 1–19.  
[8] W. Schuhmann, H. Zimmermann, K. V. Habermuller, V. Laurinavicius, *Faraday Discuss.* **2000**, *116*, 245–255.  
[9] S. Shleev, J. Tkac, A. Christenson, T. Ruzgas, A. I. Yaropolov, J. W. Whittaker, L. Gorton, *Biosens. Bioelectron.* **2005**, *20*, 2517–2554.  
[10] Y. Zhou, N. Hu, Y. Zeng, J. F. Rusling, *Langmuir* **2002**, *18*, 211–219.  
[11] B. Ge, F. Lisdat, *Anal. Chim. Acta* **2002**, *454*, 53–64.  
[12] E. E. Ferapontova, V. G. Grigorenko, A. M. Egorov, T. Borchers, T. Ruzgas, L. Gorton, *Biosens. Bioelectron.* **2001**, *16*, 147–157.  
[13] M. Fedurco, *Coord. Chem. Rev.* **2000**, *209*, 263–331.  
[14] a) M. J. Eddowes, H. A. O. Hill, *J. Chem. Soc. Chem. Commun.* **1977**, *21*, 771; b) P. Yeh, T. Kuwana, *Chem. Lett.* **1977**, *10*, 1145.  
[15] a) R. A. Clark, E. F. Bowden, *Langmuir* **1997**, *13*, 559–565; b) P. Bianco, J. Haladjian, *Electrochim. Acta* **1994**, *39*, 911–916; c) Z. Q. Feng, S. Imabayashi, T. Kakiuchi, K. Niki, *J. Chem. Soc. Faraday Trans.* **1997**, *93*, 1367–1370; d) K. J. McKenzie, F. Marken, *Langmuir* **2003**, *19*, 4327–4331.  
[16] T. Pellegrino, S. Kudera, T. Liedl, A. Muñoz Javier, L. Manna, W. J. Parak, *Small* **2005**, *1*, 48–63.  
[17] S. J. Rosenthal, A. Tomlinson, E. M. Adkins, S. Schroeter, S. Adams, L. Swafford, J. McBride, Y. Q. Wang, L. J. DeFelice, R. D. Blakely, *J. Am. Chem. Soc.* **2002**, *124*, 4586–4594.  
[18] I. Sondi, O. Siiman, S. Koester, E. Matijevic, *Langmuir* **2000**, *16*, 3107–3118.  
[19] E. P. A. M. Bakkers, A. L. Roest, A. W. Marsman, L. W. Jenneskens, L. I. de Jong-van Steensel, J. J. Kelly, D. Vanmaekelbergh, *J. Phys. Chem. B* **2000**, *104*, 7266–7272.  
[20] S. N. Sharma, Z. S. Pillai, P. V. Kamat, *J. Phys. Chem. B* **2003**, *107*, 10088–10093.  
[21] S. Licht, N. Myung, Y. Sun, *Anal. Chem.* **1996**, *68*, 954–959.  
[22] D. G. Hafemen, J. W. Parce, M. McConnell, *Science* **1988**, *240*, 1182–1185.  
[23] a) P. Reiss, J. Bleuse, A. Pron, *Nano Lett.* **2002**, *2*, 781–784; b) B. O. Dabbousi, J. Rodriguez-Viejo, F. V. Mikulec, J. R. Heine, H. Mattoussi, R. Ober, K. F. Jensen, M. G. Bawendi, *J. Phys. Chem. B* **1997**, *101*, 9463–9475.  
[24] E. P. M. A. Bakkers, E. Reitsma, J. J. Kelly, D. Vanmaekelbergh, *J. Phys. Chem. B* **1999**, *103*, 2781–2788.

Received: November 11, 2005

Published online on March 24, 2006

## **E.4 Catalytic and seeded shape-selective synthesis of II–VI semiconductor nanowires**

A. FASOLI, A. COLLI, S. KUDERA, L. MANNA, S. HOFMANN, C. DUCATI, J. ROBERTSON, A.C. FERRARI

*Physica E* **37**(1–2), pp. 138–141, 2007

We demonstrate catalytic and seeded shape-selective growth of CdSe nanostructures by a steady-state vapor-transport process. By varying the powder and sample temperatures, we observe a transition from a regime where catalytic growth is dominant to a metal-free self-induced nucleation regime. We then show that the best structural and optical quality are obtained by using CdSe colloidal nanocrystals as seeds for metal-free growth, as indicated by electron microscopy, X-ray diffraction and photoluminescence.



Available online at [www.sciencedirect.com](http://www.sciencedirect.com)



Physica E 37 (2007) 138–141

**PHYSICA E**

[www.elsevier.com/locate/physe](http://www.elsevier.com/locate/physe)

## Catalytic and seeded shape-selective synthesis of II–VI semiconductor nanowires

A. Fasoli<sup>a,\*</sup>, A. Colli<sup>a</sup>, S. Kudera<sup>b</sup>, L. Manna<sup>b</sup>, S. Hofmann<sup>a</sup>,  
C. Ducati<sup>c</sup>, J. Robertson<sup>a</sup>, A.C. Ferrari<sup>a</sup>

<sup>a</sup>*Engineering Department, Cambridge University, Cambridge CB3 0FA, UK*

<sup>b</sup>*National Nanotechnology Laboratory, Lecce, Italy*

<sup>c</sup>*Department of Materials Science and Metallurgy, Cambridge University, Cambridge CB2 3QZ, UK*

Available online 6 September 2006

### Abstract

We demonstrate catalytic and seeded shape-selective growth of CdSe nanostructures by a steady-state vapor-transport process. By varying the powder and sample temperatures, we observe a transition from a regime where catalytic growth is dominant to a metal-free self-induced nucleation regime. We then show that the best structural and optical quality are obtained by using CdSe colloidal nanocrystals as seeds for metal-free growth, as indicated by electron microscopy, X-ray diffraction and photoluminescence.

© 2006 Elsevier B.V. All rights reserved.

PACS: 61.46.-w

Keywords: CdSe; Nanostructures; Vapor transport; Colloids

### 1. Introduction

High-aspect-ratio semiconductor nanostructures are of great interest due to their potential applications in electronics and photonics [1–3]. II–VI materials, in particular, can be grown in a variety of different shapes such as nanowires (NWs), nanoribbons (NRs), nanosaws (NSs), nanorods (NRDs) or multi-branched structures [4–7]. Vapor-phase deposition techniques usually involve the use of a metal catalyst particle to promote NW nucleation [1,2,6–8]. Within this approach, however, the metal may result in a source of contamination, leading to the formation of detrimental scattering centers and intra-bandgap deep-level states [9].

Vapor transport in a single-zone quartz tube furnace is a widely employed approach for nanostructure synthesis [6,7,10,11]. Several groups reported catalyst-free NWs or NRDs by this technique [6,10,12]. In some cases, it was claimed that homo- or hetero-epitaxial nucleation on pre-

existing crystalline surfaces was needed as a driving force for NRD growth [6,12], although similar results were also obtained on amorphous substrates [10]. On the other hand, wet-chemistry also allows metal-free synthesis of NRDs in solution [4,13]. Their dimensions, though, do not exceed a few hundreds nanometers, limiting their potential for some applications. Also, they cannot be selectively grown and aligned on a substrate in well-defined positions, but require post-deposition handling.

CdSe is one of the most investigated II–VI semiconductors [4,6]. With its bulk direct bandgap of 1.73 eV, it is a very promising candidate for photovoltaics applications. Here we identify three different growth regimes for CdSe nanostructures synthesis: catalytic, self-seeded and colloidal seeded growth. We then report the catalyst-free synthesis of CdSe NRDs and multipods by vapor transport.

### 2. Experimental

CdSe nanostructures are synthesized by vapor transport in a horizontal tube, single-zone furnace reactor. Key features of our system and synthesis procedures are

\*Corresponding author. Tel.: +44 1223 748377; fax: +44 1223 748348.

E-mail addresses: af343@hermes.cam.ac.uk (A. Fasoli), acf26@eng.cam.ac.uk (A.C. Ferrari).

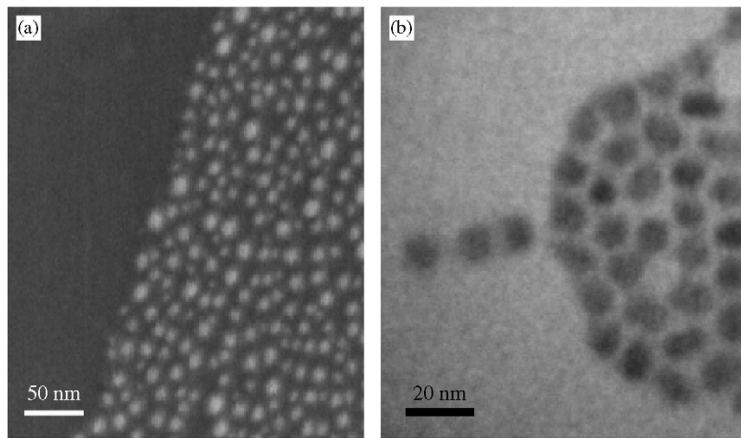


Fig. 1. (a) FEGSEM image of Au nanoislands resulting from the splitting of the patterned catalyst layer. (b) TEM image of CdSe colloids used for colloid-assisted growth [13].

described elsewhere [8]. For the set of experiments described here, we use Au-patterned (0.5 nm) oxidized Si  $\langle 100 \rangle$  substrates for catalytic NW growth. During the heating ramp, the catalyst layer splits into nanoislands about 10 nm in diameter, as shown in Fig. 1(a). Bare-oxidized Si  $\langle 100 \rangle$  chips are used for seeded growth. CdSe nanocrystals (5–10 nm in diameter), produced by solution methods [14] are dispersed from chloroform onto oxidized Si substrates for colloid-assisted growth (Fig. 1(b)). CdSe nanostructures are characterized by field-emission-gun scanning electron microscopy (FEGSEM), transmission electron microscopy (TEM), X-ray diffraction (XRD) and photoluminescence (PL). PL measurements are acquired by using an Ar-ion laser coupled to a micro-Raman spectrometer.

### 3. Results and discussion

We previously demonstrated that Au-catalyzed shape-selective synthesis of CdSe nanostructures is ruled by an interplay between surface kinetics and precursor impinging rate [8]. For our vapor-transport furnace reactor, these two parameters are driven by substrate and powder temperature, respectively ( $T_S$ ,  $T_P$ ). The lower triangle of the diagram in Fig. 2 summarizes the general trends observed for NW, NR and NS synthesis [8,15]. The main idea behind position and shape selectivity relies on the different CdSe vapor sticking and kinetics on different surfaces. In our particular case, interactions between CdSe<sub>(V)</sub>–Au, CdSe<sub>(V)</sub>–CdSe<sub>(S)</sub>, and CdSe<sub>(V)</sub>–SiO<sub>2(S)</sub> (V = vapor, S = solid) have to be considered. Due to the higher sticking coefficient of CdSe on Au, Au-catalyzed NWs can be grown, with no excess CdSe deposited on the NW sidewalls or on the uncoated SiO<sub>2</sub> areas of the substrate (Fig. 2, lower vertex). At higher powder temperatures, however, the thermal energy is no longer sufficient to fully desorb the incoming precursor. Thus homoepitaxial CdSe growth occurs on the NW sidewalls, leading eventually to a NR or NS

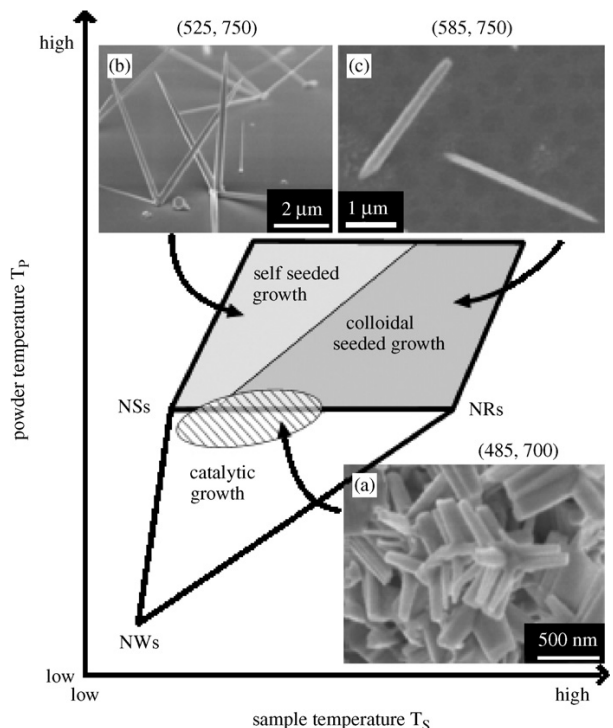


Fig. 2. Shape diagram of CdSe nanostructures obtained by varying powder and sample temperatures. Three growth regimes are found.

morphology (Fig. 2). Hence, a proper combination of parameters allows us to control the nanocrystal shape [8]. It should be noted that, within the NWs–NRs–NSs region of Fig. 2, position selectivity can always be achieved by patterning the Au catalyst. This because the sticking of CdSe vapor on SiO<sub>2</sub> is still suppressed for these conditions [8,16].

Within the NS regime ( $T_P > 650^\circ\text{C}$ ,  $450^\circ\text{C} < T_S < 500^\circ\text{C}$ ), elongated NRD branches begin to form on Au-catalyzed

NWs or NRs (Fig. 2(a)) [8]. This indicates that Au-free CdSe NRDs may be synthesized at higher  $T_P$  compared to their Au-catalyzed NW counterpart, though still requiring an existing CdSe surface to promote initial nucleation. By further increasing  $T_P$ , however, the local CdSe vapor density becomes enough for CdSe nanoislands to nucleate even on the bare  $\text{SiO}_2$  substrate. This is the regime marked as self-seeded growth in Fig. 2. For such a combination of parameters, it is possible to grow nanopods and NRDs on bare-oxidized Si chips, without the need of any metal catalyst or surface preparation (Fig. 2(b)). In fact, two separate mechanisms take place in a self-seeded process. The first is the nucleation of a CdSe seed on  $\text{SiO}_2$ . For fixed  $T_P$ , a higher density of seeds is achieved by *lowering*  $T_S$ . Then, as soon as the seed is formed, this constitutes a preferential sticking point to promote further anisotropic epitaxial growth, similar to what happens for a NS teeth. However, we find that the formation of regular rods versus multipods or more disordered structures is enhanced by *increasing*  $T_S$  (for fixed  $T_P$ ). The overlap between seed formation and NRDs growth is thus very narrow and a compromise has to be reached between final density and morphology of the resulting nanostructures.

In order to overcome these limitations, we decouple NRD growth and seed preparation by dispersing spherical CdSe colloidal nanocrystals on Si chips prior to loading the substrates in the vapor-transport reactor. In this case, initial condensation of CdSe vapor on  $\text{SiO}_2$  is no longer necessary and NRD formation can be achieved at higher  $T_S$  compared to self-seeded growth (Fig. 2, colloidal-seeded growth region). The best uniformity in terms of NRD morphology, length and diameter is found by following this approach (Fig. 2(c)). In addition, colloid-seeded NRDs tend to exhibit a spontaneous vertical alignment.

XRD measurements performed on self-seeded multipods (Fig. 1(b)) and colloid-seeded NRDs are shown in Fig. 3. Several powder-diffraction peaks are detected for the self-seeded sample, which can be assigned both to cubic and hexagonal CdSe (Fig. 3(a)). A single phase (wurtzite) is revealed by the  $2\theta$  scan in Fig. 3(b) instead. Peaks related to Cd oxides (marked as “\*” in Fig. 3) are seen in both cases, probably due to post-growth surface oxidation when exposing the samples to atmosphere. XRD results indicate that NRDs grown at higher  $T_S$  by means of colloidal seeds also offers a superior crystallographic quality. It has been reported that CdSe tetrapods grown by solution-based techniques exhibit a zinc blende (cubic) core and wurtzite (hexagonal) branches [13]. However, there is also evidence that such proposed dual-phase nucleation is not responsible for tetrapods formation but rather this is triggered by the presence of crystal twinnings within the wurtzite tetrapod core [17]. Due to the wide shape distribution of our self-seeded nanostructures, we believe that the mixed phase detected in Fig. 3(a) accounts more for highly disordered crystals rather than for regular cubic-core/wurzite-branch tetrapods. On the other hand, colloidal nanocrystals guarantee a much better seed uniformity, both in terms of shape and size distribution. As an additional advantage, we emphasize

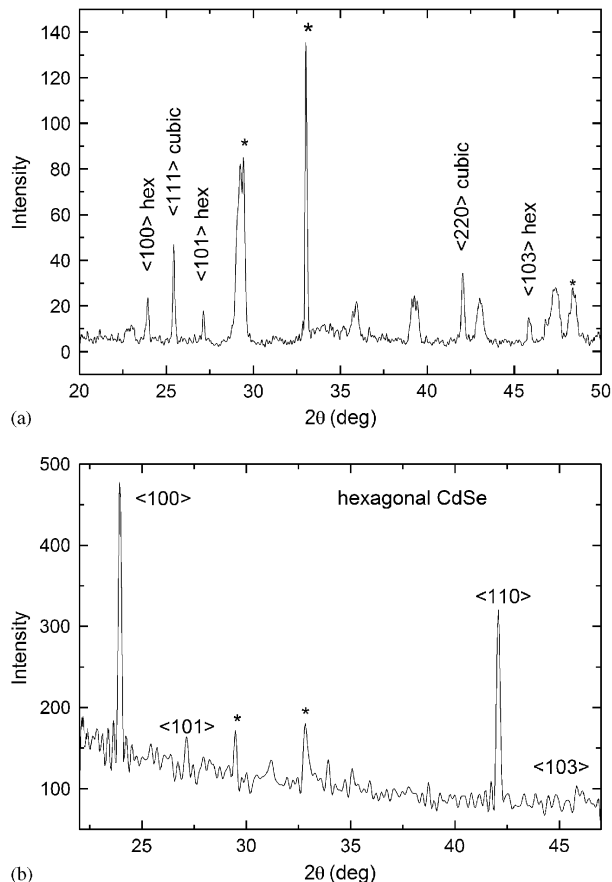


Fig. 3. XRD spectra comparing the internal structure of (a) self-seeded CdSe multi-branched nanostructures, presenting both zinc blende (cubic) and wurtzite (hexagonal) phases and (b) colloid-assisted CdSe NRDs, where wurtzite phase is dominant. Peaks labeled by “\*” are assigned to  $\text{CdO}_2$  [17].

that colloidal seeds might be pre-patterned *ex situ* on Si substrates by means of various techniques [4,18], whereas the *in situ* self-seeding process occurs randomly on the surface with no possible selective placement.

Finally, Fig. 4 compares the temperature-dependent optical emission of Au-catalyzed CdSe NWs and colloid-seeded CdSe NRDs. PL spectra in Fig. 4(a) show a broad and structured low-energy emission band around 1.7 eV, which may be attributed to electron-to-shallow-acceptor and shallow-donor-to-acceptor transitions [19]. Compared to the near-band-edge emission, such band is dominant at low temperatures and disappears above 170 K, as expected [19]. No low-energy band is found for the NRDs in Fig. 4(b). The possibility for the Au catalyst being responsible for the differences in PL emission is currently under investigation.

As a final remark, we note that, unlike the CdSe colloids PL emission (Fig. 1), NBE emission of CdSe NWs and NRDs occurs at the bulk CdSe bandgap energy. No quantum confinement effects are observed as the Bohr radius for CdSe is as low as 5 nm [20] (our Au-catalyzed

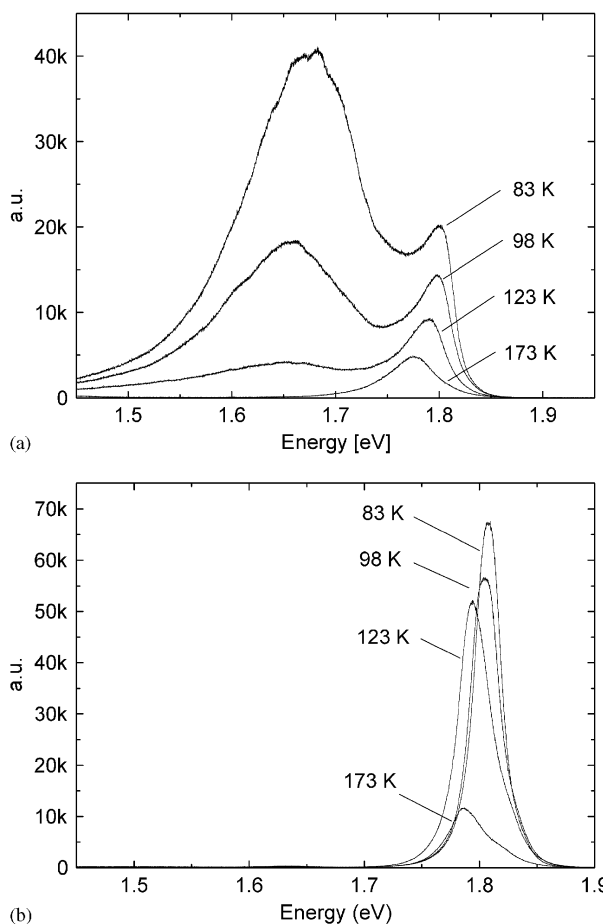


Fig. 4. PL spectra of (a) catalytically synthesized NRDs and (b) NRDs from colloid-assisted growth. No low-energy peaks associated to lattice defects or impurities are found for the colloid-assisted NRDs, suggesting their superior crystal quality.

NW are typically  $\sim 50$  nm in diameter [8]). The NRD diameter ( $\sim 100$ – $200$  nm) is also much larger than the size of the original CdSe colloids (5 nm). The dispersed nanocrystals act only as seeds to initiate NR formation, and do not appear to limit the NR diameter (as opposed to Au seeds for catalytic growth). In principle, *any* particle or material with higher sticking coefficient than SiO<sub>2</sub> could be potentially suitable for such purpose. However, by choosing nanocrystal seeds *made of the same material* as the NRDs we can rule out undesirable contamination. Self-driven anisotropic growth for catalyst-free NRDs is believed to arise from a combination of material-related properties (such as surface energy and polarity [10]) and experimental conditions [21].

#### 4. Conclusion

In summary, we demonstrated the catalytic, self-seeded and colloidal-assisted growth of CdSe nanostructures by

thermal evaporation in a single-zone furnace tube. Use of CdSe colloids made possible the metal-free homoepitaxial synthesis of NRDs in a high- $T_P$  regime, overcoming this intrinsic self-seeded growth limitation. This solution provides the best NRDs in terms of uniformity of morphology, diameter, and length. Comparison of XRD spectra on self-seeded and colloidal-assisted grown nanostructures demonstrates the superior crystallographic quality of the high- $T_P$  NRDs, which exhibit uniform hexagonal structural arrangement. Good optical quality was confirmed by low-temperature PL measurements.

#### Acknowledgements

AF acknowledges funds from ETRI, EPSRC, Cambridge European Trust and Pembroke College. ACF acknowledges funding from The Royal Society and The Leverhulme Trust. This work was supported by the Ministry of Information and Communication, Republic of Korea, under project No. A1100-0501-0073.

#### References

- [1] M. Law, J. Goldberger, P. Yang, *Annu. Rev. Mater. Res.* 34 (2004) 83.
- [2] X.F. Duan, Y. Huang, R. Agarwal, C.M. Lieber, *Nature* 421 (2003) 241.
- [3] W.U. Huynh, J.J. Dittmer, A.P. Alivisatos, *Science* 295 (2002) 2425.
- [4] L. Manna, D.J. Milliron, A. Meisel, E.C. Scher, A.P. Alivisatos, *Nat. Mater.* 2 (2003) 382.
- [5] Z.L. Wang, *Mater. Today* 7 (2004) 26.
- [6] C. Ma, Y. Ding, D. Moore, X. Wang, Z.L. Wang, *J. Am. Chem. Soc.* 126 (2004) 708.
- [7] A. Colli, S. Hofmann, A.C. Ferrari, C. Ducati, F. Martelli, S. Rubini, S. Cabriti, A. Franciosi, J. Robertson, *Appl. Phys. Lett.* 86 (2005) 153103.
- [8] A. Colli, A. Fasoli, S. Hofmann, C. Ducati, J. Robertson, A.C. Ferrari, *Nanotechnology* 17 (2006) 1046.
- [9] P.J. Dean, B.J. Fitzpatrick, R.N. Bhargava, *Phys. Rev. B* 26 (1982) 2016.
- [10] Z.R. Dai, Z.W. Pan, Z.L. Wang, *Adv. Funct. Mater.* 13 (2003) 9.
- [11] D.D.D. Ma, C.S. Lee, F.C.K. Au, S.Y. Tong, S.T. Lee, *Science* 299 (2003) 1874.
- [12] R.C. Wang, C.P. Liu, J.L. Huang, S.J. Chen, *Appl. Phys. Lett.* 86 (2005) 251104.
- [13] L. Manna, E.C. Scher, A.P. Alivisatos, *J. Am. Chem. Soc.* 122 (2000) 12700.
- [14] Z.A. Peng, X.G. Peng, *J. Am. Chem. Soc.* 123 (2001) 183.
- [15] A. Fasoli, A. Colli, S. Hofmann, C. Ducati, J. Robertson, A.C. Ferrari, *Phys. Status Solidi*, in press.
- [16] D.P. Masson, D. Landheer, T. Quance, J.E. Hulse, *J. Appl. Phys.* 84 (1998) 4911.
- [17] L. Carbone, S. Kudera, E. Carlino, W.J. Parak, C. Giannini, R. Cingolani, L. Manna, *J. Am. Chem. Soc.* 128 (2006) 748.
- [18] R.A. McMillan, C.D. Paavola, J. Howard, S.L. Chan, N.J. Zaluzec, J.D. Trent, *Nat. Mater.* 1 (2002) 247.
- [19] D.L. Rosen, Q.X. Li, R.R. Alfano, *Phys. Rev. B* 31 (1985) 2396.
- [20] H. Fu, L.W. Wang, A. Zunger, *Phys. Rev. B* 59 (1999) 5568.
- [21] V.B. Shenoy, *Appl. Phys. Lett.* 85 (2004) 2376.

## **E.5 Temperature and Size Dependence of Nonradiative Relaxation and Exciton-Phonon Coupling in Colloidal CdTe Quantum Dots**

G. MORELLO, M. DE GIORGI, S. KUDERA, L. MANNA, R. CINGOLANI, M. ANNI  
*J. Phys. Chem. C* **11**(16), pp. 5846–5849, 2007

We report on the temperature and size dependence of the photoluminescence of core CdTe colloidal quantum dots (QDs). We show that at temperatures lower than 170 K a thermally activated transition between two different states separated by about 12-20 meV takes place. At temperatures higher than 170 K, the main nonradiative process is thermal escape assisted by multiple longitudinal optical (LO) phonons absorption. Moreover, we show that quantum confinement affects both the exciton-acoustic phonons and the exciton-LO phonons coupling. The coupling constant with acoustic phonons is strongly enhanced in QDs (up to 31eV/K) with respect bulk CdTe (0.7eV/K). On the contrary, the exciton-LO phonons coupling constant decreases as the dot size decreases (down to 14 meV with respect 24.5 meV in the bulk).

## ARTICLES

## Temperature and Size Dependence of Nonradiative Relaxation and Exciton–Phonon Coupling in Colloidal CdTe Quantum Dots

G. Morello,<sup>\*,†</sup> M. De Giorgi,<sup>†</sup> S. Kudera,<sup>†</sup> L. Manna,<sup>†</sup> R. Cingolani,<sup>†</sup> and M. Anni<sup>‡</sup>

Distretto Tecnologico ISUFI and Dipartimento di Ingegneria dell’Innovazione, National Nanotechnology Laboratory (NNL) of CNR-INFM, Università degli Studi di Lecce, Via per Arnesano 73100 Lecce, Italy

Received: December 4, 2006; In Final Form: February 6, 2007

We report on the temperature and size dependence of the photoluminescence of core CdTe colloidal quantum dots (QDs). We show that at temperatures lower than 170 K a thermally activated transition between two different states separated by about 12–20 meV takes place. At temperatures higher than 170 K, the main nonradiative process is thermal escape assisted by multiple longitudinal optical (LO) phonons absorption. Moreover, we show that quantum confinement affects both the exciton–acoustic phonons and the exciton–LO phonons coupling. The coupling constant with acoustic phonons is strongly enhanced in QDs (up to 31  $\mu\text{eV/K}$ ) with respect bulk CdTe (0.7  $\mu\text{eV/K}$ ). On the contrary, the exciton–LO phonons coupling constant decreases as the dot size decreases (down to 14 meV with respect 24.5 meV in the bulk).

## I. Introduction

Semiconductor nanocrystals have attracted considerable interest in the last years, because of their potential applications to light emitting diodes (LEDs),<sup>1,2</sup> photovoltaic cells,<sup>3</sup> and optically pumped lasers.<sup>4</sup> Colloidal semiconductor quantum dots (QDs) have been also coupled to biological molecules such as proteins and DNA.<sup>5,6</sup> These QDs bioconjugates can be used as biomedical fluorescence labels for investigating biomolecular interactions and developing high-sensitivity detection and imaging systems.<sup>5,6</sup> Nowadays, advanced colloidal synthesis techniques allow the growth of highly monodispersed<sup>7</sup> II–VI QDs with high-photoluminescence (PL) quantum yield.<sup>8,9</sup> A detailed study of the QDs photophysics with a particular attention to nonradiative processes is not only interesting for fundamental physics, but it is also relevant to the exploitation of nanocrystals in practical applications. To date, several relaxation processes have been proposed to explain the photophysics of CdSe QDs, including the thermally activated exciton transition from dark to bright states<sup>10</sup> and carriers surface localization in trap states.<sup>11</sup> Moreover, it has been shown that at room temperature the main nonradiative process in CdSe/ZnS core/shell QDs is thermal escape, assisted by multiple longitudinal optical (LO) phonons absorption,<sup>12</sup> while at low temperature evidence for carrier trapping at surface defects was found. Despite these results, the role and the chemical origin<sup>37</sup> of the surface defect states in the radiative and nonradiative relaxation in nanocrystals has not been clarified completely. The existence of surface states due to unpassivated dangling bonds has been invoked to explain the anomalous red-shifted emission bands in colloidal nanocrystals.

On the contrary, it has been recently shown that above-gap trap states<sup>13</sup> affect the ultrafast relaxation dynamics<sup>14</sup> and the single nanoparticle PL spectra of CdSe quantum rods<sup>15</sup> due to charge trapping and local electric field fluctuations. These effects are expected to be dependent on the chemical composition of the QDs on the density of surface defects and on the nanocrystals size.

In this work, we performed a detailed analysis of the PL temperature dependence of colloidal CdTe core QDs with diameters varying between 4.2 and 5.9 nm. We found that the QDs PL is due to a thermally activated transition between two different states at low temperatures.

Moreover, we investigated the size dependence of the coupling with both acoustical and optical phonons. We show that the acoustic phonons coupling constant is strongly increased, up to 31  $\mu\text{eV/K}$  with respect to the bulk CdTe (0.7  $\mu\text{eV/K}$ ). On the other hand, the LO phonons coupling constant is reduced down to 14 meV for the smallest dots with respect to the bulk (24.5 meV). We show that the main nonradiative process affecting the PL quantum yield at high temperature is thermal escape assisted by multiple LO phonons absorption. The average number of phonons assisting the thermal escape increases from 4 for the 5.9 nm diameter dots up to 6 for the 4.2 nm ones, which is in quantitative agreement with the increased energy splitting occurring in the smaller dots.

## II. Experiment

We prepared CdTe QDs of different sizes, following the method described in ref 16. The average diameter of the dots was estimated by TEM measurements to be 4.2, 4.9, and 5.9 nm for samples A1, A2, and A3, respectively. The QDs have been deposited by drop casting from chloroform solution on Si–SiO<sub>2</sub> substrates. For each sample, we performed PL measurements in the temperature range of 15–300 K in steps of

\* Corresponding author. E-mail address: giovanni.morello@unile.it.  
Alternate address: ISUFI + Institute for Advanced Interdisciplinary Studies, Università degli Studi di Lecce, Via per Arnesano 73100 Lecce, Italy.

<sup>†</sup> Distretto Tecnologico ISUFI.

<sup>‡</sup> Dipartimento di Ingegneria dell’Innovazione.

Colloidal CdTe Quantum Dots

*J. Phys. Chem. C*, Vol. 111, No. 16, 2007 **5847**

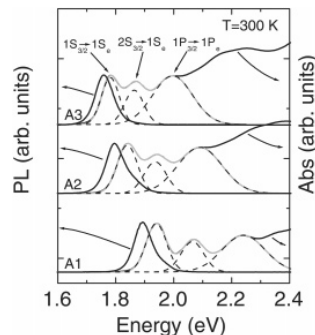


**Figure 1.** Room-temperature absorption and PL spectra of the investigated samples in chloroform solutions (black lines) and best fit Gaussians (gray lines).

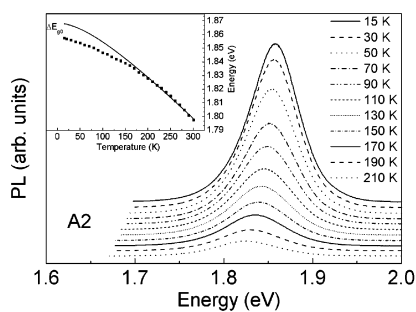


**Figure 2.** PL spectra as a function of temperature for sample A2. Inset: experimental energy gap for the same sample (full squares), and best fit curve (continuous line).

10 K. The samples were excited by ion Argon laser ( $\lambda = 458$  nm). The sample emission was dispersed by a monochromator (0.32 m focal length) and detected by a Si-CCD camera. The PL measurements were performed in vacuum in a closed-cycle He cryostat. The absorption spectra were measured in solution with a spectrophotometer.

### III. Results and Discussion

The absorption spectra of the QDs at room temperature (see Figure 1) show several peaks, corresponding to different optical transitions. The first three resonances can be reproduced by the superposition of three Gaussian bands (see Figure 1). The best fit peak energies clearly show the blue-shift of the first absorption peak and the increase of the energy splitting among the confined states, as the dots size decreases. The three first absorption peaks are due to  $1S_{3/2} \rightarrow 1S_e$ ,  $2S_{3/2} \rightarrow 1S_e$ , and  $1P_{3/2} \rightarrow 1P_e$  transitions.<sup>17,18</sup>

A typical temperature dependence of the PL spectra is reported in Figure 2, for sample A2. The spectra exhibit a weak low-energy tail (not visible in solution) that can be assigned to emission from the larger dots in the size distribution, enhanced by Förster transfer (FRET)<sup>19</sup> from the smaller dots. As the temperature increases, the PL spectra show a red-shift of the peak energy, increasing broadening and decreasing intensity.

In semiconductor nanostructures, the temperature dependence of the energy gap is usually similar to the bulk semiconductor one,<sup>20–22</sup> except for a temperature-independent energy off-set due to the quantum confinement. The experimental PL temperature dependence is thus well reproduced by the Varshni relation

$$E_g(T) = E_{g0} - \alpha \frac{T^2}{(T + \beta)} \quad (1)$$

with  $\alpha$  and  $\beta$  consistent with the bulk values. In eq 1,  $E_{g0}$  is the energy gap at 0 K,  $\alpha$  is the temperature coefficient, and the value of  $\beta$  is close to the Debye temperature  $\theta_D$  of the material. On the other hand, the experimental PL peak energy temperature dependence cannot be reproduced by the Varshni relation with “bulk-like”  $\alpha$  and  $\beta$  when transitions between different states take place in the investigated temperature range.<sup>10,11</sup> In our case the experimental data can be fitted to eq 1 with  $\alpha$  and  $\beta$  values consistent with bulk CdTe only for  $T \geq 150–170$  K, while a weaker temperature dependence is present at low temperature. Values of  $\alpha$  and  $\beta$  not consistent with CdTe are instead obtained by all the data or only the  $T \leq 150$  K ones. Keeping  $\beta$  fixed<sup>24</sup> at the bulk value<sup>22</sup> of 158 K we find a best fit value for  $\alpha = 3.2 \times 10^{-4}$  eV/K very close to the bulk value ( $3 \times 10^{-4}$  eV/K) reported in literature.<sup>23</sup> For temperatures below 170 K, the experimental emission energy is lower than the extrapolated value of the  $T \geq 170$  K best fit curve with a maximum difference  $\Delta E_{g0}$  at 15 K of the order of 12–20 meV in the three samples. We observe that for all the samples, the experimental data follow a bulklike best fit curve for  $k_B T \geq \Delta E_{g0}$  (where  $k_B$  is the Boltzmann constant) suggesting that a thermally activated transition between two different states energetically separated by  $\Delta E_{g0}$ , takes place. This transition could be due to different possible processes, like the dark-bright exciton transition,<sup>10</sup> or the transitions between intrinsic and surface states, such as detrapping from surface trap states to intrinsic electronic states,<sup>11</sup> or transition from intrinsic states to higher energy-localized surface states.<sup>14</sup> The dark-bright exciton transition can be ruled out as the typical activation energies<sup>25</sup> are much smaller than the  $\Delta E_{g0}$  values (typically a few meV) and are strongly size dependent, whereas in our case  $\Delta E_{g0}$  does not show any regular variation with the QDs size (see Table 1). This suggests that a thermally activated transition involving surface and core states is responsible for the PL peak temperature dependence. Moreover, the Stokes shift at room temperature shows an expected increase by decreasing size<sup>26</sup> (see Figure 1): 24 meV, 42 meV, and 52 meV for sample A3, A2, and A1, respectively. This trend suggests that the nature of the emitting state at room temperature is intrinsic.

To determine the different nonradiative processes affecting carriers relaxation, we studied the PL intensity variations with temperature. In Figure 3 we show the PL intensity dependence on  $1/k_B T$ . For all the samples, the photoluminescence intensity is almost constant up to about 40 K, while a first thermally activated PL decrease is visible in the range 40–170 K, followed by a stronger exponential decrease up to 300 K. In general, the relaxation processes in QDs include radiative relaxation, Auger nonradiative scattering,<sup>27,28</sup> Förster energy transfer between dots of different dimensions, thermal escape from the dot,<sup>31</sup> and carriers localization at surface states.<sup>32,33</sup> In our excitation regime (few W cm<sup>-2</sup>) the Auger interaction can be neglected, as the average excitation per dot is ( $N_0$ )  $\ll 1$ .<sup>34</sup> Moreover, FRET can be neglected because we do not observe significant differences between the PL spectra obtained from liquid and solid samples.

Assuming a temperature-independent radiative lifetime due to the strong confinement regime,<sup>29</sup> the temperature dependence of the PL intensity, taking into account the radiative relaxation, a thermally activated nonradiative process (with activation energy  $E_a$ ),<sup>30</sup> and the thermal escape is given by<sup>12</sup>

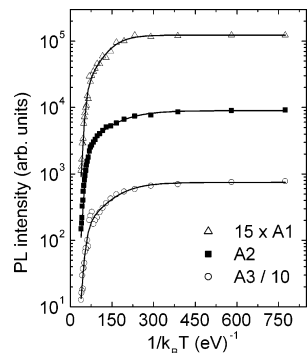


**Figure 3.** Integrated PL intensity dependence on the samples' temperature (symbols) and best fit curves (continuous lines) to eq 3. The data are scaled for clarity.

$$I_{PL}(T) = \frac{I_0}{1 + a(e^{-E_a/k_B T}) + b(e^{E_{LO}/k_B T} - 1)^{-m}} \quad (2)$$

where  $I_{PL}(T)$  is the integrated PL intensity at temperature  $T$ ,  $I_0$  is the 0 K integrated PL intensity, and  $m$  is the number of LO phonons involved in thermal escape of carriers and  $E_{LO}$  is their energy.<sup>35</sup> The best fit parameters are reported in Table 1.

We observe that the best fit value of  $E_a$  is, for all the samples, very similar to the  $\Delta E_{g0}$  values extracted from the PL peak energy analysis. This suggests that the low-temperature PL quenching process is due to the same thermally activated transition between intrinsic and defect states that affect the PL peak temperature dependence. In epitaxial QDs, simultaneous presence of an anomalous energy gap temperature dependence and of a PL quenching process with an activation energy of a few tens of meV is typical of transitions between intrinsic and defect states.<sup>36</sup> In colloidal nanocrystals, some experiments on CdTe and CdSe QDs showed the presence of emitting surface states lying several tens of meV below the band edge emission,<sup>37,38</sup> while theoretical results on potentially emitting surface defect states that resonant with or at higher energy than the band edge are also present.<sup>13</sup> However, the exact chemical origin of these surface states is not yet known.<sup>37</sup> Our results can be due to a thermally induced detrapping from a surface defect state to a weakly radiatively coupled intrinsic state or to an unusual thermally activated trapping. Further experiments, like time-resolved PL, have to be performed to attribute our results to trapping or detrapping. Another possible process can be a thermally activated exciton migration from larger to smaller dots.<sup>39</sup> However, this process is unlikely because the average distance between different QDs in our samples is of the order of microns, too large to permit efficient FRET from small to large dots. At  $T \geq 170$  K, we observe a thermal escape process, where the average number of LO phonons absorbed in the process clearly increases as the dot diameter decreases from about 4 to about 6. This is consistent with the increasing energy difference between adjacent states due to the stronger confinement of smaller dots, which leads to an increase of the energy that a carrier has to absorb to jump from one state to the following one. To confirm this conclusion, a quantitative comparison between the total energy absorbed from the LO phonons in the thermal escape given by  $E_{\text{escape}} = m(E_{LO})$  and the energy difference between the excited states involved in the process is required. First of all, we remember that the thermal escape mainly involves the carrier with the smallest energy difference between consecutive confined state, which in our case is the hole, due to its higher effective mass.<sup>23</sup> Moreover, as shown in Figure 1, the two first absorption peaks are due to

**TABLE 1: Best Fit Values of the Activation Energy  $E_a$  of the Low-Temperature Quenching Process and of the Number  $m$  of LO Phonons Absorbed in the Thermal Escape<sup>a</sup>**

sample	$E_a$ (meV)	$m$	$\Delta E_{g0}$ (meV)	$E_{LO}$ (meV)	$\Delta E_{1,2}$ (meV)	$E_{\text{escape}}$ (meV)
A1	$23.5 \pm 2.0$	$5.6 \pm 1.7$	21	$20 \pm 5$	124.5	$110 \pm 30$
A2	$13.6 \pm 0.7$	$4.9 \pm 0.2$	12	$19.1 \pm 1.5$	96.5	$94 \pm 4$
A3	$15.6 \pm 1.7$	$4.0 \pm 0.3$	17	$22 \pm 4$	82.2	$92 \pm 7$

<sup>a</sup>  $\Delta E_{1,2}$  is the energy difference between the two first absorption peaks, while  $E_{\text{escape}} = m(E_{LO})$ . The values of  $E_{LO}$  and  $\Delta E_{g0}$  are also reported for clarity.

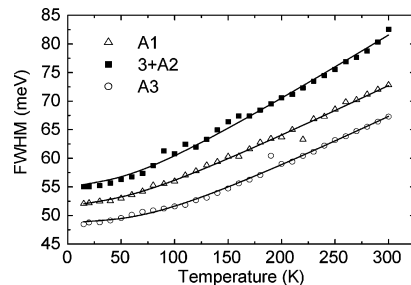


**Figure 4.** The fwhm of the PL spectra as a function of temperature (symbols) for the three samples and respective best fit curves (continuous lines). The data of the sample A2 are vertically translated by 3 meV for clarity.

**TABLE 2: Best Fit Values of  $\sigma$ ,  $\Gamma_{LO}$ , and  $E_{LO}$  for the Three Samples**

sample	$\sigma$ ( $\mu\text{eV/K}$ )	$\Gamma_{LO}$ (meV)	$E_{LO}$ (meV)
A1	$31 \pm 7$	$14 \pm 3$	$20 \pm 5$
A2	$33 \pm 6$	$18.3 \pm 0.9$	$20 \pm 1.5$
A3	$14 \pm 5$	$21 \pm 4$	$22 \pm 4$

$1S_{3/2} \rightarrow 1S_e$  and  $2S_{3/2} \rightarrow 1S_e$  transitions.<sup>17,18</sup> This allows us to estimate the energy difference between the  $1S_{3/2}$  and the  $2S_{3/2}$  hole states simply as the difference between the first two absorption peaks energies ( $\Delta E_{1,2}$  in Table 1). From the comparison of  $\Delta E_{1,2}$  with  $E_{\text{escape}} = m(E_{LO})$  (see Table 1), we observe an overall very good agreement for all the samples, suggesting that the thermal escape involves hole states.

Finally, to study the size dependence of exciton–phonon coupling, we analyzed the temperature dependence of the PL broadening obtained from the Gaussian deconvolution. The experimental values of the PL spectrum Full Width at Half-Maximum (FWHM) (see Figure 4), obtained from a Gaussian best fit of the spectra, clearly show that the FWHM increases with the temperature. As the PL broadening is partially inhomogeneous and partially homogeneous, because of exciton–phonons scattering, we fitted the experimental FWHM to the following equation:<sup>40</sup>

$$\Gamma(T) = \Gamma_{\text{inh}} + \sigma T + \Gamma_{LO}(e^{E_{LO}/k_B T} - 1)^{-1} \quad (3)$$

Here,  $\Gamma_{\text{inh}}$  is the inhomogeneous broadening, which is temperature independent, and it is due to fluctuations in size, shape, and composition of the nanocrystals,  $\sigma$  is the exciton–acoustic phonons coupling coefficient,  $\Gamma_{LO}$  represents the exciton–LO phonons coupling coefficient,  $E_{LO}$  is the LO phonon energy, and  $k_B$  is the Boltzmann constant. In all the investigated samples, the best fit curve well reproduces the experimental data for the best fit parameters reported in Table 2.

We observe that the best fit values of the exciton–acoustic phonons coupling constant  $\sigma$  are about 3 orders of magnitude

## Colloidal CdTe Quantum Dots

higher than the theoretical value estimated by Rudin et al.<sup>41</sup> (about  $0.72 \mu\text{eV}/\text{K}$ ) for bulk CdTe. This result is consistent with the theoretical prediction of a strong increase of the coupling with acoustic phonons in zero-dimensional systems.<sup>12</sup> Moreover, our results are also in qualitative agreement with the increase of the acoustic phonons coupling with the increasing two-dimensional confinement observed in CdTe quantum wells.<sup>42</sup> Despite this qualitative agreement, we observe that the  $\sigma$  value, which determines the low-temperature broadening increase, could be affected by the intrinsic-defects state transition that takes place below 170 K. On the contrary, the best fit values of the carrier-LO phonons coupling coefficient  $\Gamma_{\text{LO}}$ , obtained in a temperature range where the emission is intrinsic, is smaller than the theoretical bulk value<sup>41</sup> ( $\Gamma_{\text{LO}} = 24.5 \text{ meV}$ ) and decreases as the QDs size decreases. This result can also be ascribed to quantum confinement, and it is consistent with theoretical prediction and experimental observation.<sup>12,43,44</sup> Finally, we did not find any dependence on the quantum confinement for the LO phonon energy, as reported in literature,<sup>45</sup> but its value is within the fitting error consistent with the bulk value (21.1 meV<sup>23</sup>).

## IV. Conclusions

In conclusion, we studied the temperature and size dependence of the PL spectra in colloidal CdTe core QDs. We demonstrated that at temperatures lower than about 150–170 K a thermally activated transition between two different states separated by about 12–20 meV takes place.

We demonstrated that at higher temperature, the main nonradiative process that limits the quantum efficiency is thermal escape, induced by multiphonon absorption. The number  $m$  of phonons involved in the process is dependent on the dots size and varies from 4, in smallest dots, to about 6 for the largest ones. Finally, we have studied the size dependence of the exciton–phonons coupling. We found that it is strongly dependent on the quantum confinement. In particular, the coupling with acoustic phonons increases with respect bulk material, and the exciton–optical phonons coupling increases in larger dots.

## References and Notes

(1) Coe, S.; Woo, W. K.; Bawendi, M. G.; Bulovic, V. *Nature* **2002**, *420*, 800.

(2) Tessler, N.; Medvedev, V.; Kazes, M.; Kan, S. H.; Banin, U. *Science* **2002**, *295*, 1506.

(3) Greenham, N. C.; Peng, X.; Alivisatos, A. P. *Phys. Rev. B* **1996**, *54*, 17628.

(4) Klimov, V. I. *Science* **2003**, *28*, 214.

(5) Bruchez, M., Jr.; Moranna, M.; Gin Pand Weiss, S. *Science* **1998**, *281*, 2013.

(6) Pathak, S.; Choi, S. K.; Arnheim, N.; Thompson, M. E. *J. Am. Chem. Soc.* **2001**, *123*, 4103.

(7) Murray, C. B.; Norris, D. J.; Bawendi, M. G. *J. Am. Chem. Soc.* **1993**, *115*, 8706.

(8) Dabbousi, B. O.; Rodriguez-Viejo, J.; Mikulec, F. V.; Heine, J. R.; Mattoussi, H.; Ober, R.; Jensen, K. F.; Bawendi, M. G. *J. Phys. Chem. B* **1997**, *101*, 9463.

(9) Reiss, P.; Bleuse, J.; Pron, A. *Nano Lett.* **2002**, *2*, 781.

(10) Crooker, S. A.; Barrick, T.; Hollingsworth, J. A.; Klimov, V. I. *Appl. Phys. Lett.* **2003**, *82*, 2793.

(11) Lee, W. Z.; Shu, G. W.; Wang, J. S.; Shen, J. L.; Lin, C. A.; Chang, W. H.; Ruan, R. C.; Chou, W. C.; Lu, H. C.; Lee, Y. C. *Nanotechnology* **2005**, *16*, 1517.

(12) Valerini, D.; Creti, A.; Lomascolo, M.; Manna, L.; Cingolani, R.; Anni, M. *Phys. Rev. B* **2005**, *71*, 235409.

(13) Bawendi, M. G.; Carroll, P. J.; Wilson, W. L.; Brus, L. E. *J. Chem. Phys.* **1992**, *96*, 946.

(14) Creti, A.; Anni, M.; Zavelani Rossi, M.; Lanzani, G.; Leo, G.; Della Sala, F.; Manna, L.; Lomascolo, M. *Phys. Rev. B* **2005**, *72*, 125346.

(15) Rothenberg, E.; Kazes, M.; Shaviv, E.; Banin, U. *Nano Lett.* **2005**, *5*, 1581.

(16) Peng, Z. A.; Peng, X. G. *J. Am. Chem. Soc.* **2001**, *123*, 183.

(17) Richard, T.; Lefebvre, P.; Mathieu, H.; Allegre, J. *Phys. Rev. B* **1996**, *53*, 7287.

(18) Efros, Al. L.; Rosen, M. *Phys. Rev. B* **1998**, *58*, 7120.

(19) Kagan, C. R.; Murray, C. B.; Bawendi, M. G. *Phys. Rev. B* **1996**, *54*, 8633.

(20) Tari, D.; De Giorgi, M.; Cingolani, R.; Foti, E.; Coriasso, C. *J. Appl. Phys.* **2005**, *97*, 043705.

(21) Brusafoni, L.; Sanguinetti, S.; Grilli, E.; Guzzi, M.; Bignazzi, A.; Bogani, F.; Carraresi, L.; Colocci, M.; Bosacchi, A.; Frigeri, P.; Franchi, S. *Appl. Phys. Lett.* **1996**, *69*, 3354.

(22) Pal, U.; Herrera Pérez, J. L.; Piqueras, J.; Dieguéz, E. *Mater. Sci. Eng., B* **1996**, *42*, 297.

(23) *Landolt-Bornstein Numerical Data and Functional Relationship in Science and Technology*, Group II–VI; Hellwege, K. H.; ed.; Springer-Verlag: Berlin, Germany, 1982; Vol. 17a.

(24) The best fit is performed in a temperature range in which  $E_g(T)$  is weakly dependent on  $\beta$  and it is mainly dependent on  $\alpha$ . This prevents the extraction of accurate best fit values of  $\beta$  by leaving it free in the fitting session.

(25) Efros, Al. L.; Rosen, M.; Kuno, M.; Nirmal, M.; Norris, D. J.; Bawendi, M. *Phys. Rev. B* **1996**, *54*, 4843.

(26) Yu, Z.; Li, J.; O'Connor, D. B.; Wang, L. W.; Barbara, P. F. *J. Phys. Chem. B* **2003**, *107*, 5670.

(27) Ghanassi, M.; Schanne-Klein, M.; Hache, F.; Ekimov, A.; Ricard, D. *Appl. Phys. Lett.* **1993**, *62*, 78.

(28) Klimov, V. I.; McBranch, D. W. *Phys. Rev. B* **1997**, *55*, 13173.

(29) Gotoh, H.; Ando, H.; Takagahara, T. *J. Appl. Phys.* **1997**, *81*, 1785.

(30) The assumption of a single thermally activated process is the simplest to describe the observed exponential decrease of the PL intensity in the range 40–170 K. We observe that a similar PL temperature dependence could result also from more complicated processes, like the thermal activation of trapping in a distribution of defects at slightly different energies.

(31) Yang, W.; Lowe-Webb, R. R.; Lee, H.; Sercel, P. C. *Phys. Rev. B* **1997**, *56*, 13314.

(32) Klimov, V. I.; Bolivar, P. H.; Kurz, H. *Phys. Rev. B* **1996**, *53*, 1463.

(33) Nuss, M. C.; Zinth, W.; Kaiser, W. *Appl. Phys. Lett.* **1986**, *49*, 1717.

(34) Klimov, V. I.; McBranch, D. W.; Leatherdale, C. A.; Bawendi, M. G. *Phys. Rev. B* **1999**, *60*, 13740.

(35) De Giorgi, M.; Lingk, C.; von Plessen, G.; Feldmann, J.; De Rinaldis, S.; Passaseo, A.; De Vittorio, M.; Cingolani, R.; Lomascolo, M. *Appl. Phys. Lett.* **2001**, *79*, 3968.

(36) Wu, Yi-hong; Arai, K.; Yao, T. *Phys. Rev. B* **1996**, *53*, R10485.

(37) Wang, X.; Yu, W. W.; Zhang, J.; Aldana, J.; Peng, X.; Xiao, M. *Phys. Rev. B* **2003**, *68*, 125318.

(38) Chen, W.; Joly, A. G.; McCready, D. E. *J. Chem. Phys.* **2005**, *122*, 224708.

(39) Patané, A.; Levin, A.; Polimeni, A.; Eaves, L.; Main, P. C.; Henini, M.; Hill, G. *Phys. Rev. B* **2000**, *62*, 11084.

(40) Lee, J.; Koteles, E. S.; Vassell, M. O. *Phys. Rev. B* **1986**, *33*, 5512.

(41) Rudin, S.; Reinecke, T. L.; Segall, B. *Phys. Rev. B* **1990**, *42*, 11218.

(42) Mayer, E. J.; Pelekanos, N. T.; Kuhl, J.; Magnea, N.; Mariette, H. *Phys. Rev. B* **1995**, *51*, R17263.

(43) Gindele, F.; Hild, K.; Langbein, W.; Woggon, U. *J. Lumin.* **2000**, *87*–*89*, 381.

(44) Nomura, S.; Kobayashi, T. *Phys. Rev. B* **1992**, *45*, 1305.

(45) Trallero-Giner, C.; Debernardi, A.; Cardona, M.; Menéndez-Proupin, E.; Ekimov, A. I. *Phys. Rev. B* **1998**, *57*, 4664.